

Targeting the Latent Persistence of KSHV through Inhibition of LANA-DNA Interaction

Dissertation

Zur Erlangung des Grades des Doktors der Naturwissenschaften der
Naturwissenschaftlich-Technischen Fakultät der Universität des Saarlandes

von

M. Sc. Philine Elea Kirsch

Saarbrücken 2020

Tag des Kolloquiums: 02.07.2020

Dekan: Prof. Dr. Guido Kickelbick

Berichterstatter: Prof. Dr. Rolf W. Hartmann
Prof. Dr. Christian Ducho

Akademisches Mitglied: Dr. Josef Zapp

Vorsitz: Prof. Dr. Andreas Speicher

Die vorliegende Arbeit wurde von Januar 2016 bis Februar 2020 unter Anleitung von Herrn Dr. Martin Empting und Univ. Prof. Dr. Rolf W. Hartmann in der Fachrichtung Pharmazeutische und Medizinische Chemie der Naturwissenschaftlich-Technischen Fakultät der Universität des Saarlandes sowie am Helmholtz-Institut für Pharmazeutische Forschung Saarland (HIPS) in der Abteilung Drug Design and Optimization (DDOP) angefertigt.

Acknowledgements

Ich möchte mich ganz herzlich bei allen bedanken, die zum Gelingen dieser Arbeit beigetragen haben!

Ein ganz besonderer Dank gilt Dr. Martin Empting, der mir die Möglichkeit gegeben hat meine Promotion in diesem interessanten und vielseitigen Projekt zu bearbeiten und mir die Freiheit gegeben hat mich in diesem Projekt zu verwirklichen. Außerdem möchte ich mich für die sehr gute Betreuung und die konstruktive Unterstützung zu jeder Zeit bedanken.

Ein weiterer besonderer Dank gilt Prof. Dr. Rolf Hartmann, der mir die Möglichkeit gab, meine Promotion in seinem Arbeitskreis anfertigen zu können, für die sehr gute und sehr angenehme wissenschaftliche Begleitung und für die Übernahme des Erstgutachtens.

Bei Prof. Dr. Christian Ducho möchte ich mich herzlich für die gute wissenschaftliche Begleitung und die Übernahme des Zweitgutachtens bedanken.

Ein großer Dank gilt auch unseren Kooperationspartnern von der Medizinischen Hochschule Hannover, die wesentlich zum Gelingen dieser Arbeit beigetragen haben. Ich bedanke mich herzlich bei Prof. Dr. Thomas Schulz und Dr. Saskia Stein für die unkomplizierte, konstruktive und äußerst sympathische Zusammenarbeit und Kommunikation.

Außerdem möchte ich Dr. Joseph Zapp von der Universität des Saarlandes danken, der stets sehr hilfsbereit war und uns konstruktive Unterstützung bei all unseren Problemen mit dem NMR und den STD-NMR Messungen gegeben hat.

Ganz besonders möchte mich bei meinen engsten Kollegen bedanken, die den Laboralltag abwechslungsreich, lustig und zu einer unvergesslichen Zeit gemacht haben. Dies gilt vor allem für Christian Schütz, Valentin Jakob, Alwin Hartman, Andreas Kany, Isabell Walter und Christina Kosch. Außerdem möchte ich der ganzen Arbeitsgruppe für das gute und freundliche Arbeitsklima und die gute Zusammenarbeit im Labor bedanken.

Ein ganz großes Dankeschön gilt Christian Schütz dem besten Laborpartner den man sich wünschen kann. Mit ihm wurden vor allem auch die langen Labortage nie langweilig. Er hat mich in jeder Lebenslage unterstützt, sich mit mir gefreut und mit mir geweint.

Außerdem möchte ich mich sehr bei meinen HIWI-Studentinnen Aylin Berwanger und Julia Rinkes bedanken, die mich bei der Synthese neuer Derivate unterstützt haben und immer für gute und angenehme Stimmung im Labor gesorgt haben.

Ein ganz wichtiger Dank gilt meiner Familie und meinen Freunden, die mich privat immer unterstützt haben und immer für mich da sind und um die wertvolle Zeit außerhalb der Arbeit.

Insbesondere möchte mich bei meinen Eltern bedanken, Anke und Hans-Jürgen Kirsch, ohne die ich es niemals soweit geschafft hätte und die mich immer unterstützen in all meinen guten und schlechten Entscheidungen. Außerdem möchte ich mich auch bei meinem Freund Sebastian Koch bedanken, der immer für die notwendige Ablenkung und Unterstützung neben der Arbeit gesorgt hat.

Summary

The Kaposi's sarcoma herpesvirus (KSHV/HHV-8), is a human herpesvirus. This virus is the etiological agent of Kaposi's Sarcoma and is known to be involved in the pathogenesis of multicentric Castleman's disease and pleural effusion lymphomas. Like all herpesviruses, KSHV establishes a lifelong latent infection in its host organism. Usually, KSHV is not pathogenic for healthy individuals, but for immunosuppressed patients suffering e.g. from HIV or transplant recipients, it causes significant morbidity and mortality. To date, the treatments are still limited and no specific drugs which interfere with the life cycle of KSHV are available. This means, KSHV is still incurable. The key player for the latent persistence is the latency-associated nuclear antigen (LANA). By tethering the viral genome to the host nucleosomes, LANA ensures the persistence of the virus throughout the lifetime of its host. The inhibition of the interaction between LANA and the viral genome should prevent the latent persistence of KSHV in the infected cells.

In this thesis, the discovery of first inhibitors, which were able to inhibit the interaction between LANA and the viral DNA is described. Two different screening approaches were applied for the identification of LANA-DNA inhibitors. A fragment-based screening lead to a first hit. Fragment-growing strategies were used to grow and optimize this hit regarding functional activity. The elucidation of structure activity relationships and further characterizations resulted in a validated and very promising LANA-DNA interaction inhibitor. Further LANA-DNA inhibitors were identified and qualified from a fluorescence-polarization-based screening of our in-house library. The inhibitors were able to disturb the LANA-DNA interaction, although they were binding at different binding sites. In a follow-up hit-to-lead medicinal chemistry optimization study performed on the first hit, further SAR insights and a significant boost of efficiency against wild-type LANA was achieved.

Zusammenfassung

Das Kaposi's Sarkoma Herpesvirus (KSHV/HHV-8) ist ein humanes Herpesvirus. Dieses Virus ist der Erreger des Kaposi Sarkoms und ist bekanntermaßen an der Pathogenese der multizentrischen Morbus Castleman Krankheit und Pleuraerguss-Lymphomen beteiligt. Wie alle Herpesviren verursacht KSHV eine lebenslange latente Infektion im Wirtsorganismus. Normalerweise ist KSHV für gesunde Menschen nicht pathogen, aber bei immunsupprimierten Patienten, die zum Beispiel an HIV leiden oder Transplantatempfängern sind, verursacht es eine signifikante Morbidität und Mortalität. Bis heute sind die Therapien noch begrenzt und es sind keine spezifischen Medikamente verfügbar, die den Lebenszyklus von KSHV beeinträchtigen. Das bedeutet, KSHV ist immer noch unheilbar. Der Hauptfaktor für die latente Persistenz ist das Latenz-assoziierte Kern Antigen (LANA). Durch die Bindung des Virusgenoms an die Nukleosomen des Wirts stellt LANA die Persistenz des Virus während der gesamten Lebensdauer des Wirts sicher. Die Hemmung der Interaktion zwischen LANA und dem Virusgenom sollte die latente Persistenz von KSHV in den infizierten Zellen verhindern.

In dieser Arbeit wird die Entdeckung erster Inhibitoren beschrieben, die die Interaktion zwischen LANA und der viralen DNA hemmen können. Für die erste Identifizierung von LANA-DNA-Inhibitoren wurden zwei verschiedene Screening-Ansätze angewendet. Ein Fragment basiertes Screening führte zu einem ersten Hit. Fragment Wachstumsstrategien wurden verwendet, um diesen Hit in Bezug auf funktionelle Aktivität zu vergrößern und zu optimieren. Die Aufklärung von Strukturaktivitätsbeziehungen und weitere Charakterisierungen führten zu einem validierten und vielversprechenden LANA-DNA-Interaktionsinhibitor. Weitere LANA-DNA-Inhibitoren wurden bei einem funktionellen Screening unserer in-house Library identifiziert und qualifiziert. Die Inhibitoren konnten die LANA-DNA-Wechselwirkung inhibieren, obwohl sie an unterschiedlichen Bindungsstellen binden. In einer weiterführenden Studie zur Optimierung des zuerst identifizierten LANA Inhibitors, wurden weitere Struktur Aktivität Beziehungserkenntnisse und eine signifikant höhere Effizienz der Inhibitoren gegen das wild-typ LANA generiert.

Publications Included in this Thesis

Publication 1: Philine Kirsch, Alwin M. Hartman, Anna K. H. Hirsch and Martin Empting; Concepts and Core Principles of Fragment-based Drug Design; **2019**, *Molecules*, *24*, 4309, 0-22.

Publication 2: Philine Kirsch, Valentin Jakob, Kevin Oberhausen, Saskia C. Stein, Ivano Cucarro, Thomas F. Schulz and Martin Empting; Fragment-Based Discovery of a Qualified Hit Targeting the Latency-Associated Nuclear Antigen of the Oncogenic Kaposi's Sarcoma-Associated Herpesvirus/Human Herpesvirus 8; **2019**, *J. Med. Chem*, *62*, 3924-3939.

Publication 3: Philine Kirsch, Valentin Jakob, Walid A. M. Elgaher, Christine Walt, Kevin Oberhausen, Thomas F. Schulz and Martin Empting; Discovery of Novel Latency-Associated Nuclear Antigen Inhibitors as Antiviral Agents Against Kaposi's Sarcoma-Associated Herpesvirus; **2020**, *ACS Chemical biology*.

Publication 4: Philine Kirsch, Saskia C. Stein, Aylin Berwanger, Julia Rinkes, Valentin Jakob, Thomas F. Schulz and Martin Empting; Hit-to-Lead Optimization of a Latency-associated Nuclear Antigen Inhibitor against Kaposi's Sarcoma-associated Herpesvirus Infections; submitted on 11 February **2020** to *European Journal of Medicinal Chemistry*.

Contribution Report

Publication 1:

- Wrote parts of the manuscript (Review)

Publication 2:

- Designed and synthesized all target compounds
- Functional evaluation of all target compounds using FP-based competition assay
- Performed MST and STD-NMR measurements for compound validation
- Wrote main parts of the manuscript and experimental section, created most of the figures

Publication 3:

- Selected hit compounds observed from screening for further investigations
- Was involved in SPR measurements
- Performed STD-NMR competition experiments
- Wrote main parts of the manuscript and experimental section, created most of the figures

Publication 4:

- Designed and synthesized target compounds
- Functional evaluation of all target compounds using FP-based competition assay
- Performed STD-NMR measurements for compound validation
- Wrote main parts of the manuscript and experimental section, created most of the figures

Abbreviations

AcOH	acetic acid
Ac ₂ O	acetic anhydride
AIDS	Acquired Immune Deficiency Syndrome
AIDS-KS	Acquired Immune Deficiency Syndrome-related Kaposi's sarcoma
aq.	aqueous
CTD	C-terminal domain
DCM	dichloromethane
DMSO	dimethylsulfoxide
DNA	deoxyribonucleic acid
DBD	DNA binding domain
DMF	dimethylformamid
DIPEA	Diisopropylethylamin
DSF	differential scanning fluorimetry
EBV	Epstein-Barr virus
EBNA1	Epstein-Barr nuclear antigen 1
EDC	1-ethyl-3-(3-dimethylaminopropyl) carbodiimide hydrochloride
EE/EtOAc	ethyl acetate
EtOH	ethanol
EMSA	electrophoretic mobility shift assay
FA	formic acid
FP	fluorescence polarization
HPLC	high pressure liquid chromatography
HHV-8	human herpesvirus-8
KS	Kaposi Sarcoma
KSHV	Kaposi's Sarcoma-associated Herpesvirus
LANA	latency associated nuclear antigen
LBS	LANA binding site
LE	ligand efficiency
LCMS	liquid chromatography mass spectrometer
MeCN	acetonitrile
MeOH	methanol

MST	microscale thermophoresis
NHS	<i>N</i> -hydroxy succinimide
PBS	phosphate buffered saline
PE	petroleum benzene
prep.	preparative
SAR	structure activity relationship
sat.	saturated
STD NMR	saturation transfer difference Nuclear Magnetic Resonance
SPR	surface plasmon resonance
TBHP	<i>tert</i> -butyl hydroperoxide
<i>tert</i> -BuOH	<i>tert</i> -butanol
TMSN ₃	trimethylsilyl azide
TSA	thermal shift assay
TR	terminal repeat

Table of Contents

Acknowledgements	IV
Summary	VI
Zusammenfassung	VII
Publications Included in this Thesis	VIII
Contribution Report.....	IX
Abbreviations	X
1 Introduction	1
1.1 Human Herpesviridae	1
1.2 Kaposi Sarcoma and Kaposi's Sarcoma-associated Diseases.....	1
1.3 Kaposi's Sarcoma-associated Herpesvirus.....	2
1.4 The Latency-associated Nuclear Antigen.....	3
1.5 Oligomerization-deficient KSHV LANA Mutant	5
1.6 Copper-Catalyzed Alkyne-Azide Cycloaddition (CuAAC).....	6
1.7 Fragment-Based Drug Design in Drug Discovery.....	7
2 Aim and Scope	30
3 Results	31
3.1 Chapter A: Fragment-Based Discovery of first KSHV-LANA Inhibitors	31
3.2 Chapter B: Discovery of KSHV-LANA Inhibitors via In-House Library Screening	48
3.3 Chapter C: Hit-to-Lead Optimization of a LANA Inhibitor against KSHV Infections	57
4 Final Discussion.....	88
4.1 Identification of first LANA-DNA Interaction Inhibitors.....	88
4.1.1 Fragment-based Drug Design	88
4.1.2 In-House Library Screening.....	91
4.2 Hit-to-Lead Optimization a LANA Inhibitor	93
5 Conclusion and Outlook	96
6 References	98
7 Appendix.....	102
7.1 Supporting Information Chapter A.....	102
7.2 Supporting Information Chapter B	175
7.3 Supporting Information Chapter C.....	197

1 Introduction

1.1 Human Herpesviridae

The human herpesvirus family consists of eight members and commonly infects all humans. Almost the whole adult population is infected with one or more herpesviruses.^{1,2} The known human herpesviruses are: Herpes Simplex virus type 1 and 2 (HSV-1 and -2/HHV-1 and -2), Varicella-Zoster virus (VZV/HHV-3), Epstein-Barr virus (EBV/HHV-4), Cytomegalovirus (CMV/HHV-5), Roseolovirus (HHV-6 and -7), and Kaposi's Sarcoma-associated herpesvirus (KSHV/HHV-8).^{1,3} Each virus has special characteristics and they can be divided into three different classes. This classification mainly refers to genome characteristics such as size, genetic organization and replication strategies.^{4,5} HSV-1, HSV-2 and VZV belong to the subfamily alpha herpesviruses, CMV, HHV-6 and HHV-7 to beta herpesviruses and EBV and KSHV to gamma herpesviruses.^{6,7} All of these herpesviruses establish a latent infection and persist lifelong in the host organism after a primary infection.⁸ In healthy immunocompetent individuals, these herpesviruses usually do not cause severe diseases. Many people are carrying them and never have any symptoms.^{1,4} Often, the primary infection with a virus causes a short outbreak and different symptoms like blisters, pain, fever and enlarged lymph nodes can occur. Over time, the viruses establish a latent infection and in some cases recurrent infection symptoms occur. However, for immunodeficient as well as very young and very old individuals, herpesviruses can cause several diseases with differing severities.⁹ Especially for immunosuppressed patients, these herpesvirus infections often cause mortality and morbidity. Importantly, until now, there are no specific antiviral drugs for the treatment or for the prevention of herpes viral infections, which interfere with their lifecycle, available. This means that these infections are still not curable. There are some antiviral drugs on the market, e. g., Aciclovir, Valaciclovir or Foscarnet, which are used for the treatment of different symptoms caused by herpesviral infections, but these medications cannot clear the host of the virus.^{10,11}

1.2 Kaposi Sarcoma and Kaposi's Sarcoma-associated Diseases

Kaposi Sarcoma (KS) was first reported by Moritz K. Kaposi in 1872. He described the KS lesions as an idiopathic multiple pigmented sarcoma of the skin (Figure 1A).¹² At that time the causative agent of KS



Figure 1: Different clinical manifestations of AIDS-related KS (a, b, d and e) and classic KS (c). (adapted from E. Cesarman *et al.*, 2019)¹⁶

was unknown, however, it was recognized, that the development of KS is dependent on several cofactors. It was also observed that KS is a very common neoplasm, which occurs in acquired immune deficiency syndrome (AIDS) patients.^{13,14} In 1994, the human herpesvirus-8 (HHV-8), later termed as Kaposi's Sarcoma-associated Herpesvirus (KSHV), was first characterized as previously unknown and unique DNA sequences in Kaposi Sarcoma (KS) tissue.¹⁴ In this context, KSHV was

identified as the etiological agent of KS. An increased development of KSHV-associated disease is frequently seen in patients suffering from immunodeficiency, particularly patients with HIV infection or transplant recipients.¹⁵ Additionally, KSHV was also found to be involved in the pathogenesis of two other diseases, Multicentric Castleman's disease (MCD) and primary effusion lymphoma (PEL).^{16,17} The World Health Organization classified KSHV as a carcinogenic agent Group I in humans.^{18,19} However, for healthy individuals KSHV is usually not pathogenic. The seroprevalence of KSHV is dependent on geographical location. The KSHV prevalence in sub-Saharan Africa reaches over 40% and in some regions up to 95%. In contrast, in the northern part of Europe, in Asia, and in the most parts of North America the prevalence is below 10%, while in the Mediterranean regions it is around 20–30%. The reasons for the geographical variation are not fully understood yet, but it can be assumed that environmental factors and co-infections play a role.²⁰ The transmission of KSHV most likely takes place via saliva and other body secretions.²¹ As mentioned in the beginning, KSHV and KSHV-associated diseases are difficult to treat particularly in countries with poor medical care.

1.3 Kaposi's Sarcoma-associated Herpesvirus

KSHV is one of the nine known human herpesviruses and is also named Human Herpesvirus-8 (HHV-8). This virus belongs to the class of γ_2 -herpesviruses (Rhadinovirus) and infects mainly B-lymphocytes and other cell types like endothelial cells and primary mesenchymal stem cells.²² The virus episome exists

as a double-stranded linear DNA sequence with a coding region of 140 kb.^{21,23} Inside the host cell, the KSHV genome circulates at the 801-bp-long GC-rich terminal repeat region (TR).^{24,25} The genome encodes approximately 90 open reading frames (ORFs), 17 micro-RNAs and 14 cellular gene homologues.^{21,26} One important characteristic of KSHV is the “silent” persistence in infected cells, without being noticed by the immune system of the host organism.²⁷ During the latent phase, only a small set of proteins are important for the persistence and were expressed.^{28,29} These transcripts originate from the same genomic region referred to as the latent gene cluster (Figure 2). This includes the latency-associated nuclear antigen (LANA/ORF73), v-Cyclin (ORF72), v-FLIP (ORF71), viral microRNAs and kaposins (K12).^{21,30,31}

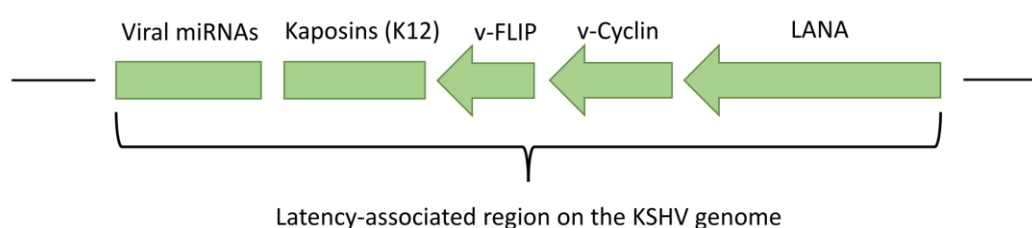


Figure 2: The latent gene cluster of KSHV.

All these transcripts are responsible for host cell survival and growth, they control proliferative and inflammatory signals in the host cells as well as the latent viral genome replication. Furthermore, they are involved in transcriptional regulation and in stable episome segregation during cell mitosis.^{30,32}

1.4 The Latency-associated Nuclear Antigen

LANA is the main and most prominent latent viral protein that is expressed in all known forms of KSHV-associated malignancies.^{33,34} This protein is expressed from the open reading frame 73 (ORF73), which is located in the latency-associated cluster gene region on the KSHV genome (Figure 2). LANA has a molecular weight of 222–234 kDa and can interact with different cellular and other viral proteins.^{35,36} This multifunctional protein is actively involved in viral episome maintenance and transcriptional regulation associated with viral oncogenes.^{34,28} During latency, LANA was found to be localized in the nucleus forming large aggregate structures, also called LANA speckles.³⁴ The most important function of LANA is a successful transfer of the viral episome into the dividing daughter cells to ensure the persistence of the virus in the host organism.^{36,37} LANA has the ability to simultaneously bind the viral episome at the TR region with its C-terminal and host nucleosomes with its N-terminal domain.^{38,39}

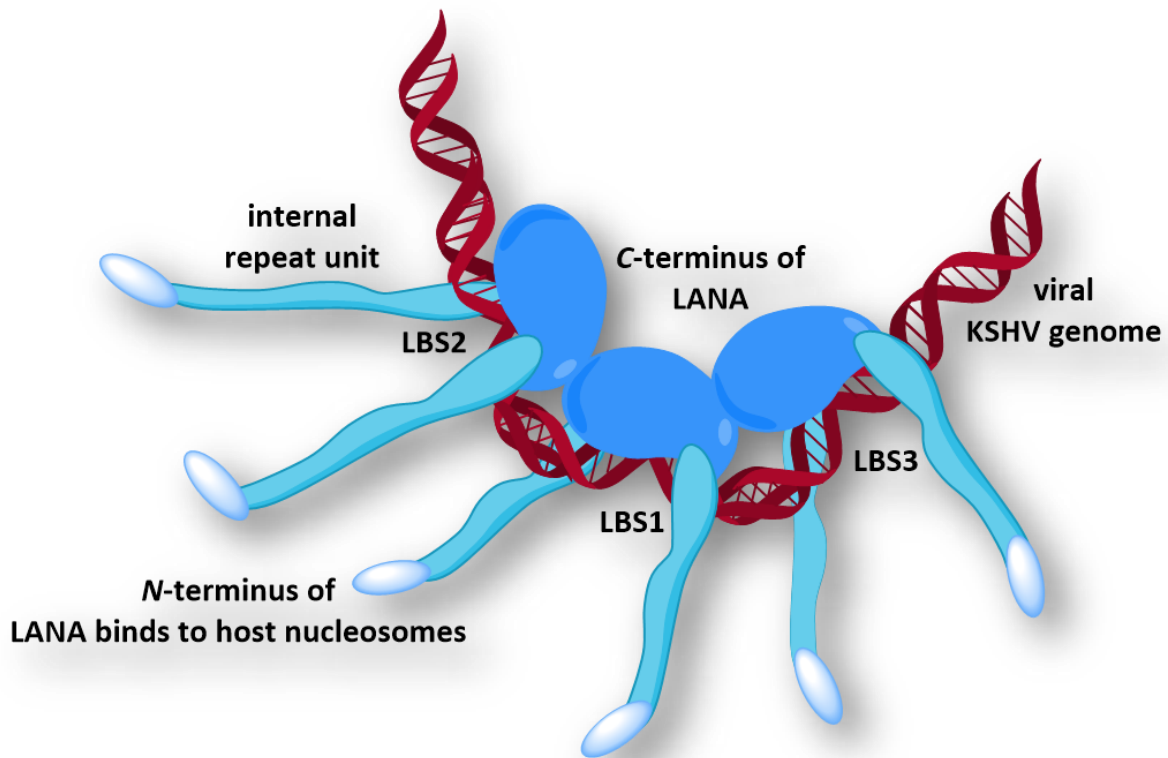


Figure 3: Schematic illustration of KSHV LANA interaction with the viral KSHV genome. C-terminus of three LANA homo dimers bound to the LANA binding sites, LBS1, LBS2 and LBS3 on the viral genome. N-terminus and C-terminus of LANA are connected via a large internal repeat unit and the N-terminus binds to the host nucleosomes.

N-terminus and C-terminus are connected by a large internal repeat unit, which is only poorly structured. The C-terminal domain is highly ordered and binds in a sequence specific manner to the TR region.⁴⁰ Additionally, through an oligomerization interface, LANA binds cooperatively to the viral DNA and forms higher-order oligomers.⁴¹ The TR region has a length of 78 bp and contains three LANA binding sites (LBS). These LBS are named LBS1, LBS2 and LBS3 (Figure 3). Each LBS consists of 20 bp. They show different binding affinities to LANA, whereby LBS1, is placed in the center between the other two LANA binding sites and has the highest affinity. LBS2 and LBS3 are arranged to either side and show a hundred fold lower affinity to LANA compared to LBS1.⁴⁰

LANA shows structural and functional homologies to related viral proteins like the Epstein-Barr nuclear antigen 1 (EBNA1) from Epstein-Barr virus (EBV) and the E2 protein from human papillomavirus (HPV). These viral proteins are also sequence-specific DNA binding proteins and have similar functions in the infected host cells like LANA.^{42,43}

1.5 Oligomerization-deficient KSHV LANA Mutant

The crystal structure of the C-terminal binding domain of KSHV LANA without its target DNA has been described by different groups.^{44,45} However, crystallization of the wild-type (wt) LANA C-terminal domain (CTD) in complex with DNA was not successful. The interaction between wt LANA CTD and DNA results in a quantitative precipitation of both components.⁴⁶ LANA CTD forms a homodimeric structure in solution and has a highly basic surface. Additionally, the protein consists of a mainly cationic DNA binding interface, which binds the viral DNA in a sequence-specific manner, and two additional positively charged regions on the surface: a so-called lysine patch and an arginine patch. Furthermore, wild-type LANA CTD has the ability to form higher-order homo oligomers by the interaction of a hydrophobic patch.

These properties influence the solubility of LANA CTD in presence of DNA and are responsible for the low solubility. To increase the solubility of the C-terminus of LANA, different point mutations were inserted into the LANA wild-type CTD sequence (Figure 4).⁴⁶

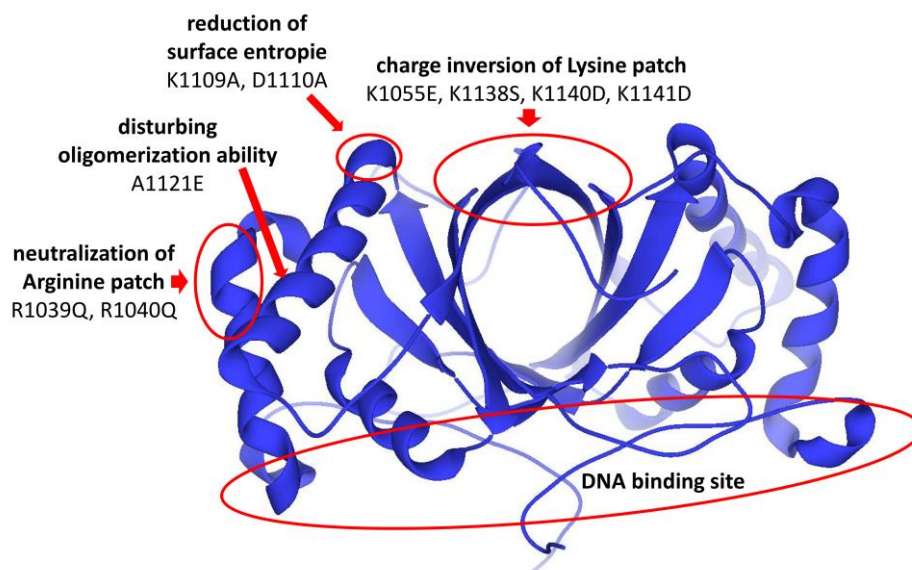


Figure 4: Structure of designed oligomerization-deficient LANA mutant. The scheme was modeled using coordinates of PDB entry 4uzb.

The arginine patch was neutralized by two mutations, R1039Q and R1040Q, and the lysine patch was charged inverted by K1055E, K1138S, K1149D and K1141D. Additionally, a single point mutation A1121E was included to disturb the ability to oligomerize and a lysine and an aspartic acid were substituted, K1109A and D1110A, to reduce the surface entropy. Since, particularly, the LANA-DNA interaction is of interest, these mutations were not located at the DNA binding region (Figure 4).^{46,40}

Using this multiple point-mutated oligomerization-deficient LANA DNA binding domain (DBD) a co-crystal structure with its target DNA LBS1 was solved by Hellert *et al.*⁴⁰ In this protein-DNA complex, homodimeric LANA retains its symmetry, whereas the DNA shows significant asymmetry.⁴⁰ In contrast to wild-type LANA, the oligomerization-deficient LANA DBD mutant binds to each LBS independently, without forming higher order oligomers or cooperative binding.⁴⁰

1.6 Copper-Catalyzed Alkyne-Azide Cycloaddition (CuAAC)

The copper-catalyzed alkyne-azide cycloaddition (CuAAC), also named click reaction, was independently discovered by the group of K. Barry Sharpless and the group of Morten Meldal in 2002.^{47,48} Since then, a very high number of articles has been published in different fields of organic chemistry and biomolecular chemistry using this technique.⁴⁹ In general, an alkyne and an azide react in a copper(I)-catalyzed 1,3-dipolar cycloaddition to a strongly stabilized disubstituted 1,2,3-triazole. For organic synthesis, click chemistry has clear advantages, the reaction conditions are very simple, a wide range of solvents can be used and the reaction is insensitive in presence of oxygen and water. Furthermore, other functional groups in the reactants are accepted and do not interfere with the chemical reaction. For click reactions a high diversity of building blocks are commercially available and ready for use. The underlying reaction mechanism of a CuAAC reaction is depicted in Figure 5.⁵⁰ The key step is the formation of the copper(I) acetylide (blue) intermediate, followed by azide (red) coordination with a second copper(I) and alkylation of the nitrogen. This regioselective mechanism finally leads to a 1,4-disubstituted 1,2,3-triazole product.

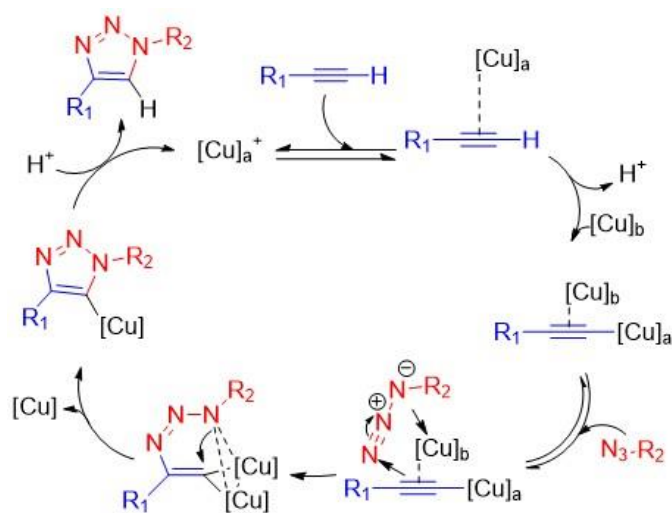


Figure 5: Reaction mechanism of CuAAC – “click” reaction.

In the context of drug development, click chemistry is a newer approach for the synthesis of drug like compounds and offers a lot of advantages in drug design.⁵¹ For medicinal chemistry optimization approaches it is an important toolbox and accelerates the drug discovery process. Furthermore, this method is very efficient in creating compound libraries using combinatorial chemistry and increases high throughput synthesis as well as improves quality and diversity of compound libraries. Moreover, a number of triazole scaffolds are found in biologically active compounds with antiviral and antibacterial activities.⁵² In conclusion click chemistry is a nice tool for the development of new drug candidates.

1.7 Fragment-Based Drug Design in Drug Discovery

Title:

Concepts and Core Principles of Fragment-based Drug Design - Review

Authors:

Philine Kirsch, Alwin M. Hartman, Anna K. H. Hirsch and Martin Empting

Bibliographic Data:

Molecules,

Volume 24, 4309, Pages 0 - 22,

November 27, **2019**,

Doi: 10.3390/molecules24234309

Review

Concepts and Core Principles of Fragment-Based Drug Design

Philine Kirsch ^{1,2,3}, Alwin M. Hartman ^{1,2,4} , Anna K. H. Hirsch ^{1,2,4} and Martin Empting ^{1,2,3,*}

¹ Helmholtz-Institute for Pharmaceutical Research Saarland (HIPS)-Helmholtz Centre for Infection Research (HZI), Department of Drug Design and Optimization (DDOP), Campus E8.1, 66123 Saarbrücken, Germany; Philine.Kirsch@helmholtz-hzi.de (P.K.); Alwin.Hartman@helmholtz-hzi.de (A.M.H.); Anna.Hirsch@helmholtz-hzi.de (A.K.H.H.)

² Department of Pharmacy, Saarland University, Campus E8.1, 66123 Saarbrücken, Germany

³ German Centre for Infection Research (DZIF), Partner Site Hannover-Braunschweig, 66123 Saarbrücken, Germany

⁴ Stratingh Institute for Chemistry, University of Groningen, Nijenborgh 7, 9747 AG Groningen, The Netherlands

* Correspondence: Martin.Empting@helmholtz-hzi.de; Tel.: +49-681-988-062-031

Academic Editor: Brian J. Stockman

Received: 28 October 2019; Accepted: 20 November 2019; Published: 26 November 2019



Abstract: In this review, a general introduction to fragment-based drug design and the underlying concepts is given. General considerations and methodologies ranging from library selection/construction over biophysical screening and evaluation methods to in-depth hit qualification and subsequent optimization strategies are discussed. These principles can be generally applied to most classes of drug targets. The examples given for fragment growing, merging, and linking strategies at the end of the review are set in the fields of enzyme-inhibitor design and macromolecule–macromolecule interaction inhibition. Building upon the foundation of fragment-based drug discovery (FBDD) and its methodologies, we also highlight a few new trends in FBDD.

Keywords: fragment-based drug design; biophysical screening; rule-of-three; ligand efficiency; fragment optimization

1. Introduction

Fragment-based drug discovery (FBDD) has become of increasing importance and interest in the past decades, especially in academia [1]. FBDD uses the advantages of biophysical and biochemical methods for the detection of very small molecules or so-called “fragments” binding to a specific target. If selected by thorough evaluation, fragment hits provide fascinating and facile starting points for the generation of drug leads. Initial identification can be achieved by the application of an array of different biophysical methods, which we discuss in the main part of our review [2]. Typically, FBDD starts with a screening of a small library of low molecular weight compounds for binding to a particular target. The key advantage of fragments is their low degree of complexity. Actually, these scaffolds should hit a sweet spot, which enables them to still be big enough to undergo a few directed attractive interactions with the protein of interest so that biophysical detection of target binding is possible. On the other hand, they should retain a sufficiently small size to limit the danger of unfavourable interactions, such as steric clashes [3]. Hence, fragments that are identified usually represent ideal binding motifs as desirable starting points for further optimization. The initial fragment hits generally have a weak binding affinity to their target, usually in a μM – mM range [4]. This can be explained by the fact that fragments possess fewer heavy atoms able to form multiple attractive interactions with the surface of

the protein in comparison to larger molecules [5]. Additionally, fragments are small enough for binding to regions, which are often hard to target; for example; allosteric sites or essential small binding pockets termed hot spots, which are often central in protein-protein interactions. Enhancing the potency of the fragments after hit identification can be achieved by fragment linking, merging or growing strategies, which are key approaches for fragment-based drug design. The benefits of FBDD compared to the traditional high-throughput screening (HTS) have been well documented, rendering the former as a valuable alternative method in drug discovery. The main differences between FBDD and HTS are the specific compositions and the sizes of the libraries, and the assay methods used for hit identification. Fragment-based biophysical screening techniques require a high degree of sensitivity in order to detect weak binders, whereas HTS assays need to be more specific to exclude false positives [6]. The ligand efficiencies of small ligands are usually higher than for larger ligands, and generation of lead compounds starting from fragment hits is primed to result in improved physicochemical properties [7].

2. Library Construction, Preselection, and General Considerations

2.1. General Principles for Library Design

Fragment-based drug discovery usually starts with screening of a relatively small compound library comprised of compounds with low molecular weights, up to 300 Da, called fragments [8]. The library compounds should be highly structurally diverse so that 500–1000 congeners are sufficient for sampling a large structural space. Typically, fragments have fewer than 20 heavy atoms and low molecular complexity [8,9]. In a fragment-based approach, the throughput compared to HTS is rather low, which is why, the selection and construction of the compound library should be carefully considered to generate high-quality hits. Additionally, it is essential to take the purpose of a library into account and deliberately select those dedicated to specific target classes; for instance, using a focused library for matrix-metalloproteinases (MMPs). To assemble a project-focused fragment library with a high chemical and structural diversity, there are some criteria which are important to consider. The outcome of an FBDD project is directly influenced by the composition of the library being applied [10]. Firstly, commercially available fragments and fragment libraries should be analysed. It is important to use a library that meets some primary criteria depending on the profile of the respective target [11]. Usually, commercially available fragment libraries have been selected based on chemical and size diversity, and different, well-balanced properties to cover most of the important features. The overall diversity of the library can also be improved by using a pharmacophore-based selection. Secondly, a set of natural products or natural-product-inspired fragments are often useful and could be included [12]. Additionally, for future plans it is important to identify a series of non-commercially available fragments, which came from synthetic chemistry efforts; for example, from an in-house library or collaborating groups. Such scaffolds can provide a basis for future medicinal chemistry optimization strategies [13,14].

However, it must be noted that since these fragments are small, they may bind multiple targets, rendering them less sensitive to target classes. Selectivity can be generated in the course of fragment optimization [15]. Fragments should ideally hit the sweet spot between low molecular weight and still being big enough to realize specific interactions to a target [9]. Usually, fragments are more hydrophilic than compounds found in HTS libraries. Hence, the likeliness of specific hydrogen bonding is increased, resulting in favorable enthalpy-driven binding [16]. The small size of the compounds usually provides a suitable starting point and ample opportunities for a medicinal chemist to embark on optimization efforts facilitating the generation of drug-like molecules.

2.2. The Rule of Three

Typically, fragments obey the rule-of-three (RO3), requiring the following properties [5,17]:

The molecular weight is ≤ 300 Da;

The number of hydrogen-bond donors ≤ 3 ;

Number of hydrogen-bond acceptors ≤ 3 ;
The logP is ≤ 3 .

Furthermore, a number of rotatable bonds (NROT) ≤ 3 and a polar surface area (PSA) ≤ 60 can be beneficial [18]. The rule-of-three is closely related to the prominent Lipinski's rule of five (RO5), which makes use of the same molecular descriptors but using a less restricted value of five as the cutoff (molecular weight ≤ 500 Da, number of hydrogen bond donors ≤ 5 , number of hydrogen bond acceptors ≤ 10 , logP ≤ 5). Importantly, the latter was derived to provide a predictor for the oral bioavailability of a drug candidate at hand, while the former is used to evaluate fragments regarding their suitability to be optimized into RO5-obeying drug candidates. RO3 as well as RO5, should be considered as rough guidelines in drug design for achieving orally bioavailable compounds. Importantly, it has to be noted that eventual drugs and clinical candidates can still have good bioavailability, whilst violating the Lipinski rules [19]. In line with this notion, library design trends that differ significantly to that suggested by the RO3 are being more frequently applied, as was reported by Pickett and coworkers [20].

2.3. Application of Electrophilic Fragments

In 2016, Backus et al. have described the use of a chemical proteomic method in order to perform fragment-based ligand discovery in native biological systems [21]. The authors report on the quantitative analysis of cysteine-reactive, small-molecule fragments that were screened against human proteomes and cells. Lysate as well as intact cells were treated with DMSO or an electrophilic fragment in a first step. In a second step, a cysteine-reactive probe containing an alkyne functional group was attached through copper-mediated, azide-alkyne cycloaddition with an azide-biotin tag. It was found that the druggability of the human proteome is larger than previously known, by expanding the search to proteins which were not known to interact with small molecules. More importantly, the applicability of reactive electrophilic fragments for the identification of covalent target binders has been demonstrated in further studies [22].

3. Fragment Hit Identification

The main challenge is to detect and select those fragments which are specifically binding to the target of interest. There are some tasks necessary for a successful FBDD campaign, such as carefully selecting the fragment library, applying several orthogonal methods to confirm that the fragment is binding to the target, and characterizing of the fragment's binding mode. In this regard, orthogonal screening methods refer to, e.g., biophysical or biochemical techniques, which interrogate the ligand-target binding but rely on different measurement principles. This enables identification of the most promising fragment, which will be used for the generation of a lead compound [3]. Starting a fragment-screening campaign requires a robust screening cascade consisting of different biophysical binding assays to detect and confirm fragment binding [23]. Because of the low affinity of fragments, usually, high concentrations up to 1 or 2 mM are used for the primary selection. Due to the fact, that in a fragment screening the rate of non-specific binding and detection of false positives is particularly high, at least one orthogonal secondary screening method is required for hit confirmation [3]. After the primary screen with direct binding techniques, usually, a number of fragment hits have been identified as target binders. Afterwards, qualified hits can be optimized by various medicinal chemistry approaches and the new derivatives can be evaluated with the previously used binding techniques [24]. Compounds with a ligand efficiency (LE, *vide infra*) of 0.3 are considered good enough to be optimized to a drug that obeys the Lipinski rules for oral bioavailability [25]. Small fragments having such an LE value might not be detectable by all detection methods which are usually used for FBDD. Therefore, the usage of different and orthogonal methods as well as high testing concentrations of the fragments (μM – mM) are required. For this reason, fluorescence-based competition assays or cell-based assays are usually not suitable for a fragment screening. Such functional assays are used after a successful hit identification to guide hit qualification

and optimization. In the following sections, we describe different binding-affinity assays which are used as key technologies for initial hit identification [26,27]. Every technique has its advantages and disadvantages, which are discussed accordingly.

3.1. Virtual Screening and Pan-Assay Interference Compounds Filters

As a prescreen, virtual screening (VS), a computer-based method for predicting binding compounds from very large compound libraries to a target protein, can be used. The VS approach allows one to reduce the number of compounds to-be-tested from up to ten million conceivable scaffolds down to a moderate number around one thousand. Virtual hits can be directly tested in different biophysical assays or used to inspire the design of a focused library. Because of the increased accuracy of the computationally programs, virtual screening methods have become more common in FBDD [20]. Several recent reviews cover this topic in detail [28–30]. Usually, the VS procedure is designed in a project-specific manner to account for the information available on the target and/or already-known ligands. Often-used approaches involve purely ligand-based pharmacophore modelling and structure-based (target-focused) screenings [31]. Nevertheless, given the considerably smaller size of fragment libraries, VS is usually not required.

Additionally the ligand-based pharmacophore approach, which avoids the need for the macromolecule target structure, has its utility. In this case, a small library of structurally diverse compounds, which are known to interact to a specific target are used to calculate and extract the essential molecular features and functional groups that are important for binding [32,33]. This, of course, requires a significant amount of knowledge about target-interacting compounds to inform the VS campaign, which is not always available.

The target-based approach, also called structure-based virtual screening, starts with docking a defined ligand into a protein target associated with a prediction of the optimal binding mode. Hence, these methods can give an idea how ligands and fragments could bind to a target protein. The advantage of this approach is, that only the X-ray structure of the target protein, e.g., holoenzyme, is needed to conduct the *in silico* experiment. It should be mentioned, however, that these experiments are hypothetical and have to be followed up with experimental testing [34].

Finally, machine and deep learning principles can be incorporated into the ligand—as can receptor-based VS pipelines, especially when dealing with large data sets [35]. Varieties of these methods have been applied, and the underlying algorithms and concepts range from classical descriptor-driven approaches, e.g., linear quantitative structure-activity relationships (QSAR), to complex, bioinformatics-heavy approaches [35,36]. In the future, it will be interesting to see whether these techniques will hold up to their promise of enabling to design drug molecules from scratch completely *in silico* [37].

In addition to virtual screening as a prescreening step, so-called pan-assay interference compounds' (PAINs) can be systematically excluded for further experiments. PAINs often cause false-positive assay results due to unspecific or covalent binding, redox effects, autofluorescence, or degradation. Especially for the selection of a fragment-based library, it is of high importance to identify and eliminate PAINs before applying biophysical screening methods. Obviously, there is an exception to this rule when deliberately using electrophilic fragments for targeting nucleophilic residues in enzymes.

3.2. Biophysical Detection Methods for Fragment Screening

3.2.1. Surface Plasmon Resonance

Surface plasmon resonance (SPR) technique is a very powerful tool for the determination of binding events [38]. SPR can be used to measure the binding affinity, specificity, and kinetic parameters of biomolecular interactions between a variety of proteins, DNA/RNA, and small/complex molecules [39,40]. The target protein is first immobilized on a gold or silver sensor surface. Subsequently, a solution of probe flows over the target surface and induces an increase in the

refractive index, if binding to the target occurs [41]. In a nutshell, SPR determines changes in reflected light before and after probe–target binding [42]. Dose–response analysis can be applied for determination of dissociation constants K_D and binding stoichiometry [43,44]. Additionally, the rate constants for association (k_{on}) and dissociation (k_{off}) can be determined. Importantly, this methodology is well suited for the detection of very weak probe–target interactions mediated by fragments because of its high sensitivity. The real time monitoring provides the possibility to conduct so-called off-rate screening (ORS), which provides an easy way to observe how long the molecules are interacting with the target. Especially for the FBDD approach, this technique was demonstrated to be very effective for the identification of new fragment hits [45]. The ORS approach provides the possibility to assess the potency of very weak binders and even analyse crude compounds or reaction mixtures by looking at the accompanying dissociation kinetics. Noteworthy compounds with slow off rates possibly have a higher potential to be improved in potency than others [46]. Additionally, the drug residence time of a ligand in complex with its target protein ($t_R = 1/k_{off}$) can be an important parameter for the functional efficacy of a compound in complex environments such as whole cells [47].

The immobilization of the target on the SPR biosensor can be achieved for a wide range of proteins, including challenging ones, such as transmembrane proteins or G-protein receptors [3,48]. SPR is a label-free technique; hence, the detection of false positives due to fluorescence quenching can be excluded. Additionally, SPR competition assays can be used to gain information on whether a fragment binds competitively to a known substrate or not. Due to the very low protein consumption, the possibility to use SPR in a high-throughput mode, and its cost-efficiency, it is very often used and is effective as a primary selection filter for screenings of large fragment libraries [49,50]. However, direct information about the binding site or interacting groups of a fragment cannot be derived.

3.2.2. Thermal Shift Assay

The thermal shift assay (TSA) is a very reliable and simple technique, which quantifies the denaturation temperature of a protein. The stability of a protein correlates with its melting temperature, which can vary under different conditions; for example, pH-value, buffer composition, amino acid mutations, or binding of a ligand/fragment. Fluorescence-based TSA techniques are the most common ones and are usually referred to as thermofluor assays or differential scanning fluorimetry (DSF) [51]. In principle, the fluorescence of a protein solution is measured in a temperature gradient. An added fluorescence dye (e.g., SYPRO Orange) shows a low fluorescence signal in a polar environment and a high signal in an apolar environment [52]. By denaturation of a protein, the hydrophobic core is exposed, which leads to an increase of the fluorescence signal. Consequently, the melting temperature of the protein can be determined [53,54]. As mentioned before, a ligand–protein interaction can increase or decrease the melting temperature significantly. Hence, a change of this parameter provides important information about protein stabilization or destabilization. In any case, it is now commonly accepted that a change in either direction implies a ligand–protein interaction event [55,56]. Besides the thermofluor variant of TSA, there are also other detection methods for protein stability, such as *N*-[4-(7-diethylamino-4-methyl-3-coumarinyl)phenyl] maleimide (CPM), as a thiol-specific reaction dye; 4-(dicyanovinyl)julolidine (DCVJ), which is rigidity sensitive; or just measuring the intrinsic tryptophan fluorescence lifetime, which differentiates between folded or unfolded proteins [57–59]. Non-labelling methods based on detecting changes in the fluorescence of tryptophan are especially easy to use and applicable for all proteins [60,61]. The fluorescence of tryptophan is strongly dependent on the close environment of the protein. A binding event can influence protein folding and/or stability, and by detecting changes in tryptophan fluorescence, the chemical and thermal stability can be determined [60,62]. The nanoDSF technology (Prometheus Series from NanoTemper or nanoDSF from 2bind molecular interactions), e.g., requires only low sample quantities (5 $\mu\text{g}/\text{mL}$), and the measurements are independent from any buffer or detergent. Another similar non-labeling TSA technique for detecting protein stability, called Tycho technology from NanoTemper, relies on protein native fluorescence. It is a simple and rapid technique to check a protein for quality and stability and for

analysing ligand–protein binding. An additional advantage of this method is a fast and easy analysis of the quality of a protein during any step of purification, characterization, or assay development.

However, TSA may not be suitable for all target proteins, due to the indirect readout of the melting temperature. Nevertheless, a wide range of applicability, easy and fast handling, and the variable detection methods render this method quite valuable. Due to a high-throughput option and high sensitivity especially, this technique is a useful and powerful method applicable for FBDD as a primary screening step [63]. Still, researchers have to be aware of a usually relatively-high number of false positives. Hence, an orthogonal filtering step is imperative to confirming which compounds are true binders.

3.2.3. Microscale Thermophoresis

Microscale thermophoresis (MST) has been well-established as a technique to detect specific probe–target interactions in recent years. It is a biophysical technique for the characterization of any kind of biomolecular interaction [64,65]. It can be used for proteins, small and complex molecules, fragments, nucleic acids, liposomes, nanoparticles, or ions. In principle, it detects the change in the fluorescence of a labelled target in a temperature gradient as a function of the concentration of a non-fluorescent ligand. The temperature gradient is generated by an IR-laser, and the fluorescence distribution is monitored inside a capillary. This change in fluorescence is based on two main effects. First, the temperature gradient can induce a change in fluorescence. This effect can be influenced by a binding event. Second, thermophoresis of the labelled protein occurs, which is basically the movement of molecules in a temperature gradient. The specific properties of a biomolecule in solution, such as size, surface charge, or hydration shell, influence the thermophoretic profile of the molecule [66]. If a ligand binds to the target, the chemical microenvironment is changed, which leads to a change in the specific thermophoretic profile of the molecule [67]. The detection of the thermophoretic change of a target molecule in relation to varying ligand concentrations can be used to calculate K_D values. In various studies, it has been demonstrated that MST can also detect weak binders, such as fragments, and is amenable for implementation into HTS campaigns [68,69]. Advantages over other methods are the very low protein consumption and the large number of compounds that can be screened, thanks to short experimentation times [70]. Furthermore, it should be mentioned that the samples are measured directly in solution and there is no need to immobilize proteins, as there is when using, for example, SPR. For MST, mainly, three simple protein labeling techniques are used. These involve crosslinker reactive groups like *N*-hydroxysuccinimide (NHS)-esters for the reaction with primary amines, maleimide functions for labelling sulfhydryl groups, and Tris-NTA for His-tag labelling. Additionally, the shape of the MST traces provides information on protein aggregation or denaturation and hints at specific or unspecific ligand–protein binding during the measurements. Additionally, fluorescence-interfering compounds can directly be identified when analysing fluorescence homogeneity. Using MST can maximize the efficacy of fragment screening campaigns due to the large spectrum of applications and easy handling [69]. All these advantages render this technique applicable and attractive for FBDD [68].

3.2.4. X-ray Methods

Macromolecular X-ray analysis is a key method for FBDD, as it generates very detailed information about the protein–ligand interaction. By this means, it provides the opportunity to conduct structure-based-design studies to improve the ligand affinity efficiently [71,72]. Suitable crystals can be achieved using two different methods, co-crystallization or soaking. To obtain crystals using the co-crystallization method, the ligand is added to the mixture before crystal formation starts. In the soaking technique, the ligand is added directly to a mixture with pre-existing crystals [73]. Both methods can be challenging, since not all proteins are easily crystalized and some ligands can disrupt the crystal lattice. As a prescreening for crystallization, thermal shift assays are often used to determine which compounds stabilize the protein fold, and are therefore favoured. Binding sites, which are occupied by a variety of different fragments, can be identified as “hot-spots” of a given target.

By generating various co-crystals, each with a different fragment, the different modes of binding can enable rational fragment linking or merging. Co-crystallization usually is historically not used for a primary screen because it usually requires large amounts (10–50 mg) of highly pure protein [74]. Interestingly, it has become possible to individually screen up to 1000 compounds in less than one week. This, however, requires dedicated instrumentation and highly streamlined processes; e.g., those established by XChem at the Diamond light source or with Astex's Pyramid Discovery Platform [75].

Astonishingly, it has been demonstrated that even low-affinity binders are detectable by this X-ray technique. Having a co-crystal structure in hand, which resolves the fragment binding site in atomic detail, truly fosters subsequent optimization efforts [76]. However, determining structure–activity relationships is not possible by crystallography alone, because it does not provide direct information about binding affinities.

At Helmholtz Zentrum Berlin (HZB), researchers have developed a workflow for the detection of hit fragments [77]. Firstly, a fragment library is selected which is to be screened for during the campaign. There are several academic libraries that can be chosen from; for example, the F2X-Universal Library, which contains over 1100 compounds, or a sub-selection of 96 fragments called the F2X-Entry Screen. Commercial libraries can be purchased from, for example, Cambridge, Enamin, LiverpoolChiroChem, JBS FragXtal Screen, and MedChemExpress—the MCE Fragment Library. Secondly, co-crystals are formed, and crystallographic data is collected. Thirdly, the data is processed and refined automatically using the programs XDSAPP and PHENIX [78,79]. Lastly, together with the hits after the refinement pipeline, PanDDA analysis allows for the identification of binding ligands from weak signals, which previously would not have been analysable [80].

Another example of a fragment screening platform based on crystallography is FragMAX. This platform follows, in general, the same protocol as described above: firstly, crystallization conditions are optimized; secondly, co-crystals are prepared either via co-crystallization or soaking; and thirdly, data collection and processing lead to hit fragments [81].

3.2.5. Nuclear Magnetic Resonance Methods

The nuclear magnetic resonance (NMR)-based techniques are among the most frequently used methods for analysing ligands and protein–ligand interactions as well as protein structures and dynamics in solution [82]. These are, in principle, very robust techniques and can be used in primary screens for the identification of target binders or to provide deep insights into structural characteristics of specific ligand–protein interactions [83,84]. Advantages of the NMR-based methods are that interactions can be determined on a molecular level and in a non-destructive manner [85]. Additionally, K_D values can be determined in the μM – mM range. However, NMR-spectrometers are expensive instruments, especially those with large magnets providing more than 700 MHz resolution, and usually need expert support for data processing and analysis. There are three NMR methods, which are most widely used in the FBDD field.

Saturation-Transfer Difference NMR

Saturation-transfer difference (STD) NMR is a very simple and powerful technique, especially for detecting weak interactions between ligand and target [86]. It is applicable for initial screens, evaluations of hit or lead structures, and for gaining important information on the binding orientation of a ligand to its target. This ligand-observing method does not require any isotope-labelling of the target protein, nor does it need high protein concentrations (10–50 μM). The technique relies on the dissociation mechanism between ligand and protein (K_D μM – mM). In theory, an STD spectrum (I_{STD}) is a difference spectrum between the bound state (on-resonance, I) and the free ligand state (off-resonance, I_o) spectrum of ligand and protein, $I_{STD} = I - I_o$ [87]. By irradiating only the protein, the saturation is transferred from the protein to the bound ligand. By this means, strongly interacting ligand groups show a higher enhancement than less strongly or non-interacting groups in the STD spectrum. Based on this requirement of proximity, the STD effect can give key information about the orientation of the

ligand to the protein. It is also possible to discriminate between specific or non-specific binders [86,88]. Additionally, dissociation constants in the μM – mM range are detectable by performing dose-response experiments [82]. Competition experiments with known binders can also be performed and will provide information whether the fragment in question binds to the same area.

Chemical-Shift Perturbation NMR Spectroscopy

The chemical-shift perturbation NMR method is a protein-observing NMR method. It relies on the chemical-shift perturbation of amino acid signals caused by covalent or non-covalent interactions between ligand and protein [89]. For protein detection via NMR, ^{15}N and/or ^{13}C -protein labelling is required. An NMR spectrum of the labelled protein and one with labelled protein in complex with the ligand have to be measured and compared. Upon ligand–protein binding to a specific site of the protein, the local chemical environment of the amino acids is affected. By this means, a chemical shift of these specific amino acid signals is detectable. The sensitivity of this method brings a lot of advantages, as it can easily detect weak ligand–protein interactions in mM ranges and provides direct information about which amino acids make up the interaction interface [90]. However, protein-observing NMR methods are often time consuming, especially with large proteins because a chemical shift mapping of the single protein is required first. Furthermore, the isotope labelling techniques must be established for the protein beforehand [3].

^{19}F Fluorine NMR Spectroscopy

^{19}F -NMR spectroscopy can be performed in protein-observing as well as ligand-observing modes. The former method works similarly to the chemical shift perturbation NMR methods using ^{15}N or ^{13}C -labeled proteins described above and requires the introduction of a fluorinated label into the biomacromolecule, usually via non-natural amino acids [91]. Chemical shifts of ^{19}F are extremely sensitive to changes in the local environment induced by protein–ligand interactions or conformational changes of the protein [92]. Compared to ^{13}C labelling, ^{19}F offers a higher natural abundance and less signal overlap [93]. Additionally, ^{19}F has a very broad chemical shift range (500 ppm) and less complexity [94]. The ligand-observed method is used quite regularly, employing specially composed fluorine-rich compound libraries. For this purpose, labelling of the target protein is not required. Interestingly, when using fluorine in both protein and ligand simultaneously, information on the dynamics of the ligand–protein interaction and binding pose can be obtained [95].

3.2.6. Isothermal Titration Calorimetry

Isothermal titration calorimetry (ITC) is a biophysical method to determine thermodynamic parameters of ligand–target interactions in solution [96]. Typically, this method is used to analyze the binding of a ligand or small molecule (e.g., fragment) to a macromolecule (e.g., protein or DNA) [97]. An ITC instrument consists of two cells, a reference cell as a control (containing e.g., buffer) and a sample cell for detecting the specific interaction of interest. The difference in temperature between these two cells is precisely measured. The sample cell contains the macromolecule, and the ligand or small molecule is titrated into the mixture. From the heat measured, which is released due to the binding event, the enthalpy change (ΔH) and the Gibbs free energy (ΔG) can be determined. This allows for the calculation of the binding affinity (K_d) and the change in entropy (ΔS) [98,99]. Additionally, binding stoichiometry and interactions between more than two molecules can be studied. The discrimination between entropy and enthalpy-driven binders especially, is one of the main advantages. Information about the thermodynamic profile of the binding event can support the understanding of relations between ligand affinities and physicochemical properties [100]. The enthalpic contribution to a binding event can be expressed as the enthalpic efficacy index EE ($EE = \Delta H/Q$, Q = number of heavy atoms, vide infra). Importantly, fragments mostly bind in an enthalpy-driven manner to the protein surface and often interact at energetically favoured regions—so called hot spots. These hot spots are usually polar residues, which are surrounded by apolar amino acids providing a hydrophobic environment.

Highly enthalpy-driven fragments tend to increase the chances of generating high affinity and selective binders [101,102]. Unfortunately for FBDD approaches, this method is often not used as a standard procedure, as fragment interactions are usually too weak for detection [103]. Furthermore, a large amount of protein is required, and ITC is not applicable for high-throughput screening. However, it is particularly beneficial for not only gaining insights in the binding affinity of ligand–target interactions, but the thermodynamic profile of the binding event [104]. Hence, it should be applied as a secondary or tertiary compound evaluation method driving hit prioritization for subsequent optimization [105,106].

3.2.7. Bio-Layer Interferometry

Bio-Layer Interferometry (BLI) is a real-time, label-free (RT-LF) optical technique that allows for monitoring the interaction between an immobilized target on a biosensor surface and a ligand in solution. Binding events can be followed through a shift in wavelength, which is caused by an increase in optical thickness at the surface. It is possible to determine the affinities of small molecules to targets via solution competition experiments [107]. However, it is mostly used to screen for biomolecules; e.g., antibodies [108,109].

4. Fragment-Hit Qualification

4.1. General Considerations

The methodologies described above should help scientists to identify fragment-sized hits for a given target of interest. In order to embark on a subsequent lead-generation campaign, hits need to be prioritized to be able to focus medicinal-chemistry resources on the most promising starting points. Prioritization of fragment hits is subject to a multi-parameter consideration. Obviously, biological activity is one primary criterion on which to select the starting points for fragment optimization. To this end, effects observed in the orthogonal screening and functional assays should be evaluated together in terms of validated target binding and ligand efficiency (LE) or a related metric to allow a proper comparison. To this end, several quantifiable metrics have been invented to serve as activity-related guideposts for compound selection and optimization. As fragments are of small molecular weight, heavy atom count or a related structure-inherent parameter is usually taken into account to evaluate the quality of the investigated target–ligand interaction. The most straightforward metric in this regard is ligand efficiency (LE). It reflects the ratio between the Gibbs free energy of binding ($\Delta_B G$) and the number non-hydrogen atoms (N) (see Equation (1)) [110]. A value of greater than or equal to 0.3 for the LE is considered a suitable starting point for further optimization.

$$LE = (\Delta_B G)/N \quad \text{with } \Delta_B G = -RT \ln K_i \quad (1)$$

It can be simplified to Equation (2) [111].

$$LE = 1.4(\text{pIC}_{50})/N \quad (2)$$

Several modifications of this equation exist, replacing, for example, the potency term ($\Delta_B G$) either by pIC_{50} (as in Equation (2)), the percentage of inhibition, or the enthalpic contribution of the thermodynamic binding profile (enthalpic efficiency, EE; see also ITC section); another is exchanging the size parameter (N) by molecular weight or total polar surface area. The EE necessitates the implementation of potentially cumbersome ITC experiments, but is particularly suited for discriminating between enthalpy and entropy-driven binders among the set of hits. The former are considered to form a higher number of oriented, specific, and geometrically well-defined interactions, rendering enthalpy-driven binding highly desirable.

Furthermore, some metrics have been devised taking other compound parameters into account. The ligand-lipophilicity efficiency (LLE) or lipophilic efficiency (LiPE) aims at identifying hits of low hydrophobicity (Equation (3)) [7]. Usually, these compounds can be optimized in an easier fashion,

as the enlargement process inherently tends to introduce further lipophilic groups into the compound. Hence, starting from a hydrophilic hit can be advantageous. A special variant of the LLE metric has been devised at Astex Therapeutics, which is referred to as the LLE_{AT} [112]. In that, potency, lipophilicity, and compound size are considered at once (Equation (4)) [7].

$$LLE = pIC_{50} \text{ or } K_i - \text{clog}P/D \quad (3)$$

$$LLE_{AT} = 0.111 + [(1.37 \times LLE)/N] \quad (4)$$

Again a value of $LLE_{AT} \geq 0.3$ is considered a suitable starting point for hit-to-lead optimization [112].

In the opinion of the authors, enthalpic efficiency (EE) and LLE_{AT} are particularly useful metrics for the evaluation of fragment hits. The former is, however, not, in any case, a feasible option, as it depends on the availability of a thermodynamic binding profile, which can be difficult to obtain. A variety of additional metrics of potential utility are available for implementation in to the drug discovery pipeline [7].

Additional compound parameters, which should be considered before embarking on an in-depth hit-optimization campaign, are solubility, synthetic tractability, the availability of commercial analogues, and the availability of structural information on the binding mode. The latter can be gathered on the atomic level via X-ray crystallographic analysis of target–ligand complexes or more seldomly through 2D NMR solution structures [113]. This will allow for the analysis of structure-based binding pharmacophores and potentially the comparison to already reported structures. However, especially in early stages of drug discovery projects, such data is often not yet available. Hence, alternative routes to acquiring structural insights into the ligand binding modality can be worth exploring. If at least a holoenzyme structure is available, a few indirect methods become exploitable. For example, combining biophysical methods such as SPR or ITC with single amino acid mutations within the active site of the enzyme can provide essential information about the binding region of the fragment of interest [114]. Additionally, quite often, target enzymes employ reactive residues in order to perform their biological function. The signal molecule synthase PqsD from *Pseudomonas aeruginosa*, for example, utilizes the thiol nucleophile of the Cys112 side chain in order to generate a thioester-bound anthraniloyl reaction intermediate through consumption of anthraniloyl-CoA. This enzyme was previously identified as a suitable anti-biofilm target to tackle *P. aeruginosa* infections [115]. The covalently blocked active site intermediate can be generated on an SPR sensor chip by addition of the anthraniloyl-CoA substrate, and then used for the characterization of fragment hits (Figure 1) [114,116,117]. This enabled researchers, for example, to classify PqsD inhibitor 1 as an active-site binder.

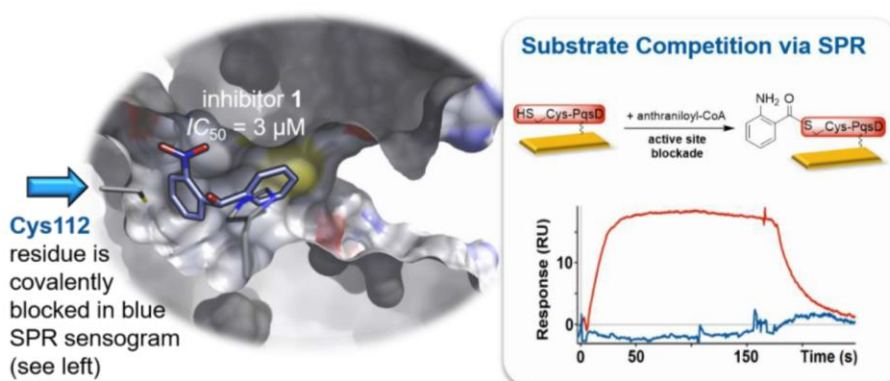


Figure 1. Schematic depiction illustrating the SPR-based competition experiment. (Left) The docking mode of inhibitor 1 bound to the target enzyme PqsD and the active site cysteine (Cys112) are indicated. (Right) SPR sensorgrams with (blue) and without (red) covalent active-site blockade via substrate preconditioning ($RU = \text{SPR response units}$) are given. The lack of SPR response (blue) indicates that inhibitor 1 is binding at the active site [114].

Other possibilities for setting up informative competition experiments can involve, for example STD, NMR, or ITC methodologies. It has to be noted, however, that such approaches only provide low-resolution information of the approximate binding region and usually need to be supported by docking experiments involving inherent ambiguities. Importantly, the more detailed the structural information that is available, the more straightforwardly subsequent optimization steps can be conducted, significantly increasing the chances of success for the fragment-to-lead phase. Hence, the presence of co-crystal structures is highly favoured for fragment-based drug discovery.

4.2. Enzyme Targeting

A usual ligand-based approach aims at finding new enzyme inhibitors by deriving them from known structures of their substrates, cofactors, or intermediates. If such a rational design is not successful, the screening tools described above may yield fragment-based hits as alternative starting points [118]. Again, fragments have comparatively weak binding affinities and low functional efficacy. However, the high ligand efficiencies and above-mentioned advantages can pave the way for generating very potent and selective enzyme inhibitors. Evaluating activity in a functional enzyme assay as early as possible in the inhibitor identification and optimization pipeline is an essential cornerstone for a successful medicinal-chemistry campaign. However, in the case of fragment-based drug design, relatively high concentrations of pure, stable, and soluble enzymes are required for reliable assay readouts due to the low affinities of fragments.

X-ray crystallography is also a suitable tool for evaluating the potential of a fragment to inhibit an enzyme after optimization. It is important to have access to robust and high diffraction-quality crystals of the enzyme [76]. Furthermore, the binding site of the enzyme should be devoid of interfering endogenous ligands, so that low affinity fragments are able to bind [119]. Well-defined and deep pockets are often easier to target than shallow grooves [120].

For the identification and characterization of new hot spots for fragment binding, the aforementioned computational screening methods can be beneficial as docking experiments, being able to predict initial structure–activity relationships [121].

4.3. Functional Enzyme Assays

For the evaluation of enzymatic inhibitors/optimized fragments and for studying kinetics of the enzymes, several methods are well-established and easily applicable for a wide range of enzymes.

A very sensitive technique to study enzyme inhibition or kinetics is based on mass-spectrometry (MS) detection. Via liquid chromatographic-MS (LC-MS), the specific enzymatic reaction products can be detected and quantified using the reaction mixture aided by LC separation. Benefits of this technique are that it is label-free and that there is no need for substrate modification [122]. Furthermore, it is applicable for most enzymatic reactions and for concentration-dependent enzyme inhibition studies.

In case of targeting proteases, the inhibitory effects of inhibitors are often determined by highly sensitive fluorescence resonance energy transfer (FRET)-based fluorogenic enzyme assays. Typically, a short peptide sequence similar to the sequence for a natural cleavage site of the target enzyme is synthesized and labelled at opposite ends with donor and acceptor/quencher molecules within the FRET distance. The enzymatic activity is determined by monitoring the change in fluorescence intensity. As soon as the labelled substrate molecule is cleaved by the enzyme and the donor–acceptor pair drifts apart, the FRET efficiency drops to zero, leading to an increase in fluorescence [123].

For NADH-dependent enzymes, an enzyme-dependent fluorescence recovery after photobleaching (ED-FRAP) assay can also be used [124]. It relies on the photobleaching of a fluorophore as a product of an enzymatic reaction; in this case, NADH. The oxidative UV photolysis of NADH to NAD⁺ is monitored and correlates with the enzymatic activities. It is applicable for in vitro samples as well as in living cell experiments as an imaging method [125].

Another tool for determining specific enzymatic activities is the usage of fluorogenic and chromogenic substrates. In the latter case, substrates increase or decrease the absorption of light at a

specific wavelength by conversion of the substrate to the product by the enzyme. An often-used example for a chromogenic substrate is *p*-nitrophenyl phosphate (pNPP), which is specific for phosphatases. The phosphatases hydrolyse the pNPP to *p*-nitrophenol and inorganic phosphorus leading to a yellow colour of the solution. As a fluorogenic substrate, for example, fluorescein di-phosphate (FDP) can be used. By hydrolysis of FDP by alkaline phosphatases, non-fluorescent FDP is converted into highly fluorescent FDP [126]. Of course, the examples given are just a small selection of available enzyme-assay modalities. In any case, a functional assay should be thoroughly adapted to the targeted system of interest as it will guide the subsequent hit-to-lead optimization phase.

5. Fragment-To-Lead Optimization

5.1. Growing

The most straightforward approach of turning a fragment-based hit obeying the rule-of-three into a lead-like compound with rule-of-five characteristics is fragment growing. The aim is to install novel target–interaction hot spots by increasing the size of the molecule and attaching additional functional groups. In order to achieve this in a rational design fashion, so-called growth vectors need to be identified. These are essentially positions of the fragment scaffold to which additional atoms, functional groups, or even other dedicated binding scaffolds can be attached. In this regard, the modality of increasing the size of the molecule might play an important role and is characterized by directionality (geometry), substituent size, and the flexibility of the attachment. Actually, identifying these growth vectors might pose a first big hurdle in the process, especially if co-crystal structures are not available. In such scenarios, gaining basic information on inhibitor binding modes, as described above, is key. In the following example, we show how a combination of different biophysical screening and evaluation methods allowed for the identification of the first inhibitors of the protein–DNA interaction between the herpesviral target Latency-associated nuclear antigen (LANA) and its binding sites on the viral episome [127]. Figure 2 shows the screening cascade used for hit identification. First, an SPR screening was conducted, yielding 52 positives. Then, an orthogonal DSF (TSA) filter was applied to preselect 20 target binders. These 20 initial hit compounds were tested for in vitro functionality using a fluorescent polarization (FP)-based competition assay for the quantitative evaluation of target interaction inhibition. In this manner, three very promising fragment hits were prioritized for further optimization and evaluation. In this example fragment 2 has been used for growth vector identification and fragment growing (Figure 2). Fragment 2 showed a low inhibitory effect of 25% at 1 mM in the functional interaction inhibition assay, which is promising, considering the size of the fragment hit.

First, initial analogues were generated to identify a suitable growth vector for subsequent enlargement. That way, it was observed that introducing substituents at the imidazole moiety improves activity. In particular, compound 4 (Figure 2) could improve the inhibitory effect to 91% at 1 mM. Additionally, different functional groups at the phenyl ring instead of the NH₂-group were tested, showing that a carboxylic acid (compound 3) improves activity to an IC₅₀ value of 333 μM. These first derivatisation results of initial hit 2 led to further optimization studies with a combichem approach using click chemistry. Replacing the imidazole moiety with a triazole core, keeping the carboxylic acid function at the phenyl ring, and increasing the size of the molecule at the Eastern part led to a small compound library of 29 new derivatives. This procedure facilitated the discovery of compound 5 by the introduction of a bulky pyridine ring. Still possessing a fragment-like size, this compound represents a promising inhibitory activity (IC₅₀ = 17 μM). Additionally, it shows favourable physicochemical properties (low clogP of 2.00, good solubility) and suitable ligand efficiency (LE = 0.33). Hence, it is a promising starting point for a follow-up lead-generation campaign. As this example demonstrates, fragment growing and, in general, compound enlargement can be attempted with and without structural information. Although, for obvious reasons, the latter usually requires more effort and is less likely to be successful.

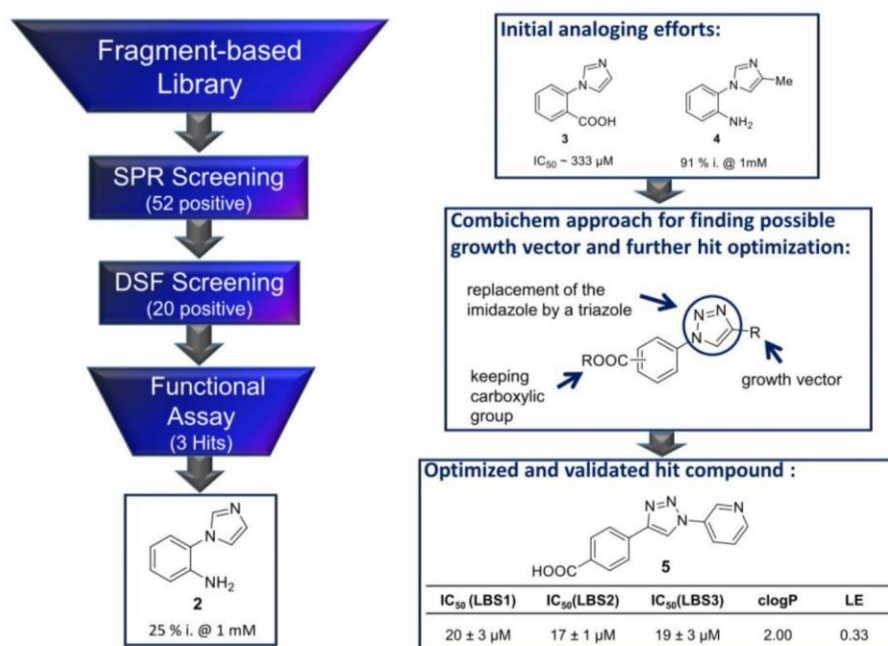


Figure 2. Fragment screening cascade using: SPR and DSF selection steps, followed by functional evaluation via fluorescence polarization, which resulted in three fragment hits. Growth vector identification through initial analoging allowed for growing of fragment 2 into a double-digit micromolar validated hit.

5.2. Merging

If two ligands or fragments bind to overlapping regions of the target protein, motifs of both can be merged into one compound. Ideally, the favourable affinity-mediating features of both compounds work additively or even synergistically when fused into one unit. Fragment merging can be attempted when obvious structural similarities of the two ligands in question are present. For example, if it is plausible to assume that both share a certain prominent binding motif or coordinate to an active-site transition metal, but do otherwise not align well, they might diverge into different regions of the active site. The geometry and attachment patterns of the combined binding groups is key for productive cooperative binding. Hence, several possible merging opportunities should be explored to identify the optimal shape of the resulting merged compound. Here, and especially in cases where the to-be-merged compounds share no obvious structural similarity, structural data of ligand–target complexes are necessary to guide this approach. Again, X-ray co-crystal structures as well as NMR solution structures deliver the most reliable and detailed source of information. Nevertheless, wet-lab experiment-guided docking studies may also provide insights robust enough to justify the syntheses of merged compounds. One such example is provided below. In previous studies, two distinct inhibitor classes of the bacterial target enzyme PqsD were identified (Figure 3) [114,128]. Docking as well as SPR competition experiments suggested that fragment 1 (vide supra) and compound 6 had overlapping binding sites and shared a common phenylmethanol feature. Hence, compound 7 was synthesized to merge both units into one scaffold [129]. Unfortunately, the resulting fused molecule did not show better potency on the target enzyme than the frontrunner compound 6. Nevertheless, the substantial modifications applied to the inhibitor were tolerated and brought about respectable activity. This example nicely illustrates the general strategy and emphasises the need for structural information, which has to be acquired beforehand.

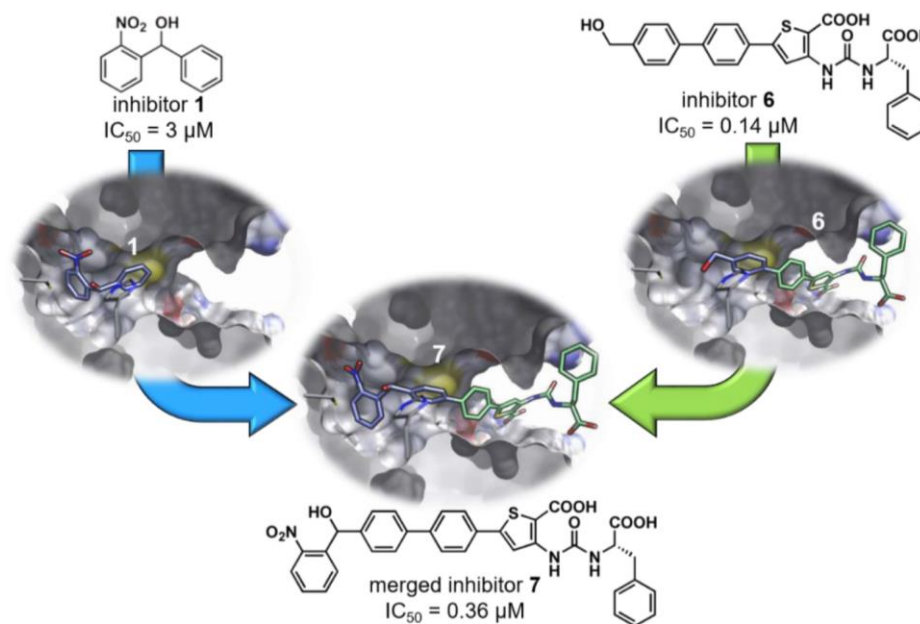


Figure 3. An example of a compound merging attempt. Fragment 1 and compound 6 were merged, guided by an SPR-informed docking poses, yielding inhibitor 7. If X-ray structures for the individual inhibitors were available, this attempt could be improved by adjusting the merging modality [129]. Light blue: carbon atoms of inhibitor 1 and carbons resembling an overlapping motif in inhibitor 6. Light green: the other carbon atoms of inhibitor 6. Blue: nitrogen. Red: oxygen. Hydrogen omitted for clarity.

5.3. Linking

For a fragment linking approach, two or more fragments have to bind to different but adjacent sites of the enzyme active site [3]. This approach is similar to the fragment merging strategy laid out above. However, it introduces one additional component into the ligand system: a linker moiety. Finding the right linker motif, which orients the individual fragment units in the favourable geometry in relation to each other without introducing too much flexibility whilst maintaining the binding poses of both fragments, can be very challenging. If successful, the combination of two fragments with rather low affinity could result in significantly higher affinity and has the potential to result in “superadditive” contributions of both binding motifs. The challenge in fragment linking is the exploration of the binding mode of both fragments and the identification of an optimal linker. Only in this case, the overall reduced so-called rigid body entropy translates into synergistically-improved affinity. By binding of a fragment to a target protein, rotational and translational entropy are lost. This entropy penalty has to be overcompensated by attractive interactions formed between the ligand and the target. When two fragments bind in parallel to adjacent sites, each has to pay this entropy penalty. When these two fragments are linked together in an ideal way, the resulting singular compound only encounters the loss of rigid body entropy once. Hence, the affinity observed will be much greater than only the sum of the individual affinities [130]. The additional binding energy gained is often also referred to as linker energy. To overcome the challenges associated with fragment linking, we pioneered a synergistic combination with dynamic combinatorial chemistry (DCC). For this proof-of-concept study, we used the model enzyme endothiapsin [131]. Generally, such aspartic proteases are found in fungi, vertebrates, plants, and retroviruses such as HIV. The class of enzymes plays a causative role in diseases such as malaria, Alzheimer’s disease, hypertension, and AIDS. X-ray crystal structures of endothiapsin in complex with fragment inhibitors 8 and 9 (PDB IDs: 4KUP and 3T7P) identified by DCC were used as a starting point for fragment linking studies facilitated by DCC. Hits 8 and 9 displayed IC_{50} values of 12.8 μ M and 14.5 μ M and LEs of 0.27 and 0.29, respectively. These hit

compounds are not typical small fragments. However, as was previously mentioned, also structures which do not follow the RO3 principles can be used in FBDD approaches. After superimposing the binding modes of the two hit structures, it was envisioned that these moieties could possibly be linked, since they occupy different pockets in the protein. The linking of **8** and **9** should, therefore, generate an inhibitor that occupies multiple binding pockets of endothiapepsin (Figure 4).

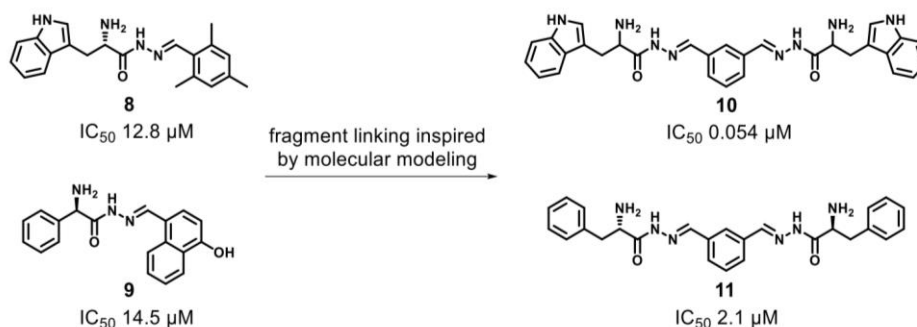


Figure 4. Structures of hits **8** and **9** and linked bisacylhydrazone linked inhibitors **10** and **11** [131].

Using molecular modelling, an acylhydrazone motif was selected as a suitable linker structure. The acylhydrazone linker provides H-bond donor and acceptor sites, which could enhance the binding affinity. Acylhydrazones can be formed in a reversible fashion from the condensation reaction between hydrazides and aldehydes. Reversibility is key for DCC, as it allows an external stimulus, such as a protein target, to influence the equilibrium. In the so called target-directed DCC, the target can stabilize certain members of the dynamic combinatorial library (DCL), giving rise to an amplification of ligands with high affinity at the cost of other DCL members (Figure 5). In this way, a moderate number of molecules can be screened for, without having to synthesize, purify, and analyse each molecule separately [132,133].

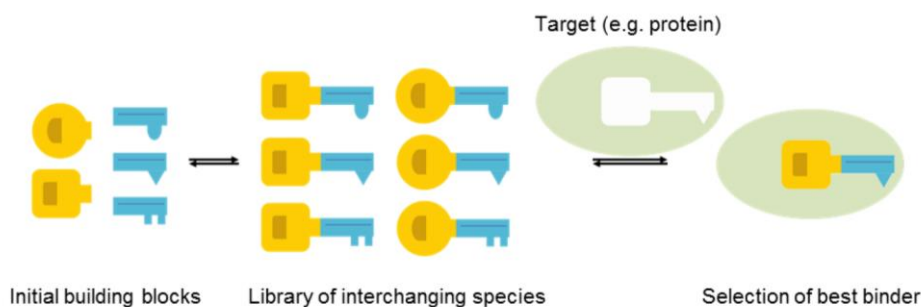


Figure 5. Schematic representation of target-directed dynamic combinatorial chemistry.

The homo-bis-acylhydrazones **10** and **11** were hits from the DCC experiments and were synthesized and evaluated accordingly. Compared to compound **9**, the potency of inhibitor **10** was increased 240-fold, yielding an IC_{50} value of 0.054 μ M and a LE value of 0.29. For inhibitor **11** an IC_{50} of 2.1 μ M and a LE value of 0.25 was determined (Figure 4) [106]. Obviously, only the symmetric linking modality resulted in efficient cooperative binding.

6. Conclusions

FBDD has become a respectable alternative to high-throughput screening of large compound libraries. Due to the moderate instrumentation requirements as well as general cost-effectiveness, this approach is attractive for both the academic and industrial drug discovery settings. However, as laid out in this review, expertise from fields of organic chemistry, biophysical screening, structural biology, compound profiling, and hit qualification have to work together right from the beginning to facilitate

successful fragment-based drug discovery. Hence, integrated medicinal chemistry teams have to be established on site in order to tackle the challenges occurring en route to lead-like compounds or even preclinical candidates. The importance of structural data and an in-depth qualification of fragment hits cannot be emphasized enough in order to enable rationally guided fragment growing, merging, or linking trials. If all ends meet up, FBDD represents a facile, target-driven strategy for finding suitable starting points ideal for lead generation circumventing HTS.

Author Contributions: Conceptualization, M.E. and P.K.; writing—original draft preparation, P.K. and M.E.; writing—review and editing, P.K., A.M.H., A.K.H.H., and M.E.; supervision, M.E.; funding acquisition, M.E. and A.K.H.H.

Funding: This research was funded by the German Centre for Infection Research (DZIF) and the Netherlands Organization for Scientific Research (NWO, VIDI grant 723.014.008).

Conflicts of Interest: The authors declare no conflict of interest.

References

1. Erlanson, D.A. Introduction to fragment-based drug discovery. *Top. Curr. Chem.* **2012**, *317*, 1–32. [[CrossRef](#)] [[PubMed](#)]
2. Chen, H.; Zhou, X.; Wang, A.; Zheng, Y.; Gao, Y.; Zhou, J. Evolutions in fragment-based drug design: The deconstruction–reconstruction approach. *Drug Discov. Today* **2014**, *20*, 105–113. [[CrossRef](#)] [[PubMed](#)]
3. Erlanson, D.A.; Jahnke, W. *Fragment-based Drug Discovery. Lessons and Outlook*; Wiley-VCH: Weinheim, Germany, 2016; ISBN 9783527337750.
4. Murray, C.W.; Rees, D.C. The rise of fragment-based drug discovery. *Nat. Chem.* **2009**, *1*, 187. [[CrossRef](#)] [[PubMed](#)]
5. Jhoti, H.; Williams, G.; Rees, D.C.; Murray, C.W. The rule of three for fragment-based drug discovery: Where are we now? *Nat. Rev. Drug Discov.* **2013**, *12*, 644. [[CrossRef](#)]
6. Wermuth, C.G. *The Practice of Medicinal Chemistry*; Elsevier: Amsterdam, The Netherlands, 2015; ISBN 9780124172050.
7. Hopkins, A.L.; Keserü, G.M.; Leeson, P.D.; Rees, D.C.; Reynolds, C.H. The role of ligand efficiency metrics in drug discovery. *Nat. Rev. Drug Discov.* **2014**, *13*, 105. [[CrossRef](#)]
8. Schuffenhauer, A.; Ruedisser, S.; Marzinzik, A.; Jahnke, W.; Selzer, P.; Jacoby, E. Library Design for Fragment Based Screening. *CTMC* **2005**, *5*, 751–762. [[CrossRef](#)]
9. Jacquemard, C.; Kellenberger, E. A bright future for fragment-based drug discovery: What does it hold? *Expert Opin. Drug Discov.* **2019**, *14*, 413–416. [[CrossRef](#)]
10. Shi, Y.; Itzstein, M.V. How Size Matters: Diversity for Fragment Library Design. *Molecules* **2019**, *24*, 2838. [[CrossRef](#)]
11. Heidrich, J.; Sperl, L.E.; Boeckler, F.M. Embracing the Diversity of Halogen Bonding Motifs in Fragment-Based Drug Discovery—Construction of a Diversity-Optimized Halogen-Enriched Fragment Library. *Front. Chem.* **2019**, *7*, 9. [[CrossRef](#)]
12. Liu, M.; Quinn, R.J. Fragment-based screening with natural products for novel anti-parasitic disease drug discovery. *Expert Opin. Drug Discov.* **2019**, *14*, 1283–1295. [[CrossRef](#)]
13. Kutchukian, P.S.; So, S.-S.; Fischer, C.; Waller, C.L. Fragment library design: Using cheminformatics and expert chemists to fill gaps in existing fragment libraries. *Methods Mol. Biol.* **2015**, *1289*, 43–53. [[CrossRef](#)] [[PubMed](#)]
14. Sandomenico, A.; Caporale, A.; Doti, N.; Cross, S.; Cruciani, G.; Chambery, A.; de Falco, S.; Ruvo, M. Synthetic Peptide Libraries. From random mixtures to in Vivo testing. *Curr. Med. Chem.* **2018**. [[CrossRef](#)]
15. Guillon, R.; Rahimova, R.; Preeti; Egron, D.; Rouanet, S.; Dumontet, C.; Aghajari, N.; Jordheim, L.P.; Chaloin, L.; Peyrottes, S. Lead optimization and biological evaluation of fragment-based cN-II inhibitors. *Eur. J. Med. Chem.* **2019**, *168*, 28–44. [[CrossRef](#)] [[PubMed](#)]
16. Ferenczy, G.G.; Keserü, G.M. On the enthalpic preference of fragment binding. *Med. Chem. Commun.* **2016**, *7*, 332–337. [[CrossRef](#)]
17. Rees, D.C.; Congreve, M.; Murray, C.W.; Carr, R. Fragment-based lead discovery. *Nat. Rev. Drug Discov.* **2004**, *3*, 660. [[CrossRef](#)] [[PubMed](#)]

18. Brown, N. *In Silico Medicinal Chemistry*; Royal Society of Chemistry: Cambridge, UK, 2015; ISBN 978-1-78262-163-8.
19. Doak, B.C.; Over, B.; Giordanetto, F.; Kihlberg, J. Oral druggable space beyond the rule of 5: Insights from drugs and clinical candidates. *Chem. Biol.* **2014**, *21*, 1115–1142. [[CrossRef](#)] [[PubMed](#)]
20. Keserű, G.M.; Erlanson, D.A.; Ferenczy, G.G.; Hann, M.M.; Murray, C.W.; Pickett, S.D. Design Principles for Fragment Libraries: Maximizing the Value of Learnings from Pharma Fragment-Based Drug Discovery (FBDD) Programs for Use in Academia. *J. Med. Chem.* **2016**, *59*, 8189–8206. [[CrossRef](#)] [[PubMed](#)]
21. Backus, K.M.; Correia, B.E.; Lum, K.M.; Forli, S.; Horning, B.D.; González-Páez, G.E.; Chatterjee, S.; Lanning, B.R.; Teijaro, J.R.; Olson, A.J.; et al. Proteome-wide covalent ligand discovery in native biological systems. *Nature* **2016**, *534*, 570–574. [[CrossRef](#)]
22. Prothiwa, M.; Englmaier, F.; Böttcher, T. Competitive Live-Cell Profiling Strategy for Discovering Inhibitors of the Quinolone Biosynthesis of *Pseudomonas aeruginosa*. *J. Am. Chem. Soc.* **2018**, *140*, 14019–14023. [[CrossRef](#)]
23. Tanaka, D. Fragment-based Drug Discovery: Concept and Aim. *Yakugaku Zasshi* **2010**, *130*, 315–323. [[CrossRef](#)]
24. Wasley, J.W. Book Review of Fragment-Based Drug Discovery. A Practical Approach. *J. Med. Chem.* **2009**, *52*, 6168. [[CrossRef](#)]
25. Schultes, S.; de Graaf, C.; Haaksma, E.E.; de Esch, I.J.; Leurs, R.; Krämer, O. Ligand efficiency as a guide in fragment hit selection and optimization. *Drug Discov. Today Technol.* **2010**, *7*, e147–e202. [[CrossRef](#)]
26. Orita, M.; Ohno, K.; Warizaya, M.; Amano, Y.; Niimi, T. Lead generation and examples opinion regarding how to follow up hits. *Meth. Enzymol.* **2011**, *493*, 383–419. [[CrossRef](#)] [[PubMed](#)]
27. Howard, S.; Abell, C. *Fragment-based Drug Discovery*; The Royal Society of Chemistry: Cambridge, UK, 2015; ISBN 9781849739085.
28. Singh, M.; Tam, B.; Akabayov, B. NMR-Fragment Based Virtual Screening: A Brief Overview. *Molecules* **2018**, *23*, 233. [[CrossRef](#)]
29. Gimeno, A.; Ojeda-Montes, M.J.; Tomás-Hernández, S.; Cereto-Massagué, A.; Beltrán-Debón, R.; Mulero, M.; Pujadas, G.; Garcia-Vallvé, S. The Light and Dark Sides of Virtual Screening: What Is There to Know? *Int. J. Mol. Sci.* **2019**, *20*, 1375. [[CrossRef](#)]
30. Bielska, E.; Lucas, X.; Czerwoniec, A.; Kasprzak, J.M.; Kaminska, K.H.; Bujnicki, J.M. Virtual screening strategies in drug design-methods and applications. *BioTechnologia* **2011**, *92*, 249–264. [[CrossRef](#)]
31. Yamaotsu, N.; Hirono, S. In silico fragment-mapping method: A new tool for fragment-based/structure-based drug discovery. *J. Comput. Aided Mol. Des.* **2018**, *32*, 1229–1245. [[CrossRef](#)]
32. Wang, T.; Wu, M.-B.; Chen, Z.-J.; Chen, H.; Lin, J.-P.; Yang, L.-R. Fragment-Based Drug Discovery and Molecular Docking in Drug Design. *Curr. Pharm. Biotechnol.* **2015**, *16*, 11–25. [[CrossRef](#)]
33. Yang, S.-Y. Pharmacophore modeling and applications in drug discovery: Challenges and recent advances. *Drug Discov. Today* **2010**, *15*, 444–450. [[CrossRef](#)]
34. Zhu, T.; Cao, S.; Su, P.-C.; Patel, R.; Shah, D.; Chokshi, H.B.; Szukala, R.; Johnson, M.E.; Hevener, K.E. Hit identification and optimization in virtual screening: Practical recommendations based on a critical literature analysis. *J. Med. Chem.* **2013**, *56*, 6560–6572. [[CrossRef](#)]
35. Melville, J.L.; Burke, E.K.; Hirst, J.D. Machine learning in virtual screening. *Comb. Chem. High Throughput Screen.* **2009**, *12*, 332–343. [[CrossRef](#)] [[PubMed](#)]
36. Lavecchia, A. Machine-learning approaches in drug discovery: Methods and applications. *Drug Discov. Today* **2015**, *20*, 318–331. [[CrossRef](#)] [[PubMed](#)]
37. Chen, H.; Engkvist, O.; Wang, Y.; Olivecrona, M.; Blaschke, T. The rise of deep learning in drug discovery. *Drug Discov. Today* **2018**, *23*, 1241–1250. [[CrossRef](#)] [[PubMed](#)]
38. Navratilova, I.; Hopkins, A.L. Fragment Screening by Surface Plasmon Resonance. *ACS Med. Chem. Lett.* **2010**, *1*, 44–48. [[CrossRef](#)]
39. Renaud, J.-P.; Neumann, T.; van Hijfte, L. Fragment-Based Drug Discovery. In *Small Molecule Medicinal Chemistry: Strategies and Technologies*; Czechtizky, W., Hamley, P., Eds.; John Wiley & Sons: Hoboken, NJ, USA, 2016; pp. 221–249, ISBN 9781118771723.
40. Grädler, U.; Schwarz, D.; Blaesse, M.; Leuthner, B.; Johnson, T.L.; Bernard, F.; Jiang, X.; Marx, A.; Gilardone, M.; Lemoine, H.; et al. Discovery of novel Cyclophilin D inhibitors starting from three dimensional fragments with millimolar potencies. *Bioorg. Med. Chem. Lett.* **2019**, 126717. [[CrossRef](#)]

41. Cooper, M.A.; Mayr, L. *Label-Free Technologies for Drug Discovery*; Wiley-Blackwell: Oxford, UK, 2011; ISBN 0470746831.
42. Schneider, C.S.; Bhargav, A.G.; Perez, J.G.; Wadajkar, A.S.; Winkles, J.A.; Woodworth, G.F.; Kim, A.J. Surface plasmon resonance as a high throughput method to evaluate specific and non-specific binding of nanotherapeutics. *J. Control. Release* **2015**, *219*, 331–344. [[CrossRef](#)]
43. Bleiweis, A.S. Identification of cariogenic bacteria by fluorescent antibody and other techniques: An international symposium. New York City, April 3–4, 1975. Preface. *J. Dent. Res.* **1976**, *55*, A4. [[CrossRef](#)]
44. Kroeck, K.G.; Sacco, M.D.; Smith, E.W.; Zhang, X.; Shoun, D.; Akhtar, A.; Darch, S.E.; Cohen, F.; Andrews, L.D.; Knox, J.E.; et al. Discovery of dual-activity small-molecule ligands of *Pseudomonas aeruginosa* LpxA and LpxD using SPR and X-ray crystallography. *Sci. Rep.* **2019**, *9*, 15450. [[CrossRef](#)]
45. Murray, J.B.; Roughley, S.D.; Matassova, N.; Brough, P.A. Off-rate screening (ORS) by surface plasmon resonance. An efficient method to kinetically sample hit to lead chemical space from unpurified reaction products. *J. Med. Chem.* **2014**, *57*, 2845–2850. [[CrossRef](#)]
46. Wang, Y.; Edalji, R.P.; Panchal, S.C.; Sun, C.; Djuric, S.W.; Vasudevan, A. Are We There Yet? Applying Thermodynamic and Kinetic Profiling on Embryonic Ectoderm Development (EED) Hit-to-Lead Program. *J. Med. Chem.* **2017**, *60*, 8321–8335. [[CrossRef](#)]
47. Copeland, R.A. *Evaluation of Enzyme Inhibitors in Drug Discovery*; Wiley: London, UK, 2013; ISBN 9781118488133.
48. Nguyen, H.H.; Park, J.; Kang, S.; Kim, M. Surface plasmon resonance: A versatile technique for biosensor applications. *Sensors* **2015**, *15*, 10481–10510. [[CrossRef](#)] [[PubMed](#)]
49. Neumann, T.; Junker, H.-D.; Schmidt, K.; Sekul, R. SPR-based fragment screening: Advantages and applications. *Curr. Top. Med. Chem.* **2007**, *7*, 1630–1642. [[CrossRef](#)] [[PubMed](#)]
50. Chavanieu, A.; Pugnière, M. Developments in SPR Fragment Screening. *Expert Opin. Drug Discov.* **2016**, *11*, 489–499. [[CrossRef](#)] [[PubMed](#)]
51. Senisterra, G.; Chau, I.; Vedadi, M. Thermal denaturation assays in chemical biology. *Assay Drug Dev. Technol.* **2012**, *10*, 128–136. [[CrossRef](#)] [[PubMed](#)]
52. Lo, M.-C.; Aulabaugh, A.; Jin, G.; Cowling, R.; Bard, J.; Malamas, M.; Ellestad, G. Evaluation of fluorescence-based thermal shift assays for hit identification in drug discovery. *Anal. Biochem.* **2004**, *332*, 153–159. [[CrossRef](#)]
53. Grøtthauge, M.K.; Hajizadeh, N.R.; Swann, M.J.; Pohl, E. Protein-ligand interactions investigated by thermal shift assays (TSA) and dual polarization interferometry (DPI). *Acta Crystallogr. D Biol. Crystallogr.* **2015**, *71*, 36–44. [[CrossRef](#)]
54. Niesen, F.H.; Berglund, H.; Vedadi, M. The use of differential scanning fluorimetry to detect ligand interactions that promote protein stability. *Nat. Protoc.* **2007**, *2*, 2212. [[CrossRef](#)]
55. Zhang, R.; Monsma, F. Fluorescence-based thermal shift assays. *Curr. Opin. Drug Discov. Dev.* **2010**, *13*, 389–402.
56. Silvestre, H.L.; Blundell, T.L.; Abell, C.; Ciulli, A. Integrated biophysical approach to fragment screening and validation for fragment-based lead discovery. *Proc. Natl. Acad. Sci. USA* **2013**, *110*, 12984–12989. [[CrossRef](#)]
57. Hofmann, L.; Gulati, S.; Sears, A.; Stewart, P.L.; Palczewski, K. An effective thiol-reactive probe for differential scanning fluorimetry with a standard real-time polymerase chain reaction device. *Anal. Biochem.* **2016**, *499*, 63–65. [[CrossRef](#)]
58. Nagarajan, S.; Lapidus, L.J. Fluorescent Probe DCVJ Shows High Sensitivity for Characterization of Amyloid β -Peptide Early in the Lag Phase. *Chembiochem* **2017**, *18*, 2205–2211. [[CrossRef](#)] [[PubMed](#)]
59. Bruce, D.; Cardew, E.; Freitag-Pohl, S.; Pohl, E. How to Stabilize Protein: Stability Screens for Thermal Shift Assays and Nano Differential Scanning Fluorimetry in the Virus-X Project. *J. Vis. Exp.* **2019**. [[CrossRef](#)] [[PubMed](#)]
60. Magnusson, A.O.; Szekrenyi, A.; Joosten, H.-J.; Finnigan, J.; Charnock, S.; Fessner, W.-D. nanoDSF as screening tool for enzyme libraries and biotechnology development. *FEBS J.* **2019**, *286*, 184–204. [[CrossRef](#)]
61. Mork-Jansson, A.E.; Eichacker, L.A. A strategy to characterize chlorophyll protein interaction in LIL3. *Plant Methods* **2019**, *15*, 1. [[CrossRef](#)] [[PubMed](#)]

62. Makowska, J.; Żamojć, K.; Wyrzykowski, D.; Wiczak, W.; Chmurzyński, L. Copper(II) complexation by fragment of central part of FBP28 protein from *Mus musculus*. *Biophys. Chem.* **2018**, *241*, 55–60. [[CrossRef](#)] [[PubMed](#)]
63. Mashalidis, E.H.; Śledź, P.; Lang, S.; Abell, C. A three-stage biophysical screening cascade for fragment-based drug discovery. *Nat. Protoc.* **2013**, *8*, 2309. [[CrossRef](#)]
64. Jerabek-Willemsen, M.; André, T.; Wanner, R.; Roth, H.M.; Duhr, S.; Baaske, P.; Breitsprecher, D. MicroScale Thermophoresis: Interaction analysis and beyond. *J. Mol. Struct.* **2014**, *1077*, 101–113. [[CrossRef](#)]
65. Mueller, A.M.; Breitsprecher, D.; Duhr, S.; Baaske, P.; Schubert, T.; Längst, G. MicroScale Thermophoresis: A Rapid and Precise Method to Quantify Protein-Nucleic Acid Interactions in Solution. *Methods Mol. Biol.* **2017**, *1654*, 151–164. [[CrossRef](#)]
66. Schubert, T.; Längst, G. Studying epigenetic interactions using MicroScale Thermophoresis (MST). *AIMS Biophys.* **2015**, *2*, 370–380. [[CrossRef](#)]
67. Asmari, M.; Ratih, R.; Alhazmi, H.A.; El Deeb, S. Thermophoresis for characterizing biomolecular interaction. *Methods* **2018**, *146*, 107–119. [[CrossRef](#)]
68. Rainard, J.M.; Pandarakalam, G.C.; McElroy, S.P. Using Microscale Thermophoresis to Characterize Hits from High-Throughput Screening: A European Lead Factory Perspective. *SLAS Discov.* **2018**, *23*, 225–241. [[CrossRef](#)] [[PubMed](#)]
69. Linke, P.; Amaning, K.; Maschberger, M.; Vallee, F.; Steier, V.; Baaske, P.; Duhr, S.; Breitsprecher, D.; Rak, A. An Automated Microscale Thermophoresis Screening Approach for Fragment-Based Lead Discovery. *J. Biomol. Screen.* **2016**, *21*, 414–421. [[CrossRef](#)] [[PubMed](#)]
70. Lamoree, B.; Hubbard, R.E. Current perspectives in fragment-based lead discovery (FBLD). *Essays Biochem.* **2017**, *61*, 453–464. [[CrossRef](#)] [[PubMed](#)]
71. Chilingaryan, Z.; Yin, Z.; Oakley, A.J. Fragment-Based Screening by Protein Crystallography: Successes and Pitfalls. *Int. J. Mol. Sci.* **2012**, *13*, 12857–12879. [[CrossRef](#)] [[PubMed](#)]
72. Davies, T.G.; Hyvönen, M.; Arnold, E. *Fragment-based Drug Discovery and X-ray Crystallography*; Springer: Heidelberg, Germany, 2012; ISBN 9783642275401.
73. Müller, I. Guidelines for the successful generation of protein–ligand complex crystals. *Acta Crystallogr. D Struct. Biol.* **2017**, *73*, 79–92. [[CrossRef](#)] [[PubMed](#)]
74. Tounge, B.A.; Parker, M.H. Designing a diverse high-quality library for crystallography-based FBDD screening. *Meth. Enzymol.* **2011**, *493*, 3–20. [[CrossRef](#)]
75. Source, D.L. Fragment Screening-XChem-MX-Diamond Light Source. Available online: <https://diamond.ac.uk/Instruments/Mx/Fragment-Screening.html> (accessed on 18 June 2019).
76. Hartshorn, M.J.; Murray, C.W.; Cleasby, A.; Frederickson, M.; Tickle, I.J.; Jhoti, H. Fragment-based lead discovery using X-ray crystallography. *J. Med. Chem.* **2005**, *48*, 403–413. [[CrossRef](#)]
77. Schiebel, J.; Krimmer, S.G.; Röwer, K.; Knörlein, A.; Wang, X.; Park, A.Y.; Stieler, M.; Ehrmann, F.R.; Fu, K.; Radeva, N.; et al. High-Throughput Crystallography: Reliable and Efficient Identification of Fragment Hits. *Structure* **2016**, *24*, 1398–1409. [[CrossRef](#)]
78. Adams, P.D.; Afonine, P.V.; Bunkóczi, G.; Chen, V.B.; Davis, I.W.; Echols, N.; Headd, J.J.; Hung, L.-W.; Kapral, G.J.; Grosse-Kunstleve, R.W.; et al. PHENIX: A comprehensive Python-based system for macromolecular structure solution. *Acta Crystallogr. D Biol. Crystallogr.* **2010**, *66*, 213–221. [[CrossRef](#)]
79. Sparta, K.M.; Krug, M.; Heinemann, U.; Mueller, U.; Weiss, M.S. XDSAPP2.0. *J Appl Crystallogr.* **2016**, *49*, 1085–1092. [[CrossRef](#)]
80. Pearce, N.M.; Krojer, T.; Bradley, A.R.; Collins, P.; Nowak, R.P.; Talon, R.; Marsden, B.D.; Kelm, S.; Shi, J.; Deane, C.M.; et al. A multi-crystal method for extracting obscured crystallographic states from conventionally uninterpretable electron density. *Nat. Commun.* **2017**, *8*, 15123. [[CrossRef](#)] [[PubMed](#)]
81. FragMAX-BioMAX Fragment Screening Platform. Available online: <https://maxiv.lu.se/accelerators-beamlines/beamlines/biomax/user-access/fragmax-biomax-fragment-screening-platform/> (accessed on 11 November 2019).
82. Dias, D.M.; Ciulli, A. NMR approaches in structure-based lead discovery: Recent developments and new frontiers for targeting multi-protein complexes. *Prog. Biophys. Mol. Biol.* **2014**, *116*, 101–112. [[CrossRef](#)] [[PubMed](#)]
83. Harner, M.J.; Frank, A.O.; Fesik, S.W. Fragment-based drug discovery using NMR spectroscopy. *J. Biomol. NMR* **2013**, *56*, 65–75. [[CrossRef](#)] [[PubMed](#)]

84. Aguirre, C.; ten Brink, T.; Guichou, J.-F.; Cala, O.; Krimm, I. Comparing binding modes of analogous fragments using NMR in fragment-based drug design: Application to PRDX5. *PLoS ONE* **2014**, *9*, e102300. [[CrossRef](#)] [[PubMed](#)]
85. Grant, D.M.; Harris, R.K. *Encyclopedia of Magnetic Resonance EMR*; Wiley InterScience: New York, NY, USA, 2007; ISBN 9780470034590.
86. Cala, O.; Krimm, I. Ligand-Orientation Based Fragment Selection in STD NMR Screening. *J. Med. Chem.* **2015**, *58*, 8739–8742. [[CrossRef](#)] [[PubMed](#)]
87. Viegas, A.; Manso, J.; Nobrega, F.L.; Cabrita, E.J. Saturation-Transfer Difference (STD) NMR: A Simple and Fast Method for Ligand Screening and Characterization of Protein Binding. *J. Chem. Educ.* **2011**, *88*, 990–994. [[CrossRef](#)]
88. Bhunia, A.; Bhattacharjya, S.; Chatterjee, S. Applications of saturation transfer difference NMR in biological systems. *Drug Discov. Today* **2012**, *17*, 505–513. [[CrossRef](#)]
89. Williamson, M.P. Using chemical shift perturbation to characterise ligand binding. *Prog. Nucl. Magn. Reson. Spectrosc.* **2013**, *73*, 1–16. [[CrossRef](#)]
90. Pellecchia, M.; Sem, D.S.; Wüthrich, K. Nmr in drug discovery. *Nat. Rev. Drug Discov.* **2002**, *1*, 211. [[CrossRef](#)]
91. Arntson, K.E.; Pomerantz, W.C.K. Protein-Observed Fluorine NMR: A Bioorthogonal Approach for Small Molecule Discovery. *J. Med. Chem.* **2016**, *59*, 5158–5171. [[CrossRef](#)]
92. Okaru, A.O.; Brunner, T.S.; Ackermann, S.M.; Kuballa, T.; Walch, S.G.; Kohl-Himmelseher, M.; Lachenmeier, D.W. Application of ¹⁹F NMR Spectroscopy for Content Determination of Fluorinated Pharmaceuticals. *J. Anal. Methods Chem.* **2017**, 2017. [[CrossRef](#)] [[PubMed](#)]
93. Tengel, T.; Fex, T.; Emtenas, H.; Almqvist, F.; Sethson, I.; Kihlberg, J. Use of ¹⁹F NMR spectroscopy to screen chemical libraries for ligands that bind to proteins. *Org. Biomol. Chem.* **2004**, *2*, 725–731. [[CrossRef](#)] [[PubMed](#)]
94. Martino, R.; Gilard, V.; Desmoulin, F.; Malet-Martino, M. Interest of fluorine-19 nuclear magnetic resonance spectroscopy in the detection, identification and quantification of metabolites of anticancer and antifungal fluoropyrimidine drugs in human biofluids. *Chemotherapy* **2006**, *52*, 215–219. [[CrossRef](#)] [[PubMed](#)]
95. Vulpetti, A.; Dalvit, C. Design and generation of highly diverse fluorinated fragment libraries and their efficient screening with improved (¹⁹F) NMR methodology. *ChemMedChem* **2013**, *8*, 2057–2069. [[CrossRef](#)]
96. Leavitt, S.; Freire, E. Direct measurement of protein binding energetics by isothermal titration calorimetry. *Curr. Opin. Struct. Biol.* **2001**, *11*, 560–566. [[CrossRef](#)]
97. Damian, L. Isothermal titration calorimetry for studying protein-ligand interactions. *Methods Mol. Biol.* **2013**, *1008*, 103–118. [[CrossRef](#)]
98. Ward, W.H.J.; Holdgate, G.A. 7 Isothermal Titration Calorimetry in Drug Discovery. In *Progress in Medicinal Chemistry*; King, F.D., Oxford, A.W., Eds.; Elsevier: Amsterdam, The Netherlands, 2001; pp. 309–376, ISBN 9780444506368.
99. Wiseman, T.; Williston, S.; Brandts, J.F.; Lin, L.N. Rapid measurement of binding constants and heats of binding using a new titration calorimeter. *Anal. Biochem.* **1989**, *179*, 131–137. [[CrossRef](#)]
100. Schönauer, E.; Kany, A.M.; Hauptenthal, J.; Hüsecken, K.; Hoppe, I.J.; Voos, K.; Yahiaoui, S.; Elsässer, B.; Ducho, C.; Brandstetter, H.; et al. Discovery of a Potent Inhibitor Class with High Selectivity toward Clostridial Collagenases. *J. Am. Chem. Soc.* **2017**, *139*, 12696–12703. [[CrossRef](#)]
101. Ferenczy, G.G.; Keserü, G.M. Thermodynamics of fragment binding. *J. Chem. Inf. Model.* **2012**, *52*, 1039–1045. [[CrossRef](#)]
102. Williams, G.; Ferenczy, G.G.; Ulander, J.; Keserü, G.M. Binding thermodynamics discriminates fragments from druglike compounds: A thermodynamic description of fragment-based drug discovery. *Drug Discov. Today* **2017**, *22*, 681–689. [[CrossRef](#)]
103. Rees, D. Fragment-based Drug Discovery: Lessons and Outlook. Edited by Daniel, A. Erlanson and Wolfgang Jahnke; Series Editors: Raimund Mannhold, Hugo Kubinyi, and Gerd Folkers. *ChemMedChem* **2016**, *11*, 1667. [[CrossRef](#)]
104. Torres, F.E.; Recht, M.I.; Coyle, J.E.; Bruce, R.H.; Williams, G. Higher throughput calorimetry: Opportunities, approaches and challenges. *Curr. Opin. Struct. Biol.* **2010**, *20*, 598–605. [[CrossRef](#)] [[PubMed](#)]
105. Murray, C.W.; Verdonk, M.L. Entropic consequences of linking ligands. In *Fragment-Based Approaches in Drug Discovery*; WILEY-VCH: Weinheim, Germany, 2006; ISBN 9783527312917.
106. Davis, B.J.; Erlanson, D.A. Learning from our mistakes: The ‘unknown knowns’ in fragment screening. *Bioorg. Med. Chem. Lett.* **2013**, *23*, 2844–2852. [[CrossRef](#)] [[PubMed](#)]

107. Abdiche, Y.; Malashock, D.; Pinkerton, A.; Pons, J. Determining kinetics and affinities of protein interactions using a parallel real-time label-free biosensor, the Octet. *Anal. Biochem.* **2008**, *377*, 209–217. [[CrossRef](#)] [[PubMed](#)]
108. Kamat, V.; Rafique, A. Designing binding kinetic assay on the bio-layer interferometry (BLI) biosensor to characterize antibody-antigen interactions. *Anal. Biochem.* **2017**, *536*, 16–31. [[CrossRef](#)]
109. Yu, Y.; Mitchell, S.; Lynaugh, H.; Brown, M.; Nobrega, R.P.; Zhi, X.; Sun, T.; Caffry, I.; Cao, Y.; Yang, R.; et al. Understanding ForteBio's Sensors for High-Throughput Kinetic and Epitope Screening for Purified Antibodies and Yeast Culture Supernatant. *J. Biomol. Screen.* **2016**, *21*, 88–95. [[CrossRef](#)]
110. Hopkins, A.L.; Groom, C.R.; Alex, A. Ligand efficiency: A useful metric for lead selection. *Drug Discov. Today* **2004**, *9*, 430–431. [[CrossRef](#)]
111. Shultz, M.D. Setting expectations in molecular optimizations: Strengths and limitations of commonly used composite parameters. *Bioorg. Med. Chem. Lett.* **2013**, *23*, 5980–5991. [[CrossRef](#)]
112. Mortenson, P.N.; Murray, C.W. Assessing the lipophilicity of fragments and early hits. *J. Comput. Aided Mol. Des.* **2011**, *25*, 663–667. [[CrossRef](#)]
113. Marion, D. An introduction to biological NMR spectroscopy. *Mol. Cell. Proteomics* **2013**, *12*, 3006–3025. [[CrossRef](#)]
114. Storz, M.P.; Brengel, C.; Weidel, E.; Hoffmann, M.; Hollemeyer, K.; Steinbach, A.; Müller, R.; Empting, M.; Hartmann, R.W. Biochemical and biophysical analysis of a chiral PqsD inhibitor revealing tight-binding behavior and enantiomers with contrary thermodynamic signatures. *ACS Chem. Biol.* **2013**, *8*, 2794–2801. [[CrossRef](#)] [[PubMed](#)]
115. Storz, M.P.; Maurer, C.K.; Zimmer, C.; Wagner, N.; Brengel, C.; de Jong, J.C.; Lucas, S.; Müsken, M.; Häussler, S.; Steinbach, A.; et al. Validation of PqsD as an anti-biofilm target in *Pseudomonas aeruginosa* by development of small-molecule inhibitors. *J. Am. Chem. Soc.* **2012**, *134*, 16143–16146. [[CrossRef](#)] [[PubMed](#)]
116. Allegretta, G.; Weidel, E.; Empting, M.; Hartmann, R.W. Catechol-based substrates of chalcone synthase as a scaffold for novel inhibitors of PqsD. *Eur. J. Med. Chem.* **2015**, *90*, 351–359. [[CrossRef](#)]
117. Weidel, E.; Negri, M.; Empting, M.; Hinsberger, S.; Hartmann, R.W. Composing compound libraries for hit discovery—rationality-driven preselection or random choice by structural diversity? *Future Med. Chem.* **2014**, *6*, 2057–2072. [[CrossRef](#)] [[PubMed](#)]
118. Cohen, S.M. A Bioinorganic Approach to Fragment-Based Drug Discovery Targeting Metalloenzymes. *Acc. Chem. Res.* **2017**, *50*, 2007–2016. [[CrossRef](#)] [[PubMed](#)]
119. Ciulli, A.; Abell, C. Fragment-based approaches to enzyme inhibition. *Curr. Opin. Biotechnol.* **2007**, *18*, 489–496. [[CrossRef](#)]
120. Ciulli, A.; Williams, G.; Smith, A.G.; Blundell, T.L.; Abell, C. Probing hot spots at protein-ligand binding sites: A fragment-based approach using biophysical methods. *J. Med. Chem.* **2006**, *49*, 4992–5000. [[CrossRef](#)]
121. Landon, M.R.; Lancia, D.R.; Yu, J.; Thiel, S.C.; Vajda, S. Identification of hot spots within druggable binding regions by computational solvent mapping of proteins. *J. Med. Chem.* **2007**, *50*, 1231–1240. [[CrossRef](#)]
122. Deng, G.; Gu, R.-F.; Marmor, S.; Fisher, S.L.; Jahic, H.; Sanyal, G. Development of an LC-MS based enzyme activity assay for MurC: Application to evaluation of inhibitors and kinetic analysis. *J. Pharm. Biomed. Anal.* **2004**, *35*, 817–828. [[CrossRef](#)]
123. Sundberg, S. High-throughput and ultra-high-throughput screening: Solution- and cell-based approaches. *Curr. Opin. Biotechnol.* **2000**, *11*, 47–53. [[CrossRef](#)]
124. Moreno, A.; Kuzmiak-Glancy, S.; Jaimes, R.; Kay, M.W. Enzyme-dependent fluorescence recovery of NADH after photobleaching to assess dehydrogenase activity of isolated perfused hearts. *Sci. Rep.* **2017**, *7*, 45744. [[CrossRef](#)] [[PubMed](#)]
125. Combs, C.A.; Balaban, R.S. Direct Imaging of Dehydrogenase Activity within Living Cells Using Enzyme-Dependent Fluorescence Recovery after Photobleaching (ED-FRAP). *Biophys. J.* **2001**, *80*, 2018–2028. [[CrossRef](#)]
126. Fahs, S.; Lujan, P.; Köhn, M. Approaches to Study Phosphatases. *ACS Chem. Biol.* **2016**, *11*, 2944–2961. [[CrossRef](#)] [[PubMed](#)]
127. Kirsch, P.; Jakob, V.; Oberhausen, K.; Stein, S.C.; Cucarro, I.; Schulz, T.F.; Empting, M. Fragment-Based Discovery of a Qualified Hit Targeting the Latency-Associated Nuclear Antigen of the Oncogenic Kaposi's Sarcoma-Associated Herpesvirus/Human Herpesvirus 8. *J. Med. Chem.* **2019**, *62*, 3924–3939. [[CrossRef](#)] [[PubMed](#)]

128. Sahner, J.H.; Brengel, C.; Storz, M.P.; Groh, M.; Plaza, A.; Müller, R.; Hartmann, R.W. Combining in silico and biophysical methods for the development of *Pseudomonas aeruginosa* quorum sensing inhibitors: An alternative approach for structure-based drug design. *J. Med. Chem.* **2013**, *56*, 8656–8664. [[CrossRef](#)] [[PubMed](#)]
129. Sahner, J.H.; Empting, M.; Kamal, A.; Weidel, E.; Groh, M.; Börger, C.; Hartmann, R.W. Exploring the chemical space of ureidothiophene-2-carboxylic acids as inhibitors of the quorum sensing enzyme PqsD from *Pseudomonas aeruginosa*. *Eur. J. Med. Chem.* **2015**, *96*, 14–21. [[CrossRef](#)]
130. Murray, C.W.; Verdonk, M.L. The consequences of translational and rotational entropy lost by small molecules on binding to proteins. *J. Comput. Aided Mol. Des.* **2002**, *16*, 741–753. [[CrossRef](#)]
131. Mondal, M.; Radeva, N.; Fanlo-Virgós, H.; Otto, S.; Klebe, G.; Hirsch, A.K.H. Fragment Linking and Optimization of Inhibitors of the Aspartic Protease Endothiapepsin: Fragment-Based Drug Design Facilitated by Dynamic Combinatorial Chemistry. *Angew. Chem. Int. Ed. Engl.* **2016**, *55*, 9422–9426. [[CrossRef](#)]
132. Mondal, M.; Hirsch, A.K.H. Dynamic combinatorial chemistry: A tool to facilitate the identification of inhibitors for protein targets. *Chem. Soc. Rev.* **2015**, *44*, 2455–2488. [[CrossRef](#)]
133. Frei, P.; Hevey, R.; Ernst, B. Dynamic Combinatorial Chemistry: A New Methodology Comes of Age. *Chemistry* **2019**, *25*, 60–73. [[CrossRef](#)]



© 2019 by the authors. Licensee MDPI, Basel, Switzerland. This article is an open access article distributed under the terms and conditions of the Creative Commons Attribution (CC BY) license (<http://creativecommons.org/licenses/by/4.0/>).

2 Aim and Scope

The options of a therapeutic treatment against KSHV and KSHV-associated diseases is still very limited.⁵³ Today's therapeutic approaches range from no treatment to the application of different chemotherapeutic agents, radiotherapy or surgical excision of the lesions.⁵⁴ Importantly, a specific treatment, which can interfere with the latent phase of the KSHV life cycle is not available, yet. This means, KSHV is a disease, which is currently still incurable and therefore innovative anti-KSHV drugs are urgently needed.

The objective of this thesis was the discovery of the first LANA-DNA interaction inhibitors. This should be achieved by using two different approaches and a subsequent hit-to-lead optimization of a qualified LANA-DNA inhibitor.

In the first part of this work, a fragment-based approach should be used to identify first LANA-DNA interaction inhibitors. In a previous work at HIPS-DDOP, a fragment library was screened using SPR and DSF screening methods (see section 1.7) to identify first LANA binders. Additionally, a functional fluorescence polarization-based LANA-DNA interaction inhibition assay was established. The aim of this work was the functional evaluation and medicinal chemistry optimization of hit compounds. Furthermore, the design and synthesis of more potent as well as establishment of a structure-activity-relationships were additional goals. The most active compounds should be further characterized and prioritized through biophysical and biochemical characterization using different techniques such as electrophoretic mobility shift assay (EMSA), microscale thermophoresis (MST) and saturation transfer difference (STD) NMR. These efforts are shown in Chapter 3.1.

In the second part of this work, the in-house HIPS library should be employed to identify further LANA-DNA interaction inhibitors. For a first selection the fluorescence polarization-based LANA-DNA interaction inhibition assay should be used to perform a functional screening. Further work aimed at the biological and biophysical characterization and prioritization of selected hit compounds. The results were described in Chapter 3.2.

The third part of this work covered hit-to-lead optimization studies of the best and most promising LANA inhibitor, which resulted from the previous fragment-based approach (Chapter 3.1). As co-crystal structures of inhibitors in complex with LANA were not available, a rational ligand-based design should be used for medicinal chemistry optimization. The synthetic efforts towards successful fragment growing delivered new and more potent structures as demonstrated by functional as well as biochemical and biophysical evaluation. The optimization efforts are described in Chapter 3.3.

3 Results

3.1 Chapter A: Fragment-Based Discovery of first KSHV-LANA Inhibitors

Title:

Fragment-Based Discovery of a Qualified Hit Targeting the Latency-Associated Nuclear Antigen of the Oncogenic Kaposi's Sarcoma-Associated Herpesvirus/Human Herpesvirus 8

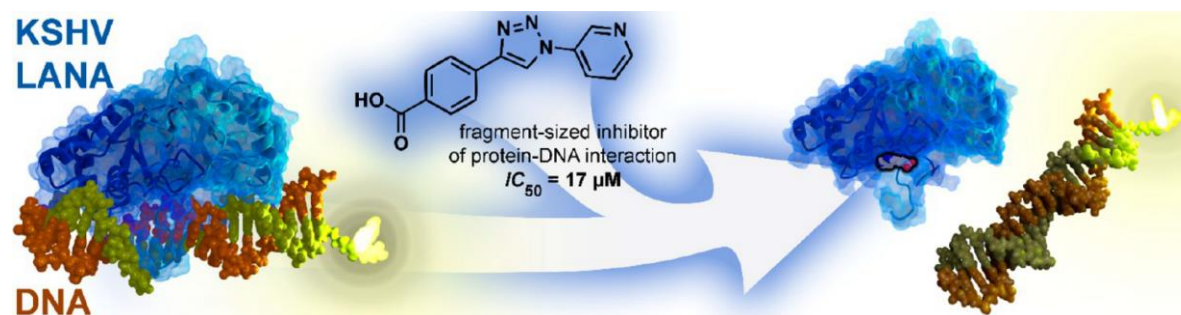
Authors:

Philine Kirsch, Valentin Jakob, Kevin Oberhausen, Saskia C. Stein, Ivano Cuccaro, Thomas F. Schulz and Martin Empting

Bibliographic Data:

Journal of Medicinal Chemistry,
Volume 8, Issue 62, Pages 3924-3939,
March 19, 2019,
Doi: 10.1021/acs.jmedchem.8b01827

Graphical Abstract:



Fragment-Based Discovery of a Qualified Hit Targeting the Latency-Associated Nuclear Antigen of the Oncogenic Kaposi's Sarcoma-Associated Herpesvirus/Human Herpesvirus 8

Philine Kirsch,^{‡,§,||} Valentin Jakob,^{‡,§} Kevin Oberhausen,^{‡,§} Saskia C. Stein,^{||,⊥} Ivano Cucarro,^{‡,§} Thomas F. Schulz,^{||,⊥} and Martin Empting^{*,‡,§,||}

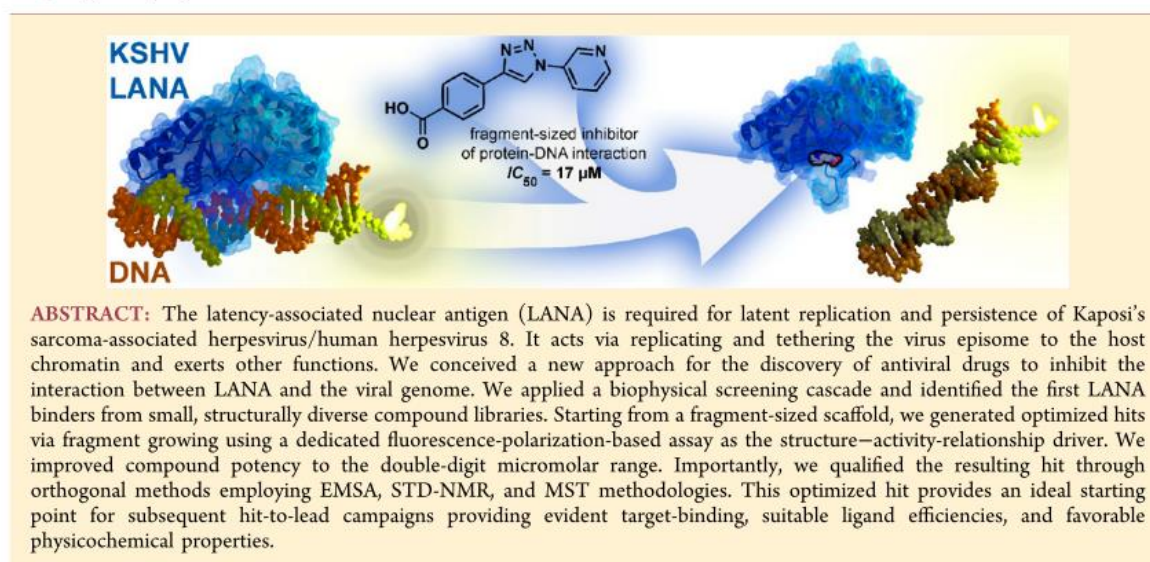
[‡]Department of Drug Design and Optimization (DDOP), Helmholtz-Institute for Pharmaceutical Research Saarland (HIPS)-Helmholtz Centre for Infection Research (HZI), Campus E8.1, 66123 Saarbrücken, Germany

[§]Department of Pharmacy, Saarland University, Campus E8.1, 66123 Saarbrücken, Germany

^{||}German Centre for Infection Research (DZIF), Partner Site Hannover-Braunschweig, 66123 Saarbrücken, Germany

[⊥]Institute of Virology, Hannover Medical School, Carl-Neuberg-Strasse 1, 30625 Hannover, Germany

 Supporting Information



INTRODUCTION

Kaposi's sarcoma-associated herpesvirus (KSHV; taxonomic name human herpesvirus 8) is a human gammaherpesvirus and is classified as a carcinogenic agent Group I by the World Health Organization.^{1,2} It was identified as the etiological agent of Kaposi sarcoma (KS) and lymphoproliferative disorders. After a first infection, it establishes a lifelong latent infection in the host organism. KSHV is usually not pathogenic in healthy individuals, but AIDS-related Kaposi's sarcoma (AIDS-KS), KS in transplant recipients, and endemic KS in East/Central Africa cause significant morbidity and mortality in affected patients.³ In latently infected cells, KSHV expresses only a limited set of proteins, which are important for its persistence. One of these is the latency-associated nuclear antigen (ORF73/LANA).^{4,5} LANA plays an important role for the latency and regulation of the viral genome in the host organism. Previous studies have shown that LANA exerts several functions in the host cell like

cell survival, transcriptional control, latent viral DNA replication, and stable episome segregation during mitosis.⁶ The C-terminal domain of LANA binds to the terminal repeat (TR) region of the viral genome in a sequence-specific manner.^{7,2} The TR consists of three adjacent LANA binding sites (LBS), which are referred to as LBS1, LBS2, and LBS3 (Figures 1 and 2).⁷ The N-terminal domain of LANA is very poorly structured and is tethered to the host nucleosome.^{8,9} It is separated by a large internal repeat sequence from the C-terminal DNA-binding domain (Figure 1).^{10,11}

To date, the options for treating KSHV-associated diseases are limited.¹² While several inhibitors of herpesviral DNA polymerases are active against KSHV productive replication, they are not effective against KS or other KSHV associated

Received: November 22, 2018

Published: March 19, 2019

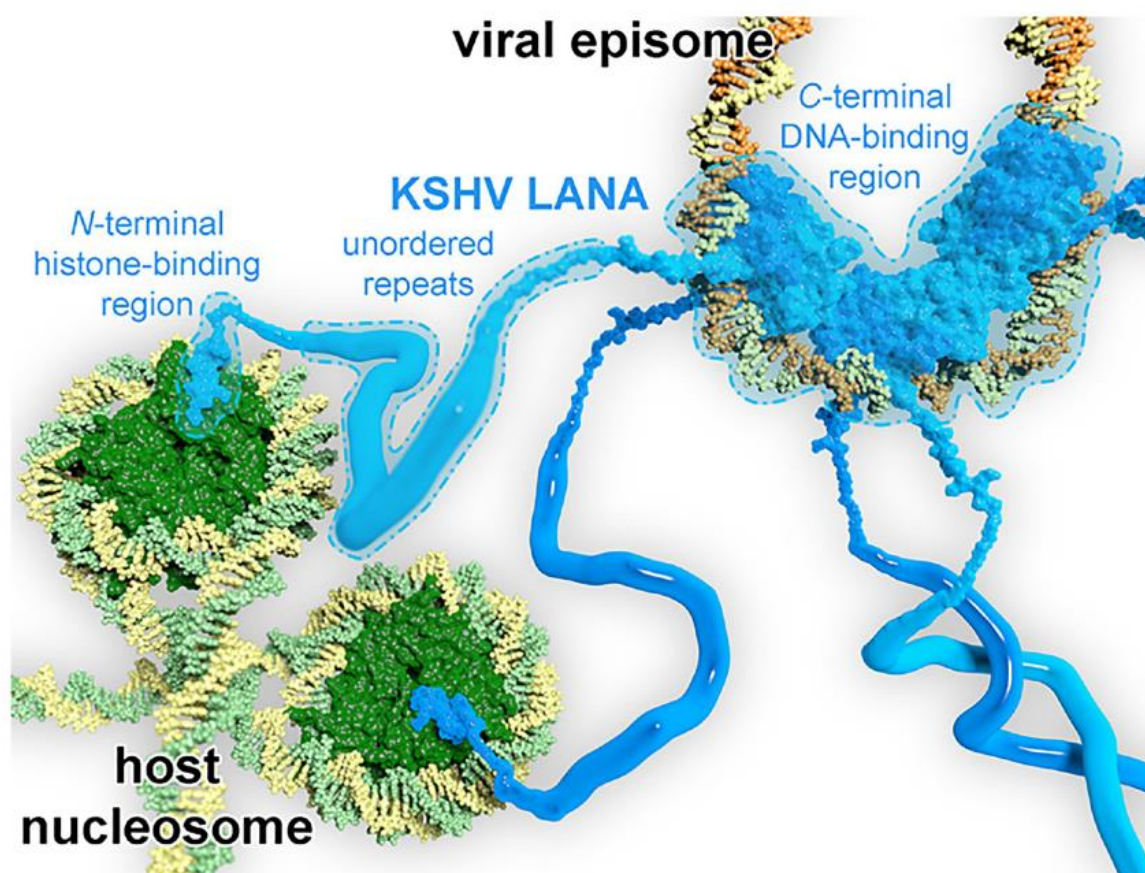


Figure 1. Illustration of molecular interactions between KSHV LANA, viral episome, and host nucleosome, rationalizing the C-terminal DNA-binding domain of KSHV LANA as an antiviral drug target as it links viral DNA (yellow and orange) to host histones (dark green) and attached host DNA (yellow and green). Three KSHV LANA dimers (blue) are shown, and unordered repeats are displayed as tubes. Illustration was modeled using coordinates of PDB entries 1zla, 4uzb, and 4uzc.

malignancies.¹² LANA represents a very promising target for the discovery and development of new anti-KSHV drugs that, in contrast to currently available compounds, would interfere with the latent phase of the viral life cycle. Based on the knowledge that LANA is involved in binding to viral latent episomal DNA and tethering it to host nucleosomes^{7,6} we conceived a new approach for the discovery of specific KSHV inhibitors. Our concept aims at the inhibition of the interaction between LANA and the viral genome. This should ultimately prevent latent persistence of KSHV, which could result in the gradual loss of infected cells and in a decrease in viral load in infected individuals. In the present work, we present our efforts to exploit this strategy through identification of the first functional LANA–DNA-interaction inhibitors by using fragment-based drug design. As a first step, we made use of different biological and biophysical methods to screen fragment libraries for identification of LANA binders. Subsequently, we established a fluorescence polarization (FP)-based assay to determine the inhibitory activities of our hits, and we used it for further optimization steps. Furthermore, we confirmed target binding of our best compound via orthogonal assays using saturation-transfer difference (STD) NMR and microscale thermophoresis

(MST) methodologies. Finally, we qualified the optimized hit scaffold for future lead-generation campaigns in an orthogonal interaction inhibition assay, namely, the electrophoretic mobility shift assay (EMSA). This provides an ideal starting point for subsequent medicinal chemistry efforts toward specific anti-KSHV agents. To the best of our knowledge, this study is the first report of inhibitors targeting the DNA-binding domain of LANA. A similar approach, however, has been previously applied to the EBNA1 protein, the functional homologue of LANA in Epstein–Barr virus (EBV).¹³ However, these conceptually related studies as well as experiments with a DNA-binding site mutant of LANA provide a sufficient basis for the validity of this antiviral drug target.¹⁴

RESULTS AND DISCUSSION

Screening and Hit Identification. To discover the first small molecules that can bind to LANA, we used orthogonal biophysical methods to screen two different small-molecule libraries from synthetic and natural sources.^{15,16} For the primary selection, we used two protein binding assays, surface plasmon resonance (SPR) and differential scanning fluorimetry (DSF), due to their high sensitivity and low protein

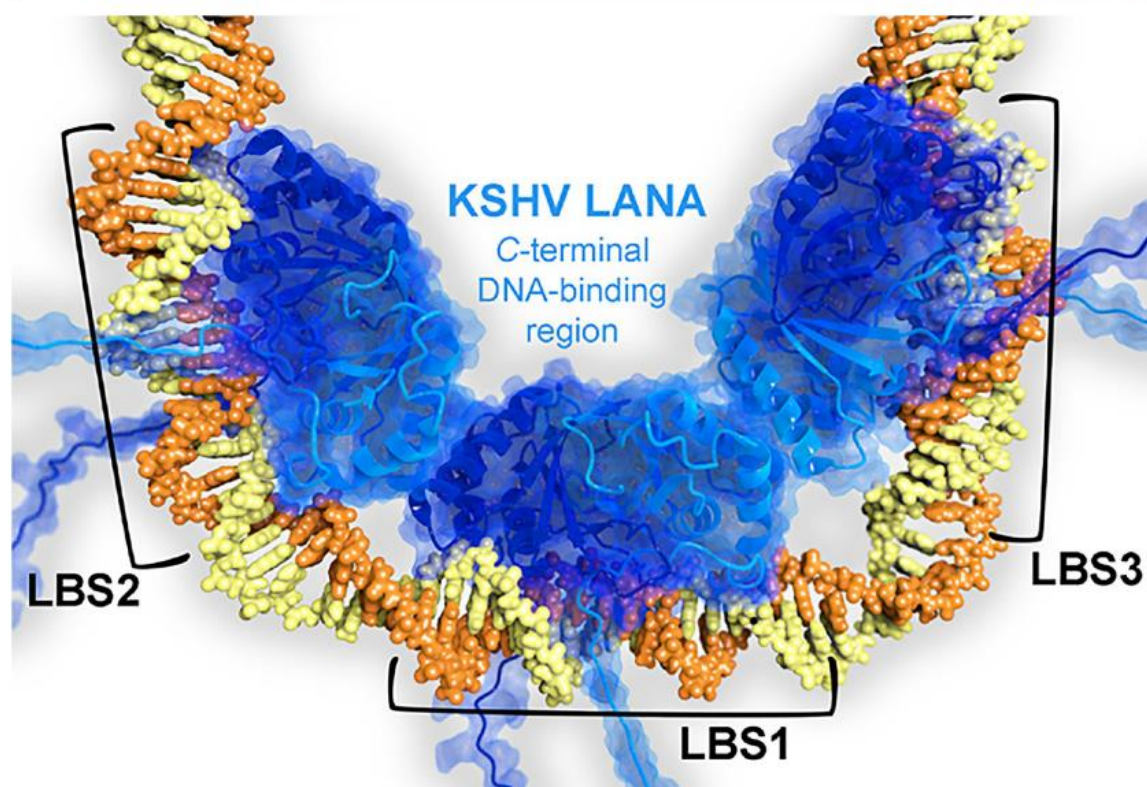


Figure 2. Model of the C-terminal DNA-binding domain of three KSHV dimers bound to adjacent LANA-binding sites LBS1, 2, and 3. Protein chains are shown as ribbon representations (chain A: blue, chain B: light blue). Viral DNA (yellow orange) is shown in space-filling representation. The model was generated using pdb entries 4uzb and 4uzc.

consumption. First, we conducted SPR screening at a constant concentration to preselected putative LANA binders. Subsequently, we applied DSF (thermal shift assay, TSA) as a secondary filter.

This methodology enabled us to select 20 compounds for further testing. In order to test for functionalities of our LANA binders *in vitro*, we established an FP-based assay, which allows for the quantitative evaluation of the LANA–DNA interaction and its inhibition by small molecules. In this manner, we identified three promising small molecule hit scaffolds for further consideration. In this report, we will focus on our hit optimization efforts, starting from the fragment-sized hit **1** (Figure 3).

SPR- and DSF-Based Primary Screening. Two different libraries, containing a total of 720 highly structurally diverse hit-like small molecules with molecular weights below 398 g/mol, were screened.^{15,16} We started with SPR spectroscopy using the wild-type LANA C-terminal domain (CTD) as the ligand and the library compounds at a constant concentration of 500 μ M. Compounds that showed a response higher than 9 μ -refractive index units were selected from this screening, which yielded 52 primary binders (for detailed results, see the Supporting Information Figure S1). In a second step, we employed DSF experiments as a secondary filter. This assay quantifies a change in thermal denaturation temperature of the wild-type LANA C-terminal domain by binding to a compound. Generally, an increase of melting temperature

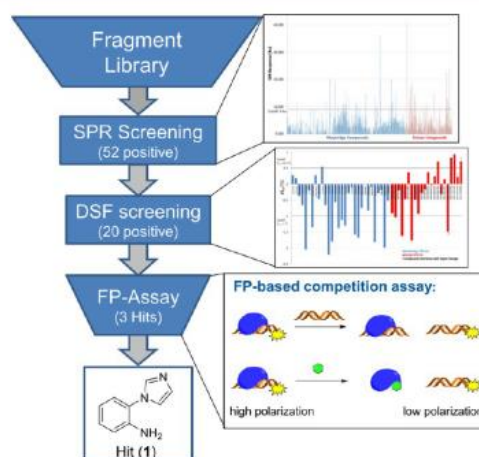
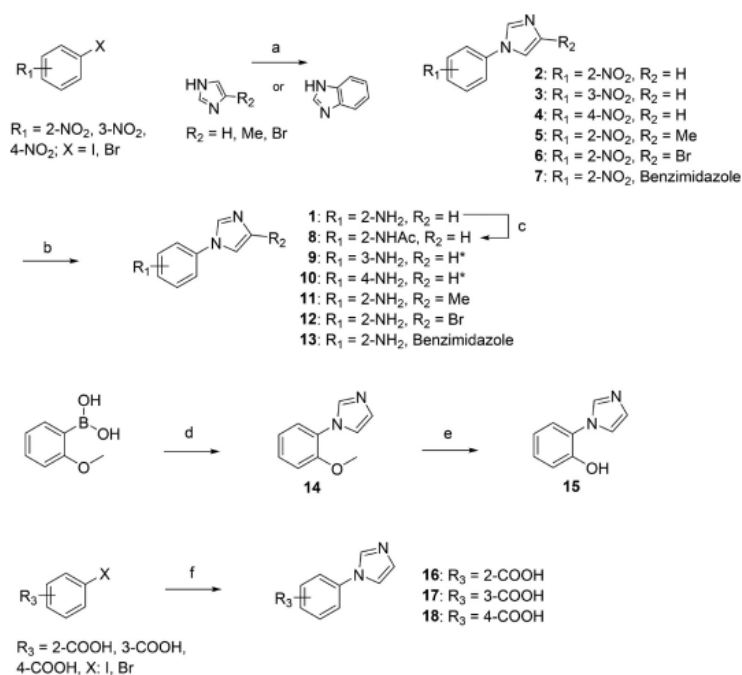


Figure 3. Screening procedure using two different fragment libraries targeting LANA. In total, 720 compounds were screened using SPR experiments, followed by DSF. An FP-based assay was used to identify promising interaction inhibitors, which resulted in three promising hits.

indicates a stabilization of the protein due to binding of a small molecule. Our experiments showed for almost all compounds a decrease in melting temperature for LANA. A decrease of

Scheme 1. Synthesis of Hit 1 and 1*H*-Imidazole-1-yl Derivatives^a

^aReagents and conditions: (a) K_3PO_4 , CuI abs. DMF, 110 °C, 24 h; (b) SnCl_2 , EtOH, 80 °C, 30 min; (c) H_2SO_4 , AcOH, Ac_2O , rt, 16 h; (d) imidazole, CuCl, MeOH, 80 °C, 16 h; (e) 48% aq HBr, 100 °C, 16 h; (f) K_2CO_3 , CuCl, N,N' -dimethylmethanediamine, DMF, 120 °C, 24 h.

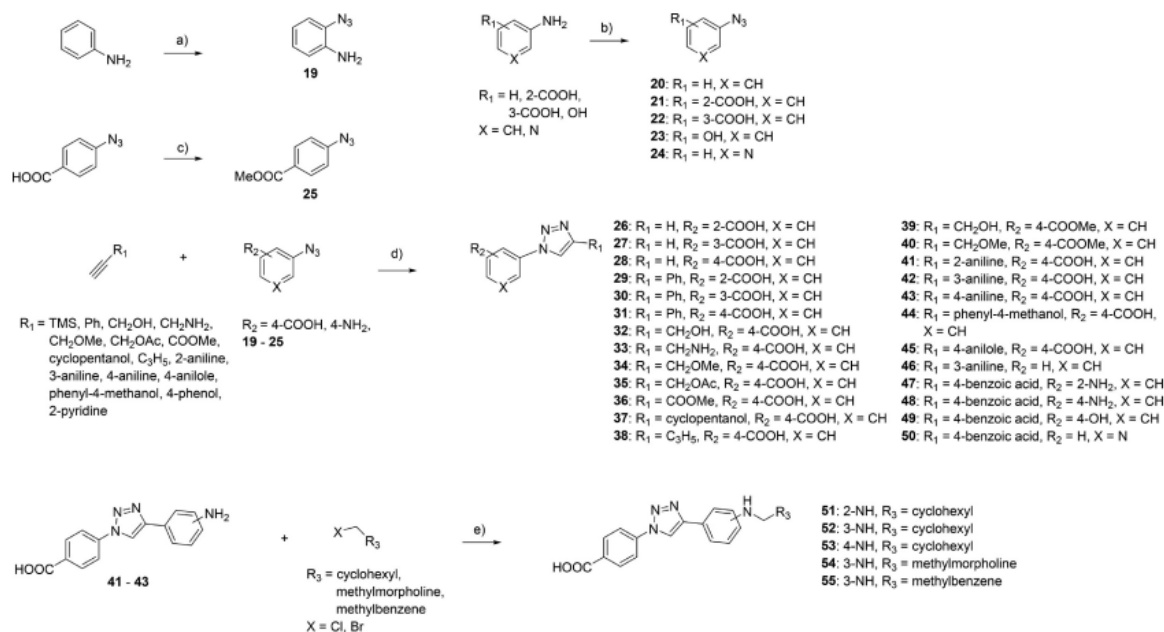
melting temperature may indicate a destabilization of the protein by compound binding. Although usually an increase in protein stability and, thus, increase in melting temperature are observed for target binders, also negative shifts are commonly considered as binding events.¹⁷ As a consequence, we selected 20 compounds that showed significant thermal shifts $T_M \geq +0.5$ °C and $T_M \leq -1.0$ °C for further investigations (for detailed results see the Supporting Information, Figure S2).

Establishment of FP Assay. For further characterization and optimization, our compounds were tested for inhibition of the DNA–LANA interaction using an FP-based competition assay. The FP assay is a rapid and quantitative method for identification of small molecular macromolecule–macromolecule interaction inhibitors.¹⁸ For this process we used a mutant of the KSHV LANA C-terminal DNA-binding domain (DBD) (aa1008-1146) that lacked the ability to form oligomers of LANA DBD dimers.⁷ In previous studies it was observed that the wild-type LANA C-terminal domain (LANA CTD (aa934-1162)) precipitated readily following the addition of either specific or unspecific DNA.¹⁹ It has the ability to form higher-order oligomers, which contribute to the low solubility in the presence of DNA. For avoiding these solubility problems, multiple point mutations were inserted into the basic patch and the oligomerization interface of LANA DBD; none of these mutations are located at the specific DNA-binding site of LANA, while the basic patch mutations suppress unspecific DNA binding. This C-terminal LANA mutant with the amino acid mutations K1055E, K1138S, K1140D, K1141D, R1039Q, R1040Q, A1121E, K1109A, and D1110A shows a high solubility also in the presence of oligonucleotides representing

the viral LANA-binding sites (LBS) in the viral terminal repeat subunit.^{19,7,14}

A fluorescence-labeled DNA sequence was employed as a competitive binding partner, which corresponds to LANA-binding site 2 (LBS2) in a KSHV terminal repeat subunit.⁷ We chose LBS2 as the fluorescence probe because of its lower affinity for the LANA DBD and used varying concentrations of unlabeled LBS1, LBS2, and LBS3 to validate and optimize our assay conditions (see the Supporting Information, Figures S3 and S4). In accordance with previous reports, we obtained a difference in affinity between the LBS sequences.⁷

FP-Based Functional Screening. In order to assess the effect of identified screening hits on LANA–DNA-interaction inhibition we tested them in our FP-based assay using LBS2 as the fluorescent probe. Due to their high solubility, the compounds could be tested at high concentrations (1 mM or 500 μM), allowing for the identification of even weak inhibitory effects usually observed with fragment-like scaffolds. Each compound was measured in duplicate and in two independent experiments. Three of the 20 tested compounds showed promising results (Table S9, Supporting Information). In this paper we will present the hit optimization and validation for hit 1. Despite its fragment-like size with a molecular weight of only 159.08 g/mol, this compound showed an inhibitory effect of $25 \pm 9\%$ at 1 mM (Figure 3; SPR at 500 μM : 15.69 ± 9.3 RU; DSF at 500 μM : $T_M -1.80 \pm 1.41$ °C). Considering the large interaction site between LANA and its target DNA sequence, this result was promising and encouraged medicinal chemistry optimization of this fragment hit.

Scheme 2. Synthesis of Azide Intermediates and Reaction of Aryl Azides with Different Alkynes Using Click Chemistry and Derivatives^a

^aReagents and conditions: (a) TMSN_3 , CuBr, TBHP, MeCN, 0 °C \rightarrow rt, 16 h; (b) concd H_2SO_4 or concd HCl, NaNO_2 , NaN_3 , H_2O , 0 °C, 1.5 h; (c) SOCl_2 , MeOH, 0 °C \rightarrow rt, 16 h; (d) $\text{CuSO}_4 \cdot 5\text{H}_2\text{O}$, sodium ascorbate, $\text{H}_2\text{O}/\text{tert-BuOH}$ (1:1), DIPEA, rt, 16 h; (e) Cs_2CO_3 , DMF, 5 h, 90 °C.

The fragment-like structure of hit **1** provided reasonable opportunities for fragment-growing strategies toward generating drug like LANA–DNA inhibitors. Unfortunately, no X-ray or NMR structure was available when starting this hit optimization endeavor. Hence, structure-guided fragment-linking or -merging approaches were not feasible.

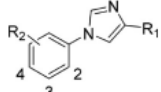
Chemistry. The synthesis of hit **1** was carried out starting from commercially available 2-iodonitrobenzene in two steps. Hit **1** and further imidazole derivatives **9–13** were synthesized via an Ullmann-type coupling reaction with a halogen nitrobenzene and the appropriate imidazole.²⁰ In a second step, the nitro group was reduced with tin(II) chloride to the amine to yield the target compounds **1** and **9–13**.²¹ The *N*-acetyl derivative **8** was obtained by acetylation with acetyl anhydride. Furthermore, the 2-methoxyphenyl imidazole (**14**) was synthesized via copper salt catalyzed coupling of imidazole with (2-methoxyphenyl)boronic acid²² and by cleaving the methyl group with aqueous HBr, affording the hydroxyl derivative **15**.²³ The synthesis of the benzoic acid derivatives was done by copper catalyzed coupling with the appropriate halo-benzoic acid and 1*H*-imidazole in a one-step reaction (Scheme 1).²⁴ Generation of 1-azidoaniline (**19**) was achieved by copper catalyzed C–H activation of aniline.²⁵ The azido intermediates (**20–24**) were synthesized from the corresponding anilines using standard azidation methods (concd H_2SO_4 or concd HCl, NaNO_2 , NaN_3 in H_2O).²⁶ Methyl azidobenzoate (**25**) was synthesized by activation with thionyl chloride followed by treatment with methanol.²⁷ The 1,2,3-triazoles (**26–50**) were synthesized using standard copper(I)-catalyzed click reaction conditions. The appropriate alkyne was dissolved in 1:1 *tert*-butanol/water and treated with DIPEA, $\text{CuSO}_4 \cdot 5\text{H}_2\text{O}$, and sodium ascorbate under an argon atmosphere,

followed by the addition of the corresponding azide. Amino-phenyl-substituted compounds (**51–55**) were synthesized from the appropriate amino-phenyl scaffold by treatment with different halogen alkyl analogues under basic conditions in DMF (Scheme 2).

Stepwise Hit Optimization and Biological Evaluation.

For measuring the inhibitory effect of our compounds, we performed dose–response experiments using constant concentrations of the mutated LANA DBD (aa1008–1146) and fluorescence-labeled LBS2 with varying concentrations of the test compound. To exclude false positives through interaction with DNA or via fluorescence quenching, we conducted the dose-dependent experiments with and without addition of LANA. We did not observe any noticeable assay-interfering effect for any of the compounds. The results obtained with our FP-based interaction inhibition assay are listed in Table 1.

The aim of this first series of derivatives was to identify possible growth vectors to increase size and potency of the compound. Hence, substituents at the imidazole (R_1) as well as the phenyl ring (R_2) were introduced. Notably, moieties of different sizes (**11–13**) were tolerated at R_1 . In particular, the methyl derivative **11** showed an improved inhibitory effect of $91 \pm 8\%$ at 1 mM. We concluded that position R_1 should be further explored (*vide infra*) as a possible growth vector. Regarding R_2 , we first varied the position of the amino group at the phenyl ring and investigated the effect of acetylation (compounds **8–10**). However, these modifications did not improve the inhibitory effect on the DNA–LANA interaction significantly. Hence, we introduced different hydrophilic moieties like nitro (**2–4**), methoxy (**14**), hydroxyl (**15**), and carboxy (**16–18**) groups instead. To our surprise, the presence of a carboxylic acid on the aromatic moiety was tolerated. For

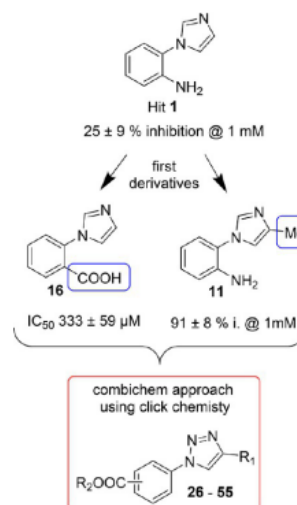
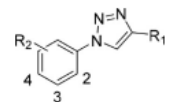
Table 1. Inhibitory Activities of 1*H*-Imidazole-1-yl Derivatives in FP Assay at 1 mM


Cpd	R ₁	R ₂	inhibition [%] at 1 mM or IC ₅₀ [μM] (LBS2)
1	H	2-NH ₂	25 ± 9 %
11	Me	2-NH ₂	91 ± 8 %
12	Br	2-NH ₂	13 ± 4 %
13	Benzimidazole	2-NH ₂	32 ± 9 %
8	H	2-NHAc	32 ± 16 %
9	H	3-NH ₂	n. i.
10	H	4-NH ₂	n. i.
2	H	2-NO ₂	74 ± 16 %
3	H	3-NO ₂	21 ± 16 %
4	H	4-NO ₂	22 ± 16 %
14	H	2-OMe	15 ± 12 %
15	H	2-OH	51 ± 13 %
16	H	2-COOH	333 ± 59 μM ^a
17	H	3-COOH	19 ± 9 %
18	H	4-COOH	13 ± 1 %

^aMaximum effect was 50% displacement.

compound **16** we were able to plot a full sigmoidal inhibition curve providing an IC₅₀ value of 333 ± 59 μM, with a restriction that the maximum effect leveled out at 50% displacement. Considering the rather basic interaction surface at the DNA-binding domain of LANA, the effectiveness of the acidic moiety in compound **16** was indeed a plausible finding in hindsight. Furthermore, it rendered an unfavorable compound–DNA interaction as the cause for the observed activity in the FP assay very unlikely.

These initial findings inspired us to conduct a combinatorial chemistry approach exploiting the copper(I)-catalyzed alkyne-azide cycloaddition as a straightforward synthetic method for the rapid generation of a reasonable number of new derivatives. This prototypic click chemistry provides very efficient and robust reactions under mild conditions and has become a powerful tool in drug discovery.²⁸ Assuming that the replacement of the imidazole moiety by a triazole core is tolerated, this strategy would dramatically accelerate the establishment of structure–activity relationships. Further considerations for the design of the click library were the envisioned fragment growth in the direction of residue R1 (Figure 4) as well as the switch from the amino to the carboxylic group in the western part of the molecule. Hence, we first checked whether this strategy was valid by synthesizing compounds **26–31** (Table 2).

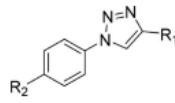
**Figure 4.** From our initial screening hit **1** first derivatizations lead to compounds **11** and **16**, which served as a starting point for a CombiChem approach using click chemistry.**Table 2.** Inhibition of the First Series of 1,2,3-Triazole Compounds in FP Assay


Cpd	R ₁	R ₂	IC ₅₀ (LBS2) [μM] or Inhibition [%] ^a
26	H	2-COOH	12 ± 10 %
27	H	3-COOH	98 ± 1 %
28	H	4-COOH	35 ± 3 %
29	Ph	2-COOH	13 ± 1 %
30	Ph	3-COOH	43 ± 17 %
31	Ph	4-COOH	232 ± 10 μM

^aInhibition (%) at 1 mM.

Indeed, by comparing the carboxylic acid imidazole compounds (**16–18**) and the carboxylic acid triazole analogues (**26–28**), the introduction of a 1,2,3-triazole was accepted, although the preference for the orientation of the carboxylic acid was shifted from position 2 to 3. This trend even continued when introducing a bulky phenyl moiety in the eastern part of the molecule (**29–31**). In this case, position 4 was favored for the carboxylic group implying a shift in interaction geometries and/or binding modes between LANA and the inhibitors when moving from imidazolyl to triazolyl to enlarged triazolyl compounds. Derivative **31** showed reasonable potency (IC₅₀ value of 232 ± 10 μM) with a significant improvement over inhibitor **16** and additionally provided the

Table 3. Inhibitory Activities of Further 1,2,3-Triazole Derivatives in FP Assay



Cpd	R ₁	R ₂	IC ₅₀ (LBS2) [μM]	Cpd	R ₁	R ₂	IC ₅₀ (LBS2) [μM]
32		COOH	79 ± 2	42		COOH	109 ± 3
33		COOH	30 ± 2	43		COOH	14 ± 1
34		COOH	210 ± 31	44		COOH	27 ± 4
35		COOH	n. i.	45		COOH	20 ± 3 % ^a
36		COOH	163 ± 30	46		H	n. i.
37		COOH	159 ± 2	51		COOH	n. i.
38		COOH	694 ± 41	52		COOH	n. i.
39		COOMe	84 ± 53	53		COOH	n. i.
40		COOMe	237 ± 33	54		COOH	n. i.
41		COOH	28 ± 1	55		COOH	n. i.

^aInhibition (%) at 500 μM.

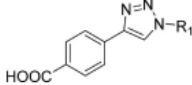
opportunity for further modifications replacing the newly introduced bulky phenyl ring. Consequently, we chose this scaffold as the basis for the click library design (Table 3) keeping the carboxylic acid in the *para* position at the aromatic ring in the western part and varying the substituents on the eastern side of the molecule.

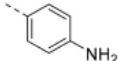
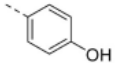
A rather general observation when varying the residue R₁ was that introducing hydrogen-bond-donating groups gave a boost in potency. In detail, direct attachment of a primary hydroxyl or amino group to the triazole core could improve the inhibitory effect by 3- to 4-fold (32: IC₅₀ 79 ± 2 μM, 33: IC₅₀ 30 ± 2 μM). A methyl ether (34) or methyl ester (36), on the other hand, showed just a small potency enhancement compared to compound 29, while the acetylated analogue 35 resulted in a complete loss of activity. Moving from the primary (32) to a tertiary alcohol (37) by addition of a cyclopentyl motif led to a decrease in activity. However, this derivative shows that obviously bulkier substituents could be tolerated at this position. Also, a rather hydrophobic cyclopropyl residue (38) did not yield a potent compound.

In parallel, we synthesized two additional compounds with a methyl ester instead of the carboxylic acid at the aromatic ring, 39 and 40. By comparing compound 32 with 39 and 34 with 40 it seems that also a methyl ester is well accepted, which certainly provides opportunities for future optimization efforts. Additionally, it becomes clear that the beneficial effect of the carboxylic group is not fully relying on a possible ionic interaction with the protein surface. As laid out above, our aim was to explore R₁ as a growth vector. Hence, we synthesized aniline derivatives (41–43). Introducing the amino group in the *ortho* (41) or *para* (43) position resulted in the most active compounds to date with IC₅₀ values in the low double-digit micromolar range. A loss of activity was observed with *m*-aniline (42) and *p*-anisole (45). Also, the phenyl methanol analogue (44) showed a rather potent IC₅₀ value of 27 ± 4 μM. Keeping the aniline residue and deleting the carboxylic acid at the aromatic region we observed a total loss in activity (46). In order to further grow the LANA inhibitor, compounds substituted at the aniline (51–55) were synthesized. Unfortunately, none of these derivatives were active regardless

of the position of the attached substituent. Probably these residues incorporated in 37–41 are too bulky and are, thus, not tolerated. Nevertheless, more research should be done in this area of the molecule when moving the project into the lead-generation phase. Finally, we synthesized a series of compounds with an inverted orientation of the 1,2,3-triazole core using 4-ethyl carboxylic acid and an array of azido benzenes. Compounds 47 and 48 were similar to the previous compounds 41 and 43 showing good IC_{50} values in the same range. Modifying the *para* aniline analogue to a *para* phenol (49) resulted in slight loss of activity. Besides that, for the 2-pyridine derivative 50 we observed an IC_{50} of $17 \pm 1 \mu M$ (Table 4).

Table 4. Inhibitory Activities of Compounds with Inverted Orientation of the 1,2,3-Triazole Core in FP Assay



Cpd	R ₁	IC_{50} (LBS2) [μM]
47		18 ± 3
48		19 ± 1
49		52 ± 3
50		17 ± 1

Qualification of Obtained Optimized Hits. *Comparison of the Inhibition of the Interaction between LANA and LBS1, 2, and 3.* In order to investigate whether inhibitors of the LANA–LBS2 interaction would also interfere with protein binding to the other LANA binding sites, we modified our FP assay protocol to also include labeled LBS1 and LBS3 sequences as fluorescent probes. We selected six compounds (37, 41–43, 47, 50) with differing activities against LBS2 for this assessment, and the determined IC_{50} values are summarized in Table 5. Notably, we observed IC_{50} values in a similar range compared to the inhibition against the LBS2 probe. Additionally, we calculated the log P value and the ligand efficiency (LE) for these compounds to provide a metric for comparing the most potent hits taking potency and molecular weight into account.²⁹ The log P value is defined as the partition coefficient of a given compound between octanol and water. It provides information about its hydrophobicity, and log P values below 3 are found generally in an aqueous medium (e.g. blood serum).³⁰ The LE value is defined as the binding energy of a compound for its target divided by its number of heavy atoms, and hence, it enables to identify those hits, which interact efficiently with most of their atoms. In practice, an LE of 0.3 or greater is considered to characterize a suitable hit for the optimization to a drug-like compound.³¹

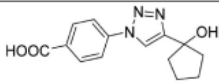
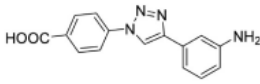
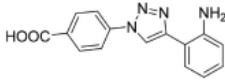
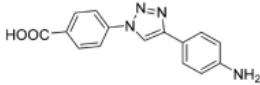
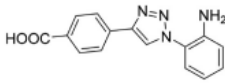
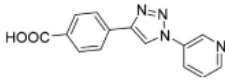
Notably, compounds 41, 43, 47, and 50 displayed an LE value of 0.3 or higher and log P values below 3, hence, are suitable scaffolds for further optimization efforts. Considering that these hits have to compete with a macromolecule (DNA) upon binding to a rather flat interaction surface, these results are encouraging.

EMSA (Electrophoretic Mobility Shift Assay) as Orthogonal Interaction Inhibition Assay. As an orthogonal interaction inhibition assay, EMSA was used to probe the ability of these six selected compounds to inhibit the DNA–LANA interaction (Figure 5). In this assay, solutions of protein, nucleic acid, and inhibitor were combined and the resulting mixtures were subjected to electrophoresis under native conditions.³² We evaluated the effects of the compounds using fixed concentrations of DNA probes of 20 nM, LANA DBD mutant of 200 nM, and compounds of 500 μM . The probes were Dy-682-modified, and a purified GST protein was used as the control. We performed the EMSA with two different DNA probes: An oligonucleotide representing only LBS1 for comparing the results with the results of our previous FP assay (Figure 5A) and a longer oligonucleotide containing both of the LBS1 and LBS2 sequences (Figure 5B). The latter also forms trimeric complexes with LANA (Supporting Information, Figure S6). In both experiments, we observed that the compounds with IC_{50} values in the triple-digit micromolar range have no specific effect on the DNA–LANA interaction at the concentration used. Importantly, the aniline analogue having an IC_{50} value in the lower double-digit micromolar range caused a significant decrease in the intensity of the DNA–LANA complexes and an increase in the intensity of the band representing the free DNA probe. This clearly indicated that these compounds inhibit the interaction of the LANA DBD mutant with LBS1 and/or LBS1 + 2.

The most effective inhibitor was the pyridine analogue (50, IC_{50} $17 \pm 1 \mu M$). The single LBS1 probe (Figure 5A) could be displaced almost completely and the combined LBS1–LBS2 probe (Figure 5B) to a significant extent. Additionally, we performed further dose-dependent EMSA experiments with the most efficient compound 50 using LBS1 as the probe and the LANA DBD mutant as well as the wild-type LANA C-terminal domain (CTD) (aa934–1162) as the protein (for more information see the Supporting Information, EMSA gels: Figures S9 and S10; calculated IC_{50} values see Figure S11, IC_{50} (LANA DBD mutant) $426 \pm 2 \mu M$ and IC_{50} (LANA CTD wild-type) $435 \pm 6 \mu M$).

MST and STD NMR Studies for Further Characterization of Ligand Binding. We used MST to quantify the binding affinity of compound 50 to the LANA DBD mutant and determined the dissociation constant K_D .³³ The binding assay was performed using the labeled LANA DBD mutant protein at a concentration of 50 nM and starting the dose–response curve with a ligand concentration of 1 mM. The calculated K_D for the binding of compound 50 to LANA was determined to be $23 \pm 1 \mu M$. The detected binding curve is shown in Figure 6A. We also attempted to perform crystallography on the LANA DBD–inhibitor complex but have so far not been successful. With the aim to gather information on the mode of binding, we performed ligand-observed STD NMR studies with compounds 41, 47, and 50. The STD NMR can provide information on the putative orientation of a given binder to the target of interest in the absence of any structural data of the protein. In this assay, protons that are closest to the protein upon binding show the strongest STD effect. In our

Table 5. Comparison of IC₅₀ Values Obtained by Using LBS1, 2, or 3 as Fluorescent Probes, c log P, and LE

Cpd	structure	IC ₅₀ LBS1	IC ₅₀ LBS2	IC ₅₀ LBS3	clogP	LE
37		104 ± 33 μM	159 ± 2 μM	39 ± 4 μM	1.80	0.26
42		136 ± 27 μM	109 ± 3 μM	106 ± 32 μM	2.78	0.26
41		25 ± 1 μM	28 ± 1 μM	26 ± 1 μM	2.78	0.30
43		19 ± 55 μM	14 ± 1 μM	12 ± 1 μM	2.78	0.32
47		25 ± 1 μM	18 ± 3 μM	26 ± 1 μM	2.78	0.32
50		20 ± 3 μM	17 ± 1 μM	19 ± 3 μM	2.00	0.33

measurement, samples contained a 40-fold excess of the compound (1 mM) relative to the LANA DBD mutant (25 μM) and were recorded at 298 K (Figure 6B). The STD effects (I/I_0) were measured and calculated for each proton of the ligand. The STD effect of compound 50 is shown in Figure 6B. The overlaid spectra were normalized to the signals of H-1 and H-2, which gave the strongest enhancement and, hence, can be assumed to interact the most with the protein surface. These observable variations of the STD effects suggest that the compound binds in a defined orientation to the protein where the pyridine moiety faces the protein surface with its aromatic nitrogen. It can be assumed that this motif acts as a hydrogen bond acceptor. STD effects of H-3 and H-4 (53 and 61% of H-3 and H-4, respectively) suggest that these protons are not in direct contact with the protein and should be further investigated as potential growth vectors. Indeed, inactive compounds 51–55 were already grown in this direction and led to abolished activities.

However, the introduced residues were rather large leaving the option of smaller less bulky substituents to be tried. The four protons referred to by H-8 and H-9 presumably divide into two populations: two hydrogens, which are closer to the protein surface, and two, which are more remote (see Figure 6B). As these are indistinguishable in the STD NMR experiment, the observed effect should be a mean of the signals from both populations. As a consequence, growth of the compound breaking this ambiguity is a potential path forward in future optimization efforts.

For compounds 41 and 47 we observed similar STD effects (see Figure S12, Supporting Information). The protons from the aniline next to the amino group gave the strongest enhancement. This also implies that the NH₂ plays an

important role as a hydrogen bond acceptor or donor for binding.

Molecular Docking. In order to generate a possible binding mode of the optimized hit 50 to LANA, we performed docking experiments taking the STD-NMR data into account. Importantly, we specifically searched for target–ligand complex geometries, which are in line with the gathered experimental data. As we demonstrated that this compound binds to LANA (FP assay, MST, STD NMR) and is able to displace the DNA (FP assay, EMSA), we directed our docking experiment to the DNA-binding site of the target (Figure 7A). This approach intentionally neglects a possible allosteric mechanism of our compound, which we consider to be rather unlikely due to the rigidity of the DNA-binding domain.

In order to identify the initial docking site, we selected those LANA residues, which were in close proximity (4.5 Å) to the DNA atoms found in PDB entry 4uzb.⁷ Docking to this large interaction surface yielded three distinct clusters (Figure 7A). We searched for a binding pose of our inhibitor capable of prominently displacing the DNA from the protein. In general, cluster site 2 was located at the center of the LANA–nucleic acid interaction and would enable to disrupt major as well as minor groove interactions. Sites 1 and 3 were located on the peripheral areas of the LANA–DNA interface. Hence, we selected cluster site 2 for a more focused redocking experiment and screened the yielded binding poses for compliance with the STD NMR data (see Figure 6B). We selected the highest scoring pose, which met the criterion of bringing protons 1 and 2 as well as one pair of protons 8 and 9 into close proximity to the protein surface, while exposing protons 3, 4, and 5 as well as the other 8 and 9 pair (Figure S13, Supporting Information and Figure 6B). This pose was further refined through local

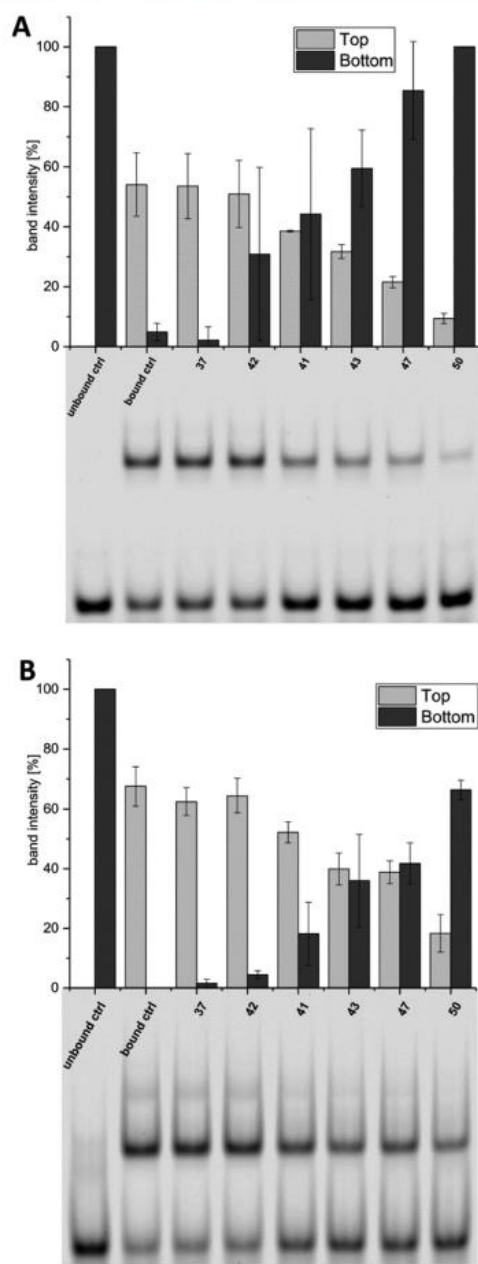


Figure 5. EMSA analysis of compounds 37, 41, 42, 43, 47, and 50 using (A) LBS1 and (B) LBS1 + 2 as probes. Representative EMSA gels of one independent experiment are shown containing unbound control (GST + LBS1 or LBS1 + 2), bound control (DMSO + LANA + LBS1 or LBS1 + 2), and compounds (Cpd + LANA + LBS1, or LBS1 + 2). Bar graphs are shown with normalized data points (inhibition from 0–100%) representing mean intensities of top band values (LANA–LBS complex) and bottom band values (single LBS). The experiment was performed in duplicate, and the standard deviations were given; each compound was used at 500 μ M, proteins were used at 200 nM, and DNA probe concentration was 20 nM.

energy minimization and is depicted in Figure 7B,C. A very prominent interaction partner suggested by this pose is Gln1015. Due to the symmetrical assembly of the LANA dimer, each Gln1015 from either of the two protein chains can contribute to inhibitor binding by acting as hydrogen-bond donors to the carboxyl group. Furthermore, Gln1073 and Val1019 form hydrogen-mediated interactions with the pyridine motif of 50. As seen from the 2D interaction profile (Figure 7C), the proton at position 2 is detected as “solvent exposed” although it was in van der Waals contact with the protein (see Figure S13, Supporting Information). However, this is in agreement with the observation that introduction of an aniline motif is tolerated in this position (43). Finally, we postulate a possible cation– π interaction between nearby Lys1069 and the central triazole motif, which would further add to the attractive forces between LANA and the inhibitor. At this point, we would like to stress that the preferential docking pose is hypothetical and needs further validation through wet lab experiments, for example, via single-amino acid mutation of the strongly interacting Glu1015. Nonetheless, it is in line with currently available data and, hence, a plausible binding mode to base structure-guided modifications on. Next optimization efforts will be directed toward exploration of the proposed growth vectors (Figure 6B). The surface of LANA at the DNA-binding site is densely covered with possible hydrogen-bonding donors and acceptors, which could be exploited for further attractive interactions.

CONCLUSIONS

In this study, we successfully obtained a qualified fragment-sized hit capable of displacing a viral nucleic acid sequence from the DNA-binding domain of the latency-associated nuclear antigen (LANA)—a potential antiviral drug target to treat Kaposi’s sarcoma herpesvirus (KSHV) infections. We achieved this by means of fragment-based drug design employing biophysical screening via SPR and DSF as two orthogonal selection filters followed by functional evaluation through fluorescence polarization (FP). FP also guided hit optimization toward low micromolar activity. Favorable ligand efficiency (>0.3) and low lipophilicity combined with additional EMSA, MST, and STD NMR experiments corroborating specific target interaction qualify hit 50 as a suitable starting point for a follow-up lead-generation campaign. Future optimization efforts will be aided by a wet lab-informed docking pose and amenability of the described scaffold to facilitate CombiChem-driven derivatization via click chemistry. In parallel, continuing efforts are underway to identify a suitable crystallographic system for the generation of protein–ligand complex structures, which would ultimately enable structure-based drug design. The ability to inhibit a nucleic-acid-involving macromolecule–macromolecule interaction by a small molecular scaffold is encouraging. The same is true for the promise to break the latent replication cycle of a herpesviral infection. In our opinion, both concepts are challenging yet worthwhile endeavors.

EXPERIMENTAL SECTION

Materials and Methods. All reagent-grade chemicals were obtained from commercial suppliers and were used as received. All reactions were carried out under an argon atmosphere. Automated column flash chromatography (CombiFlash Rf + von Teledyne ISCO, Lincoln, NE, USA) was performed on silica gel (Axel Semrau, Sprockhövel, Germany). Preparative high pressure liquid chromatog-

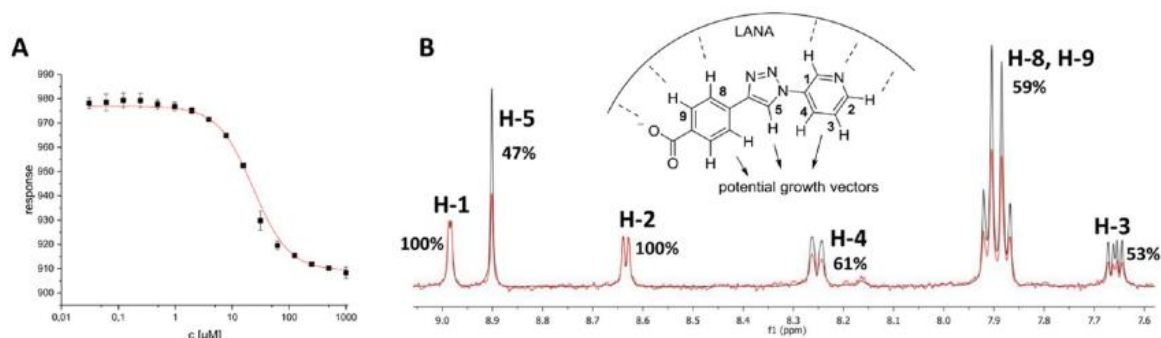


Figure 6. (A) Dose-dependent MST interaction curve of compound **50** with LANA DBD mutant. (B) STD experiments of compound **50** in complex with LANA DBD mutant. The reference spectrum is displayed in black (STD-off) and STD difference spectra (STD-on) in red. Overlaid spectra were normalized to the signals for H-1 and H-2, which showed the strongest enhancement.

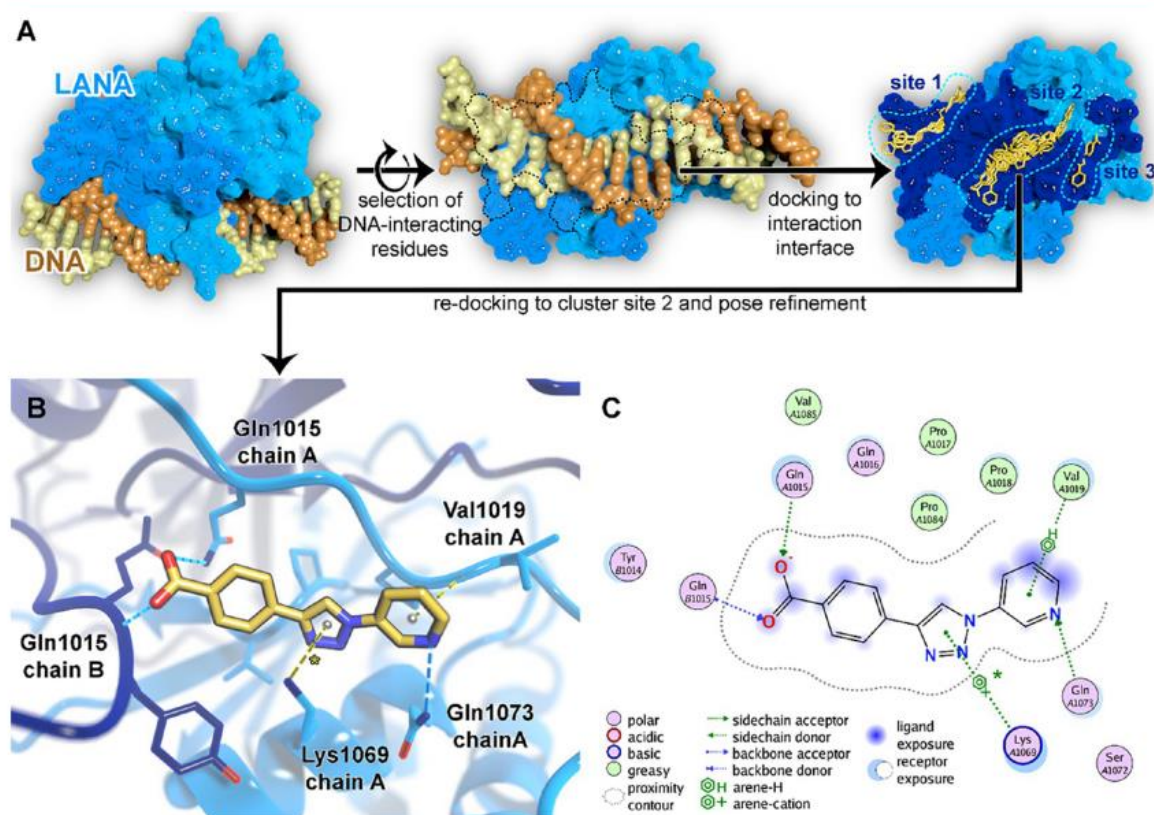


Figure 7. Design (A) and result (B,C) of STD-NMR-informed docking study performed on **50**. (A) Docking was conducted using PDB entry 4uzb (left). Residues that make up the docking site were selected based on proximity (4.5 Å) to DNA in complex structure (dashed black lines, middle; dark blue surface, right). First docking resulted in three distinct clusters (light blue dashed lines; right). Cluster site 2 was selected for redocking and subsequent pose refinement. (B) 3D and (C) 2D representation of the plausible binding pose of **50**. A putative cation- π interaction mediated by Lys1069 is shown and marked with an asterisk.

raphy (HPLC, Ultimate 3000 UHPLC+ focused, Thermo Scientific) purification was performed on a reversed-phase column (C18 column, 5 μ m, Macherey-Nagel, Germany). For gradient elution a mobile phase consisting of acetonitrile containing 0.05% formic acid (FA) (v/v) and water containing 0.05% FA (v/v) was used. The syntheses were not optimized regarding yields. ^1H and ^{13}C NMR were recorded on a Bruker Fourier spectrometers (300/500 or 176/126/75 MHz).

Chemical shifts (δ) are reported in parts per million (ppm) relative to each reference solvent. The chemical shifts recorded as δ values in ppm units by reference to the hydrogenated residues of the deuterated solvent as the internal standard. Coupling constants (J) are given in hertz (Hz), and splitting patterns are designated as follows: s, singlet; d, doublet; dd, doublet of doublets; t, triplet; m, multiplet; br., broad signal. Purity of all final compounds was measured on the UV trace

recorded at a wavelength of 254 nm and was determined to be >95% by a reversed-phase liquid chromatography mass spectrometer (LCMS). High resolution mass spectra of all final compounds were measured on a Thermo Scientific Q Exactive Focus (Germany) equipped with a DIONEX ultimate 3000 UHPLC+ focused and can be found in the Supporting Information.

Procedure I: General Synthesis of 1-(Nitrophenyl)-1H-imidazole 2–7. The appropriate halo-nitrobenzene (1 equiv) was dissolved in DMF and treated with K_2CO_3 (1.2 equiv), CuI (0.1 equiv), and substituted 1H-imidazole (1.2 equiv) or 1H-benzimidazole (1.2 equiv) under an argon atmosphere. The mixture was stirred at 120 °C for 24 h. After cooling to room temperature, the solids were filtered off and washed with ethyl acetate (3 \times). The combined filtrate was concentrated under reduced pressure. The resulting product was purified by column chromatography. Experimental details can be found in the Supporting Information. Compound **2** is presented as an example. 1-(2-Nitrophenyl)-1H-imidazole **2** was prepared according to general procedure I using 2-iodonitrobenzene (100 mg, 0.40 mmol), K_2CO_3 (66 mg, 0.48 mmol), CuI (7.5 mg, 0.04 mmol), 1H-imidazole (33 mg, 0.48 mmol), and DMF (3 mL). The obtained crude was purified by column chromatography (PE:EE 1:9) to yield the title compound (36 mg, 0.19 mmol, 49%). 1H NMR (300 MHz, $CDCl_3$) δ ppm: 7.10 (s, 1 H), 7.25 (s, 1 H), 7.48 (dd, $J = 7.82, 1.21$ Hz, 1 H), 7.57–7.71 (m, 2 H), 7.71–7.79 (m, 1 H), 8.01 (dd, $J = 8.06, 1.35$ Hz, 1 H); ^{13}C NMR (75 MHz, $CDCl_3$) δ ppm: 125.35, 128.65, 129.62, 130.66, 133.70, 137.23.

Procedure II: General Synthesis of (1H-Imidazol-1-yl)anilines 1 and 9–13. 1-(Nitrophenyl)-1H-imidazole derivatives (1 equiv) were dissolved in ethanol and treated with tin(II) chloride (5 equiv). The mixture was refluxed for 30 min, and after cooling to room temperature, the solids were filtered off and washed with ethanol. The filtrate was combined, and the solvent was removed under reduced pressure. The crude was dissolved in ethyl acetate and extracted with saturated $NaHCO_3$ solution. The combined organic layers were dried over sodium sulfate and concentrated under reduced pressure. The products were purified by flash chromatography or by reversed-phase HPLC and were dried at a lyophilisator. Experimental details can be found in the Supporting Information. Compound **1** is presented as an example. 2-(1H-Imidazol-1-yl)aniline **1** was prepared by the general procedure II using 1-(2-nitrophenyl)-1H-imidazole **2** (150 mg, 0.79 mmol), $SnCl_2$ (890 mg, 3.96 mmol), and ethanol (20 mL). The obtained crude was purified by flash column chromatography (gradient elution, DCM/MeOH 95:5–90:10) to yield the target compound (108 mg, 0.67 mmol, 68%). 1H NMR (300 MHz, $CDCl_3$) δ ppm: 3.80 (br. s, 2 H), 6.91–7.02 (m, 2 H), 7.20–7.31 (m, 2 H), 7.34–7.43 (m, 2 H), 7.79 (s, 1 H); ^{13}C NMR (75 MHz, $CDCl_3$) δ ppm: 116.35, 118.54, 120.09, 123.25, 127.11, 129.79, 129.92, 137.64, 141.90.

N-(2-(1H-Imidazol-1-yl)phenyl)acetamide (8). 2-(1H-Imidazol-1-yl)aniline **1** (50 mg, 0.31 mmol) was dissolved in a mixture of acetic acid (4 mL) and acetic acid anhydride (2 mL). One drop of sulfuric acid was added, and the solution was stirred at room temperature for 16 h. The reaction mixture was neutralized with aqueous 10% NaOH solution and extracted with DCM (2 \times). The combined organic phases were dried over sodium sulfate and concentrated under reduced pressure to give the crude, which was purified by HPLC (reversed-phase, mobile phase consisting of acetonitrile containing 0.05% FA (v/v) and water containing 0.05% FA (v/v), gradient elution: 5:95–60:40) to yield the target compound (8 mg, 0.04 mmol, 13%). 1H NMR (300 MHz, $CDCl_3$) δ ppm: 2.12 (s, 3 H), 7.06–7.11 (m, 1 H), 7.19 (d, $J = 1.02$ Hz, 1 H), 7.23 (s, 1 H), 7.24 (s, 1 H), 7.43–7.51 (m, 1 H), 7.51–7.54 (m, 1 H), 7.74 (s, 1 H), 8.25 (d, $J = 8.20$ Hz, 1 H); ^{13}C NMR (75 MHz, $CDCl_3$) δ ppm: 24.28, 120.20, 123.78, 124.99, 126.79, 129.83, 130.30, 133.36, 137.63, 168.90.

1-(2-Methoxyphenyl)-1H-imidazole (14). (2-Methoxyphenyl)-boronic acid (150 mg, 0.98 mmol), 1H-imidazole (80 mg, 1.18 mmol), and CuCl (5 mg, 0.05 mmol, 5 mol %) were dissolved in methanol (10 mL) and refluxed for 16 h. After cooling to room temperature the solvent was removed under reduced pressure, and the

obtained crude was dissolved in ethyl acetate and extracted with water. The combined organic phases were dried over sodium sulfate and concentrated under reduced pressure to give the crude. The crude was purified by column chromatography (DCM/MeOH 95:5) to yield the title compound (70 mg, 0.40 mmol, 41%). 1H NMR (300 MHz, methanol- d_4) δ ppm: 3.87 (s, 3 H), 7.01–7.13 (m, 2 H), 7.22 (d, $J = 8.29$ Hz, 1 H), 7.30–7.48 (m, 3 H), 7.88 (s, 1 H); ^{13}C NMR (75 MHz, methanol- d_4) δ ppm: 56.58, 113.90, 122.15, 122.30, 126.91, 127.62, 128.75, 130.77, 139.18, 154.33.

2-(1H-Imidazol-1-yl)phenol (15). 1-(2-Methoxyphenyl)-1H-imidazole **14** (50 mg, 0.28 mmol) was dissolved in 48% hydrobromic acid in water (6 mL) and refluxed for 16 h. The mixture was neutralized with saturated $NaHCO_3$ solution and extracted with ethyl acetate (2 \times). The combined organic phases were dried over sodium sulfate and concentrated under reduced pressure to give the crude, which was purified by column chromatography (DCM/MeOH 95:5) to yield the title compound (40 mg, 0.25 mmol, 90%). 1H NMR (300 MHz, $DMSO-d_6$) δ ppm: 6.91 (td, $J = 7.59, 1.40$ Hz, 1 H), 6.98–7.11 (m, 2 H), 7.16–7.26 (m, 1 H), 7.33 (dd, $J = 7.87, 1.63$ Hz, 1 H), 7.45 (s, 1 H), 7.94 (s, 1 H), 10.27 (br. s, 1 H); ^{13}C NMR (75 MHz, $DMSO-d_6$) δ ppm: 116.90, 119.54, 124.75, 125.25, 128.47, 150.23.

Procedure III: General Procedure of (1H-Imidazol-1-yl)benzoic Acids 16–18. The appropriate halo-benzoic acid (1 equiv) was dissolved in DMF (0.1 M) and treated with N_1,N_2 -dimethylethane-1,2-diamine (0.2 equiv), K_2CO_3 (2.2 equiv), CuCl (0.1 equiv), and 1H-imidazole (1.5 equiv) under an argon atmosphere. The mixture was stirred at 120 °C for 24 h. After cooling to room temperature the solids were filtered off and washed with ethyl acetate. The combined filtrate was concentrated under reduced pressure. The resulting product was purified using preparative HPLC (reversed-phase, mobile phase consisting of acetonitrile containing 0.05% FA (v/v) and water containing 0.05% FA (v/v); gradient elution, 5:95–90:10) to yield the target compound. Experimental details can be found in the Supporting Information. Compound **16** is presented as example. 2-(1H-Imidazol-1-yl)benzoic acid **16** was prepared according to general procedure III using 2-iodobenzoic acid, N_1,N_2 -dimethylethane-1,2-diamine, K_2CO_3 , CuCl, 1H-imidazole, and DMF. 1H NMR (500 MHz, $DMSO-d_6$) δ ppm: 7.40 (br. s, 1 H), 7.57 (br. s, 1 H), 7.59–7.72 (m, 2 H), 7.72–7.84 (m, 1 H), 7.99 (br. s, 1 H), 8.51 (br. s, 1 H); ^{13}C NMR (126 MHz, $DMSO-d_6$) δ ppm: 119.23, 120.21, 123.52, 126.37, 127.64, 130.14, 130.25, 135.58, 138.45, 166.53.

2-Azidoaniline (19). Aniline (500 mg, 5.4 mmol) was dissolved in acetonitrile (100 mL). *tert*-Butylhydroperoxide (1.5 mL, 8.1 mmol) and copper(I) bromide (77 mg, 0.5 mmol) were added, and the mixture was cooled to 0 °C. At 0 °C $TMSN_3$ (1.4 mL, 10.7 mmol) was added dropwise, and the reaction mixture was stirred at room temperature overnight. The solvent was removed under reduced pressure, and the crude product was purified by flash chromatography (PE:EE, gradient elution, 1:0–9:1) to yield the target compound (230 mg 1.72 mmol, 32%). 1H NMR (300 MHz, $CDCl_3$) δ ppm: 7.05 (d, 1 H, $J = 9$ Hz), 6.97 (dd, 1 H, $J = 7.5$ Hz), 6.80 (dd, 1 H, $J = 7.5$ Hz), 6.71 (d, 1 H, $J = 3$ Hz), 3.81 (br. s, 2 H); ^{13}C NMR (75 MHz, $CDCl_3$) δ ppm: 138.1, 125.6, 125.2, 119.1, 118.3, 115.8.

Azido Benzene (20). Aniline (364 mg, 4.0 mmol) was dissolved in ethyl acetate (8 mL) and cooled to 0 °C, and water (1 mL) and concentrated HCl (2.4 mL) were added. Sodium nitrite (469 mg, 6.8 mmol, 1.7 equiv) dissolved in water (1 mL) was added slowly. The reaction mixture was stirred for 30 min at 0 °C. Subsequently, sodium azide (442 mg, 6.8 mmol, 1.7 equiv) in water (1 mL) was added slowly at 0 °C. After stirring at room temperature for 1.5 h, TLC indicated full conversion and the mixture was neutralized and extracted with ethyl acetate (2 \times). The combined organic phases were dried over sodium sulfate and concentrated under reduced pressure to give the crude. The crude product (300 mg) was used as obtained in the next step without further purifications.

2-Azidobenzoic Acid (21). Anthranilic acid (300 mg, 2.2 mmol) were dissolved in a mixture of water (10 mL) and sulfonic acid (2 mL) and cooled to 0 °C. Sodium nitrite (151 mg, 2.2 mmol) was dissolved in water (1 mL) and added dropwise. The reaction mixture was stirred for 15 min at 0 °C. Subsequently, sodium azide (172 mg,

2.6 mmol) in water (1 mL) was added slowly at 0 °C. After stirring at room temperature for 2 h, TLC indicated full conversion and the mixture was diluted with water and extracted with ethyl acetate (2×). The combined organic phases were dried over sodium sulfate and concentrated under reduced pressure to give the crude. The crude product (250 mg) was used as obtained in the next step without further purifications. MS (ESI⁻) *m/z* 162 (M - H).

3-Azidobenzoic Acid (22). 3-Aminobenzoic acid (300 mg, 2.2 mmol) was dissolved in a mixture of water (10 mL) and sulfonic acid (2 mL) and cooled to 0 °C. Sodium nitrite (151 mg, 2.2 mmol) was dissolved in water (1 mL) and added dropwise. The reaction mixture was stirred for 15 min at 0 °C. Subsequently, sodium azide (172 mg, 2.6 mmol) in water (1 mL) was added slowly at 0 °C. After stirring at room temperature for 2 h, TLC indicated full conversion and the mixture was diluted with water and extracted with ethyl acetate. The combined organic phases were dried over sodium sulfate and concentrated under reduced pressure to give the crude. The crude product (220 mg) was used as obtained in the next step without further purifications. MS (ESI⁻) *m/z* 162 (M-H).

4-Azido Phenol (23). 4-Aminophenol (436 mg, 4.0 mmol) was dissolved in 6 M HCl (15 mL). Sodium nitrite (469 mg, 6.8 mmol, 1.7 equiv) was dissolved in water (3 mL) and added. The reaction mixture was stirred for 30 min at 0 °C. Subsequently, sodium azide (442 mg, 6.8 mmol, 1.7 equiv) in water (1 mL) was added slowly at 0 °C. After stirring at room temperature for 1.5 h, TLC indicated full conversion and the mixture was neutralized and extracted with ethyl acetate (2×). The combined organic phases were dried over sodium sulfate and concentrated under reduced pressure to give the crude. The crude product (290 mg) was used as obtained in the next step without further purifications.

3-Azido Pyridine (24). 3-Aminopyridine (376 mg, 4.0 mmol) was dissolved in ethyl acetate (8 mL) and cooled to 0 °C, and water (1 mL) and concentrated HCl (2.4 mL) were added. Sodium nitrite (469 mg, 6.8 mmol, 1.7 equiv) dissolved in water (1 mL) was added dropwise. The reaction mixture was stirred for 30 min at 0 °C. Subsequently, sodium azide (442 mg, 6.8 mmol, 1.7 equiv) in water (1 mL) was added slowly at 0 °C. After stirring at room temperature for 1.5 h, TLC indicated full conversion and the mixture was basified with saturated Na₂CO₃ solution (pH 10) and extracted with ethyl acetate (2×). The combined organic phases were dried over sodium sulfate and concentrated under reduced pressure to give the crude. The crude product (280 mg) was used as obtained in the next step without further purifications.

Methyl 4-Azidobenzoate (25). 4-Azidobenzoic acid (300 mg, 1.8 mmol) was dissolved in methanol (10 mL) and cooled to 0 °C. Thionyl chloride (297 μL, 4.14 mmol) was added dropwise at 0 °C, and the reaction mixture was stirred at room temperature overnight. The solvent was removed, and the obtained crude was purified by flash chromatography (PE:EE, gradient elution, 1:0–95:5) to yield the product (305 mg, 1.7 mmol, 94%). MS (ESI⁺) *m/z* 178 (M + H).

Procedure IV: General Synthetic Procedure for (1H-1,2,3-Triazol-1-yl)benzoic Acids 26–28. Ethynyltrimethyl silane (1.0 equiv) was suspended in 1:1 mixture of water and methanol under an argon atmosphere. Copper sulfate heptahydrate (0.5 equiv) and sodium ascorbate (0.5 equiv) were added. After addition of the corresponding azide (1.0 equiv) the mixture was stirred for 24 h at room temperature. After full conversion (TLC control) the mixture was acidified with 1 M HCl for cleaving the TMS group and extracted with dichloromethane (2×). The combined organic phases were dried over sodium sulfate and concentrated under reduced pressure to give the crude. The crude product was purified using preparative HPLC (reversed-phase, mobile phase consisting of acetonitrile containing 0.05% FA (v/v) and water containing 0.05% FA (v/v); gradient elution, 5:95–90:10) and dried on a lyophilizer to yield the target compound. Experimental details can be found in the Supporting Information. Compound 26 is presented as example. 2-(1H-1,2,3-Triazol-1-yl)benzoic acid 26 was synthesized according to procedure IV using 2-azidobenzoic acid and ethynyltrimethylsilane as starting materials. ¹H NMR (500 MHz, DMSO-*d*₆) δ ppm: 7.60 (s, 1 H), 7.63–7.70 (m, 1 H), 7.73–7.79 (m, 1 H), 7.91 (d, *J* = 8.70 Hz, 2 H),

8.51 (s, 1 H); ¹³C NMR (126 MHz, DMSO-*d*₆) δ ppm: 126.47, 126.53, 129.84, 130.38, 132.29, 133.35, 135.36, 166.62.

Procedure V: General Synthetic Procedure for Synthesis of Copper Catalyzed Click Reaction of Alkynes and Azides (Compounds 29–50). Under an argon atmosphere the appropriate alkyne (1.0 equiv) was suspended in a 1:1 mixture of water and *tert*-butanol. DIPEA (2.0 equiv), copper sulfate heptahydrate (0.5 equiv), and sodium ascorbate (0.5 equiv) were added. After addition of the corresponding azide (1.0 equiv) the mixture was stirred for 16 h at room temperature. After full conversion (TLC control) the mixture was acidified with 1 M HCl and the product was precipitated. The solids were collected, washed with water, and dried under vacuum to obtain the crude product. The products were purified by preparative HPLC (reversed-phase, mobile phase consisting of acetonitrile containing 0.05% FA (v/v) and water containing 0.05% FA (v/v); gradient elution, 5:95–90:10) and dried on a lyophilizer. The reactions and purification steps were not optimized regarding yields. Experimental details can be found in the Supporting Information. Compound 31 is presented as an example. 4-(4-Phenyl-1H-1,2,3-triazol-1-yl)benzoic acid 31 was synthesized according to procedure V using 4-azidobenzoic acid and ethynyl benzene as starting materials. ¹H NMR (300 MHz, DMSO-*d*₆) δ ppm: 7.39 (dd, *J* = 7.39 Hz, *J* = 7.39 Hz, 1 H), 7.50 (dd, *J* = 7.50 Hz, *J* = 7.50 Hz, 2 H), 7.95 (d, *J* = 7.45 Hz, 2 H), 8.16 (s, 3 H), 9.41 (s, 1 H); ¹³C NMR (75 MHz, DMSO-*d*₆) δ ppm: 119.65, 125.37, 128.38, 129.01, 129.99, 139.46, 147.56, 167.52.

Procedure VI: General Procedure for 4-(4-((Cyclohexylmethyl)amino)phenyl)-1H-1,2,3-triazol-1-yl)benzoic Acid 51–53. The appropriate 4-(4-(aminophenyl)-1H-1,2,3-triazol-1-yl)benzoic acid (30 mg, 0.11 mmol, 1 equiv), cesium carbonate (107 mg, 0.33 mmol, 3 equiv), and (bromomethyl)cyclohexane (39 mg, 0.22 mmol, 2 equiv) were dissolved in DMF (5 mL) and stirred at 90 °C for 5 h. After cooling to room temperature 1 M HCl was added and the mixture was extracted with DCM (2×). The combined organic phases were dried over sodium sulfate and concentrated under reduced pressure to give the crude. Purification was done by flash column chromatography (DCM/MeOH, gradient elution, 95:5–90:10) to yield the target compound. Experimental details can be found in the Supporting Information. Compound 51 is presented as example and was obtained with 72% (29 mg, 0.08 mmol) yield. ¹H NMR (500 MHz, CDCl₃) δ ppm 1.03–1.16 (m, 2 H) 1.19–1.35 (m, 4 H) 1.73 (d, *J* = 12.05 Hz, 1 H) 1.77–1.83 (m, 2 H) 1.83–1.90 (m, 2 H) 4.20 (d, *J* = 6.26 Hz, 2 H) 5.48 (br. s., 1 H) 6.73–6.86 (m, 2 H) 7.15–7.23 (m, 1 H) 7.46 (dd, *J* = 7.71, 1.30 Hz, 1 H) 7.92 (d, *J* = 8.54 Hz, 2 H) 8.18–8.33 (m, 3 H); ¹³C NMR (126 MHz, CDCl₃) δ ppm 25.68, 26.35, 29.76, 34.68, 37.24, 70.54, 112.96, 116.93, 117.54, 117.56, 119.99, 127.89, 129.59, 130.78, 131.36, 139.93, 145.30, 149.43, 165.47.

4-(4-(3-((2-Morpholinoethyl)amino)phenyl)-1H-1,2,3-triazol-1-yl)benzoic Acid (54). 4-(4-(3-Aminophenyl)-1H-1,2,3-triazol-1-yl)benzoic acid 42 (30 mg, 0.11 mmol, 1 equiv), cesium carbonate (107 mg, 0.33 mmol, 3 equiv), and 4-(2-chloroethyl)morpholine (331 mg, 0.22 mmol, 2 equiv) were dissolved in DMF (5 mL) and stirred at 90 °C for 5 h. After cooling to room temperature the solvent was removed under reduced pressure and purified by flash column chromatography (DCM/MeOH, gradient elution, 95:5–90:10) to yield the target compound (16 mg, 0.04 mmol, 36%). ¹H NMR (500 MHz, CDCl₃) δ ppm: 2.57–2.63 (m, 4 H), 2.81 (t, *J* = 5.87 Hz, 2 H), 3.72–3.76 (m, 5 H), 3.81 (br. s., 2 H), 4.52 (t, *J* = 5.87 Hz, 2 H), 6.72 (dt, *J* = 7.52, 1.74 Hz, 1 H), 7.21–7.26 (m, 2 H), 7.36 (s, 1 H), 7.92 (d, *J* = 8.54 Hz, 2 H), 8.22 (s, 2 H), 8.24 (s, 1 H); ¹³C NMR (126 MHz, CDCl₃) δ ppm: 53.88, 57.08, 62.69, 66.97, 112.36, 115.38, 116.15, 117.24, 119.85, 129.93, 130.20, 130.77, 131.39, 140.17, 147.00, 148.94, 165.32.

4-(4-(3-(Phenethylamino)phenyl)-1H-1,2,3-triazol-1-yl)benzoic Acid (55). 4-(4-(3-Aminophenyl)-1H-1,2,3-triazol-1-yl)benzoic acid 42 (30 mg, 0.11 mmol), cesium carbonate (107 mg, 0.33 mmol, 3 equiv), and (2-bromoethyl)benzene (41 mg, 0.22 mmol, 2 equiv) were dissolved in DMF (5 mL) and stirred at 90 °C for 5 h. After cooling to room temperature 1 M HCl was added and the mixture

was extracted with DCM (2×). The combined organic phases were dried over sodium sulfate and concentrated under reduced pressure to give the crude. Purification was done by flash column chromatography (DCM/MeOH, gradient elution, 95:5–90:10) to yield the target compound (20 mg, 0.05 mmol, 45%). ¹H NMR (500 MHz, CDCl₃) δ ppm: 3.13 (t, *J* = 6.94 Hz, 2 H), 3.81 (br. s, 1 H), 4.59 (t, *J* = 6.94 Hz, 2 H), 6.72 (d, *J* = 7.63 Hz, 1 H), 7.21–7.26 (m, 2 H), 7.28–7.33 (m, 3 H), 7.35 (d, *J* = 7.63 Hz, 3 H), 7.89–7.92 (m, 2 H), 8.18–8.21 (m, 2 H), 8.22 (s, 1 H); ¹³C NMR (126 MHz, CDCl₃) δ ppm: 35.19, 65.86, 112.36, 115.36, 116.14, 117.26, 119.81, 126.70, 128.57, 128.60, 128.90, 128.94, 129.91, 130.29, 130.78, 131.33, 131.36, 137.67, 140.10, 147.00, 148.90, 165.32.

Expression and Purification of His-Tagged Oligomerization-Deficient Mutant of the KSHV LANA C-Terminal DNA-Binding Domain (DBD; aa1008–1146). For the expression of KSHV His-tagged oligomerization-deficient LANA DBD (aa1008–1146) protein pETRO1.01 vector BL21 (DE3) cells were used.⁷ The His-tagged LANA DBD target protein was purified by Ni-NTA affinity chromatography (HisTrap HP column) using ÄKTApur (GE Healthcare). For more details see the Supporting Information.

Screening Library. The screening library contained 220 diverse fragment compounds from Asinex (Winston-Salem, NC, USA) and 500 from Maybridge (Loughborough, U.K.). The compounds possessing molecular weights (MWs) from 142 to 398 g/mol and were dissolved in DMSO to 10 or 20 mM stocks.

Surface Plasmon Resonance (SPR) Screening. SPR experiments were performed in running buffer (10 mM PBS, pH = 7.4, 5% DMSO (v/v), 0.05% Tween20 (v/v)) using a Reichert SR7500 biosensor (Buffalo, NY, USA) with research-grade CMD-500 M sensor chips provided by XanTec Bioanalytics (Düsseldorf, Germany) at 18 °C. All experiments were performed in two independent experiments. Scrubber 2 software (Version 2.0c 2008, BioLogic Software) was used for processing and analyzing the data. Changes in the refractive index due to DMSO-dependent solvent effects were corrected by using a calibration curve (seven solutions, 4.75–5.75% DMSO in buffer).

We immobilized the wild-type LANA C-terminal domain (LANA CTD (aa934–1162)) on CMD500 sensor chips using standard amine coupling with ddH₂O as immobilization buffer at 25 °C. The carboxymethyl dextran surface was first prepared with sodium borate (1 M, pH 9.5) (5 injections) and was activated with a 7 min injection of a 1:1 ratio of 0.4 M 1-ethyl-3-(3-dimethylaminopropyl)-carbodiimide hydrochloride (EDC) to 0.1 M *N*-hydroxysuccinimide (NHS). LANA CTD was diluted into sodium acetate (10 mM, pH 4.5) to 10 mM solution and coupled to the surface with a 1.5 min injection. Remaining activated groups were blocked with a 7 min injection of 1 M ethanolamine (pH 8.5).

Binding experiments were performed at a constant flow rate of 20 μL/min, and before starting the experiments, 12 warm-up blank injections were done. Zero-buffer blank injections were included for referencing. For SPR screening, all compounds were tested at 500 μM. Each sample was injected twice on two different sensor chips. To collect the binding response the sample was dissolved in running buffer and injected for 120 s association and 300 s dissociation. Compounds that showed a response higher than 9 RU were selected from the first screening (52 compounds). Results are shown in Figure S1.

Differential Scanning Fluorimetry (DSF) Screening. DSF experiments were performed in running buffer (10 mM PBS, pH = 7.4, 5% DMSO (v/v), 0.05% Tween20 (v/v)) using a StepOne Plus Real Time PCR System (Biosystem, Life Technologies Corporation), StepOne Software (StepOne and StepOne Plus Real Time PCR System Version 2.3) as collecting data software, and Applied Biosystem (Protein Thermal Shift Software Version 1.1) as analyzing software. Final concentrations of 20 μM wild-type LANA C-terminal domain (LANA CTD (aa934–1162)) and 500 μM compounds were used. The 52 positive compounds from SPR screening were tested. Compounds showing *T*_M > +0.5 °C and *T*_M < –1 °C were selected for further investigations. Results are shown in Figure S2.

Fluorescence Polarization (FP) Assay. FP was recorded in black 384 well microtiter plates (Greiner Bio-One, catalog number 781900) using a CLARIOstar microplate reader (BMG LABTECH, Ortenberg, Germany) with an extinction filter at 485 nm and emission filter at 520 nm. Gain adjustment was performed before starting each measurement to achieve maximum sensitivity. The FP values were measured in millipolarization units (mP). The experiments were performed in two independent experiments, and each sample was tested in duplicate. In all experiments the inhibitor and His-tagged oligomerization-deficient LANA DBD (aa1008–1146) mutant (final concentration 200 nM) were preincubated for 60 min. After addition of fluorescent labelled DNA (LBS1_flc, LBS2_flc, or LBS3_flc, final concentration 10 nM) the samples were incubated for 90 min. The assay was performed in FP-Buffer (10 mM HEPES, 150 mM NaCl, 0.005% (v/v) Tween20, DEPC water) with 5% DMSO. Assay optimization studies can be found in Figure S3.

Microscale Thermophoresis (MST). According to the MST (nanotemper-technologies.com) guided procedure, the His-tagged oligomerization-deficient LANA DBD (aa1008–1146) mutant was labeled using the Monolith NTTM His-Tag Labeling Kit RED-tris NTA. The binding assay was performed as described in the MST guided procedure, and MST-Buffer (10 mM HEPES, 150 mM NaCl, 2 mM DTT, 0.005% (v/v) Tween20, DEPC water) with 5% DMSO was used.

Electrophoretic Mobility Shift Assay (EMSA). The EMSA was carried out with slight modifications as described in Hellert et al.¹⁴ The His-tagged oligomerization-deficient LANA DBD (aa1008–1146) mutant protein (200 nM final) was incubated with the compounds (500 μM final) for 1 h at RT in the dark in a reaction volume of 15 μL. The reaction buffer consisted of 30 mM Tris HCl pH 7.5, 50 mM KCl, 10 mM MgCl₂, 1 mM DTT, 1 mM EDTA, 10% glycerol, 0.25% Tween 20, 0.5 mg/mL BSA, and 0.05 mg/mL poly(dI-dC). After the initial incubation period the 5'-Dy682-labeled double stranded DNA probe (IBA Lifesciences) (20 nM final) was added to the reaction and incubated for another 30 min at RT in the dark. 10 μL of the reaction was run on a pre-run native 5% acrylamide gel for 45 min at 100 V with tris-borate-EDTA buffer. Images of the gels were acquired with the Odyssey (Licor) using the Image Studio software. Raw data can be found in Figures S7 and S8.

Saturation-Transfer Difference (STD) NMR. The STD experiments were recorded at 298 K on a Bruker Fourier spectrometer (500 MHz). The samples contained a 40-fold excess of compound (1 mM final) relative to the C-terminal His-tagged oligomerization-deficient LANA DBD (aa1008–1146) mutant (25 μM final). The control spectra were recorded under the same conditions containing the free compound to test for artifacts. The STD buffer considered 20 mM bis-tris-Cl, 300 mM NaCl, 2 mM DTT, pH 6.5 in D₂O containing 5% DMSO-*d*₆. The experiments were recorded with a carrier set at 0 ppm for the on-resonance and –40 ppm for the off-resonance irradiation. Selective protein saturation was carried out at 2 s by using a train of 50 ms Gauss-shaped pulses, each separated by a 1 ms delay. The difference in intensity due to saturation transfer was quantified using $STD_{\text{effect}} = (I_0 - I_{\text{sat}})/I_0$ and constitutes an indication of binding. *I*_{sat} is the intensity of a signal in the on-resonance NMR spectrum, and *I*₀ is the intensity of one signal in the off-resonance or reference NMR spectrum.

Molecular Docking. All docking experiments were performed with MOE 2018.01 (Molecular Operating Environment, Chemical Computing Group),³⁴ while graphic processing for manuscript figures was done using YASARA structure (YASARA Biosciences GmbH)³⁵ and POV-Ray 3.7.0. First, 4uzb was loaded into MOE. LANA residues in 4.5 Å proximity to DNA atoms were selected and used as initial docking sites. Then compound 50 was docked in its deprotonated form to this site ignoring solvent, using "Triangle Matcher" as the placement method and "London dG" as the scoring function with 300. Refinement was done using the "Induced Fit" method and "GBVI/WSA dG" scoring function with 50 poses. Amber10:EHT was used as the force field. For the redocking experiment we used the 14 ligand poses found in cluster 2 as docking sites ignoring solvent, using Triangle Matcher as the placement method and London dG as the

scoring function with 100. Refinement was done using the Induced Fit method and GBVI/WSA dG scoring function with 10 poses. Amber10:EHT was used as the force field. The proposed binding pose depicted in Figure 7 was selected from the resulting array of poses based on the following criteria: (1) compliance to STD-NMR data (see also Figure S12); (2) docking score; and (3) number of occurrence. The highest score of the selected pose was position 35, and it occurred eight times within the 140 generated poses. Refinement of the selected pose was done using the built-in "QuickPrep" function with standard parameters and the Amber10:EHT force field.

■ ASSOCIATED CONTENT

Supporting Information

The Supporting Information is available free of charge on the ACS Publications website at DOI: 10.1021/acs.jmedchem.8b01827.

Synthetic procedures and characterizations of compounds 3–7, 11–13, 17, 18, 27–30, 32–50, 52, and 53, high resolution mass spectra of all final compounds, more details to SPR screening results, DSF screening results and FP assay condition optimizations as well as concentration-dependent FP experiments of compounds 37, 41–43, 47, and 50, EMSA row data for compounds 37, 41–43, 47, and 50, concentration-dependent EMSA for compound 50 and further STD NMR spectra for compounds 41 and 47 (PDF).

Docking was performed only with PDB entry 4uzb (PDB)

Docking was performed only with PDB entry 4uzb (PDB)

Molecular formula strings and some data (CSV)

■ AUTHOR INFORMATION

Corresponding Author

*E-mail: Martin.Empting@helmholtz-hzi.de. Phone: +(49) 681 988062031.

ORCID

Martin Empting: 0000-0002-0503-5830

Author Contributions

All authors have given approval to the final version of the manuscript.

Funding

This work was financially supported by the German Centre for Infection Research (DZIF) and the DFG Collaborative Research Centre 900, project C1.

Notes

The authors declare no competing financial interest.

■ ACKNOWLEDGMENTS

We thank Prof. Dr. Rolf W. Hartmann for his continuous support and guiding expertise. For the help with the SPR and DSF screening we thank Dr. Elisabeth Weidel, and for helping with the establishment of the FP-based assay, Dr. Christine Maurer and Dr. Jan Hellert.

■ ABBREVIATIONS

AcOH, acetic acid; Ac₂O, acetic anhydride; AIDS-KS, acquired immune deficiency syndrome-related Kaposi's sarcoma; CTD, C-terminal domain; DCM, dichloromethane; DMSO, dimethylsulfoxide; DNA, deoxyribonucleic acid; DBD, DNA-binding domain; DMF, dimethylformamide; DIPEA, diisopro-

pylethylamine; DSF, differential scanning fluorimetry; EBV, Epstein–Barr virus; EBNA1, Epstein–Barr nuclear antigen 1; EDC, 1-ethyl-3-(3-dimethylaminopropyl) carbodiimide hydrochloride; EE, ethyl acetate; EtOH, ethanol; EMSA, electrophoretic mobility shift assay; FA, formic acid; FP, fluorescence polarization; HPLC, high pressure liquid chromatography; HHV-8, human herpesvirus 8; KS, Kaposi Sarcoma; KSHV, Kaposi's sarcoma-associated herpesvirus; LANA, latency associated nuclear antigen; LBS, LANA binding site; LE, ligand efficiency; LCMS, liquid chromatography mass spectrometer; MeCN, acetonitrile; MeOH, methanol; MST, microscale thermophoresis; NHS, N-hydroxysuccinimide; PBS, phosphate-buffered saline; PE, petroleum benzene; STD NMR, saturation transfer difference nuclear magnetic resonance; SPR, surface plasmon resonance; TBHP, *tert*-butyl hydroperoxide; *tert*-BuOH, *tert*-butanol; TMSN₃, trimethylsilyl azide; TSA, thermal shift assay; TR, terminal repeat

■ REFERENCES

- (1) World Health Organization - International Agency for Research on Cancer. *A Review of Human Carcinogens*; World Health Organization: Lyon, France, 2012; Vol 100 B.
- (2) Weidner-Glunde, M.; Mariggio, G.; Schulz, T. F. Kaposi's sarcoma-associated herpesvirus latency-associated nuclear antigen: replicating and shielding viral DNA during viral persistence. *J. Virol.* **2017**, *91*, No. e01083-16.
- (3) Mariggio, G.; Koch, S.; Schulz, T. F. Kaposi sarcoma herpesvirus pathogenesis. *Philos. Trans. R. Soc., B* **2017**, *372*, 21060275.
- (4) Rainbow, L.; Platt, G. M.; Simpson, G. R.; Sarid, R.; Gao, S. J.; Stoiber, H.; Herrington, C. S.; Moore, P. S.; Schulz, T. F. The 222- to 234-kilodalton latent nuclear protein (LNA) of kaposi's sarcoma-associated herpesvirus (human herpesvirus 8) is encoded by *orf73* and is a component of the latency-associated nuclear antigen. *J. Virol.* **1997**, *71*, 5915–5921.
- (5) Kedes, D. H.; Ganem, D.; Ameli, N.; Bacchetti, P.; Greenblatt, R. The prevalence of serum antibody to human herpesvirus 8 (kaposi sarcoma-associated herpesvirus) among HIV-seropositive and high-risk HIV-seronegative women. *JAMA* **1997**, *277*, 478–481.
- (6) Verma, S. C.; Lan, K.; Robertson, E. Structure and function of latency-associated nuclear antigen. *Curr. Top. Microbiol. Immunol.* **2007**, *312*, 101–136.
- (7) Hellert, J.; Weidner-Glunde, M.; Krausz, J.; Lünsdorf, H.; Ritter, C.; Schulz, T. F.; Lührs, T. The 3D structure of kaposi sarcoma herpesvirus LANA C-terminal domain bound to DNA. *Proc. Natl. Acad. Sci. U. S. A.* **2015**, *112*, 6694–6699.
- (8) Barbera, A. J.; Chodaparambil, J. V.; Kelley-Clarke, B.; Joukov, V.; Walter, J. C.; Luger, K.; Kaye, K. M. The nucleosomal surface as a docking station for kaposi's sarcoma herpesvirus LANA. *Science* **2006**, *311*, 856–861.
- (9) Chodaparambil, J. V.; Barbera, A. J.; Lu, X.; Kaye, K. M.; Hansen, J. C.; Luger, K. A charged and contoured surface on the nucleosome regulates chromatin compaction. *Nat. Struct. Mol. Biol.* **2007**, *14*, 1105–1107.
- (10) Alkharsah, K. R.; Schulz, T. F. A role for the internal repeat of the kaposi's sarcoma-associated herpesvirus latent nuclear antigen in the persistence of an episomal viral genome. *J. Virol.* **2012**, *86*, 1883–1887.
- (11) Russo, J. J.; Bohenzky, R. A.; Chien, M.-C.; Chen, J.; Yan, M.; Maddalena, D.; Parry, J. P.; Peruzzi, D.; Edelman, I. S.; Chang, Y.; Moore, P. S. Nucleotide sequence of the kaposi sarcoma-associated herpesvirus (HHV8). *Proc. Natl. Acad. Sci. U. S. A.* **1996**, *93*, 14862–14867.
- (12) Coen, N.; Duraffour, S.; Snoeck, R.; Andrei, G. KSHV targeted therapy: an update on inhibitors of viral lytic replication. *Viruses* **2014**, *6*, 4731–4759.
- (13) Li, N.; Thompson, S.; Schultz, D. C.; Zhu, W.; Jiang, H.; Luo, C.; Lieberman, P. M. Discovery of selective inhibitors against EBNA1

via high throughput in silico virtual screening. *PLoS One* **2010**, *5*, No. e10126.

(14) Hellert, J.; Weidner-Glunde, M.; Krausze, J.; Richter, U.; Adler, H.; Fedorov, R.; Pietrek, M.; Rückert, J.; Ritter, C.; Schulz, T. F.; Lührs, T. A structural basis for BRD2/4-mediated host chromatin interaction and oligomer assembly of kaposi sarcoma-associated herpesvirus and murine gammaherpesvirus LANA proteins. *PLoS Pathog.* **2013**, *9*, No. e1003640.

(15) Maurer, C. K.; Fruth, M.; Empting, M.; Avrutina, O.; Hoßmann, J.; Nadmid, S.; Gorges, J.; Herrmann, J.; Kazmaier, U.; Dersch, P.; Müller, R.; Hartmann, R. W. Discovery of the first small-molecule CsrA-RNA interaction inhibitors using biophysical screening technologies. *Future Med. Chem.* **2016**, *8*, 931–947.

(16) Weidel, E.; Negri, M.; Empting, M.; Hinsberger, S.; Hartmann, R. W. Composing compound libraries for hit discovery-rationality-driven preselection or random choice by structural diversity? *Future Med. Chem.* **2014**, *6*, 2057–2072.

(17) Cimperman, P.; Baranauskienė, L.; Jachimovičiūtė, S.; Jachno, J.; Torresan, J.; Michailoviene, V.; Matulienė, J.; Sereikaitė, J.; Bumelis, V.; Matulis, D. A quantitative model of thermal stabilization and destabilization of proteins by ligands. *Biophys. J.* **2008**, *95*, 3222–3231.

(18) Lea, W. A.; Simeonov, A. Fluorescence polarization assays in small molecule screening. *Expert Opin. Drug Discovery* **2011**, *6*, 17–32.

(19) Hellert, J.; Krausze, J.; Schulz, T. F.; Lührs, T. Crystallization, room-temperature X-ray diffraction and preliminary analysis of kaposi's sarcoma herpesvirus LANA bound to DNA. *Acta Crystallogr. F Struct. Biol. Commun.* **2014**, *70*, 1570–1574.

(20) Wang, X.; Jin, Y.; Zhao, Y.; Zhu, L.; Fu, H. Copper-catalyzed aerobic oxidative intramolecular C-H amination leading to imidazobenzimidazole derivatives. *Org. Lett.* **2012**, *14*, 452–455.

(21) Campiani, G.; Morelli, E.; Gemma, S.; Nacci, V.; Butini, S.; Hamon, M.; Novellino, E.; Greco, G.; Cagnotto, A.; Goegan, M.; Cervo, L.; Dalla Valle, F.; Fracasso, C.; Caccia, S.; Mennini, T. Pyrroloquinoxaline Derivatives as High-Affinity and Selective 5-HT₃ Receptor Agonists: Synthesis, Further Structure–Activity Relationships, and biological studies. *J. Med. Chem.* **1999**, *42*, 4362–4379.

(22) Lan, J.-B.; Chen, L.; Yu, X.-Q.; You, J.-S.; Xie, R.-G. A simple copper salt catalyzed the coupling of imidazole with arylboronic acids in protic solvent. *Chem. Commun.* **2004**, 188–189.

(23) Pratt, D. A.; Pesavento, R. P.; van der Donk, W. A. Model studies of the histidine-tyrosine cross-link in cytochrome C oxidase reveal the flexible substituent effect of the imidazole moiety. *Org. Lett.* **2005**, *7*, 2735–2738.

(24) He, Z.; Bae, M.; Wu, J.; Jamison, T. F. Synthesis of highly functionalized polycyclic quinoxaline derivatives using visible-light photoredox catalysis. *Angew. Chem. Int. Ed Engl.* **2014**, *53*, 14451–14455.

(25) Tang, C.; Jiao, N. Copper-catalyzed C-H azidation of anilines under mild conditions. *J. Am. Chem. Soc.* **2012**, *134*, 18924–18927.

(26) Hu, M.; Li, J.; Yao, S. Q. In situ “click” assembly of small molecule matrix metalloprotease inhibitors containing zinc-chelating groups. *Org. Lett.* **2008**, *10*, 5529–5531.

(27) Addy, P. S.; Erickson, S. B.; Italia, J. S.; Chatterjee, A. A chemoselective rapid azo-coupling reaction (CRACR) for unclickable bioconjugation. *J. Am. Chem. Soc.* **2017**, *139*, 11670–11673.

(28) Hou, J.; Liu, X.; Shen, J.; Zhao, G.; Wang, P. G. The impact of click chemistry in medicinal chemistry. *Expert Opin. Drug Discovery* **2012**, *7*, 489–501.

(29) Mortenson, P. N.; Murray, C. W. Assessing the lipophilicity of fragments and early hits. *J. Comput.-Aided Mol. Des.* **2011**, *25*, 663–667.

(30) Shargel, L.; Wu-Pong, S.; Yu, A. B. C. *Applied Biopharmaceutics & Pharmacokinetics* 5. ed; McGraw-Hill Medical Publ. Division: New York, NY, 2005.

(31) Erlanson, D. A.; Jahnke, W., Eds. *Fragment-based Drug Discovery*; Wiley-VCH Verlag GmbH & Co. KGaA: Weinheim, 2016.

(32) Hellman, L. M.; Fried, M. G. Electrophoretic mobility shift assay (EMSA) for detecting protein-nucleic acid interactions. *Nat. Protoc.* **2007**, *2*, 1849–1861.

(33) Jerabek-Willemsen, M.; André, T.; Wanner, R.; Roth, H. M.; Duhr, S.; Baaske, P.; Breitsprecher, D. Microscale thermophoresis: interaction analysis and beyond. *J. Mol. Struct.* **2014**, *1077*, 101–113.

(34) *Molecular Operating Environment (MOE)*, 2013.08 Chemical computing group ULC 2018.

(35) Krieger, E.; Koraimann, G.; Vriend, G. Increasing the precision of comparative models with YASARA NOVA—a self-parameterizing force field. *Proteins* **2002**, *47*, 393–402.

3.2 Chapter B: Discovery of KSHV-LANA Inhibitors via In-House Library Screening

Title:

Discovery of Novel Latency-Associated Nuclear Antigen Inhibitors as Antiviral Agents Against Kaposi's Sarcoma-Associated Herpesvirus

Authors:

Philine Kirsch,[‡] Valentin Jakob,[‡] Walid A. M. Elgaher, Christine Walt, Kevin Oberhausen, Thomas F. Schulz and Martin Empting ([‡] contributed equally)

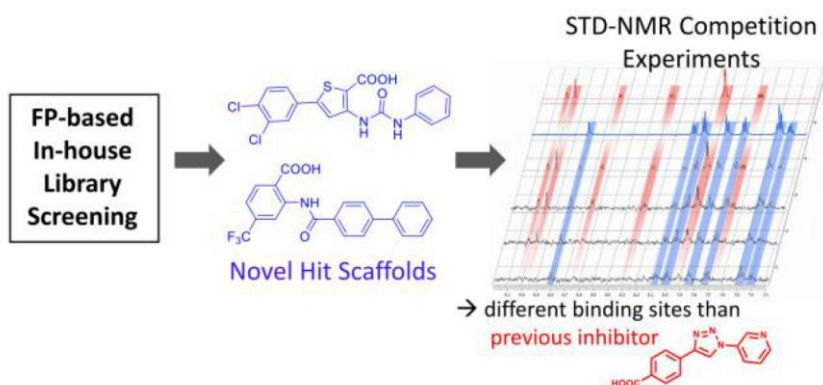
Bibliographic Data:

ACS Chemical Biology,

Publication Date: January 16, **2020**,

Doi: 10.1021/acscchembio.9b00845

Graphical Abstract:



Discovery of Novel Latency-Associated Nuclear Antigen Inhibitors as Antiviral Agents Against Kaposi's Sarcoma-Associated Herpesvirus

Philine Kirsch,¹ Valentin Jakob,¹ Walid A. M. Elgaher, Christine Walt, Kevin Oberhausen, Thomas F. Schulz, and Martin Empting*

Cite This: <https://dx.doi.org/10.1021/acscchembio.9b00845>

Read Online

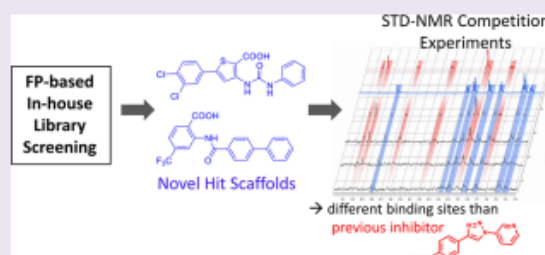
ACCESS |

Metrics & More

Article Recommendations

Supporting Information

ABSTRACT: With the aim to develop novel antiviral agents against Kaposi's Sarcoma Herpesvirus (KSHV), we are targeting the latency-associated nuclear antigen (LANA). This protein plays an important role in viral genome maintenance during latent infection. LANA has the ability to tether the viral genome to the host nucleosomes and, thus, ensures latent persistence of the viral genome in the host cells. By inhibition of the LANA–DNA interaction, we seek to eliminate or reduce the load of the viral DNA in the host. To achieve this goal, we screened our in-house library using a dedicated fluorescence polarization (FP)-based competition assay, which allows for the quantification of LANA–DNA-interaction inhibition by small organic molecules. We successfully identified three different compound classes capable of disrupting this protein–nucleic acid interaction. We characterized these compounds by IC₅₀ dose–response evaluation and confirmed the compound–LANA interaction using surface plasmon resonance (SPR) spectroscopy. Furthermore, two of the three hit scaffolds showed only marginal cytotoxicity in two human cell lines. Finally, we conducted STD-NMR competition experiments with our new hit compounds and a previously described fragment-sized inhibitor. Based on these results, future compound linking approaches could serve as a promising strategy for further optimization studies in order to generate highly potent KSHV inhibitors.



Kaposi's sarcoma herpesvirus (KSHV, also known as HHV-8) is a human γ_2 -herpesvirus that was identified as the etiological agent of Kaposi's sarcoma (KS) and two lymphoproliferative disorders, primary effusion lymphoma (PEL) and the plasma cell variant of multicentric Castlemann's disease (MCD).¹ Most of the disease burden caused by KSHV occurs in immunocompromised individuals, mainly patients suffering from the acquired immunodeficiency syndrome (AIDS) and transplant recipients. In contrast, KSHV-associated disease is infrequent in otherwise healthy individuals; however, KSHV also causes "classic" KS mainly in elderly men from KSHV-endemic areas and "endemic" KS in East and Central Africa.^{2–5} No specific treatments directed against the latent phase of the KSHV life cycle and KSHV-associated diseases are available.⁶ For the latent persistence and the regulation of KSHV in the human host, the latency-associated nuclear antigen (LANA) plays an important role.^{7–9} All KSHV-infected tumor cells express LANA, which is hence used as a biomarker for diagnostics by immunohistochemistry.^{10,11} It functions as an origin-binding protein via tethering the viral genome with its C-terminus and the host nucleosome with its N-terminus.^{12–14} LANA ensures a stable and latent persistence of the viral genome in the human cells.¹⁵ There are three adjacent LANA binding sites (LBSs) located in the terminal repeat (TR) region on the viral genome, which are referred to as LBS1, LBS2, and LBS3.^{13,16} Previous studies showed that

disruption of LANA expression leads to a reduction of viral DNA copies.¹⁷ On the basis of these findings, we aim to prevent latent KSHV persistence and reduce the viral load of infected cells through inhibition of the interaction between LANA and the viral genome.¹⁸ In a previous work, we discovered first inhibitors that interfere with the LANA–DNA interaction using a fragment-based drug-discovery approach.¹² The functional activity of our LANA–DNA interaction inhibitors was evaluated using a fluorescence polarization (FP)-based competition assay as a rapid and quantitative method. The most promising fragment-sized inhibitor I showed an IC₅₀ value of $17 \pm 1 \mu\text{M}$ (Figure 1). Additionally, target binding was confirmed via microscale thermophoresis (MST) and saturation transfer difference (STD)-NMR experiments as well as in an electrophoretic mobility shift assay (EMSA) measuring the interaction between the LANA DNA-binding domain (DBD) and DNA oligonucleotides representing LBS1 and LBS2.¹²

Received: October 21, 2019

Accepted: January 16, 2020

Published: January 16, 2020

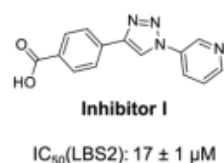


Figure 1. Previously discovered LANA–DNA interaction inhibitor I using a fragment-based approach.

In this present study, we exploit our FP-based competition assay as a new screening tool to search our in-house HIPS library for compounds with the ability to disturb the LANA–DNA interaction. In order to exclude assay artifacts, we used surface plasmon resonance (SPR) spectroscopy to confirm target binding and affinity of the screening hits and assessed their applicability by determining their cytotoxic potential. Moreover, with the view to compare the novel hit scaffolds with inhibitor I, we performed STD-NMR-based competition experiments. By this means, we were able to demonstrate nonoverlapping binding sites for two of our novel scaffolds with inhibitor I. Our screening protocol served as an effective strategy for the discovery of LANA–DNA interaction inhibitors and the identification of novel scaffolds for future medicinal chemistry campaigns.

RESULTS AND DISCUSSION

General Screening Protocol and Hit Evaluation. In order to identify new potential scaffolds, we decided to screen our in-house HIPS-library (670 compounds) comprising various chemical classes of small molecules with diverse biological activities. We used an FP-based competition assay, which we have established and described previously.¹² By this assay, we are able to quantitatively assess the functional activity of compounds in terms of LANA–DNA interaction inhibition. We employ a mutant of the C-terminal DBD of LANA, which is multimerization deficient. A fluorescence-labeled double-stranded DNA oligomer is used as the probe. Hit identification

was done in two steps as shown in Figure 2A. The first screening step was carried out at a single fixed concentration (100 μM) for preselection. Then, a three-point dose-dependency test was performed for evaluating the activity profiles. This procedure resulted in nine hits that can be clustered into three classes according to their chemical structure (Figure 2B). Subsequently, we determined the IC_{50} values using our FP-based competition assay and confirmed target binding via SPR measurements of the hit compounds. Moreover, we investigated the binding mode of the most promising inhibitors using STD-NMR competition experiments with the inhibitor I.

Library Screening Using FP-Based Assay. To apply our FP-based competition assay as a medium-to-high throughput screening method, we modified assay conditions slightly. For the primary screening, we used the same concentrations of LANA DBD mutant and LBS2 probe as described before.¹² The library compounds were screened in two independent experiments at a final concentration of 100 μM . Additionally, we used a high control (HC) comprising samples with LANA DBD mutant, LBS2 probe, and DMSO in buffer without any compound and low control (LC) containing the same components without LANA DBD mutant in each screening plate. Compounds that contained strong chromophores or precipitated under assay conditions were neglected to exclude false positives. Compounds showing an inhibitory effect greater than 50% were defined as hits. According to these criteria, we selected 86 compounds out of 670 (hit rate 12.8%) for further investigations (Figure S1). Next, we tested the 86 primary actives in a concentration-dependent three-point test in two independent FP-based experiments at final concentrations of 100 μM , 50 μM , and 10 μM (Figure S2–S4). By this means, we were able to focus on well-behaved compounds that can display a concentration-dependent inhibition of the LANA–DNA interaction and avoid being misguided by a strong initial effect in the spot test. The largest of the three classes (class I) comprises 64 2-ureidothiophene-3-carboxylic acid derivatives.^{19,20} This scaffold was previously described as a dual

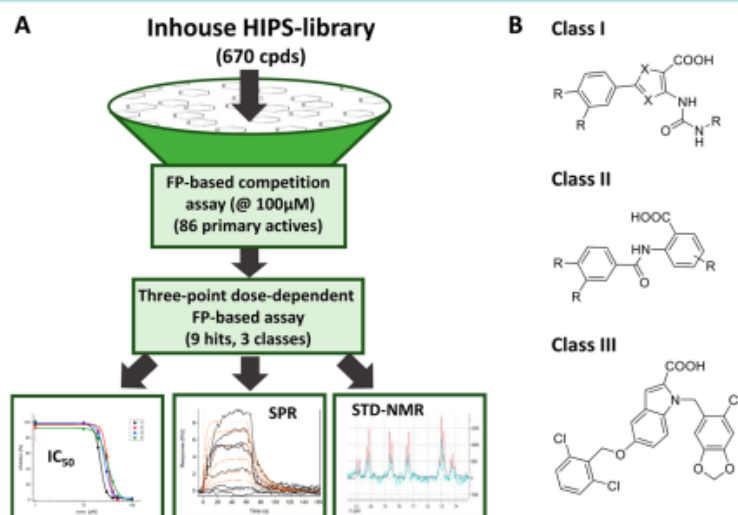


Figure 2. (A) Flowchart illustrating the screening procedure and the following hit evaluation methods. Using FP-based primary screening for identification of LANA–DNA interaction inhibitors and dose-dependent screening as secondary filters. IC_{50} determination, SPR, and STD-NMR experiments were performed for hit characterization and to confirm target binding. (B) Core structures of our screening hit compound classes.

B

<https://dx.doi.org/10.1021/acscchembio.9b00845>
ACS Chem. Biol. XXXX, XXX, XXX–XXX

Table 1. Characterization of Hit Compounds 1–9

Compd	Structure	MW [g/mol]	IC ₅₀ [μM] (FP assay)	Response [RU] at 100 μM (SPR)	K _D [μM] (SPR)
1		407.27	24 ± 1	9.5 ± 0.7	131.0 ± 9.0
2		437.29	33 ± 1	14.4 ± 0.6	n.d. ^a
3		500.37	26 ± 2	8.6 ± 0.1	n.d.
4		516.57	31 ± 2	42.3 ± 0.8	n.d.
5		396.24	33 ± 5	22.1 ± 1.2	n.d.
6		385.34	30 ± 2	12.2 ± 0.6	9.9 ± 0.4
7		412.24	38 ± 1	10.1 ± 0.5	n.d.
8		399.46	11 ± 2	21.2 ± 1.1	n.d.
9		504.74	11 ± 1	9.1 ± 0.7	9.3 ± 0.4

^aNot determined.

antibacterial and antiviral inhibitor for methicillin-resistant *Staphylococcus aureus* (MRSA) and human immunodeficiency virus type 1 (HIV-1) co-infections.²¹ The antibacterial activity can be attributed to the inhibition of RNA polymerase (RNAP) activity, which is an essential enzyme for bacterial viability. RNAP is responsible for the transcription of double-stranded DNA into single-stranded RNA. Antiviral potency of these compounds was rooted in their ability to inhibit the HIV-reverse transcriptase (HIV-RT), which reversibly transcribes the single-stranded viral RNA to double-stranded DNA.²¹ Obviously, there is a certain degree of functional relationship between these two targets and our target LANA, as all three possess the ability to interact with DNA or RNA (nucleic acids). The second class (class II) consists of 21 carboxamido benzoic acid derivatives, which were also identified as bacterial RNAP inhibitors.²² Additionally, we identified a unique compound in our LANA–DNA interaction inhibition assay possessing an indole-2-carboxylic acid scaffold (class III).

Based on these results, we selected representative examples from class I (compounds 1–4, Table 1) and class II (compounds 5–8, Table 1), which show suitable concentration-dependent activity and structural diversity in addition to the single member of class III (compound 9, Table 1) for further investigations.

Hit Characterization. Selected hits were further characterized for their relative potency and target affinity. We carried out dose-dependent FP-assay experiments using serial dilutions

up to 100 μM or 125 μM with and without addition of LANA DBD mutant. Importantly, for none of our hit compounds we observed fluorescence quenching or enhancement. Representative curves show the results of compounds 1–9 (Figures 3A–C and S6–S14). Curves were fitted to a four-parameter dose–response model using OriginPro 2018 to calculate IC₅₀ values. Generally, the observed IC₅₀ values are in the low micromolar range (Table 1). Importantly, we carried out SPR experiments to confirm that our hits are real target binders and not interfering with the DNA. We screened the hit compounds at a final concentration of 100 μM for binding to an immobilized LANA DBD mutant. For all hit compounds, we observed a significant binding response (Figure S16A–I). The bar diagram (Figure 3D) shows the mean of SPR response values in RU normalized to the molecular weight (MW) of the compounds. These results indicate that protein–DNA–interaction inhibition is most probably due to LANA binding rather than DNA or fluorescence-interfering effects.

Within class I (1–4), compound 1 showed the lowest IC₅₀ value of 24 ± 1 μM and the lowest MW (Table 1). The IC₅₀ values of hits 2–4 are in the same low micromolar range. However, bulkiness and complexity are increased compared to hit 1. In the SPR study, compounds 1–3 displayed reproducible responses between 9–14 RU and their sensorgrams showed clear association and dissociation phases indicating a typical reversible binding to LANA (Figure S16A–C). Hit 4 showed a relatively high response value (42

C

<https://dx.doi.org/10.1021/acscchembio.9b00845>
ACS Chem. Biol. XXXX, XXX, XXX–XXX

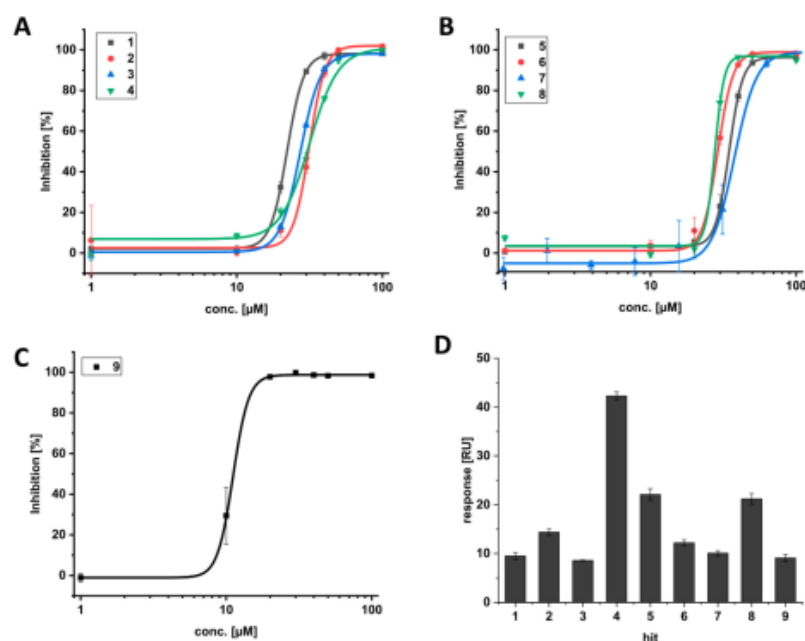


Figure 3. (A–C) Dose-dependent FP-based competition experiments for hit compounds 1–9. Curves were based on normalized data points (inhibition from 0–100%) from FP values of duplicates \pm standard deviation; (D) Mean of SPR response values (RU) of duplicates \pm standard deviation of the screened compounds at 100 μ M injected over an immobilized LANA DBD mutant.

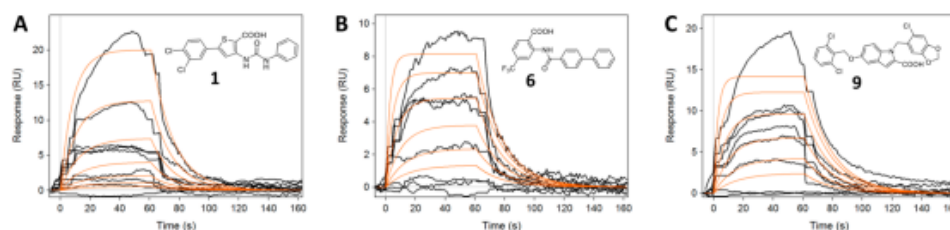


Figure 4. SPR sensorgrams (black) of the hit compounds 1 (A), 6 (B), and 9 (C) at concentrations of 1.6–100.0 μ M using immobilized LANA. Global fitting of the association and dissociation curves (red).

RU), which may indicate unspecific binding because of the two carboxylic acid motifs. Based on these results, we picked out hit 1 showing the lowest MW, least structure complexity, best IC_{50} value, and good SPR response for further characterization. For class II (5–8), hit compound 8 showed the highest inhibitory activity (IC_{50} value, $11 \pm 2 \mu$ M). Moreover, all hits displayed prominent SPR responses and binding curves (Figure S16E–H). Interestingly, sensorgram of compound 6 revealed a slow dissociation interaction with LANA among this set compounds (5–8) and a potential high affinity. Accordingly, we choose compound 6 for further evaluation as it represents class II preferably, having the lowest MW, low IC_{50} value ($30 \pm 2 \mu$ M), and favorable binding kinetics. Furthermore, compound 6 showed the highest solubility in our assay conditions. In addition, compound 9 (class III) showed also high activity (IC_{50} value, $11 \pm 1 \mu$ M), as well as binding response, and was selected for further investigations.

Next, we evaluated compounds 1, 6, and 9 for affinity to LANA and determined binding kinetics using SPR. Compounds 6 and 9 showed high affinity to LANA (K_D values, 9–10 μ M) and about 13-fold stronger than compound 1 (K_D

value, 131 μ M) (Table 1 and Figure 4). The on-rate of compounds 6 and 9 was 1 order of magnitude faster than that of compound 1, while all compounds displayed a comparable off-rate (see Figure S17–S19 and Table S2 for detailed results including Langmuir isotherms and kinetic parameters). The dissociation rate constant (k_{off}) and the ligand–protein residence time ($1/k_{off}$) are known to play a major role in potency, efficacy, and duration of effect.²³ Interestingly, we found that the inhibitory activities (IC_{50} values) obtained from the FP assay show a better correlation with the off-rates of the compounds rather than the binding affinities (K_D values). Such a correlation is known to be target-specific and was observed previously for other protein targets.^{23,24} These results indicate that the dissociation rate and consequently the duration of binding seem to be the driving force for the activity on LANA.

Saturation Transfer Difference (STD) NMR Competition Experiments. As the new hits were able to compete with the DNA in the FP-based competition experiments, they seem to bind to the DNA binding site of LANA. Having confirmed compound–LANA binding by the SPR study, we were interested in studying the LANA–ligand interactions and

D

<https://dx.doi.org/10.1021/acscchembio.9b00845>
ACS Chem. Biol. XXXX, XXX, XXX–XXX

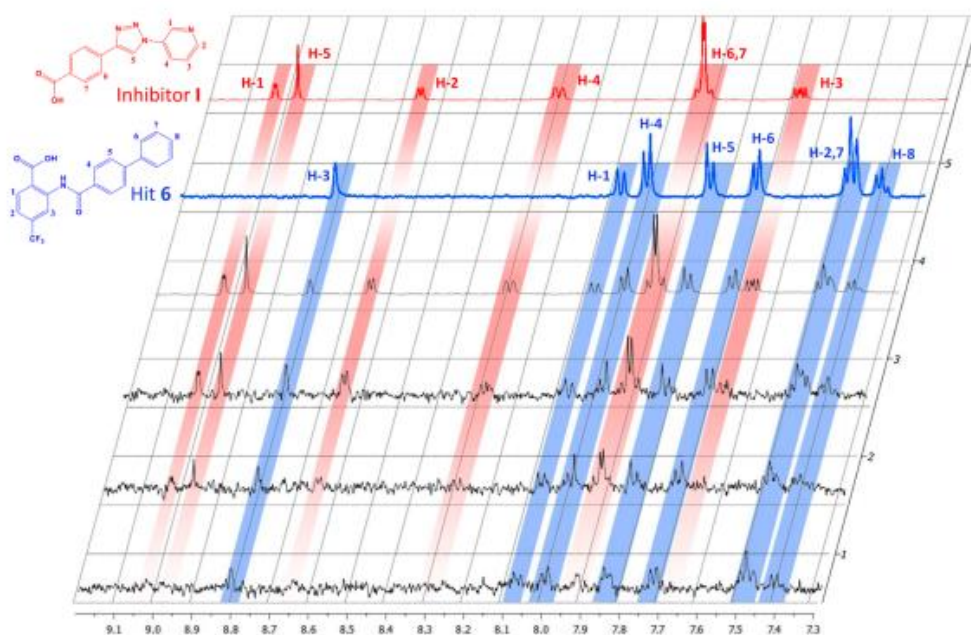


Figure 5. STD-NMR competition experiments with inhibitor **1** and hit **6** in complex with LANA DBD mutant. The respective protons of each compound are highlighted with a corresponding color, inhibitor **1** in red and hit **6** in blue; spectrum **6** (red), off resonance spectrum of inhibitor **1** with final concentration of 250 μM ; spectrum **5** (blue), off resonance spectrum of hit **6** with final concentration of 250 μM ; spectrum **4**, off resonance spectrum of inhibitor **1** mixed with hit **6**, each with a final concentration of 250 μM ; spectrum **3**, STD spectrum of inhibitor **1** mixed with hit **6**, inhibitor **1** with a final concentration of 500 μM and hit **6** with a final concentration of 250 μM ; spectrum **2**, STD spectrum of inhibitor **1** mixed with hit **6**, each with a final concentration of 250 μM ; spectrum **1**, STD spectrum of inhibitor **1** mixed with hit **6**, inhibitor **1** with a final concentration of 125 μM and hit **6** with a final concentration of 250 μM .

getting insights into the mode of binding. To this end, we performed ligand-observed STD-NMR studies using compounds **1**, **6**, and **9** in a competition experiment with our previously discovered inhibitor **1** (Figure 1). STD-NMR competition experiments can provide important information on the putative binding of the hit compounds to the target in the absence of any structural data of the protein.²⁵ In our previous work, we observed a defined binding orientation for inhibitor **1** to LANA where the pyridine moiety of inhibitor **1** interacts strongly with the LANA surface.¹² A competition experiment should allow for evaluating whether the new hit compounds bind at the same binding site as inhibitor **1** or if they bind simultaneously at different binding regions. For the STD studies, we used a fixed concentration (250 μM) of compound **1**, **6**, or **9** and different concentrations (125 μM , 250 μM , and 500 μM) of inhibitor **1**. The observed STD spectra for hit **6** in competition to inhibitor **1** is shown in Figure 5. Spectrum **6** (red) shows the off resonance spectrum of inhibitor **1**, and spectrum **5** (blue) shows the off resonance spectrum of compound **6**. The next spectrum (**4**) is the off resonance spectrum of inhibitor **1** mixed with **6**. The spectra **1**–**3** show the STD signals with fixed concentration of 250 μM of compound **6** and increasing concentrations of inhibitor **1**. The observed STD effects indicate that both compounds can bind simultaneously to the LANA surface as signals for compound **6** have identical peak intensities regardless any concentration of inhibitor **1**. The STD signals for inhibitor **1** increase with increasing concentration of inhibitor **1** as expected. For the STD competition experiments with compound **1** and inhibitor **1**, we observed similar results (see

Figure S26). Unfortunately, we were not able to observe STD-NMR data for compound **9**.

It is quite possible that compounds **1** and **6** bind in different binding modes and on different binding sites of LANA considering the huge DNA binding interface of LANA. Another explanation could be that the hit compounds have an allosteric effect on LANA, which could prevent the LANA–DNA interaction. Importantly, with the STD-NMR competition experiments, we demonstrated that different and non-overlapping binding sites for our novel scaffolds do exist compared to inhibitor **1**.

Cytotoxicity. We complemented our hit characterization by testing the compounds for cytotoxicity. Hit **1** and **6** showed only a marginal cytotoxicity on Hek293 and HepG2 cells, whereas compound **9** seems to be highly toxic (Table 2). Cytotoxicity assessment is very important in prospect of testing cell-based activities of antiviral compounds, which renders hit **6** the most promising starting point for subsequent optimization efforts as it showed the lowest cytotoxic potential.

Table 2. Cytotoxicity Data of Compounds **1**, **6**, and **9**

hit	relative viability after 48 h [%] at 100 μM	
	HepG2	Hek293
1	114 \pm 42	43 \pm 3
6	147 \pm 12	85 \pm 3
9	20 \pm 9	7 \pm 6

E

<https://dx.doi.org/10.1021/acscchembio.9b00845>
ACS Chem. Biol. XXXX, XXX, XXX–XXX

However, also scaffolds found in classes I (1) and III (9) might provide valuable structural motifs to be exploited in compound merging studies.

Conclusion. We have identified three chemical scaffolds as novel LANA–DNA interaction inhibitors by screening our in-house library using a dedicated FP-based competition assay. These new LANA inhibitors were found to inhibit the LANA–DNA interaction with IC_{50} values in the low micromolar range providing a very good starting point for medicinal chemistry optimization. Additionally, we applied SPR to confirm target binding and exclude DNA interaction in the FP assay. All hit compounds displayed a significant binding to LANA, and the obtained affinity (K_D) results were comparable to the inhibitory activity (IC_{50} values). Furthermore, we performed STD-NMR competition experiments with previously discovered inhibitor I. We found that compounds 1 and 6 are binding at a different binding site on the LANA surface than inhibitor I. Cytotoxicity was also evaluated for one representative compound from each class, whereby compounds 1 and 6 only show a marginal cytotoxicity and in contrast compound 9 was highly toxic. Importantly, our study demonstrated that our FP-based competition assay can be used as a fast and simple method to identify new LANA–DNA interaction inhibitors, which can open up avenues for further studies. Moreover, the results obtained in this study can serve as a starting point for further development of LANA–DNA interaction inhibitors with greater potency and selectivity as future therapeutic agents against latent KSHV infections.

METHODS

Expression of His-Tagged Oligomerization-Deficient LANA DBD (aa1008–1146) Mutant. The expression of His-tagged oligomerization-deficient LANA DBD (aa1008–1146) mutant was done as described previously.^{12,13}

FP-Based Library Screening. The in-house HIPS small molecule library contained 670 compounds dissolved in DMSO to 10 mM stock solutions. The fluorescence polarization assay was performed as described previously¹² with slight modifications. All experiments were performed in two independent experiments and each sample was tested in duplicate. The primary spot-test screening was performed with a final concentration of 100 μ M of each compound. The three-point secondary screening was carried out with final compound concentrations of 10 μ M, 50 μ M, and 100 μ M. LANA DBD mutant was used with a final concentration of 200 nM, and fluorescently labeled LBS2 oligomer was used with a final concentration of 10 nM.¹² IC_{50} determination of the final screening hits was performed as described previously.¹² Curves were fit to a four-parameter dose–response model using OriginPro 2018 to calculate IC_{50} values. For data reliability, high control (HC) comprising 24 samples with LANA DBD mutant, LBS2 probe, and DMSO (5% [v/v] final) in buffer without any compound and low control (LC) comprising 24 samples containing the same components without LANA DBD mutant were distributed over each screening plate.

Binding Studies Using Surface Plasmon Resonance (SPR). The SPR experiments were performed using a Reichert SR7500DC surface plasmon resonance spectrometer (Reichert Technologies, Depew, NY, USA), and medium density carboxymethyl dextran hydrogel CMD500 M sensor chips (XanTec Bioanalytics, Düsseldorf, Germany). Double distilled (dd) water was used as the running buffer for immobilization. Phosphate-buffered saline (PBS) buffer (10 mM Na_2HPO_4 , 1.8 mM KH_2PO_4 , 137 mM NaCl, 2.7 mM KCl, 0.05% [v/v] tween 20, pH 7.4) containing 5% [v/v] DMSO was used as the running buffer for binding study. All running buffers were filtered and degassed prior to use. The LANA 1008–1146 (17.653 kDa) was immobilized in one of the two flow cells by amine coupling procedure. The other flow cell was left blank to serve as a reference.

The system was initially primed with borate buffer 100 mM (pH 9.0); then the carboxymethyl dextran matrix was activated by a 1:1 mixture of *N*-ethyl-*N'*-(3-(dimethylamino)propyl)carbodiimide hydrochloride (EDC) 100 mM and *N*-hydroxysuccinimide (NHS) 100 mM at a flow rate of 10 μ L min⁻¹ for 7 min. The LANA protein (aa1008–1146) was diluted to a final concentration of 50 μ g mL⁻¹ in 10 mM sodium acetate buffer (pH 4.0) and was injected at a flow rate of 10 μ L min⁻¹ for 7 min. Nonreacted surface was quenched by 1 M ethanolamine hydrochloride (pH 8.5) at a flow rate of 25 μ L min⁻¹ for 3 min. A series of 7 buffer injections was run initially on both reference and active surfaces to equilibrate the system resulting in a stable immobilization level of approximately 5000 micro-refractive index units (μ RIU). Binding experiments were performed at 20 °C. Compounds dissolved in DMSO were diluted with PBS buffer (final DMSO concentration of 5% [v/v]) and were injected (in duplicate) at a flow rate of 30 μ L min⁻¹. Single-cycle kinetics were applied for K_D determination. The association time was set to 60 s, and the dissociation phase was recorded for 120 s. Ethylene glycol 80% in the running buffer or 10 mM glycine hydrochloride (pH 2.0) was used for regeneration of the surface. Differences in the bulk refractive index due to DMSO were corrected by a calibration curve (nine concentrations: 3–7% [v/v] DMSO in PBS buffer). Data processing and analysis were performed by Scrubber software (version 2.0c, 2008, BioLogic Software). Sensorgrams were calculated by sequential subtractions of the corresponding curves obtained from the reference flow cell and the running buffer (blank). SPR responses are expressed in resonance units (RU). Concentration-dependent SPR experiments were performed at final compound concentrations of 100 μ M, 50 μ M, 25 μ M, 12.5 μ M, 6.25 μ M, and 3.125 μ M. The K_D values were calculated by global fitting of the kinetic curves.

Saturation-Transfer Difference (STD) NMR. The STD experiments were recorded at 298 K on a Bruker Fourier spectrometer (500 MHz). The samples contained 5 μ M (final concentration) C-terminally His-tagged oligomerization-deficient LANA DBD (aa1008–1146) mutant and different compound concentrations. The control spectra were recorded under the same conditions containing the free compound to test for artifacts. The STD buffer for experiments using compound 1 and inhibitor I consisted of 5 mM HEPES, 125 mM NaCl, pH 8.5, in D₂O containing 10% [v/v] DMSO-*d*₆. The experiments were recorded with a carrier set at -1 ppm for the on-resonance and -40 ppm for the off-resonance irradiation. Selective protein saturation was carried out at 1 s using a train of 50 ms Gauss-shaped pulses, each separated by a 1 ms delay. For all experiments, a constant concentration of 250 μ M of 1 was used combined with different concentrations of inhibitor I (125 μ M, 250 μ M, and 500 μ M). The STD buffer for experiments using compound 6 and inhibitor I consisted of 20 mM Tris-Cl, 150 mM NaCl, pH 7.4, in D₂O containing 10% [v/v] DMSO-*d*₆. The experiments were recorded with a carrier set at -2 ppm for the on-resonance and -40 ppm for the off-resonance irradiation. Selective protein saturation was carried out at 1.5 s using a train of 50 ms Gauss-shaped pulses, each separated by a 1 ms delay. For all experiments, a constant concentration of 250 μ M of 6 was used combined with different concentrations of inhibitor I (125 μ M, 250 μ M, and 500 μ M).

Cytotoxicity Assay. HepG2 and Hek193 cells (2×10^5 cells per well) were seeded in 24-well flat bottom plates. The procedure for culturing the cells, incubation times, and OD measurements were performed as described previously²⁶ with slight modifications. Twenty-four hours after seeding the cells, the compounds were added (final DMSO concentration of 1%) and incubated for 24 h. The living cell mass was determined after 24 h. Each compound was tested in two independent experiments.

ASSOCIATED CONTENT

Supporting Information

The Supporting Information is available free of charge at <https://pubs.acs.org/doi/10.1021/acscchembio.9b00845>.

F

<https://dx.doi.org/10.1021/acscchembio.9b00845>
ACS Chem. Biol. XXXX, XXX, XXX–XXX

Data of primary and secondary FP-based library screening, concentration-dependent FP experiments, SPR response curves, information on K_D determination via SPR, STD-NMR spectra, and cytotoxicity assay data (PDF)

AUTHOR INFORMATION

Corresponding Author

Martin Empting – Department of Drug Design and Optimization (DDOP), Helmholtz-Institute for Pharmaceutical Research Saarland (HIPS) - Helmholtz Centre for Infection Research (HZI), 66123 Saarbrücken, Germany; Department of Pharmacy, Saarland University, 66123 Saarbrücken, Germany; German Centre for Infection Research (DZIF), Partner Site Hannover-Braunschweig, 66123 Saarbrücken, Germany; orcid.org/0000-0002-0503-5830; Phone: +49681-98806 2031; Email: Martin.Empting@helmholtz-hips.de

Authors

Philine Kirsch – Department of Drug Design and Optimization (DDOP), Helmholtz-Institute for Pharmaceutical Research Saarland (HIPS) - Helmholtz Centre for Infection Research (HZI), 66123 Saarbrücken, Germany; Department of Pharmacy, Saarland University, 66123 Saarbrücken, Germany; German Centre for Infection Research (DZIF), Partner Site Hannover-Braunschweig, 66123 Saarbrücken, Germany

Valentin Jakob – Department of Drug Design and Optimization (DDOP), Helmholtz-Institute for Pharmaceutical Research Saarland (HIPS) - Helmholtz Centre for Infection Research (HZI), 66123 Saarbrücken, Germany; Department of Pharmacy, Saarland University, 66123 Saarbrücken, Germany; German Centre for Infection Research (DZIF), Partner Site Hannover-Braunschweig, 66123 Saarbrücken, Germany

Walid A. M. Elgaher – Department of Drug Design and Optimization (DDOP), Helmholtz-Institute for Pharmaceutical Research Saarland (HIPS) - Helmholtz Centre for Infection Research (HZI), 66123 Saarbrücken, Germany; orcid.org/0000-0002-8766-4568

Christine Walt – Department of Drug Design and Optimization (DDOP), Helmholtz-Institute for Pharmaceutical Research Saarland (HIPS) - Helmholtz Centre for Infection Research (HZI), 66123 Saarbrücken, Germany

Kevin Oberhausen – Department of Drug Design and Optimization (DDOP), Helmholtz-Institute for Pharmaceutical Research Saarland (HIPS) - Helmholtz Centre for Infection Research (HZI), 66123 Saarbrücken, Germany

Thomas F. Schulz – German Centre for Infection Research (DZIF), Partner Site Hannover-Braunschweig, 66123 Saarbrücken, Germany; Institute of Virology, Hannover Medical School, 30625 Hannover, Germany

Complete contact information is available at: <https://pubs.acs.org/10.1021/acscchembio.9b00845>

Author Contributions

[†]P.K. and V.J. contributed equally.

Funding

This work was financial supported by the German Centre for Infection Research (DZIF) and the DFG Collaborative Research Centre 900, project C1.

Notes

The authors declare no competing financial interest.

ACKNOWLEDGMENTS

We thank Prof. Dr. R. W. Hartmann for his continuous support and guiding expertise. For the help with the STD NMR experiments, we thank Dr. J. Zapp.

ABBREVIATIONS

AIDS, acquired immune deficiency syndrome; DMSO, dimethyl sulfoxide; DBD, DNA binding domain; EDC, 1-ethyl-3-(3-(dimethylamino)propyl) carbodiimide hydrochloride; FP, fluorescence polarization; HHV-8, human herpesvirus 8; HIPS, Helmholtz Institute for Pharmaceutical Research Saarland; KS, Kaposi sarcoma; KSHV, Kaposi's sarcoma-associated herpesvirus; LANA, latency-associated nuclear antigen; LBS, LANA binding site; MST, microscale thermophoresis; NHS, N-hydroxysuccinimide; PBS, phosphate-buffered saline; STD NMR, saturation transfer difference nuclear magnetic resonance; SPR, surface plasmon resonance; TR, terminal repeat

REFERENCES

- Schulz, T. F. (2006) The pleiotropic effects of Kaposi's sarcoma herpesvirus. *J. Pathol.* 208, 187–198.
- Greene, W., Kuhne, K., Ye, F., Chen, J., Zhou, F., Lei, X., and Gao, S.-J. (2007) Molecular biology of KSHV in relation to AIDS-associated oncogenesis. *Cancer Treat. Res.* 133, 69–127.
- Zlatkovskaia, N. M., Penner, I. D., Sosnova, M. A., Abramova, V. A., and Duovitskaia, N. F. (1975) Clinical characteristics of intestinal coli infection in the city of Frunze. *Zdravookhr Kirg.* 23–27.
- World Health Organization - International Agency for Research (2012) Biological agents. Volume 100 B. A review of human carcinogens. *IARC Monogr. Eval. Carcinog. Risks. Hum.* 100, 1–441.
- Bouvard, V., Baan, R., Straif, K., Grosse, Y., Secretan, B., El Ghissassi, F., Benbrahim-Tallaa, L., Guha, N., Freeman, C., Galichet, L., and Cogliano, V. (2009) A review of human carcinogens—Part B: biological agents. *Lancet Oncol.* 10, 321–322.
- Coen, N., Duraffour, S., Snoeck, R., and Andrei, G. (2014) KSHV targeted therapy: an update on inhibitors of viral lytic replication. *Viruses* 6, 4731–4759.
- Bhutani, M., Polizzotto, M. N., Uldrick, T. S., and Yarchoan, R. (2015) Kaposi sarcoma-associated herpesvirus-associated malignancies: epidemiology, pathogenesis, and advances in treatment. *Semin. Oncol.* 42, 223–246.
- Rainbow, L., Platt, G. M., Simpson, G. R., Sarid, R., Gao, S. J., Stoiber, H., Herrington, C. S., Moore, P. S., and Schulz, T. F. (1997) The 222- to 234-kilodalton latent nuclear protein (LNA) of Kaposi's sarcoma-associated herpesvirus (human herpesvirus 8) is encoded by orf73 and is a component of the latency-associated nuclear antigen. *J. Virol.* 71, 5915–5921.
- Kedes, D. H., Ganem, D., Ameli, N., Bacchetti, P., and Greenblatt, R. (1997) The prevalence of serum antibody to human herpesvirus 8 (Kaposi sarcoma-associated herpesvirus) among HIV-seropositive and high-risk HIV-seronegative women. *JAMA* 277, 478–481.
- Mariggio, G., Koch, S., and Schulz, T. F. (2017) Kaposi sarcoma herpesvirus pathogenesis. *Philos. Trans. R. Soc., B* 372, 20160275.
- Yamada, M., Katano, H., Yotsumoto, M., Hashimoto, H., Muramatsu, T., Shiotsuka, M., Fukutake, K., and Kuroda, M. (2014) Unique expression pattern of viral proteins in human herpesvirus 8-positive plasmablastic lymphoma: a case report. *Int. J. Clin. Exp. Pathol.* 7, 6415–6418.
- Kirsch, P., Jakob, V., Oberhausen, K., Stein, S. C., Cucarro, L., Schulz, T. F., and Empting, M. (2019) Fragment-Based Discovery of a Qualified Hit Targeting the Latency-Associated Nuclear Antigen of the Oncogenic Kaposi's Sarcoma-Associated Herpesvirus/Human Herpesvirus 8. *J. Med. Chem.* 62, 3924–3939.

- (13) Hellert, J., Weidner-Glunde, M., Krausze, J., Lünsdorf, H., Ritter, C., Schulz, T. F., and Lührs, T. (2015) The 3D structure of Kaposi sarcoma herpesvirus LANA C-terminal domain bound to DNA. *Proc. Natl. Acad. Sci. U. S. A.* *112*, 6694–6699.
- (14) Barbera, A. J., Chodaparambil, J. V., Kelley-Clarke, B., Joukov, V., Walter, J. C., Luger, K., and Kaye, K. M. (2006) The nucleosomal surface as a docking station for Kaposi's sarcoma herpesvirus LANA. *Science* *311*, 856–861.
- (15) Chodaparambil, J. V., Barbera, A. J., Lu, X., Kaye, K. M., Hansen, J. C., and Luger, K. (2007) A charged and contoured surface on the nucleosome regulates chromatin compaction. *Nat. Struct. Mol. Biol.* *14*, 1105–1107.
- (16) Weidner-Glunde, M., Mariggio, G., and Schulz, T. F. (2017) Kaposi's Sarcoma-Associated Herpesvirus Latency-Associated Nuclear Antigen: Replicating and Shielding Viral DNA during Viral Persistence. *J. Virol.* *91*, No. e01083-16.
- (17) Verma, S. C., Lan, K., and Robertson, E. (2007) Structure and Function of Latency-Associated Nuclear Antigen. *Curr. Top. Microbiol. Immunol.* *312*, 101–136.
- (18) Hellert, J., Weidner-Glunde, M., Krausze, J., Richter, U., Adler, H., Fedorov, R., Pietrek, M., Rückert, J., Ritter, C., Schulz, T. F., and Lührs, T. (2013) A structural basis for BRD2/4-mediated host chromatin interaction and oligomer assembly of Kaposi sarcoma-associated herpesvirus and murine gammaherpesvirus LANA proteins. *PLoS Pathog.* *9*, No. e1003640.
- (19) Elgaher, W. A. M., Fruth, M., Groh, M., Hauptenthal, J., and Hartmann, R. W. (2014) Expanding the scaffold for bacterial RNA polymerase inhibitors: design, synthesis and structure-activity relationships of ureido-heterocyclic-carboxylic acids. *RSC Adv.* *4*, 2177–2194.
- (20) Sahner, J. H., Empting, M., Kamal, A., Weidel, E., Groh, M., Börger, C., and Hartmann, R. W. (2015) Exploring the chemical space of ureidothiophene-2-carboxylic acids as inhibitors of the quorum sensing enzyme PqsD from *Pseudomonas aeruginosa*. *Eur. J. Med. Chem.* *96*, 14–21.
- (21) Elgaher, W. A. M., Sharma, K. K., Hauptenthal, J., Saladini, F., Pires, M., Real, E., Mély, Y., and Hartmann, R. W. (2016) Discovery and Structure-Based Optimization of 2-Ureidothiophene-3-carboxylic Acids as Dual Bacterial RNA Polymerase and Viral Reverse Transcriptase Inhibitors. *J. Med. Chem.* *59*, 7212–7222.
- (22) Hinsberger, S., Hüsecken, K., Groh, M., Negri, M., Hauptenthal, J., and Hartmann, R. W. (2013) Discovery of novel bacterial RNA polymerase inhibitors: pharmacophore-based virtual screening and hit optimization. *J. Med. Chem.* *56*, 8332–8338.
- (23) Copeland, R. A. (2016) The drug-target residence time model: a 10-year retrospective. *Nat. Rev. Drug Discovery* *15*, 87–95.
- (24) Doornbos, M. L. J., Cid, J. M., Haubrich, J., Nunes, A., van de Sande, J. W., Vermond, S. C., Mulder-Krieger, T., Trabanco, A. A., Ahnaou, A., Drinkenburg, W. H., Lavreysen, H., Heitman, L. H., Ijzerman, A. P., and Tresadern, G. (2017) Discovery and Kinetic Profiling of 7-Aryl-1,2,4-triazolo[4,3-*a*]pyridines: Positive Allosteric Modulators of the Metabotropic Glutamate Receptor 2. *J. Med. Chem.* *60*, 6704–6720.
- (25) Lepre, C. A., Moore, J. M., and Peng, J. W. (2004) Theory and applications of NMR-based screening in pharmaceutical research. *Chem. Rev.* *104*, 3641–3676.
- (26) Hauptenthal, J., Baehr, C., Zeuzem, S., and Piiper, A. (2007) RNase A-like enzymes in serum inhibit the anti-neoplastic activity of siRNA targeting polo-like kinase 1. *Int. J. Cancer* *121*, 206–210.

3.3 Chapter C: Hit-to-Lead Optimization of a LANA Inhibitor against KSHV Infections

The following persons contributed experimentally to this chapter:

Philine Kirsch: designed and synthesized target compounds, performed FP-based competition assay for functional evaluation of all target compounds, performed STD-NMR experiments

Saskia C. Stein: performed EMSA experiments for functional evaluation of target compounds, expressed and purified CTD LANA wild-type.

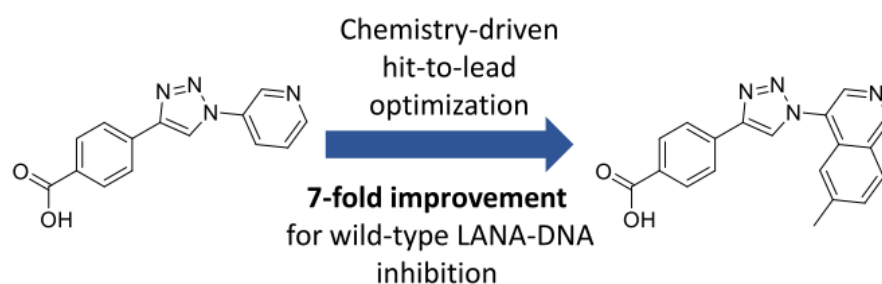
Aylin Berwanger: was involved in the synthesis of target compounds.

Julia Rinkes: was involved in the synthesis of target compounds.

Valentin Jakob: expressed and purified LANA DBD mutant.

This part of the thesis has been submitted to European Journal of Medicinal Chemistry on 11 February 2020.

Graphical Abstract:



Hit-to-Lead Optimization of a Latency-associated Nuclear Antigen Inhibitor against Kaposi's Sarcoma-associated Herpesvirus Infections

Philine Kirsch,^{1,2,3} Saskia C. Stein,^{3,4} Aylin Berwanger,^{1,2,3} Julia Rinke,^{1,2,3} Valentin Jakob,^{1,2,3} Thomas F. Schulz^{3,4} and Martin Empting^{*,1,2,3}

¹Department of Drug Design and Optimization (DDOP), Helmholtz-Institute for Pharmaceutical Research Saarland (HIPS) - Helmholtz Centre for Infection Research (HZI), Campus E8.1, 66123 Saarbrücken, Germany.

²Department of Pharmacy, Saarland University, Campus E8.1, 66123 Saarbrücken, Germany.

³German Centre for Infection Research (DZIF), Partner Site Hannover-Braunschweig, 66123 Saarbrücken, Germany.

⁴Institute of Virology, Hannover Medical School, Carl-Neuberg-Strasse 1, 30625 Hannover, Germany.

Abstract

The Latency-associated nuclear antigen (LANA) plays a central role for the latent persistence of the Kaposi's Sarcoma Herpesvirus (KSHV) in the human host and helps to establish lifelong infections. Herein, we report our efforts towards hit-to-lead generation starting from a previously discovered LANA-DNA inhibitor. By tethering the viral genome to the host nucleosomes, LANA ensures the segregation and persistence of the viral DNA during mitosis. LANA is also required for the replication of the latent viral episome during the S phase of the cell cycle. We aim to inhibit the interaction between LANA and the viral genome to prevent the latent persistence of KSHV in the host organism. Medicinal chemistry-driven optimization studies and structure-activity-relationship investigation led to the discovery of an improved LANA inhibitor. The functional activity of our compounds was evaluated using a fluorescence polarization (FP)-based interaction inhibition assay and electrophoretic mobility shift assay (EMSA). Even though a crystal structure of the ligand protein complex was not available, we successfully conducted hit optimization toward a low micromolar protein-nucleic acid-interaction inhibitor. Additionally, we applied STD-NMR studies to corroborate target binding and to

gain insights into the binding orientation of our most potent inhibitor, providing opportunities for further rational design of more efficient LANA-targeting anti KSHV agents in future studies.

Keywords: hit-to-lead optimization, latency-associated nuclear antigen (LANA), Kaposi's Sarcoma Herpesvirus (KSHV), fluorescence polarization (FP)-based interaction inhibition assay, electrophoretic mobility shift assay (EMSA), CuAAC, STD-NMR

Introduction

Kaposi's Sarcoma Herpesvirus (KSHV) is a human gamma herpesvirus and establishes a lifelong latent infection in B-cells and endothelial cells.^{1,2} The virus was identified as the etiological agent of Kaposi's Sarcoma (KS) and is involved in two other neoplastic diseases, multicentric Castleman's disease and pleural effusion lymphoma.^{1,3} In healthy individuals, KSHV-associated diseases are rare. However, in immunosuppressed patients, e.g., transplant recipients or patients with the acquired immunodeficiency syndrome (AIDS), KSHV is highly oncogenic.^{4,5} However, classic KS mainly can also occur in elderly men especially from KSHV-endemic areas and endemic KS in East and Central Africa.⁶ The main key player for the establishment and maintenance of the latent infection is the latency-associated nuclear antigen (LANA).⁷⁻⁹ It is an origin-binding protein, whose C-terminal domain binds to the viral genome and whose N-terminal region interacts simultaneously with host nucleosomes.¹⁰⁻¹² This allows the segregation of latent viral episomes during mitosis and their partitioning to daughter cells.¹³ LANA has also additional functions like latent viral replication, transcriptional control and survival in the host cell.¹⁴⁻¹⁶ The C-terminal DNA-binding domain (DBD) of LANA binds the viral genome in a sequence-specific manner.¹⁷ Located on the terminal repeats (TRs) are three specific LANA binding sites (LBS), LBS1, LBS2 and LBS3. LBS1 has a hundred fold higher affinity to LANA compared to LBS2 and LBS3.¹⁷ In the majority of KSHV-associated cancer cells the viral genome is present and LANA is expressed.¹⁸ It has been shown, that the persistence of viral DNA is affected by disturbing or influencing LANA.¹⁵ The inhibition of the interaction between LANA and viral DNA could lead to a reduction or loss of viral genomes in the infected cells. Today's treatment of KSHV and KSHV-associated diseases is difficult and still limited.^{19,20} It is clear, that there is an urgent need for specific drugs, which interfere with novel steps in the KSHV lifecycle. In view of its central role during latent viral persistence, LANA is considered to be a very promising target for the development of specific antiviral therapeutics against KSHV.

In a study previously published by us in 2019, we described the discovery of first inhibitors, which interfere with the LANA-DNA interaction.¹¹ Further inhibitor scaffolds have been identified using a functional screen and an in-house compound library.²¹ Starting with a fragment-based drug discovery approach, we successfully developed a fragment-sized inhibitor **I** capable to compete with the viral DNA (Figure 1). For the evaluation of functional activity of our compounds, we used a fluorescence-polarization (FP)-based assay and electrophoretic mobility shift assay (EMSA) experiments. For our most promising fragment-sized inhibitor **I**, we observed an IC_{50} value of $17 \pm 1 \mu\text{M}$ in our FP-assay using a LANA DNA binding domain (DBD) mutant and $435 \pm 6 \mu\text{M}$ in the EMSA studies using the wild-type LANA C-terminal domain (CTD).

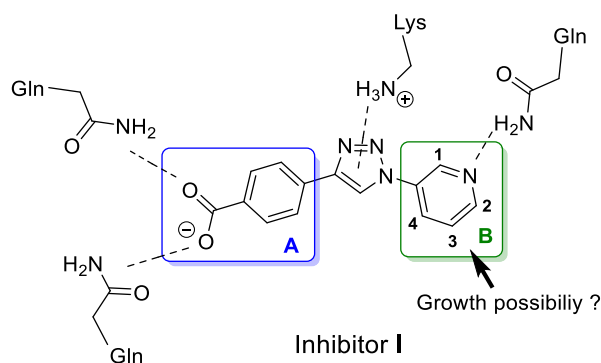


Figure 1: Previously described LANA-DNA interaction inhibitor **I** and its predicted binding node which provides the basis for structural optimization by rational design and growth vector exploration.

We confirmed target binding using microscale thermophoresis (MST) and saturation transfer difference (STD)-NMR experiments. Additionally, the STD-NMR experiments and molecular docking studies provided important information on the putative orientation of Inhibitor **I** when bound to LANA. Based on the STD-NMR studies and docking results we suggested that the nitrogen at the pyridine core acts as a hydrogen bond acceptor and protons 2, 3 and 4 are not in direct interaction with the protein surface, hence these positions should be further investigated as potential growth vectors. Furthermore, two glutamines are presumably involved in hydrogen-bond interactions with the carboxyl group. However, it was not clear whether the carboxylic acid function is necessary for binding.¹¹

Based on these findings, we embarked on structure-activity relationship (SAR) studies and further medicinal chemistry optimization to improve the potency of our hit compounds. Herein, we report our

recent advances in improving our LANA-DNA-interaction inhibitors using compound **I** as a starting point. Unfortunately, our efforts in solving a co-crystal structure of inhibitor **I** in complex with LANA have not been successful to date. This renders unambiguous experiment-supported structure-based optimization unfeasible. Therefore, we systematically investigated the LANA-DNA-interaction inhibition of new synthesized compounds using FP-based competition assay and EMSA experiments as the SAR drivers.

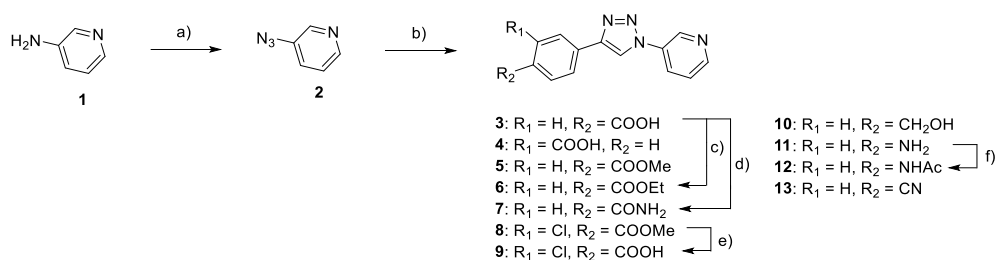
Design Concept

Based on the previously applied STD-NMR and docking studies we modified Inhibitor **I** in a step-by-step manner. Inhibitor **I** was divided in two regions, the benzoic acid part **A** and the pyridine core **B** (Figure 1). The triazole core was not yet modified in order to exploit the robust and facile Copper(I)-catalyzed azide-alkyne cycloaddition (CuAAC) click chemistry. First, region **A** was modified and variations of the carboxylic acid were introduced. As a second step, we have modified the pyridine moiety, region **B**. From our previous results we assumed that the nitrogen at the pyridine motif is essential for binding and functions as hydrogen bond acceptor. STD-NMR data revealed that Proton 1 interacts tightly with LANA while proton 2 is also in close proximity to the protein surface. However, our docking studies suggested that the latter might be at least partially solvent exposed. In contrast, protons at position 3 and 4 did not show direct contact with the LANA surface according to their weak STD-NMR effects. These observations inspired us to investigate positions 2, 3 and 4 as potential growth vectors in the presented study.

Results and Discussion

Chemistry

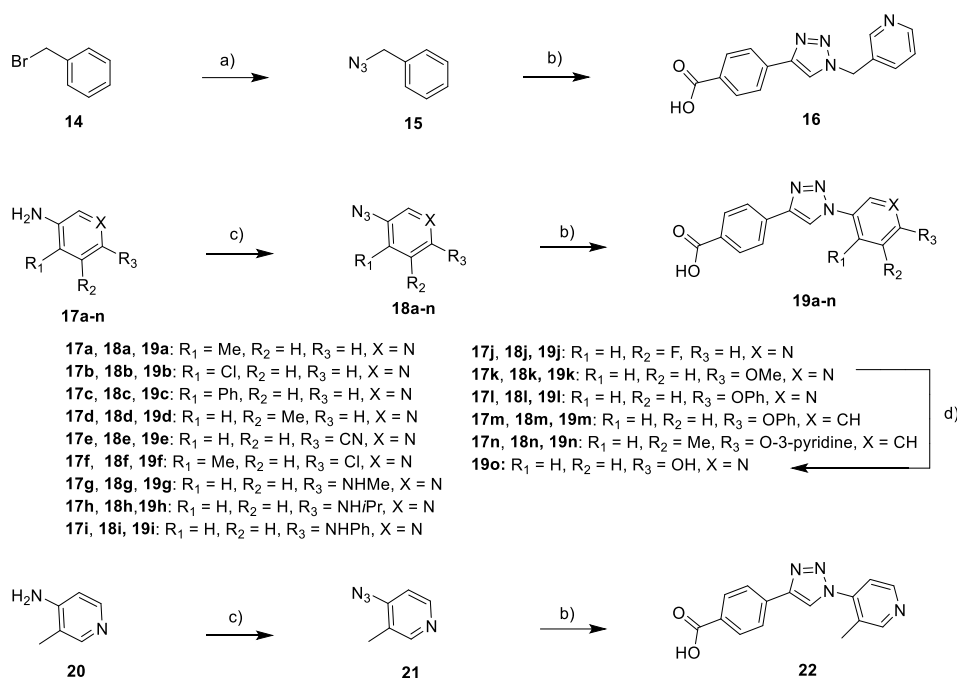
Modifications of region A. 3-azidopyridine **2** was generated by a standard azidation method using 3-aminopyridine **1**, NaNO₂ and NaN₃ in a mixture of EtOAc and 6M HCl.^{11,22} In a second step, as depicted in scheme 1, various commercially available ethynylbenzene derivatives were used in a standard copper-catalyzed CuAAC reaction with 3-azidopyridine to provide the triazoles **3 - 5, 8, 10, 11**, and **13**.¹¹

Scheme 1. Modification of region A.^a

^aReagents and conditions: a) NaNO₂, NaN₃, EtOAc, 6M HCl, 0°C → rt, 2 h; b) corresponding ethynylbenzene, CuSO₄•5H₂O, Na-Ascorbate, DIPEA, MeOH, H₂O, rt, 16 h; c) 1. SOCl₂, DMF, 60°C, 1 h, 2. EtOH, DIPEA, rt, 16 h; d) 1. SOCl₂, DMF, 60°C, 1 h, 2. NH₄OH, rt, 16 h; e) 2 M NaOH, MeOH, rt, 16 h; f) Acetyl chloride, Et₃N, DCM, DMF, rt, 16 h.

The ethyl ester **6** and amide **7** analogue were generated from the carboxylic acid **3** by thionyl chloride-mediated activation and subsequent treatment with ethanol or aq. ammonia solution. The hydrolysis of 3-chloro-4-methylester intermediate **8** with NaOH in ethanol produced the corresponding acid **9**. The *N*-acetyl analogue **12** was synthesized from amine **11** with acetyl chloride under basic conditions.

Modifications of region B. Compound **16** bearing an additional CH₂-linker between triazole and pyridine core was synthesized starting from (bromomethyl)benzene **14**, which was converted to the azide **15** using NaN₃ in DMSO²³, followed by a click reaction with 4-ethynylbenzoic acid. Different arylazides **17a-n** and **20** decorated with various substitutions were generated by reaction of the corresponding commercially available amines **18a-n** and **21** with NaNO₂ and NaN₃ in 6 M HCl and EtOAc (Scheme 2). The subsequent CuAAC click reaction with 4-ethynylbenzoic acid provided the target molecules **19a-n** and **22**. The hydroxypyridine **19o** analogue was generated from the methoxypyridine **19k** by treating with 48% aqueous HBr solution at 80 °C.

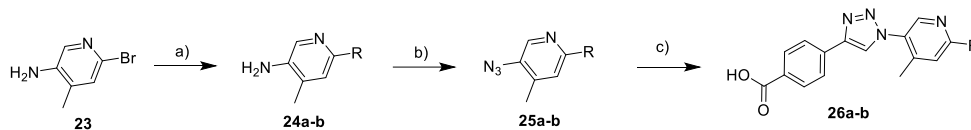
Scheme 2: Azide synthesis and CuAAC click reaction.^a

^aReagents and conditions: a) NaN₃, Et₃N, DMSO, rt, 16 h; b) 4-ethynylbenzoic acid, CuSO₄•5H₂O, Na-Ascorbate, DIPEA, MeOH, H₂O, rt, 16 h; c) NaNO₂, NaN₃, EtOAc, 6M HCl, 0°C → rt, 2 h; d) 48% aq. HBr, 80°C, 12 h.

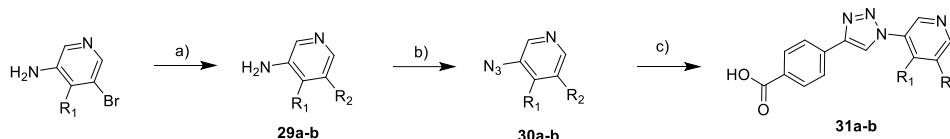
As depicted in Scheme 3, the syntheses of target compounds via Suzuki coupling was achieved using two different synthetic routes. In route 1, Suzuki coupling with different commercially available boronic acids and halogenated pyridine-3-amines **23**, **27** and **28** in presence of Pd(PPh₃)₄ achieved phenyl-substituted pyridine amines **24a-b** and **29a-b** in the first step. Subsequently, the amines were converted to the corresponding azides **25a-b** and **30a-b** followed by a CuAAC click reaction with 4-ethynylbenzoic acid to obtain the target compounds **26a-b** and **31a-b**. In parallel, the alternative route 2 was established for late stage modifications via Suzuki coupling. First, halogenated pyridine-3-amines **32a-b** were converted to the corresponding azide **33a-b**, followed by click reaction with 4-ethynylbenzoate to obtain the corresponding triazole intermediates **34a-b**. Subsequently, phenyl-substituted compounds **35a-k** were achieved via Suzuki coupling using corresponding boronic acids and Pd(PPh₃)₄.

Scheme 3: Synthesis of target compounds via Suzuki coupling using two different routes.^a

Route 1:



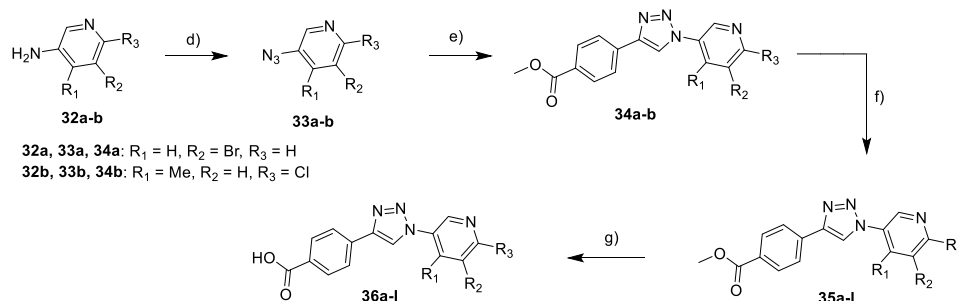
24a, 25a, 26a: R = 2-phenol
24b, 25b, 26b: R = 3-(hydroxymethyl)phenyl



27: R₁ = H, R₂ = Br, R₃ = H
28: R₁ = Cl, R₂ = Br, R₃ = H

29a, 30a, 31a: R₁ = H, R₂ = 3-(hydroxymethyl)phenyl
29b, 30b, 31b: R₁ = Cl, R₂ = Ph

Route 2:



32a, 33a, 34a: R₁ = H, R₂ = Br, R₃ = H

32b, 33b, 34b: R₁ = Me, R₂ = H, R₃ = Cl

35a, 36a: R₁ = H, R₂ = Ph, R₃ = H

35b, 36b: R₁ = H, R₂ = 2-methoxyphenyl, R₃ = H

35c, 36c: R₁ = H, R₂ = 3-methoxyphenyl, R₃ = H

35d, 36d: R₁ = H, R₂ = 4-methoxyphenyl, R₃ = H

35e, 36e: R₁ = H, R₂ = 3-hydroxyphenyl, R₃ = H

35f, 36f: R₁ = H, R₂ = 3,4-dimethylphenyl, R₃ = H

35g, 36g: R₁ = H, R₂ = 3,4-difluorophenyl, R₃ = H

35h, 36h: R₁ = H, R₂ = 4-(hydroxymethyl)phenyl, R₃ = H

35i, 36i: R₁ = H, R₂ = 3-fluoro-5-methoxyphenyl, R₃ = H

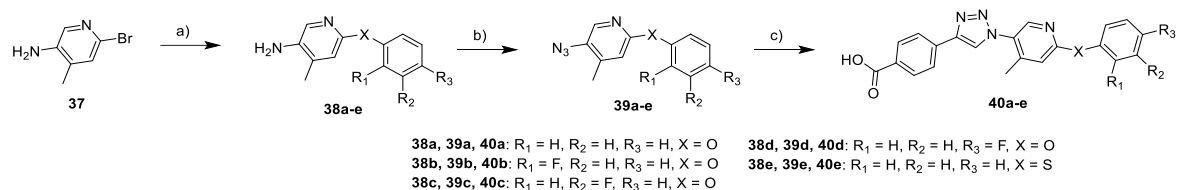
35j, 36j: R₁ = H, R₂ = 3-furanyl, R₃ = H

35k, 36k: R₁ = Me, R₂ = H, R₃ = Ph

35l, 36l: R₁ = Me, R₂ = H, R₃ = 4-chlorobenzene

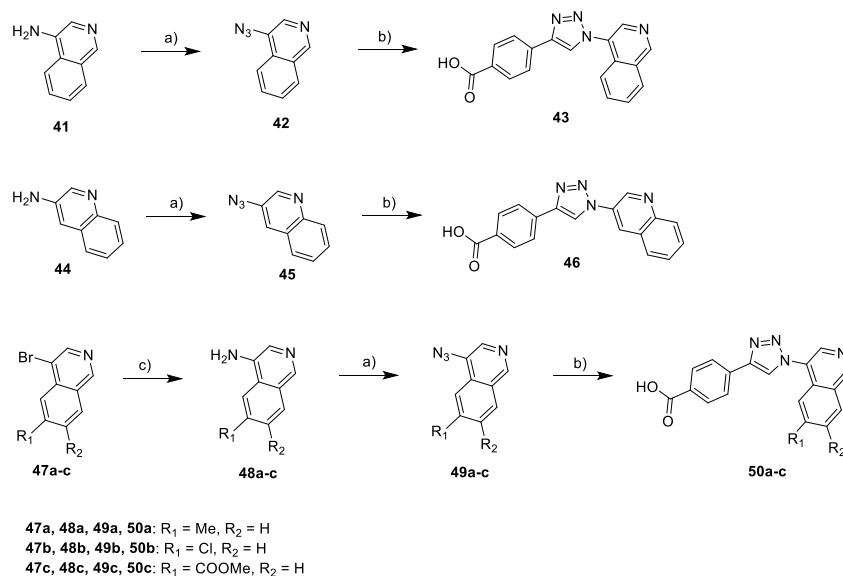
^aReagents and conditions: a) corresponding boronic acid, Na₂CO₃, Pd(P(Ph)₃)₄, 1,4-dioxan, H₂O, 90 °C, 16h; b) NaN₃, EtOAc, 6M HCl, 0 °C → rt, 2 h; c) 4-ethynyl benzoic acid, CuSO₄•5H₂O, Na-Ascorbate, DIPEA, MeOH, H₂O, rt, 16 h; d) NaN₃, EtOAc, 6M HCl, 0 °C → rt, 2 h; e) 4-ethynyl benzoate, CuSO₄•5H₂O, Na-Ascorbate, DIPEA, MeOH, H₂O, rt, 16 h; f) corresponding boronic acid, Na₂CO₃, Pd(P(Ph)₃)₄, 1,4-dioxan, H₂O, 90 °C, 16h; g) 2 M NaOH, MeOH, rt, 16 h.

Finally, the hydrolysis of the esters with NaOH in methanol produced the target carboxylic acid compounds **36a-k**. As depicted in Scheme 4, for the synthesis of the series of pyridine-phenoxy target compounds **40a-e**, copper-catalyzed Ullmann reaction was used in the first step using 6-bromo-4-methylpyridin-3-amine **37**, the corresponding phenol derivative or thiophenol, Cs₂CO₃ and CuI to obtain the aminopyridine-phenoxy intermediates **38a-e**.

Scheme 4: Synthesis of target compounds via Ullmann Reaction.^a

^aReagents and conditions: a) corresponding phenol or thiophenol, Cs₂CO₃, CuI, DMF, 130 °C, 16 h; b) NaNO₂, NaN₃, EtOAc, 6M HCl, 0°C → rt, 2 h; c) 4-ethynyl benzoic acid, CuSO₄•5H₂O, Na-Ascorbate, DIPEA, MeOH, H₂O, rt, 16 h.

The obtained amines were transformed into the corresponding azides **39a-e** as described above. Last step was a CuAAC reaction of azides with 4-ethynylbenzoic acid to obtain the target compounds **40a-e**. The isoquinoline **43** and quinoline **46** analogue were synthesized starting from isoquinoline-4-amin **41** and quinoline-3-amin **44** by standard azidation to **42** and **45**, followed by CuAAC click reaction with 4-ethynylbenzoic acid. Further isoquinoline derivatives **50a-c** were synthesized in a 3 step procedure (Scheme 5).

Scheme 5: Synthesis of isoquinoline derivatives.^a

^aReagents and conditions: a) NaNO₂, NaN₃, EtOAc, 6M HCl, 0°C → rt, 2 h; b) 4-ethynyl benzoic acid, CuSO₄•5H₂O, Na-Ascorbate, DIPEA, MeOH, H₂O, rt, 16 h; c) NaN₃, Na₂CO₃, CuSO₄•5H₂O, Na-Ascorbate, L-proline, DMF, H₂O, 85 °C, 24 h

A direct transformation of bromo isoquinolines **47a-c** into the corresponding azides using NaN_3 , Cu(I) and Na_2CO_3 at 85°C over night as described in literature was not efficient.²⁴ LCMS-guided reaction monitoring showed the formation the primary amine and other side products. For this reason, we extended the reaction time until we detected full conversion into the corresponding primary amine **48a-c** with the aim to subsequently transform these intermediates into the corresponding azides. Indeed, we achieved successful azidation (intermediates **49a-c**) and CuAAC coupling, respectively, using amines **48a-c** and the conditions described above yielding the desired isoquinoline products **50a-c**.

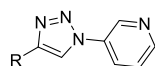
Functional Evaluation using LANA-DNA Interaction Inhibition Assays and SAR Studies.

The target compounds were tested for functional activity in the FP-based LANA-DNA interaction inhibition assay using LBS2 as the probe and an oligomerization-deficient LANA DBD mutant.¹¹ All compounds showing an IC_{50} values greater than $250\ \mu\text{M}$ were further tested in an orthogonal LANA-DNA interaction inhibition assay employing EMSA methodology, the same LANA DBD mutant and LBS1 as probe. As described above, the latter oligo has a higher affinity to the target rendering the EMSA experiment a more stringent read out for compound efficacy.

For the first series of compounds, we investigated the significance of the carboxylic acid in the Western part of the molecule (region A) by varying its position, attaching additional groups or substituting it by other polar functional groups capable of participating in hydrogen bonding. The results are shown in Table 1.

Moving the carboxylic acid from *para* (inhibitor **1**) to *meta* position (**4**) decreases the activity significantly. Also an additional chlorine atom attached in *meta* position (**9**) lead to a complete loss of activity. The replacement of the carboxylic acid by a methyl ester (**5**), ethyl ester (**6**) or amide (**7**) was also detrimental. Furthermore, moving from the carboxylic acid to the methyl alcohol (**10**), amine (**11**), acetamide (**12**) or nitrile (**13**) also resulted in inactive compounds. These results indicate that the carboxylic acid in *para* position in region A is essential for inhibitory activity. Therefore, we kept the *p*-carboxylic acid in region A fixed for further optimization studies and focused on the modifications at the pyridine core in region B. First, we examined the effect on inserting a short linker between the triazole and the pyridine core (**16**).

Table 1: Inhibition activities of compounds with modification in region A demonstrating that *p*-carboxylic acid is essential for inhibitory activity.



Cpd	FP Assay (LBS2) ^a		Cpd	FP Assay (LBS2)	
	R	IC ₅₀		R	IC ₅₀
Inhibitor I		17 ± 1 μM	9		n.i.
4		>250 μM	10		n.i.
5		n.i. ^b	11		>250 μM
6		n.i.	12		n.i.
7		n.i.	13		>250 μM

^aFluorescence-polarization assay using LBS2 as probe, data representing average of duplicates ± standard deviation; ^bNo inhibition.

This, however, resulted in loss of activity. As described before, from previous STD-NMR and molecular docking experiments we expected, that growing the fragment-sized Inhibitor I in different positions at the pyridine core (region B) would potentially increase potency.

To explore the influence of larger structural motifs at the pyridine core in position 4 we introduced a variety of residues. As listed in Table 2, growing in this position is accepted and resulted in moderate to potent inhibitory effects in FP assay ranging from IC₅₀ values of 86 ± 6 μM (**19a**) to 18 ± 4 μM (**19c**). The size of the introduced residue seems to play an important role. While a small methyl group is not favorable, but accepted (**19a**, IC₅₀ 86 ± 6 μM), further increasing the size from chlorine (**19b**) to phenyl (**19c**) improves IC₅₀ values to 29 ± 1 μM μM and 18 ± 4 μM, respectively. This observation might hint at a steric *ortho* effect. The additional bulky phenyl ring strongly hinders the rotation of the bond between triazole and pyridine and, therefore, might fix the nitrogen in the pyridine core in a more favorable orientation. In EMSA experiments, 4-substituted compounds **19b** (EMSA: 94% inhibition @ 500 μM) and **19c** (EMSA: 100% inhibition @ 500 μM) showed a higher efficiency compared to Inhibitor I (EMSA: 83% inhibition @ 500 μM).¹¹ Additionally, we shifted the nitrogen of the pyridine core from *meta* (**19a**) to *para* position (**22**) which resulted in an inactive compound. The improvements in the EMSA assay for compounds **19b-c** over our initial hit compound I were not perfectly mirrored by the

FP IC₅₀ values, which presumably is rooted in the usage of different DNA probes (LBS1 vs LBS2, respectively).

Table 2. Inhibitory activities of analogues modified in position 4 – observing higher efficiency for 4-substituted compounds

cpd	R	FP Assay (LBS2) ^a	EMSA (LBS1) ^b
		IC ₅₀	inhibition @ 500 μM
16		>250 μM	n.d. ^d
19a		86 ± 6 μM	39 %
19b		29 ± 1 μM	94 %
19c		18 ± 4 μM	100 %
22		n.i. ^c	n.d.

^aFluorescence-polarization assay using LBS2 as probe, data representing average of duplicates ± standard deviation;

^bElectrophoretic mobility shift assay using LBS1 as probe; ^cNo inhibition; ^dNot determined.

Nevertheless, the results for compounds **19b** and **19c** were a major step towards achieving LANA inhibitors suitable for cellular assays and encouraged us to explore the potential of growing the hit scaffold in this direction even further.

In the next series of compounds, Inhibitor I was grown in position 3 at the pyridine core by introducing a variety of aromatic rings. As listed in table 3, a small methyl residue in position 3 (**19d**, IC₅₀ of 45 ± 5 μM; EMSA: 78% inhibition @ 500 μM) is tolerated, but the fluorinated analogue **19j** and most of the phenyl substituted compounds **36a-d**, **36f-i**, and **31a** showed a complete loss or only moderate activity.

Table 3. Inhibitory activities of analogues modified in position 3. Most derivatives substituted in this position (R₂) showed a significant decrease in activity.

cpd	R ₁	R ₂	FP Assay (LBS2)	EMSA (LBS1)
			IC ₅₀	Inhibition @ 500 μM
19d	H	Me	45 ± 5 μM	78 %
19j	H	F	n. i.	n. d.
36a	H		>250 μM	n. d.
36f	H		n.i.	n. d.
36g	H		>250 μM	n. d.
36b	H		n. i.	n. d.
36c	H		110 ± 32 μM	n. i.
36d	H		n. i.	n. d.
36i	H		n. i.	n. d.
36e	H		153 ± 7 μM	20 %
31a	H		>250 μM	n. d.
36h	H		>250 μM	n. d.
36j	H		19 ± 2 μM	34 %
31b	Cl		38 ± 3 μM	100 %

^aFluorescence-polarization assay using LBS2 as probe, data representing average of duplicates ± standard deviation;

^bElectrophoretic mobility shift assay using LBS1 as probe; ^cNo inhibition; ^dNot determined.

However, compounds with an additional hydroxyl function attached to the phenyl ring (**36e**, IC₅₀ of 153 ± 7 μM, EMSA: 20% inhibition @ 500 μM) showed moderate activity.

Moving from a phenyl **36a** to a smaller and more polar furanyl residue **36j** the potency was restored (IC₅₀ of 19 ± 2 μM). Unfortunately, in EMSA experiments we observed only a weak effect (34% inhibition @ 500 μM) for this compound. Interestingly, by attaching an additional chlorine atom in position 4 and having a phenyl in position 3 (**31b**) resulted in a highly potent compound with IC₅₀ of 38 ± 3 μM and full inhibition in FP and EMSA assays, respectively. These results further corroborate the notion of a beneficial *ortho* effect.

To explore the influence of growing inhibitor **I** at the pyridine core in position 2, a set of different target compounds was synthesized (Table 3 and 4). The direct attachment of a nitrile group to the pyridine was tolerated (**19e**: IC₅₀ 52 ± 37 μM, EMSA: n. i.). Moving to chlorine, hydroxy or methoxy group we observed a significant loss in activity (**19f**: IC₅₀ >250 μM; **19o**: IC₅₀ 214 ± 24 μM and **19k**: IC₅₀ 218 ± 192 μM). Also in EMSA experiments **19j** (75% inhibition @ 500μM) and **19k** (11% inhibition @ 500μM) did not show a significant effect. An increase in activity was observed by introducing bulkier substituents and an additional methyl group for R₁. In detail, an unpolar bulky phenyl or *p*-chlorophenyl was accepted in position 2 and we observed IC₅₀ values of 36 ± 5 μM for **36k** and 58 ± 7 μM for **36l** and moderate inhibition in EMSA. Analogues **26a** and **26b** with polar hydroxyl groups attached at the phenyl showed good potency with IC₅₀ values of 21 ± 3 μM and 25 ± 1 μM, respectively. Furthermore, the efficiency of these two analogues in our EMSA studies was high with a full inhibition @ 500 μM. By attaching methylamine (**19g**), isopropylamine (**19h**) and phenylamine (**19i**) at position 2 we observed an increase in activity from small to bigger size, whereby the methylamine compound **19g** was completely inactive and the phenylamine analogue **19i** showed a moderate activity of IC₅₀ of 110 μM and 29% inhibition in EMSA.

Additionally, a series of compounds was synthesized with a more flexible and bulky phenoxy group in position 2 (Table 5). The phenoxy analogue **19l**, similar to the aminophenyl compound **19i**, was inactive, indicating that an amino linker between pyridine and phenyl is more suitable for activity compared to the oxygen linker. By attaching an additional methylgroup in position 4 (R₁) at the pyridine core **40a** an increase in activity compared to **19l** was observed leading to a moderate IC₅₀ of 198 ± 8 μM. The fluorinated analogues **40b-d** also showed moderate activities like compound **40a** while the *o*-flour analogue **40b** possessed the best IC₅₀ of 64 ± 2 μM. For the *m*- (**40c**) and *p*-flour (**40d**) derivatives IC₅₀s of 122 ± 3 μM and 134 ± 2 μM were observed, respectively. Unfortunately, all these compounds showed no effect in EMSA experiments.

Table 4. Inhibitory activities of analogues modified in position 2. Attaching polar hydroxyl benzene groups increases inhibitory activity.

cpd	R ₁	R ₂	FP Assay (LBS2)	EMSA (LBS1)
			IC ₅₀	Inhibition @ 500 μM
19e	H	CN	52 ± 37 μM	n.i.
19f	Me	Cl	>250 μM	n.d.
19o	H	OH	214 ± 24 μM	75 %
19k	H	OMe	218 ± 192 μM	11 %
36k	Me		36 ± 5 μM	36 %
36l	Me		58 ± 7 μM	30 %
26a	Me		21 ± 3 μM	100 %
26b	Me		25 ± 1 μM	100 %
19g	H		n.i.	n.d.
19h	H		>250 μM	n.d.
19i	H		110 ± 20 μM	29 %

^aFluorescence-polarization assay using LBS2 as probe, data representing average of duplicates ± standard deviation;

^bElectrophoretic mobility shift assay using LBS1 as probe; ^cNo inhibition; ^dNot determined.

Exchanging the oxygen linker by a sulfur (**40e**, IC₅₀ 175 ± 10 μM) was tolerated (compare with **40a**, IC₅₀ 198 ± 8 μM). As expected, by removing the nitrogen in the pyridine core resulted in an inactive compound (**19m**). Astonishingly, moving the nitrogen to the phenoxy residue (**19n**) yielded a highly potent compound with an IC₅₀ of 19 ± 1 μM showing also full inhibition in the EMSA experiments.

Table 5. Inhibitory activities of Phenoxy analogues. Shifting nitrogen to the phenoxy residue improves inhibitory efficiency.

cpd	R ₂	FP Assay (LBS2)	EMSA (LBS1)
		IC ₅₀	inhibition @ 500 μM
19l		n. i.	n. d.
40a		198 ± 8 μM	n. i.
40b		64 ± 2 μM	n. i.
40c		122 ± 3 μM	n. i.
40d		134 ± 2 μM	n. i.
40e		175 ± 10 μM	n. i.
19m		n.i.	n. d.
19n		19 ± 1 μM	100 %

^aFluorescence-polarization assay using LBS2 as probe, data representing average of duplicates ± standard deviation;

^bElectrophoretic mobility shift assay using LBS1 as probe; ^cNo inhibition; ^dNot determined.

Intrigued by the notion that fragment growing in position 3 was possible in combination with *ortho*-substituents, we focused our efforts on further exploring these two positions by installing a connected structural motif. To this end, we designed and synthesized isoquinoline analogues (Table 6). In general, isoquinoline analogues were pleasingly effective. The unsubstituted isoquinoline **43** showed an FP IC₅₀ value of 33 ± 1 μM and 96% inhibition in EMSA experiments. Moving from isoquinoline to quinoline **46** resulted in a slight loss in activity compared to **43** (**46**, IC₅₀ 70 ± 34 μM, 61% inhibition in EMSA).

Table 6. Inhibitory activities of Isoquinoline derivatives. Adding an annulated ring structure in direction of identified growth vector results in the most efficient inhibitors to date.

Cpd	R	FP Assay (LBS2)	EMSA (LBS1)
		IC ₅₀	inhibition @ 500 μM
43		33 ± 1 μM	96%
46		70 ± 34 μM	61%
50a		8 ± 1 μM	100%
50b		17 ± 1 μM	100%
50c		>250 μM	n. d.

^aFluorescence-polarization assay using LBS2 as probe, data representing average of duplicates ± standard deviation;

^bElectrophoretic mobility shift assay using LBS1 as probe; ^cNo inhibition; ^dNot determined.

Attaching an additional methyl (**50a**) or chlorine (**50b**) at the isoquinoline motif was beneficial for the inhibitory effect. Noteworthy, **50a** showed the lowest FP IC₅₀ of 8 ± 1 μM reported to date, while **50b** also possessed a decent IC₅₀ of 17 ± 1 μM. Furthermore, in EMSA experiments 100% inhibition was detected for both compounds at 500 μM. Finally, an isoquinoline methylester analogue **50c** was inactive, however.

Further Characterization and EMSA Studies using wild-type LANA.

For further evaluation and characterization the most promising compounds were selected. On the bases of our results, we chose compounds **19c**, **31b**, **26a-b**, **19n**, **50a**, and **50b**, which possessed the best IC₅₀ values in the FP-based assay and showed strong inhibitory effects at 500 μM in EMSA using the LANA DBD mutant.

First, these compounds were initially tested for inhibition at 250 μ M using LANA DBD mutant (Figure 2, A) to see if they are also able to disturb the LANA-DNA interaction at a lower concentration in EMSA and compared these results also with inhibitor **I**. Inhibitor **I** and the compounds **19c**, **31b**, and **26b** showed no inhibitory effect on the LANA_{mut}-DNA interaction at 250 μ M. However, strong inhibitory effects were observed at this concentration for compounds **26a**, **19n**, **50a**, and **50b** as observed by the disappearance of the bands for the LANA_{mut}-DNA complex (upper band, Figure 2A).

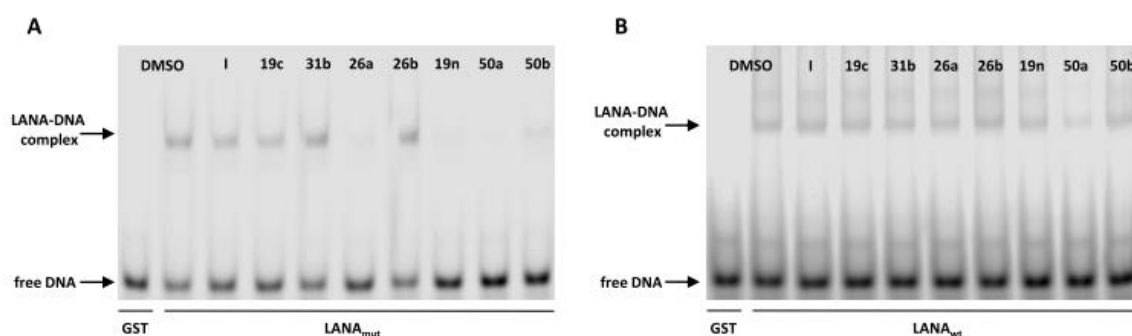


Figure 2: EMSA gels with inhibitor **I**, **19c**, **31b**, **26a-b**, **19n**, **50a-b**. Compounds were tested at a final concentration of 250 μ M and LBS1 was used as probe. **(A)** Using an oligomerization-deficient LANA DBD mutant, a strong inhibitory effect (disappearance of LANA-DNA complex band) was observed for compounds **26a**, **19n** and **50a-b** **(B)** Using wild-type LANA CTD, a significant inhibitory effect for compound **50a** was observed.

We also determined the inhibitory activity of our best compounds against the interaction between wild-type LANA CTD (aa934-1162) and viral LBS1 (Figure 2, B) in EMSA. The compounds were also tested at 250 μ M. Unfortunately, no inhibitory effect was observed for compounds **I**, **19c**, **31b**, **26a-b**, **19n**, and **50b**. However, Compound **50a** showed a significant effect and was able to inhibit the interaction between wild-type LANA CTD and LBS1.

Furthermore, we titrated the compounds showing an effective inhibition in EMSA using the LANA DBD mutant (Figure 2, A), in EMSA experiments using the LANA DBD mutant and LBS1 as a probe to determine the IC₅₀ values. The results are listed in Table 7 and detailed information can be found in the supporting information.

Table 7: Comparison of most efficient LANA-DNA inhibitors.

Cpd	Structure	FP-Assay ^a	FP-Assay	FP-Assay	EMSA ^b
		IC ₅₀ (LBS2) (LANA _{mut})	IC ₅₀ (LBS1) (LANA _{mut})	IC ₅₀ (LBS3) (LANA _{mut})	IC ₅₀ (LBS1) (LANA _{mut})
Inhibitor I		17 ± 1 μM	20 ± 3 μM	19 ± 3 μM	426 ± 2 μM
19c		18 ± 4 μM	52 ± 2 μM	42 ± 3 μM	n.i. at 250 μM ^c
31b		38 ± 3 μM	55 ± 7 μM	45 ± 4 μM	n.i. at 250 μM
26a		21 ± 3 μM	30 ± 2 μM	34 ± 3 μM	156 ± 27 μM
26b		25 ± 1 μM	64 ± 1 μM	63 ± 8 μM	n.i. at 250 μM
19n		19 ± 1 μM	15 ± 1 μM	25 ± 1 μM	64 ± 12 μM
50a		8 ± 1 μM	9 ± 2 μM	8 ± 1 μM	53 ± 43 μM
50b		17 ± 1 μM	14 ± 1 μM	15 ± 1 μM	93 ± 8 μM

^aFluorescence-polarization assay using LBS1, LBS2 and LBS3 as probe, data representing average of duplicates ± standard deviation; ^bElectrophoretic mobility shift assay using LBS1 as probe; ^cNo inhibition at 250 μM.

As reported earlier by us, inhibitor I showed an IC₅₀ in FP assay (LBS2) of 17 ± 1 μM and an IC₅₀ in EMSA of 426 ± 2 μM using LANA DBD mutant.¹¹ The observed IC₅₀ values using LBS2 for the most promising inhibitors were basically in the same range. Additionally, we also tested the most promising inhibitors in FP assay using LBS1 and LBS3, respectively. Compound 50a showed a 2-fold better IC₅₀ of 8–9 μM against all LBS compared to I. Furthermore, we could increase the inhibitory activity in EMSA experiments using LBS1 by 7-fold. As a consequence compounds 19n and 50a are the most potent LANA-LBS1-inhibitors reported so far (IC₅₀ values of 64 ± 12 μM and 53 ± 3 μM). Interestingly, compounds showing increased IC₅₀ values of 50-60 μM against LBS1 and LBS3 in FP assay were also not

effective in EMSA at 250 μM . Excepted is however inhibitor **I**, which showed also IC_{50} values around 20 μM against LBS1 and LBS3, but no effect at 250 μM in EMSA.

As described above, only compound **50a** showed an inhibitory effect at a concentration of 250 μM in EMSA using wild-type LANA CTD (Figure 3 A). A dose-response EMSA experiment with wild-type LANA CTD yielded an IC_{50} value of $60 \pm 4 \mu\text{M}$ (Figure 3 B).

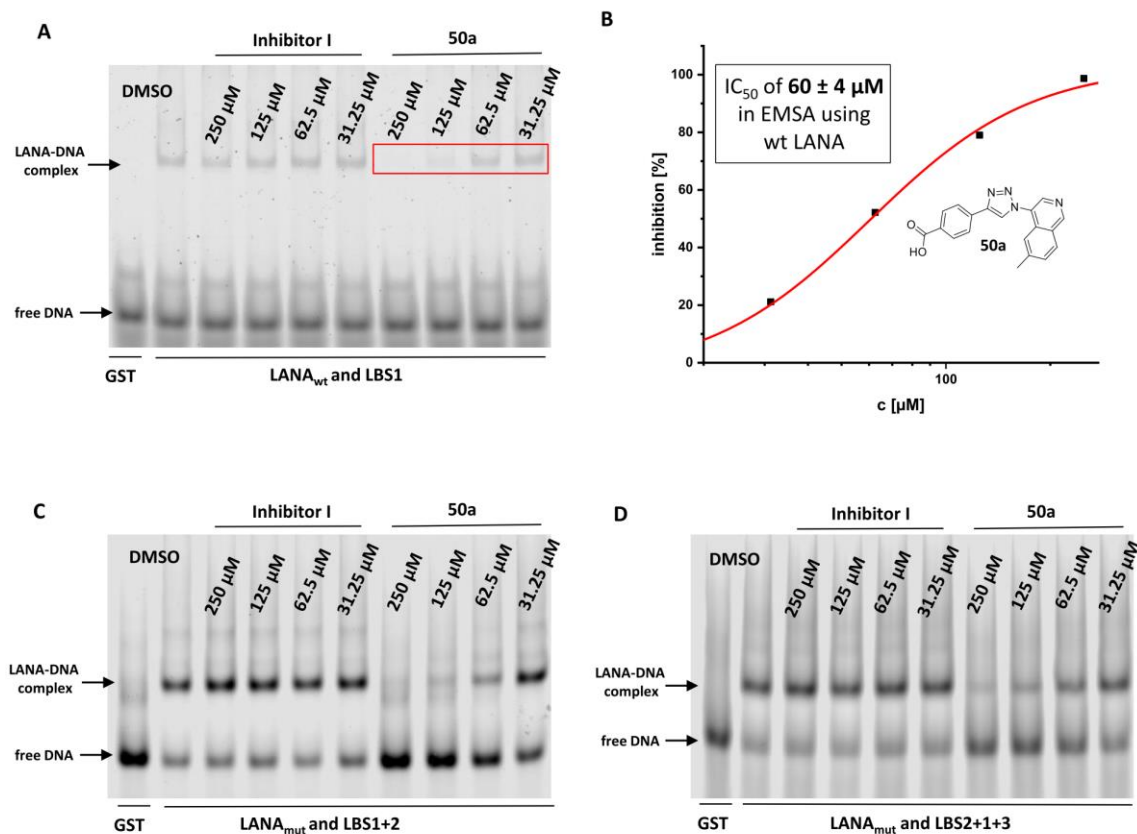


Figure 3: (A) Dose-dependent EMSA experiment using wild-type LANA CTD, LBS1 as probe and Compound **50a**.

(B) Curve shows normalized data points (inhibition from 0 - 100%) representing intensities of LANA-DNA-complex bands (Figure 3 (A), upper bands, marked in red) from dose-dependent EMSA experiment. IC_{50} value

was calculated using a four-parameter dose-response model. (C) Dose-dependent EMSA experiment using

LANA DBD mutant, a combination of LBS1+2 as probe and Inhibitor **I** and Compound **50a**. (D) Dose-dependent EMSA experiment using LANA DBD mutant, a combination of LBS2+1+3 as probe and Inhibitor **I** and Compound

50a.

These results indicate that compound **50a** is equally potent against wild-type LANA CTD and the oligomerization-deficient LANA DBD mutant. In comparison to inhibitor **I** (IC_{50} of $435 \pm 6 \mu\text{M}$ against wild-type LANA CTD in EMSA) these results represent a huge potency improvement.¹¹ Furthermore,

we tested if compound **50a** is also able to disturb the LANA-DNA interaction when using longer oligonucleotides comprising LBS1+2 as well as LBS2+1+3, in an arrangement that is present on the viral KSHV genome.¹⁷ Each LBS is able to associate with one LANA dimer. Hence, LANA and the LBS1+2 oligomer can form a trimeric complex while the LBS2+1+3 oligomer gives rise to a quaternary complex. In order to test the efficacy of our inhibitors against the formation of these higher-order aggregates, dose-dependent EMSA experiments using LBS1+2 and LBS2+1+3 with the LANA DBD mutant were performed (Figure 3, C and D). We compared the effects of inhibitor **I** and Compound **50a** in this setup. As expected, inhibitor **I** showed no inhibitory effects in both experiments. However, Compound **50a** was still able to significantly inhibit the LANA LBS1+2 interaction at a concentration of 62.5 μM (Figure 3, C) and additionally inhibited the LANA LBS2+1+3 interaction at 125 μM (Figure 3, D). These results provide a basis for testing these inhibitors in cell based assays in the future.

The similar IC_{50} values of compound **50a** observed against wild-type LANA and LANA DBD mutant corroborates our hypothesis that our inhibitor binds at the DNA binding interface and is able to compete with the DNA. The DBD mutant involves nine point mutations, which are all located outside of the DNA binding site.²⁵ The goal of generating and using this mutant was to disturb the higher oligomerization in solution, which resulted in improved handling characteristics of the protein and better solubility of LANA-DNA complexes. Figure 4 illustrates the LANA DBD surface (blue) and its single point mutations (yellow) bound to double-stranded DNA (red).

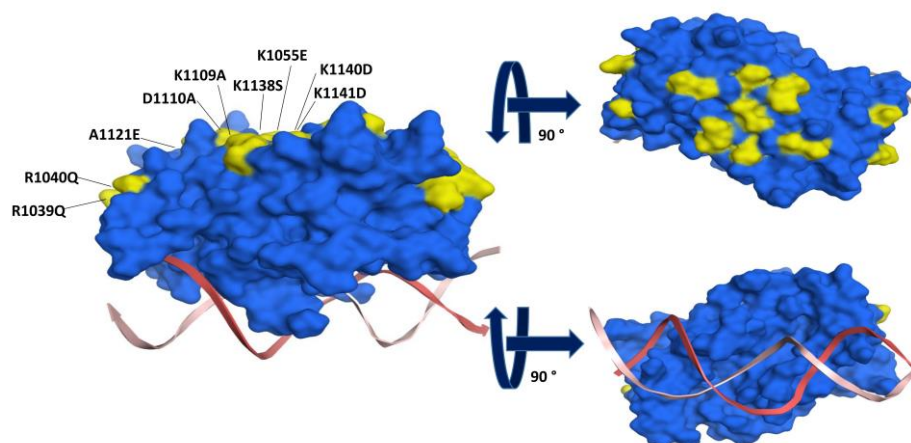


Figure 4: Illustration of the nine single point mutations (yellow) of oligomerisation interface and basic patch LANA mutant (blue) bound to DNA (red) assuming that our inhibitors bind at the LANA-DNA interaction interface.

The distribution of these mutations distant from the DNA-interaction interface combined with the observed similar IC_{50} values of our compound against wild-type and DBD mutant provide strong evidence, that we are targeting the LANA DNA interaction interface and that we do not unintentionally target one of the mutated regions on the LANA surface.

Taken together, compound **50a** is the most effective inhibitor against LANA DBD mutant and wild-type LANA CTD reported to date. To complement our studies, we applied STD-NMR experiments in order to identify further growth vectors.

STD-NMR Studies for Insight on Ligand Binding Modes

Finally, we complemented our lead generation campaign by STD-NMR experiments with the aim to gather information on the binding orientation and to identify further growth vectors. In parallel, we attempted to solve co-crystal structures of our inhibitors in complex with LANA, unfortunately without success. However, we could successfully confirm previous STD-NMR and molecular docking results for inhibitor **I** by the obtained SAR in the present study and we were able to enlarge inhibitor **I** in the suggested direction. In order to inform our next optimization steps, we again performed STD-NMR experiments of our best inhibitor **50a**.

The protons of the tested compound, which are in closest proximity to the protein surface upon binding, are showing the strongest STD effects. In Figure 5 an overlay of the on- (red) and off- (black) resonance STD-NMR spectra of the aromatic region are shown. The spectra were normalized to the strongest signal, which was observed for proton 1. The STD effects were calculated for each proton of inhibitor **50a** ($\text{Effect}_{\text{STD}} = I/I_0$). The results suggest that compound **50a** has a binding orientation to LANA similar to that of inhibitor **I**.¹¹

The nitrogen of the pyridine ring presumably acts as a proton acceptor and thereby anchors proton 1 close to the LANA surface. The proton in position 2 showed also a strong STD effect of 89%. The corresponding proton in inhibitor **I** showed a slightly stronger effect of 100%.¹¹ The bulky isoquinoline moiety and the additional methyl group cause an *ortho* effect, which hinders the rotation of the bond between the triazole core and the isoquinoline. We hypothesize, that this effect brings the nitrogen in an even more favorable orientation to the LANA surface and in turn leaves proton 2 now slightly more exposed.

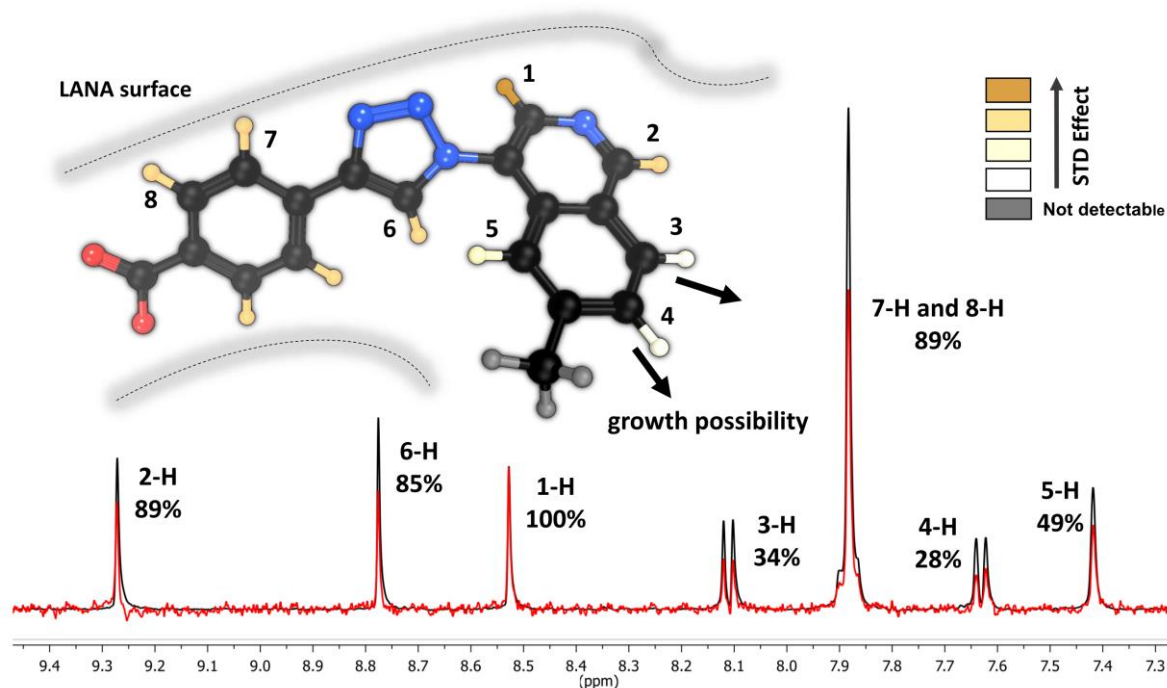


Figure 5: STD experiments of compound **50a** in complex with LANA DBD mutant. The reference spectrum is displayed in black (STD-off) and STD difference spectra (STD-on) in red. Overlaid spectra were normalized to the signal for 1-H, which showed the strongest enhancement.

Furthermore, proton 6 located in the triazole core shows a stronger STD effect of 85% (47% in inhibitor I),¹¹ which leads us to suspect that the triazole is also now interacting more favorably with LANA. The four protons at the benzoic acid moiety, 7-H and 8-H, were found under one signal displaying a prominent STD effect of 89%. In contrast, the protons at the second ring of the isoquinoline motif showed a significantly lower STD effect (3-H: 34%, 4-H: 28% and 5-H: 49%). Hence, we conclude that these protons are not in direct contact with the protein and should be further investigated as potential secondary growth vectors. Unfortunately, the STD effect of the methyl group could not be determined, because signals of buffer ingredients were in the same chemical shift range. For future medicinal chemistry optimization studies, further growing of the isoquinoline analogues in positions 3, 4 and 5 should be investigated. Additionally, a combination of the isoquinoline **50a** and compounds elongated in position 2 (see **19n** and **26a**) should be attempted.

Conclusion

In this study we synthesized a series of new derivatives of our LANA inhibitor **I**¹¹ and evaluated them for LANA-DNA interaction inhibition in an FP-assay and in EMSA experiments in order to generate more potent LANA-DNA inhibitors. Based on the previously discovered fragment-sized inhibitor **I**, medicinal chemistry optimization led to new inhibitors with improved potency. In particular, the replacement of the pyridine core (inhibitor **I**) by a methyl-isoquinoline (**50a**) led to an increase of inhibitory potency of 7-fold against the wild-type LANA CTD interaction with viral LBS1. Moreover, compound **50a** was also able to inhibit the interaction between LANA DBD mutant and LBS1+2 and LBS2+1+3, respectively, in the lower micromolar range. Additionally, step-by-step modification studies gave new and important SAR insights for future medicinal chemistry optimizations towards lead structures. Furthermore, STD-NMR measurements of the most potent inhibitor **50a** in complex with LANA revealed important details about the binding orientation and allowed for the identification of a new potential growth vector. The ability to inhibit the wild-type LANA DNA interaction in a low micro molar range ($IC_{50} 60 \pm 4 \mu\text{M}$) with such a small molecule scaffold is striking as such a macromolecule-macromolecule-interaction is usually considered to be highly challenging, if not “undruggable”. Unexpectedly, we were able to significantly improve the inhibitory effects of our inhibitors using a chemistry-driven approach without having any structural information from a co-crystal about the binding mode and location on the LANA surface. Our results pave the way for the generation of a LANA-targeting anti-KSHV agent.

Experimental Section

All reagent-grade chemicals were purchased from commercial suppliers and were used as received. The purifications were performed using automated column flash chromatography (CombiFlash Rf+, Teledyne ISCO, Lincoln, NE, USA) on silica gel 0.04 – 0.063 mm (RediSep Rf Kartuschen, Axel Semrau, Spocklhövel, Germany) or using preparative high performance liquid chromatography (HPLC, Ultimate 3000 UHPLC+ focused, Thermo Scientific) on a reversed-phase column (C18 column, 5 μm , Macherey-Nagel, Germany). The solvents used for column flash chromatography were EtOAc and cyclohexane or DCM and MeOH. The solvents used for HPLC were water (containing 0.05% [v/v] FA) and MeCN (containing 0.05% [v/v] FA) (gradient elution, MeCN:H₂O 1:9 \rightarrow 9:1). Reaction progress was monitored by TLC on TLC Silica Gel 60 F₂₅₄ plates (Merk, Darmstadt, Germany) or by a reversed-phase liquid chromatography mass spectrometer (LCMS). ¹H and ¹³C NMR were recorded on a Bruker Fourier

spectrometers (500 or 126 MHz). Chemical shifts (δ) were reported in parts per million (ppm) relative to the corresponding reference solvent. The chemical shifts recorded as δ values in ppm units by reference to the hydrogenated residues of the deuterated solvent as the internal standard. Coupling constants (J) are given in hertz (Hz) and splitting patterns are designated as follows: s, singlet; d, doublet; dd, doublet of doublets; t, triplet; m, multiplet; br., broad signal. Purity of all final compounds was measured on the UV trace recorded at a wavelength of 254 nm and was determined to be >95% by a reversed-phase liquid chromatography mass spectrometer (LCMS). Representative ^1H and ^{13}C spectra of all final compounds can be found in the supporting information. High resolution mass spectra of all final compounds were measured on a Thermo Scientific Q Exactive Focus (Germany) combined with a DIONEX ultimate 3000 UHPLC+ focused and results can be found in the supporting information. The reactions and purification steps were not optimized regarding yields.

General procedure for azide formation (GP1) for Compounds 2, 18a-n, 21, 25a-b, 30a-b, 33a-b, 39a-e, 42, 45, 49a-c: The appropriate aryl amine (1 eq.) was dissolved in EtOAc, cooled to 0 °C and 6 M HCl was added. Sodium nitrite (1.7 eq.) was dissolved in water and added slowly. The reaction mixture was stirred for 30 min at 0 °C. Subsequently, sodium azide (1.7 eq.) in water was added slowly at 0 °C. The mixture was stirred at room temperature for 2 h. TLC control indicated full conversion and the mixture was basified with saturated NaHCO_3 solution and was extracted with EtOAc (2 \times). The combined organic layers were dried over sodium sulfate and concentrated under reduced pressure to give the crude. The crude product was used as obtained in the next step without further purifications. Compound **2** is presented as an example. 3-azidopyridine (**2**): The azide was synthesized according to **GP1** using pyridin-3-amine **1** (376 mg, 4 mmol), sodium nitrite (1.7 eq., 469 mg, 6.8 mmol), sodium azide (1.7 eq., 442 mg, 6.8 mmol), EtOAc (8 mL), 6 M HCl (5 mL). The crude product (245 mg, 2 mmol, 50%) was used as obtained in the next step without further purifications. $R_f = 0.37$ (PE/EtOAc 7:3)

General procedure for synthesis of amino isoquinolin derivatives (GP2) for compounds 48a-c: Under argon atmosphere the appropriate bromo isoquinoline (1 eq.), L-proline (0.1 eq.), sodium azide (1.3 eq.) and sodium carbonate (1.3 eq.) was dissolved in a 2:1 mixture of DMF and water. Subsequently, sodium ascorbate (1.3 eq.) and copper sulfate hepta hydrate (1 eq.) were added and the reaction mixture was stirred over night at 85 °C. After full conversion (LCMS control) the mixture was cooled to room temperature and EtOAc and sat. aqueous NaHCO_3 solution were added. The mixture was extracted with EtOAc (3 \times), the combined organic layers were dried over sodium sulfate and concentrated under reduced pressure to obtain the crude. The obtained products were used as obtained without further purification. Compound **48a** is presented as an example. 6-methylisoquinolin-4-amine (**48a**): The amino isoquinoline was synthesized according to **GP2** using 4-

bromo-6-methylisoquinoline **47a** (100 mg, 0.46 mmol), L-proline (0.1 eq., 0.05 mmol, 5 mg), sodium azide (1.3 eq., 0.60 mmol, 34 mg), sodium carbonate (1.3 eq., 0.60 mmol, 64 mg), sodium ascorbate (1.3 eq., 0.60 mmol, 119 mg), copper sulfate heptahydrate (1 eq., 0.46 mmol, 115 mg), DMF (4 mL) and water (2 mL). The crude product (70 mg, 0.44 mmol, 97%) was used as obtained in the next step without further purifications. MS (ESI+) m/z 159 (M + H).

General procedure for copper catalyzed click reaction (GP3) for compounds 3-11, 13, 16, 19a-n, 22, 26a-b, 31a-b, 34a-b, 40a-e, 50a-c: Under argon atmosphere the appropriate alkyne (1 eq.) was suspended in a 1:1 mixture of water and MeOH. Subsequently, DIPEA (2.0 eq.), copper sulfate heptahydrate (0.5 eq.) and sodium ascorbate (0.5 eq.) were added. After addition of the corresponding azide (1.2 eq.) the mixture was stirred for 16 h at room temperature. After full conversion (LCMS control) the mixture was acidified with 1 M HCl and the product was precipitated. The solids were collected, washed with water, and dried under vacuum to obtain the crude product. The products were purified using preparative HPLC. The solvents used were water (containing 0.05% [v/v] FA) and MeCN (containing 0.05% [v/v] FA) (gradient elution, MeCN:H₂O 1:9 → 9:1). Compound **4** is presented as an example. 3-(1-(pyridin-3-yl)-1H-1,2,3-triazol-4-yl)benzoic acid (**4**): The triazole was synthesized according to **GP3** using 3-ethynylbenzoic acid (92 mg, 0.64 mmol) and 3-azidopyridine **2** (1.3 eq., 100 mg, 0.83 mmol) as starting materials. The crude was obtained as a white solid (110 mg, 0.41 mmol, 64%). Purification was done using preparative HPLC. ¹H NMR (500 MHz, DMSO-*d*₆) δ ppm 7.66 (br. s., 1 H) 7.68 - 7.79 (m, 1 H) 7.88 - 8.06 (m, 1 H) 8.19 (d, *J*=7.63 Hz, 1 H) 8.41 (d, *J*=8.24 Hz, 1 H) 8.53 (s., 1 H) 8.76 (s., 1 H) 9.25 (s., 1 H) 9.55 (s, 1 H) 13.23 (br. s., 1 H); ¹³C NMR (126 MHz, DMSO-*d*₆) δ ppm 120.56, 124.96, 127.82, 129.40, 141.24, 146.80, 149.81, 167.30

General procedure for Suzuki coupling (GP4) for compounds 24a-b, 29a-b, 35a-l: Under argon atmosphere the appropriate aryl halide 1 (eq.) was dissolved in water and 1,4-dioxane (1:1). Sodium carbonate (3 eq.), the corresponding boronic acid (1.2 eq.) and tetrakis (triphenylphosphine) palladium (0.1 eq.) were added. The reaction mixture was heated to 90 °C for 16 h. After full conversion (LCMS control) the mixture was cooled to room temperature and EtOAc and sat. aqueous NaHCO₃ solution were added. The mixture was extracted with EtOAc (3x), the combined organic layers were dried over sodium sulfate and concentrated under reduced pressure to obtain the crude. The purification was done using automated flash chromatography (cyclohexane/EtOAc 1:0 → 0:1). Compound **24a** is presented as an example. 2-(5-amino-4-methylpyridin-2-yl)phenol (**24a**): The coupling was done according to **GP4** using 6-bromo-4-methylpyridin-3-amine **23** (130 mg, 0.69 mmol), (2-hydroxyphenyl)boronic acid (1.2 eq., 113 mg, 0.83 mmol), sodium carbonate (3 eq., 218 mg, 2.08

mmol,) and tetrakis (triphenylphosphine) palladium (0.1 eq., 78 mg, 0.07 mmol) in 1,4-dioxan:water (1:1, 6 mL). **24b** was obtained as yellow solid (103 mg, 0.52 mmol, 75%). MS (ESI+) m/z 201 (M + H).

General procedure for hydrolysis of methyl ester (GP5) for compounds 36a-l: The appropriate methyl ester was dissolved in MeOH and aqueous 0.5 M NaOH solution (1:1). The mixture was stirred at room temperature for 16 h. After full conversion (LCMS control) the mixture was acidified with 1 M HCl and the product was precipitated. The solids were collected, washed with water, and dried under vacuum to obtain the crude product. The products were purified using preparative HPLC. Compound **36a** is presented as an example. 4-(1-(5-phenylpyridin-3-yl)-1H-1,2,3-triazol-4-yl)benzoic acid (**36a**): The synthesis was done according to **GP5** using methyl 4-(1-(5-phenylpyridin-3-yl)-1H-1,2,3-triazol-4-yl)benzoate **35a** (20 mg, 0.06 mmol). The crude was obtained as a white solid (13 mg, 0.04 mmol, 66%). Purification was done using preparative HPLC. ^1H NMR (500 MHz, $\text{DMSO-}d_6$) δ ppm 7.49 - 7.54 (m, 1 H) 7.56 - 7.61 (m, 2 H) 7.84 - 7.95 (m, 2 H) 8.02 - 8.16 (m, 4 H) 8.65 (t, $J=2.21$ Hz, 1 H) 9.07 (d, $J=1.98$ Hz, 1 H) 9.22 (d, $J=2.29$ Hz, 1 H) 9.64 (s, 1 H); ^{13}C NMR (126 MHz, $\text{DMSO-}d_6$) δ ppm 121.41, 125.29, 125.57, 127.30, 128.97, 129.30, 130.22, 133.38, 133.97, 135.68, 136.49, 139.93, 146.65, 147.70, 167.01

General procedure for Ullmann reaction (GP6) for compounds 38a-e: Under argon atmosphere 6-bromo-4-methylpyridin-3-amine (1 eq.) was dissolved in DMF and the appropriate phenol derivative (1.2 eq.), cesium carbonate (3 eq.) and CuI (0.05 eq.) were added. The mixture was stirred for 16 h at 130 °C. LCMS control indicated full conversion and the mixture was cooled to room temperature. EtOAc and sat. aqueous NaHCO_3 solution were added. The mixture was extracted with EtOAc (3x), the combined organic layers were dried over sodium sulfate and concentrated under reduced pressure to obtain the crude. Compound **38a** is presented as an example. 4-methyl-6-phenoxy-pyridin-3-amine (**38a**): The aryl ether was synthesized according to **GP6** using 6-bromo-4-methylpyridin-3-amine **37** (100 mg, 0.53 mmol), phenol (1.2 eq., 0.60 mmol, 70 mg), cesium carbonate (3 eq., 1.61 mmol, 523 mg) and CuI (0.1 eq., 0.05 mmol, 9 mg) in DMF (3 mL). The product was purified using automated flash chromatography (DCM/MeOH 1:0 \rightarrow 9:1). Yield: (30 mg, 0.15 mmol, 28%) MS (ESI+) m/z 201 (M + H).

Protein expression and purification: The expression and purification of His-tagged oligomerization-deficient LANA DNA binding domain (DBD; aa1008–1146) mutant and GST-tagged KSHV LANA C-terminal domain (CTD; aa934-1162) were described previously and the protocol was adopted.^{10,11}

Fluorescence Polarization (FP) assay: The FP assay was performed, analyzed and evaluated as described previously.¹¹

Electrophoretic mobility shift assay (EMSA): The EMSA was performed, analyzed and evaluated as described previously.¹¹

Saturation-Transfer Difference (STD) NMR: The STD experiments were recorded at 298 K on a Bruker Fourier spectrometer (500 MHz). The samples contained 10 μ M (final concentration) His-tagged oligomerization-deficient LANA DBD (aa1008–1146) mutant and a final compound concentration of 500 μ M. The control spectra were recorded under the same conditions containing the free compound to test for artifacts. The STD buffer for experiments consists of 10 mM HEPES, 150 mM NaCl, pH 7.4 in D₂O containing 10% [v/v] DMSO-d₆. The experiments were recorded with a carrier set at -1 ppm for the on-resonance and -40 ppm for the off-resonance irradiation. Selective protein saturation was carried out at 2 s by using a train of 50 ms Gauss-shaped pulses, each separated by a 1 ms delay.

Declaration of competing interest

The authors declare no competing financial interest.

Corresponding Author

*E-mail: Martin.Empting@helmholtz-hzi.de. Phone: +(49) 681 988062031

Acknowledgments

The authors acknowledge the financial support by the German Centre for Infection Research (DZIF) and the DFG Collaborative Research Centre 900, project C1.

Abbreviations

AIDS, acquired immune deficiency syndrome; CTD, C-terminal domain; DCM, dichloromethane; DMSO, dimethylsulfoxide; DBD, DNA binding domain; DMF, dimethylformamide; DIPEA, diisopropylethylamine; EE, ethyl acetate; EtOH, ethanol; EMSA, electrophoretic mobility shift assay; FA, formic acid; FP, fluorescence polarization; HPLC, high pressure liquid chromatography; HHV-8, human herpesvirus 8; KS, Kaposi Sarcoma; KSHV, Kaposi's sarcoma-associated herpesvirus; LANA, latency associated nuclear antigen; LBS, LANA binding site; LCMS, liquid chromatography mass spectrometer; MeCN, acetonitrile; MeOH, methanol; MST, microscale thermophoresis; PBS, phosphate-buffered saline; PE, petroleum benzene; STD NMR, saturation transfer difference nuclear magnetic resonance; SPR, surface plasmon resonance; TR, terminal repeat; wild-type, wt

Appendix A. Supplementary Data

Supplementary data to this article is available. Synthetic procedures and characterizations of all synthesized compounds, representative ^1H , ^{13}C NMR spectra and high resolution mass spectra of all final compounds, concentration-dependent FP experiments of compounds **19c**, **31b**, **26a-b**, **19n** and **50a-b** using LBS1, LBS2 and LBS3, concentration-dependent EMSA gels for compounds **1**, **19n**, **26a-b**, **31b**, **50a-b**, as well as curves from dose-dependent EMSA experiments for IC_{50} calculation for compounds **26a**, **19n** and **50a-b**.

References

1. Weidner-Glunde, M.; Marigliò, G.; Schulz, T.F. Kaposi's Sarcoma-Associated Herpesvirus Latency-Associated Nuclear Antigen: Replicating and Shielding Viral DNA during Viral Persistence. *J. Virol.* **2017**, *91*, doi:10.1128/JVI.01083-16.
2. Wang, L.; Damania, B. Kaposi's sarcoma-associated herpesvirus confers a survival advantage to endothelial cells. *Cancer Res.* **2008**, *68*, 4640–4648, doi:10.1158/0008-5472.CAN-07-5988.
3. Purushothaman, P.; Dabral, P.; Gupta, N.; Sarkar, R.; Verma, S.C. KSHV Genome Replication and Maintenance. *Front. Microbiol.* **2016**, *7*, 54, doi:10.3389/fmicb.2016.00054.
4. Marigliò, G.; Koch, S.; Zhang, G.; Weidner-Glunde, M.; Rückert, J.; Kati, S.; Santag, S.; Schulz, T.F. Kaposi Sarcoma Herpesvirus (KSHV) Latency-Associated Nuclear Antigen (LANA) recruits components of the MRN (Mre11-Rad50-NBS1) repair complex to modulate an innate immune signaling pathway and viral latency. *PLoS Pathog.* **2017**, *13*, e1006335, doi:10.1371/journal.ppat.1006335.
5. Kedes, D.H.; Operskalski, E.; Busch, M.; Kohn, R.; Flood, J.; Ganem, D. The seroepidemiology of human herpesvirus 8 (Kaposi's sarcoma-associated herpesvirus): distribution of infection in KS risk groups and evidence for sexual transmission. *Nat. Med.* **1996**, *2*, 918–924, doi:10.1038/nm0896-918.
6. Yan, L.; Majerciak, V.; Zheng, Z.-M.; Lan, K. Towards Better Understanding of KSHV Life Cycle: from Transcription and Posttranscriptional Regulations to Pathogenesis. *Virol. Sin.* **2019**, *34*, 135–161, doi:10.1007/s12250-019-00114-3.
7. Rainbow, L.; Platt, G.M.; Simpson, G.R.; Sarid, R.; Gao, S.J.; Stoiber, H.; Herrington, C.S.; Moore, P.S.; Schulz, T.F. The 222- to 234-kilodalton latent nuclear protein (LNA) of Kaposi's sarcoma-

- associated herpesvirus (human herpesvirus 8) is encoded by orf73 and is a component of the latency-associated nuclear antigen. *J. Virol.* **1997**, *71*, 5915–5921.
8. Uppal, T.; Banerjee, S.; Sun, Z.; Verma, S.C.; Robertson, E.S. KSHV LANA—the master regulator of KSHV latency. *Viruses* **2014**, *6*, 4961–4998, doi:10.3390/v6124961.
 9. Juillard, F.; Tan, M.; Li, S.; Kaye, K.M. Kaposi's Sarcoma Herpesvirus Genome Persistence. *Front. Microbiol.* **2016**, *7*, 1149, doi:10.3389/fmicb.2016.01149.
 10. Hellert, J.; Weidner-Glunde, M.; Krausze, J.; Richter, U.; Adler, H.; Fedorov, R.; Pietrek, M.; Rückert, J.; Ritter, C.; Schulz, T.F.; et al. A structural basis for BRD2/4-mediated host chromatin interaction and oligomer assembly of Kaposi sarcoma-associated herpesvirus and murine gammaherpesvirus LANA proteins. *PLoS Pathog.* **2013**, *9*, e1003640, doi:10.1371/journal.ppat.1003640.
 11. Kirsch, P.; Jakob, V.; Oberhausen, K.; Stein, S.C.; Cucarro, I.; Schulz, T.F.; Empting, M. Fragment-Based Discovery of a Qualified Hit Targeting the Latency-Associated Nuclear Antigen of the Oncogenic Kaposi's Sarcoma-Associated Herpesvirus/Human Herpesvirus 8. *J. Med. Chem.* **2019**, *62*, 3924–3939, doi:10.1021/acs.jmedchem.8b01827.
 12. Alkharsah, K.R.; Schulz, T.F. A role for the internal repeat of the Kaposi's sarcoma-associated herpesvirus latent nuclear antigen in the persistence of an episomal viral genome. *J. Virol.* **2012**, *86*, 1883–1887, doi:10.1128/JVI.06029-11.
 13. Leo, A. de; Deng, Z.; Vladimirova, O.; Chen, H.-S.; Dheekollu, J.; Calderon, A.; Myers, K.A.; Hayden, J.; Keeney, F.; Kaufer, B.B.; et al. LANA oligomeric architecture is essential for KSHV nuclear body formation and viral genome maintenance during latency. *PLoS Pathog.* **2019**, *15*, e1007489, doi:10.1371/journal.ppat.1007489.
 14. Singh, R.K.; Lamplugh, Z.L.; Lang, F.; Yuan, Y.; Lieberman, P.; You, J.; Robertson, E.S. KSHV-encoded LANA protects the cellular replication machinery from hypoxia induced degradation. *PLoS Pathog.* **2019**, *15*, e1008025, doi:10.1371/journal.ppat.1008025.
 15. Verma, S.C.; Lan, K.; Robertson, E. Structure and Function of Latency-Associated Nuclear Antigen. *Curr. Top. Microbiol. Immunol.* **2007**, *312*, 101–136.
 16. Wei, F.; Gan, J.; Wang, C.; Zhu, C.; Cai, Q. Cell Cycle Regulatory Functions of the KSHV Oncoprotein LANA. *Front. Microbiol.* **2016**, *7*, 334, doi:10.3389/fmicb.2016.00334.
 17. Hellert, J.; Weidner-Glunde, M.; Krausze, J.; Lünsdorf, H.; Ritter, C.; Schulz, T.F.; Lührs, T. The 3D structure of Kaposi sarcoma herpesvirus LANA C-terminal domain bound to DNA. *Proc. Natl. Acad. Sci. U. S. A.* **2015**, *112*, 6694–6699, doi:10.1073/pnas.1421804112.
 18. Parravicini, C.; Chandran, B.; Corbellino, M.; Berti, E.; Paulli, M.; Moore, P.S.; Chang, Y. Differential Viral Protein Expression in Kaposi's Sarcoma-Associated Herpesvirus-Infected Diseases : Kaposi's

-
- Sarcoma, Primary Effusion Lymphoma, and Multicentric Castleman's Disease. *Am. J. Pathol.* **2000**, *156*, 743–749.
19. Coen, N.; Duraffour, S.; Snoeck, R.; Andrei, G. KSHV Targeted Therapy: An Update on Inhibitors of Viral Lytic Replication. *Viruses* **2014**, *6*, 4731–4759, doi:10.3390/v6114731.
 20. Hoffmann, C.; Sabranski, M.; Esser, S. HIV-Associated Kaposi's Sarcoma. *Oncol. Res. Treat.* **2017**, *40*, 94–98, doi:10.1159/000455971.
 21. Kirsch, P.; Jakob, V.; Elgaher, W.A.M.; Walt, C.; Oberhausen, K.; Schulz, T.F.; Empting, M. Discovery of Novel Latency-Associated Nuclear Antigen Inhibitors as Antiviral Agents Against Kaposi's Sarcoma-Associated Herpesvirus. *ACS Chem. Biol.* **2020**, doi:10.1021/acscchembio.9b00845.
 22. Cui, J.; Hu, L.'A.; Shi, W.; Cui, G.; Zhang, X.; Zhang, Q.-W. Design, Synthesis and Anti-Platelet Aggregation Activity Study of Ginkgolide-1,2,3-triazole Derivatives. *Molecules* **2019**, *24*, doi:10.3390/molecules24112156.
 23. Dou, D.; He, G.; Li, Y.; Lai, Z.; Wei, L.; Alliston, K.R.; Lushington, G.H.; Eichhorn, D.M.; Groutas, W.C. Utilization of the 1,2,3,5-thiatriazolidin-3-one 1,1-dioxide scaffold in the design of potential inhibitors of human neutrophil proteinase 3. *Bioorg. Med. Chem.* **2010**, *18*, 1093–1102, doi:10.1016/j.bmc.2009.12.057.
 24. Liu, Y.; Xiao, Q.; Liu, Y.; Li, Z.; Qiu, Y.; Zhou, G.-B.; Yao, Z.-J.; Jiang, S. Biological evaluation of new mimetics of annonaceous acetogenins: alteration of right scaffold by click linkage with aromatic functionalities. *Eur. J. Med. Chem.* **2014**, *78*, 248–258, doi:10.1016/j.ejmech.2014.03.062.
 25. Hellert, J.; Krausze, J.; Schulz, T.F.; Lühns, T. Crystallization, room-temperature X-ray diffraction and preliminary analysis of Kaposi's sarcoma herpesvirus LANA bound to DNA. *Acta Crystallogr. F Struct. Biol. Commun.* **2014**, *70*, 1570–1574, doi:10.1107/S2053230X14019906.
-

4 Final Discussion

The aim of this thesis was the discovery of the first LANA-DNA interaction inhibitors. LANA plays a key role for the latent persistence of KSHV in human host cells. The inhibition of the interaction between LANA and the viral genome should lead to a loss of the viral genome over time, which will prevent the persistence of KSHV in the human host. Hence, LANA is considered to be a very promising target for the development of anti-KSHV drugs.

We successfully discovered the first LANA-DNA interaction inhibitors using two different strategies (Chapter 3.1 and 3.2): a fragment-based drug design approach and an in-house library screening. One central part was the design, synthesis and biological evaluation of novel and improved LANA-DNA interaction inhibitors. Furthermore, a set of biochemical and biophysical methods were utilized to characterize the most promising hit compounds. Both hit identification strategies will be discussed below.

In the second part (Chapter 3.3), initial hit-to-lead optimization studies have been performed on the basis of the qualified fragment-sized inhibitor from Chapter 3.1 and further SAR insights were obtained. Medicinal chemistry optimizations were conducted aiming at growing the fragment into a drug-like compound. Most promising inhibitors were further characterized and prioritized using previously applied biophysical and biological methods. By this means, we successfully discovered a highly potent inhibitor against wild-type LANA.

For clear understanding, the compounds mentioned and discussed in the following part of the thesis are denominated with the capital letter A, B or C referring to the respective manuscript of the Chapter and the corresponding Arabic number of the numbering in the respective manuscript.

4.1 Identification of first LANA-DNA Interaction Inhibitors

4.1.1 Fragment-based Drug Design

In the first part of this thesis, a fragment-based drug discovery (FBDD) approach was applied, which has a lot of advantages for drug discovery. Usually, a macromolecule-macromolecule interaction like the LANA-DNA interaction is difficult to target or even undruggable by small organic molecules.⁵⁵ LANA has no well-defined binding pocket, but only a rather flat and huge binding site. Hence, it is quite

difficult to identify interaction hot spots. In general, using fragment screening campaigns, low affinity binders can be discovered by different biochemical and biophysical approaches and subsequent medicinal chemistry efforts can be used to generate potent inhibitors.^{56,57} In recent years, notable progress has been made using FBDD for inhibiting protein-protein interactions, which are also macromolecule-macromolecule interactions and considered to be challenging to target.⁵⁸ Another interesting benefit of using FBDD is that potentially allosteric sites can be targeted by these small molecules. This can provide an alternative mode-of-action facilitating to inhibit such macromolecule-macromolecule interactions. Addressing an allosteric site usually results in conformational changes in the protein, which modulate its functionality.⁵⁹ Targeting an allosteric site on the LANA surface could prevent, e. g., LANA dimer formation, which subsequently would hinder DNA binding. However, based on our results we assume that our compounds are more likely competitive inhibitors.

We analyzed 720 fragment-sized compounds using SPR and TSA to detect protein binding, which also allows to detect very weak binding fragments. This resulted in the identification of 20 LANA binders, which were further evaluated regarding functionality. Functional LANA-DNA interaction inhibition was determined using a fluorescence polarization (FP)-based competition assay resulting in three fragment-sized hit compounds. For further medicinal chemistry optimizations we chose Hit **A1** showing an inhibitory effect of 25% inhibition at 1 mM. Even though the activity of hit **A1** was not very high, the small size and the low molecular weight served as a good starting point and provided a lot of possibilities to optimize this fragment regarding size and potency. The other two identified hit compounds showed slightly lower responses in SPR and less prominent changes in melting temperature of the protein in TSA. These inferior outcomes prompted us to first focus on optimizing hit **A1**. However, the other two hit scaffolds are still quite interesting and will be further explored in future studies.

A main part in this chapter was the design, synthesis and functional evaluation as well as the SAR elucidation of newly synthesized inhibitors towards LANA-DNA interaction. A first series of derivatives based on the structure of **A1** was synthesized and evaluated for functionality. The goal was the identification of a potential growth vector to increase the size and the potency. To summarize this, 14 new derivatives have been synthesized and for compounds **A11** and **A16** an increase of activity was observed. Attaching a methyl group at the imidazole moiety (**A11**) increased the activity and we decided, growing the fragment in this position seemed to be favorable and should be further explored. Furthermore, the carboxylic acid analogue **A16** increased the activity significantly. The positive effect of negatively charged carboxylic acid function is very plausible considering the highly positively charged DNA interaction interface of the LANA surface. Based on these first findings, a combinatorial chemistry

approach was applied. The imidazole could be easily exchanged by a triazole because of their structural similarities. Moving to a triazole core was beneficial, because new target compounds could be easily synthesized using Copper(I)-catalyzed azide-alkyne cycloaddition (CuAAC, click reaction). Furthermore, our combinatorial chemistry approach using click chemistry facilitated the synthesis of a reasonably sized and diverse compound library in a short time to establish an SAR. Moreover, a lot of building blocks for click reactions are commercially available and usually not expensive. First, we could confirm that the triazole was tolerated and the attachment of a bulky phenyl residue at the triazole (**A31**) increased the activity significantly.

On the basis of these results, a small compound library was synthesized via click chemistry by keeping the carboxylic acid in para position constant, while a variety of different groups attached to the triazole core was introduced. Overall, 29 new compounds have been synthesized at this step and the activity (IC_{50} values) could be improved into the double-digit μM range. We selected six of the LANA-DNA inhibitors with different activities for further evaluation and characterization. In the former FP-based competition assays, LBS2 was used as fluorescent probe. It has been reported by other groups that LBS1 has a 100-fold higher affinity to LANA compared to LBS2 and LBS3. Interestingly, IC_{50} values for most tested compounds were similar in competition with LBS1, 2, and 3. This was surprising and underscore the suitability of our compounds to displace LANA from all three possible binding sites on the viral DNA. Additionally, as an orthogonal LANA-DNA interaction inhibition assay, EMSA experiments with the six inhibitors were conducted. For these experiments LBS1 and a combination of LBS1 and LBS2 was used as probe. In both EMSA experiments similar results were observed and the pyridine analogue **A50** showed the strongest inhibitory effect compared to the other inhibitors. The physicochemical properties and biological activities of compound **A50** are summarized in Figure 6.

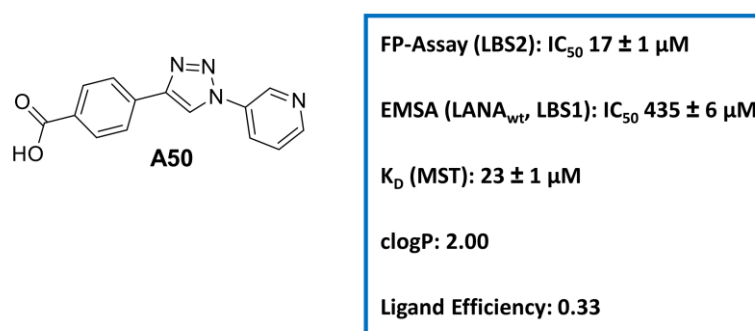


Figure 6: LANA-DNA interaction inhibitor **A50** observed from fragment-based screening.

Along with the highest ligand efficiency of 0.33 and a low clogP of 2.00, compound **A50** was considered to be the most efficient inhibitor at this stage. Target binding was also confirmed via MST and a K_D value of $23 \pm 1 \mu\text{M}$ was determined. Taken all these results together, Inhibitor **A50** is a very promising starting point for further hit-to-lead medicinal chemistry optimization studies in order to generate a highly potent and druglike LANA-DNA inhibitor.

4.1.2 In-House Library Screening

As a different approach for the identification of further LANA-DNA inhibitors, we screened our HIPS in-house library. As a first filter, we used our functional FP-based competition assay, which was also used in the previously fragment-based approach. Hence, compounds with the ability to inhibit the LANA-DNA interaction could be identified directly. Using primary protein binding assays like SPR or TSA, which we used first in the fragment-based screening were not necessary. The in-house library comprised 670 druglike compounds which were already optimized for specific targets from different projects at HIPS. Applying a primary one-spot screen followed by a secondary three-point dose-dependent screening, three different compound classes were identified and out of each class compounds were selected for further evaluation. IC_{50} values were determined in the lower double-digit micromolar range. Additionally, using SPR, the binding affinity to LANA was confirmed for these hit compounds. The most promising hit compounds out of each class were selected: **B1**, **B6** and **B9** (Figure 7).

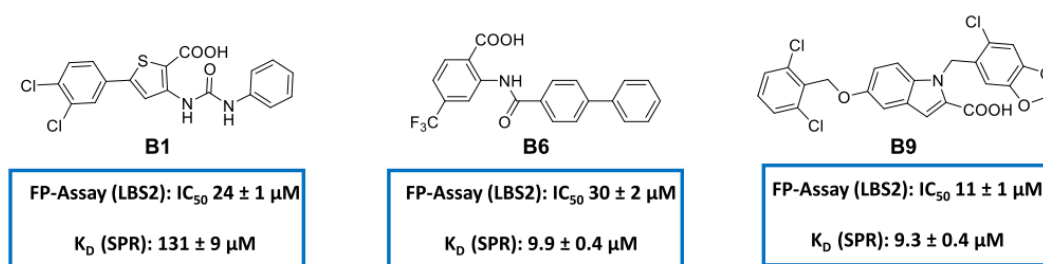


Figure 7: LANA-DNA interaction inhibitors **B1**, **B6** and **B9** observed from HIPS in-house library screening.

These compounds were previously found to be active against other nucleic acid binding proteins, what makes the observed activity for inhibiting the LANA-DNA interaction quite plausible. Nevertheless, it can be assumed that the binding selectivity to one specific target is not very high. In cells, compounds can interact with many different biomolecules or other small molecules and especially unselective

compounds often cause a lot of unexpected and unintentional interactions leading to various side effects. In a drug discovery, achieving selectivity is one important objective that should be considered. However, these new identified LANA inhibitors are primary screening hits, which could be further optimized regarding higher activity and selectivity to LANA and, thus, serve as starting points for future hit-to-lead optimization studies. Primary structural simplification, followed by rationally growing and optimizing the compounds could improve the efficiency and selectivity. Beyond this, the established screening and hit evaluation procedure is a very simple, fast and generic method for the identification of new LANA-DNA interaction inhibitors suitable for other compound libraries as well.

4.1.2.1 Putative Binding Mode of Discovered Inhibitors in Complex with LANA

Solving a co-crystal structure of **A50** in complex with LANA would have been an essential asset for unambiguous structure-based optimization of our inhibitors with improved activities providing important information on the binding site and the binding mode of our inhibitors. On the basis of a co-crystal, we would be able to identify interactions between the functional groups of our inhibitors and the amino acids of LANA. Unfortunately, all efforts to solve a co-crystal structure failed. However, using STD-NMR in combination with molecular docking experiments, we were able to deduce information on the inhibitor-target interaction and suggest a putative binding mode. We concluded that the pyridine nitrogen acts as an important proton acceptor and the proton of position 1 (see Figure A6 and A7) seems to be the closest to the LANA surface. In contrast, positions 2, 3 and 4 are exposed and could serve as possible growth vectors. The carboxylic acid seems to interact with two glutamine residues and the triazole core with a positively charged lysine. Nevertheless, these results have to be confirmed by co-crystal structures. Furthermore, we were interested, if Inhibitor **A50** and Inhibitors **B1**, **B6** and **B9** were binding at the same position on the LANA surface. Therefore, STD-based competition experiments were performed. With these experiments, we showed that the inhibitors were able to bind simultaneously to the LANA surface implying that they are binding to different binding sites. These findings are plausible considering the large LANA-DNA binding interface and the relatively small size of the inhibitors. If we could solve co-crystal structures of LANA in complex with the individual inhibitors in future studies, compound linking or merging strategies could be used to generate highly potent inhibitors by combining them.

4.1.2.2 Comparison of LANA-DNA Inhibitors

In conclusion, both approaches successfully led to potent and very promising LANA-DNA inhibitors. The identified inhibitors showed IC_{50} values in the lower μM range and LANA binding was confirmed while determined K_D values were usually in agreement with the inhibitory activities. Interestingly, all inhibitors were decorated with a carboxylic acid function, which seems to be important for LANA binding. However, inhibitor **A50** has a significantly lower molecular weight compared to inhibitors **B1**, **B6** and **B9**. The compounds **B1** and **B6** do also interact with other nucleic acid binding proteins, which makes them quite unselective. To increase the selectivity and activity to LANA, further optimization efforts need to be undertaken. Furthermore, the physicochemical properties like solubility need to be optimized, too. Under our assay conditions, **A50** showed a 10-fold higher solubility compared to **B1**, **B6** and **B9**. Because, of the promising physicochemical properties of inhibitor **A50** including molecular weight and a good water solubility, inhibitor **A50** was considered to be the most promising starting point for a follow up hit-to-lead optimization. Furthermore, we already conducted SAR studies while the synthetic access to this scaffold was firmly established. Also the in chapter 3.1 revealed possible binding mode of **A50** providing several possibilities for medicinal chemistry optimizations via fragment growing strategies. Nevertheless, the other inhibitors were also interesting due to the fact that they are addressing different binding sites on LANA. Medicinal chemistry optimizations should be conducted starting first with simplification, followed by in-depth SAR studies.

4.2 Hit-to-Lead Optimization a LANA Inhibitor

As described in the previous chapters, LANA-DNA inhibitor **A50** was identified and validated as a promising hit to undergo more extensive optimization in a hit-to-lead process (chapter 3.3). The goal was the improvement of inhibitory activity by using fragment growing strategies. From previous experiments it was not clear how essential the carboxylic acid in the Western part of the molecule was for binding. Additionally, positions 2, 3 and 4 at the pyridine core were identified as possible growth vectors. In this chapter, I aimed at increasing the potency of our inhibitors in a step-by-step manner starting from inhibitor **A50**. In this process, additional SAR insights have been gathered and potent inhibitors were generated. The target compounds were evaluated first using FP-based interaction inhibition assay followed by EMSA experiments.

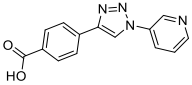
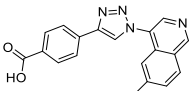
Exchanging the carboxylic acid was detrimental for activity for every tested derivative and we concluded, that the carboxylic acid is essential for inhibitory activity and should be kept constant for

further optimization steps. Now, we focused on modifications at the pyridine core. By growing the compound in position 4, we observed that the inhibitory effect was correlating to the size of the attached residue improving from methyl to phenyl. We hypothesized, that this effect is at least partly due to a steric *ortho* effect. A bulky residue hinders the rotation of the bond between pyridine and triazole, which presumably brings the nitrogen of the pyridine core, acting as proton acceptor, in a favorable angle to the LANA surface. As a next step, the pyridine core was grown in position 3 by introducing different aromatic rings with varying substitutions. In conclusion, a small methyl residue was tolerated, but all compounds decorated with more bulky substituted phenyl residues showed only moderate or a complete loss of activity. Interestingly, making additional use of an *ortho* substituent improved activity (**C31b**). Subsequently, further improvements were observed by growing **A50** in position 2. Different functional groups were introduced, as well as small and big residues were attached. In general, most of these modifications were accepted and additional polar hydroxyl substituents (**26a-b**) boosted the inhibitory potency. Furthermore, the phenoxy analogue **C19n**, which had the nitrogen shifted into the second phenyl ring, was highly potent. Also in these series of compounds, exploiting the *ortho* effect had a positive influence on the inhibitory activity. To further explore this *ortho* effect, a series of isoquinoline analogues was designed resulting in very efficient compounds. The best LANA inhibitor to date, **C50a**, showed a potent IC_{50} of $8 \pm 1 \mu M$ in FP-assay and full inhibition in EMSA (at a concentration of 500 μM).

So far, for the LANA inhibitor discovery and optimization process, a LANA DBD mutant was used. As described in the introduction, this mutant was not modified at the LANA DNA binding site. Nevertheless, LANA inhibitors necessarily should also be able to inhibit wild-type LANA. Therefore, the most efficient inhibitors showing the best IC_{50} values in the FP-based assay and full inhibition in EMSA at 500 μM (**C19c**, **C31b**, **C26a-b**, **C19n**, **C50a-b**) were further evaluated. Using wild-type LANA CTD, only the isoquinoline analogue **C50a** was able to inhibit the protein-DNA interaction (at 250 μM) and from dose-dependent experiments a promising IC_{50} of $60 \pm 4 \mu M$ was calculated.

By comparing the inhibitory activities of our initially discovered inhibitor **A50** and the new promising frontrunner **C50a**, we generated a 2-fold improved IC_{50} value in FP-based assay and a 7-fold more potent IC_{50} in EMSA experiments using LANA DBD mutant (Table C1) and wild-type LANA CTD (Table 1).

Table 1: Comparison LANA-DNA inhibitors **A50** and **C50a**.

Cpd	Structure	MW	FP-Assay	EMSA
			IC ₅₀ (LANA _{mut} , LBS2)	IC ₅₀ (LANA _{wt} , LBS1)
A50		266.26 g/mol	17 ± 1 μM	435 ± 6 μM
C50a		330.35 g/mol	8 ± 1 μM	60 ± 4 μM

In addition, dose-dependent EMSA experiments with inhibitor **A50** and **C50a** using LBS1+2 and LBS2+1+3 as probes showed also, that **C50a** can effectively inhibit the interaction between LANA and the full length of the LBSs at lower micromolar concentrations, whereas for **A50** was not that effective.

It is encouraging that such a still small inhibitor, can interfere with the wild-type LANA CTD nucleic-acid interaction and is able to compete with the DNA in the lower micromolar range. The potential to generate even more potent inhibitors starting from lead inhibitor **C50a** is encouraging. Furthermore, with the additional SAR information, we were able to corroborate the previously observed binding mode from STD-NMR and molecular docking experiments of **A50**. Unfortunately, solving a co-crystal structure still failed despite all the efforts that were undertaken by us and our collaborators (T. Krey, MHH). Therefore, it is impressive, that we were able to optimize our inhibitors with 7-fold improvement against wild-type LANA applying a chemistry-driven optimization using FP-competition assay and EMSA experiments as SAR drivers. For further optimization and growing studies, again, a putative binding mode of **C50a** could be deduced from STD-NMR experiments. We hypothesize that the binding orientation of **A50** and **C50a** were quite similar. Proton 1 showed the strongest enhancement for both compounds. For inhibitor **C50a** stronger STD effects of protons from the benzoic acid and triazole regions compared to **A50** were detected. This suggests that the whole molecule is closer to the LANA surface and binds in a more favorable orientation. Due to the *ortho* effect of the isoquinoline of **C50a**, proton 2 seems to be more exposed as equivalent proton 2 from the pyridine ring of **A50**. Furthermore, lower STD effects were observed from the second ring of the isoquinoline. These positions should be further exploited as new potential growth vectors. These insights open up new possibilities for further medicinal chemistry optimizations.

5 Conclusion and Outlook

The aim of this thesis was the development of first inhibitors targeting the interaction between LANA and the viral DNA. Indeed, effective LANA-DNA interaction inhibitors were identified by two different approaches. Furthermore, in a hit-to-lead optimization campaign a more potent inhibitor has been generated with the ability to disturb also wild-type LANA interaction with viral DNA in the lower micro molar range. The potent inhibitory effect of the still small sized inhibitor **C50a** is encouraging and the promising results that were obtained in this study will serve as an excellent starting point for the further development of LANA-DNA inhibitors with greater potency and selectivity. In the future, these LANA inhibitors could be used as therapeutic agents against latent KSHV infections and KSHV-associated diseases.

LANA has structural and functional homologies to the viral proteins EBNA1 from EBV and E2 from HPV. In a quite similar approach to ours, small-molecule EBNA1-DNA interaction inhibitors were discovered in the group of Lieberman *et al.*⁶⁰ From a fragment-based approach two low affinity fragments were identified. Based on co-crystal structure fragment linking strategies and medicinal chemistry optimizations were used to generate highly potent inhibitors. EBNA1 inhibitors showed high selectivity in multiple cell-based assays and were able to block tumor growth and expression of EBV RNA in mice. These results are astonishing. A comparison of the potencies of these EBNA-1 inhibitors (IC_{50} of 0.388 μ M; ALPHA assay) and our best LANA inhibitor **C50a** (IC_{50} of 8 μ M; FP assay) let us suggest, that we were not too far away from generating similar activities. Hence, we feel encouraged to continue optimizations of our LANA-DNA inhibitors. In our opinion the potential to develop antiviral agents against KSHV on the basis of our still small LANA inhibitors is very high.

The next milestone in this project would be to demonstrate activity in a cell-based virus infection assay. The impact of our compounds are currently tested by our collaborators in the lab of Thomas Schulz (MHH) by analyzing the loss of the viral genome in KSHV infected cells over time. Additionally, the pharmacokinetic properties of the inhibitors should be determined and, when necessary, optimized by additional modifications.

Furthermore, solving a co-crystal structure of the most promising inhibitors in complex with LANA would provide the opportunity for a structure-based optimization, which might accelerate the whole optimization process. Additionally, the putative binding mode of **A50** and **C50a**, deduced from STD-NMR and molecular docking results could be confirmed by this means. Furthermore, it would be

also of high interest to identify the different binding sites of **A50**, **B1** and **B6** on LANA to enable linking or merging of the different inhibitor scaffolds.

As it stands, the question whether our inhibitors are sufficiently potent or big enough to disturb the strong interaction between LANA and the viral genome in a complex cell system is still unanswered. However, it is already encouraging that such small inhibitors were able to inhibit this macromolecular-macromolecular interaction *in vitro*.

A different approach to eliminate LANA in the KSHV infected cells might provide the so-called PROTAC (proteolysis targeting chimera) strategy.⁶¹ It exploits the ubiquitin proteasome system (UPS) of the mammalian cells and thus can be used to achieve a targeted protein degradation. The degradation of LANA within the infected cells would also prevent the latent persistence of KSHV. For this approach, the synthesis and evaluation of a PROTAC-based LANA degraders has to be established. These conjugates should consist of two independent binding moieties, one binding to the target protein LANA and one binding to the E3 ligase.⁶² If these two motifs are linked together in an appropriate manner, the resulting compound should be able to induce ubiquitination of the target protein LANA. The ubiquitylated LANA would be recognition by the proteasome and, hence, be eliminated from the cell by proteolytic degradation. One example for a putative PROTAC-based LANA degrader is shown in Figure 8. The LANA inhibitor **C50a** (black) is connected by a linker (red) to a known E3 ligase ligand, e. g. pomalidomide (blue).

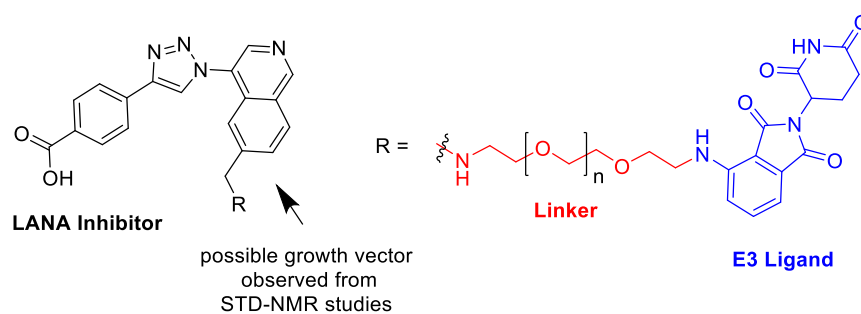


Figure 8: Design of a possible PROTAC-based LANA degrader.

To date, a few promising studies have been published in the field of antiviral PROTACs, but such approaches are relatively underexploited.^{63,64} Such a targeted protein degradation strategy could serve as a relatively new and innovative approach in the area of antiviral drug discovery.

6 References

1. Grinde, B. Herpesviruses: latency and reactivation - viral strategies and host response. *J. Oral Microbiol.* **2013**, *5*, doi:10.3402/jom.v5i0.22766.
2. Virgin, H.W.; Wherry, E.J.; Ahmed, R. Redefining chronic viral infection. *Cell* **2009**, *138*, 30–50, doi:10.1016/j.cell.2009.06.036.
3. Davison, A.J. *Human Herpesviruses: Biology, Therapy, and Immunoprophylaxis. Overview of classification*; Cambridge, 2007, ISBN 9780521827140.
4. Davison, A.J. Herpesvirus systematics. *Vet. Microbiol.* **2010**, *143*, 52–69, doi:10.1016/j.vetmic.2010.02.014.
5. Whitley, R.J. *Medical Microbiology. Herpesviruses*, 4th; Galveston (TX), 1996, ISBN 0963117211.
6. *Human herpesviruses. Biology, therapy and immunoprophylaxis*; Arvin, A., Ed.; Cambridge Univ. Press: Cambridge, 2007, ISBN 0521827140.
7. Goto-Tamura, R.; Takesue, Y.; Takesue, S. Immunological similarity between NADH-cytochrome b5 reductase of erythrocytes and liver microsomes. *Biochim. Biophys. Acta* **1976**, *423*, 293–302, doi:10.1016/0005-2728(76)90186-9.
8. Jordan, M.C.; Jordan, G.W.; Stevens, J.G.; Miller, G. Latent herpesviruses of humans. *Ann. Intern. Med.* **1984**, *100*, 866–880, doi:10.7326/0003-4819-100-6-866.
9. Sehrawat, S.; Kumar, D.; Rouse, B.T. Herpesviruses: Harmonious Pathogens but Relevant Cofactors in Other Diseases? *Front. Cell. Infect. Microbiol.* **2018**, *8*, 177, doi:10.3389/fcimb.2018.00177.
10. Mocroft, A.; Youle, M.; Gazzard, B.; Morcinek, J.; Halai, R.; Phillips, A.N. Anti-herpesvirus treatment and risk of Kaposi's sarcoma in HIV infection. Royal Free/Chelsea and Westminster Hospitals Collaborative Group. *AIDS* **1996**, *10*, 1101–1105.
11. Zuckerman, A.J.; Banatvala, J.E.; Schoub, B.D.; Griffiths, P.D.; Mortimer, P. *Principles and Practice of Clinical Virology*; John Wiley & Sons, Ltd: Chichester, UK, 2009, ISBN 9780470741405.
12. Kaposi. Idiopathisches multiples Pigmentsarkom der Haut. *Arch. f. Dermat.* **1872**, *4*, 265–273, doi:10.1007/BF01830024.
13. Beral, V.; Bull, D.; Darby, S.; Weller, I.; Came, C.; Beecham, M.; Jaffe, H. Risk of Kaposi's sarcoma and sexual practices associated with faecal contact in homosexual or bisexual men with AIDS. *The Lancet* **1992**, *339*, 632–635, doi:10.1016/0140-6736(92)90793-3.
14. Chang, Y.; Cesarman, E.; Pessin, M.S.; Lee, F.; Culpepper, J.; Knowles, D.M.; Moore, P.S. Identification of herpesvirus-like DNA sequences in AIDS-associated Kaposi's sarcoma. *Science* **1994**, *266*, 1865–1869, doi:10.1126/science.7997879.
15. Schulz, T.F. The pleiotropic effects of Kaposi's sarcoma herpesvirus. *J. Pathol.* **2006**, *208*, 187–198, doi:10.1002/path.1904.
16. Cesarman, E.; Chang, Y.; Moore, P.S.; Said, J.W.; Knowles, D.M. Kaposi's sarcoma-associated herpesvirus-like DNA sequences in AIDS-related body-cavity-based lymphomas. *N. Engl. J. Med.* **1995**, *332*, 1186–1191, doi:10.1056/NEJM199505043321802.
17. Soulier, J.; Grollet, L.; Oksenhendler, E.; Cacoub, P.; Cazals-Hatem, D.; Babinet, P.; d'Agay, M.F.; Clauvel, J.P.; Raphael, M.; Degos, L. Kaposi's sarcoma-associated herpesvirus-like DNA sequences in multicentric Castlemann's disease. *Blood* **1995**, *86*, 1276–1280.
18. Biological agents. Volume 100 B. A review of human carcinogens. *IARC Monogr. Eval. Carcinog. Risks Hum.* **2012**, *100*, 1–441.

19. Bouvard, V.; Baan, R.; Straif, K.; Grosse, Y.; Secretan, B.; El Ghissassi, F.; Benbrahim-Tallaa, L.; Guha, N.; Freeman, C.; Galichet, L.; et al. A review of human carcinogens--Part B: biological agents. *Lancet Oncol.* **2009**, *10*, 321–322.
20. Cesarman, E.; Damania, B.; Krown, S.E.; Martin, J.; Bower, M.; Whitby, D. Kaposi sarcoma. *Nature Reviews Disease Primers* **2019**, *5*, 9, doi:10.1038/s41572-019-0060-9.
21. Mesri, E.A.; Cesarman, E.; Boshoff, C. Kaposi's sarcoma and its associated herpesvirus. *Nat. Rev. Cancer* **2010**, *10*, 707–719, doi:10.1038/nrc2888.
22. Schulz, T.F.; Cesarman, E. Editorial overview: Viruses and cancer: How tumor viruses affect the cellular genome. *Curr. Opin. Virol.* **2017**, *26*, vi–vii, doi:10.1016/j.coviro.2017.10.005.
23. Russo, J.J.; Bohenzky, R.A.; Chien, M.C.; Chen, J.; Yan, M.; Maddalena, D.; Parry, J.P.; Peruzzi, D.; Edelman, I.S.; Chang, Y.; et al. Nucleotide sequence of the Kaposi sarcoma-associated herpesvirus (HHV8). *Proc. Natl. Acad. Sci. U. S. A.* **1996**, *93*, 14862–14867, doi:10.1073/pnas.93.25.14862.
24. Hu, J.; Renne, R. Characterization of the Minimal Replicator of Kaposi's Sarcoma-Associated Herpesvirus Latent Origin. *Journal of Virology* **2005**, *79*, 2637–2642, doi:10.1128/JVI.79.4.2637-2642.2005.
25. Lagunoff, M.; Ganem, D. The Structure and Coding Organization of the Genomic Termini of Kaposi's Sarcoma-Associated Herpesvirus (Human Herpesvirus 8). *Virology* **1997**, *236*, 147–154, doi:10.1006/viro.1997.8713.
26. Cai, Q.; Verma, S.C.; Lu, J.; Robertson, E.S. Molecular Biology of Kaposi's Sarcoma-associated Herpesvirus and Related Oncogenesis. In *Advances in virus research*; Maramorosch, K., Ed.; Elsevier Science Publishing Co, 2010; pp 87–142, ISBN 9780123850324.
27. Zhong, W.; Wang, H.; Herndier, B.; Ganem, D. Restricted expression of Kaposi sarcoma-associated herpesvirus (human herpesvirus 8) genes in Kaposi sarcoma. *Proc. Natl. Acad. Sci. U. S. A.* **1996**, *93*, 6641–6646, doi:10.1073/pnas.93.13.6641.
28. Rainbow, L.; Platt, G.M.; Simpson, G.R.; Sarid, R.; Gao, S.J.; Stoiber, H.; Herrington, C.S.; Moore, P.S.; Schulz, T.F. The 222- to 234-kilodalton latent nuclear protein (LNA) of Kaposi's sarcoma-associated herpesvirus (human herpesvirus 8) is encoded by orf73 and is a component of the latency-associated nuclear antigen. *Journal of Virology* **1997**, *71*, 5915–5921.
29. Kedes, D.H. The Prevalence of Serum Antibody to Human Herpesvirus 8 (Kaposi Sarcoma—Associated Herpesvirus) Among HIV-Seropositive and High-Risk HIV-Seronegative Women. *JAMA* **1997**, *277*, 478, doi:10.1001/jama.1997.03540300046032.
30. Dittmer, D.; Lagunoff, M.; Renne, R.; Staskus, K.; Haase, A.; Ganem, D. A Cluster of Latently Expressed Genes in Kaposi's Sarcoma-Associated Herpesvirus. *Journal of Virology* **1998**, *72*, 8309–8315.
31. Yan, L.; Majerciak, V.; Zheng, Z.-M.; Lan, K. Towards Better Understanding of KSHV Life Cycle: from Transcription and Posttranscriptional Regulations to Pathogenesis. *Virol. Sin.* **2019**, *34*, 135–161, doi:10.1007/s12250-019-00114-3.
32. Sarid, R.; Wiezorek, J.S.; Moore, P.S.; Chang, Y. Characterization and Cell Cycle Regulation of the Major Kaposi's Sarcoma-Associated Herpesvirus (Human Herpesvirus 8) Latent Genes and Their Promoter. *Journal of Virology* **1999**, *73*, 1438–1446.
33. Parravicini, C.; Chandran, B.; Corbellino, M.; Berti, E.; Paulli, M.; Moore, P.S.; Chang, Y. Differential Viral Protein Expression in Kaposi's Sarcoma-Associated Herpesvirus-Infected Diseases. *The American Journal of Pathology* **2000**, *156*, 743–749, doi:10.1016/S0002-9440(10)64940-1.
34. Verma, S.C.; Lan, K.; Robertson, E. Structure and Function of Latency-Associated Nuclear Antigen. *Curr. Top. Microbiol. Immunol.* **2007**, *312*, 101–136.

35. Wei, F.; Gan, J.; Wang, C.; Zhu, C.; Cai, Q. Cell Cycle Regulatory Functions of the KSHV Oncoprotein LANA. *Front. Microbiol.* **2016**, *7*, 334, doi:10.3389/fmicb.2016.00334.
36. Uppal, T.; Banerjee, S.; Sun, Z.; Verma, S.C.; Robertson, E.S. KSHV LANA--the master regulator of KSHV latency. *Viruses* **2014**, *6*, 4961–4998, doi:10.3390/v6124961.
37. Hu, J.; Garber, A.C.; Renne, R. The latency-associated nuclear antigen of Kaposi's sarcoma-associated herpesvirus supports latent DNA replication in dividing cells. *Journal of Virology* **2002**, *76*, 11677–11687, doi:10.1128/JVI.76.22.11677–11687.2002.
38. Kirsch, P.; Jakob, V.; Oberhausen, K.; Stein, S.C.; Cucarro, I.; Schulz, T.F.; Empting, M. Fragment-Based Discovery of a Qualified Hit Targeting the Latency-Associated Nuclear Antigen of the Oncogenic Kaposi's Sarcoma-Associated Herpesvirus/Human Herpesvirus 8. *J. Med. Chem.* **2019**, *62*, 3924–3939, doi:10.1021/acs.jmedchem.8b01827.
39. Juillard, F.; Tan, M.; Li, S.; Kaye, K.M. Kaposi's Sarcoma Herpesvirus Genome Persistence. *Front. Microbiol.* **2016**, *7*, 1883, doi:10.3389/fmicb.2016.01149.
40. Hellert, J.; Weidner-Glunde, M.; Krausze, J.; Lünsdorf, H.; Ritter, C.; Schulz, T.F.; Lühns, T. The 3D structure of Kaposi sarcoma herpesvirus LANA C-terminal domain bound to DNA. *Proc. Natl. Acad. Sci. U. S. A.* **2015**, *112*, 6694–6699, doi:10.1073/pnas.1421804112.
41. Garber, A.C.; Hu, J.; Renne, R. Latency-associated nuclear antigen (LANA) cooperatively binds to two sites within the terminal repeat, and both sites contribute to the ability of LANA to suppress transcription and to facilitate DNA replication. *J. Biol. Chem.* **2002**, *277*, 27401–27411, doi:10.1074/jbc.M203489200.
42. Rawlins, D.R.; Milman, G.; Hayward, S.D.; Hayward, G.S. Sequence-specific DNA binding of the Epstein-Barr virus nuclear antigen (EBNA-1) to clustered sites in the plasmid maintenance region. *Cell* **1985**, *42*, 859–868, doi:10.1016/0092-8674(85)90282-x.
43. Hegde, R.S. The papillomavirus E2 proteins: structure, function, and biology. *Annu. Rev. Biophys. Biomol. Struct.* **2002**, *31*, 343–360, doi:10.1146/annurev.biophys.31.100901.142129.
44. Domsic, J.F.; Chen, H.-S.; Lu, F.; Marmorstein, R.; Lieberman, P.M. Molecular Basis for Oligomeric-DNA Binding and Episome Maintenance by KSHV LANA. *PLoS Pathog* **2013**, *9*, e1003672, doi:10.1371/journal.ppat.1003672.
45. Hellert, J.; Weidner-Glunde, M.; Krausze, J.; Richter, U.; Adler, H.; Fedorov, R.; Pietrek, M.; Rückert, J.; Ritter, C.; Schulz, T.F.; et al. A Structural Basis for BRD2/4-Mediated Host Chromatin Interaction and Oligomer Assembly of Kaposi Sarcoma-Associated Herpesvirus and Murine Gammaherpesvirus LANA Proteins. *PLoS Pathog* **2013**, *9*, e1003640, doi:10.1371/journal.ppat.1003640.
46. Hellert, J.; Krausze, J.; Schulz, T.F.; Lühns, T. Crystallization, room-temperature X-ray diffraction and preliminary analysis of Kaposi's sarcoma herpesvirus LANA bound to DNA. *Acta Crystallogr. F Struct. Biol. Commun.* **2014**, *70*, 1570–1574, doi:10.1107/S2053230X14019906.
47. Tornøe, C.W.; Christensen, C.; Meldal, M. Peptidotriazoles on solid phase: 1,2,3-triazoles by regioselective copper(i)-catalyzed 1,3-dipolar cycloadditions of terminal alkynes to azides. *J. Org. Chem.* **2002**, *67*, 3057–3064, doi:10.1021/jo011148j.
48. Rostovtsev, V.V.; Green, L.G.; Fokin, V.V.; Sharpless, K.B. A Stepwise Huisgen Cycloaddition Process: Copper(I)-Catalyzed Regioselective "Ligation" of Azides and Terminal Alkynes. *Angew. Chem. Int. Ed.* **2002**, *41*, 2596–2599, doi:10.1002/1521-3773(20020715)41:14<2596:AID-ANIE2596>3.0.CO;2-4.
49. Jiang, X.; Hao, X.; Jing, L.; Wu, G.; Kang, D.; Liu, X.; Zhan, P. Recent applications of click chemistry in drug discovery. *Expert Opin. Drug Discov.* **2019**, *14*, 779–789, doi:10.1080/17460441.2019.1614910.

-
50. Worrell, B.T.; Malik, J.A.; Fokin, V.V. Direct evidence of a dinuclear copper intermediate in Cu(I)-catalyzed azide-alkyne cycloadditions. *Science* **2013**, *340*, 457–460, doi:10.1126/science.1229506.
 51. Thirumurugan, P.; Matosiuk, D.; Jozwiak, K. Click chemistry for drug development and diverse chemical-biology applications. *Chem. Rev.* **2013**, *113*, 4905–4979, doi:10.1021/cr200409f.
 52. Tron, G.C.; Pirali, T.; Billington, R.A.; Canonico, P.L.; Sorba, G.; Genazzani, A.A. Click chemistry reactions in medicinal chemistry: applications of the 1,3-dipolar cycloaddition between azides and alkynes. *Med. Res. Rev.* **2008**, *28*, 278–308, doi:10.1002/med.20107.
 53. Coen, N.; Duraffour, S.; Snoeck, R.; Andrei, G. KSHV targeted therapy: an update on inhibitors of viral lytic replication. *Viruses* **2014**, *6*, 4731–4759, doi:10.3390/v6114731.
 54. Schwartz, R.A. Kaposi's sarcoma: an update. *J. Surg. Oncol.* **2004**, *87*, 146–151, doi:10.1002/jso.20090.
 55. Valkov, E.; Sharpe, T.; Marsh, M.; Greive, S.; Hyvönen, M. Targeting protein-protein interactions and fragment-based drug discovery. *Top. Curr. Chem.* **2012**, *317*, 145–179, doi:10.1007/128_2011_265.
 56. Jacquemard, C.; Kellenberger, E. A bright future for fragment-based drug discovery: what does it hold? *Expert Opin. Drug Discov.* **2019**, *14*, 413–416, doi:10.1080/17460441.2019.1583643.
 57. Kirsch, P.; Hartman, A.M.; Hirsch, A.K.H.; Empting, M. Concepts and Core Principles of Fragment-Based Drug Design. *Molecules* **2019**, *24*, doi:10.3390/molecules24234309.
 58. Valenti, D.; Hristeva, S.; Tzalis, D.; Ottmann, C. Clinical candidates modulating protein-protein interactions: The fragment-based experience. *Eur. J. Med. Chem.* **2019**, *167*, 76–95, doi:10.1016/j.ejmech.2019.01.084.
 59. *Targeting Protein-Protein Interactions by Small Molecules*; Sheng, C.; Georg, G.I., Eds.; Springer Singapore: Singapore, 2018, ISBN 978-981-13-0772-0.
 60. Messick, T.E.; Smith, G.R.; Soldan, S.S.; McDonnell, M.E.; Deakyne, J.S.; Malecka, K.A.; Tolvinski, L.; van den Heuvel, A.P.J.; Gu, B.-W.; Cassel, J.A.; et al. Structure-based design of small-molecule inhibitors of EBNA1 DNA binding blocks Epstein-Barr virus latent infection and tumor growth. *Sci. Transl. Med.* **2019**, *11*, doi:10.1126/scitranslmed.aau5612.
 61. Pei, H.; Peng, Y.; Zhao, Q.; Chen, Y. Small molecule PROTACs: an emerging technology for targeted therapy in drug discovery. *RSC Adv.* **2019**, *9*, 16967–16976, doi:10.1039/C9RA03423D.
 62. Konstantinidou, M.; Li, J.; Zhang, B.; Wang, Z.; Shaabani, S.; Ter Brake, F.; Essa, K.; Dömling, A. PROTACs- a game-changing technology. *Expert Opin. Drug Discov.* **2019**, *14*, 1255–1268, doi:10.1080/17460441.2019.1659242.
 63. Wispelaere, M. de; Du, G.; Donovan, K.A.; Zhang, T.; Eleuteri, N.A.; Yuan, J.C.; Kalabathula, J.; Nowak, R.P.; Fischer, E.S.; Gray, N.S.; et al. Small molecule degraders of the hepatitis C virus protease reduce susceptibility to resistance mutations. *Nat. Commun.* **2019**, *10*, 3468, doi:10.1038/s41467-019-11429-w.
 64. Montrose, K.; Krissansen, G.W. Design of a PROTAC that antagonizes and destroys the cancer-forming X-protein of the hepatitis B virus. *Biochem. Biophys. Res. Commun.* **2014**, *453*, 735–740, doi:10.1016/j.bbrc.2014.10.006.
-

7 Appendix

7.1 Supporting Information Chapter A

SUPPORTING INFORMATION

Fragment-based discovery of a qualified hit targeting the Latency-associated Nuclear Antigen of the oncogenic Kaposi's Sarcoma-associated Herpesvirus/Human Herpesvirus 8

Philine Kirsch†^{1,2,3}, Valentin Jakob^{1,2}, Kevin Oberhausen^{1,2}, Saskia C. Stein^{3,4}, Ivano Cucarro^{1,2}, Thomas F. Schulz^{3,4}, Martin Empting^{1,2,3*}

¹Helmholtz-Institute for Pharmaceutical Research Saarland (HIPS)-Helmholtz Centre for Infection Research (HZI), Department of Drug Design and Optimization (DDOP), Campus E8.1, 66123 Saarbrücken, Germany

²Department of Pharmacy, Saarland University, Campus E8.1, 66123 Saarbrücken, Germany

³German Centre for Infection Research (DZIF), Partner Site Hannover-Braunschweig, Saarbrücken, Germany

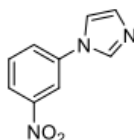
⁴Institute of Virology, Hannover Medical School, Carl-Neuberg-Strasse 1, 30625 Hannover, Germany

Contents

1. Materials and Methods	3
1.1. Chemistry.....	3
2. Biology	15
2.1. Expression and purification of a His-tagged oligomerization-deficient mutant of the KSHV LANA C-terminal DNA binding domain (DBD; aa1008-1146)	15
2.2. Expression and purification of a GST-tagged KSHV LANA C-terminal domain (CTD; aa934-1162)	15
2.3. SPR-based Screening	16
2.4. DSF-based Screening	17
2.5. Fluorescence Polarization Assay	18
2.5.1. DNA Hybridisation:	18
2.5.2. FP-Assay Optimization Studies	18
2.5.3. Dose-dependent Studies with LBS1, 2 and 3.....	20
2.5.4. Dose dependent Studies of Compounds 37, 41 - 43, 47 and 50	21
2.6. Calculation of LogP and Ligand Efficiency (LE)	21
2.7. Electrophoretic Mobility Shift Assay (EMSA)	22
2.7.1. EMSA Experiments for Compounds 37, 41, 42, 43, 47, and 50.....	22
2.7.2. Dose-dependent EMSA Experiments with Compound 50.....	25
2.8. Saturation-Transfer Difference NMR (STD-NMR)	28
2.9. Molecular Docking.....	29
2.10. Additional information to Hit 1 and alternative Hits 1a and 1b.....	29
3. High Resolution Mass Spectrometry (HRMS).....	30
References.....	Fehler! Textmarke nicht definiert.

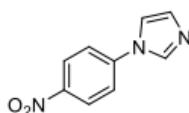
1. Materials and Methods

1.1. Chemistry



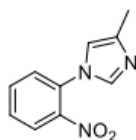
1-(3-nitrophenyl)-1H-imidazole

1-(3-nitrophenyl)-1H-imidazole (3): **3** was prepared according to general procedure I using 3-bromo-nitrobenzene (150 mg, 0.74 mmol), K_2CO_3 (122 mg, 0.89 mmol), CuCl (7.0 mg, 0.04 mmol), 1H-imidazole (73 mg, 0.89 mmol) and DMF (5 mL). Additionally, *N*1,*N*2-dimethylethane-1,2-diamine (13 mg, 0.08 mmol) was added and the reaction mixture was heated up to 150 °C in a crimp vial. The obtained crude was purified by column chromatography (PE:EE 1:9) to yield the title compound (45 mg, 0.23 mmol, 31 %) 1H NMR (300 MHz, $DMSO-d_6$) δ ppm 7.32 (m, $J = 8.75$ Hz, 2 H) 7.75 (m, $J = 8.75$ Hz, 2 H) 7.84 - 7.96 (m, 1 H) 8.23 (t, $J = 1.72$ Hz, 1 H) 9.70 (t, $J = 1.35$ Hz, 1 H); ^{13}C NMR (75 MHz, $DMSO-d_6$) δ ppm 119.72, 120.43, 120.59, 121.03, 123.40, 134.25, 139.41, 140.05.



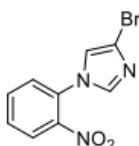
1-(4-nitrophenyl)-1H-imidazole

1-(4-nitrophenyl)-1H-imidazole (4): **4** was prepared according to general procedure I using 4-iodo-nitrobenzene (150 mg, 0.60 mmol), K_2CO_3 (99 mg, 0.72 mmol), CuCl (7.0 mg, 0.06 mmol), 1H-imidazole (73 mg, 0.89 mmol) and DMF (5 mL). Additionally, *N*1,*N*2-dimethylethane-1,2-diamine (19 mg, 0.12 mmol) was added. The obtained crude was purified by column chromatography (PE:EE 1:9) to yield the title compound (60 mg, 0.31 mmol, 52%) 1H NMR (300 MHz, $DMSO-d_6$) δ ppm 7.18 (s, 1 H) 7.86 - 8.02 (m, 3 H) 8.24 - 8.45 (m, 2 H) 8.50 (s, 1 H); ^{13}C NMR (75 MHz, $DMSO-d_6$) δ ppm 117.86, 120.37, 125.50, 130.78, 136.03, 141.67, 145.27.



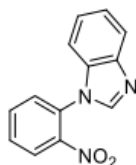
4-methyl-1-(2-nitrophenyl)-1H-imidazole

4-methyl-1-(2-nitrophenyl)-1H-imidazole (5): **5** was prepared according to general procedure I using 2-Iod-nitrobenzene (400 mg, 1.60 mmol), K_2CO_3 (263 mg, 1.90 mmol), CuI (40 mg, 0.16 mmol), 4-methyl-1H-imidazole (156 mg, 1.90 mmol) and DMF (12 mL). The obtained crude was purified by column chromatography (PE:EE 1:9) to yield the title compound (168 mg, 0.83 mmol, 52 %) MS (ESI⁺) m/z 204 (M+H).



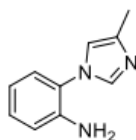
4-bromo-1-(2-nitrophenyl)-1H-imidazole

4-bromo-1-(2-nitrophenyl)-1H-imidazole (6): **6** was prepared according to general procedure I using 2-Iod-nitrobenzene (120 mg, 0.48 mmol), K_2CO_3 (79 mg, 0.57 mmol), CuI (12 mg, 0.05 mmol), 4-bromo-1H-imidazole (84 mg, 0.57 mmol) and DMF (4 mL). The obtained crude was purified by column chromatography (PE:EE 1:1) to yield the title compound (50 mg, 0.18 mmol, 38 %). MS (ESI⁺) m/z 268, 270 (M+H).



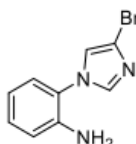
1-(2-nitrophenyl)-1H-benzo[d]imidazole

1-(2-nitrophenyl)-1H-benzo[d]imidazole (7): **7** was prepared according to general procedure I using 2-Iod-nitrobenzene (100 mg, 0.40 mmol), K_2CO_3 (66 mg, 0.48 mmol), CuI (7.5 mg, 0.04 mmol), 1H-benzimidazole (56 mg, 0.48 mmol) and DMF (3 mL). The obtained crude was purified by column chromatography (PE:EE 1:1) to yield the title compound (80 mg, 0.33 mmol, 82 %). MS (ESI⁺) m/z 240 (M+H).



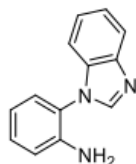
2-(4-methyl-1H-imidazol-1-yl)aniline

2-(4-methyl-1H-imidazol-1-yl)aniline (11): **11** was prepared to the general procedure II using 4-methyl-1-(2-nitrophenyl)-1H-imidazole **5** (100 mg, 0.49 mmol), SnCl₂ (553 mg, 2.46 mmol) and ethanol (10 mL). The obtained crude was purified by flash column chromatography (gradient elution, DCM:MeOH 95:5 - 90:10) to yield the target compound (53 mg, 0.30 mmol, 61%). ¹H NMR (300 MHz, CDCl₃) δ ppm 2.32 (s, 3 H) 3.70 (br. s., 2 H) 6.72 - 6.95 (m, 3 H) 7.10 (dd, *J* = 7.68, 1.26 Hz, 1 H) 7.17 - 7.26 (m, 1 H) 7.56 (br. s., 1 H); ¹³C NMR (75 MHz, CDCl₃) δ ppm 15.66, 116.30, 118.55, 123.67, 125.44, 127.06, 129.58, 141.86, 142.87.



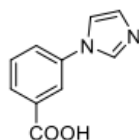
2-(4-bromo-1H-imidazol-1-yl)aniline

2-(4-bromo-1H-imidazol-1-yl)aniline (12): **12** was prepared to the general procedure II using 4-bromo-1-(2-nitrophenyl)-1H-imidazole **6** (50 mg, 0.19 mmol), SnCl₂ (209 mg, 0.93 mmol) and ethanol (7 mL). The obtained crude was purified by prep. HPLC (reversed-phase, mobile phase consisting of acetonitrile containing 0.05% FA (v/v) and water containing 0.05% FA (v/v); 5:95 - 90:10) to yield the target compound (15 mg, 0.06 mmol, 31%). ¹H NMR (300 MHz, CDCl₃) δ ppm 3.73 (br. s., 2 H) 6.75 - 6.91 (m, 2 H) 7.05 - 7.16 (m, 2 H) 7.18 - 7.33 (m, 1 H) 7.52 (d, *J* = 1.49 Hz, 1 H); ¹³C NMR (75 MHz, CDCl₃) δ ppm 116.19, 116.55, 118.66, 119.32, 122.49, 127.04, 130.31, 137.37, 141.79.

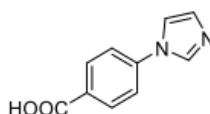


2-(1H-benzo[d]imidazol-1-yl)aniline

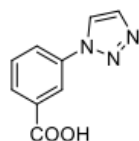
2-(1H-benzo[d]imidazol-1-yl)aniline (13): **13** was prepared to the general procedure II using 4-methyl-1-(2-nitrophenyl)-1H-imidazole **7** (80 mg, 0.33 mmol), SnCl₂ (350 mg, 1.56 mmol) and ethanol (10 mL). The obtained crude was purified by flash column chromatography (gradient elution, DCM:MeOH 98:2 - 9:1) to yield the target compound (32 mg, 0.15 mmol, 45 %). ¹H NMR (300 MHz, CDCl₃) δ ppm 3.65 (br. s., 2 H) 6.83 - 6.96 (m, 2 H) 7.19 (dd, *J* = 7.82, 1.49 Hz, 1 H) 7.23 - 7.39 (m, 4 H) 7.84 - 7.94 (m, 1 H) 7.97 - 8.05 (m, 1 H); ¹³C NMR (75 MHz, CDCl₃) δ ppm 110.79, 116.54, 118.73, 120.50, 121.16, 122.72, 123.60, 128.18, 130.24, 133.88, 142.71, 143.23, 143.51.

3-(1*H*-imidazol-1-yl)benzoic acid

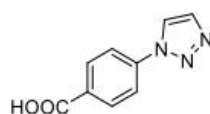
3-(1*H*-imidazol-1-yl)benzoic acid (17): 17 was prepared according to general procedure III using 3-bromo-benzoic acid, *N*1,*N*2-dimethylethane-1,2-diamine, K_2CO_3 , CuCl, 1*H*-imidazole and DMF. 1H NMR (500 MHz, $DMSO-d_6$) δ ppm 7.13 (br. s., 1 H) 7.65 (d, $J = 6.56$ Hz, 1 H) 7.84 (br. s., 1 H) 7.91 (br. s., 2 H) 8.10 (br. s., 1 H) 8.34 (br. s., 1 H); ^{13}C NMR (126 MHz, $DMSO-d_6$) δ ppm 118.18, 120.78, 124.62, 127.57, 130.14, 130.25, 135.77, 137.15, 166.64.

4-(1*H*-imidazol-1-yl)benzoic acid

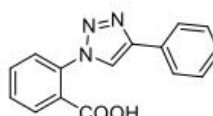
4-(1*H*-imidazol-1-yl)benzoic acid (18): 18 was prepared according to general procedure III using 4-bromo-benzoic acid, *N*1,*N*2-dimethylethane-1,2-diamine, K_2CO_3 , CuCl, 1*H*-imidazole and DMF. 1H NMR (500 MHz, $DMSO-d_6$) δ ppm 7.15 (br. s., 1 H) 7.81 (br. s., 2 H) 7.87 (br. s., 1 H) 8.05 (br. s., 2 H) 8.40 (br. s., 1 H); ^{13}C NMR (126 MHz, $DMSO-d_6$) δ ppm 117.66, 119.63, 130.22, 130.92, 135.55, 139.91, 166.42.

3-(1*H*-1,2,3-triazol-1-yl)benzoic acid

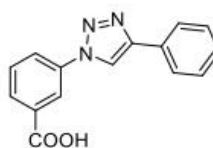
3-(1*H*-1,2,3-triazol-1-yl)benzoic acid (27): 27 was synthesized according to procedure IV using 3-azidobenzoic acid and ethynyltrimethylsilane as starting material. 1H NMR (500 MHz, $DMSO-d_6$) δ ppm 7.74 (d, $J = 6.26$ Hz, 1 H) 8.04 (s, 1 H) 8.01 (s, 1 H) 8.18 (br. s., 1 H) 8.42 (br. s., 1 H) 8.97 (br. s., 1 H) 13.43 (br. s., 1 H); ^{13}C NMR (126 MHz, $DMSO-d_6$) δ ppm 120.52, 123.45, 124.22, 129.16, 130.39, 134.68, 136.86, 166.39.

4-(1*H*-1,2,3-triazol-1-yl)benzoic acid

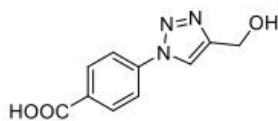
4-(1*H*-1,2,3-triazol-1-yl)benzoic acid (28): **28** was synthesized according to procedure IV using 4-azidobenzoic acid and ethynyltrimethylsilane as starting material. ^1H NMR (500 MHz, $\text{DMSO-}d_6$) δ ppm 8.03 (br. s., 1 H) 8.07 (br. s., 2 H) 8.14 (br. s., 2 H) 8.96 (br. s., 1 H); ^{13}C NMR (126 MHz, $\text{DMSO-}d_6$) δ ppm 119.86, 123.43, 131.09, 134.81, 139.54, 166.48.

2-(4-phenyl-1*H*-1,2,3-triazol-1-yl)benzoic acid

2-(4-phenyl-1*H*-1,2,3-triazol-1-yl)benzoic acid (29): **29** was synthesized according to procedure V using 2-azidobenzoic acid **21** and ethynyl benzene as starting material. ^1H NMR (300 MHz, $\text{DMSO-}d_6$) δ ppm 7.28 - 7.41 (m, 1 H) 7.44 - 7.54 (m, 2 H) 7.64 - 7.85 (m, 3 H) 7.88 - 8.01 (m, 3 H) 9.00 (s, 1 H); ^{13}C NMR (75 MHz, $\text{DMSO-}d_6$) δ ppm 123.00, 125.20, 126.48, 128.04, 128.81, 128.96, 130.01, 130.44, 130.49, 132.42, 135.32, 146.33, 166.50.

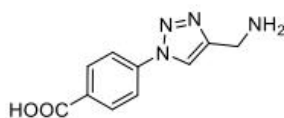
3-(4-phenyl-1*H*-1,2,3-triazol-1-yl)benzoic acid

3-(4-phenyl-1*H*-1,2,3-triazol-1-yl)benzoic acid (30): **30** was synthesized according to procedure V using 3-azidobenzoic acid **22** and ethynyl benzene as starting material. ^1H NMR (500 MHz, $\text{DMSO-}d_6$) δ ppm 4.62 (s, 2 H) 5.35 (br. s., 1 H) 7.73 (t, $J = 7.86$ Hz, 1 H) 8.02 (d, $J = 7.78$ Hz, 1 H) 8.16 (dd, $J = 8.09, 1.37$ Hz, 1 H) 8.41 (s, 1 H) 8.81 (s, 1 H) 13.42 (br. s., 1 H); ^{13}C NMR (75 MHz, $\text{DMSO-}d_6$) δ ppm 115.45, 124.36, 126.31, 128.67, 129.21, 129.99, 131.42, 131.98, 139.46, 146.56, 166.57.



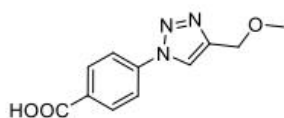
4-(4-(hydroxymethyl)-1H-1,2,3-triazol-1-yl)benzoic acid

4-(4-(hydroxymethyl)-1H-1,2,3-triazol-1-yl)benzoic acid (32): **32** was synthesized according to procedure V using 4-azidobenzoic acid and propargyl alcohol as starting material. ^1H NMR (300 MHz, $\text{DMSO-}d_6$) δ ppm 4.63 (s, 2 H) 5.37 (s, 1 H) 7.97 - 8.26 (m, 4 H) 8.80 (s, 1 H) 13.19 (br. s., 1 H); ^{13}C NMR (75 MHz, $\text{DMSO-}d_6$) δ ppm 55.39, 120.14, 121.59, 131.59, 140.14, 149.98, 158.70, 166.87.



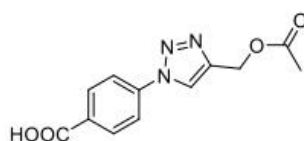
4-(4-(aminomethyl)-1H-1,2,3-triazol-1-yl)benzoic acid

4-(4-(aminomethyl)-1H-1,2,3-triazol-1-yl)benzoic acid (33): **33** was synthesized according to procedure V using 4-azidobenzoic acid and propargyl amine as starting material. ^1H NMR (500 MHz, $\text{DMSO-}d_6$) δ ppm 2.13 (s, 2 H) 5.61 (d, $J = 8.54$ Hz, 2 H) 5.90 (d, $J = 8.55$ Hz, 2 H) 6.34 (s, 1 H); ^{13}C NMR (126 MHz, $\text{DMSO-}d_6$) δ ppm 31.73, 118.59, 121.53, 129.20, 137.31, 138.39, 166.93.



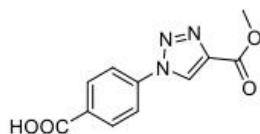
4-(4-(methoxymethyl)-1H-1,2,3-triazol-1-yl)benzoic acid

4-(4-(methoxymethyl)-1H-1,2,3-triazol-1-yl)benzoic acid (34): **34** was synthesized according to procedure V using 4-azidobenzoic acid and methyl propargyl ether as starting material. ^1H NMR (500 MHz, $\text{DMSO-}d_6$) δ ppm 3.32 (s, 3 H) 4.55 (s, 2 H) 8.06 (m, $J = 7.78$ Hz, 2 H) 8.13 (m, $J = 8.24$ Hz, 2 H) 8.84 - 9.02 (m, 1 H); ^{13}C NMR (126 MHz, $\text{DMSO-}d_6$) δ ppm 57.56, 64.85, 119.87, 122.38, 131.25, 139.58, 145.37, 166.39.



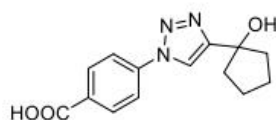
4-(4-(acetoxymethyl)-1H-1,2,3-triazol-1-yl)benzoic acid

4-(4-(acetoxymethyl)-1H-1,2,3-triazol-1-yl)benzoic acid (35): **35** was synthesized according to procedure V using 4-azidobenzoic acid and propargyl acetate as starting material. ^1H NMR (300 MHz, $\text{DMSO-}d_6$) δ ppm 2.07 (s, 3 H) 5.22 (s, 2 H) 7.98 - 8.09 (m, 2 H) 8.09 - 8.21 (m, 2 H) 8.97 (s, 1 H); ^{13}C NMR (75 MHz, $\text{DMSO-}d_6$) δ ppm 20.58, 56.83, 119.88, 123.03, 130.84, 131.05, 139.35, 143.47, 166.37, 170.07.



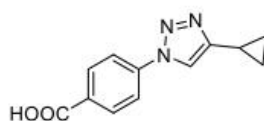
4-(4-(methoxycarbonyl)-1H-1,2,3-triazol-1-yl)benzoic acid

4-(4-(methoxycarbonyl)-1H-1,2,3-triazol-1-yl)benzoic acid (36): 36 was synthesized according to procedure V using 4-azidobenzoic acid and methyl propiolate as starting material. ^1H NMR (500 MHz, $\text{DMSO-}d_6$) δ ppm 3.91 (s., 3 H) 8.16 (br. s., 4 H) 9.65 (s., 1 H); ^{13}C NMR (126 MHz, $\text{DMSO-}d_6$) δ ppm 52.10, 120.43, 127.59, 131.05, 139.00, 139.78, 160.48, 166.44.



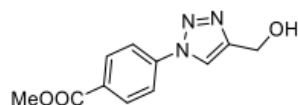
4-(4-(1-hydroxycyclopentyl)-1H-1,2,3-triazol-1-yl)benzoic acid

4-(4-(1-hydroxycyclopentyl)-1H-1,2,3-triazol-1-yl)benzoic acid (37): 37 was synthesized according to procedure V using 4-azidobenzoic acid and 1-ethynylcyclopentan-1-ol as starting material. ^1H NMR (500 MHz, $\text{DMSO-}d_6$) δ ppm 1.72 (s., 2 H) 1.86 (s., 2 H) 1.91 (d, $J = 13.28$ Hz, 2 H) 2.04 (s., 2 H) 5.18 (br. s., 1 H) 8.08 (s., 2 H) 8.11 (s., 2 H) 8.72 (s., 1 H) 13.27 (br. s., 1 H); ^{13}C NMR (126 MHz, $\text{DMSO-}d_6$) δ ppm 23.31, 40.61, 77.35, 119.58, 131.11, 139.74, 155.99, 166.47.



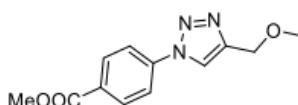
4-(4-cyclopropyl-1H-1,2,3-triazol-1-yl)benzoic acid

4-(4-cyclopropyl-1H-1,2,3-triazol-1-yl)benzoic acid (38): 38 was synthesized according to procedure V using 4-azidobenzoic acid and ethynyl cyclopropane as starting material. ^1H NMR (500 MHz, $\text{DMSO-}d_6$) δ ppm 0.81 (br. s., 2 H) 0.98 (br. s., 2 H) 1.97 - 2.12 (m, 1 H) 8.00 (s., 2 H) 8.11 (s., 2 H) 8.66 (s., 1 H) 13.18 (br. s., 1 H); ^{13}C NMR (126 MHz, $\text{DMSO-}d_6$) δ ppm 6.52, 7.83, 119.01, 119.22, 119.42, 130.28, 131.09, 131.25, 139.66, 150.70, 166.46.



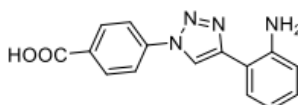
methyl 4-(4-(hydroxymethyl)-1H-1,2,3-triazol-1-yl)benzoate

methyl 4-(4-(hydroxymethyl)-1H-1,2,3-triazol-1-yl)benzoate (39): **39** was synthesized according to procedure V using methyl 4-azidobenzoate **25** and propargyl alcohol as starting material. ^1H NMR (500 MHz, $\text{DMSO-}d_6$) δ ppm 3.89 (s, 3 H) 4.62 (s, 2 H) 5.39 (br. s., 1 H) 8.05 - 8.23 (m, 4 H) 8.83 (s, 1 H); ^{13}C NMR (126 MHz, $\text{DMSO-}d_6$) δ ppm 52.44, 54.92, 119.76, 121.15, 129.18, 131.01, 139.94, 149.58, 165.38.



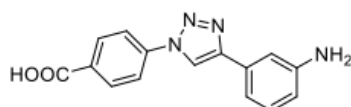
methyl 4-(4-(methoxymethyl)-1H-1,2,3-triazol-1-yl)benzoate

methyl 4-(4-(methoxymethyl)-1H-1,2,3-triazol-1-yl)benzoate (40): **40** was synthesized according to procedure V using methyl 4-azidobenzoate **25** and methyl propargyl ether as starting material. ^1H NMR (500 MHz, $\text{DMSO-}d_6$) δ ppm 3.32 (s, 3 H) 3.33 (s, 3 H) 4.56 (s, 2 H) 8.08 - 8.12 (m, 2 H) 8.14 - 8.18 (m, 2 H) 8.96 (s, 1 H); ^{13}C NMR (126 MHz, $\text{DMSO-}d_6$) δ ppm 52.25, 57.32, 64.62, 119.70, 122.19, 129.13, 130.82, 139.64, 145.19, 165.17.



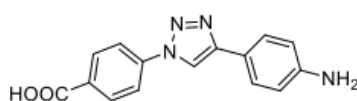
4-(4-(2-aminophenyl)-1H-1,2,3-triazol-1-yl)benzoic acid

4-(4-(2-aminophenyl)-1H-1,2,3-triazol-1-yl)benzoic acid (41): **41** was synthesized according to procedure V using 4-azidobenzoic acid and 2-ethynyl aniline as starting material. ^1H NMR (500 MHz, $\text{DMSO-}d_6$) δ ppm 6.64 (t, $J = 7.02$ Hz, 1 H) 6.81 (d, $J = 7.78$ Hz, 1 H) 7.09 (t, $J = 7.40$ Hz, 1 H) 7.61 (d, $J = 7.63$ Hz, 1 H) 8.08 - 8.31 (m, 5 H) 9.31 (s, 1 H); ^{13}C NMR (126 MHz, $\text{DMSO-}d_6$) δ ppm 112.15, 116.01, 119.92, 127.97, 129.05, 131.20, 139.53, 145.86, 148.34, 166.55.



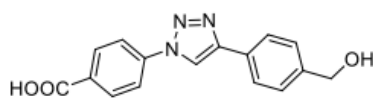
4-(4-(3-aminophenyl)-1H-1,2,3-triazol-1-yl)benzoic acid

4-(4-(3-aminophenyl)-1H-1,2,3-triazol-1-yl)benzoic acid (42): 42 was synthesized according to procedure V using 4-azidobenzoic acid and 3-ethynyl aniline as starting material. ^1H NMR (500 MHz, $\text{DMSO-}d_6$) δ ppm 5.28 (br. s., 2 H) 6.58 (s., 1 H) 7.04 (s., 1 H) 7.08 - 7.16 (m, 1 H) 7.21 (s., 1 H) 8.15 (s, 2 H) 8.11 (s, 2 H) 9.27 (s., 1 H); ^{13}C NMR (126 MHz, $\text{DMSO-}d_6$) δ ppm 59.78, 110.58, 113.25, 114.07, 119.21, 119.66, 129.50, 130.47, 131.16, 139.46, 148.32, 149.19, 154.19, 166.87.



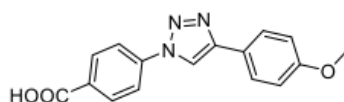
4-(4-(4-aminophenyl)-1H-1,2,3-triazol-1-yl)benzoic acid

4-(4-(4-aminophenyl)-1H-1,2,3-triazol-1-yl)benzoic acid (43): 43 was synthesized according to procedure V using 4-azidobenzoic acid and 4-ethynyl aniline as starting material. ^1H NMR (500 MHz, $\text{DMSO-}d_6$) δ ppm 6.70 (d, $J = 8.24$ Hz, 2 H) 7.63 (d, $J = 8.39$ Hz, 2 H) 8.04 - 8.10 (m, 2 H) 8.14 - 8.17 (m, 2 H) 9.14 (s, 1 H); ^{13}C NMR (126 MHz, $\text{DMSO-}d_6$) δ ppm 114.52, 117.32, 119.42, 119.64, 126.46, 130.30, 131.12, 139.69, 148.52, 166.44.



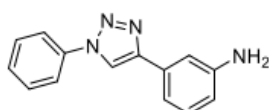
4-(4-(4-(hydroxymethyl)phenyl)-1H-1,2,3-triazol-1-yl)benzoic acid

4-(4-(4-(hydroxymethyl)phenyl)-1H-1,2,3-triazol-1-yl)benzoic acid (44): 44 was synthesized according to procedure V using 4-azidobenzoic acid and (4-ethynylphenyl) methanol as starting material. ^1H NMR (500 MHz, $\text{DMSO-}d_6$) δ ppm 4.55 (d, $J = 3.51$ Hz, 2 H) 5.26 (br. s., 1 H) 7.45 (m, $J = 8.09$ Hz, 2 H) 7.92 (m, $J = 8.09$ Hz, 2 H) 8.08 (d, $J = 7.32$ Hz, 2 H) 8.16 (d, $J = 8.39$ Hz, 2 H) 9.40 (s, 1 H) ^{13}C NMR (126 MHz, $\text{DMSO-}d_6$) δ ppm 62.63, 119.55, 125.16, 127.01, 131.07, 142.88, 147.58, 147.88, 159.71, 168.68.



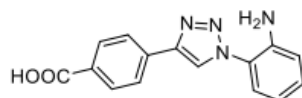
4-(4-(4-methoxyphenyl)-1H-1,2,3-triazol-1-yl)benzoic acid

4-(4-(4-methoxyphenyl)-1H-1,2,3-triazol-1-yl)benzoic acid (45): 45 was synthesized according to procedure V using 4-azidobenzoic acid and 1-ethynyl-4-methoxybenzene as starting material. ^1H NMR (500 MHz, $\text{DMSO-}d_6$) δ ppm 3.81 (s, 3 H) 7.08 (s., 2 H) 7.88 (s., 2 H) 8.10 (s., 2 H) 8.17 (s., 2 H) 9.33 (s., 1 H) 13.21 (br. s., 1 H); ^{13}C NMR (126 MHz, $\text{DMSO-}d_6$) δ ppm 55.23, 114.49, 118.68, 119.58, 126.79, 131.16, 139.58, 139.85, 147.55, 159.45, 166.58.



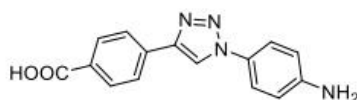
3-(1-phenyl-1H-1,2,3-triazol-4-yl)aniline

3-(1-phenyl-1H-1,2,3-triazol-4-yl)aniline (46): 46 was synthesized according to procedure V using azidobenzene 20 and 3-ethynyl aniline as starting material. ^1H NMR (500 MHz, $\text{DMSO-}d_6$) δ ppm 5.24 (br. s., 2 H) 6.50 - 6.65 (m, 1 H) 6.98 - 7.07 (m, 1 H) 7.07 - 7.17 (m, 1 H) 7.22 (t, $J = 1.83$ Hz, 1 H) 7.43 - 7.53 (m, 1 H) 7.58 - 7.79 (m, 2 H) 7.88 - 8.09 (m, 2 H) 9.15 (s, 1 H); ^{13}C NMR (126 MHz, $\text{DMSO-}d_6$) δ ppm 113.87, 114.07, 119.21, 119.66, 120.54, 128.57, 130.20, 131.16, 139.34, 148.35, 149.57.



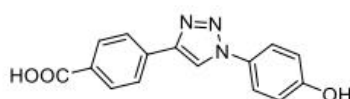
4-(1-(2-aminophenyl)-1H-1,2,3-triazol-4-yl)benzoic acid

4-(1-(2-aminophenyl)-1H-1,2,3-triazol-4-yl)benzoic acid (47): 47 was synthesized according to procedure V using 2-azido aniline 19 and 4-ethynyl benzoic acid as starting material. ^1H NMR (500 MHz, $\text{DMSO-}d_6$) δ ppm 5.48 (br. s., 2 H) 6.71 (t, $J = 7.48$ Hz, 1 H) 6.95 (d, $J = 8.24$ Hz, 1 H) 7.18 - 7.41 (m, 2 H) 7.94 - 8.17 (m, 4 H) 8.93 - 9.11 (m, 1 H) 12.99 (br. s., 1 H); ^{13}C NMR (126 MHz, $\text{DMSO-}d_6$) δ ppm 116.05, 116.69, 121.81, 123.73, 125.30, 125.66, 130.03, 130.24, 134.71, 142.64, 145.48, 167.06.



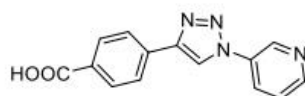
4-(1-(4-aminophenyl)-1H-1,2,3-triazol-4-yl)benzoic acid

4-(1-(4-aminophenyl)-1H-1,2,3-triazol-4-yl)benzoic acid (48): **48** was synthesized according to procedure V using 4-azido aniline and 4-ethynyl benzoic acid as starting material. ^1H NMR (500 MHz, $\text{DMSO-}d_6$) δ ppm 5.54 (br. s., 2 H) 6.72 (m, $J = 8.54$ Hz, 2 H) 7.54 (m, $J = 8.70$ Hz, 2 H) 8.04 (s, 4 H) 9.15 (s, 1 H); ^{13}C NMR (126 MHz, $\text{DMSO-}d_6$) δ ppm 113.81, 120.26, 121.60, 125.13, 125.76, 130.07, 134.68, 145.85, 149.57, 167.10.



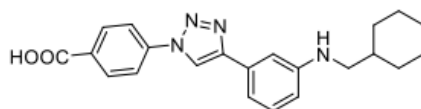
4-(1-(4-hydroxyphenyl)-1H-1,2,3-triazol-4-yl)benzoic acid

4-(1-(4-hydroxyphenyl)-1H-1,2,3-triazol-4-yl)benzoic acid (49): **49** was synthesized according to procedure V using 4-azido phenol **23** and 4-ethynyl benzoic acid as starting material. ^1H NMR (500 MHz, $\text{DMSO-}d_6$) δ ppm 6.97 (m, $J = 8.85$ Hz, 2 H) 7.72 (m, $J = 8.70$ Hz, 2 H) 8.05 (s., 4 H) 9.25 (s, 1 H); ^{13}C NMR (126 MHz, $\text{DMSO-}d_6$) δ ppm 116.10, 120.61, 121.96, 125.32, 128.66, 134.38, 146.13, 157.94.



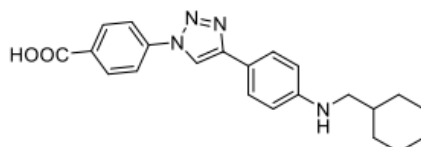
4-(1-(pyridin-3-yl)-1H-1,2,3-triazol-4-yl)benzoic acid

4-(1-(pyridin-3-yl)-1H-1,2,3-triazol-4-yl)benzoic acid (50): **50** was synthesized according to procedure V using 3-azido pyridine **24** and 4-ethynyl benzoic acid as starting material. ^1H NMR (500 MHz, $\text{DMSO-}d_6$) δ ppm 7.59 - 7.80 (m, 1 H) 8.07 (br. s., 4 H) 8.40 (d, $J = 8.24$ Hz, 1 H) 8.75 (br. s., 1 H) 9.22 (br. s., 1 H) 9.53 (s, 1 H); ^{13}C NMR (126 MHz, $\text{DMSO-}d_6$) δ ppm 121.17, 124.81, 125.38, 127.99, 130.24, 134.03, 141.35, 146.68, 149.94, 167.35.



4-(4-(3-((cyclohexylmethyl)amino)phenyl)-1H-1,2,3-triazol-1-yl)benzoic acid

4-(4-(3-((cyclohexylmethyl)amino)phenyl)-1H-1,2,3-triazol-1-yl)benzoic acid (52): **52** was synthesized according to procedure VI using 4-(4-(3-aminophenyl)-1H-1,2,3-triazol-1-yl)benzoic acid **42** (30 mg, 0.11 mmol), cesium carbonate (107 mg, 0.33 mmol) and (bromomethyl) cyclohexane (39 mg, 0.22 mmol, 2 eq.) in DMF (5 mL). Yield: 22 mg (0.06 mmol, 54 %) ^1H NMR (500 MHz, CDCl_3) δ ppm 1.04 - 1.19 (m, 2 H) 1.20 - 1.40 (m, 4 H) 1.73 (d, $J = 12.21$ Hz, 1 H) 1.76 - 1.87 (m, 4 H) 3.81 (br. s., 1 H) 4.19 (d, $J = 6.26$ Hz, 2 H) 6.72 (dt, $J = 7.32, 1.83$ Hz, 1 H) 7.17 - 7.27 (m, 2 H) 7.36 (s, 1 H) 7.91 (d, $J = 8.55$ Hz, 2 H) 8.22 (s, 1 H) 8.24 (d, $J = 8.54$ Hz, 2 H); ^{13}C NMR (126 MHz, CDCl_3) δ ppm 25.69, 26.35, 29.76, 37.24, 70.51, 112.36, 115.36, 116.17, 117.27, 119.81, 129.92, 130.59, 130.81, 131.32, 140.04, 147.00, 148.90, 165.51.



4-(4-(4-((cyclohexylmethyl)amino)phenyl)-1H-1,2,3-triazol-1-yl)benzoic acid

4-(4-(4-((cyclohexylmethyl)amino)phenyl)-1H-1,2,3-triazol-1-yl)benzoic acid (53): **53** was synthesized according to procedure VI using 4-(4-(4-aminophenyl)-1H-1,2,3-triazol-1-yl) benzoic acid **43** (30 mg, 0.11 mmol), cesium carbonate (107 mg, 0.33 mmol, 3 eq.) and (bromomethyl) cyclohexane (39 mg, 0.22 mmol, 2 eq.) in DMF (5 mL). Yield: 15 mg (0.04 mmol, 36 %) ^1H NMR (500 MHz, CDCl_3) δ ppm 1.10 (d, $J = 11.90$ Hz, 2 H) 1.23 - 1.37 (m, 4 H) 1.72 (d, $J = 12.21$ Hz, 1 H) 1.77 - 1.81 (m, 2 H) 1.86 (d, $J = 11.90$ Hz, 2 H) 3.83 (br. s., 1 H) 4.18 (d, $J = 6.10$ Hz, 2 H) 6.78 (m, $J = 8.39$ Hz, 2 H) 7.72 (m, $J = 8.39$ Hz, 2 H) 7.87 - 7.92 (m, 2 H) 8.12 (s, 1 H) 8.22 (d, $J = 8.55$ Hz, 2 H); ^{13}C NMR (126 MHz, CDCl_3) δ ppm 25.42, 26.08, 29.50, 36.98, 53.16, 70.21, 115.00, 119.43, 126.90, 131.01, 139.88, 146.67, 148.87, 165.29.

2. Biology

2.1. Expression and purification of a His-tagged oligomerization-deficient mutant of the KSHV LANA C-terminal DNA binding domain (DBD; aa1008-1146)

For the expression of the previously described¹ His-tagged oligomerization-deficient mutant of the KSHV LANA C-terminal DBD (aa1008-1146) we used the pETRO1.01 vector.

BL21 (DE3) was transformed (chemical transformation) with the plasmid pETRO1.01- LANA 1008-1146 olig-mut. An expression culture of LB-medium (Lennox) containing 100 µg/mL ampicillin was grown over night at 37 °C (200 rpm) to an OD₆₀₀ of 3.0 was reached. Cells were harvested by centrifugation (6200 rpm, 4 °C, 20 min) and the supernatant was removed. The cells were resuspended in lysis buffer (100 mM NaH₂PO₄, 10 mM Tris-Cl, 2 mM DTT, pH 8.0) followed by cell distribution with a Microfluidizer® (Microfluidics, Benchtop High-Pressure Homogenizer 25 mL) with one cycle. After removal of cellular debris by centrifugation (19000 rpm, 1 h, 4 °C) the lysate was filtered through a 0.22 µm filter. His-tagged LANA target protein was purified by Ni-NTA affinity chromatography using ÄKTAexpress (GE Healthcare). A HisTrap HP 1 mL column (GE Healthcare) was equilibrated with lysis buffer until the UV signal was stable. The lysate was applied to the column at 1 mL/min, washed with a linear washing gradient (2.5 mL/min) starting from 100% lysis buffer to 100% wash buffer (100 mM NaH₂PO₄, 10 mM Tris-Cl, 2 mM DTT, 500 mM imidazole, pH 8.0). Subsequently the target protein was eluted (2.5 mL/min) with elution buffer (100 mM NaH₂PO₄, 10 mM Tris-Cl, 2 mM DTT, 1000 mM imidazole, pH 5.8). The buffer in the protein containing fractions was exchanged to storage buffer (20 mM Bis-Tris-Cl, 300 mM NaCl, 2 mM DTT, pH 6,5) using a PD10 column (GE Healthcare) and concentrated via centrifugal filtration using Vivaspin 20 columns (MWCO 10,000 Da, Sartorius).

2.2. Expression and purification of a GST-tagged KSHV LANA C-terminal domain (CTD; aa934-1162)

The expression and purification of the GST-tagged KSHV LANA C-terminal domain (CTD; aa934-1162) was described previously and the protocol was adopted.²

2.3. SPR-based Screening

In total 720 library compounds were tested in SPR-based screening using constant concentrations of 500 μM of each compound. Compounds which showed a response higher than 9 RU were selected from the first screening which resulted in 52 compounds.

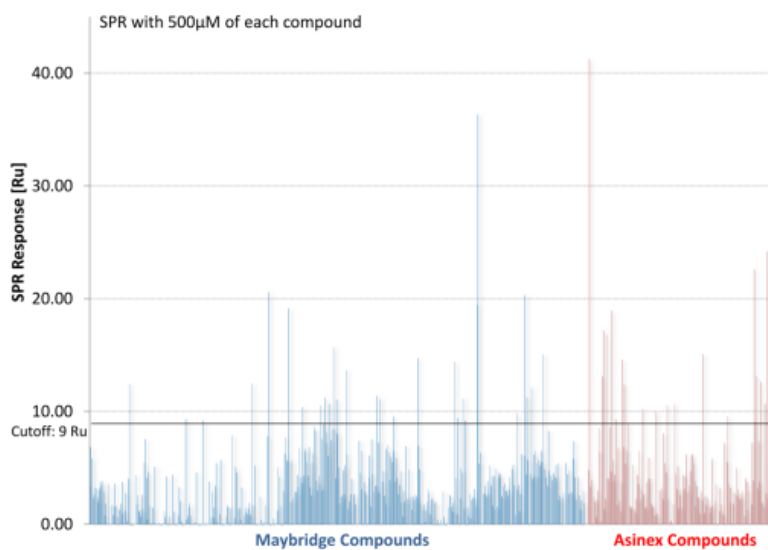


Figure S1: Results of SPR based screening of compounds from the Maybridge library (blue) and compounds from the Asinex library (red).

2.5. Fluorescence Polarization Assay

2.5.1. DNA Hybridisation:

DNA oligonucleotide stocks were always prepared freshly. DNA hybridisation was done by mixing the corresponding sense and antisense oligonucleotides in a ratio of 1:1, heating the mixture at 95 °C for 12 minutes and cooling slowly to room temperature again. The sequences of all used sense and antisense oligonucleotides are listed in table S1. All oligomers were obtained from Sigma Aldrich in HPLC purity and were used as received. Fluorescein was used as fluorescence label.

Table S1: DNA sense and antisense oligonucleotides for FP assay.

DNA	Base sequence
LBS1_sense	5'-TCCCGCCCGGGCATGGGGCC
LBS1_sense_flc	5'-TCCCGCCCGGGCATGGGGCC_flc
LBS1_antisense	5'-GGCCCATGCCCGGGCGGGA
LBS2_sense	5'-CGCCGCCGGGGCCTGCGGCG
LBS2_sense_flc	5'-CGCCGCCGGGGCCTGCGGCG_flc
LBS2_antisense	5'-CGCCGAGGCCCGGGCGGCG
LBS3_sense	5'-CCGCGCCGGGCCCTGAGGCG
LBS3_sense_flc	5'-CCGCGCCGGGCCCTGAGGCG_flc
LBS3_antisense	5'-CGCCTCAGGGCCCGGCGCGG

2.5.2. FP-Assay Optimization Studies

To determine the optimal concentrations of protein and DNA for this experiment different concentration dependent experiments were performed (Figure S3; **A**). Three different protein concentrations (400 nM, 266 nM and 134 nM final) were tested with fixed concentration of LBS2_flc (15 nM final) and increasing concentrations of LBS2. Best results were observed using a final concentration of 400 nM. Furthermore, different concentrations of labelled LBS2 (5 nM, 10 nM and 15 nM final of LBS2_flc) were tested with a constant protein concentration of 400 nM (Figure S3; **B**). Based on these experiments we chose a final concentration of 10 nM DNA_flc in subsequent assays.

Assay robustness was measured by testing control run plates (Figure S3; **C**). A high control (HC) plate contained 192 samples with LANA (400 nM), LBS2_flc (10 nM) and DMSO (5% [v/v]) in FP assay buffer while a low control (LC) plate contained the same samples without LANA. A high dynamic range, low coefficients of variations (CVs) and a Z' factor of 0.925 indicated that the assay was robust and suitable for measuring the inhibitory efficiency of our compounds.

DMSO tolerance was measured by incubating various concentrations of DMSO (0-10 % [v/v] final), a fixed concentration of LBS2_flc (10 nM final) and different concentrations of LANA (0 nM, 150 nM, 400 nM) (Figure S3; **D**). Accordingly, a final concentration of 5% DMSO was chosen for the assay.

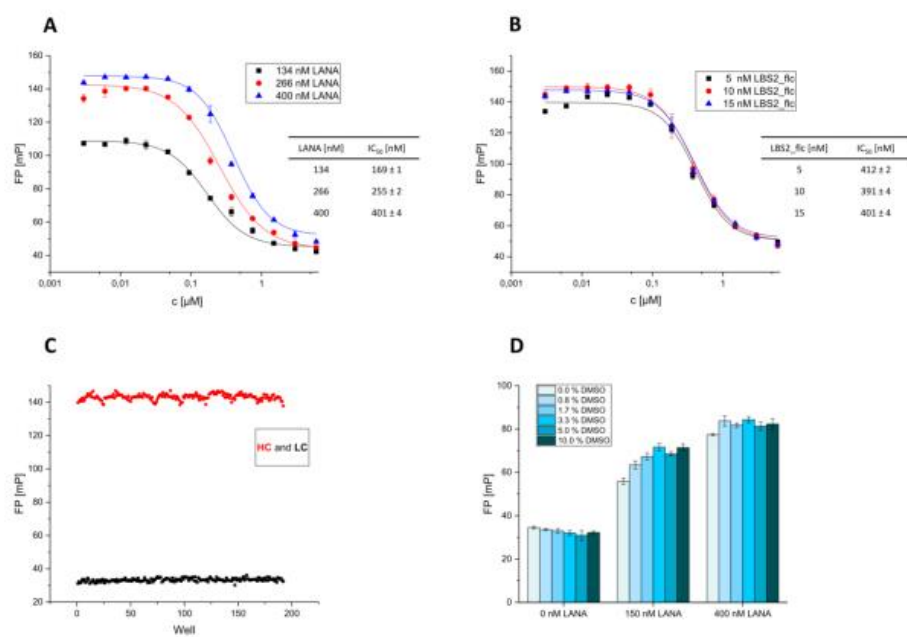


Figure S3: **A:** Dose-dependent experiments using different LANA concentrations. **B:** Dose-dependent experiments using different DNA concentrations. **C:** Determination of assay robustness, HC (red) and LC (black). **D:** DMSO tolerance measurement for different LANA and DMSO concentrations.

2.5.3. Dose-dependent Studies with LBS1, 2 and 3

We performed dose dependent experiments using LBS2 as the fluorescent probe and used varying concentrations of unlabeled LBS1, LBS2 and LBS3.

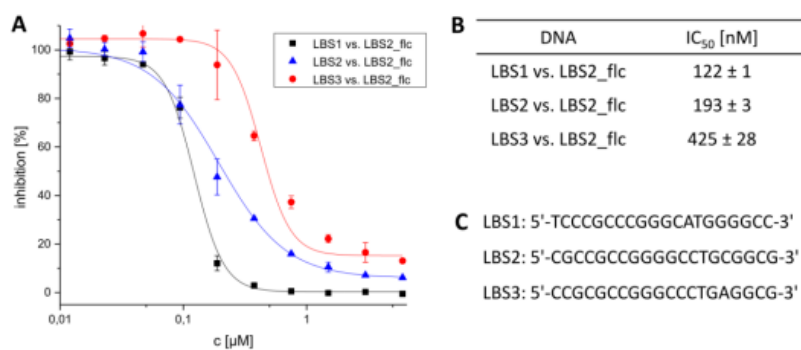


Figure S4: **A**: Dose-dependent studies with LBS1, 2 and 3 as a representative example for FP-based competition experiments. Representative curves of one independent experiment are shown with normalized data points (inhibition from 0 - 100%) representing averaged FP values of duplicates \pm standard deviation. **B**: IC₅₀ values [nM] calculated using a four-parameter dose-response model. **C**: Sequences of LBS1, 2 and 3 oligonucleotides as used in this experiment.

2.5.4. Dose dependent Studies of Compounds 37, 41 - 43, 47 and 50

We carried out dose-dependent competition studies with our compounds. Representative curves showing the results obtained with compounds 37, 41 - 43, 47 and 50 are shown in figure S5, which based on normalized data points (% inhibition from 0 - 100%) representing averaged FP values of duplicates \pm standard deviation. Curves were fit to a four-parameter dose response model using OriginLab (2016) to calculate IC_{50} values. Compounds were tested in dose dependent experiments starting at 1 mM or 500 μ M depending on solubility. LBS2_flc was used as fluorescent probe.

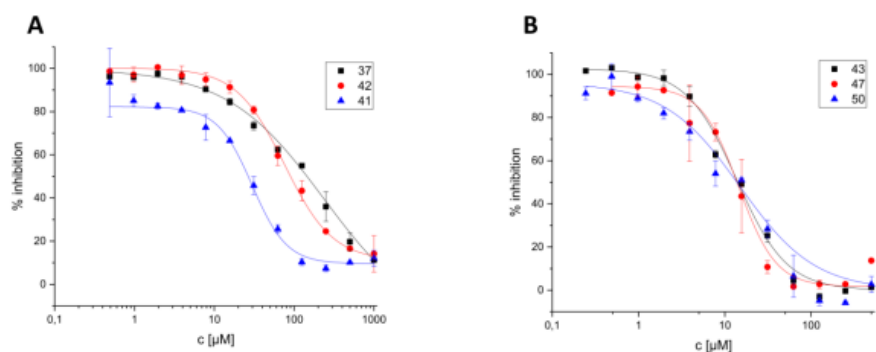


Figure S5: **A:** Dose-dependent experiments for compounds 37, 41 and 42 in FP-based competition experiments. **B:** Dose-dependent experiments for compounds 43, 47 and 50 in FP-based competition experiments.

2.6. Calculation of LogP and Ligand Efficiency (LE)

Calculation of LogP values (clogP) was done using ACD/Percepta version 2012 (Build 2203, 29 jan. 2013), ACD/Labs with the LogPGALAS model.

LE of compounds 37, 41 - 43, 47 and 50 was calculated based on their IC_{50} obtained using LBS2:

$$LE = 1.4 * \frac{pIC_{50}}{NAH}$$

$$pIC_{50} = -\log(IC_{50} [M])$$

NAH = number of heavy atoms

2.7. Electrophoretic Mobility Shift Assay (EMSA)

Table S2: sense and antisense oligonucleotides used for EMSA.

DNA	Base sequence
LBS1 sense	5'-TCCCGCCCGGGCATGGGGCC
LBS1 antisense	5'-GGCCCCATGCCCGGGCGGGA
LBS1+2 sense	5'-GGGGACGCCCGGGGCTGCGGCGCCTCCCGCCCGGGCATGGGGCC
LBS1+2 antisense	5'-GGCCCCATGCCCGGGCGGAGGCGCCGAGGCCCGGGCGCGTCCCC
Competitor sense	5'-GAGGCGGCGCGGGGACGCCCGGGGCTGCGGCGCCTCCCGCCCGGGCATGGGGCC
Competitor antisense	5'-GGCCCCATGCCCGGGCGGAGGCGCCGAGGCCCGGGCGCGTCCCCCGCGCCGCCTC

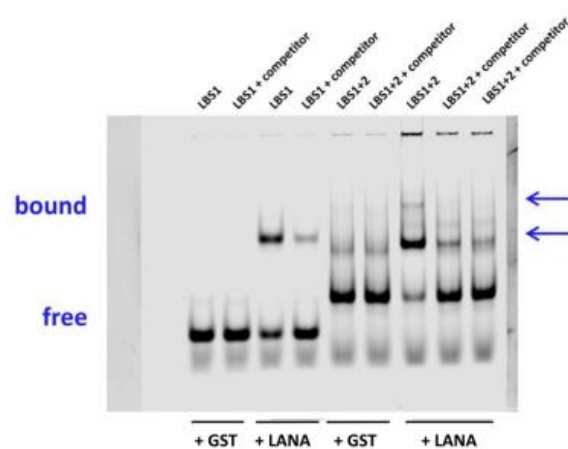


Figure S6: Gel of EMSA experiment using LBS1 and LBS1+2 as probes at 20 nM, non DNA-binding protein GST as control at 200 nM, LANA DBD mutant at 200 nM and competitor at 200 nM.

2.7.1. EMSA Experiments for Compounds 37, 41, 42, 43, 47, and 50

Calculation for normalized data for top bands:

$$(X - \text{GST} + \text{DMSO} + \text{LBS top band}) / (\text{GST} + \text{DMSO} + \text{LBS bottom band}) * 100 [\%] \quad (\text{equation 1})$$

Calculation for normalized data for bottom bands:

$$(X - \text{LANA} + \text{LBS} + \text{DMSO bottom band}) / (\text{GST} + \text{DMSO} + \text{LBS bottom band} - \text{LANA} + \text{LBS} + \text{DMSO bottom band}) * 100 [\%] \quad (\text{equation 2})$$

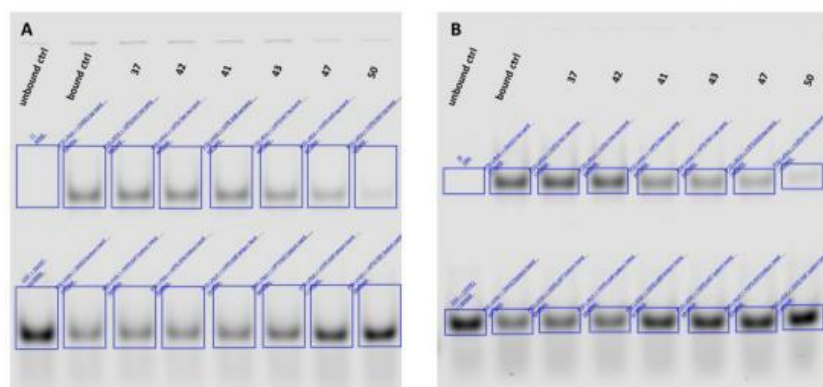


Figure S7: Two independent EMSA experiments using LBS1 as probes. Unbound control: GST+LBS1, bound control: DMSO+LANA+LBS1 and compound+LANA+LBS1 (37, 41, 42, 43, 47, and 50). A: Gel 1 and B: Gel 2. Fixed concentrations of DNA probes of 20 nM, LANA DBD mutant and GST of 200 nM and each compounds of 500 μ M were used.

Table S3: Intensities of top bands of the two independent EMSA experiments using LBS1 (Fig. S7).

Top Band	Intensities Gel 1	Intensities Gel 2	Normalized Gel 1' [%]	Normalized Gel 2' [%]	Mean [%]	Standard deviation [%]
LANA +LBS1+DMSO	7082303	7273467	43,49	64,60	54,04	10,6
LANA+LBS1+37	6949745	7250647	42,67	64,40	53,53	10,9
LANA+LBS1+42	6477320	6993989	39,76	62,12	50,94	11,2
LANA+LBS1+41	6320920	4309422	38,79	38,27	38,53	0,3
LANA+LBS1+43	4798905	3824099	29,41	33,96	31,68	2,3
LANA+LBS1+47	3220508	2636996	19,67	23,41	21,54	1,9
LANA+LBS1+50	1278539	1252071	7,69	11,11	9,40	1,7
GST+DMSO+LBS1	30900	1060	0,0	0,0	0,0	0,0

*equation 1

Table S4: Intensities of bottom bands of the two independent EMSA experiments using LBS1(Fig. S7).

Bottom Band	Intensities Gel 1	Intensities Gel 2	Normalized Gel 1' [%]	Normalized Gel 2' [%]	Mean [%]	Standard deviation [%]
LANA +LBS1+DMSO	7700812	5974719	0,00	0,00	54,04	10,6
LANA+LBS1+37	7869608	6387713	1,98	7,82	53,53	10,9
LANA+LBS1+42	7496542	6327240	-2,40	6,67	50,94	11,2
LANA+LBS1+41	7866835	9132550	1,95	59,77	38,53	0,3
LANA+LBS1+43	9040171	9815636	15,73	72,70	31,68	2,3
LANA+LBS1+47	11677697	9789259	46,72	72,20	21,54	1,9
LANA+LBS1+50	13583109	11350337	69,10	101,75	9,40	1,7
GST+DMSO+LBS1	16213805	11257853	100,00	100,00	100,00	0,00

*equation 2

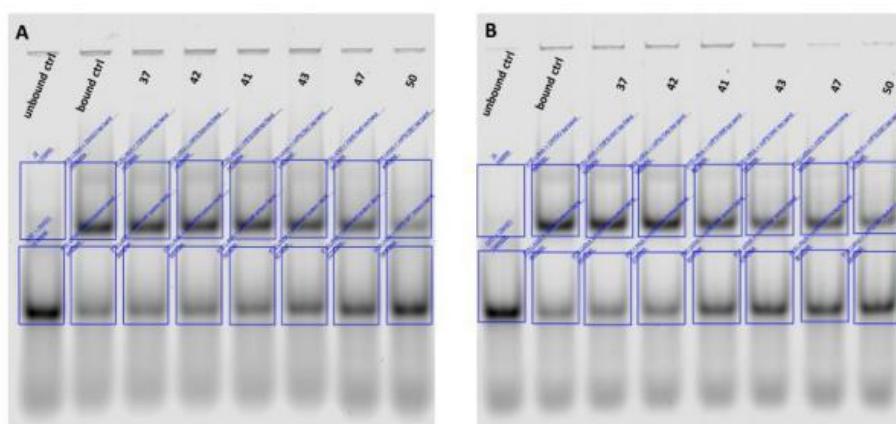


Figure S8: Two independent EMSA experiments using LBS1+2 as probes. Unbound control: GST+LBS1+2, bound control: DMSO+LANA+LBS1+2 and compound+LANA+LBS1+2 (37, 41, 42, 43, 47, and 50). A: Gel 1 and B: Gel 2. Fixed concentrations of DNA probes of 20 nM, LANA DBD mutant and GST of 200 nM and each compounds of 500 μ M were used.

Table S5: Intensities of top bands of two independent EMSA experiments using LBS1+2 (Fig. S8).

Top Band	Intensities Gel 1	Intensities Gel 2	Normalized Gel 1' [%]	Normalized Gel 2' [%]	Mean [%]	Standard deviation [%]
LANA +LBS1+DMSO	15403664	5878857	61,01	74,08	67,55	6,5
LANA+LBS1+37	14680225	5352544	57,88	67,06	62,47	4,6
LANA+LBS1+42	14875512	5587054	58,73	70,19	64,46	5,7
LANA+LBS1+41	14194824	3974357	55,78	48,66	52,22	3,6
LANA+LBS1+43	11770175	2918459	45,28	34,56	39,92	5,4
LANA+LBS1+47	9410393	3529022	35,07	42,71	38,89	3,8
LANA+LBS1+50	4083551	2174762	12,01	24,63	18,32	6,3
GST+DMSO+LBS1	1310000	330000	0,00	0,00	0,00	0,00

*equation 1

Table S6: Intensities of bottom bands of two independent EMSA experiments using LBS1+2 (Fig. S8).

Bottom Band	Intensities Gel 1	Intensities Gel 2	Normalized Gel 1' [%]	Normalized Gel 2' [%]	Mean [%]	Standard deviation [%]
LANA +LBS1+DMSO	6346736	1904508	0,00	0,00	0,00	0,0
LANA+LBS1+37	6394300	2067054	0,28	2,91	1,60	1,3
LANA+LBS1+42	6870768	2228421	3,13	5,80	4,46	1,3
LANA+LBS1+41	7621028	3512216	7,61	28,78	18,19	10,6
LANA+LBS1+43	9772169	4781537	20,45	51,51	35,98	15,5
LANA+LBS1+47	12194399	4622428	34,90	48,66	41,78	6,9
LANA+LBS1+50	17995263	5431572	69,53	63,15	66,34	3,2
GST+DMSO+LBS1	23100000	7490000	100,00	100,00	100,00	0,0

*equation 2

2.7.2. Dose-dependent EMSA Experiments with Compound 50.

We carried out dose-dependent competition studies with compound 50. EMSA gels showing the results obtained with varying concentrations of compound 50 and LANA DBD mutant are shown in figure S9. Similar experiments were performed using wild-type C-terminal LANA (Fig. S10). Dose-dependent curves which based on normalized data points (% band intensity of top bands from 0 - 100%) representing averaged FP values of duplicates \pm standard deviation. Curves were fit to a four-parameter dose response model using OriginLab (2016) to calculate IC_{50} values. Compounds were tested in dose dependent experiments starting at 2 mM. LBS1 was used as probe.

Calculation for normalized data for top bands:

$$\frac{(X + \text{GST} + \text{DMSO} + \text{LBS1 top band})}{(\text{LANA} + \text{DMSO} + \text{LBS1 top band} + \text{GST} + \text{DMSO} + \text{LBS1 top band})} * 100 [\%]$$

(equation 3)

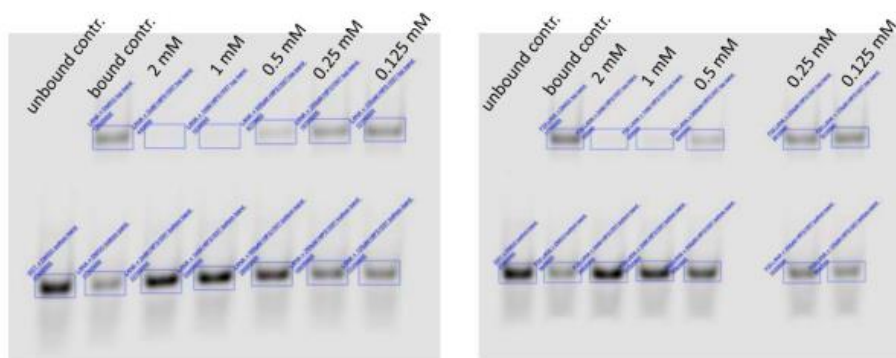


Figure S9: Two independent EMSA experiments using LBS1 as probes. Unbound control: GST+LBS1, bound control: DMSO+LANA+LBS1 and compound 50+LANA+LBS1. **A:** Gel 1 and **B:** Gel 2. Fixed concentrations of DNA probes of 20 nM, LANA DBD mutant and GST of 200 nM were used. Compound 50 was used at 2 mM, 1 mM, 500 μ M, 250 μ M and 125 μ M.

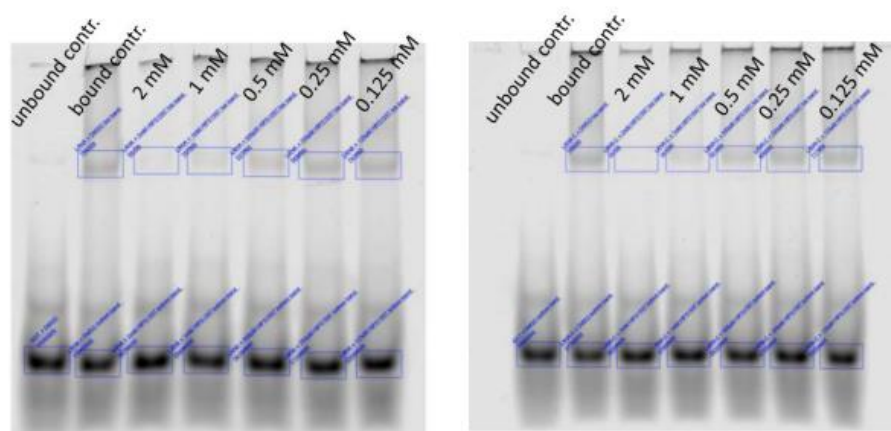


Figure S10: Two independent EMSA experiments using LBS1 as probes. Unbound control: GST+LBS1, bound control: DMSO+wild-type LANA+LBS1 and compound **50**+wild-type LANA+LBS1. **A**: Gel 1 and **B**: Gel 2. Fixed concentrations of DNA probes of 20 nM, wild-type C-terminal LANA and GST of 200 nM were used. Compound **50** was used at 2 mM, 1 mM, 500 μ M, 250 μ M and 125 μ M.

Table S7: Intensities of top bands of two independent EMSA experiments using LBS1 and LANA mutant and varying concentrations of compound **50** (see Gel Fig. S9).

Top Band	Intensities Gel 1	Intensities Gel 2	Normalized Gel 1' [%]	Normalized Gel 2' [%]	Mean [%]	Standard deviation [%]
LANA +LBS1+DMSO	12600282	11705533	100,00	100,00	100,00	0,0
LANA+LBS1+ 50 (2 mM)	490249	367666	7,49	6,09	6,79	0,7
LANA+LBS1+ 50 (1 mM)	1027522	699015	11,59	8,84	10,21	1,4
LANA+LBS1+ 50 (0.5 mM)	4270214	4041334	36,37	36,52	36,44	0,1
LANA+LBS1+ 50 (0.25 mM)	10263509	8810879	82,15	76,02	79,09	3,1
LANA+LBS1+ 50 (0.125 mM)	12146712	9232463	96,54	79,52	88,03	8,5
GST+DMSO+LBS1	490249	367666	0,00	0,00	0,00	0,00

*equation 3

Table S8: Intensities of top bands of two independent EMSA experiments using LBS1 and LANA wild-type and varying concentrations of compound **50** (see Gels Fig. S10).

Top Band	Intensities Gel 1	Intensities Gel 2	Normalized Gel 1' [%]	Normalized Gel 2' [%]	Mean [%]	Standard deviation [%]
LANA +LBS1+DMSO	746156	754214	100,00	100,00	100,00	0,0
LANA+LBS1+ 50 (2 mM)	36663	50134	9,37	12,47	10,92	1,5
LANA+LBS1+ 50 (1 mM)	160620	106993	25,20	19,53	22,37	2,8
LANA+LBS1+ 50 (0.5 mM)	360528	337027	50,74	48,13	49,44	1,3
LANA+LBS1+ 50 (0.25 mM)	607872	568304	82,34	76,89	79,61	2,7
LANA+LBS1+ 50 (0.125 mM)	717155	743068	96,30	98,61	97,45	1,2
GST+DMSO+LBS1	36663	50134	0,00	0,00	0,00	0,00

*equation 3

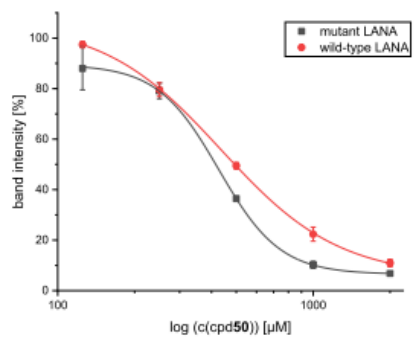


Figure S11: Dose-dependent EMSA experiments with compound **50**. LBS1 as probes and LANA DBD mutant (black) or LANA CTD wild-type (red) as target protein was used. IC_{50} (LANA DBD mutant) $426 \pm 2 \mu\text{M}$, IC_{50} (LANA CTD wild-type) $435 \pm 6 \mu\text{M}$.

2.8. Saturation-Transfer Difference NMR (STD-NMR)

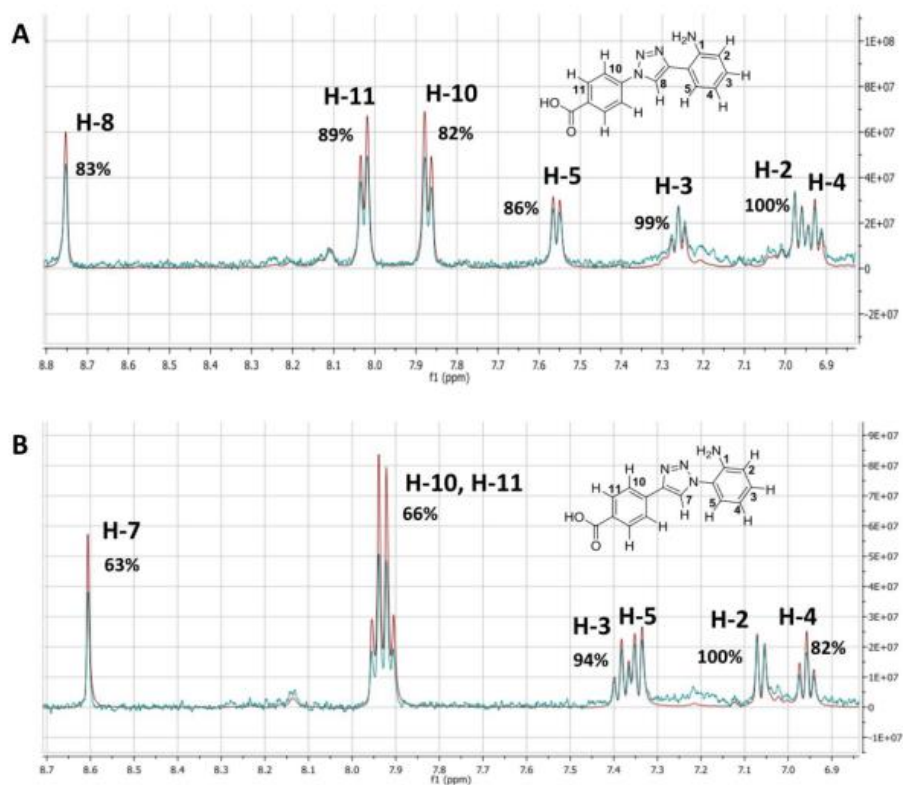


Figure S12: STD-NMR of **A**: compound **41** and **B**: compound **47** in complex with LANA DBD. The reference spectra are displaced in red (STD-off) and STD difference spectra (STD-on) in blue. Overlaid spectra were normalized to the signals which showed the strongest enhancement (A: H-2, H-4; B: H-2).

2.9. Molecular Docking

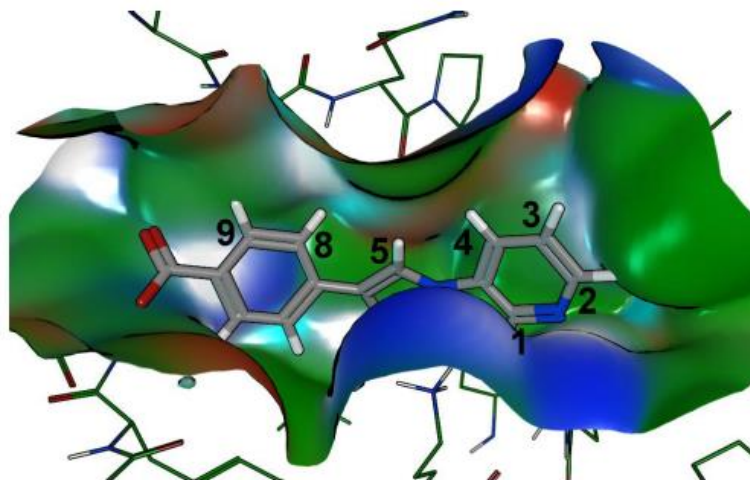


Figure S13: Docking pose of compound **50**. Surface indicates van der Waals radius of LANA residues. Protons at positions 1, 2 and one 8/9 pair are in close proximity to the protein, while protons 3, 4, 5, and the other 8/9 pair are exposed

2.10. Additional information to Hit 1 and alternative Hits 1a and 1b

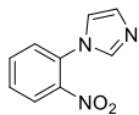
Table S9: Additional information to Hit 1, 1a, 1b.

	Chemical Formula:	Molecular Weight [g/mol]	Response [RU] (SPR @ 500 μM)	T_M [°C] (DSF @ 500 μM)
Hit 1	C ₉ H ₉ N ₃	159,19	15.69 \pm 9.3	-1.80 \pm 1.41
Hit 1a	C ₅ H ₇ N ₃	109,13	12.66 \pm 2.1	-1.36 \pm 1.5
Hit 1b	C ₁₀ H ₁₁ NO ₂	177,20	14.73 \pm 1.9	-1.55 \pm 0.83

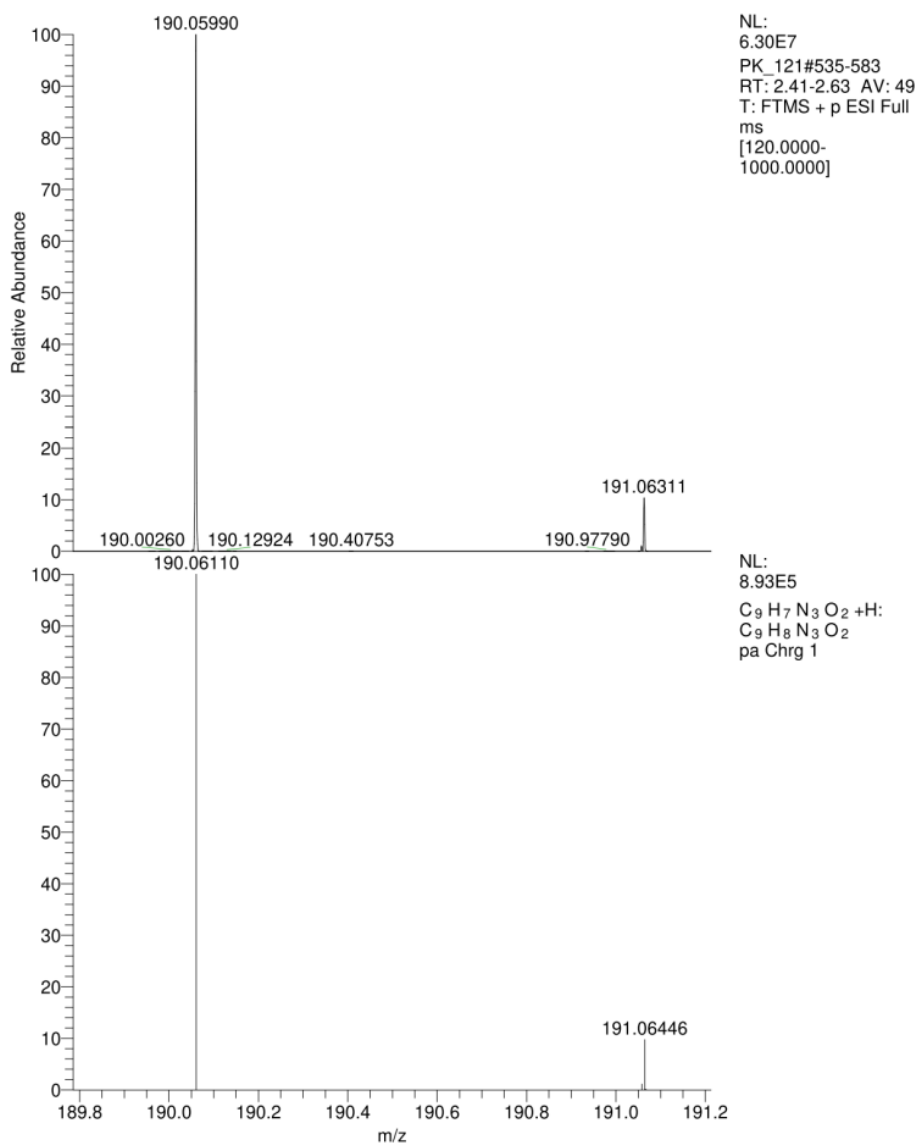
3. High Resolution Mass Spectrometry (HRMS)

HRMS were measured on a Thermo Scientific Q Exactive Focus (Germany) equipped with DIONEX ultimate 3000 UHPLC⁺ focused. For gradient elution, an EC 150/2 NUCLEODUR C18 Pyramid (3 μm) column (Machery-Nagel, Germany) was used with a mobile phase consisting of acetonitrile containing 0.1% formic acid (FA; v/v; eluent A) and water containing 0.1% FA (v/v; eluent B). Elution method was used with a total run time of 7.5 min and gradient conditions 10% A to 90% A. Mass spectrometry was used in positive or negative mode using electrospray ionisation (ESI). Measured (upper spectrum) and calculated (lower spectrum) HRMS spectra of each final synthesized compound were depicted below.

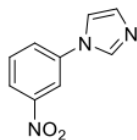
1-(2-nitrophenyl)-1H-imidazole (2)



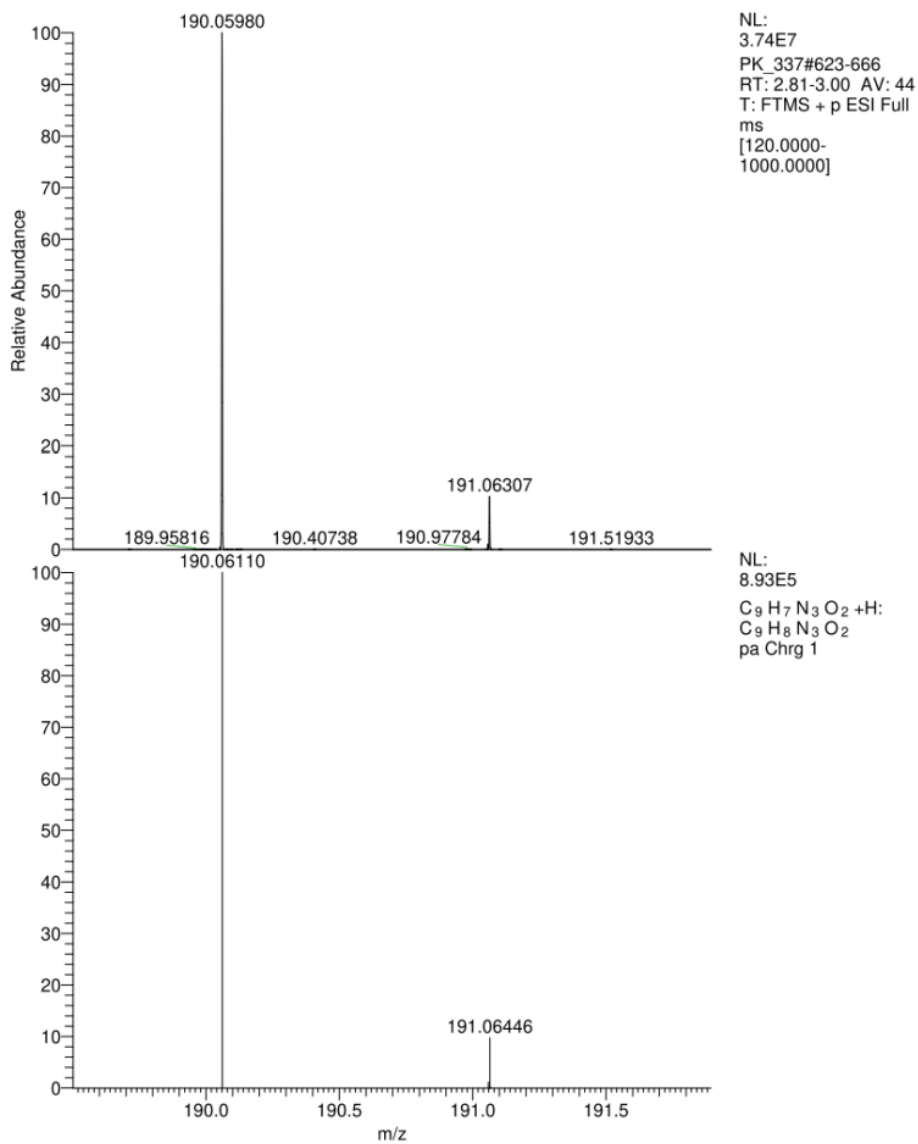
1-(2-nitrophenyl)-1H-imidazole



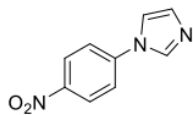
S31

1-(3-nitrophenyl)-1H-imidazole (3)

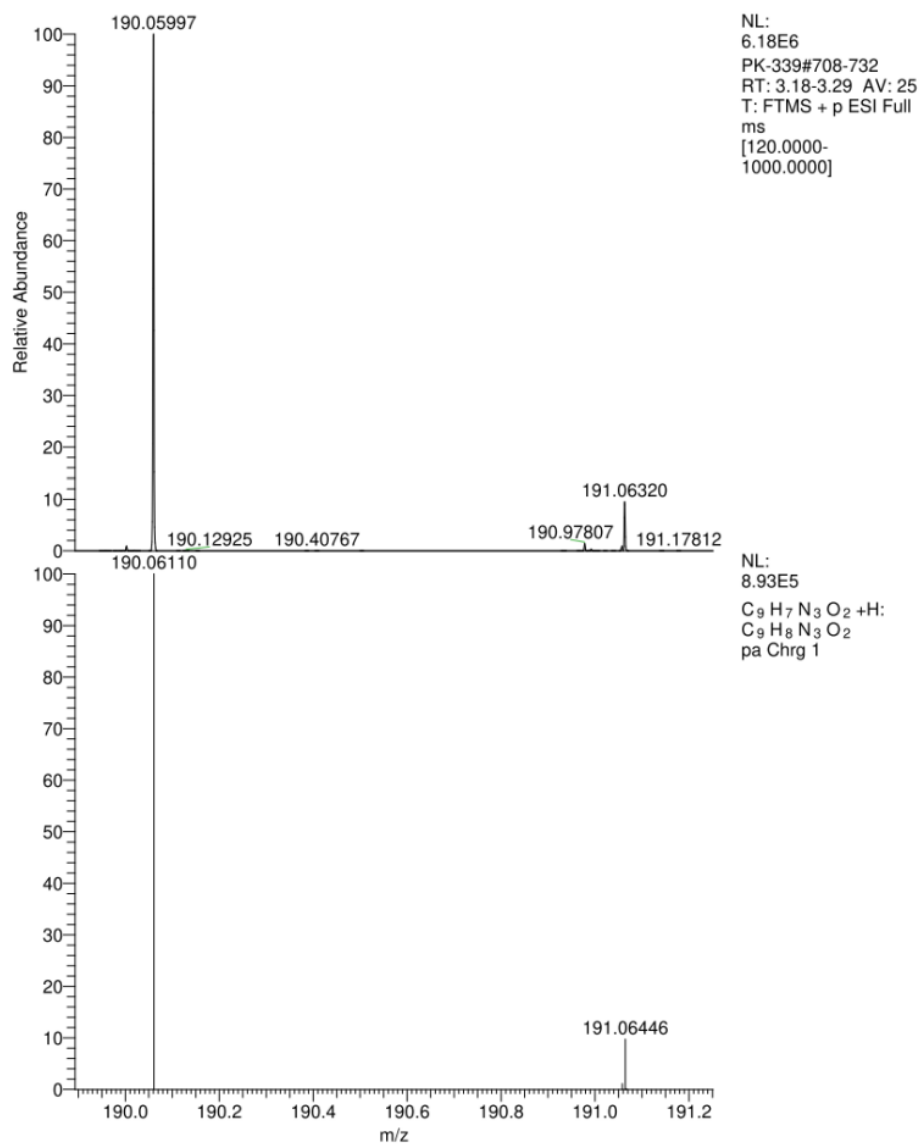
1-(3-nitrophenyl)-1H-imidazole

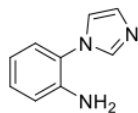
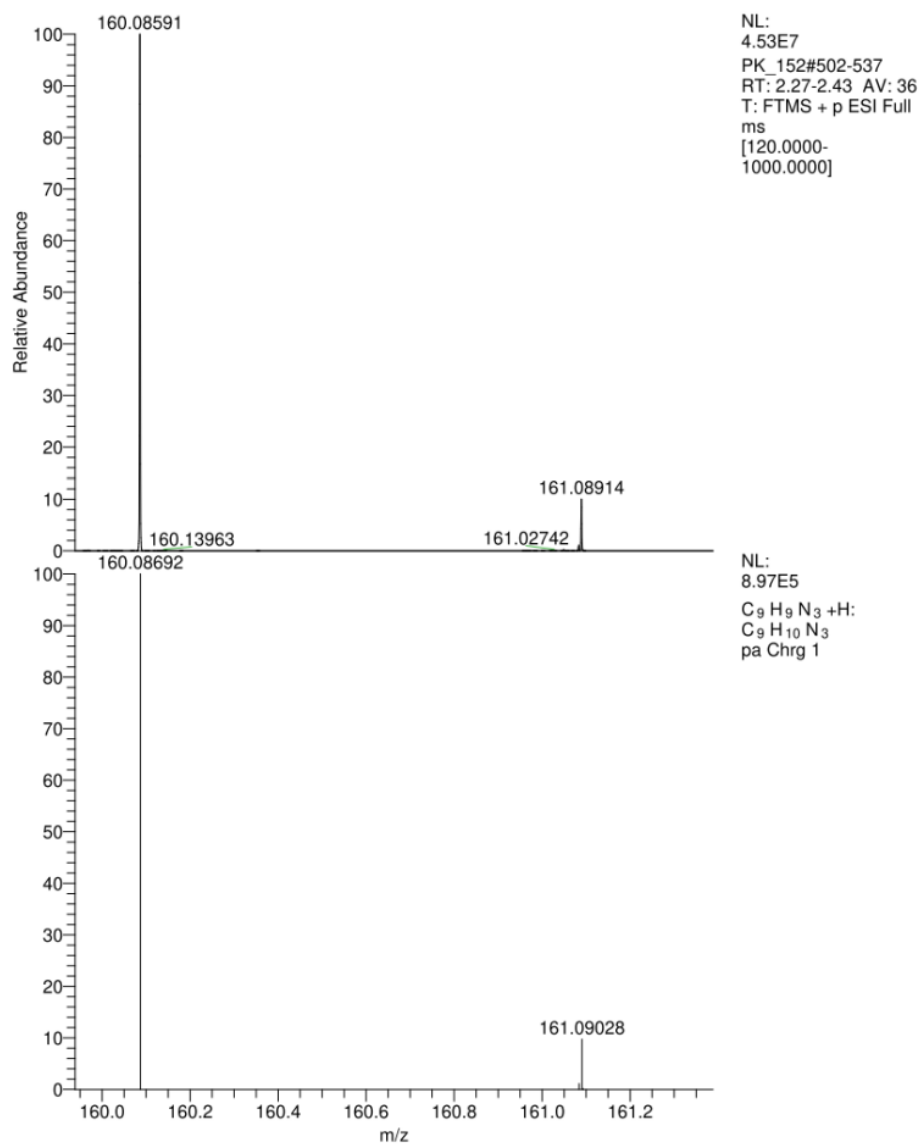


S32

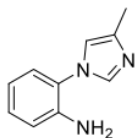
1-(4-nitrophenyl)-1H-imidazole (4)

1-(4-nitrophenyl)-1H-imidazole

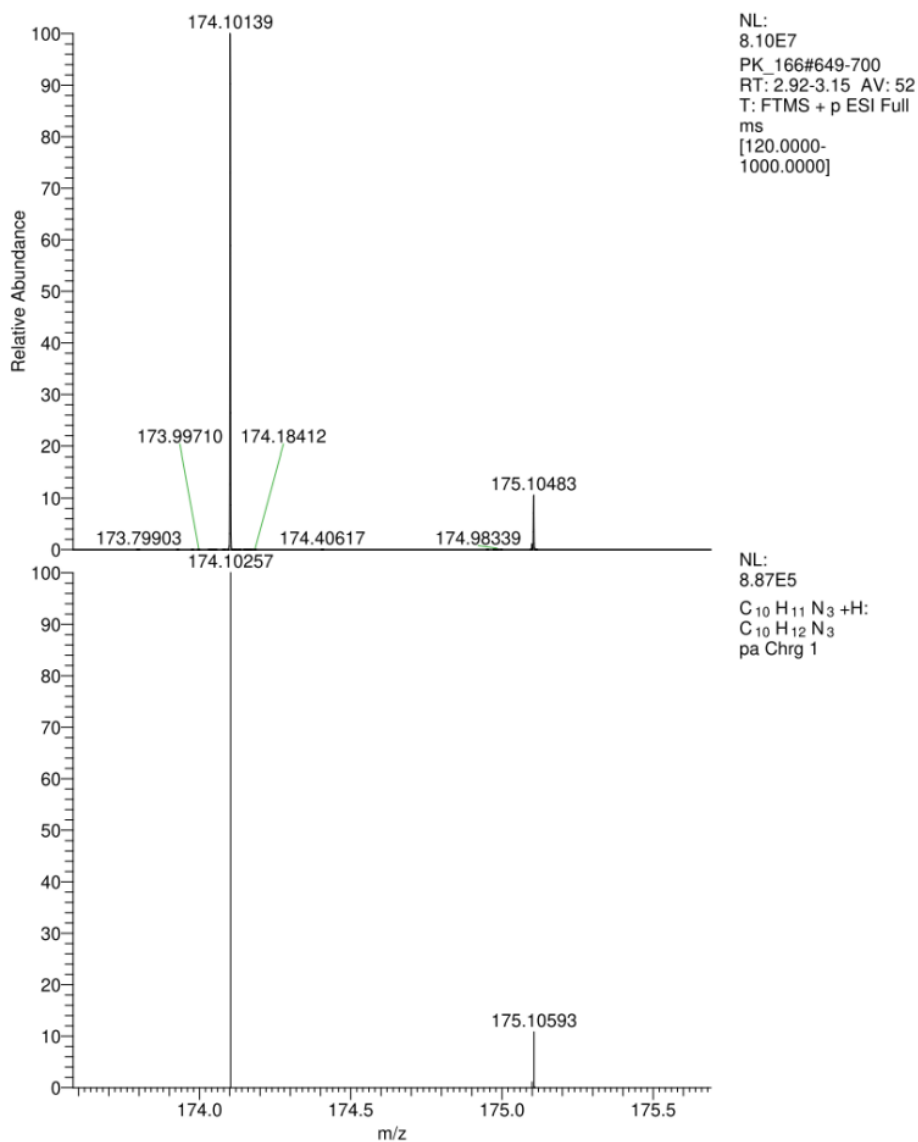


2-(1*H*-imidazol-1-yl)aniline (1)2-(1*H*-imidazol-1-yl)aniline

2-(4-methyl-1*H*-imidazol-1-yl)aniline (11)

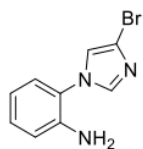


2-(4-methyl-1*H*-imidazol-1-yl)aniline

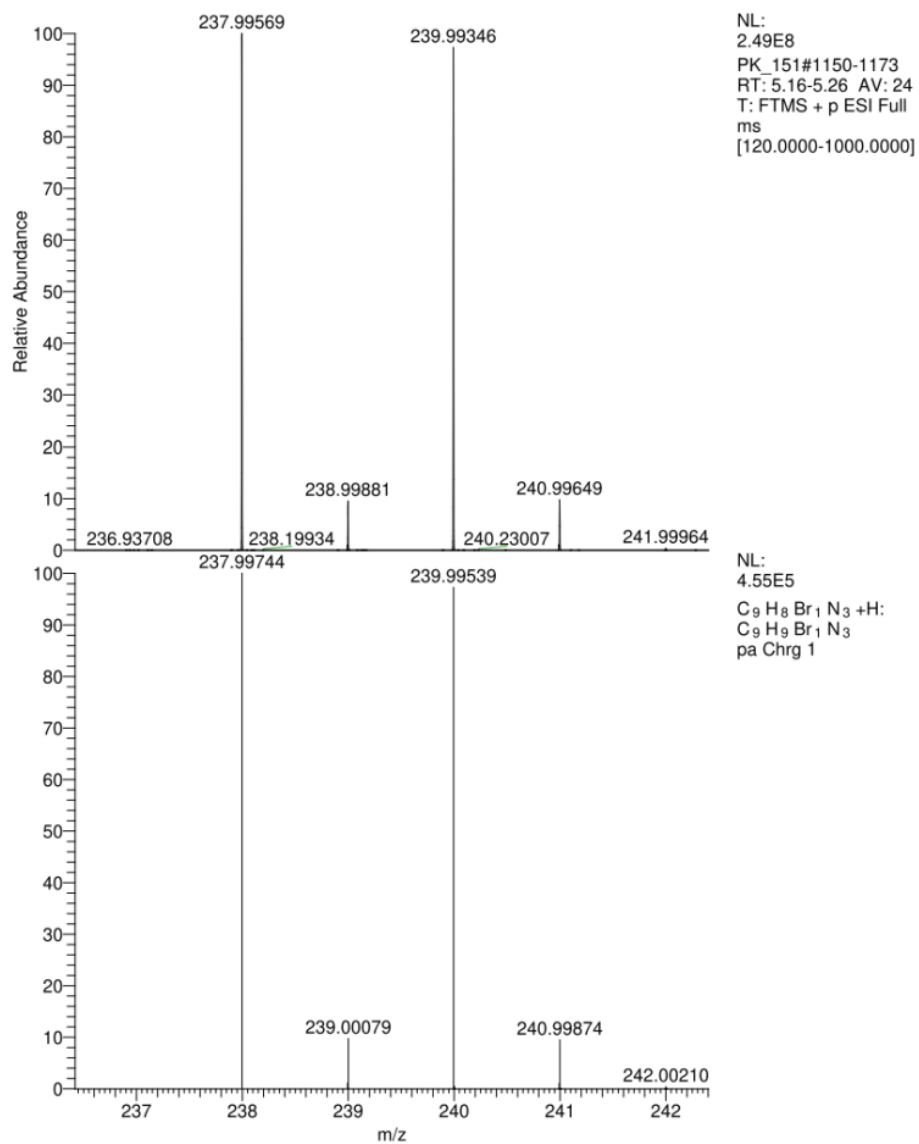


S35

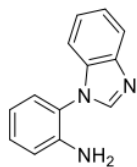
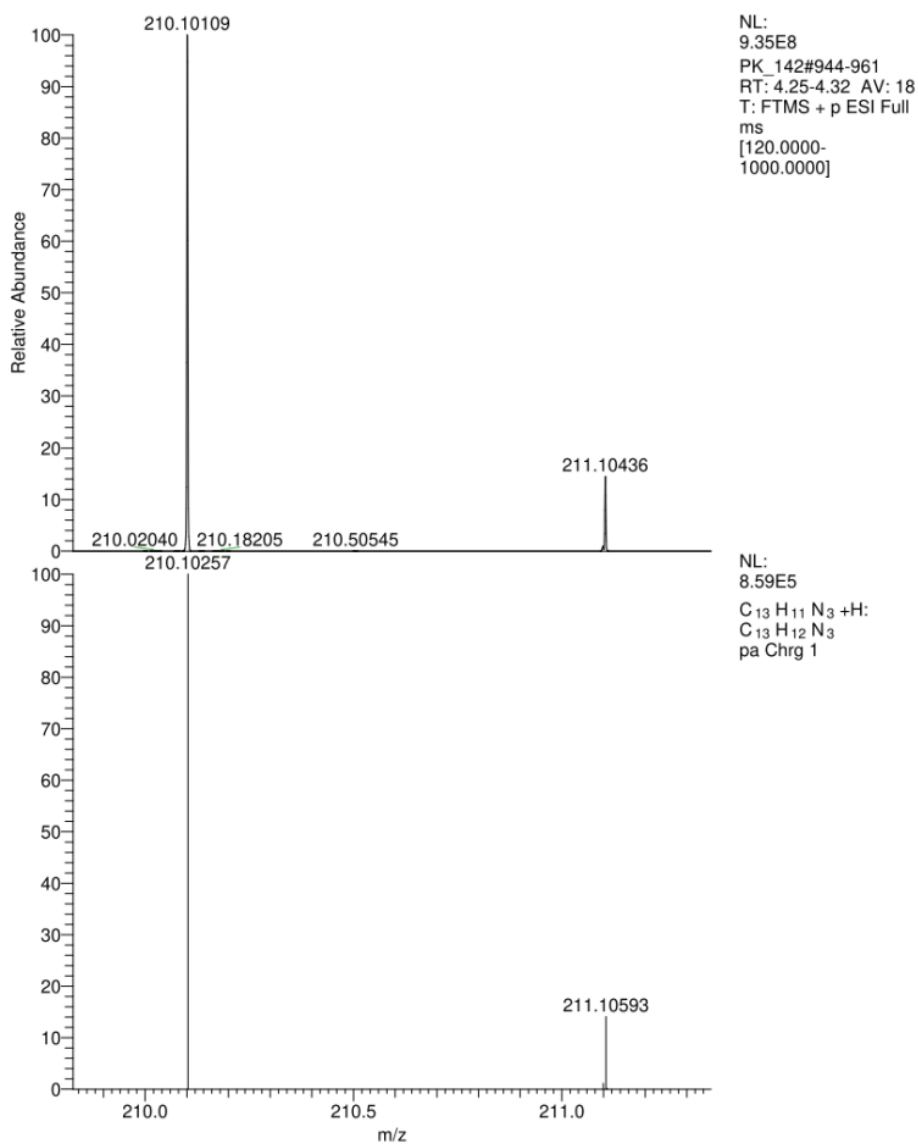
2-(4-bromo-1H-imidazol-1-yl)aniline (12)



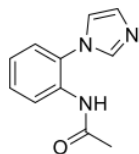
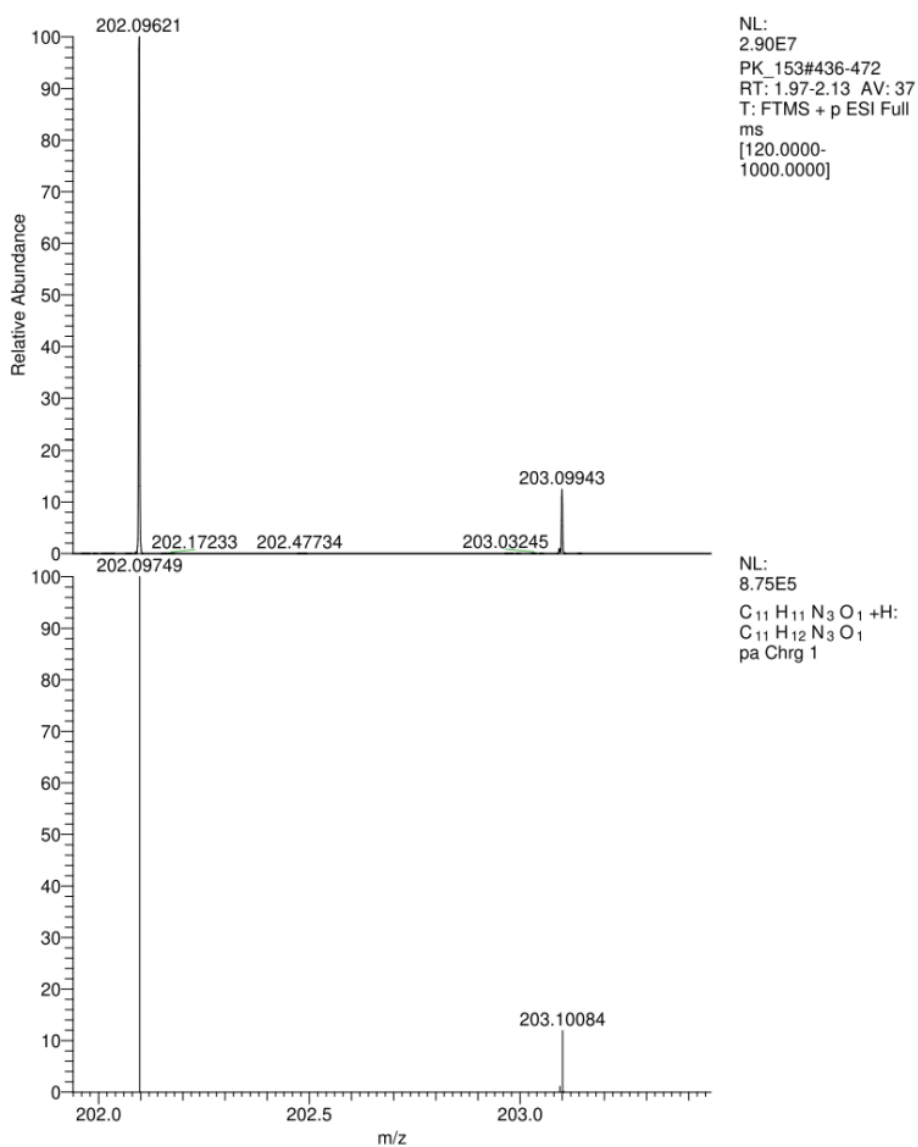
2-(4-bromo-1H-imidazol-1-yl)aniline



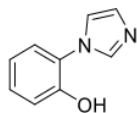
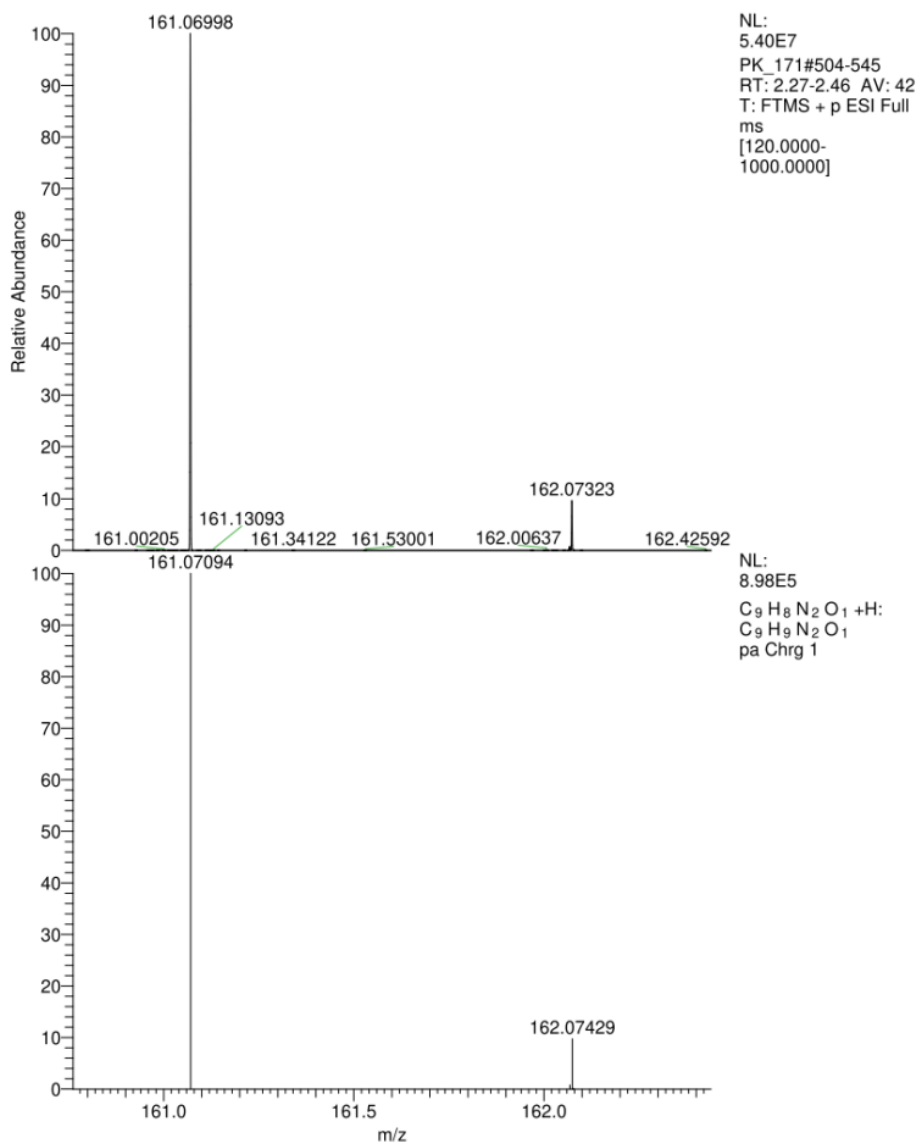
S36

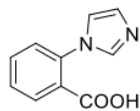
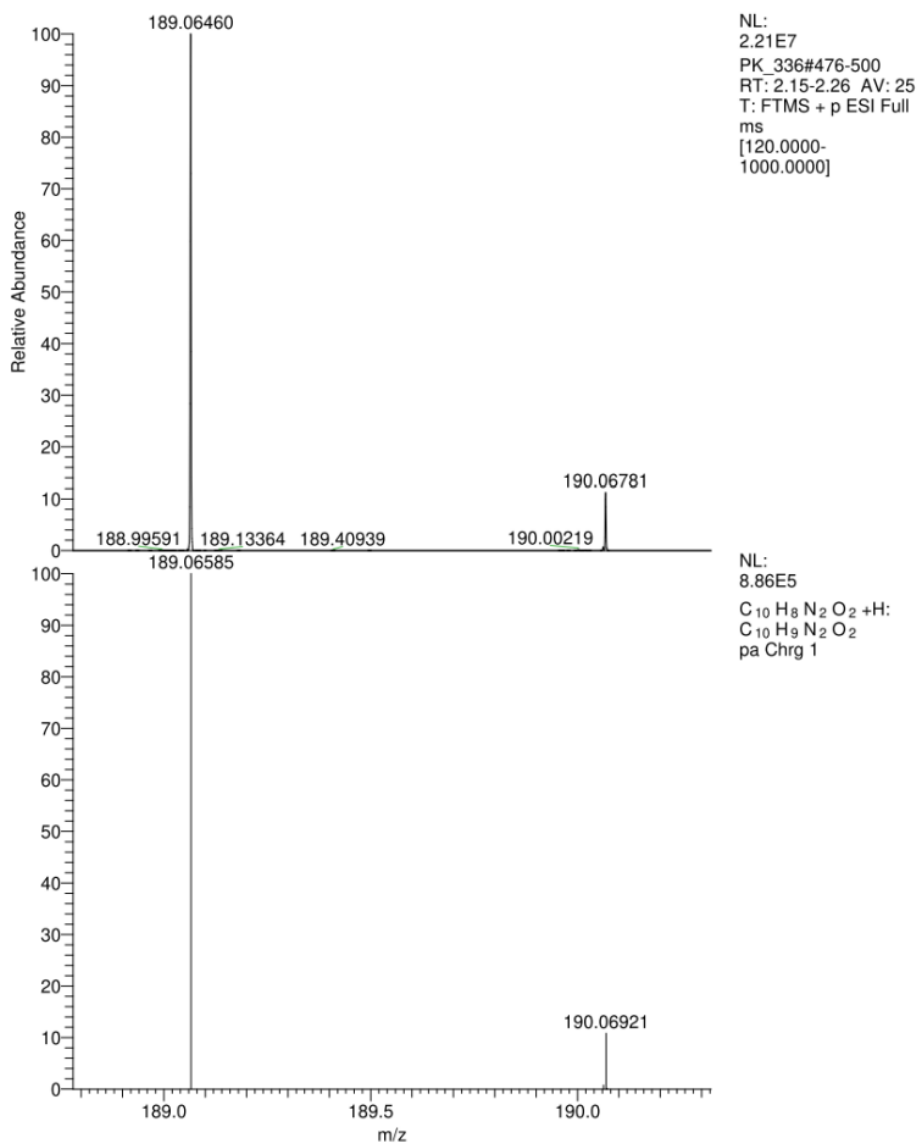
2-(1*H*-benzo[d]imidazol-1-yl)aniline (13)2-(1*H*-benzo[d]imidazol-1-yl)aniline

S37

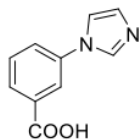
***N*-(2-(1*H*-imidazol-1-yl)phenyl)acetamide (8)***N*-(2-(1*H*-imidazol-1-yl)phenyl)acetamide

S38

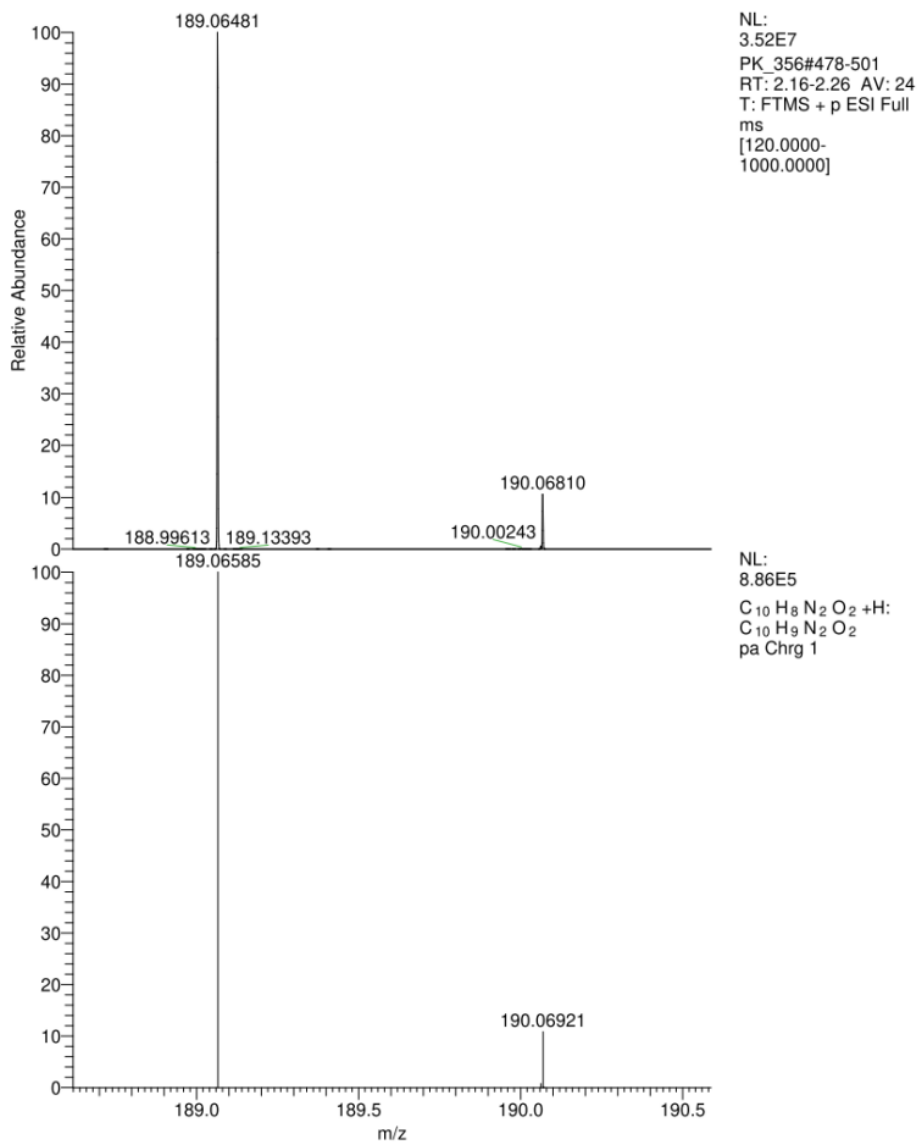
2-(1*H*-imidazol-1-yl)phenol (15)2-(1*H*-imidazol-1-yl)phenol

2-(1*H*-imidazol-1-yl)benzoic acid (16)2-(1*H*-imidazol-1-yl)benzoic acid

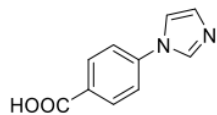
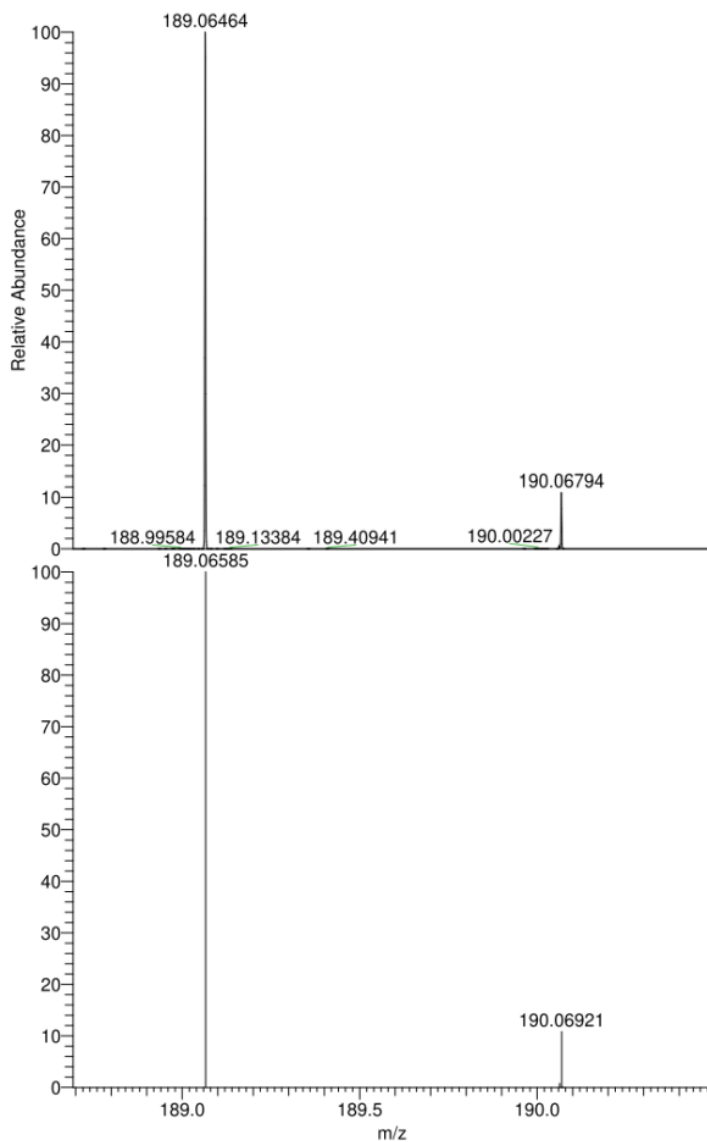
3-(1*H*-imidazol-1-yl)benzoic acid (17)



3-(1*H*-imidazol-1-yl)benzoic acid



S41

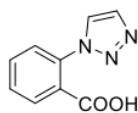
4-(1*H*-imidazol-1-yl)benzoic acid (18)4-(1*H*-imidazol-1-yl)benzoic acid

NL:
4.37E7
PK_357#472-493
RT: 2.13-2.23 AV: 22
T: FTMS + p ESI Full
ms
[120.0000-
1000.0000]

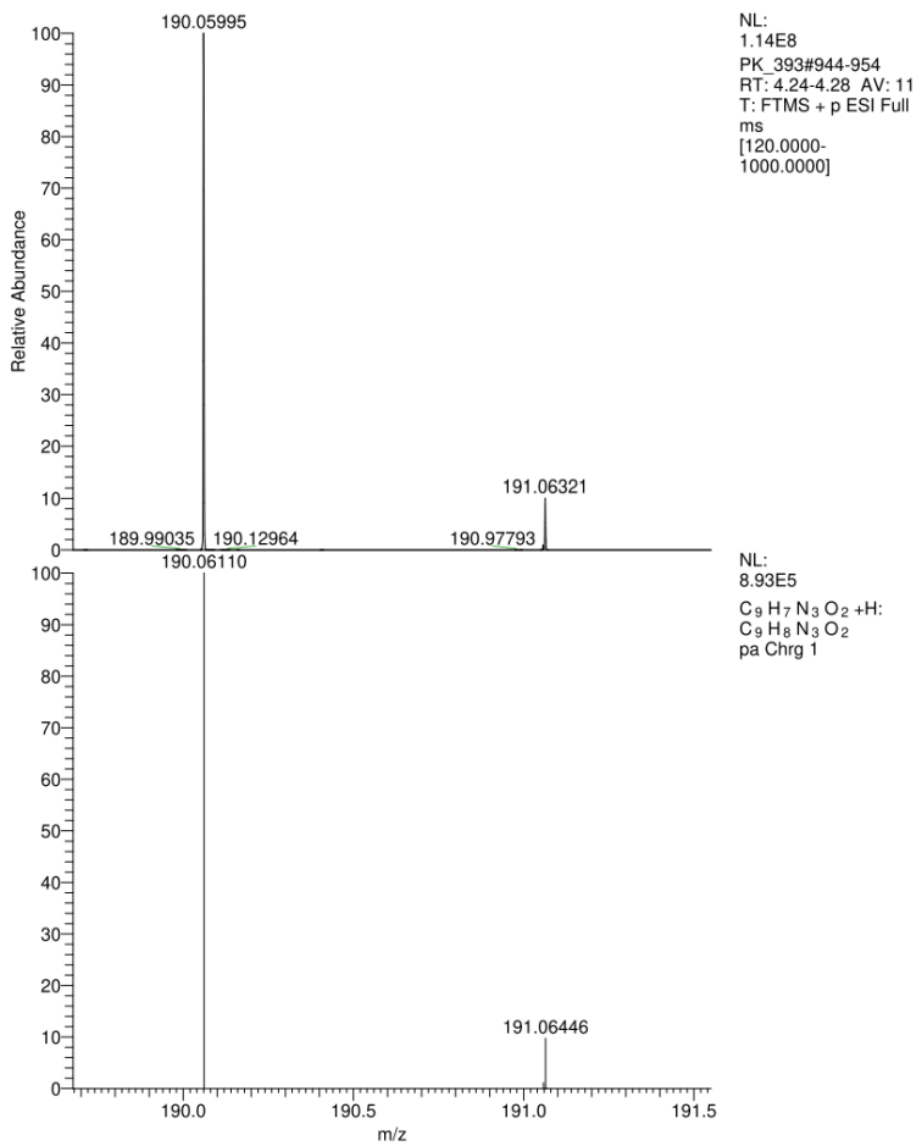
NL:
8.86E5
C₁₀H₈N₂O₂+H:
C₁₀H₉N₂O₂
pa Chrg 1

S42

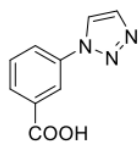
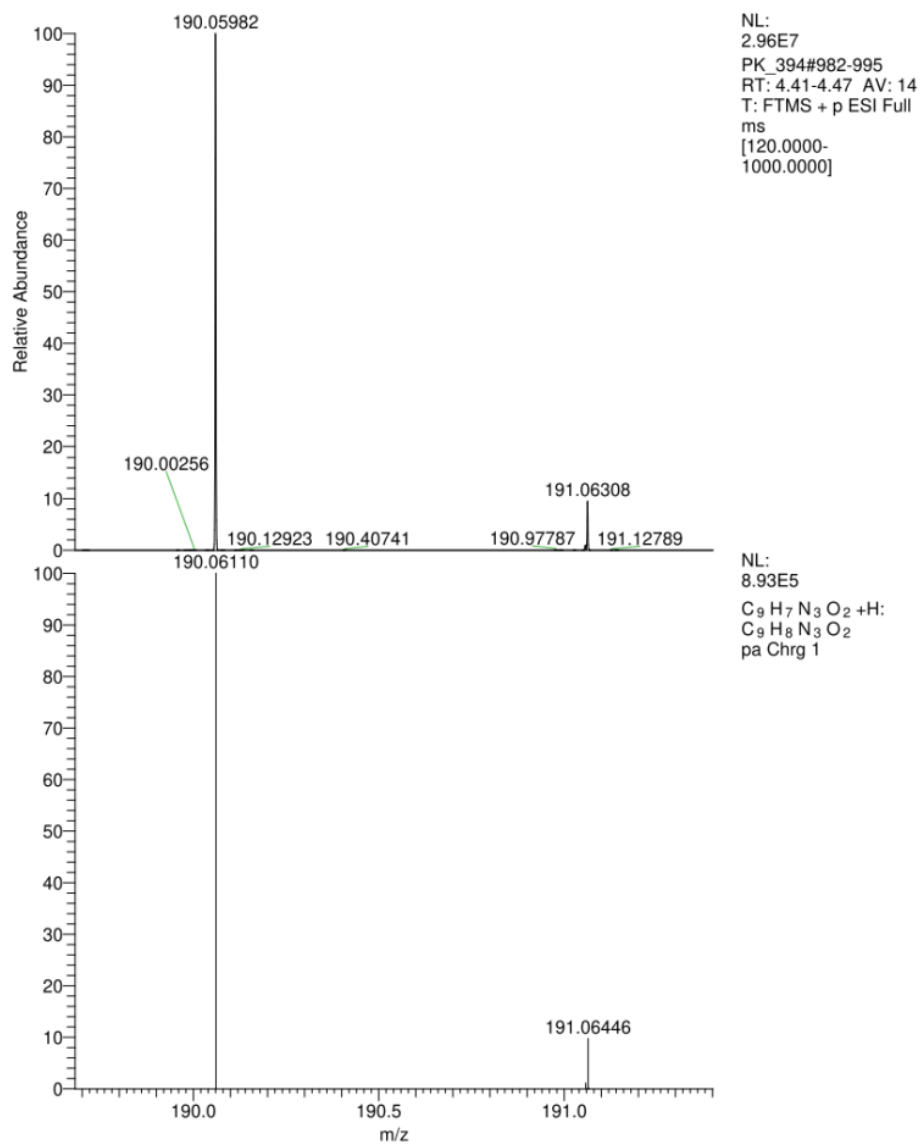
2-(1*H*-1,2,3-triazol-1-yl)benzoic acid (26)



2-(1*H*-1,2,3-triazol-1-yl)benzoic acid

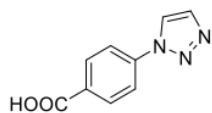


S43

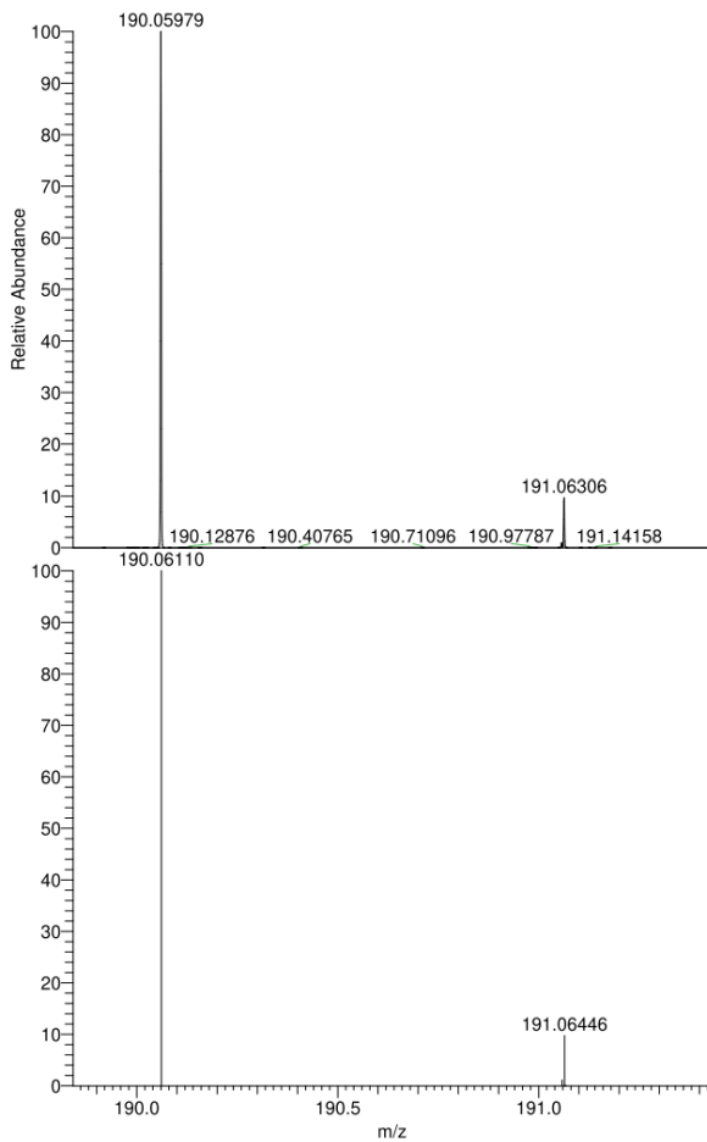
3-(1*H*-1,2,3-triazol-1-yl)benzoic acid (27)3-(1*H*-1,2,3-triazol-1-yl)benzoic acid

S44

4-(1*H*-1,2,3-triazol-1-yl)benzoic acid (28)

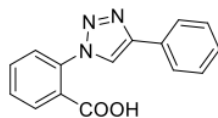
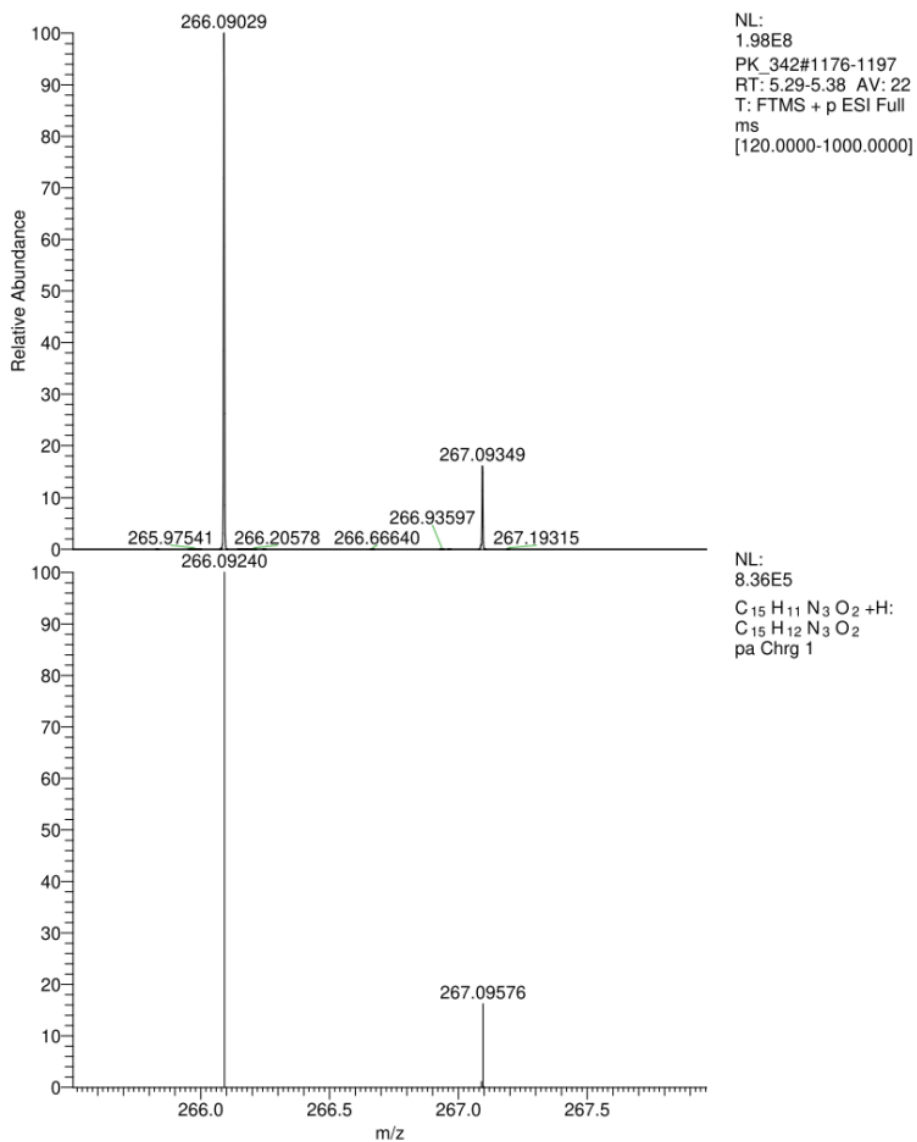


4-(1*H*-1,2,3-triazol-1-yl)benzoic acid



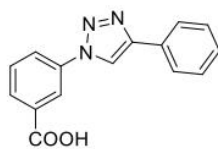
NL:
4.73E7
PK_395#973-988
RT: 4.38-4.44 AV: 16
T: FTMS + p ESI Full
ms
[120.0000-
1000.0000]

NL:
8.93E5
C₉H₇N₃O₂+H:
C₉H₈N₃O₂
pa Chrg 1

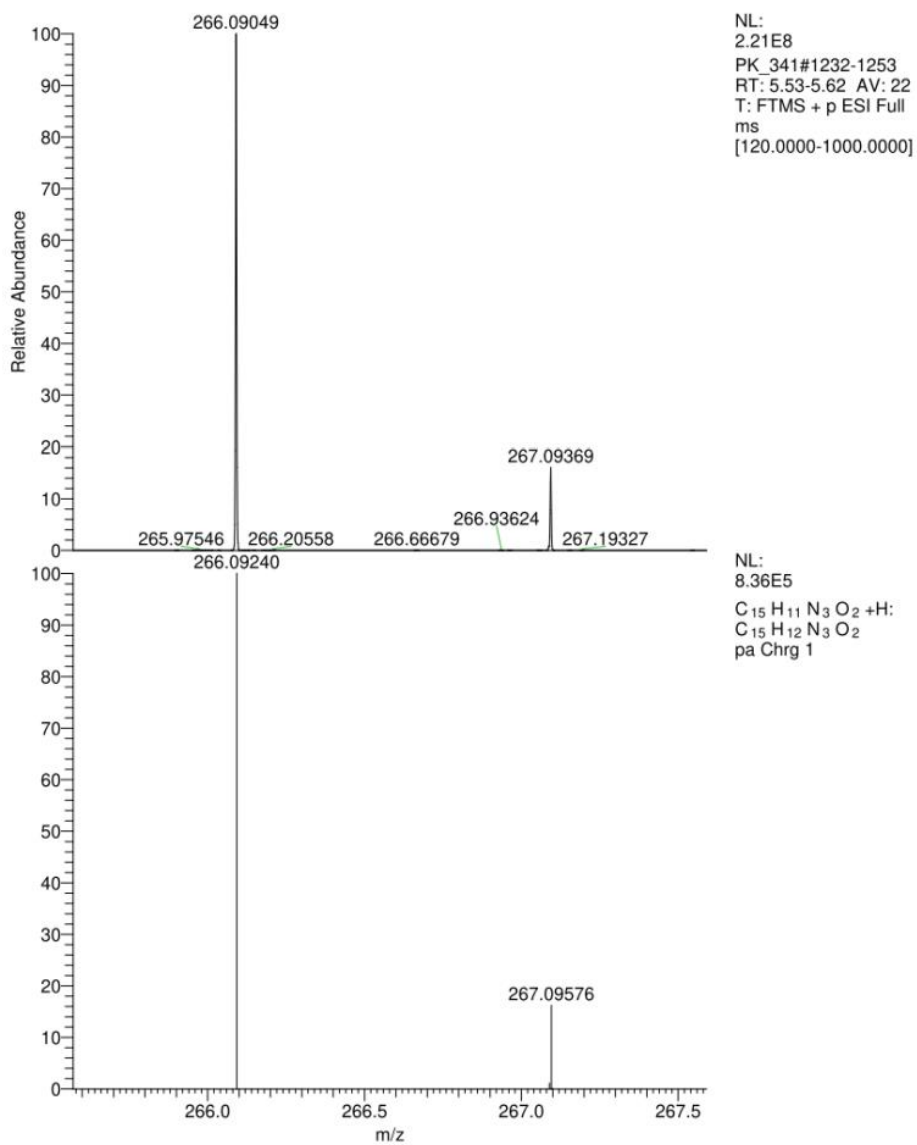
2-(4-phenyl-1*H*-1,2,3-triazol-1-yl)benzoic acid (29)2-(4-phenyl-1*H*-1,2,3-triazol-1-yl)benzoic acid

S46

3-(4-phenyl-1*H*-1,2,3-triazol-1-yl)benzoic acid (30)

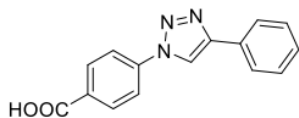


3-(4-phenyl-1*H*-1,2,3-triazol-1-yl)benzoic acid

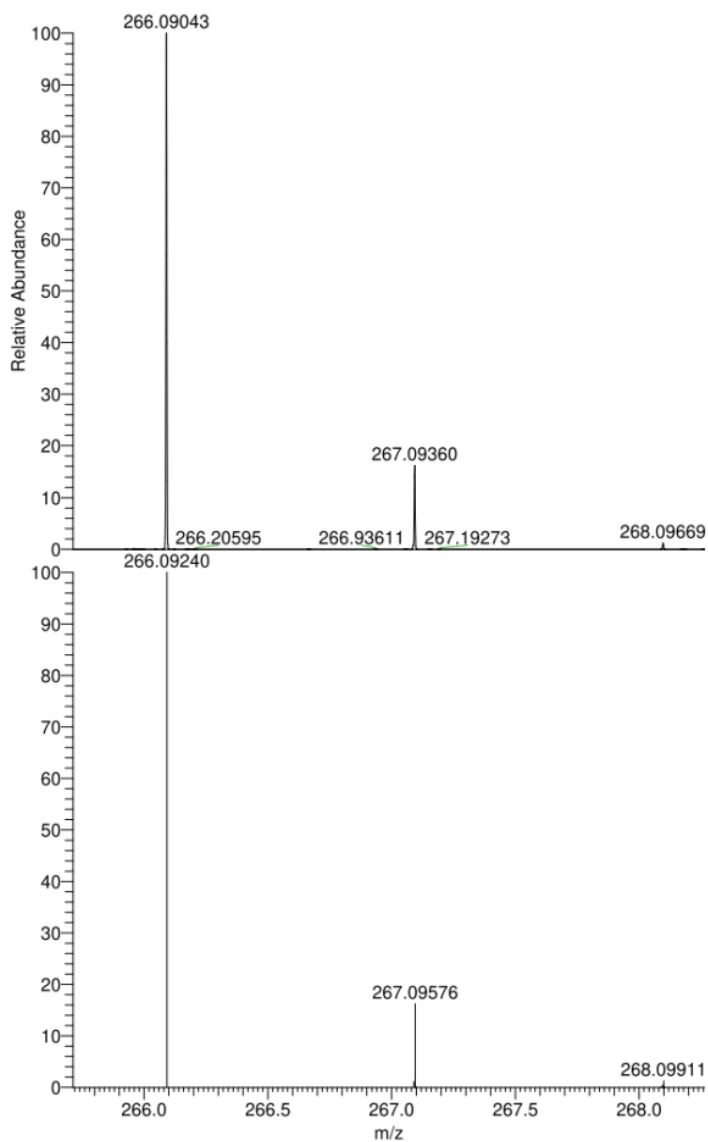


S47

4-(4-phenyl-1H-1,2,3-triazol-1-yl)benzoic acid (31)



4-(4-phenyl-1H-1,2,3-triazol-1-yl)benzoic acid

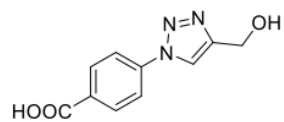


NL:
4.55E7
PK_1104#1238-1248
RT: 5.57-5.61 AV: 11
T: FTMS + p ESI Full
ms
[120.0000-1000.0000]

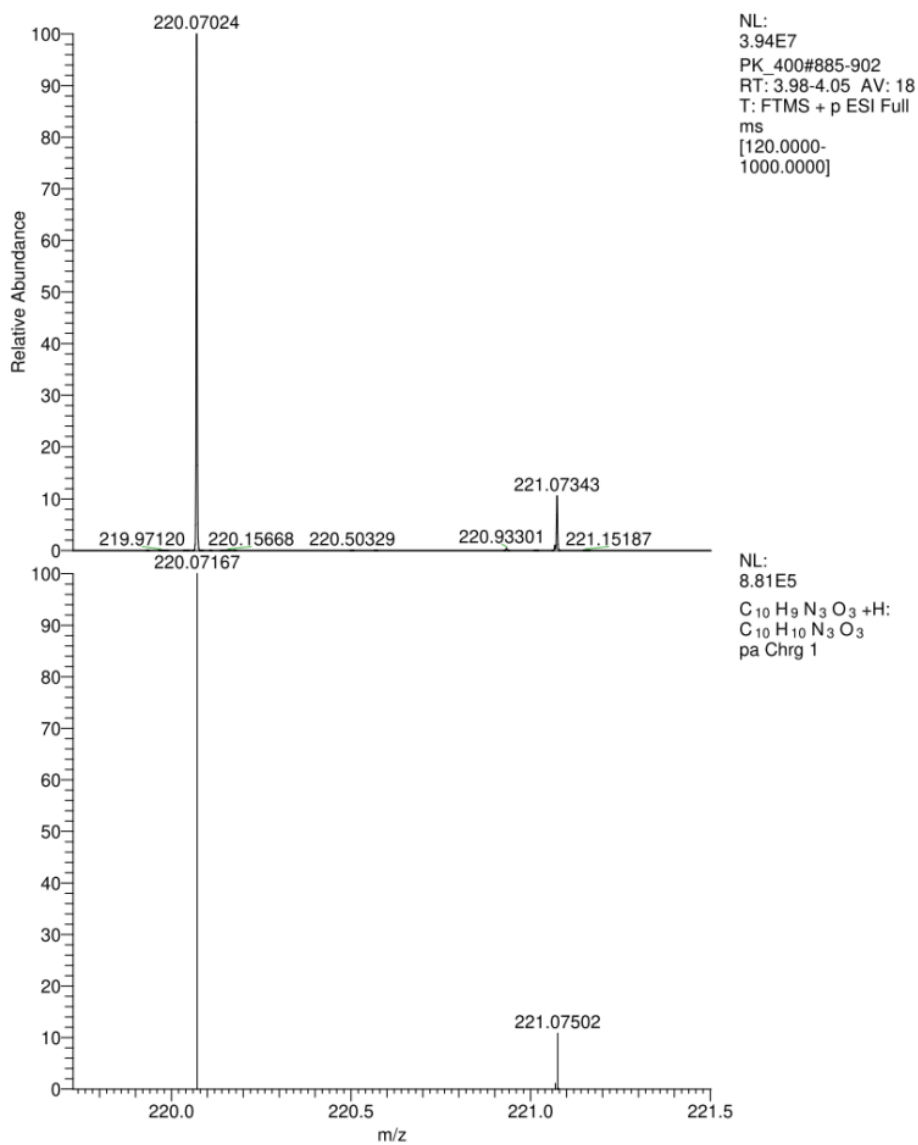
NL:
8.36E5
C₁₅ H₁₁ N₃ O₂ +H:
C₁₅ H₁₂ N₃ O₂
pa Chrg 1

S48

4-(4-(hydroxymethyl)-1H-1,2,3-triazol-1-yl)benzoic acid (32)

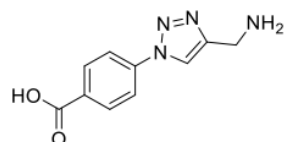


4-(4-(hydroxymethyl)-1H-1,2,3-triazol-1-yl)benzoic acid

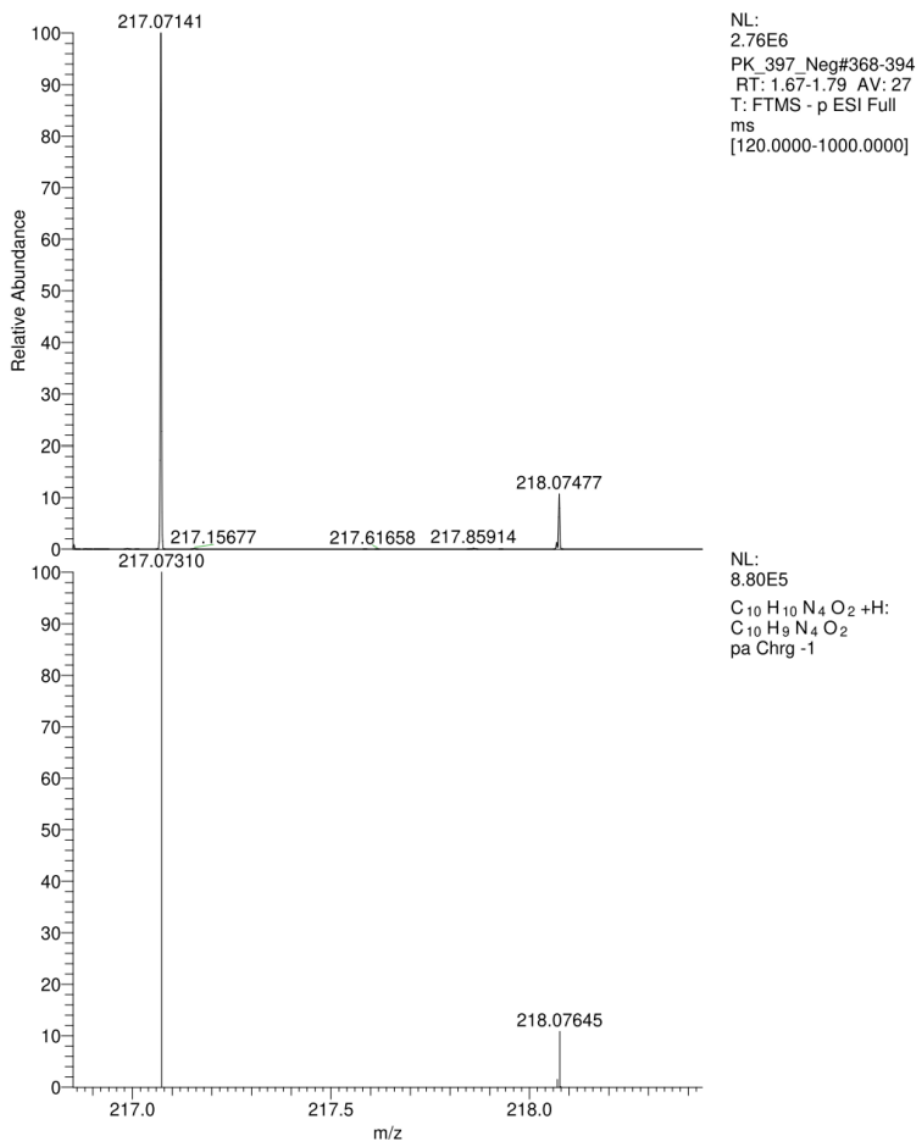


S49

4-(4-(aminomethyl)-1H-1,2,3-triazol-1-yl)benzoic acid (33)

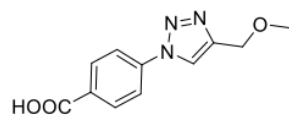


4-(4-(aminomethyl)-1H-1,2,3-triazol-1-yl)benzoic acid

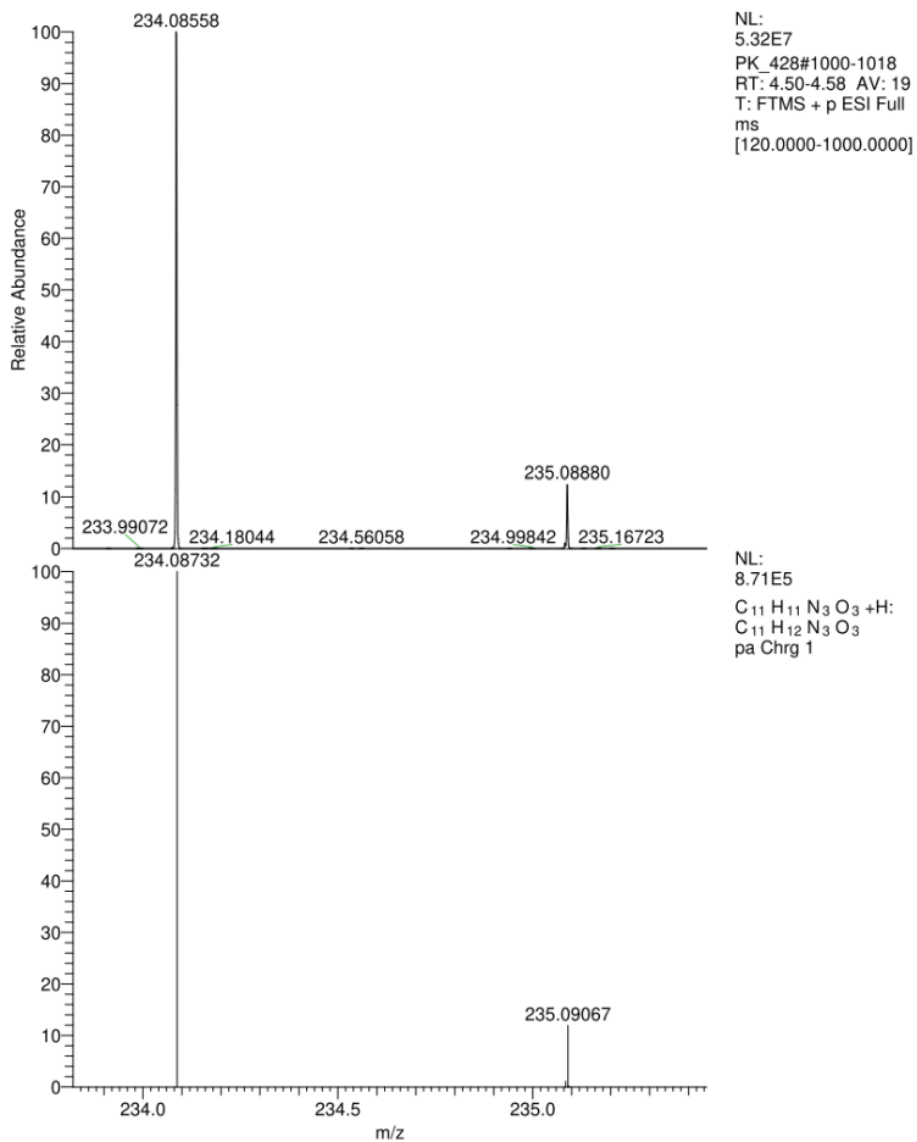


S50

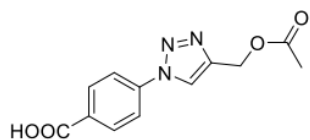
4-(4-(methoxymethyl)-1H-1,2,3-triazol-1-yl)benzoic acid (34)



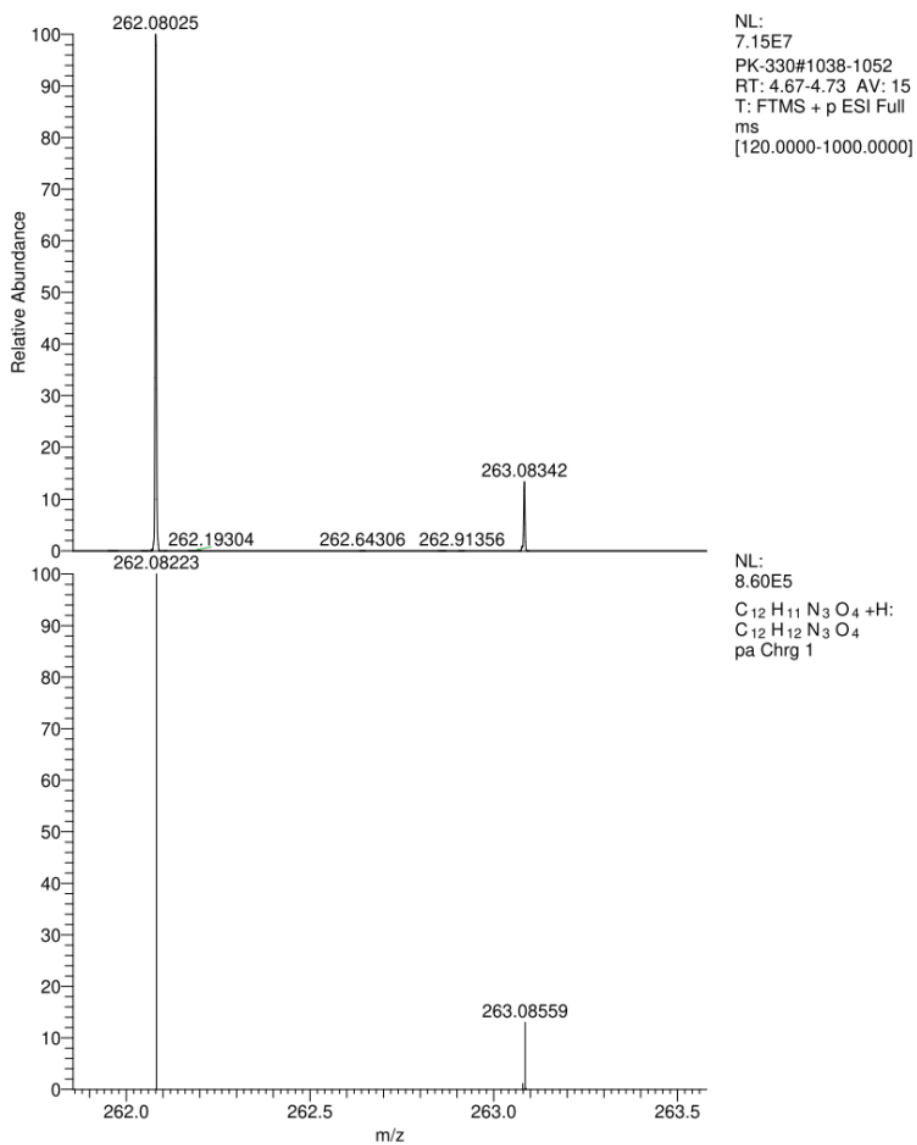
4-(4-(methoxymethyl)-1H-1,2,3-triazol-1-yl)benzoic acid



4-(4-(acetoxymethyl)-1H-1,2,3-triazol-1-yl)benzoic acid (35)

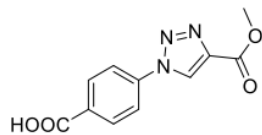


4-(4-(acetoxymethyl)-1H-1,2,3-triazol-1-yl)benzoic acid

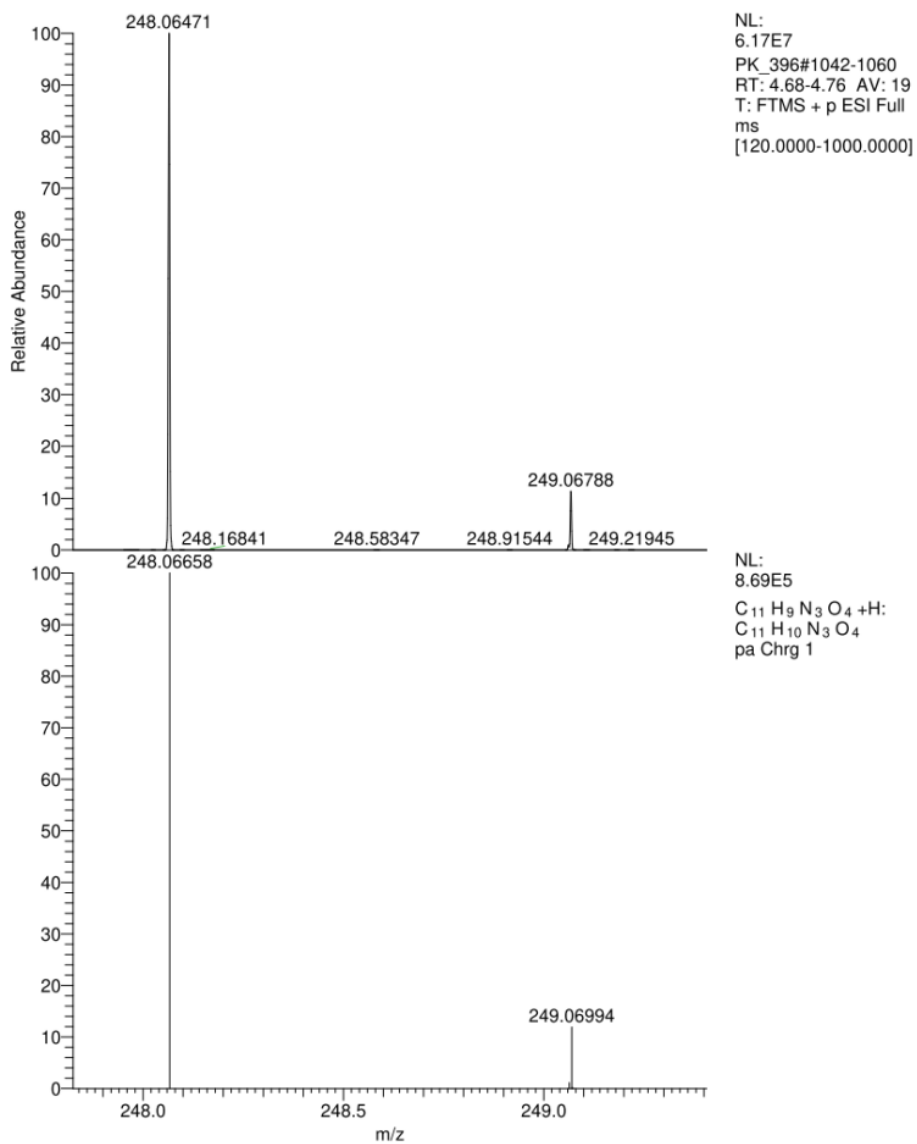


S52

4-(4-(methoxycarbonyl)-1H-1,2,3-triazol-1-yl)benzoic acid (36)

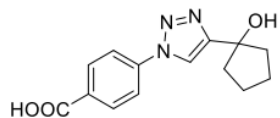


4-(4-(methoxycarbonyl)-1H-1,2,3-triazol-1-yl)benzoic acid

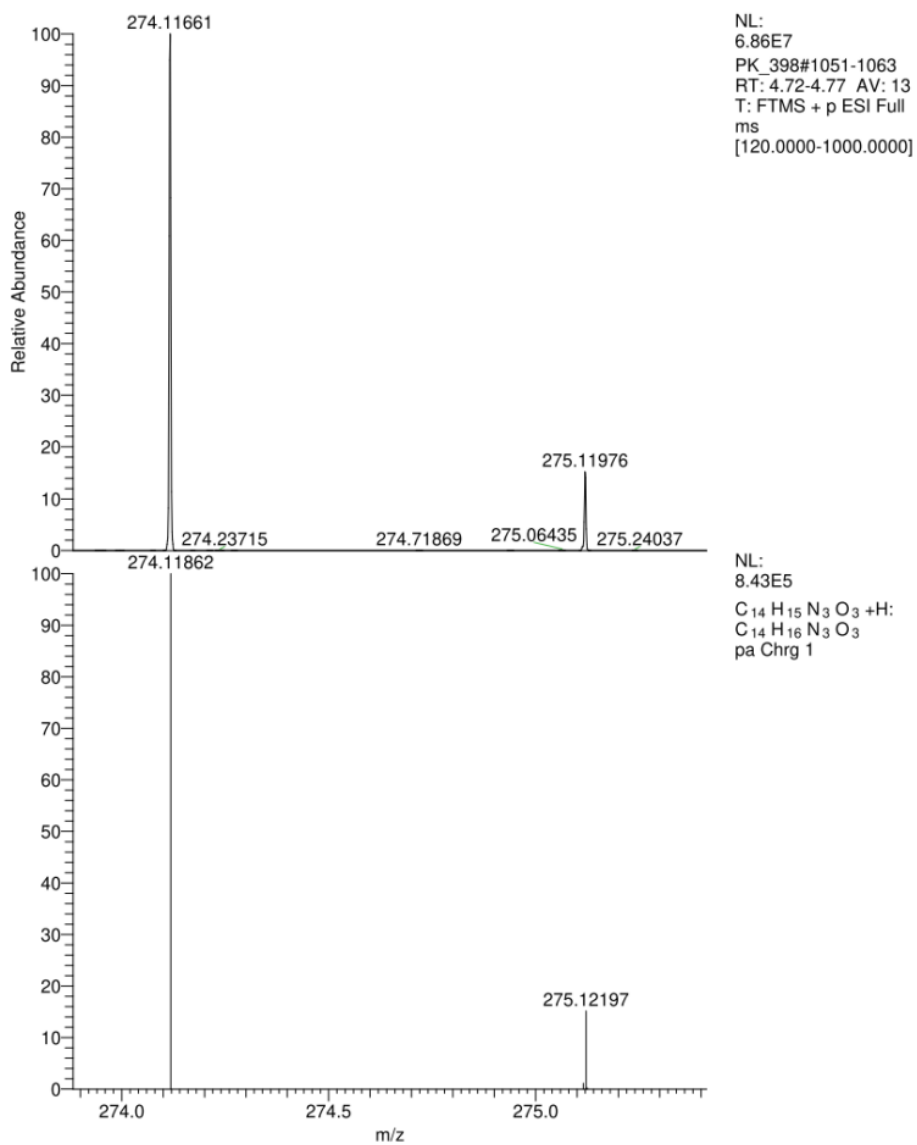


S53

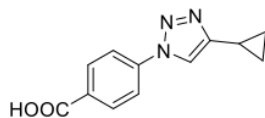
4-(4-(1-hydroxycyclopentyl)-1H-1,2,3-triazol-1-yl)benzoic acid (37)



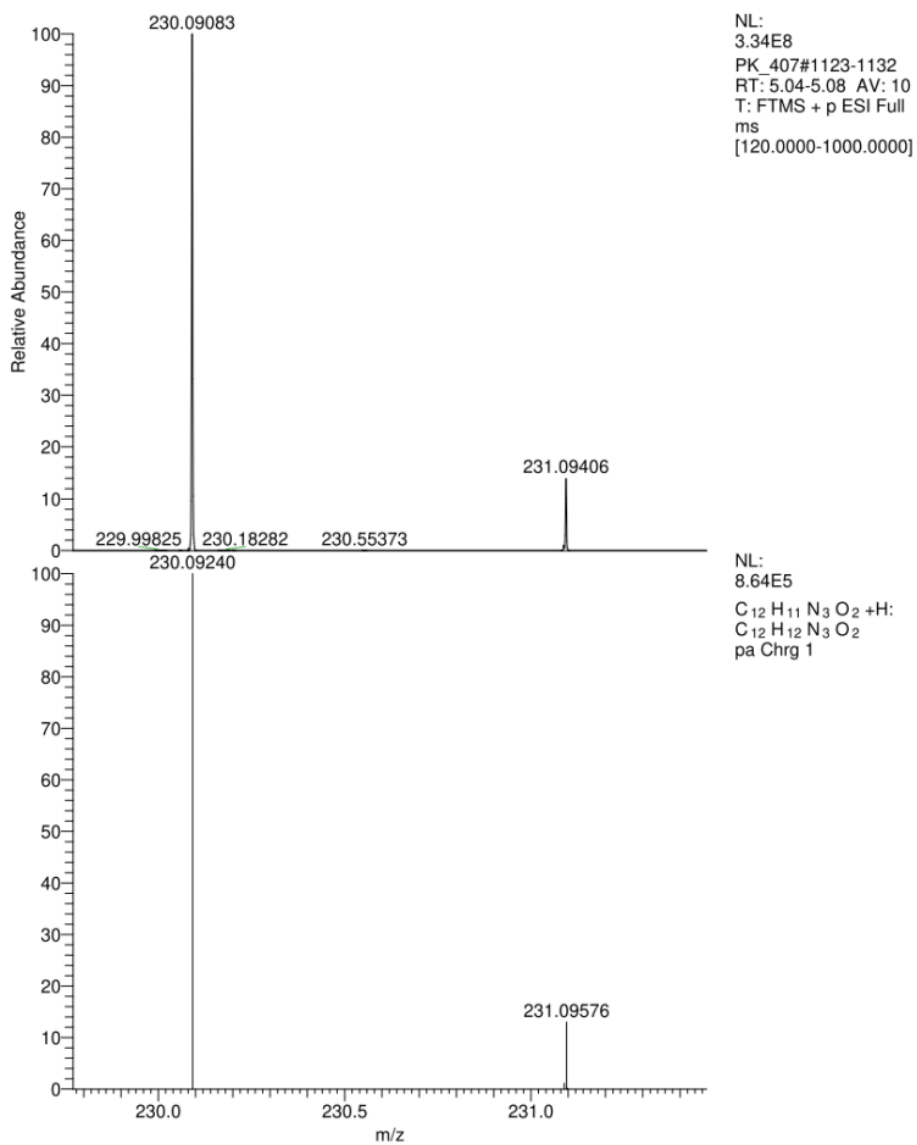
4-(4-(1-hydroxycyclopentyl)-1H-1,2,3-triazol-1-yl)benzoic acid



4-(4-cyclopropyl-1H-1,2,3-triazol-1-yl)benzoic acid (38)

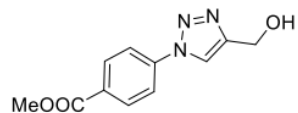


4-(4-cyclopropyl-1H-1,2,3-triazol-1-yl)benzoic acid

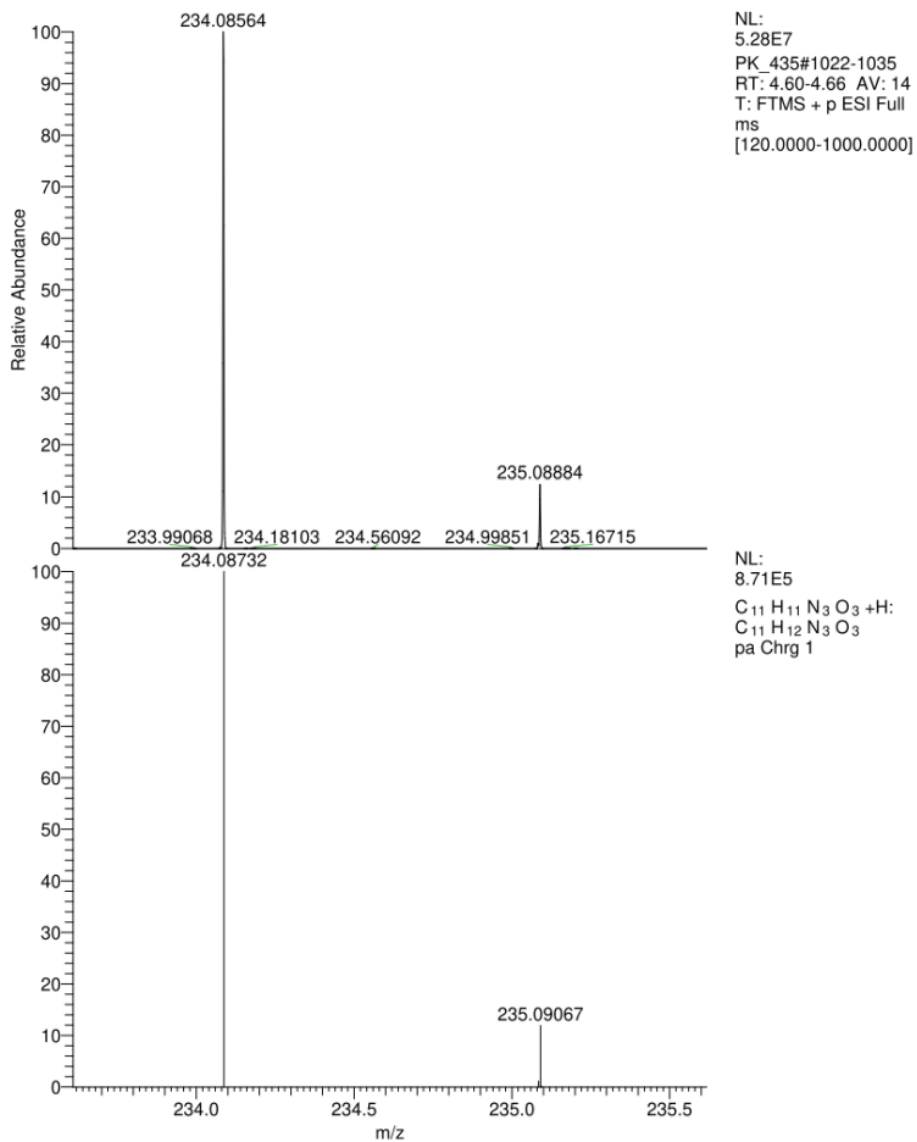


S55

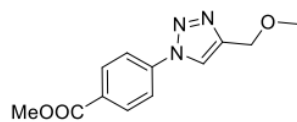
methyl 4-(4-(hydroxymethyl)-1H-1,2,3-triazol-1-yl)benzoate (39)



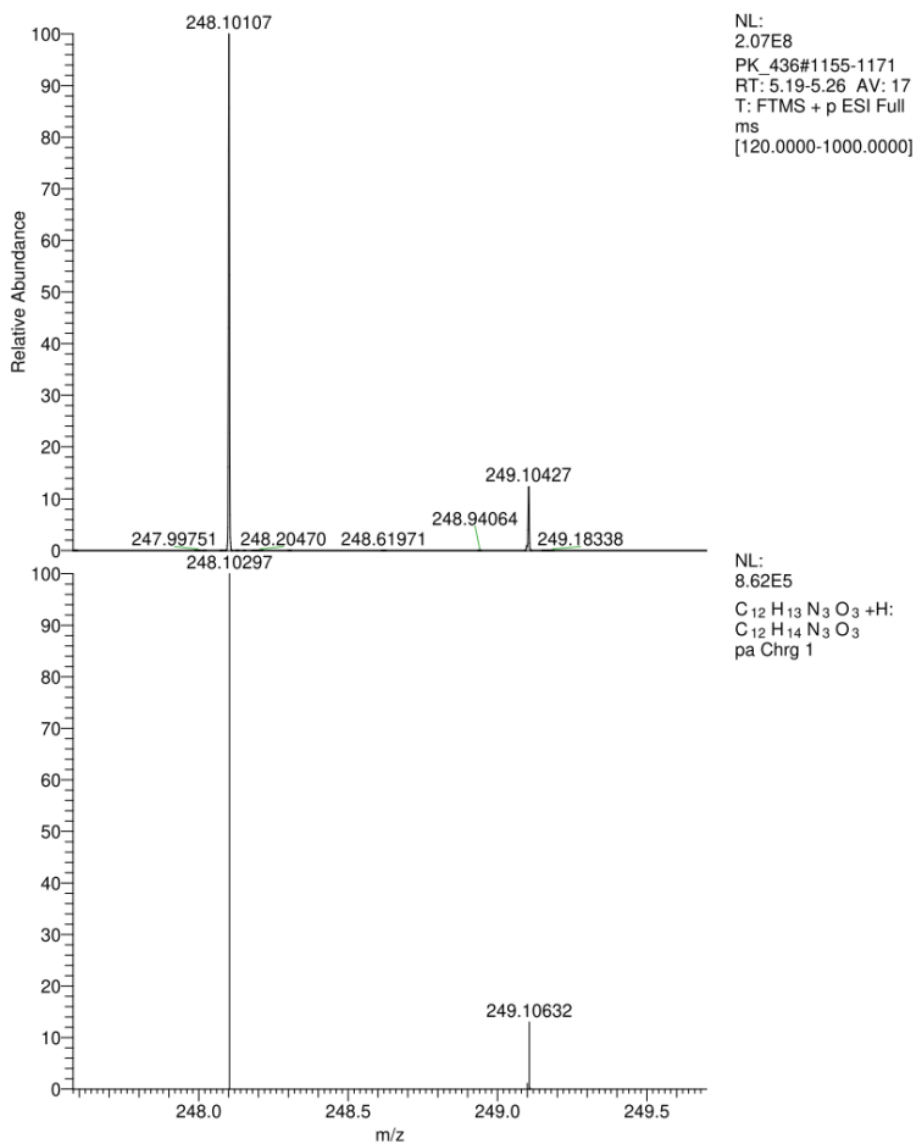
methyl 4-(4-(hydroxymethyl)-1H-1,2,3-triazol-1-yl)benzoate



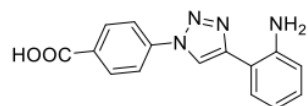
methyl 4-(4-(methoxymethyl)-1H-1,2,3-triazol-1-yl)benzoate (40)



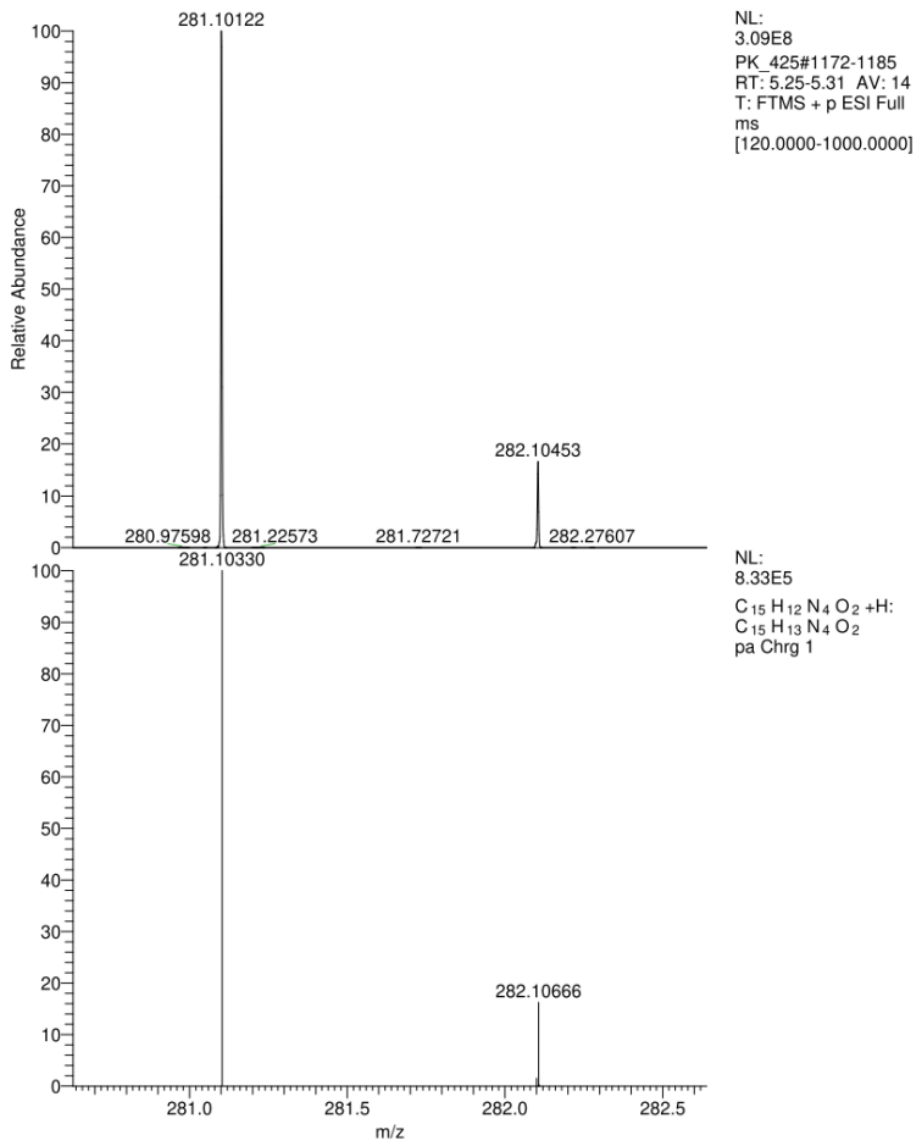
methyl 4-(4-(methoxymethyl)-1H-1,2,3-triazol-1-yl)benzoate



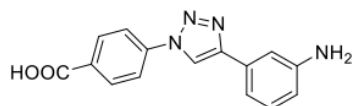
4-(4-(2-aminophenyl)-1H-1,2,3-triazol-1-yl)benzoic acid (41)



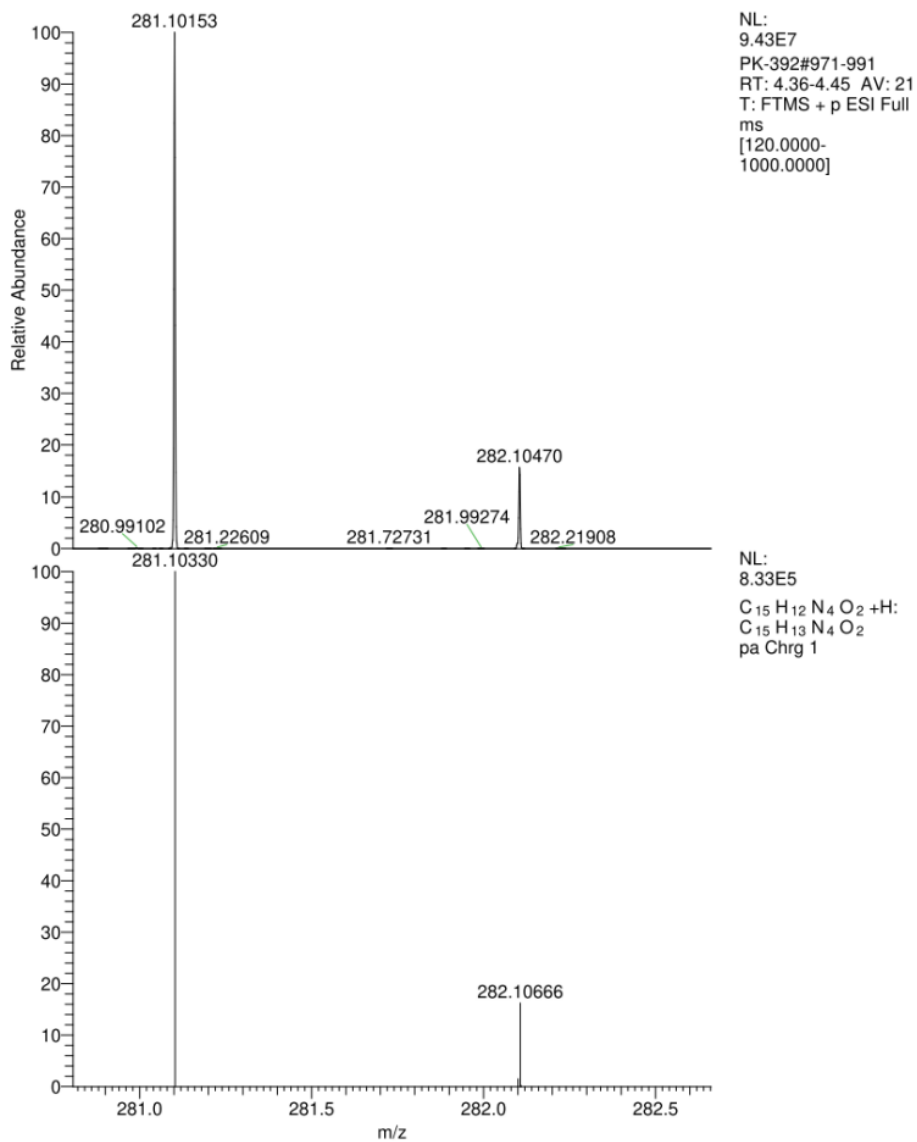
4-(4-(2-aminophenyl)-1H-1,2,3-triazol-1-yl)benzoic acid



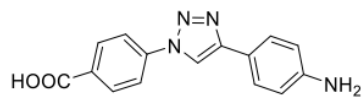
4-(4-(3-aminophenyl)-1H-1,2,3-triazol-1-yl)benzoic acid (42)



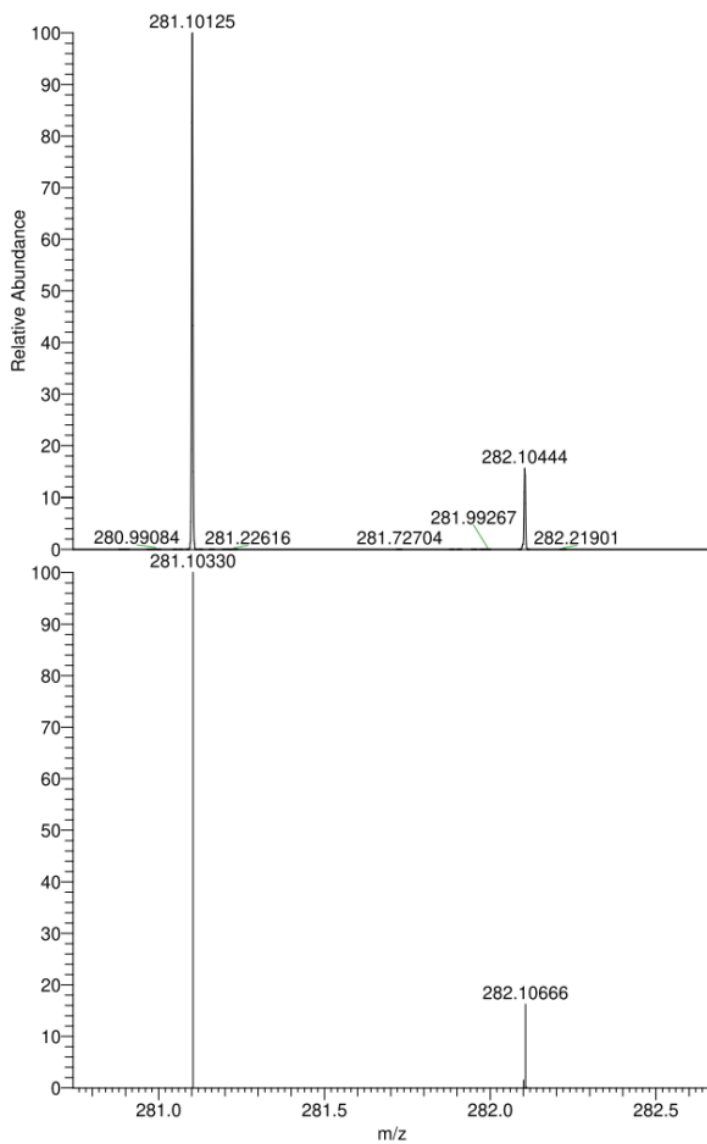
4-(4-(3-aminophenyl)-1H-1,2,3-triazol-1-yl)benzoic acid



4-(4-(4-aminophenyl)-1H-1,2,3-triazol-1-yl)benzoic acid (43)



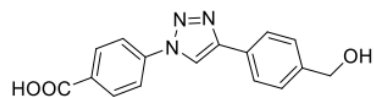
4-(4-(4-aminophenyl)-1H-1,2,3-triazol-1-yl)benzoic acid



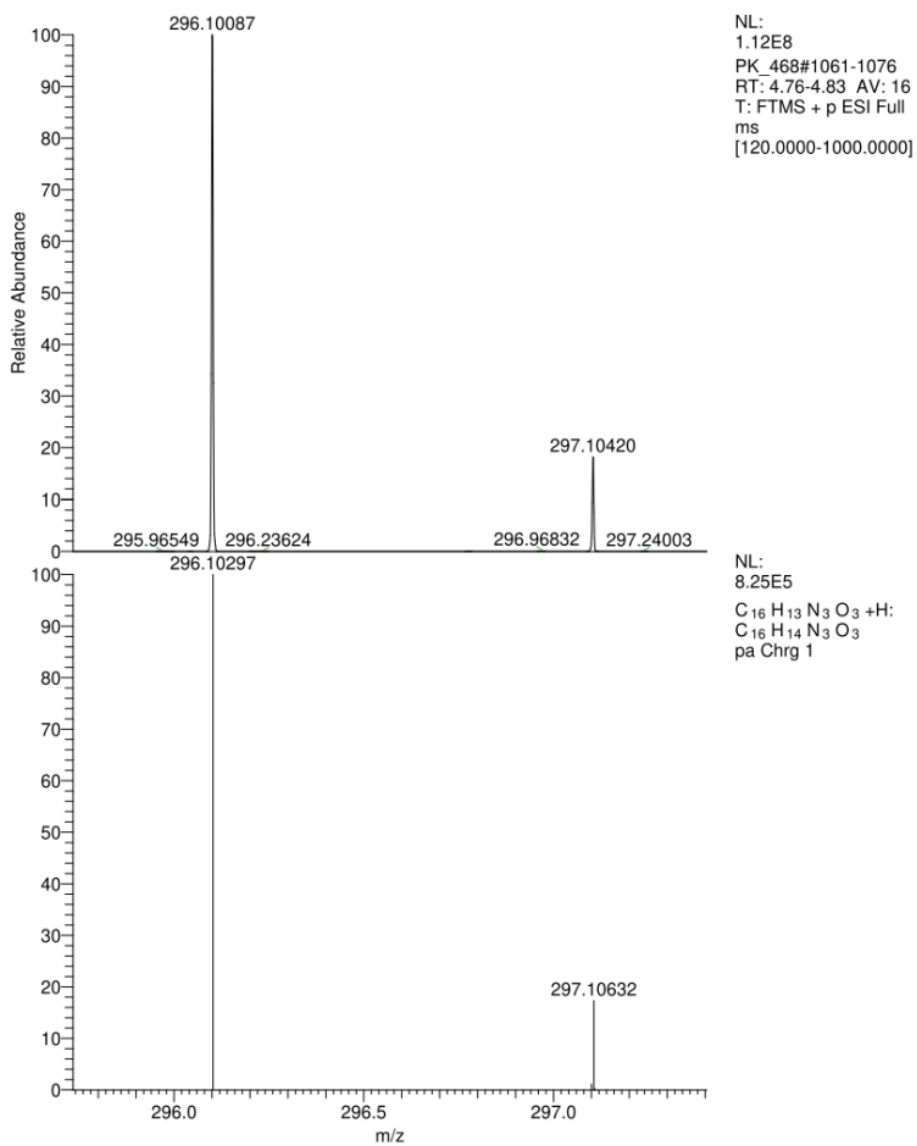
NL:
1.31E8
PK_460#968-991
RT: 4.35-4.45 AV: 24
T: FTMS + p ESI Full
ms
[120.0000-
1000.0000]

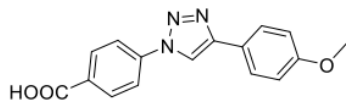
NL:
8.33E5
C₁₅ H₁₂ N₄ O₂ +H:
C₁₅ H₁₃ N₄ O₂
pa Chrg 1

4-(4-(4-(hydroxymethyl)phenyl)-1H-1,2,3-triazol-1-yl)benzoic acid (44)

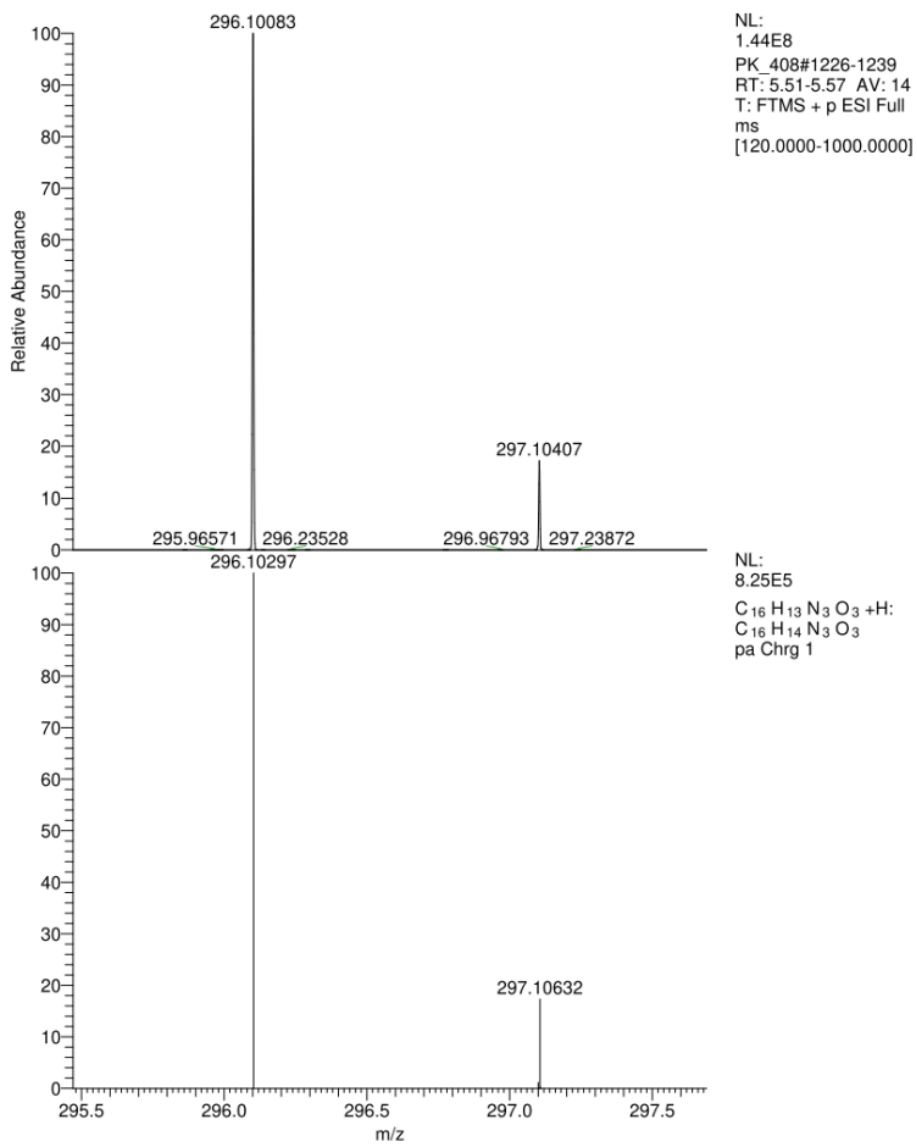


4-(4-(4-(hydroxymethyl)phenyl)-1H-1,2,3-triazol-1-yl)benzoic acid

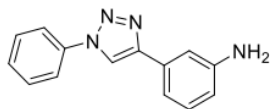


4-(4-(4-methoxyphenyl)-1H-1,2,3-triazol-1-yl)benzoic acid (45):

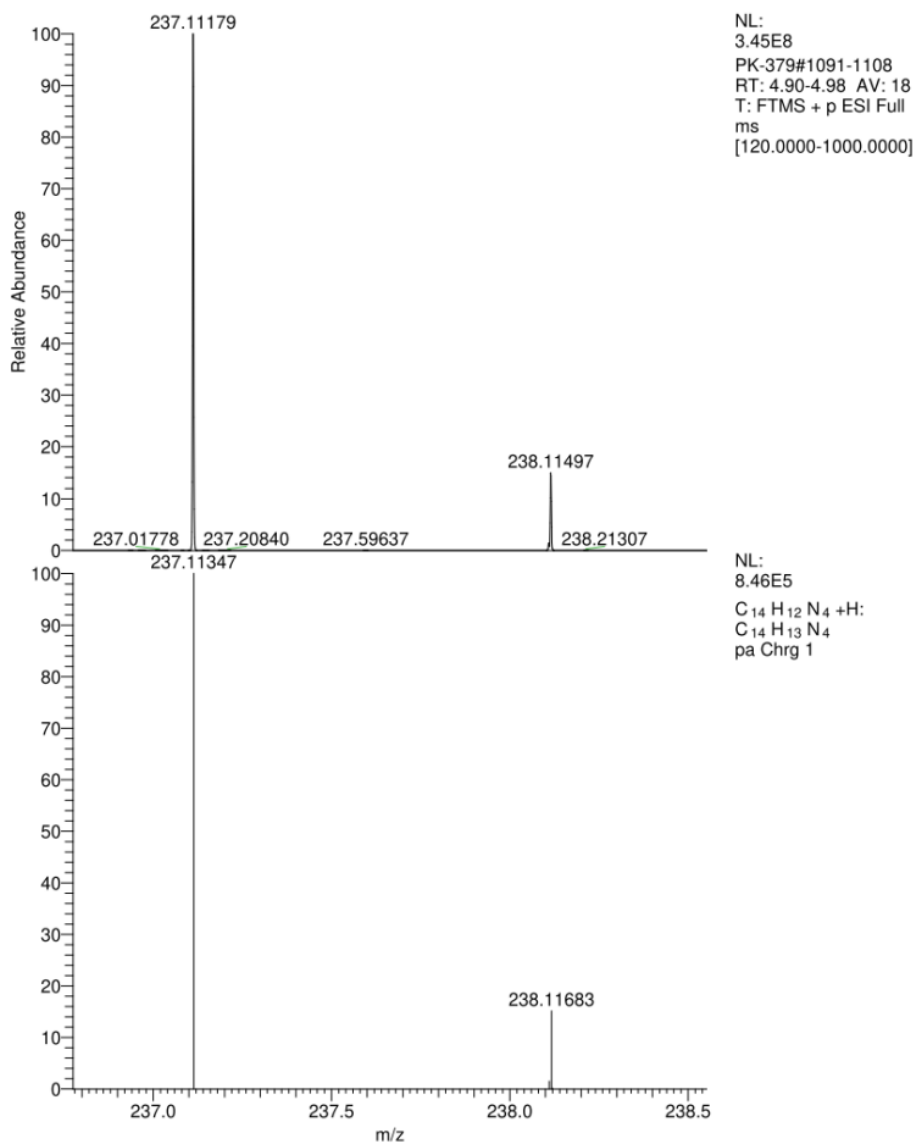
4-(4-(4-methoxyphenyl)-1H-1,2,3-triazol-1-yl)benzoic acid



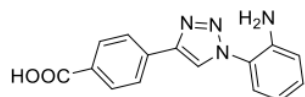
3-(1-phenyl-1H-1,2,3-triazol-4-yl)aniline (46)



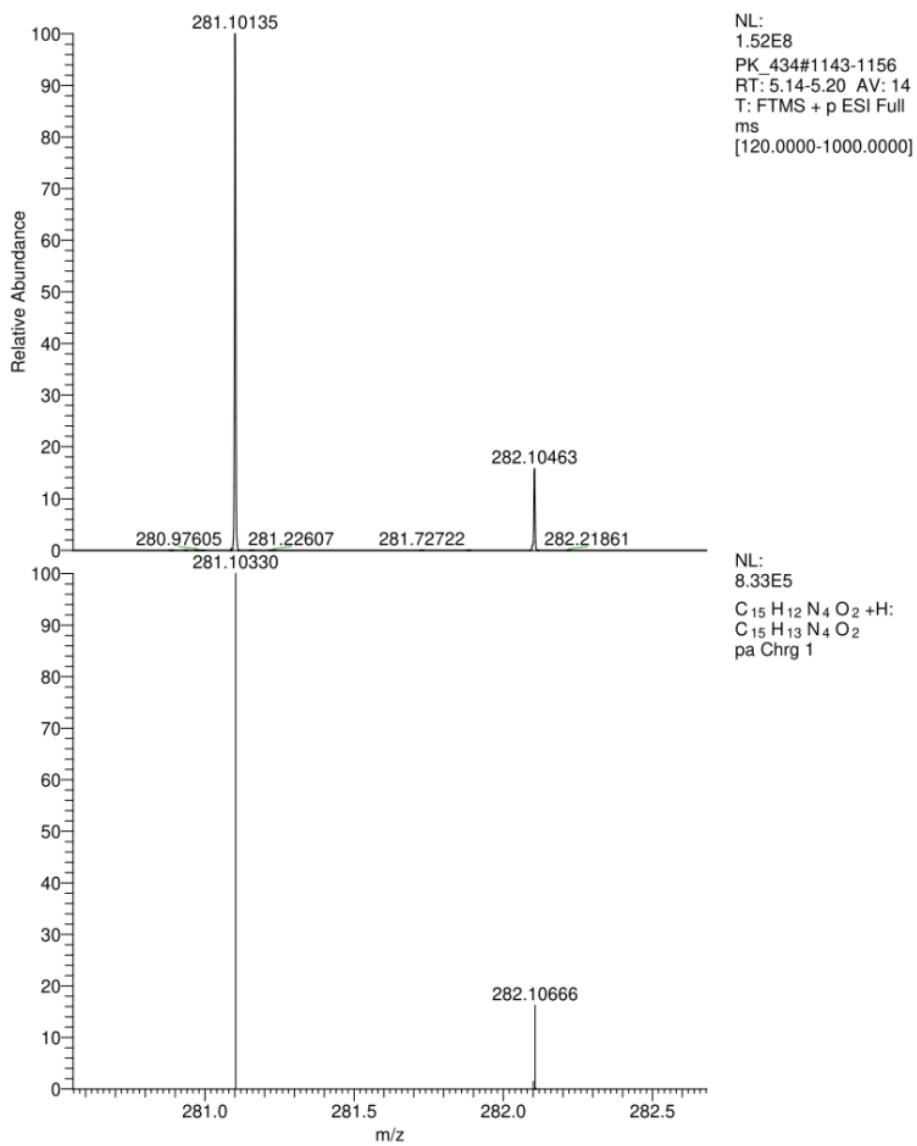
3-(1-phenyl-1H-1,2,3-triazol-4-yl)aniline



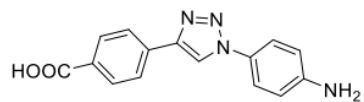
4-(1-(2-aminophenyl)-1H-1,2,3-triazol-4-yl)benzoic acid (47)



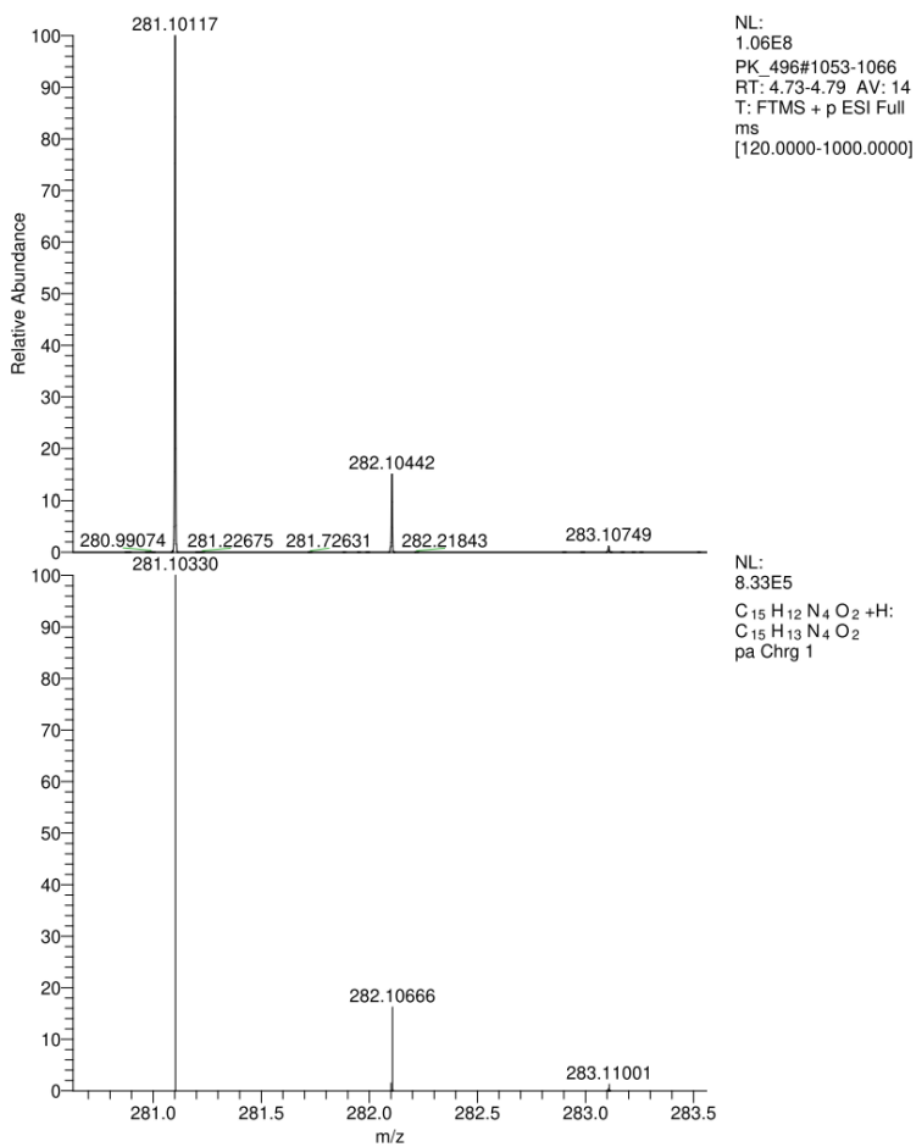
4-(1-(2-aminophenyl)-1H-1,2,3-triazol-4-yl)benzoic acid



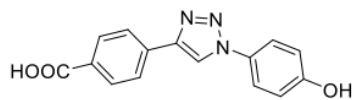
4-(1-(4-aminophenyl)-1H-1,2,3-triazol-4-yl)benzoic acid (48)



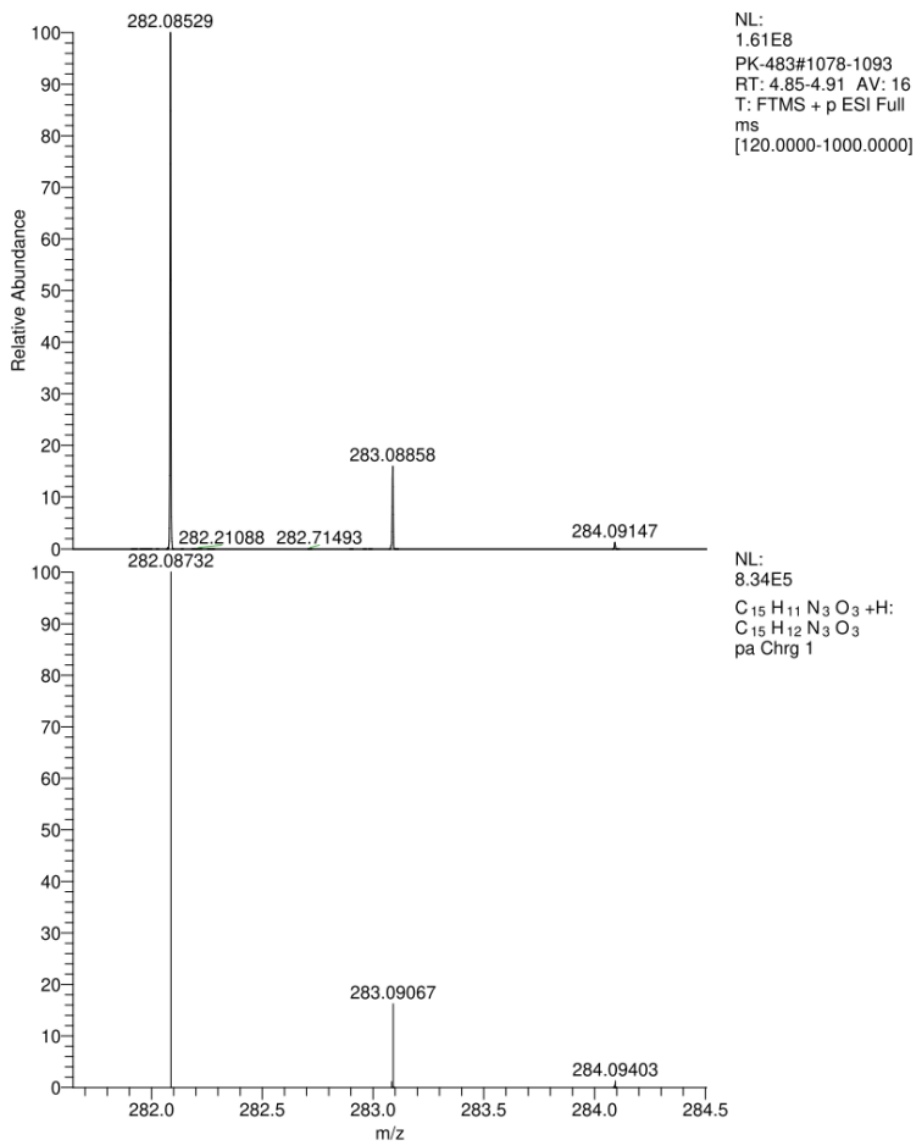
4-(1-(4-aminophenyl)-1H-1,2,3-triazol-4-yl)benzoic acid



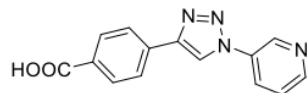
4-(1-(4-hydroxyphenyl)-1H-1,2,3-triazol-4-yl)benzoic acid (49)



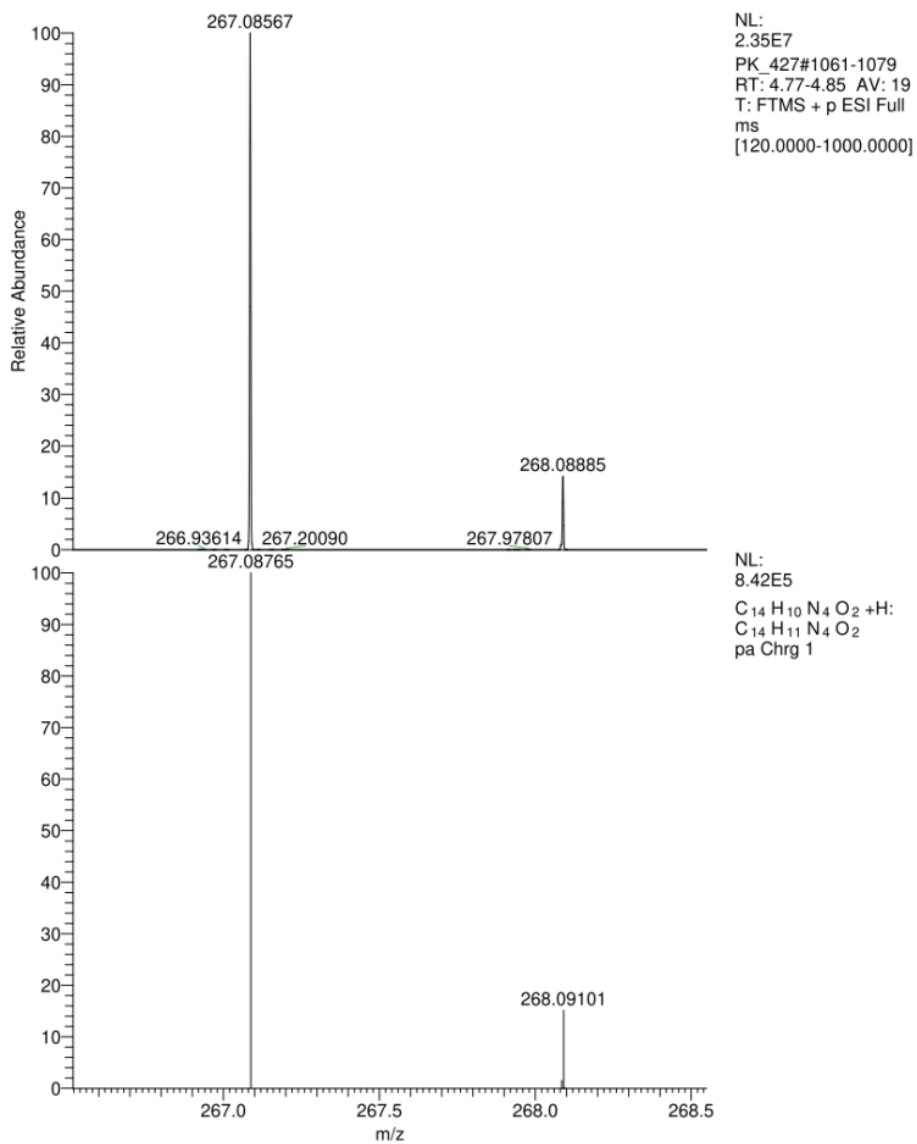
4-(1-(4-hydroxyphenyl)-1H-1,2,3-triazol-4-yl)benzoic acid



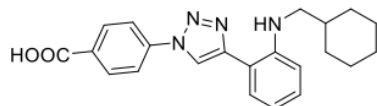
4-(1-(pyridin-3-yl)-1H-1,2,3-triazol-4-yl)benzoic acid (50)



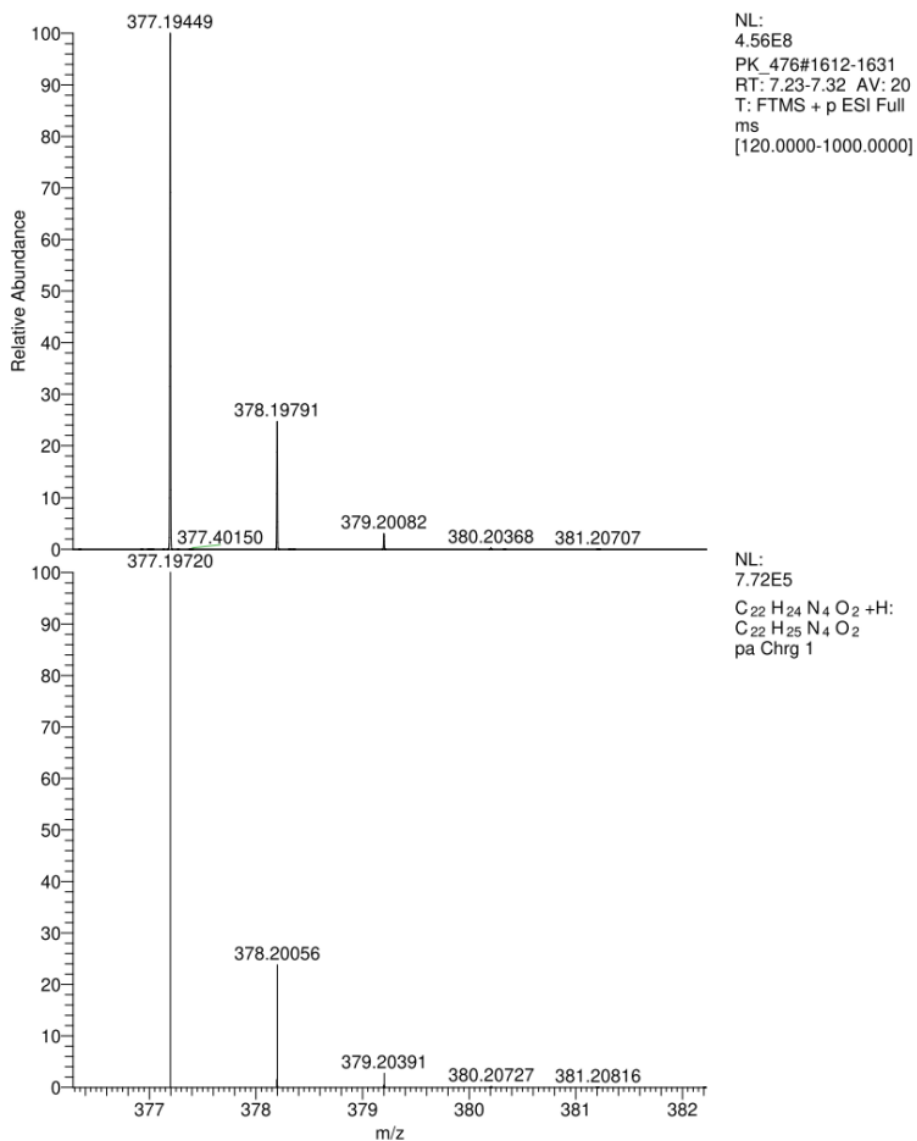
4-(1-(pyridin-3-yl)-1H-1,2,3-triazol-4-yl)benzoic acid



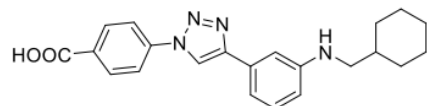
4-(4-(2-((cyclohexylmethyl)amino)phenyl)-1H-1,2,3-triazol-1-yl)benzoic acid (51)



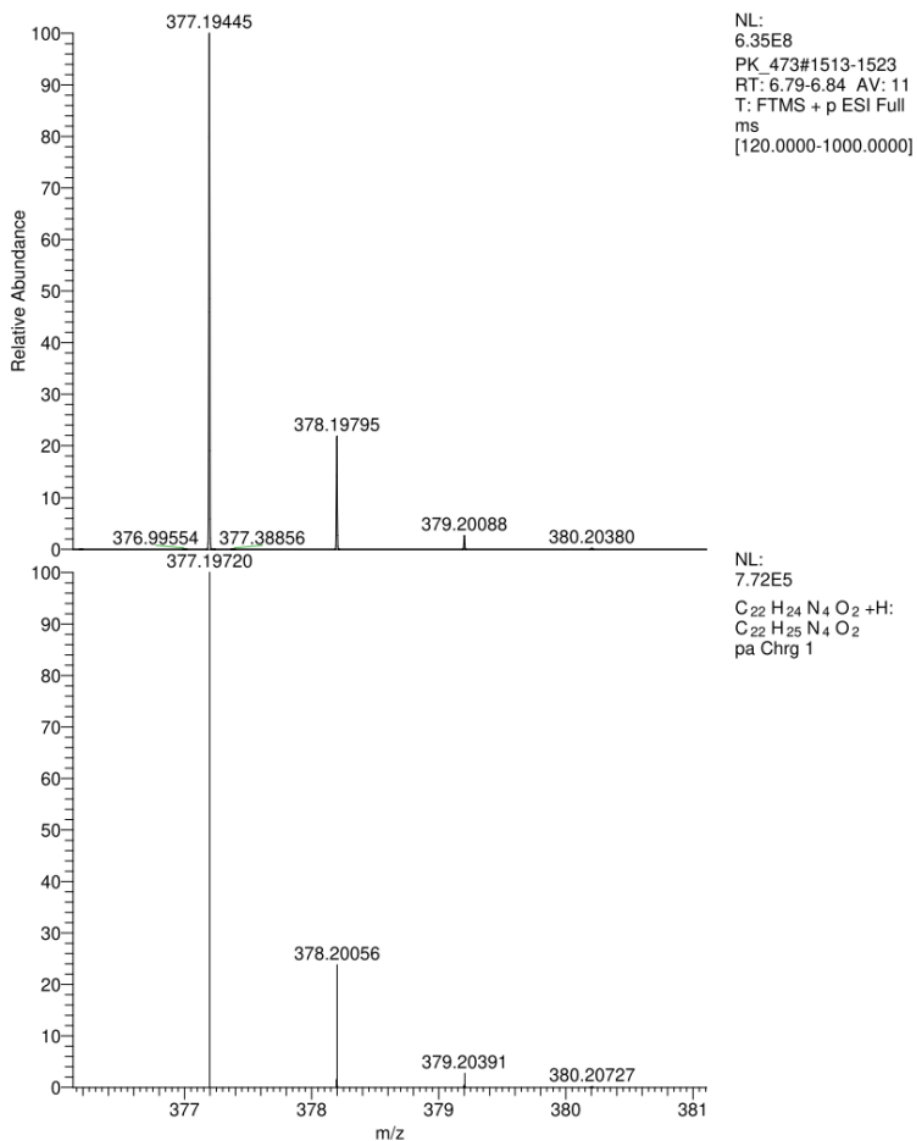
4-(4-(2-((cyclohexylmethyl)amino)phenyl)-1H-1,2,3-triazol-1-yl)benzoic acid



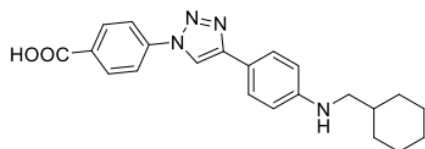
4-(4-(3-((cyclohexylmethyl)amino)phenyl)-1H-1,2,3-triazol-1-yl)benzoic acid (52)



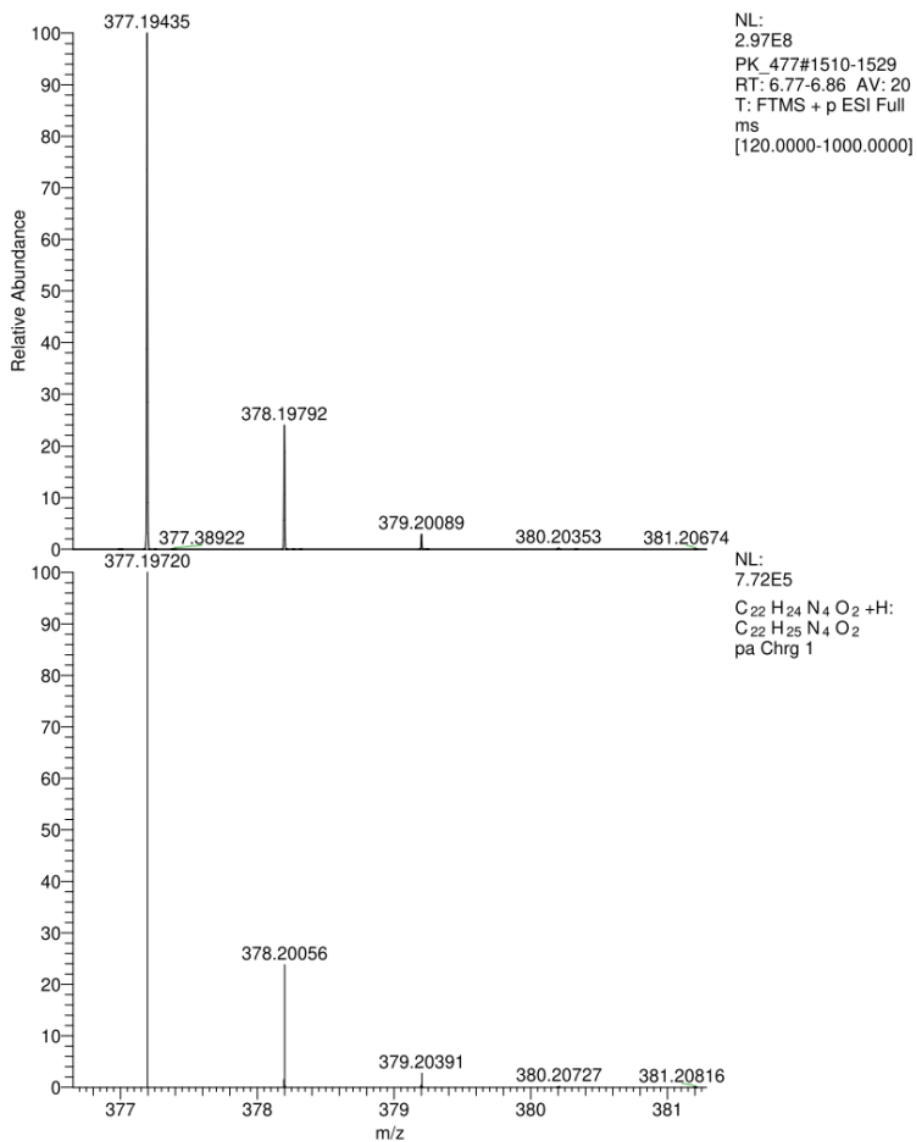
4-(4-(3-((cyclohexylmethyl)amino)phenyl)-1H-1,2,3-triazol-1-yl)benzoic acid



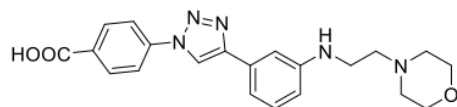
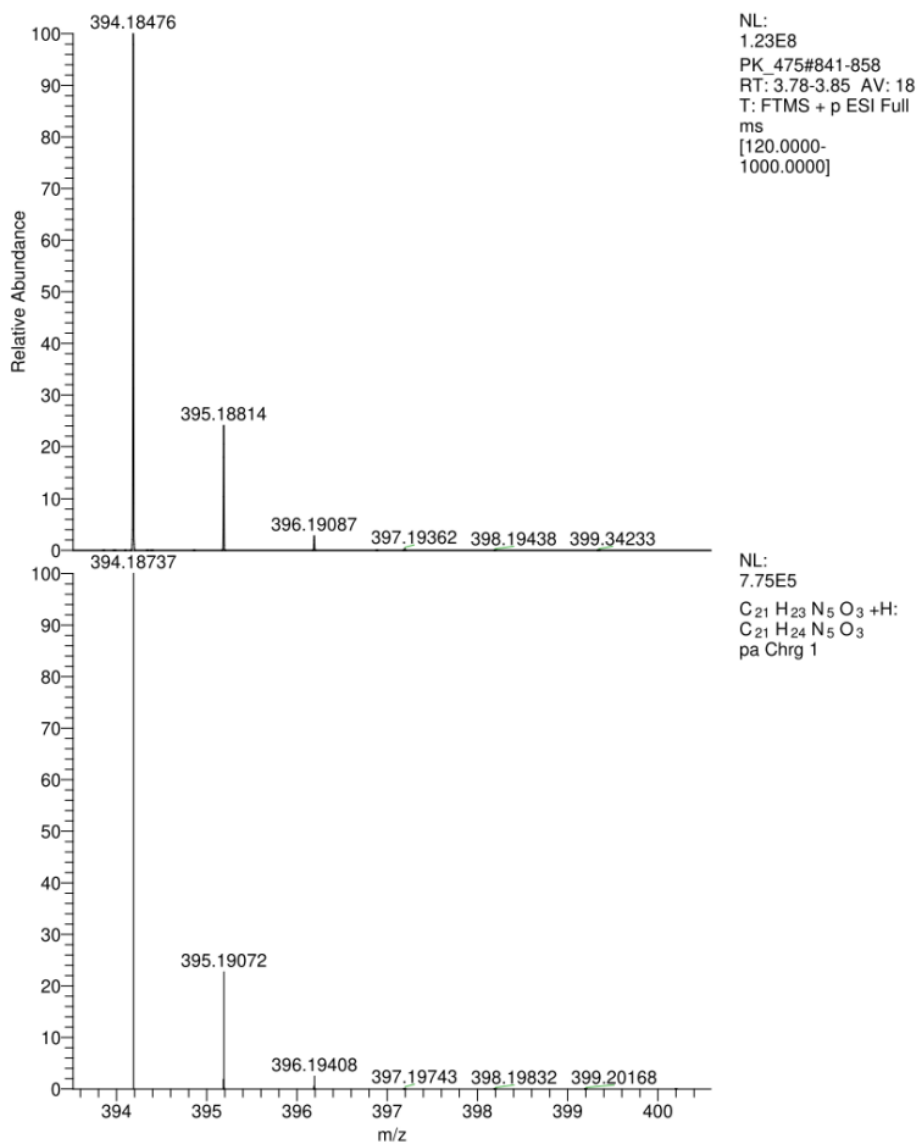
4-(4-(4-((cyclohexylmethyl)amino)phenyl)-1H-1,2,3-triazol-1-yl)benzoic acid (53)

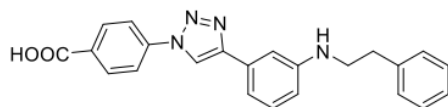


4-(4-(4-((cyclohexylmethyl)amino)phenyl)-1H-1,2,3-triazol-1-yl)benzoic acid

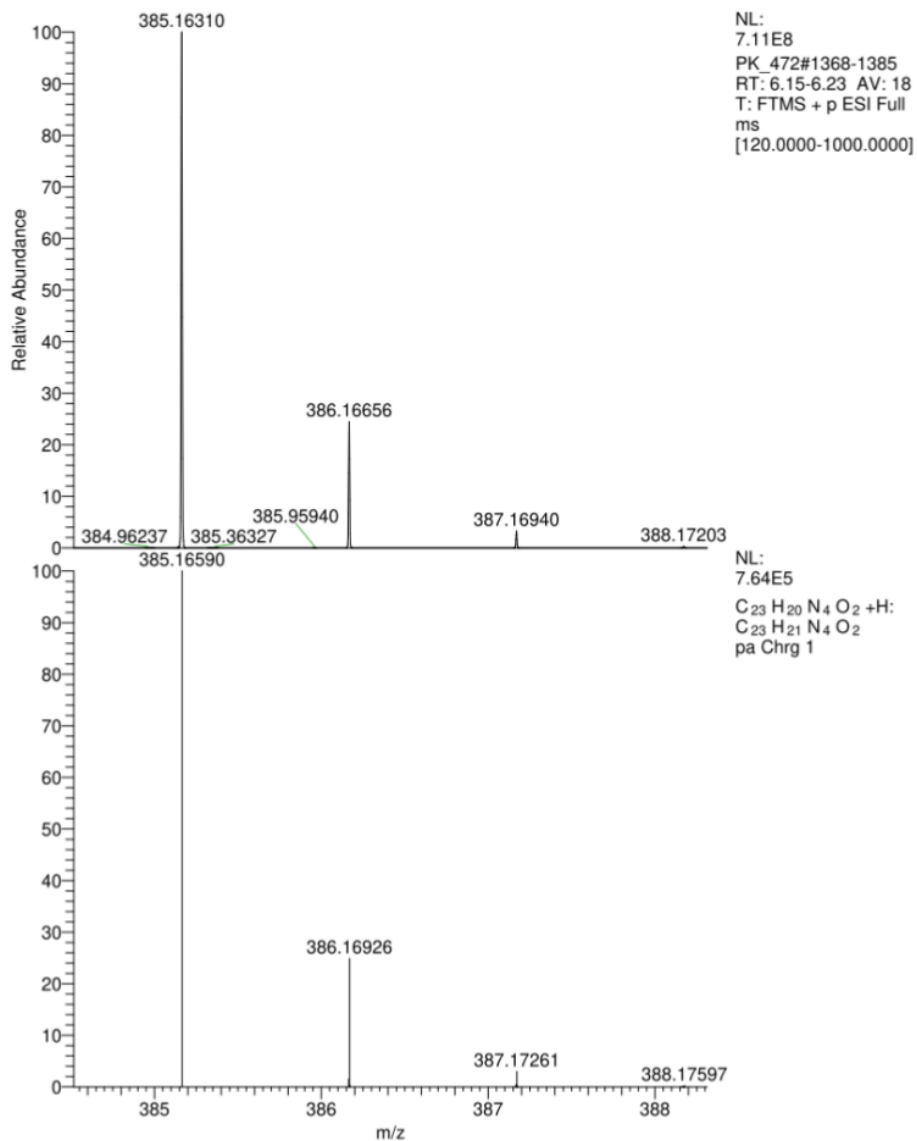


S70

4-(4-(3-((2-Morpholinoethyl)amino)phenyl)-1H-1,2,3-triazol-1-yl)benzoic acid (54)**4-(4-(3-((2-morpholinoethyl)amino)phenyl)-1H-1,2,3-triazol-1-yl)benzoic acid**

4-(4-(3-(Phenethylamino)phenyl)-1H-1,2,3-triazol-1-yl)benzoic acid (55)

4-(4-(3-(phenethylamino)phenyl)-1H-1,2,3-triazol-1-yl)benzoic acid



References

- (1) Hellert, J.; Weidner-Glunde, M.; Krausze, J.; Lünsdorf, H.; Ritter, C.; Schulz, T. F.; Lührs, T. *The 3D structure of kaposi sarcoma herpesvirus LANA C-terminal domain bound to DNA*. *Proc. Natl. Acad. Sci. U. S. A.*, **2015**, *112*, 6694–6699.
- (2) Hellert, J.; Weidner-Glunde, M.; Krausze, J.; Richter, U.; Adler, H.; Fedorov, R.; Pietrek, M.; Rückert, J.; Ritter, C.; Schulz, T. F.; Lührs, T. *A structural basis for BRD2/4-mediated host chromatin interaction and oligomer assembly of kaposi sarcoma-associated herpesvirus and murine gammaherpesvirus LANA proteins*. *PLoS Pathog.*, **2013**, *9*, e1003640.

7.2 Supporting Information Chapter B

Supporting Information

Discovery of Novel Latency-Associated Nuclear Antigen Inhibitors as Antiviral Agents Against Kaposi's Sarcoma-associated Herpesvirus

Philine Kirsch,^{1,†,‡,§} Valentin Jakob,^{1,†,‡,§} Walid A. M. Elgaher,[†] Christine Walt,[†] Kevin Oberhausen,[†] Thomas F. Schulz^{§,||} and Martin Empting^{*,†,‡,§}

[†]Department of Drug Design and Optimization (DDOP), Helmholtz-Institute for Pharmaceutical Research Saarland (HIPS) - Helmholtz Centre for Infection Research (HZI), Campus E8.1, 66123 Saarbrücken, Germany.

[‡]Department of Pharmacy, Saarland University, Campus E8.1, 66123 Saarbrücken, Germany.

[§]German Centre for Infection Research (DZIF), Partner Site Hannover-Braunschweig, 66123 Saarbrücken, Germany.

^{||}Institute of Virology, Hannover Medical School, Carl-Neuberg-Strasse 1, 30625 Hannover, Germany.

Table of Contents

1	Screening Results.....	2
1.1	FP-based competition Screening @ 100 μ M.....	2
1.2	Results of secondary dose-dependent FP-based competition screening.....	3
2	Compound Characterization.....	6
2.1	FP-based concentration-dependent competition assay and IC ₅₀ calculations for hit compounds 1–9	6
2.2	Surface Plasmon Resonance (SPR) Studies.....	11
2.3	SPR responses of compounds 1–9 injected at 100 μ M over immobilized LANA.....	12
2.4	Determination of equilibrium dissociation constant (K_D) for compounds 1, 6 and 9	14
2.5	STD-MNR Spectra for compounds 1, 6 and Inhibitor I.....	16
2.6	Cytotoxicity data for compounds 1, 6 and 9	21
3	References.....	22

1 Screening Results

1.1 FP-based Spot Test Screening @ 100 μ M

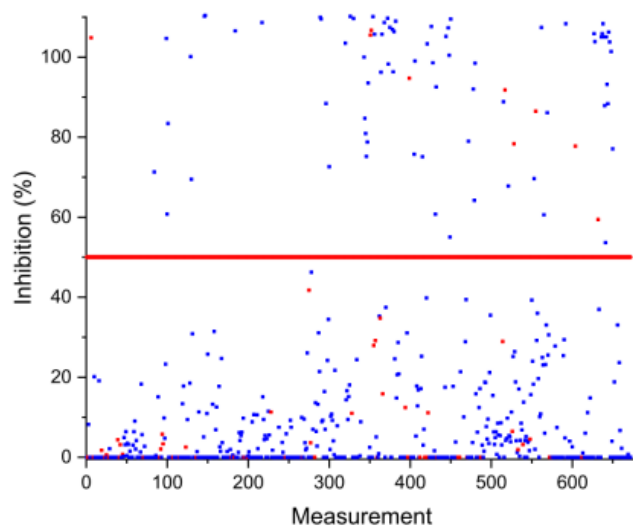


Figure S1: Results of spot test FP-based assay. Compounds were tested at 100 μ M and threshold was set to 50% inhibition. Primary screening resulted in 86 hits with 12.8% hit rate.

1.2 Results of dose-dependent FP-based competition screening

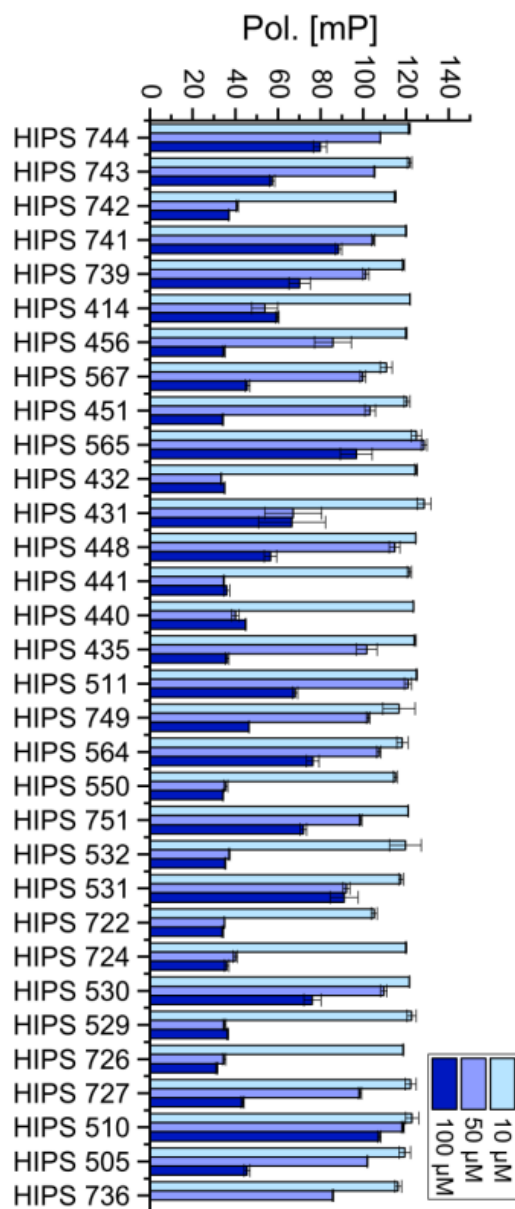


Figure S2: Results of dose-dependent FP-based screening (Class I, Part 1).

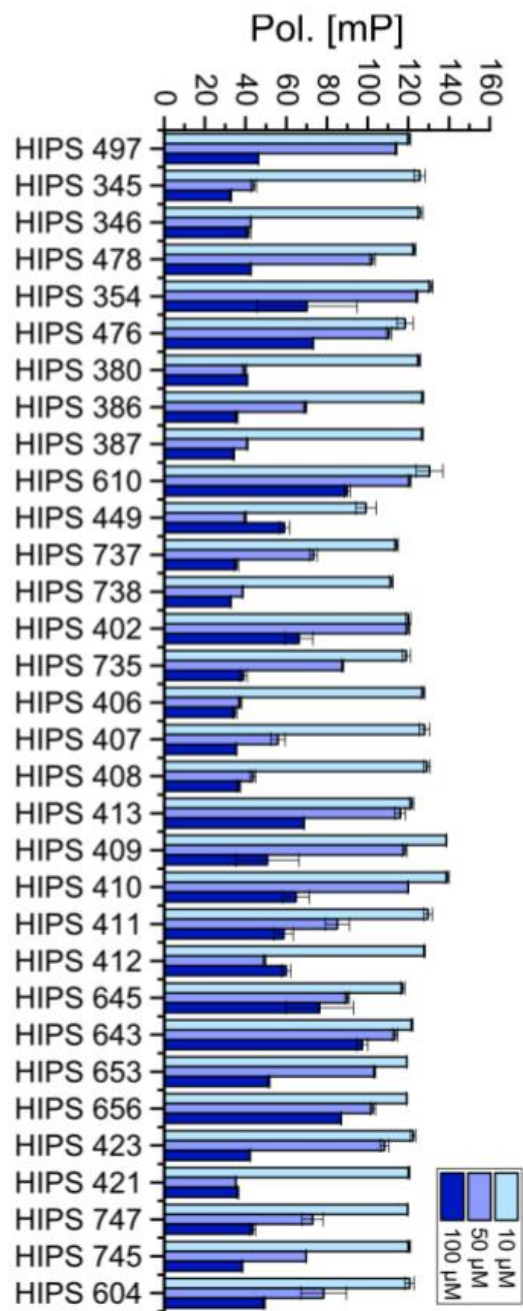


Figure S3: Results of dose-dependent FP-based screening (Class I, Part 2).

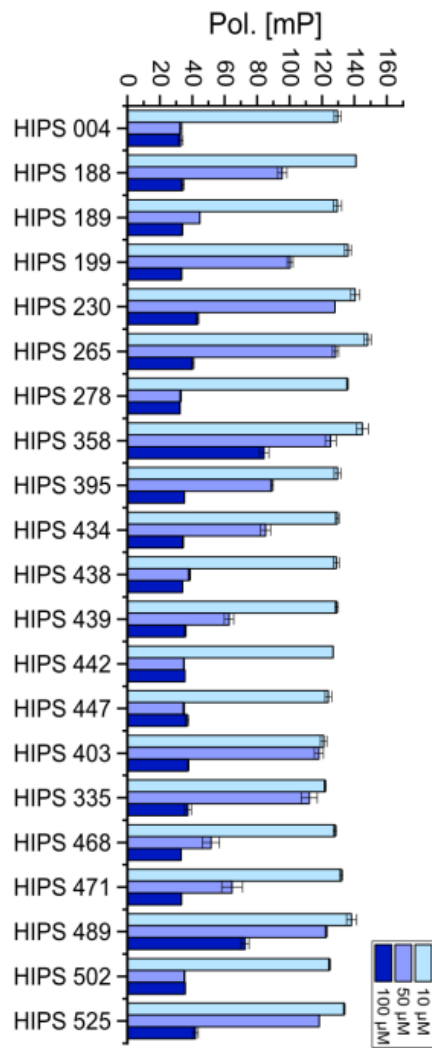


Figure S4: Results of dose-dependent FP-based screening (Class II).

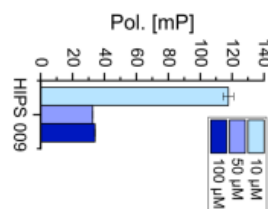


Figure S5: Results of dose-dependent FP-based screening (Class III).

2 Compound Characterization

2.1 FP-based IC₅₀ determination for hit compounds 1–9.

The curves are showing the obtained results for hit compounds **1–9** in the FP-based competition assay using LBS2 as fluorescent probe and His-tagged oligomerization-deficient LANA DBD (aa1008–1146). (1) Compounds were tested in duplicates and in two independent experiments. Curves were based on obtained FP values of duplicates \pm standard deviation. Finally, curves were fit to a four-parameter dose-response model using OriginPro 2018 to calculate IC₅₀ values.

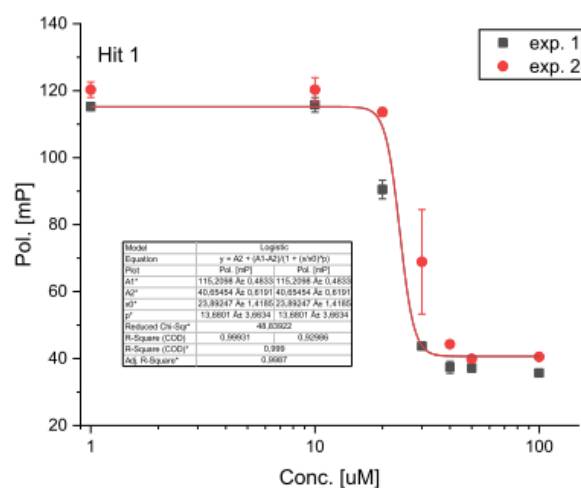


Figure S6: Results of dose-dependent FP-assay for Hit 1.

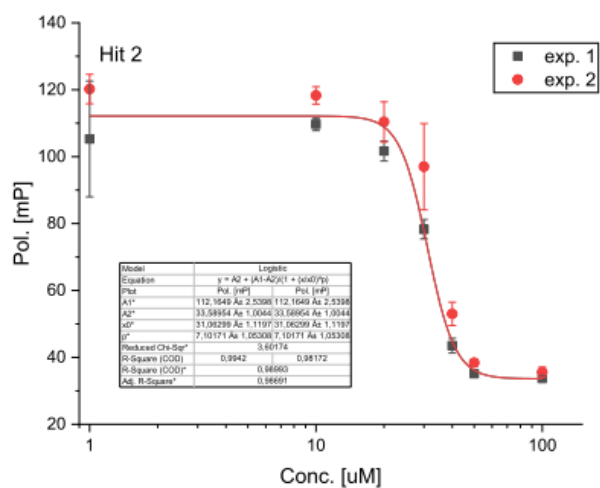


Figure S7: Results of dose-dependent FP-assay for Hit 2.

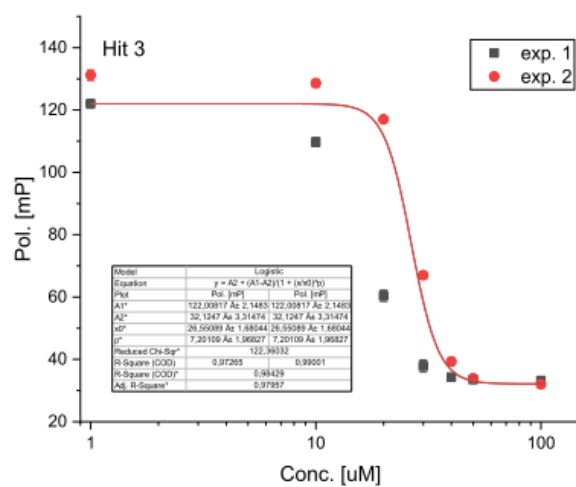


Figure S8: Results of dose-dependent FP-assay for Hit 3.

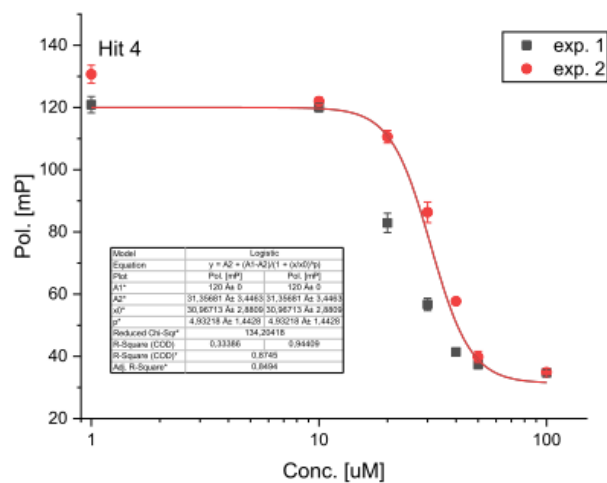


Figure S9: Results of dose-dependent FP-assay for Hit 4.

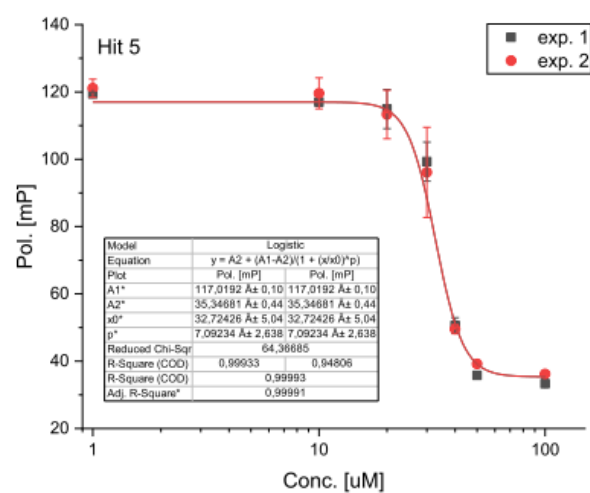


Figure S10: Results of dose-dependent FP-assay for Hit 5.

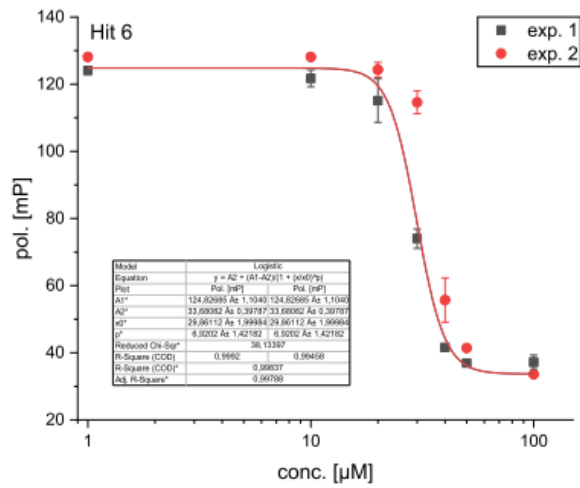


Figure S11: Results of dose-dependent FP-assay for Hit 6.

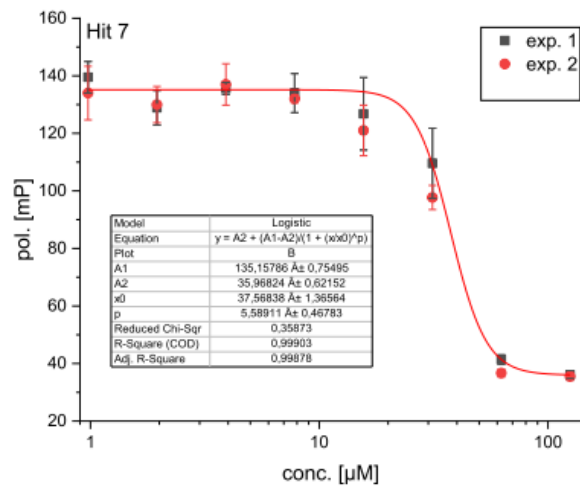


Figure S12: Results of dose-dependent FP-assay for Hit 7.

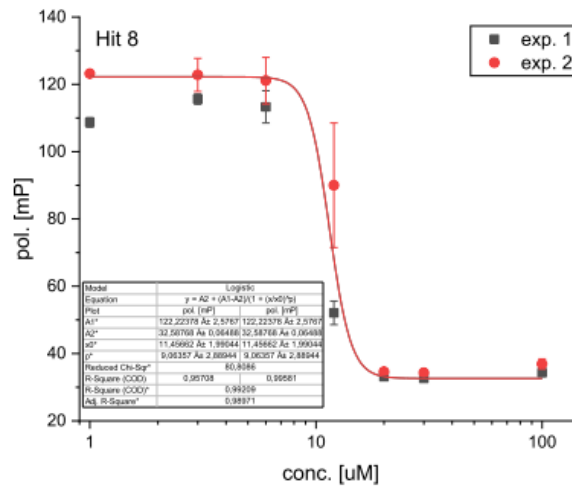


Figure S13: Results of dose-dependent FP-assay for Hit 8.

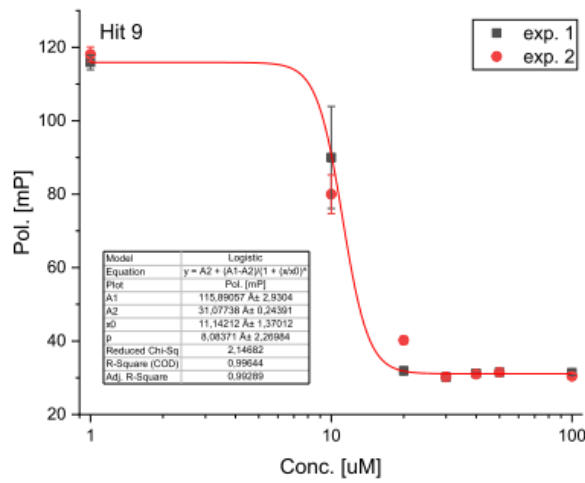


Figure S14: Results of dose-dependent FP-assay for Hit 9.

2.2 Surface Plasmon Resonance (SPR) Studies

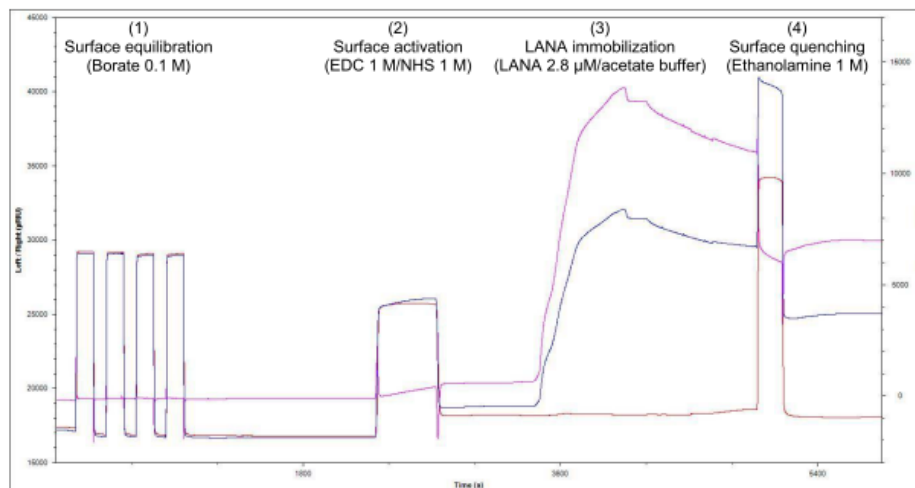


Figure S15: Sensorgram of the immobilization procedure for LANA (1008-1146) DBD mutant on CMD500M sensor chip: (1) Four injections of cleaning solution, (2) activation solution, (3) LANA 1008-1146, and (4) quenching solution. The blue, red, and magenta curves represent the left (active) channel, right (reference) channel, and the difference, respectively.

2.3 SPR responses of compounds 1–9 injected at 100 μ M over immobilized LANA.

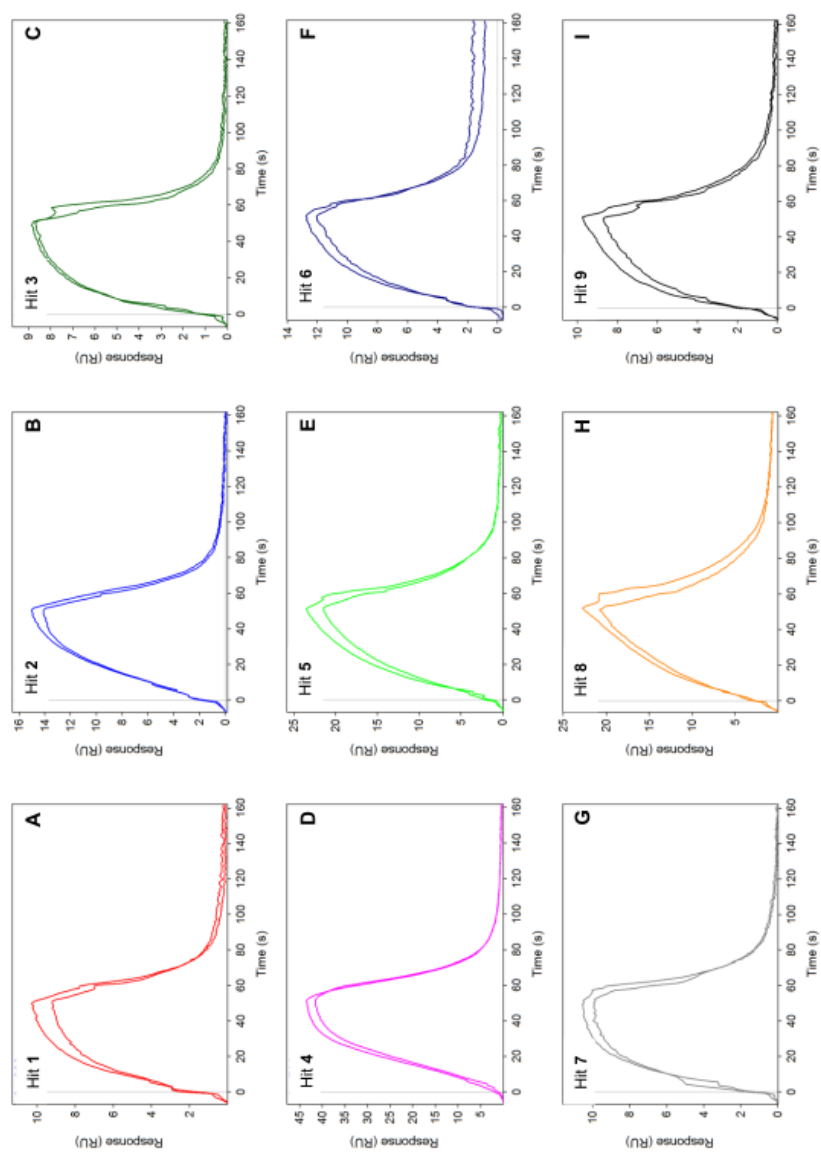


Figure S16: Sensorgrams overlay showing the SPR responses of hit compounds 1–9 injected over an immobilized LANA DBD mutant (Association phase: 60 s and dissociation phase: 120 s). Compounds were tested in two independent experiments at 100 μ M final concentration.

S12

Table S1: SPR response values (RU) of the tested compounds at 100 μ M injected over an immobilized LANA DBD mutant.

Compound	Response (RU)		
	Experiment 1	Experiment 2	Mean \pm standard deviation
1	8.8	10.2	9.5 \pm 0.7
2	13.8	15.0	14.4 \pm 0.6
3	8.5	8.7	8.6 \pm 0.1
4	43.1	41.5	42.3 \pm 0.8
5	21.0	23.3	22.1 \pm 1.2
6	11.6	12.7	12.2 \pm 0.6
7	9.6	10.6	10.1 \pm 0.5
8	20.1	22.2	21.2 \pm 1.1
9	8.4	9.7	9.1 \pm 0.7

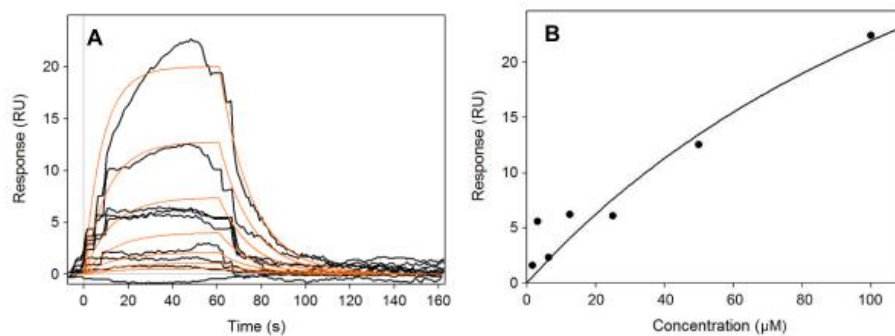
2.4 Determination of equilibrium dissociation constant (K_D) for compounds 1, 6 and 9.

Figure S17: (A) Sensorgrams overlay (black) of **1** at concentrations of 1.6–100.0 μM running over an immobilized LANA DBD mutant. Global fitting of the association and dissociation curves (red); (B) Langmuir binding isotherm (K_D value: $131 \pm 9 \mu\text{M}$).

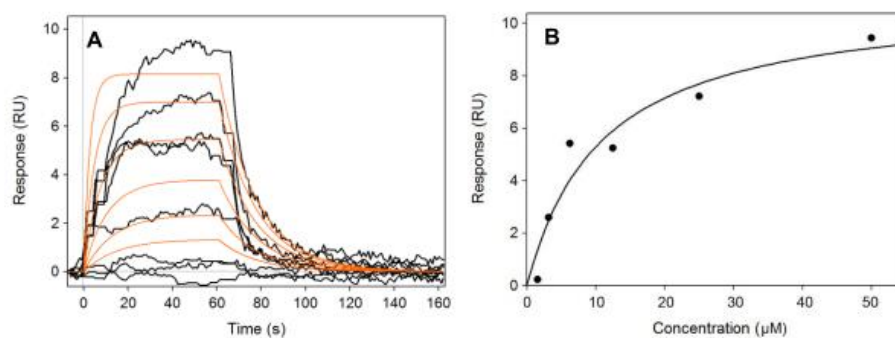


Figure S18: (A) Sensorgrams overlay (black) of **6** at concentrations of 1.6–50.0 μM running over an immobilized LANA DBD mutant. Global fitting of the association and dissociation curves (red); (B) Langmuir binding isotherm (K_D value: $10 \pm 1 \mu\text{M}$).

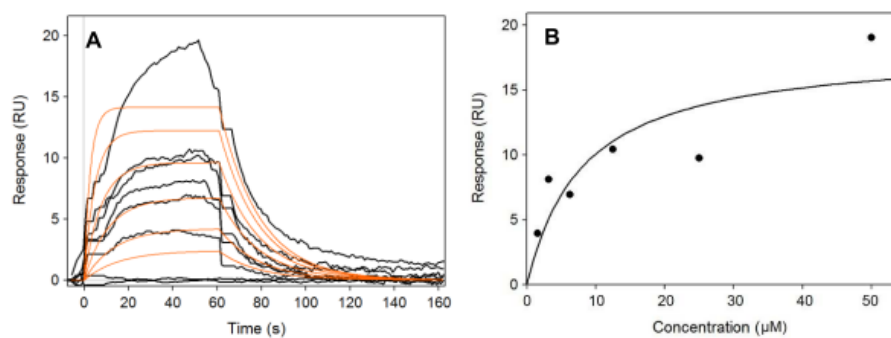


Figure S19: (A) Sensorgrams overlay (black) of **9** at concentrations of 1.6–50.0 μM running over an immobilized LANA DBD mutant. Global fitting of the association and dissociation curves (red); (B) Langmuir binding isotherm (K_D value: $9 \pm 1 \mu\text{M}$).

Table S2: The kinetic parameters of compounds **1**, **6** and **9** binding to LANA.

Compound	R_{max} (RU)	k_{on} ($\text{M}^{-1}\text{s}^{-1}$)	k_{off} (s^{-1})	K_D (μM)	Res sd
1	46 ± 2	$5.2 \pm 0.3 \times 10^2$	0.068 ± 0.002	131.0 ± 9.0	1.5
6	10 ± 1	$6.0 \pm 0.2 \times 10^3$	0.059 ± 0.001	9.9 ± 0.4	0.8
9	17 ± 1	$6.0 \pm 0.3 \times 10^3$	0.055 ± 0.002	9.3 ± 0.4	1.7

R_{max} : maximum analyte binding capacity; k_{on} : association rate constant; k_{off} : dissociation rate constant; K_D : equilibrium dissociation constant; Res sd: residual standard deviation.

2.5 STD-MNR Spectra for compounds 1, 6 and Inhibitor I

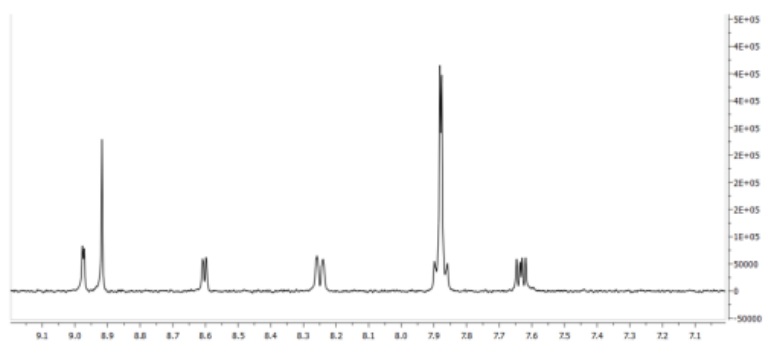


Figure S20: Off resonance NMR spectrum of Inhibitor I at a concentration of 250 μ M.

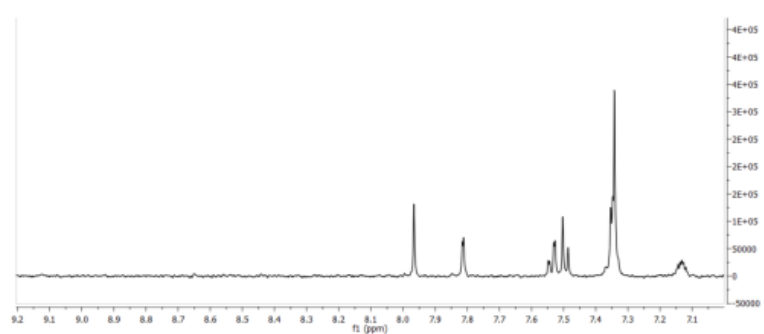


Figure S21: Off resonance NMR spectrum of Hit 1 at a concentration of 250 μ M.

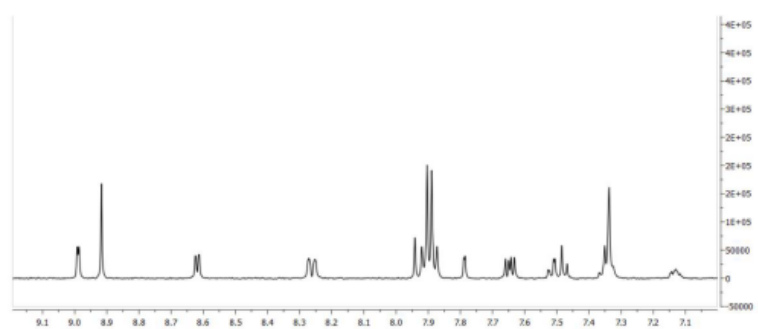


Figure S22: Off resonance NMR spectrum of Inhibitor I mixed with Hit 1, each at a concentration of 250 μ M.

S16

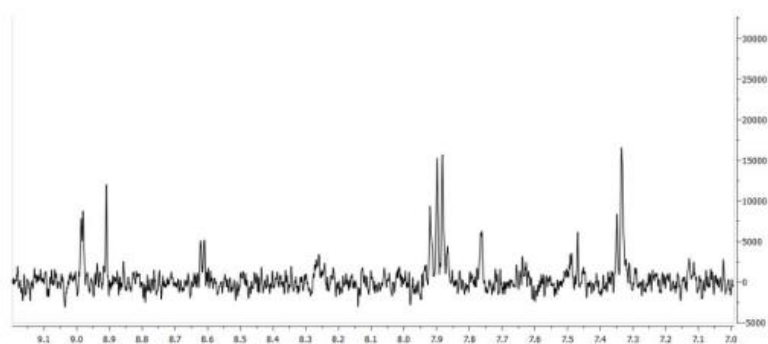


Figure S23: STD-NMR spectrum of Inhibitor I (final concentration of 500 μM) mixed with Hit **1** (final concentration of 250 μM).

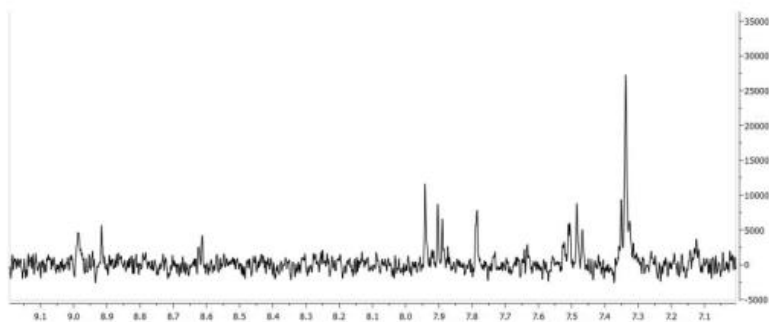


Figure S24: STD-NMR spectrum of Inhibitor I (final concentration of 250 μM) mixed with Hit **1** (final concentration of 250 μM).

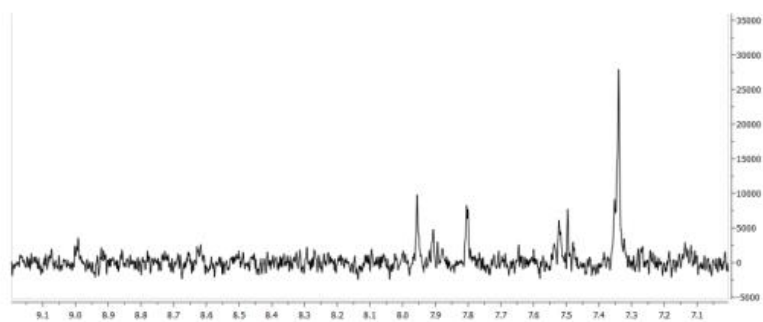


Figure S25: STD-NMR spectrum of Inhibitor I (final concentration of 125 μM) mixed with Hit **1** (final concentration of 250 μM).

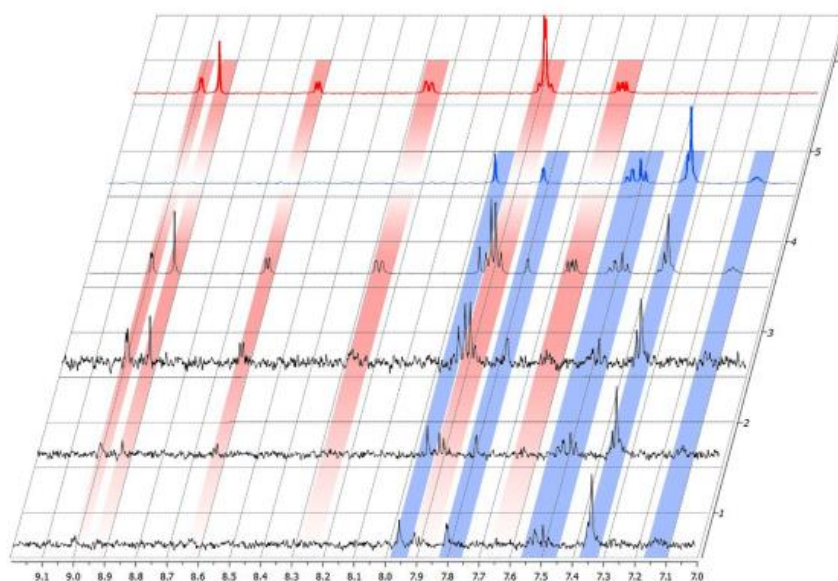


Figure S26: STD-NMR competition experiments with inhibitor **1** and hit **1** in complex with LANA DBD mutant. The respective protons of each compound are highlighted with a corresponding color, Inhibitor **1** in red and Hit **1** in blue; Spectrum 6 (red): off resonance spectrum of Inhibitor **1** with final concentration of 250 μM ; Spectrum 5 (blue): off resonance spectrum of hit **1** with final concentration of 250 μM ; Spectrum 4: off resonance spectrum of Inhibitor **1** mixed with hit **1**, each with a final concentration of 250 μM ; Spectrum 3: STD spectrum of Inhibitor **1** mixed with hit **1**, inhibitor **1** with a final concentration of 500 μM and hit **1** with a final concentration of 250 μM ; Spectrum 2: STD spectrum of Inhibitor **1** mixed with hit **1**, each with a final concentration of 250 μM ; Spectrum 1: STD spectrum of Inhibitor **1** mixed with hit **1**, inhibitor **1** with a final concentration of 125 μM and hit **1** with a final concentration of 250 μM .

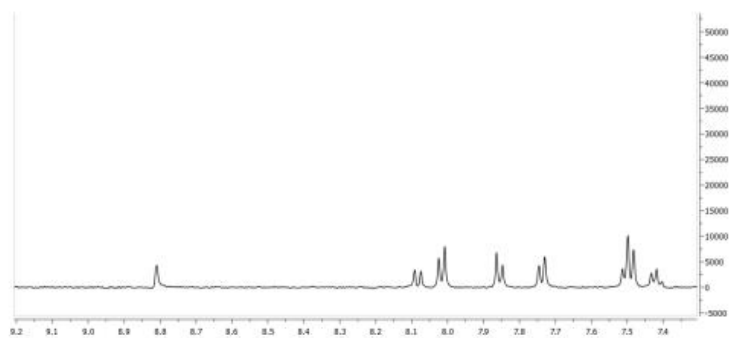


Figure S27: Off resonance NMR spectrum of Hit 6 at a concentration of 250 μM.

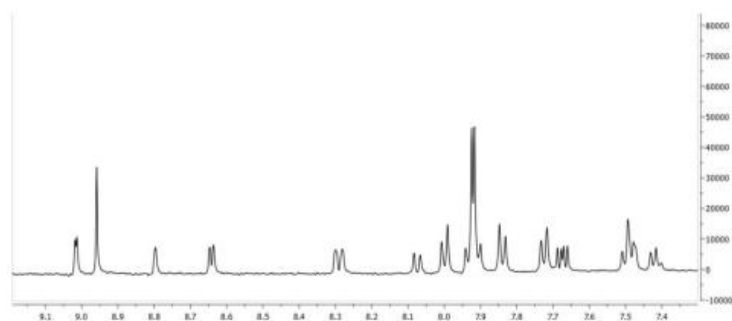


Figure S28: Off resonance NMR spectrum of Inhibitor I mixed with Hit 6, each at a concentration of 250 μM.

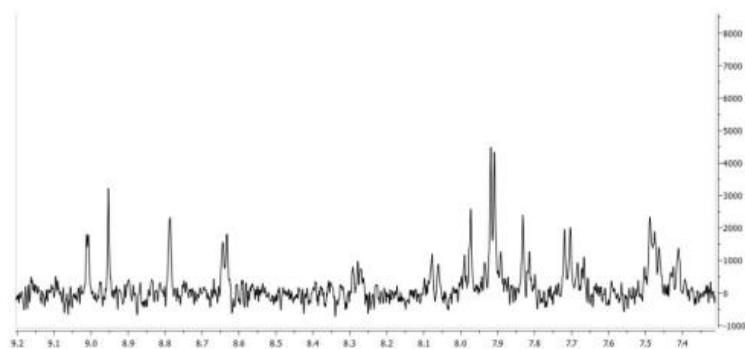


Figure S29: STD-NMR spectrum of Inhibitor I (final concentration of 500 μM) mixed with Hit 6 (final concentration of 250 μM).

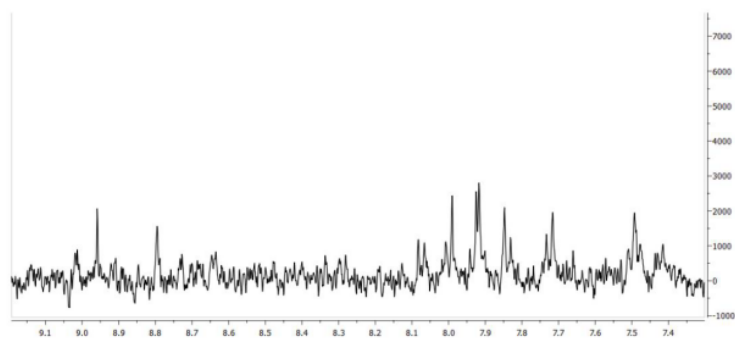


Figure S29: STD-NMR spectrum of Inhibitor I (final concentration of 250 μ M) mixed with Hit 6 (final concentration of 250 μ M).

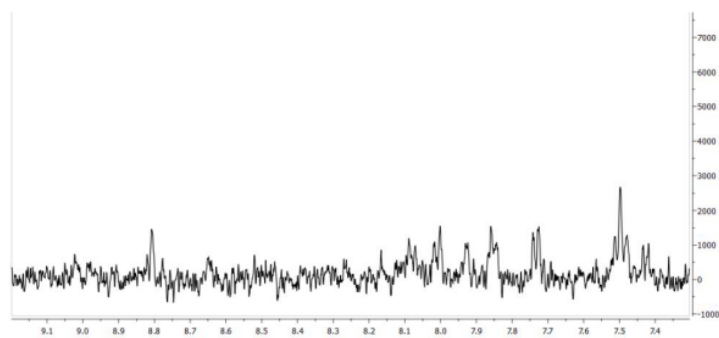


Figure S30: STD-NMR spectrum of Inhibitor I (final concentration of 125 μ M) mixed with Hit 6 (final concentration of 250 μ M).

2.6 Cytotoxicity data for compounds 1, 6 and 9.

Compounds were tested in two independent experiments at a final concentration of 100 μM .

Table S3: Cytotoxicity Assay – HepG2 cells

Compound	Concentration [μM]	HepG2 Relative viability after 48 h [%]	
		Experiment 1	Experiment 2
1	100	84.91	144.76
6	100	155.94	138.43
9	100	27.35	14.59

Table S4: Cytotoxicity Assay – Hek293 cells

Compound	Concentration [μM]	Hek293 Relative viability after 48 h [%]	
		Experiment 1	Experiment 2
1	100	41.66	45.56
6	100	82.55	87.18
9	100	11.15	2.34

3 References

1. Kirsch, P., Jakob, V., Oberhausen, K., Stein, S. C., Cucarro, I., Schulz, T. F., and Empting, M. (2019) Fragment-Based Discovery of a Qualified Hit Targeting the Latency-Associated Nuclear Antigen of the Oncogenic Kaposi's Sarcoma-Associated Herpesvirus/Human Herpesvirus 8, *Journal of medicinal chemistry* 62, 3924–3939.

7.3 Supporting Information Chapter C

Supporting Information

Hit-to-Lead Optimization of a Potent Latency-associated Nuclear Antigen Inhibitor against Kaposi's Sarcoma-associated Herpesvirus Infections

Philine Kirsch,^{1,2,3} Saskia C. Stein,^{3,4} Aylin Berwanger,^{1,2,3} Julia Rinkes,^{1,2,3} Valentin Jakob,^{1,2,3} Thomas F. Schulz^{3,4} and Martin Empting*^{1,2,3}

¹Department of Drug Design and Optimization (DDOP), Helmholtz-Institute for Pharmaceutical Research Saarland (HIPS) - Helmholtz Centre for Infection Research (HZI), Campus E8.1, 66123 Saarbrücken, Germany.

²Department of Pharmacy, Saarland University, Campus E8.1, 66123 Saarbrücken, Germany.

³German Centre for Infection Research (DZIF), Partner Site Hannover-Braunschweig, 66123 Saarbrücken, Germany.

⁴Institute of Virology, Hannover Medical School, Carl-Neuberg-Strasse 1, 30625 Hannover, Germany.

Table of Contents

1	Materials and Methods	1
1.1	Chemistry	1
1.2	Fluorescence Polarization (FP) Assay	19
1.3	Electrophoretic Mobility Shift Assay (EMSA)	21
1.4	¹ H and ¹³ C NMR Spectra and High Resolution Mass Spectrometry (HRMS)	23
2	References	128

1 Materials and Methods

1.1 Chemistry

3-azidopyridine (2): The azide was synthesized according to **GP1** using pyridin-3-amine **1** (376 mg, 4 mmol), sodium nitrite (1.7 eq., 469 mg, 6.8 mmol), sodium azide (1.7 eq., 442 mg, 6.8 mmol), EtOAc (8 mL), 6 M HCl (5 mL). The crude product (245 mg, 2 mmol, 50%) was used as obtained in the next step without further purifications. $R_f = 0.37$ (PE/EtOAc 7:3)

4-(1-(pyridin-3-yl)-1H-1,2,3-triazol-4-yl)benzoic acid (3): The triazole was synthesized according to **GP3** using 4-ethynylbenzoic acid and 3-azidopyridine **2** as described previously.¹

3-(1-(pyridin-3-yl)-1H-1,2,3-triazol-4-yl)benzoic acid (4): The triazole was synthesized according to **GP3** using 3-ethynylbenzoic acid (92 mg, 0.64 mmol) and 3-azidopyridine **2** (1.3 eq., 100 mg, 0.83 mmol) as starting materials. The crude was obtained as a white solid (110 mg, 0.41 mmol, 64%). Purification was done using prep. HPLC. ¹H NMR (500 MHz, DMSO-*d*₆) δ ppm 7.66 (br. s., 1 H) 7.68 - 7.79 (m, 1 H) 7.88 - 8.06 (m, 1 H) 8.19 (d, $J=7.63$ Hz, 1 H) 8.41 (d, $J=8.24$ Hz, 1 H) 8.53 (s., 1 H) 8.76 (s., 1 H) 9.25 (s., 1 H) 9.55 (s., 1 H) 13.23 (br. s., 1 H); ¹³C NMR (126 MHz, DMSO-*d*₆) δ ppm 120.56, 124.96, 127.82, 129.40, 141.24, 146.80, 149.81, 167.30

methyl 4-(1-(pyridin-3-yl)-1H-1,2,3-triazol-4-yl)benzoate (5): The triazole was synthesized according to **GP3** using methyl 4-ethynylbenzoate (103 mg, 0.64 mmol) and 3-azidopyridine **2** (1.3 eq., 100 mg, 0.83 mmol) as starting materials. The crude was obtained as a yellow solid (117 mg, 0.41 mmol, 49%). Purification was done using prep. HPLC. ¹H NMR (500 MHz, DMSO-*d*₆) δ ppm 3.89 (s, 3 H) 7.71 (dd, $J=8.32, 4.81$ Hz, 1 H) 8.01 - 8.18 (m, 4 H) 8.30 - 8.46 (m, 1 H) 8.74 (d, $J=4.12$ Hz, 1 H) 9.21 (br. s., 1 H) 9.56 (s, 1 H); ¹³C NMR (126 MHz, DMSO-*d*₆) δ ppm 52.24, 121.36, 124.72, 125.49, 127.99, 129.18, 130.08, 134.52, 141.33, 146.47, 149.95, 165.89

ethyl 4-(1-(pyridin-3-yl)-1H-1,2,3-triazol-4-yl)benzoate (6): 4-(1-(pyridin-3-yl)-1H-1,2,3-triazol-4-yl) benzoic acid **3** (40 mg, 0.15 mmol) was dissolved in thionyl chloride (1 mL) and a few drops of DMF. The mixture was heated to 60 °C for 1 h. After cooling to room temperature, the solvent was removed under reduced pressure. Subsequently, ice-cold ethanol (5 mL) containing a few drips DIPEA was added slowly at 0 °C and the mixture was stirred at room temperature overnight. The solvent was removed under reduced pressure and EtOAc and sat. aq. NaHCO₃ solution were added. The mixture was extracted with EtOAc (3x), the combined organic layers were dried over sodium sulfate and concentrated under reduced pressure to obtain the crude. The purification was done using automated flash chromatography (DCM/MeOH 1:0 → 9:1). **6** was obtained as white powder (23 mg, 0.08 mmol, 53%). ¹H NMR (500 MHz, DMSO-*d*₆) δ ppm 1.35 (t, $J=7.10$ Hz, 3 H) 4.35 (q, $J=7.17$ Hz, 2 H) 7.71 (dd, $J=8.32, 4.81$ Hz, 1 H) 8.10 (s, 4 H) 8.36 - 8.47 (m, 1 H) 8.74 (dd, $J=4.73, 1.53$ Hz, 1 H) 9.21 (d, $J=2.44$ Hz, 1 H) 9.56 (s, 1 H); ¹³C NMR (126 MHz, DMSO-*d*₆) δ ppm 14.67, 61.32, 121.81, 125.16, 125.93, 128.47, 129.93, 130.49, 133.69, 134.92, 141.81, 146.95, 150.41, 165.85

4-(1-(pyridin-3-yl)-1*H*-1,2,3-triazol-4-yl)benzamide (7): 4-(1-(pyridin-3-yl)-1*H*-1,2,3-triazol-4-yl)benzoic acid **3** (40 mg, 0.15 mmol) was dissolved in thionyl chloride (1 mL) and a few drops of DMF. The mixture was heated to 60 °C for 1 h. After cooling to room temperature, the solvent was removed under reduced pressure. Subsequently, ice-cold aqueous ammonium hydroxide (5 mL) was added slowly at 0 °C and the mixture was stirred at room temperature overnight. DCM and water were added. The mixture was extracted with DCM (3x), the combined organic layers were dried over sodium sulfate and concentrated under reduced pressure to obtain the crude. The purification was done using automated flash chromatography (DCM/MeOH 1:0 → 8:2). **7** was obtained as white powder (10 mg, 0.04 mmol, 27%). ¹H NMR (500 MHz, DMSO-*d*₆) δ ppm 7.44 (br. s., 1 H) 7.72 (dd, *J*=8.01, 4.35 Hz, 1 H) 8.02 (s, 4 H) 8.39 (d, *J*=8.09 Hz, 1 H) 8.76 (br. s., 1 H) 9.23 (br. s., 1 H) 9.50 (s, 1 H); ¹³C NMR (126 MHz, DMSO-*d*₆) δ ppm 120.86, 125.05, 127.93, 128.34, 132.59, 133.93, 141.31, 146.83, 149.87, 167.36

methyl 2-chloro-4-(1-(pyridin-3-yl)-1*H*-1,2,3-triazol-4-yl)benzoate (8): The triazole was synthesized according to **GP3** using methyl 2-chloro-4-ethynylbenzoate (62 mg, 0.32 mmol) and 3-azidopyridine **2** (1.3 eq., 50 mg, 0.41 mmol) as starting materials. Purification was done using flash chromatography (DCM:MeOH 1:0 → 9:1) and **8** was obtained as a white solid (81 mg, 0.26 mmol, 81%). ¹H NMR (500 MHz, DMSO-*d*₆) δ ppm 3.89 (s, 3 H) 7.72 (ddd, *J*=8.28, 4.77, 0.69 Hz, 1 H) 8.00 (d, *J*=8.09 Hz, 1 H) 8.02 - 8.07 (m, 1 H) 8.12 (d, *J*=1.53 Hz, 1 H) 8.38 (ddd, *J*=8.28, 2.63, 1.45 Hz, 1 H) 8.75 (dd, *J*=4.73, 1.37 Hz, 1 H) 9.19 (d, *J*=2.59 Hz, 1 H) 9.61 (s, 1 H); ¹³C NMR (126 MHz, DMSO-*d*₆) δ ppm 52.59, 121.91, 123.82, 124.72, 127.09, 128.00, 128.97, 132.26, 132.93, 133.13, 134.66, 141.31, 145.18, 150.04, 165.01

2-chloro-4-(1-(pyridin-3-yl)-1*H*-1,2,3-triazol-4-yl)benzoic acid (9): The synthesis was done according to **GP5** using methyl 2-chloro-4-(1-(pyridin-3-yl)-1*H*-1,2,3-triazol-4-yl)benzoate **8** (10 mg, 0.03 mmol) at 80 °C for 1 h. **9** was obtained as a white solid (5 mg, 0.02 mmol, 66%). ¹H NMR (500 MHz, DMSO-*d*₆) δ ppm 7.72 (dd, *J*=8.32, 4.81 Hz, 1 H) 7.88 - 8.03 (m, 2 H) 8.09 (d, *J*=1.37 Hz, 1 H) 8.38 (ddd, *J*=8.28, 2.63, 1.45 Hz, 1 H) 8.75 (dd, *J*=4.65, 1.30 Hz, 1 H) 9.19 (d, *J*=2.44 Hz, 1 H) 9.59 (s, 1 H) 13.53 (br. s., 1 H); ¹³C NMR (126 MHz, DMSO-*d*₆) δ ppm 122.18, 124.19, 125.20, 127.45, 128.47, 132.49, 133.63, 140.89, 141.79, 145.82, 150.48, 166.72

(4-(1-(pyridin-3-yl)-1*H*-1,2,3-triazol-4-yl)phenyl)methanol (10): The triazole was synthesized according to **GP3** using (4-ethynylphenyl)methanol (300 mg, 2.27 mmol) and 3-azidopyridine **2** (1.2 eq., 326 mg, 2.72 mmol) as starting materials. The crude was obtained as a yellow solid (466 mg, 1.86 mmol, 82%). Purification was done using prep. HPLC. ¹H NMR (500 MHz, DMSO-*d*₆) δ ppm 4.55 (d, *J*=5.65 Hz, 2 H) 5.26 (t, *J*=5.72 Hz, 1 H) 7.46 (m, *J*=8.24 Hz, 2 H) 7.70 (dd, *J*=8.24, 4.73 Hz, 1 H) 7.90 (m, *J*=8.09 Hz, 2 H) 8.36 - 8.42 (m, 1 H) 8.72 (dd, *J*=4.73, 1.22 Hz, 1 H) 9.20 (d, *J*=2.44 Hz, 1 H) 9.36 (s, 1 H); ¹³C NMR (126 MHz, DMSO-*d*₆) δ ppm 62.62, 119.74, 124.66, 125.16, 127.04, 127.83, 128.40, 133.32, 141.21, 142.88, 147.58, 149.72

4-(1-(pyridin-3-yl)-1*H*-1,2,3-triazol-4-yl)aniline (11): The triazole was synthesized according to **GP3** using 4-ethynylaniline (75 mg, 0.64 mmol) and 3-azidopyridine **2** (1.3 eq., 100 mg, 0.83 mmol) as starting materials. After full conversion (LCMS control) the mixture was basified with sat. aq. NaHCO₃ solution and the product was precipitated. The crude was obtained as a brown solid (91 mg, 0.38 mmol, 60%). Purification was done using prep. HPLC. ¹H NMR (500 MHz, DMSO-*d*₆) δ ppm 5.35 (s, 2 H) 6.62 - 6.69 (m, 2 H) 7.56 - 7.62 (m, 2 H) 7.68 (dd, *J*=8.09, 4.58 Hz, 1 H) 8.32 - 8.38 (m, 1 H) 8.72 (br.

s., 1 H) 9.09 (s, 1 H) 9.20 (br. s., 1 H); ^{13}C NMR (126 MHz, $\text{DMSO-}d_6$) δ 113.95, 117.36, 117.43, 126.46, 127.50, 140.99, 148.62, 149.16, 149.43

***N*-(4-(1-(pyridin-3-yl)-1*H*-1,2,3-triazol-4-yl)phenyl)acetamide (12)**: 4-(1-(pyridin-3-yl)-1*H*-1,2,3-triazol-4-yl) aniline **11** (35 mg, 0.14 mmol) and triethylamine (2 eq., 0.28 mmol, 28 mg) were dissolved in a mixture of DCM (2 mL) and DMF (1 mL). Acetyl chloride (1.2 eq., 0.17 mmol, 13 mg) was added slowly at room temperature and the mixture was stirred for 16 h. TLC control indicated full conversion and the solvent was removed under reduced pressure to obtain the crude. Purification was done using automated flash chromatography (DCM/MeOH 1:0 \rightarrow 9:1) to obtain **12** (5 mg, 0.02 mmol, 14%). ^1H NMR (500 MHz, $\text{DMSO-}d_6$) δ ppm 2.07 (s, 3 H) 7.61 - 7.78 (m, 3 H) 7.81 - 7.92 (m, 2 H) 8.32 - 8.41 (m, 1 H) 8.72 (dd, $J=4.73, 1.22$ Hz, 1 H) 9.19 (d, $J=2.44$ Hz, 1 H) 9.30 (s, 1 H) 10.10 (s, 1 H); ^{13}C NMR (126 MHz, $\text{DMSO-}d_6$) δ ppm 24.08, 119.29, 124.67, 125.88, 127.80, 133.34, 139.50, 141.19, 147.47, 149.72, 168.50

4-(1-(pyridin-3-yl)-1*H*-1,2,3-triazol-4-yl)benzonitrile (13): The triazole was synthesized according to **GP3** using 4-ethynylbenzonitrile (80 mg, 0.63 mmol) and 3-azidopyridine **2** (1.2 eq., 90 mg, 0.75 mmol) as starting materials. The crude was obtained as a yellow solid (100 mg, 0.40 mmol, 64%). Purification was done using prep. HPLC. ^1H NMR (500 MHz, $\text{DMSO-}d_6$) δ ppm 7.72 (dd, $J=8.24, 4.73$ Hz, 1 H) 8.01 (d, $J=8.39$ Hz, 2 H) 8.08 - 8.17 (m, 2 H) 8.35 - 8.44 (m, 1 H) 8.75 (d, $J=4.27$ Hz, 1 H) 9.19 (br. s., 1 H) 9.59 (s, 1 H); ^{13}C NMR (126 MHz, $\text{DMSO-}d_6$) δ ppm 110.67, 118.75, 121.84, 124.72, 125.93, 128.09, 133.16, 133.21, 134.48, 141.40, 145.93, 150.04

3-(azidomethyl)pyridine (15): To a solution of 3-(bromomethyl)pyridine **14** (200 mg, 1.17 mmol) in DMSO (5 mL), Et_3N (0.1 mL) and NaN_3 (1.1 eq., 84 mg, 1.29 mmol) were added. The mixture was stirred over night at room temperature, diluted with water and extracted with diethyl ether (3x). The combined organic layers were washed with brine, dried over MgSO_4 and concentrated under reduced pressure. The product was obtained as a colorless oil (123 mg, 0.92 mmol, 78%) and was used without further purification. $R_f = 0.36$ (PE/EtOAc 9:1)

4-(1-(pyridin-3-ylmethyl)-1*H*-1,2,3-triazol-4-yl)benzoic acid (16): The triazole was synthesized according to **GP3** using 4-ethynylbenzoic acid (50 mg, 0.31 mmol) and 3-(azidomethyl)pyridine **15** (1.3 eq., 53 mg, 0.40 mmol) as starting materials. The crude was obtained as a yellow solid (42 mg, 0.15 mmol, 51%). Purification was done using prep. HPLC. ^1H NMR (500 MHz, $\text{DMSO-}d_6$) δ ppm 5.88 (s, 2 H) 7.86 (br. s., 1 H) 7.94 - 7.99 (m, 3 H) 8.00 - 8.04 (m, 2 H) 8.27 (d, $J=7.93$ Hz, 1 H) 8.81 (s., 1 H) 8.85 (s, 1 H) 8.93 (s., 1 H); ^{13}C NMR (126 MHz, $\text{DMSO-}d_6$) δ ppm 49.95, 123.11, 125.14, 126.11, 130.02, 130.06, 133.89, 134.56, 142.03, 144.60, 144.82, 145.84, 166.96

3-azido-4-methylpyridine (18a): The azide was synthesized according to **GP1** using 4-methylpyridin-3-amine **17a** (150 mg, 1.4 mmol), sodium nitrite (1.7 eq., 165 mg, 2.4 mmol), sodium azide (1.7 eq., 155 mg, 2.4 mmol), EtOAc (4 mL), 6 M HCl (2.4 mL). The crude product (120 mg, 0.89 mmol, 64%) was used as obtained in the next step without further purifications. $R_f = 0.35$ (PE/EtOAc 7:3)

3-azido-4-chloropyridine (18b): The azide was synthesized according to **GP1** using 4-chloropyridin-3-amine **17b** (200 mg, 1.56 mmol), sodium nitrite (1.7 eq., 182 mg, 2.65 mmol), sodium azide (1.7 eq.,

172 mg, 2.65 mmol), EtOAc (8 mL), 6 M HCl (4.8 mL). The crude product (120 mg, 0.77 mmol, 50%) was used as obtained in the next step without further purifications. $R_f = 0.71$ (PE/EtOAc 7:3)

3-azido-4-phenylpyridine (18c): The azide was synthesized according to **GPI** using 4-phenylpyridin-3-amine **17c** (100 mg, 0.48 mmol), sodium nitrite (1.7 eq., 57 mg, 0.82 mmol), sodium azide (1.7 eq., 53 mg, 0.82 mmol), EtOAc (4 mL), 6 M HCl (2.4 mL). The crude product (92 mg, 0.47 mmol, 98%) was used as obtained in the next step without further purifications. $R_f = 0.44$ (PE/EtOAc 7:3)

3-azido-5-methylpyridine (18d): The azide was synthesized according to **GPI** using 5-methylpyridin-3-amine **17d** (150 mg, 1.4 mmol), sodium nitrite (1.7 eq., 165 mg, 2.4 mmol), sodium azide (1.7 eq., 155 mg, 2.4 mmol), EtOAc (4 mL), 6 M HCl (2.4 mL). The crude product (141 mg, 1.05 mmol, 75%) was used as obtained in the next step without further purifications. $R_f = 0.35$ (PE/EtOAc 7:3)

5-azidopicolonitrile (18e): The azide was synthesized according to **GPI** using 5-aminopicolonitrile **17e** (100 mg, 0.84 mmol), sodium nitrite (1.7 eq., 98 mg, 1.43 mmol), sodium azide (1.7 eq., 93 mg, 1.43 mmol), EtOAc (4 mL), 6 M HCl (1.2 mL). The crude product (107 mg, 0.74 mmol, 88%) was used as obtained in the next step without further purifications. $R_f = 0.69$ (PE/EtOAc 7:3)

5-azido-2-chloro-4-methylpyridine (18f): The azide was synthesized according to **GPI** using 6-chloro-4-methylpyridin-3-amine **17f** (200 mg, 1.41 mmol), sodium nitrite (1.7 eq., 165 mg, 2.40 mmol), sodium azide (1.7 eq., 155 mg, 2.40 mmol), EtOAc (8 mL), 6 M HCl (4.8 mL). The crude product (190 mg, 1.13 mmol, 80%) was used as obtained in the next step without further purifications. $R_f = 0.82$ (PE/EtOAc 7:3)

5-azido-N-methylpyridin-2-amine (18g): The azide was synthesized according to **GPI** using *N*²-methylpyridine-2,5-diamine **17g** (200 mg, 1.62 mmol), sodium nitrite (1.7 eq., 2.75 mmol, 190 mg), sodium azide (1.7 eq., 2.75 mmol, 181 mg), EtOAc (13 mL), 6 M HCl (7 mL). The crude product (234 mg, 1.57 mmol, 97%) was used as obtained in the next step without further purifications. $R_f = 0.46$ (PE/EtOAc 7:3)

5-azido-N-isopropylpyridin-2-amine (18h): The azide was synthesized according to **GPI** using *N*²-isopropylpyridine-2,5-diamine **17h** (300 mg, 1.98 mmol), sodium nitrite (1.7 eq., 3.36 mmol, 231 mg), sodium azide (1.7 eq., 3.36 mmol, 221 mg), EtOAc (10 mL), 6 M HCl (5 mL). The crude product (308 mg, 1.78 mmol, 90%) was used as obtained in the next step without further purifications. $R_f = 0.75$ (PE/EtOAc 7:3)

5-azido-N-phenylpyridin-2-amine (18i): The azide was synthesized according to **GPI** using *N*²-phenylpyridine-2,5-diamine **17i** (200 mg, 1.08 mmol), sodium nitrite (1.7 eq., 1.84 mmol, 126 mg), sodium azide (1.7 eq., 1.84 mmol, 121 mg), EtOAc (6 mL), 6 M HCl (2.5 mL). The crude product (203 mg, 0.96 mmol, 89%) was used as obtained in the next step without further purifications. $R_f = 0.78$ (PE/EtOAc 7:3)

3-azido-5-fluoropyridine (18j): The azide was synthesized according to **GP1** using 5-fluoropyridin-3-amine (100 mg, 0.91 mmol) **17j** (100 mg, 0.91 mmol), sodium nitrite (1.7 eq., 1.54 mmol, 105 mg), sodium azide (1.7 eq., 1.84 mmol, 101 mg), EtOAc (3 mL), 6 M HCl (1.25 mL). The crude product (37 mg, 0.27 mmol, 30%) was used as obtained in the next step without further purifications. $R_f = 0.54$ (PE/EtOAc 7:3)

5-azido-2-methoxypyridine (18k): The azide was synthesized according to **GP1** using 6-methoxypyridin-3-amine **17k** (100 mg, 0.81 mmol), sodium nitrite (1.7 eq., 94 mg, 1.37 mmol), sodium azide (1.7 eq., 88 mg, 1.37 mmol), EtOAc (4 mL), 6 M HCl (2.4 mL). The crude product (110 mg, 0.73 mmol, 90%) was used as obtained in the next step without further purifications. $R_f = 0.77$ (PE/EtOAc 7:3)

5-azido-2-phenoxy pyridine (18l): The azide was synthesized according to **GP1** using 6-phenoxy pyridin-3-amine **17l** (180 mg, 0.97 mmol), sodium nitrite (1.7 eq., 1.14 mmol, 77 mg), sodium azide (1.7 eq., 1.14 mmol, 74 mg), EtOAc (3 mL), 6 M HCl (6 mL). The crude product (150 mg, 0.70 mmol, 72%) was used as obtained in the next step without further purifications. $R_f = 0.85$ (PE/EtOAc 6:4)

1-azido-4-phenoxybenzene (18m): The azide was synthesized according to **GP1** using 4-phenoxyaniline **17m** (100 mg, 0.54 mmol), sodium nitrite (1.7 eq., 0.91 mmol, 61 mg), sodium azide (1.7 eq., 1.82 mmol, 58 mg), EtOAc (4 mL), 6 M HCl (7 mL). The crude product (90 mg, 0.45 mmol, 83%) was used as obtained in the next step without further purifications. $R_f = 0.43$ (PE/EtOAc 7:3)

3-(4-azidophenoxy) pyridine (18n): The azide was synthesized according to **GP1** using 4-(pyridin-3-yloxy) aniline **17n** (200 mg, 1.07 mmol), sodium nitrite (1.7 eq., 1.82 mmol, 125 mg), sodium azide (1.7 eq., 1.82 mmol, 118 mg), EtOAc (5 mL), 6 M HCl (10 mL). The crude product (190 mg, 0.89 mmol, 83%) was used as obtained in the next step without further purifications. $R_f = 0.35$ (PE/EtOAc 7:3)

4-(1-(4-methylpyridin-3-yl)-1H-1,2,3-triazol-4-yl)benzoic acid (19a): The triazole was synthesized according to **GP3** using 4-ethynylbenzoic acid (118 mg, 0.81 mmol) and 3-azido-4-methylpyridine **18a** (1.3 eq., 141 mg, 1.05 mmol) as starting materials. The crude was obtained as a white solid (45 mg, 0.16 mmol, 20%). Purification was done using prep. HPLC. $^1\text{H NMR}$ (500 MHz, $\text{DMSO-}d_6$) δ ppm 2.32 (s, 3 H) 7.60 (d, $J=5.04$ Hz, 1 H) 8.07 (s, 5 H) 8.66 (d, $J=4.73$ Hz, 1 H) 8.73 (s, 1 H) 9.20 (s, 1 H) 13.04 (br. s., 1 H); $^{13}\text{C NMR}$ (126 MHz, $\text{DMSO-}d_6$) δ ppm 17.05, 124.45, 125.32, 126.25, 130.13, 130.26, 134.27, 142.44, 145.87, 145.97, 150.53, 166.96

4-(1-(4-chloropyridin-3-yl)-1H-1,2,3-triazol-4-yl)benzoic acid (19b): The triazole was synthesized according to **GP3** using 4-ethynylbenzoic acid (83 mg, 0.56 mmol) and 3-azido-4-chloropyridine **18b** (1.3 eq., 114 mg, 0.74 mmol) as starting materials. The crude was obtained as a yellow solid (40 mg, 0.13 mmol, 23%). Purification was done using prep. HPLC. $^1\text{H NMR}$ (500 MHz, $\text{DMSO-}d_6$) δ ppm 7.97 (dd, $J=4.96, 4.20$ Hz, 1 H) 8.02 - 8.18 (m, 4 H) 8.71 - 8.89 (m, 1 H) 8.98 (br. s., 1 H) 9.27 (d, $J=3.97$ Hz, 1 H) 13.11 (br. s., 1 H); $^{13}\text{C NMR}$ (126 MHz, $\text{DMSO-}d_6$) δ ppm 124.96, 125.39, 125.51, 130.17, 131.55, 133.82, 138.59, 145.98, 148.18, 152.25, 167.01

4-(1-(4-phenylpyridin-3-yl)-1H-1,2,3-triazol-4-yl)benzoic acid (19c): The triazole was synthesized according to **GP3** using 4-ethynylbenzoic acid (53 mg, 0.36 mmol) and 3-azido-4-phenylpyridine **18c** (1.3 eq., 92 mg, 0.47 mmol) as starting materials. The crude was obtained as a white solid (30 mg, 0.09 mmol, 25%). Purification was done using prep. HPLC. ¹H NMR (500 MHz, DMSO-*d*₆) δ ppm 7.17 - 7.25 (m, 2 H) 7.31 - 7.40 (m, 3 H) 7.74 (d, *J*=5.04 Hz, 1 H) 7.89 - 7.96 (m, 2 H) 7.98 - 8.04 (m, 2 H) 8.88 (d, *J*=5.19 Hz, 1 H) 8.90 (s, 1 H) 8.93 (s, 1 H); ¹³C NMR (126 MHz, DMSO-*d*₆) δ ppm 125.05, 125.17, 125.21, 128.02, 128.83, 129.13, 130.12, 131.18, 134.01, 134.55, 144.74, 145.79, 147.47, 151.54, 166.98

4-(1-(5-methylpyridin-3-yl)-1H-1,2,3-triazol-4-yl)benzoic acid (19d): The triazole was synthesized according to **GP3** using 4-ethynylbenzoic acid (100 mg, 0.68 mmol) and 3-azido-5-methylpyridine **18d** (1.3 eq., 120 mg, 0.89 mmol) as starting materials. The crude was obtained as a yellow solid (103 mg, 0.36 mmol, 53%). Purification was done using prep. HPLC. ¹H NMR (500 MHz, DMSO-*d*₆) δ ppm 2.46 (s, 3 H) 8.00 - 8.13 (m, 4 H) 8.25 (s, 1 H) 8.59 (s, 1 H) 9.01 (s, 1 H) 9.51 (s, 1 H) 13.04 (br. s., 1 H); ¹³C NMR (126 MHz, DMSO-*d*₆) δ ppm 17.74, 121.11, 125.32, 128.06, 130.18, 130.41, 132.92, 134.09, 134.59, 138.41, 146.58, 150.25, 166.96

4-(1-(6-cyanopyridin-3-yl)-1H-1,2,3-triazol-4-yl)benzoic acid (19e): The triazole was synthesized according to **GP3** using 4-ethynylbenzoic acid (125 mg, 0.86 mmol) and 5-azidopyridinonitrile **18e** (1.3 eq., 161 mg, 1.11 mmol) as starting materials. The crude was obtained as a yellow solid (113 mg, 0.39 mmol, 45%). Purification was done using prep. HPLC. ¹H NMR (500 MHz, DMSO-*d*₆) δ ppm 8.07 (d, *J*=7.48 Hz, 4 H) 8.38 (d, *J*=8.55 Hz, 1 H) 8.66 (dd, *J*=8.47, 2.52 Hz, 1 H) 9.42 (d, *J*=2.44 Hz, 1 H) 9.67 (s, 1 H); ¹³C NMR (126 MHz, DMSO-*d*₆) δ ppm 115.35, 117.02, 121.28, 125.35, 128.55, 130.30, 131.83, 135.25, 142.55, 147.00, 166.96

4-(1-(6-chloro-4-methylpyridin-3-yl)-1H-1,2,3-triazol-4-yl)benzoic acid (19f): The triazole was synthesized according to **GP3** using 4-ethynylbenzoic acid (78 mg, 0.53 mmol) and 5-azido-2-chloro-4-methylpyridine **18f** (1.3 eq., 116 mg, 0.69 mmol) as starting materials. The crude was obtained as a white yellow solid (128 mg, 0.41 mmol, 77%). Purification was done using prep. HPLC. ¹H NMR (500 MHz, DMSO-*d*₆) δ ppm 2.33 (s, 3 H) 7.81 (s, 1 H) 8.07 (s, 4 H) 8.63 (s, 1 H) 9.20 (s, 1 H); ¹³C NMR (126 MHz, DMSO-*d*₆) δ ppm 17.21, 124.56, 125.38, 126.34, 130.18, 130.34, 132.94, 134.15, 145.98, 146.15, 146.55, 150.87, 166.98

4-(1-(6-(methylamino)pyridin-3-yl)-1H-1,2,3-triazol-4-yl)benzoic acid (19g): The triazole was synthesized according to **GP3** using 4-ethynylbenzoic acid (60 mg, 0.41 mmol) and 5-azido-*N*-methylpyridin-2-amine **18g** (1.2 eq., 73 mg, 0.49 mmol) as starting materials. The crude was obtained as a white solid (70 mg, 0.24 mmol, 59%). Purification was done using prep. HPLC. ¹H NMR (500 MHz, DMSO-*d*₆) δ ppm 2.84 (d, *J*=4.73 Hz, 3 H) 6.64 (d, *J*=9.00 Hz, 1 H) 7.05 (d, *J*=4.73 Hz, 1 H) 7.89 (dd, *J*=8.93, 2.67 Hz, 1 H) 8.00 - 8.14 (m, 4 H) 8.49 (d, *J*=2.59 Hz, 1 H) 9.21 (s, 1 H) 13.01 (br. s., 1 H); ¹³C NMR (126 MHz, DMSO-*d*₆) δ ppm 28.03, 108.01, 120.84, 123.47, 125.21, 130.12, 130.15, 134.57, 140.28, 146.01, 159.45, 167.01

4-(1-(6-(isopropylamino)pyridin-3-yl)-1H-1,2,3-triazol-4-yl)benzoic acid (19h): The triazole was synthesized according to **GP3** using 4-ethynylbenzoic acid (60 mg, 0.41 mmol) and 5-azido-*N*-isopropylpyridin-2-amine **18h** (1.2 eq., 87 mg, 0.49 mmol) as starting materials. The crude was obtained as a white solid (93 mg, 0.29 mmol, 70%). Purification was done using prep. HPLC. ¹H NMR (500 MHz, DMSO-*d*₆) δ ppm 1.17 (s, 3 H) 1.19 (s, 3 H) 4.06 (dq, *J*=13.35, 6.59 Hz, 1 H) 6.62 (d, *J*=9.00 Hz, 1 H) 6.94 (d, *J*=7.48 Hz, 1 H) 7.85 (dd, *J*=9.00, 2.75 Hz, 1 H) 7.96 - 8.17 (m, 4 H) 8.45 (d, *J*=2.59 Hz, 1 H) 9.18 (s, 1 H); ¹³C NMR (126 MHz, DMSO-*d*₆) δ ppm 22.50, 41.86, 108.53, 120.81, 123.23, 125.16, 130.09, 130.17, 134.42, 140.32, 146.01, 158.27, 167.07

4-(1-(6-(phenylamino)pyridin-3-yl)-1H-1,2,3-triazol-4-yl)benzoic acid (19i): The triazole was synthesized according to **GP3** using 4-ethynylbenzoic acid (60 mg, 0.41 mmol) and 5-azido-*N*-phenylpyridin-2-amine **18i** (1.2 eq., 104 mg, 0.49 mmol) as starting materials. The crude was obtained as a white solid (132 mg, 0.37 mmol, 90%). Purification was done using prep. HPLC. ¹H NMR (500 MHz, DMSO-*d*₆) δ ppm 6.96 (s, 1 H) 7.04 (d, *J*=8.85 Hz, 1 H) 7.32 (t, *J*=7.71 Hz, 2 H) 7.72 (d, *J*=8.24 Hz, 2 H) 8.06 (s, 4 H) 8.10 (dd, *J*=8.93, 2.67 Hz, 1 H) 8.68 (d, *J*=2.59 Hz, 1 H) 9.31 (s, 1 H) 9.48 (s, 1 H); ¹³C NMR (126 MHz, DMSO-*d*₆) δ ppm 111.04, 118.52, 120.86, 121.31, 125.25, 125.49, 128.78, 130.15, 130.49, 134.38, 139.59, 140.94, 146.21, 155.89, 167.04

4-(1-(5-fluoropyridin-3-yl)-1H-1,2,3-triazol-4-yl)benzoic acid (19j): The triazole was synthesized according to **GP3** using 4-ethynylbenzoic acid (40 mg, 0.27 mmol) and 3-azido-5-fluoropyridine **18j** (1.1 eq., 41 mg, 0.30 mmol) as starting materials. The crude was obtained as a white solid (31 mg, 0.11 mmol, 40%). Purification was done using prep. HPLC. ¹H NMR (500 MHz, DMSO-*d*₆) δ ppm 7.97 - 8.11 (m, 4 H) 8.46 (dt, *J*=9.50, 2.35 Hz, 1 H) 8.79 (d, *J*=2.59 Hz, 1 H) 9.14 (s, 1 H) 9.55 (s, 1 H); ¹³C NMR (126 MHz, DMSO-*d*₆) δ ppm 116.06, 125.67, 130.62, 137.90, 138.53, 138.78, 143.33, 155.08, 169.50

4-(1-(6-methoxypyridin-3-yl)-1H-1,2,3-triazol-4-yl)benzoic acid (19k): The triazole was synthesized according to **GP3** using 4-ethynylbenzoic acid (90 mg, 0.62 mmol) and 5-azido-2-methoxypyridine **18k** (1.3 eq., 120 mg, 0.81 mmol) as starting materials. The crude was obtained as a white solid (101 mg, 0.34 mmol, 55%). Purification was done using prep. HPLC. ¹H NMR (500 MHz, DMSO-*d*₆) δ ppm 3.95 (s, 3 H) 7.11 (dd, *J*=8.93, 0.53 Hz, 1 H) 7.97 - 8.11 (m, 4 H) 8.27 (dd, *J*=8.93, 2.82 Hz, 1 H) 8.69 - 8.81 (m, 1 H) 9.36 (s, 1 H); ¹³C NMR (126 MHz, DMSO-*d*₆) δ ppm 53.89, 111.50, 121.16, 125.16, 128.26, 130.10, 132.30, 139.03, 163.44

4-(1-(6-phenoxyphenyl)-1H-1,2,3-triazol-4-yl)benzoic acid (19l): The triazole was synthesized according to **GP3** using 4-ethynylbenzoic acid (85 mg, 0.58 mmol) and 5-azido-2-phenoxyphenylpyridine **18l** (1.2 eq., 150 mg, 0.70 mmol) as starting materials. The crude was obtained as a white solid (160 mg, 0.45 mmol, 77%). Purification was done using prep. HPLC. ¹H NMR (500 MHz, DMSO-*d*₆) δ ppm 7.18 - 7.24 (m, 2 H) 7.24 - 7.30 (m, 1 H) 7.32 (d, *J*=8.85 Hz, 1 H) 7.44 - 7.53 (m, 2 H) 8.05 (q, *J*=8.39 Hz, 4 H) 8.42 (dd, *J*=8.85, 2.75 Hz, 1 H) 8.72 (d, *J*=2.75 Hz, 1 H) 9.40 (s, 1 H); ¹³C NMR (126 MHz, DMSO-*d*₆) δ ppm 112.36, 121.25, 121.43, 125.13, 125.25, 129.54, 129.95, 130.18, 133.05, 133.76, 139.48, 146.62, 153.55, 162.88, 167.29

4-(1-(4-phenoxyphenyl)-1H-1,2,3-triazol-4-yl)benzoic acid (19m): The triazole was synthesized according to **GP3** using 4-ethynylbenzoic acid (25 mg, 0.17 mmol) and 1-azido-4-phenoxybenzene **18m**

(1.2 eq., 42 mg, 0.2 mmol) as starting materials. The crude was obtained as a white solid (32 mg, 0.09 mmol, 53%). Purification was done using prep. HPLC. ¹H NMR (500 MHz, DMSO-*d*₆) δ ppm 7.13 (dd, *J*=8.62, 0.99 Hz, 2 H) 7.20 - 7.27 (m, 3 H) 7.46 (dd, *J*=8.55, 7.48 Hz, 2 H) 7.96 (d, *J*=9.00 Hz, 2 H) 8.06 (s, 4 H) 9.40 (s, 1 H); ¹³C NMR (126 MHz, DMSO-*d*₆) δ ppm 119.23, 119.38, 120.88, 122.17, 124.22, 125.27, 130.14, 130.32, 131.97, 134.36, 146.37, 156.01, 157.11, 166.98

4-(1-(4-(pyridin-3-yloxy)phenyl)-1*H*-1,2,3-triazol-4-yl)benzoic acid (19n): The triazole was synthesized according to **GP3** using 4-ethynylbenzoic acid (25 mg, 0.17 mmol) and 3-(4-azidophenoxy)pyridine **18n** (1.2 eq., 42 mg, 0.20 mmol) as starting materials. The crude was obtained as a white solid (42 mg, 0.12 mmol, 70%). Purification was done using prep. HPLC. ¹H NMR (500 MHz, DMSO-*d*₆) δ ppm 7.33 - 7.40 (m, 2 H) 7.58 - 7.63 (m, 1 H) 7.70 - 7.76 (m, 1 H) 7.98 - 8.04 (m, 2 H) 8.07 (s, 4 H) 8.51 (br. s., 1 H) 8.59 (br. s., 1 H) 9.45 (s, 1 H); ¹³C NMR (126 MHz, DMSO-*d*₆) δ ppm 119.91, 120.97, 122.30, 125.34, 125.66, 128.02, 130.20, 130.27, 132.74, 134.38, 140.04, 143.88, 146.45, 156.15, 167.05

4-(1-(6-hydroxypyridin-3-yl)-1*H*-1,2,3-triazol-4-yl)benzoic acid (19o): 4-(1-(6-methoxypyridin-3-yl)-1*H*-1,2,3-triazol-4-yl)benzoic acid **19k** (20 mg, 0.07 mmol) was dissolved in 48% HBr aq. solution (1 mL) and was stirred at 80 °C for 12 h. After cooling to room temperature, water was added and the product precipitated. The solids were collected, washed with water, and dried under vacuum to obtain the crude product (17 mg, 0.06 mmol, 86%). The product was purified using prep. HPLC. ¹H NMR (500 MHz, DMSO-*d*₆) δ ppm 6.59 (d, *J*=9.61 Hz, 1 H) 7.99 (d, *J*=3.05 Hz, 1 H) 8.00 - 8.04 (m, 2 H) 8.04 - 8.08 (m, 2 H) 8.12 (d, *J*=2.75 Hz, 1 H) 9.21 (s, 1 H), 12.59 (br. s, 1 H); ¹³C NMR (126 MHz, DMSO-*d*₆) δ ppm 121.39, 125.20, 130.17, 134.38, 135.14, 146.01, 161.76, 166.98

4-azido-3-methylpyridine (21): The azide was synthesized according to **GP1** using 3-methylpyridin-4-amine **20** (150 mg, 1.4 mmol), sodium nitrite (1.7 eq., 165 mg, 2.4 mmol), sodium azide (1.7 eq, 155 mg, 2.4 mmol), EtOAc (4 mL), 6 M HCl (2.4 mL). The crude product (51 mg, 0.38 mmol, 4%) was used as obtained in the next step without further purifications. *R*_f = 0.31 (PE/EtOAc 7:3)

4-(1-(3-methylpyridin-4-yl)-1*H*-1,2,3-triazol-4-yl)benzoic acid (22): The triazole was synthesized according to **GP3** using 4-ethynylbenzoic acid (40 mg, 0.27 mmol) and 4-azido-3-methylpyridine **21** (1.3 eq., 51 mg, 0.35 mmol) as starting materials. Purification was done using flash chromatography (DCM:MeOH 1:0 → 9:1) and **22** was obtained as a white solid (56 mg, 0.20 mmol, 77%). ¹H NMR (500 MHz, DMSO-*d*₆) δ ppm 2.32 (s, 3 H) 7.60 (d, *J*=5.04 Hz, 1 H) 8.07 (s, 5 H) 8.66 (d, *J*=5.04 Hz, 1 H) 8.73 (s, 1 H) 9.20 (s, 1 H) 13.07 (br. s., 1 H); ¹³C NMR (126 MHz, DMSO-*d*₆) δ ppm 17.05, 124.43, 125.32, 126.25, 130.13, 130.41, 133.36, 134.22, 142.45, 145.89, 145.98, 150.54, 167.00

2-(5-amino-4-methylpyridin-2-yl)phenol (24a): The coupling was done according to **GP4** using 6-bromo-4-methylpyridin-3-amine **23** (130 mg, 0.69 mmol), (2-hydroxyphenyl)boronic acid (1.2 eq., 113 mg, 0.83 mmol), sodium carbonate (3 eq., 218 mg, 2.08 mmol,) and tetrakis (triphenylphosphine) palladium (0.1 eq., 78 mg, 0.07 mmol) in 1,4-dioxan:water (1:1, 6 mL). **24b** was obtained as yellow solid (103 mg, 0.52 mmol, 75%). MS (ESI+) *m/z* 201 (M + H).

(4'-amino-3'-methyl-[1,1'-biphenyl]-3-yl)methanol (24b): The coupling was done according to **GP4** using 6-bromo-4-methylpyridin-3-amine **23** (100 mg, 0.53 mmol), (3-(hydroxymethyl)phenyl)boronic acid (1.2 eq., 97 mg, 0.64 mmol), sodium carbonate (3 eq., 167 mg, 1.59 mmol,) and tetrakis (triphenylphosphine) palladium (0.1 eq., 57 mg, 0.05 mmol) in 1,4-dioxan:water (1:1, 6 mL). **24a** was obtained as yellow-brown solid (70 mg, 0.33 mmol, 62%). MS (ESI+) *m/z* 215 (M + H).

2-(5-azido-4-methylpyridin-2-yl)phenol (25a): The azide was synthesized according to **GP1** using 2-(5-amino-4-methylpyridin-2-yl)phenol **25a** (56 mg, 0.27 mmol), sodium nitrite (1.7 eq., 0.46 mmol, 32 mg), sodium azide (1.7 eq., 0.46 mmol, 30 mg), EtOAc (2 mL), 6 M HCl (4 mL). The crude product (58 mg, 0.25 mmol, 99%) was used as obtained in the next step without further purifications. *R_f* = 0.75 (PE/EtOAc 0:1)

(3-(5-azido-4-methylpyridin-2-yl)phenyl)methanol (25b): The azide was synthesized according to **GP1** using (4'-amino-3'-methyl-[1,1'-biphenyl]-3-yl)methanol **24a** (70 mg, 0.33 mmol), sodium nitrite (1.7 eq., 0.55 mmol, 38 mg), sodium azide (1.7 eq., 0.55 mmol, 33 mg), EtOAc (3 mL) and 6 M HCl (5 mL). The crude product (77 mg, 0.32 mmol, 98%) was used as obtained in the next step without further purifications. *R_f* = 0.80 (PE/EtOAc 0:1)

4-(1-(6-(2-hydroxyphenyl)-4-methylpyridin-3-yl)-1*H*-1,2,3-triazol-4-yl)benzoic acid (26a): The triazole was synthesized according to **GP3** using 4-ethynylbenzoic acid (32 mg, 0.22 mmol) and 2-(5-azido-4-methylpyridin-2-yl)phenol **25a** (1 eq., 50 mg, 0.22 mmol) as starting materials. The crude was obtained as a white solid (30 mg, 0.08 mmol, 36%). Purification was done using prep. HPLC. ¹H NMR (500 MHz, DMSO-*d*₆) δ ppm 2.43 (s, 3 H) 6.95 - 7.01 (m, 2 H) 7.37 (td, *J*=7.71, 1.53 Hz, 1 H) 8.06 (s, 1 H) 8.08 (s, 4 H) 8.11 (dd, *J*=8.39, 1.53 Hz, 1 H) 8.42 (s, 1 H) 8.84 (s, 1 H) 9.25 (s, 1 H) 13.22 (br. s, 1 H); ¹³C NMR (126 MHz, DMSO-*d*₆) δ ppm 17.77, 117.98, 118.97, 119.25, 122.74, 124.48, 125.32, 128.01, 130.18, 131.67, 132.00, 143.23, 144.53, 146.02, 157.43, 158.77, 167.09

4-(1-(6-(3-(hydroxymethyl)phenyl)-4-methylpyridin-3-yl)-1*H*-1,2,3-triazol-4-yl)benzoic acid (26b): The triazole was synthesized according to **GP3** using 4-ethynylbenzoic acid (36 mg, 0.26 mmol) and (3-(5-azido-4-methylpyridin-2-yl)phenyl)methanol **25a** (1.0 eq., 60 mg, 0.26 mmol) as starting materials. The crude was obtained as a white solid (50 mg, 0.13 mmol, 50%). Purification was done using prep. HPLC. ¹H NMR (500 MHz, DMSO-*d*₆) δ ppm 2.40 (s, 3 H) 4.62 (br. s., 2 H) 5.34 (br. s., 1 H) 7.45 (d, *J*=7.63 Hz, 1 H) 7.51 (t, *J*=7.63 Hz, 1 H) 8.03 - 8.06 (m, 1 H) 8.06 - 8.11 (m, 4 H) 8.16 (s, 1 H) 8.19 (s, 1 H) 8.81 (s, 1 H) 9.24 (s, 1 H) 13.07 (br. s., 1 H); ¹³C NMR (126 MHz, DMSO-*d*₆) δ ppm 17.45, 62.85, 122.49, 124.45, 124.94, 125.27, 125.33, 127.85, 128.72, 130.17, 132.25, 137.28, 143.31, 143.35, 145.79, 145.95, 156.97, 167.50

(3-(5-aminopyridin-3-yl)phenyl)methanol (29a): The coupling was done according to **GP4** using 5-bromopyridin-3-amine **27** (120 mg, 0.69 mmol), (3-(hydroxymethyl)phenyl)boronic acid (1.2 eq., 125 mg, 0.83 mmol), sodium carbonate (3 eq., 218 mg, 2.08 mmol,) and tetrakis (triphenylphosphine) palladium (0.1 eq., 78 mg, 0.07 mmol) in 1,4-dioxan:water (1:1, 6 mL). **29a** was obtained as yellow solid (96 mg, 0.48 mmol, 69%). MS (ESI+) *m/z* 201 (M + H).

4-chloro-5-phenylpyridin-3-amine (29b): The coupling was done according to **GP4** using 5-bromo-4-chloropyridin-3-amine **28** (150 mg, 0.72 mmol), phenylboronic acid (1.2 eq., 104 mg, 0.86 mmol), sodium carbonate (3 eq., 227 mg, 2.17 mmol,) and tetrakis (triphenylphosphine) palladium (0.1 eq., 78 mg, 0.07 mmol) in 1,4-dioxan:water (1:1, 7 mL). **29b** was obtained as yellow oil (30 mg, 0.15 mmol, 21%). MS (ESI+) m/z 205 (M + H).

(3-(5-azidopyridin-3-yl)phenyl)methanol (30a): The azide was synthesized according to **GP1** using (3-(5-aminopyridin-3-yl)phenyl)methanol **29a** (60 mg, 0.30 mmol), sodium nitrite (1.7 eq., 0.51 mmol, 36 mg), sodium azide (1.7 eq., 0.51 mmol, 34 mg), EtOAc (2 mL) and 6 M HCl (4 mL). The crude product (58 mg, 0.26 mmol, 86%) was used as obtained in the next step without further purifications. $R_f = 0.79$ (PE/EtOAc 0:1)

3-azido-4-chloro-5-phenylpyridine (30b): The azide was synthesized according to **GP1** using 4-chloro-5-phenylpyridin-3-amine **29b** (30 mg, 0.15 mmol sodium nitrite (1.7 eq., 0.25 mmol, 17 mg), sodium azide (1.7 eq., 0.25 mmol, 14 mg), EtOAc (1 mL), 6 M HCl (3 mL). The crude product (30 mg, 0.13 mmol, 86%) was used as obtained in the next step without further purifications. $R_f = 0.9$ (PE/EtOAc 0:1)

4-(1-(5-(3-(hydroxymethyl)phenyl)pyridin-3-yl)-1H-1,2,3-triazol-4-yl)benzoic acid (31a): The triazole was synthesized according to **GP3** using 4-ethynylbenzoic acid (30 mg, 0.20 mmol) and (3-(5-azidopyridin-3-yl)phenyl)methanol **30a** (1.2 eq., 54 mg, 0.24 mmol) as starting materials. The crude was obtained as a white solid (31 mg, 0.08 mmol, 40%). Purification was done using prep. HPLC. ^1H NMR (500 MHz, DMSO- d_6) δ ppm 4.63 (s, 2 H) 5.35 (br. s., 1 H) 7.47 (d, $J=7.63$ Hz, 1 H) 7.54 (t, $J=7.63$ Hz, 1 H) 7.77 (d, $J=7.78$ Hz, 1 H) 7.83 (s, 1 H) 8.01 - 8.23 (m, 4 H) 8.64 (t, $J=2.14$ Hz, 1 H) 9.05 (br. s., 1 H) 9.22 (br. s., 1 H) 9.65 (s, 1 H); ^{13}C NMR (126 MHz, DMSO- d_6) δ ppm 62.77, 121.43, 125.27, 125.33, 125.47, 125.64, 127.05, 129.13, 130.25, 130.64, 133.43, 134.04, 135.45, 136.67, 139.89, 143.78, 146.66, 147.68, 167.05

4-(1-(4-chloro-5-phenylpyridin-3-yl)-1H-1,2,3-triazol-4-yl)benzoic acid (31b): The triazole was synthesized according to **GP3** using 4-ethynylbenzoic acid (22 mg, 0.15 mmol) and 3-azido-4-chloro-5-phenylpyridine **30b** (1.0 eq., 35 mg, 0.15 mmol) as starting materials. The crude was obtained as a white solid (43 mg, 0.11 mmol, 76%). Purification was done using prep. HPLC. ^1H NMR (500 MHz, DMSO- d_6) δ ppm 7.53 - 7.62 (m, 5 H) 8.07 (s, 4 H) 8.85 (s, 1 H) 8.98 (s, 1 H) 9.29 (s, 1 H) 13.13 (br. s., 1 H); ^{13}C NMR (126 MHz, DMSO- d_6) δ ppm 125.21, 125.38, 128.77, 129.08, 129.62, 130.22, 131.96, 134.08, 136.85, 137.48, 145.98, 147.09, 152.41, 167.04

3-azido-5-bromopyridine (33a): The azide was synthesized according to **GP1** using 5-bromopyridin-3-amine **32a** (150 mg, 0.87 mmol), sodium nitrite (1.7 eq., 101 mg, 1.47 mmol), sodium azide (1.7 eq., 96 mg, 1.47 mmol), EtOAc (4 mL), 6 M HCl (2.4 mL). The crude product (60 mg, 0.3 mmol, 34%) was used as obtained in the next step without further purifications. $R_f = 0.75$ (PE/EtOAc 7:3)

5-azido-2-chloro-4-methylpyridine (33b): The azide was synthesized according to **GP1** using 6-chloro-4-methylpyridin-3-amine **32b** (200 mg, 1.41 mmol), sodium nitrite (1.7 eq., 165 mg, 2.40 mmol), sodium azide (1.7 eq., 155 mg, 2.40 mmol), EtOAc (8 mL), 6 M HCl (4.8 mL). The crude

product (190 mg, 1.13 mmol, 80%) was used as obtained in the next step without further purifications. $R_f = 0.82$ (PE/EtOAc 7:3)

methyl 4-(1-(5-bromopyridin-3-yl)-1*H*-1,2,3-triazol-4-yl)benzoate (34a): The triazole was synthesized according to **GP3** using methyl 4-ethynylbenzoate (200 mg, 1.25 mmol) and 3-azido-5-bromopyridine **33a** (1.2 eq, 298 mg, 1.5 mmol) as starting materials. **34a** was obtained as a yellow solid (238 mg, 0.79 mmol, 63%) and was used as obtained without further purification. MS (ESI+) m/z 360 (M + H).

methyl 4-(1-(6-chloro-4-methylpyridin-3-yl)-1*H*-1,2,3-triazol-4-yl)benzoate (34b): The triazole was synthesized according to **GP3** using methyl 4-ethynylbenzoate (230 mg, 2.0 mmol) and 5-azido-2-chloro-4-methylpyridine **33b** (1.2 eq., 400 mg, 2.4 mmol) as starting materials. The mixture was acidified with 1 M HCl, extracted with EtOAc (2x) and the combined organic layers were dried over sodium sulfate and concentrated under reduced pressure to obtain the crude (525 mg, 1.6 mmol, 80%). **34b** was used as obtained without further purification. MS (ESI+) m/z 329 (M + H).

methyl 4-(1-(5-phenylpyridin-3-yl)-1*H*-1,2,3-triazol-4-yl)benzoate (35a): The coupling was done according to **GP4** using methyl 4-(1-(5-bromopyridin-3-yl)-1*H*-1,2,3-triazol-4-yl)benzoate **34a** (30 mg, 0.08 mmol) and phenylboronic acid (1.2 eq., 12 mg, 0.10 mmol). **35a** was obtained as yellow-brown solid (21 mg, 0.06 mmol, 75%). MS (ESI+) m/z 357 (M + H).

methyl 4-(1-(5-(2-methoxyphenyl)pyridin-3-yl)-1*H*-1,2,3-triazol-4-yl)benzoate (35b): The coupling was done according to **GP4** using methyl 4-(1-(5-bromopyridin-3-yl)-1*H*-1,2,3-triazol-4-yl)benzoate **34a** (40 mg, 0.11 mmol) and (2-methoxyphenyl)boronic acid (1.5 eq., 25 mg, 0.16 mmol). **35b** was obtained as a brown solid (25 mg, 0.06 mmol, 54%). MS (ESI+) m/z 387 (M + H). NMR ABE181

methyl 4-(1-(5-(3-methoxyphenyl)pyridin-3-yl)-1*H*-1,2,3-triazol-4-yl)benzoate (35c): The coupling was done according to **GP4** using methyl 4-(1-(5-bromopyridin-3-yl)-1*H*-1,2,3-triazol-4-yl)benzoate **34a** (30 mg, 0.08 mmol) and (3-methoxyphenyl)boronic acid (1.2 eq., 15 mg, 0.10 mmol). **35c** was obtained as a yellow-brown solid (29 mg, 0.07 mmol, 87%). MS (ESI+) m/z 387 (M + H).

methyl 4-(1-(5-(4-methoxyphenyl)pyridin-3-yl)-1*H*-1,2,3-triazol-4-yl)benzoate (35d): The coupling was done according to **GP4** using methyl 4-(1-(5-bromopyridin-3-yl)-1*H*-1,2,3-triazol-4-yl)benzoate **34a** (30 mg, 0.08 mmol) and (4-methoxyphenyl)boronic acid (1.2 eq., 15 mg, 0.10 mmol). **35d** was obtained as a brown solid (26 mg, 0.07 mmol, 87%). MS (ESI+) m/z 373 (M + H).

methyl 4-(1-(5-(3-hydroxyphenyl)pyridin-3-yl)-1*H*-1,2,3-triazol-4-yl)benzoate (35e): The coupling was done according to **GP4** using methyl 4-(1-(5-bromopyridin-3-yl)-1*H*-1,2,3-triazol-4-yl)benzoate **34a** (40 mg, 0.11 mmol) and (3-hydroxyphenyl) boronic acid (1.2 eq., 18 mg, 0.13 mmol). **35e** was obtained as yellow-brown solid (15 mg, 0.04 mmol, 36 %). MS (ESI+) m/z 373 (M + H).

methyl 4-(1-(5-(3,4-dimethylphenyl)pyridin-3-yl)-1H-1,2,3-triazol-4-yl)benzoate (35f): The coupling was done according to **GP4** using methyl 4-(1-(5-bromopyridin-3-yl)-1H-1,2,3-triazol-4-yl)benzoate **34a** (40 mg, 0.11 mmol) and (3,4-dimethylphenyl) boronic acid (1.2 eq., 19 mg, 0.13 mmol). **35f** was obtained as yellow-brown solid (25 mg, 0.06 mmol, 60%). MS (ESI+) m/z 385 (M + H).

methyl 4-(1-(5-(3,4-difluorophenyl)pyridin-3-yl)-1H-1,2,3-triazol-4-yl)benzoate (35g): The coupling was done according to **GP4** using methyl 4-(1-(5-bromopyridin-3-yl)-1H-1,2,3-triazol-4-yl)benzoate **34a** (40 mg, 0.11 mmol) and (3,4-difluorophenyl)boronic acid (1.2 eq., 21 mg, 0.13 mmol). **35g** was obtained as yellow-brown solid (41 mg, 0.10 mmol, 90%). MS (ESI+) m/z 393 (M + H).

methyl 4-(1-(5-(4-(hydroxymethyl)phenyl)pyridin-3-yl)-1H-1,2,3-triazol-4-yl)benzoate (35h): The coupling was done according to **GP4** using methyl 4-(1-(5-bromopyridin-3-yl)-1H-1,2,3-triazol-4-yl)benzoate **34a** (40 mg, 0.11 mmol) and (4-(hydroxymethyl)phenyl)boronic acid (1.2 eq., 20 mg, 0.13 mmol). **35h** was obtained as a yellow solid (15 mg, 0.04 mmol, 36%). MS (ESI+) m/z 387 (M + H).

methyl 4-(1-(5-(3-fluoro-5-methoxyphenyl)pyridin-3-yl)-1H-1,2,3-triazol-4-yl)benzoate (35i): The coupling was done according to **GP4** using methyl 4-(1-(5-bromopyridin-3-yl)-1H-1,2,3-triazol-4-yl)benzoate **34a** (40 mg, 0.11 mmol) and (3-fluoro-5-methoxyphenyl) boronic acid (1.2 eq., 22 mg, 0.13 mmol). **35i** was obtained as a yellow-brown solid (8 mg, 0.02 mmol, 20%). MS (ESI+) m/z 405 (M + H).

methyl 4-(1-(5-(furan-3-yl)pyridin-3-yl)-1H-1,2,3-triazol-4-yl)benzoate (35j): The coupling was done according to **GP4** using methyl 4-(1-(5-bromopyridin-3-yl)-1H-1,2,3-triazol-4-yl)benzoate **34a** (40 mg, 0.11 mmol) and furan-3-yl boronic acid (1.2 eq., 15 mg, 0.13 mmol). **35j** was obtained as a yellow solid (28 mg, 0.08 mmol, 73%). MS (ESI+) m/z 347 (M + H).

methyl 4-(1-(4-methyl-6-phenylpyridin-3-yl)-1H-1,2,3-triazol-4-yl)benzoate (35k): The coupling was done according to **GP4** using methyl 4-(1-(6-chloro-4-methylpyridin-3-yl)-1H-1,2,3-triazol-4-yl)benzoate **34b** (40 mg, 0.12 mmol) and phenylboronic acid (1.2 eq., 18 mg, 0.14 mmol). **35k** was obtained as yellow-brown solid (38 mg, 0.10 mmol, 83%). MS (ESI+) m/z 371 (M + H).

methyl 4-(1-(6-(4-chlorophenyl)-4-methylpyridin-3-yl)-1H-1,2,3-triazol-4-yl)benzoate (35l): The coupling was done according to **GP4** using methyl 4-(1-(6-chloro-4-methylpyridin-3-yl)-1H-1,2,3-triazol-4-yl)benzoate **34b** (40 mg, 0.12 mmol) and (4-chlorophenyl)boronic acid (1.2 eq., 23 mg, 0.14 mmol). **35l** was obtained as brown solid (22 mg, 0.05 mmol, 41%). MS (ESI+) m/z 405 (M + H).

4-(1-(5-phenylpyridin-3-yl)-1H-1,2,3-triazol-4-yl)benzoic acid (36a): The synthesis was done according to **GP5** using methyl 4-(1-(5-phenylpyridin-3-yl)-1H-1,2,3-triazol-4-yl)benzoate **35a** (20 mg, 0.06 mmol). The crude was obtained as a white solid (13 mg, 0.04 mmol, 66%). Purification was done using prep. HPLC. $^1\text{H NMR}$ (500 MHz, DMSO- d_6) δ ppm 7.49 - 7.54 (m, 1 H) 7.56 - 7.61 (m, 2 H) 7.84 - 7.95 (m, 2 H) 8.02 - 8.16 (m, 4 H) 8.65 (t, $J=2.21$ Hz, 1 H) 9.07 (d, $J=1.98$ Hz, 1 H) 9.22 (d, $J=2.29$

Hz, 1 H) 9.64 (s, 1 H); ^{13}C NMR (126 MHz, $\text{DMSO-}d_6$) δ ppm 121.41, 125.29, 125.57, 127.30, 128.97, 129.30, 130.22, 133.38, 133.97, 135.68, 136.49, 139.93, 146.65, 147.70, 167.01

4-(1-(5-(2-methoxyphenyl)pyridin-3-yl)-1H-1,2,3-triazol-4-yl)benzoic acid (36b): The synthesis was done according to **GP5** using methyl 4-(1-(5-(2-methoxyphenyl)pyridin-3-yl)-1H-1,2,3-triazol-4-yl)benzoate **35b** (25 mg, 0.06 mmol). The crude was obtained as a white solid (21 mg, 0.05 mmol, 83%). Purification was done using prep. HPLC. ^1H NMR (500 MHz, $\text{DMSO-}d_6$) δ ppm 3.84 (s, 3 H) 7.14 (d, $J=0.92$ Hz, 1 H) 7.23 (d, $J=7.78$ Hz, 1 H) 7.46 - 7.51 (m, 1 H) 7.53 (dd, $J=7.48$, 1.68 Hz, 1 H) 8.08 (d, $J=2.14$ Hz, 4 H) 8.48 (t, $J=2.14$ Hz, 1 H) 8.85 (d, $J=1.83$ Hz, 1 H) 9.16 (d, $J=2.44$ Hz, 1 H) 9.59 (s, 1 H); ^{13}C NMR (126 MHz, $\text{DMSO-}d_6$) δ ppm 55.75, 111.96, 121.10, 121.33, 124.81, 125.32, 128.00, 130.20, 130.54, 130.70, 132.87, 134.68, 139.40, 146.66, 149.86, 156.32, 167.01

4-(1-(5-(3-methoxyphenyl)pyridin-3-yl)-1H-1,2,3-triazol-4-yl)benzoic acid (36c): The synthesis was done according to **GP5** using methyl 4-(1-(5-(3-methoxyphenyl)pyridin-3-yl)-1H-1,2,3-triazol-4-yl)benzoate **35c** (25 mg, 0.06 mmol). The crude was obtained as a white solid (18 mg, 0.05 mmol, 83%). Purification was done using prep. HPLC. ^1H NMR (500 MHz, $\text{DMSO-}d_6$) δ ppm 3.87 (s, 3 H) 7.01 - 7.16 (m, 1 H) 7.34 - 7.55 (m, 3 H) 8.02 - 8.15 (m, 4 H) 8.64 (t, $J=2.21$ Hz, 1 H) 9.08 (d, $J=1.98$ Hz, 1 H) 9.22 (d, $J=2.44$ Hz, 1 H) 9.64 (s, 1 H); ^{13}C NMR (126 MHz, $\text{DMSO-}d_6$) δ ppm 55.37, 112.81, 114.60, 119.53, 121.51, 125.34, 125.76, 130.25, 130.44, 133.36, 134.11, 136.38, 137.11, 140.10, 146.61, 147.85, 159.99, 166.98

4-(1-(5-(3-hydroxyphenyl)pyridin-3-yl)-1H-1,2,3-triazol-4-yl)benzoic acid (36e): The synthesis was done according to **GP5** using methyl 4-(1-(5-(3-hydroxyphenyl)pyridin-3-yl)-1H-1,2,3-triazol-4-yl)benzoate **35e** (15 mg, 0.04 mmol). Purification was done using prep. HPLC. **36e** was obtained as a white solid (6 mg, 0.02 mmol, 50%). ^1H NMR (500 MHz, $\text{DMSO-}d_6$) δ ppm 6.82 - 6.97 (m, 1 H) 7.28 (br. s., 1 H) 7.30 (d, $J=7.78$ Hz, 1 H) 7.37 (t, $J=7.78$ Hz, 1 H) 7.99 - 8.15 (m, 4 H) 8.59 (t, $J=2.14$ Hz, 1 H) 8.99 (d, $J=1.83$ Hz, 1 H) 9.21 (d, $J=2.44$ Hz, 1 H) 9.65 (s, 1 H); ^{13}C NMR (126 MHz, $\text{DMSO-}d_6$) δ ppm 114.06, 115.09, 115.91, 117.89, 121.30, 125.24, 125.38, 130.18, 130.37, 133.35, 136.63, 137.00, 139.81, 146.72, 147.52, 158.17, 167.12

4-(1-(5-(4-methoxyphenyl)pyridin-3-yl)-1H-1,2,3-triazol-4-yl)benzoic acid (36d): The synthesis was done according to **GP5** using methyl 4-(1-(5-(4-methoxyphenyl)pyridin-3-yl)-1H-1,2,3-triazol-4-yl)benzoate **35d** (25 mg, 0.06 mmol). The crude was obtained as a white solid (14 mg, 0.04 mmol, 66%). Purification was done using prep. HPLC. ^1H NMR (500 MHz, $\text{DMSO-}d_6$) δ ppm 3.84 (s, 3 H) 7.13 (m, $J=8.85$ Hz, 2 H) 7.87 (m, $J=8.85$ Hz, 2 H) 8.09 (d, $J=3.51$ Hz, 4 H) 8.59 (s, 1 H) 9.03 (d, $J=1.98$ Hz, 1 H) 9.15 (d, $J=2.29$ Hz, 1 H) 9.63 (s, 1 H); ^{13}C NMR (126 MHz, $\text{DMSO-}d_6$) δ ppm 55.36, 114.75, 121.42, 124.85, 125.32, 127.83, 128.53, 130.23, 133.37, 134.09, 136.16, 139.16, 146.60, 147.26, 160.03, 166.99

4-(1-(5-(3,4-dimethylphenyl)pyridin-3-yl)-1H-1,2,3-triazol-4-yl)benzoic acid (36f): The synthesis was done according to **GP5** using methyl 4-(1-(5-(3,4-dimethylphenyl)pyridin-3-yl)-1H-1,2,3-triazol-4-yl)benzoate **35f** (25 mg, 0.06 mmol). Purification was done using prep. HPLC. **36f** was obtained as a white solid (7 mg, 0.02 mmol, 33%). ^1H NMR (500 MHz, $\text{DMSO-}d_6$) δ ppm 2.30 (s, 3 H) 2.34 (s, 3 H) 7.33 (d, $J=7.93$ Hz, 1 H) 7.63 (dd, $J=7.78$, 1.83 Hz, 1 H) 7.70 (s, 1 H) 8.01 - 8.10 (m, 4 H) 8.60 (t, $J=2.21$ Hz, 1 H) 9.04 (d, $J=1.98$ Hz, 1 H) 9.17 (d, $J=2.29$ Hz, 1 H) 9.62 (s, 1 H); ^{13}C NMR (126 MHz,

DMSO- d_6) δ ppm 19.63, 19.96, 113.18, 118.16, 121.76, 124.97, 125.54, 125.67, 128.60, 130.62, 130.82, 133.49, 133.85, 136.95, 137.77, 137.81, 139.98, 147.19, 147.90, 167.54

4-(1-(5-(3,4-difluorophenyl)pyridin-3-yl)-1H-1,2,3-triazol-4-yl)benzoic acid (36g): The synthesis was done according to **GP5** using methyl 4-(1-(5-(3,4-difluorophenyl)pyridin-3-yl)-1H-1,2,3-triazol-4-yl)benzoate **35g** (40 mg, 0.10 mmol). Purification was done using prep. HPLC. **36g** was obtained as a white solid (12 mg, 0.03 mmol, 31%). ^1H NMR (500 MHz, DMSO- d_6) δ ppm 7.67 (dt, $J=10.57$, 8.60 Hz, 1 H) 7.78 - 7.85 (m, 1 H) 8.04 - 8.10 (m, 5 H) 8.69 (t, $J=2.21$ Hz, 1 H) 9.10 (d, $J=1.98$ Hz, 1 H) 9.24 (d, $J=2.29$ Hz, 1 H) 9.61 (s, 1 H); ^{13}C NMR (126 MHz, DMSO- d_6) δ ppm 113.00, 116.56, 116.71, 118.33, 118.47, 121.34, 124.43, 125.24, 125.80, 130.20, 133.32, 134.34, 140.38, 146.72, 147.71, 149.04, 167.06

4-(1-(5-(4-(hydroxymethyl)phenyl)pyridin-3-yl)-1H-1,2,3-triazol-4-yl)benzoic acid (36h): The synthesis was done according to **GP5** using methyl 4-(1-(5-(4-(hydroxymethyl)phenyl)pyridin-3-yl)-1H-1,2,3-triazol-4-yl)benzoate **35h** (15 mg, 0.04 mmol). Purification was done using prep. HPLC. **36h** was obtained as a white solid (7 mg, 0.02 mol, 50%). ^1H NMR (500 MHz, DMSO- d_6) δ ppm 4.59 (s, 2 H) 5.32 (br. s., 1 H) 7.51 (m, $J=8.39$ Hz, 2 H) 7.88 (m, $J=8.24$ Hz, 2 H) 7.99 - 8.10 (m, 4 H) 8.64 (t, $J=2.21$ Hz, 1 H) 9.07 (d, $J=1.83$ Hz, 1 H) 9.20 (d, $J=2.29$ Hz, 1 H) 9.61 (s, 1 H); ^{13}C NMR (126 MHz, DMSO- d_6) δ ppm 62.47, 110.60, 118.11, 125.26, 126.97, 127.20, 128.29, 130.09, 133.43, 133.92, 136.37, 139.71, 140.40, 143.54, 147.51, 151.49, 151.85, 154.97, 167.77

4-(1-(5-(3-fluoro-5-methoxyphenyl)pyridin-3-yl)-1H-1,2,3-triazol-4-yl)benzoic acid (36i): The synthesis was done according to **GP5** using methyl 4-(1-(5-(3-fluoro-5-methoxyphenyl)pyridin-3-yl)-1H-1,2,3-triazol-4-yl)benzoate **35i** (5 mg, 0.01 mmol). Purification was done using prep. HPLC. **36i** was obtained as a white solid (3 mg, 0.007 mmol, 70%). ^1H NMR (500 MHz, DMSO- d_6) δ ppm 3.89 (s, 3 H) 6.99 (dt, $J=10.95$, 2.23 Hz, 1 H) 7.35 (t, $J=1.75$ Hz, 1 H) 7.40 (dt, $J=9.69$, 1.87 Hz, 1 H) 8.01 - 8.13 (m, 4 H) 8.68 (t, $J=2.21$ Hz, 1 H) 9.11 (d, $J=1.98$ Hz, 1 H) 9.25 (d, $J=2.44$ Hz, 1 H) 9.62 (s, 1 H); ^{13}C NMR (126 MHz, DMSO- d_6) δ ppm 56.43, 102.31, 102.51, 106.66, 106.84, 109.91, 118.56, 121.80, 125.63, 126.36, 130.62, 133.80, 135.60, 138.83, 141.05, 147.23, 148.29, 161.79, 167.57

4-(1-(5-(furan-3-yl)pyridin-3-yl)-1H-1,2,3-triazol-4-yl)benzoic acid (36j): The synthesis was done according to **GP5** using methyl 4-(1-(5-(furan-3-yl)pyridin-3-yl)-1H-1,2,3-triazol-4-yl)benzoate **34a** (20 mg, 0.06 mmol). Purification was done using prep. HPLC. **36j** was obtained as a white solid (4 mg, 0.01 mmol, 16%). ^1H NMR (500 MHz, DMSO- d_6) δ ppm 2.54 (s, 4 H) 7.23 (s, 1 H) 7.88 (s, 1 H) 8.02 - 8.10 (m, 5 H) 8.51 (s, 1 H) 8.62 (s, 1 H) 9.08 (s, 1 H) 9.06 (s, 1 H) 9.54 (s, 1 H); ^{13}C NMR (126 MHz, DMSO- d_6) δ 108.67, 117.70, 121.39, 121.92, 124.28, 125.43, 128.93, 130.30, 131.53, 131.61, 139.45, 141.30, 145.10, 146.86, 167.14

4-(1-(4-methyl-6-phenylpyridin-3-yl)-1H-1,2,3-triazol-4-yl)benzoic acid (36k): The synthesis was done according to **GP5** using methyl 4-(1-(4-methyl-6-phenylpyridin-3-yl)-1H-1,2,3-triazol-4-yl)benzoate **35k** (20 mg, 0.05 mmol). Purification was done using prep. HPLC. **36k** was obtained as a white solid (7 mg, 0.02 mmol, 40%). ^1H NMR (500 MHz, DMSO- d_6) δ ppm 2.40 (s, 3 H) 7.48 - 7.53 (m, 1 H) 7.54 - 7.58 (m, 2 H) 8.07 (s, 4 H) 8.18 (s, 1 H) 8.81 (s, 1 H) 9.22 (s, 1 H); ^{13}C NMR (126 MHz, DMSO- d_6) δ ppm 17.91, 123.03, 124.82, 125.74, 127.37, 129.40, 130.23, 130.59, 132.74, 137.95, 143.77, 146.26, 157.32, 167.58

4-(1-(6-(4-chlorophenyl)-4-methylpyridin-3-yl)-1H-1,2,3-triazol-4-yl)benzoic acid (36l): The synthesis was done according to **GP5** using methyl 4-(1-(6-(4-chlorophenyl)-4-methylpyridin-3-yl)-1H-1,2,3-triazol-4-yl)benzoate **35l** (22 mg, 0.05 mmol). The mixture was extracted with DCM and 1 M HCl and after purification using prep HPLC a white solid (5 mg, 0.01 mmol, 20%) was obtained. ¹H NMR (500 MHz, DMSO-*d*₆) δ ppm 2.41 (s, 3 H) 7.63 (d, *J*=8.70 Hz, 2 H) 8.08 (s, 4 H) 8.23 (d, *J*=8.70 Hz, 2 H) 8.25 (s, 1 H) 8.83 (s, 1 H) 9.23 (s, 1 H); ¹³C NMR (126 MHz, DMSO-*d*₆) δ ppm 1.63, 17.94, 108.81, 119.67, 123.13, 124.80, 125.74, 129.14, 129.45, 130.59, 132.93, 135.13, 136.76, 143.92, 146.31, 167.54

4-methyl-6-phenoxy pyridin-3-amine (38a): The aryl ether was synthesized according to **GP6** using 6-bromo-4-methylpyridin-3-amine **37** (100 mg, 0.53 mmol), phenol (1.2 eq., 0.60 mmol, 70 mg), cesium carbonate (3 eq., 1.61 mmol, 523 mg) and CuI (0.1 eq., 0.05 mmol, 9 mg) in DMF (3 mL). The product was purified using automated flash chromatography (DCM/MeOH 1:0 → 9:1). Yield: (30 mg, 0.15 mmol, 28%) MS (ESI+) *m/z* 201 (M + H).

6-(2-fluorophenoxy)-4-methylpyridin-3-amine (38b): The aryl ether was synthesized according to **GP6** using 6-bromo-4-methylpyridin-3-amine **37** (100 mg, 0.53 mmol), 2-fluorophenol (1.2 eq., 0.64 mmol, 72 mg), cesium carbonate (3 eq., 1.61 mmol, 523 mg) and CuI (0.1 eq., 0.05 mmol, 9 mg) in DMF (3 mL). The product (102 mg, 0.47 mmol, 88%) was used as obtained without further purifications. MS (ESI+) *m/z* 219 (M + H).

6-(3-fluorophenoxy)-4-methylpyridin-3-amine (38c): The aryl ether was synthesized according to **GP6** using 6-bromo-4-methylpyridin-3-amine **37** (100 mg, 0.53 mmol), 3-fluorophenol (1.2 eq., 0.64 mmol, 72 mg), cesium carbonate (3 eq., 1.61 mmol, 523 mg) and CuI (0.1 eq., 0.05 mmol, 9 mg) in DMF (3 mL). The product (85 mg, 0.39 mmol, 73%) was used as obtained without further purifications. MS (ESI+) *m/z* 219 (M + H).

6-(4-fluorophenoxy)-4-methylpyridin-3-amine (38d): The aryl ether was synthesized according to **GP6** using 6-bromo-4-methylpyridin-3-amine **37** (100 mg, 0.53 mmol), 4-fluorophenol (1.2 eq., 0.64 mmol, 72 mg), cesium carbonate (3 eq., 1.61 mmol, 523 mg) and CuI (0.1 eq., 0.05 mmol, 9 mg) in DMF (3 mL). The product (109 mg, 0.50 mmol, 94%) was used as obtained without further purifications. MS (ESI+) *m/z* 219 (M + H).

4-methyl-6-(phenylthio)pyridin-3-amine (38e): The arylether was synthesized according to **GP6** using 6-bromo-4-methylpyridin-3-amine **37** (100 mg, 0.53 mmol), benzenethiol (1.2 eq., 0.64 mmol, 70 mg), cesium carbonate (3 eq., 1.61 mmol, 523 mg) and CuI (0.1 eq., 0.05 mmol, 9 mg) in DMF (3 mL). The crude product was purified using automated flash chromatography (DCM/MeOH 1:0 → 9:1). Yield: (54 mg, 0.25 mmol, 47%) MS (ESI+) *m/z* 217 (M + H).

5-azido-4-methyl-2-phenoxy pyridine (39a): The azide was synthesized according to **GP1** using 4-methyl-6-phenoxy pyridin-3-amine **38a** (30 mg, 0.15 mmol), sodium nitrite (1.7 eq., 0.25 mmol, 17 mg), sodium azide (1.7 eq., 0.25 mmol, 14 mg), EtOAc (1 mL), 6 M HCl (3 mL). The crude product (29 mg, 0.13 mmol, 86%) was used as obtained in the next step without further purifications. *R*_f = 0.79 (PE/EtOAc 0:1)

5-azido-2-(2-fluorophenoxy)-4-methylpyridine (39b): The azide was synthesized according to **GP1** using 6-(2-fluorophenoxy)-4-methylpyridin-3-amine **38b** (102 mg, 0.47 mmol), sodium nitrite (1.7 eq., 0.80 mmol, 55 mg), sodium azide (1.7 eq., 0.80 mmol, 52 mg), EtOAc (2.5 mL), and 6 M HCl (5 mL). The crude product (107 mg, 0.44 mmol, 93%) was used as obtained in the next step without further purifications. $R_f = 0.84$ (PE/EtOAc 7:3)

5-azido-2-(3-fluorophenoxy)-4-methylpyridine (39c): The azide was synthesized according to **GP1** using 6-(3-fluorophenoxy)-4-methylpyridin-3-amine **38c** (85 mg, 0.39 mmol), sodium nitrite (1.7 eq., 0.66 mmol, 46 mg), sodium azide (1.7 eq., 0.66 mmol, 43 mg), EtOAc (2.5 mL), 6 M HCl (5 mL). The crude product (95 mg, 0.39 mmol, 99%) was used as obtained in the next step without further purifications. $R_f = 0.84$ (PE/EtOAc 7:3)

5-azido-2-(4-fluorophenoxy)-4-methylpyridine (39d): The azide was synthesized according to **GP1** using 6-(4-fluorophenoxy)-4-methylpyridin-3-amine **38d** (109 mg, 0.50 mmol), sodium nitrite (1.7 eq., 0.85 mmol, 59 mg), sodium azide (1.7 eq., 0.85 mmol, 55 mg), EtOAc (2.5 mL), 6 M HCl (5 mL). The crude product (120 mg, 0.49 mmol, 98%) was used as obtained in the next step without further purifications. $R_f = 0.84$ (PE/EtOAc 7:3)

5-azido-4-methyl-2-(phenylthio) pyridine (39e): The azide was synthesized according to **GP1** using 4-methyl-6-(phenylthio) pyridin-3-amine **38e** (54 mg, 0.25 mmol), sodium nitrite (1.7 eq., 0.42 mmol, 30 mg), sodium azide (1.7 eq., 0.42 mmol, 23 mg), EtOAc (2 mL), 6 M HCl (4 mL). The crude product (41 mg, 0.17 mmol, 70%) was used as obtained in the next step without further purifications. $R_f = 0.81$ (PE/EtOAc 0:1)

4-(1-(4-methyl-6-phenoxy pyridin-3-yl)-1H-1,2,3-triazol-4-yl)benzoic acid (40a): The triazole was synthesized according to **GP3** using 4-ethynylbenzoic acid (15 mg, 0.11 mmol) and 5-azido-4-methyl-2-phenoxy pyridine **39a** (1.2 eq., 29 mg, 0.13 mmol) as starting materials. 1 M HCl was added and the mixture was extracted with EtOAc (3x), the combined organic layers were dried over sodium sulfate and concentrated under reduced pressure to obtain the crude. Purification was done using flash chromatography (PE:EtOAc 1:0 → 1:0). **40a** was obtained as a white solid (21 mg, 0.05 mmol, 45%). $^1\text{H NMR}$ (500 MHz, DMSO- d_6) δ ppm 2.27 (s, 3 H) 7.19 - 7.23 (m, 2 H) 7.24 (s, 1 H) 7.25 - 7.29 (m, 1 H) 7.44 - 7.50 (m, 2 H) 7.99 - 8.13 (m, 5 H) 8.32 (s, 1 H) 9.12 (s, 1 H); $^{13}\text{C NMR}$ (126 MHz, DMSO- d_6) δ ppm 17.28, 112.78, 121.54, 124.75, 125.13, 125.35, 129.57, 129.92, 130.19, 130.29, 134.35, 144.21, 145.83, 147.15, 153.43, 163.58, 167.05

4-(1-(6-(2-fluorophenoxy)-4-methylpyridin-3-yl)-1H-1,2,3-triazol-4-yl)benzoic acid (40b): The triazole was synthesized according to **GP3** using 4-ethynylbenzoic acid (65 mg, 0.45 mmol) and 5-azido-2-(2-fluorophenoxy)-4-methylpyridine **39b** (1.2 eq., 129 mg, 0.53 mmol) as starting materials. The crude was obtained as a white solid (140 mg, 0.36 mmol, 80%). Purification was done using prep. HPLC. $^1\text{H NMR}$ (500 MHz, DMSO- d_6) δ ppm 2.29 (s, 3 H) 7.27 - 7.31 (m, 1 H) 7.31 - 7.36 (m, 1 H) 7.37 (s, 1 H) 7.38 - 7.44 (m, 2 H) 8.05 (s, 5 H) 8.30 (s, 1 H) 9.13 (s, 1 H) 13.06 (br. s., 1 H); $^{13}\text{C NMR}$ (126 MHz, DMSO- d_6) δ ppm 17.26, 112.04, 116.81, 116.95, 124.37, 124.75, 125.30, 125.37, 125.40, 126.97, 127.03, 129.87, 130.17, 130.44, 134.25, 140.01, 140.10, 144.04, 145.84, 147.49, 153.28, 155.24, 162.66, 167.05

4-(1-(6-(3-fluorophenoxy)-4-methylpyridin-3-yl)-1H-1,2,3-triazol-4-yl)benzoic acid (40c): The triazole was synthesized according to **GP3** using 4-ethynylbenzoic acid (65 mg, 0.45 mmol) and 5-azido-2-(3-fluorophenoxy)-4-methylpyridine **39c** (1.2 eq., 129 mg, 0.53 mmol) as starting materials. The crude was obtained as a white solid (160 mg, 0.41 mmol, 93%). Purification was done using prep. HPLC. ¹H NMR (500 MHz, DMSO-*d*₆) δ ppm 2.29 (s, 3 H) 7.08 (dd, *J*=8.01, 1.75 Hz, 1 H) 7.10 - 7.15 (m, 1 H) 7.18 (dt, *J*=10.15, 2.33 Hz, 1 H) 7.30 (s, 1 H) 7.50 (td, *J*=8.24, 6.87 Hz, 1 H) 8.06 (s, 4 H) 8.35 (s, 1 H) 9.12 (s, 1 H); ¹³C NMR (126 MHz, DMSO-*d*₆) δ ppm 17.29, 109.27, 109.46, 111.92, 112.09, 113.04, 117.66, 117.69, 124.69, 125.31, 129.89, 130.17, 131.04, 131.12, 134.23, 144.19, 145.86, 147.34, 154.48, 154.57, 161.65, 163.04, 163.60, 167.06

4-(1-(6-(4-fluorophenoxy)-4-methylpyridin-3-yl)-1H-1,2,3-triazol-4-yl)benzoic acid (40d): The triazole was synthesized according to **GP3** using 4-ethynylbenzoic acid (65 mg, 0.45 mmol) and 5-azido-2-(4-fluorophenoxy)-4-methylpyridine **39d** (1.2 eq., 129 mg, 0.53 mmol) as starting materials. The crude was obtained as a white solid (155 mg, 0.39 mmol, 86%). Purification was done using prep. HPLC. ¹H NMR (500 MHz, DMSO-*d*₆) δ ppm 2.27 (s, 3 H) 7.25 (s, 1 H) 7.26 - 7.32 (m, 4 H) 8.06 (s, 4 H) 8.32 (s, 1 H) 9.11 (s, 1 H) 13.08 (br. s., 1 H); ¹³C NMR (126 MHz, DMSO-*d*₆) δ ppm 17.25, 112.61, 116.32, 116.51, 123.44, 124.70, 125.31, 129.59, 130.17, 130.40, 134.28, 144.10, 145.84, 147.17, 149.37, 158.28, 160.19, 163.57, 167.06

4-(1-(4-methyl-6-(phenylthio)pyridin-3-yl)-1H-1,2,3-triazol-4-yl)benzoic acid (40e): The triazole was synthesized according to **GP3** using 4-ethynylbenzoic acid (19 mg, 0.13 mmol) and 5-azido-4-methyl-2-(phenylthio)pyridine **39e** (1.2 eq., 40 mg, 0.16 mmol) as starting materials. The crude was obtained as a white solid (25 mg, 0.06 mmol, 46%). Purification was done using prep. HPLC. ¹H NMR (500 MHz, DMSO-*d*₆) δ ppm 2.18 (s, 3 H) 7.18 (s, 1 H) 7.44 - 7.60 (m, 3 H) 7.61 - 7.77 (m, 2 H) 7.95 - 8.14 (m, 4 H) 8.56 (s, 1 H) 9.13 (s, 1 H) 13.09 (br. s., 1 H); ¹³C NMR (126 MHz, DMSO-*d*₆) δ ppm 17.22, 122.67, 124.51, 125.33, 129.41, 129.71, 130.03, 130.17, 130.82, 134.22, 134.91, 143.68, 145.86, 145.90, 161.32, 167.04

4-azidoisoquinoline (42): The azide was synthesized according to **GP1** using isoquinolin-4-amine **41** (150 mg, 1 mmol), sodium nitrite (1.7 eq., 122 mg, 1.7 mmol), sodium azide (1.7 eq. 115 mg, 1.7 mmol), EtOAc (4 mL), 6 M HCl (2.4 mL). The crude product (143 mg, 0.84 mmol, 84%) was used as obtained in the next step without further purifications. *R*_f = 0.63 (PE/EtOAc 7:3)

4-(1-(isoquinolin-4-yl)-1H-1,2,3-triazol-4-yl)benzoic acid (43): The triazole was synthesized according to **GP3** using 4-ethynylbenzoic acid (95 mg, 0.65 mmol) and 4-azidoisoquinoline **42** (1.3 eq., 143 mg, 0.84 mmol) as starting materials. The crude was obtained as a yellow solid (183 mg, 0.58 mmol, 90%). Purification was done using prep. HPLC. ¹H NMR (500 MHz, DMSO-*d*₆) δ ppm 7.80 - 7.86 (m, 1 H) 7.89 (ddd, *J*=8.09, 7.02, 1.07 Hz, 1 H) 7.92 - 7.99 (m, 1 H) 8.06 - 8.11 (m, 2 H) 8.11 - 8.19 (m, 2 H) 8.39 (d, *J*=8.24 Hz, 1 H) 8.86 (s, 1 H) 9.38 (s, 1 H) 9.60 (s, 1 H) 13.06 (br. s., 1 H); ¹³C NMR (126 MHz, DMSO-*d*₆) δ ppm 121.42, 125.32, 125.43, 128.26, 128.45, 128.51, 128.85, 130.00, 130.15, 130.31, 132.83, 134.28, 139.26, 146.00, 154.60, 166.98

3-azidoquinoline (45): The azide was synthesized according to **GP1** using quinolin-3-amine **44** (100 mg, 0.69 mmol), sodium nitrite (1.7 eq., 81 mg, 1.63 mmol), sodium azide (1.7 eq., 77 mg, 1.63

mmol), EtOAc (3.5 mL), 6 M HCl (2.0 mL). The crude product (107 mg, 0.63 mmol, 91%) was used as obtained in the next step without further purifications. $R_f = 0.73$ (PE/EtOAc 7:3)

4-(1-(quinolin-3-yl)-1*H*-1,2,3-triazol-4-yl)benzoic acid (46): The triazole was synthesized according to **GP3** using 4-ethynylbenzoic acid (60 mg, 0.41 mmol) and 3-azidoquinoline **45** (1.2 eq., 83 mg, 0.49 mmol) as starting materials. The crude was obtained as a white solid (70 mg, 0.22 mmol, 54%). Purification was done using prep. HPLC. $^1\text{H NMR}$ (500 MHz, DMSO- d_6) δ ppm 7.73 - 7.80 (m, 1 H) 7.90 (ddd, $J=8.35, 6.98, 1.30$ Hz, 1 H) 8.10 (s, 4 H) 8.18 (t, $J=8.62$ Hz, 2 H) 9.01 (d, $J=2.29$ Hz, 1 H) 9.53 (d, $J=2.59$ Hz, 1 H) 9.67 (s, 1 H); $^{13}\text{C NMR}$ (126 MHz, DMSO- d_6) δ ppm 121.33, 125.35, 126.02, 127.09, 128.24, 128.70, 128.99, 130.13, 130.22, 130.63, 134.01, 143.16, 146.69, 147.02, 167.07

6-methylisoquinolin-4-amine (48a): The amino isoquinolin was synthesized according to **GP2** using 4-bromo-6-methylisoquinoline **47a** (100 mg, 0.46 mmol), L-proline (0.1 eq., 0.05 mmol, 5 mg), sodium azide (1.3 eq., 0.60 mmol, 34 mg), sodium carbonate (1.3 eq., 0.60 mmol, 64 mg), sodium ascorbate (1.3 eq., 0.60 mmol, 119 mg), copper sulfate heptahydrate (1 eq., 0.46 mmol, 115 mg), DMF (4 mL) and water (2 mL). The crude product (70 mg, 0.44 mmol, 97%) was used as obtained in the next step without further purifications. MS (ESI+) m/z 159 (M + H).

7-chloroisoquinolin-4-amine (48b): The amino isoquinolin was synthesized according to **GP2** using 4-bromo-7-chloroisoquinoline **47b** (100 mg, 0.36 mmol), L-proline (0.1 eq., 0.04 mmol, 4 mg), sodium azide (1.3 eq., 0.46 mmol, 30 mg), sodium carbonate (1.3 eq., 0.49 mmol, 64 mg), sodium ascorbate (1.3 eq., 0.46 mmol, 92 mg), copper sulfate heptahydrate (1 eq., 0.36 mmol, 89 mg), DMF (4 mL) and water (2 mL). The crude product (56 mg, 0.31 mmol, 88%) was used as obtained in the next step without further purifications. MS (ESI+) m/z 179 (M + H).

methyl 4-aminoisoquinoline-7-carboxylate (48c): The amino isoquinolin was synthesized according to **GP2** using methyl 4-bromoisoquinoline-7-carboxylate **47c** (50 mg, 0.18 mmol), L-proline (0.1 eq., 0.02 mmol, 2 mg), sodium azide (1.3 eq., 0.24 mmol, 16 mg), sodium carbonate (1.3 eq., 0.24 mmol, 26 mg), sodium ascorbate (1.3 eq., 0.24 mmol, 48 mg), copper sulfate heptahydrate (1 eq., 0.18 mmol, 46 mg), DMF (2 mL) and water (1 mL). The crude product (33 mg, 0.16 mmol, 90%) was used as obtained in the next step without further purifications. MS (ESI+) m/z 203 (M + H).

4-azido-6-methylisoquinoline (49a): The azide was synthesized according to **GP1** using 6-methylisoquinolin-4-amine **48a** (70 mg, 0.44 mmol), sodium nitrite (1.7 eq., 0.75 mmol, 52 mg), sodium azide (1.7 eq., 0.75 mmol, 48 mg), EtOAc (2 mL), 6 M HCl (4 mL). The crude product (74 mg, 0.40 mmol, 91%) was used as obtained in the next step without further purifications. $R_f = 0.33$ (PE/EtOAc 7:3)

4-azido-7-chloroisoquinoline (49b): The azide was synthesized according to **GP1** using 7-chloroisoquinolin-4-amine **48b** (56 mg, 0.31 mmol), sodium nitrite (1.7 eq., 0.52 mmol, 36 mg), sodium azide (1.7 eq., 0.52 mmol, 34 mg), EtOAc (2.5 mL), 6 M HCl (5 mL). The crude product (57 mg, 0.28 mmol, 90%) was used as obtained in the next step without further purifications. $R_f = 0.47$ (PE/EtOAc 7:3)

methyl 4-azidoisoquinoline-7-carboxylate (49c): The azide was synthesized according to **GP1** using methyl 4-aminoisoquinoline-7-carboxylate **48c** (33 mg, 0.16 mmol), sodium nitrite (1.7 eq., 0.27 mmol, 19 mg), sodium azide (1.7 eq., 0.27 mmol, 17 mg), EtOAc (2 mL), 6 M HCl (4 mL). The crude product (25 mg, 0.11 mmol, 68%) was used as obtained in the next step without further purifications. $R_f = 0.36$ (PE/EtOAc 7:3)

4-(1-(6-methylisoquinolin-4-yl)-1H-1,2,3-triazol-4-yl)benzoic acid (50a): The triazole was synthesized according to **GP3** using 4-ethynylbenzoic acid (28 mg, 0.19 mmol) and 4-azido-6-methylisoquinoline **49a** (1.2 eq., 42 mg, 0.23 mmol) as starting materials. The crude was obtained as a white solid (16 mg, 0.04 mmol, 21%). Purification was done using prep. HPLC. $^1\text{H NMR}$ (500 MHz, $\text{DMSO-}d_6$) δ ppm 2.54 (s, 3 H) 7.59 (s, 1 H) 7.73 (dd, $J=8.47, 1.30$ Hz, 1 H) 8.09 (m, $J=8.55$ Hz, 2 H) 8.14 (m, $J=8.55$ Hz, 2 H) 8.29 (d, $J=8.39$ Hz, 1 H) 8.79 (s, 1 H) 9.36 (s, 1 H) 9.52 (s, 1 H); $^{13}\text{C NMR}$ (126 MHz, $\text{DMSO-}d_6$) δ ppm 21.94, 119.93, 125.32, 125.44, 128.14, 130.17, 130.38, 130.98, 134.28, 139.55, 143.45, 146.00, 154.14, 167.13

4-(1-(7-chloroisoquinolin-4-yl)-1H-1,2,3-triazol-4-yl)benzoic acid (50b): The triazole was synthesized according to **GP3** using 4-ethynylbenzoic acid (44 mg, 0.30 mmol) and 4-azido-7-chloroisoquinoline **49b** (1.2 eq., 73 mg, 0.36 mmol) as starting materials. The crude was obtained as a white solid (35 mg, 0.10 mmol, 33%). Purification was done using prep. HPLC. $^1\text{H NMR}$ (500 MHz, $\text{DMSO-}d_6$) δ ppm 7.92 - 7.99 (m, 2 H) 8.05 - 8.11 (m, 4 H) 8.56 (d, $J=1.98$ Hz, 1 H) 8.90 (s, 1 H) 9.37 (s, 1 H) 9.57 (s, 1 H); $^{13}\text{C NMR}$ (126 MHz, $\text{DMSO-}d_6$) δ ppm 121.63, 124.31, 125.16, 125.36, 127.03, 128.45, 129.19, 130.14, 131.55, 133.15, 133.23, 139.53, 146.19, 153.76, 166.36

4-(1-(7-(methoxycarbonyl)isoquinolin-4-yl)-1H-1,2,3-triazol-4-yl)benzoic acid (50c): The triazole was synthesized according to **GP3** using 4-ethynylbenzoic acid (23 mg, 0.16 mmol) and methyl 4-azidoisoquinoline-7-carboxylate **49c** (1.2 eq., 43 mg, 1.9 mmol) as starting materials. The crude was obtained as a white solid (15 mg, 0.04 mmol, 25%). Purification was done using prep. HPLC. $^1\text{H NMR}$ (500 MHz, $\text{DMSO-}d_6$) δ ppm 3.98 (s, 3 H) 8.00 (d, $J=8.85$ Hz, 1 H) 8.07 - 8.15 (m, 5 H) 8.38 (dd, $J=8.93, 1.75$ Hz, 1 H) 9.00 (s, 1 H) 9.09 (d, $J=1.22$ Hz, 1 H) 9.40 (s, 1 H) 9.81 (s, 1 H) 13.07 (br. s., 1 H); $^{13}\text{C NMR}$ (126 MHz, $\text{DMSO-}d_6$) δ ppm 52.75, 122.63, 125.32, 125.45, 127.88, 128.41, 129.46, 130.18, 130.87, 131.40, 132.00, 141.34, 146.13, 156.07, 165.34, 167.02

1.2 Fluorescence Polarization (FP) Assay

Representative curves of dose-dependent competition studies with compounds **19c**, **19n**, **31b**, **26a-b** and **50a-b** were shown in Figure S1, which based on normalized data points (% polarization from 0 - 100%) representing averaged FP values of duplicates \pm standard deviation. Curves were fit to a four-parameter dose response model using OriginLab (2019) to calculate IC_{50} values. Compounds were tested in two independent experiments using LBS1_flc, LBS2_flc and LBS3_flc, respectively, as fluorescent probe.

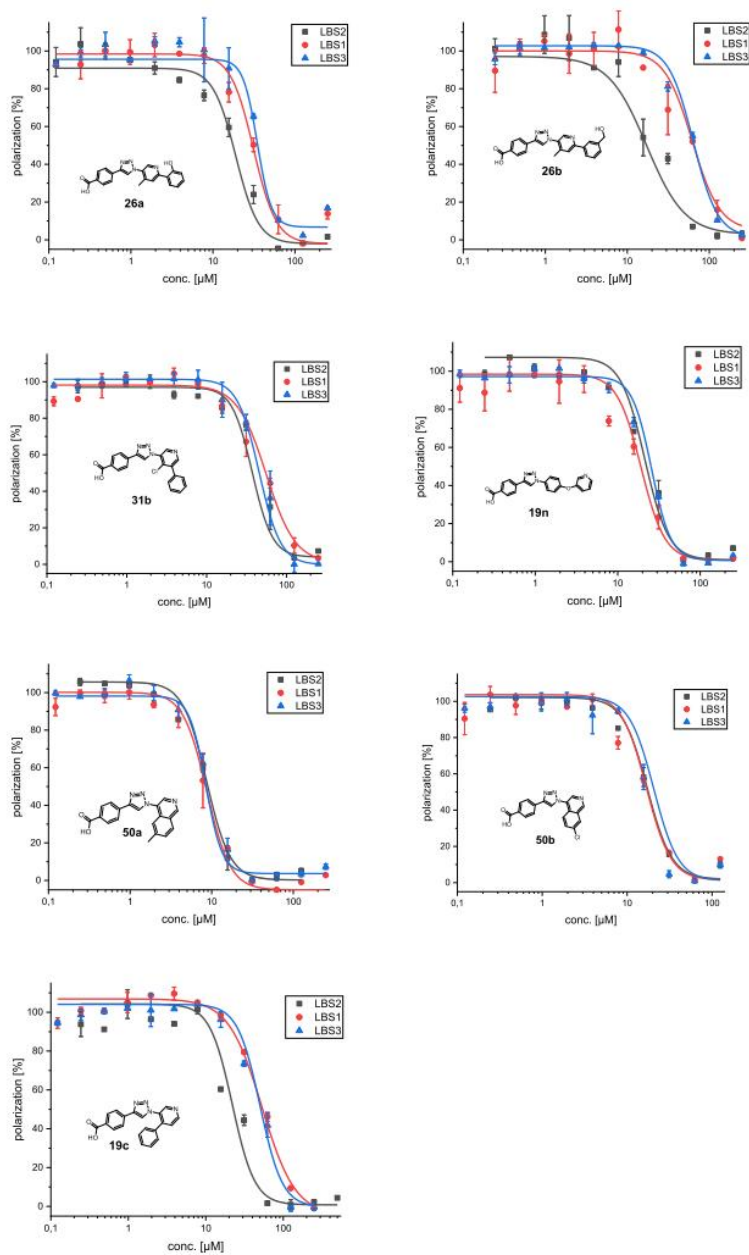


Figure S1: A: Representative curves of dose-dependent experiments for compounds **19c**, **31b**, **26a-b**, **19n** and **50a-b** in FP-based competition experiments using LANA DBD mutant (1008-1146) and fluorescence labeled LBS1, LBS2 and LBS3, respectively.

1.3 Electrophoretic Mobility Shift Assay (EMSA)

Gels of dose-dependent EMSA experiments of compounds **19c**, **31b**, **26a-b**, **19n** and **50a-b** are shown in Figure S2 and S3. Curves are shown with normalized data points (inhibition from 0 - 100%) representing intensities of LANA-DNA-complex bands. IC₅₀ values were calculated using a four-parameter dose-response model (Figure S4)

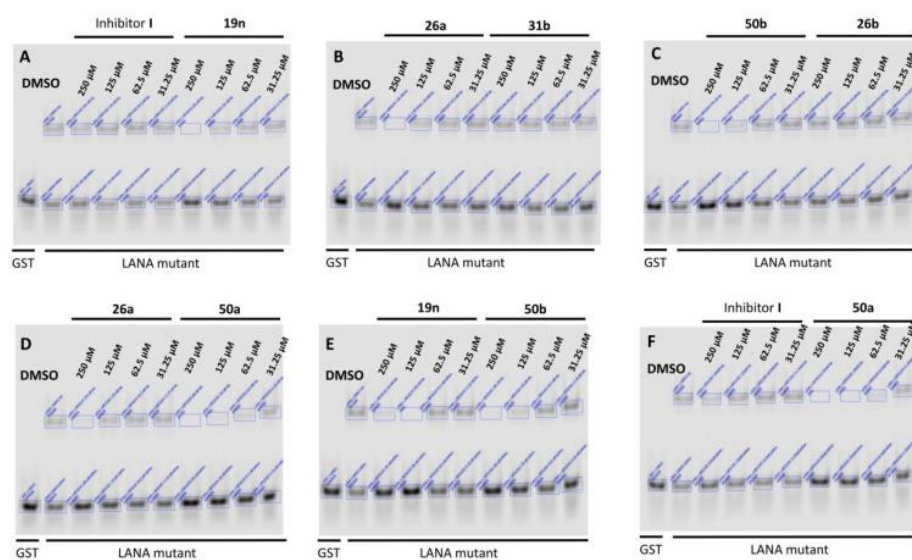


Figure S2: Gels of dose-dependent EMSA experiments using LANA DBD mutant and LBS1. (A) Inhibitor **I** and compound **19n**. (B) Compounds **26a** and **31b** (C) Compounds **50b** and **26b**. (D) Compounds **26a** and **50a**. (E) Compounds **19n** and **50b**. (F) Inhibitor **I** and **50a**.

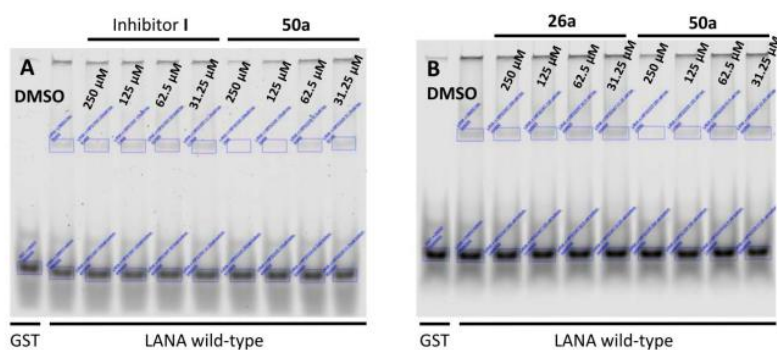


Figure S3: Gels of dose-dependent EMSA experiments. (A) Inhibitor **I** and **50a** using wild-type LANA CTD and LBS1. (B) Inhibitor **26a** and **50a** using wild-type LANA CTD and LBS1.

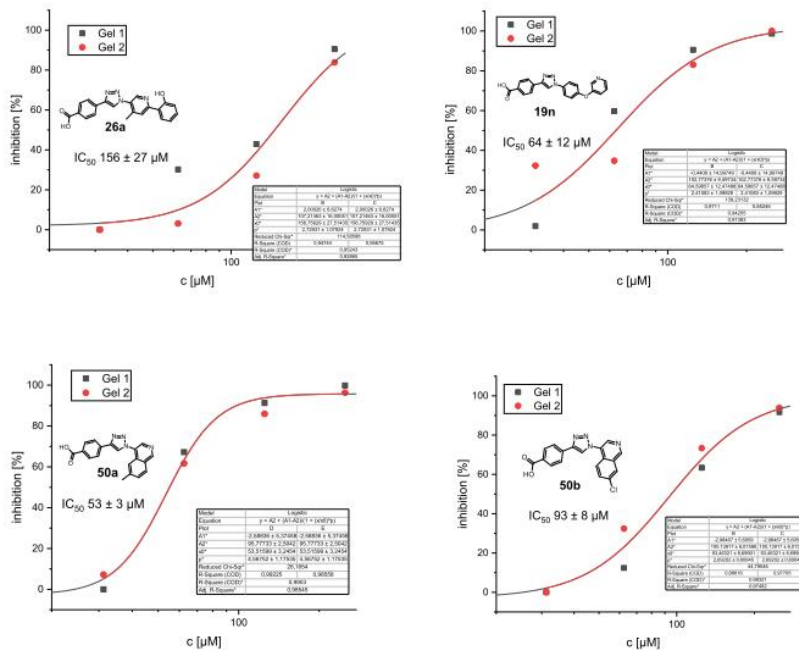
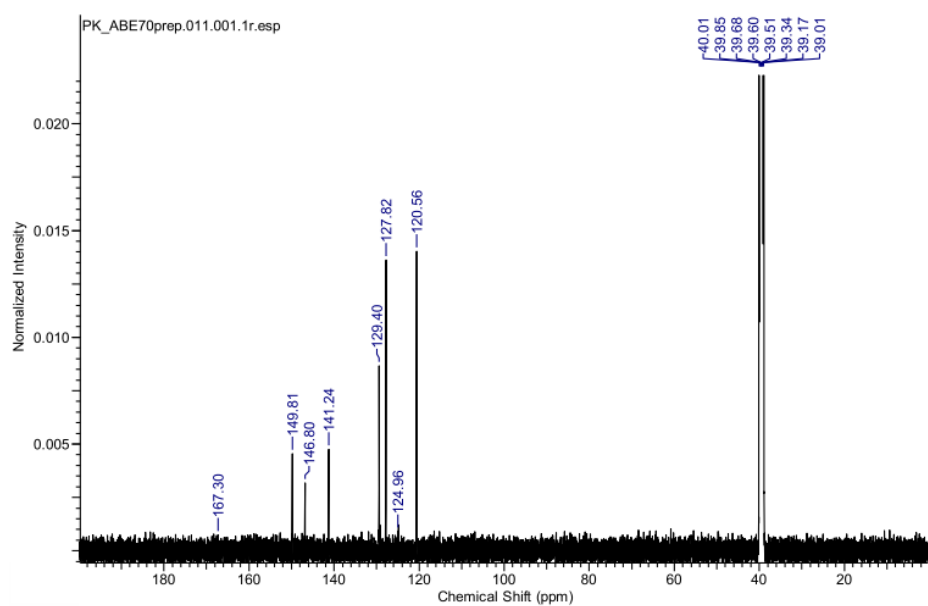
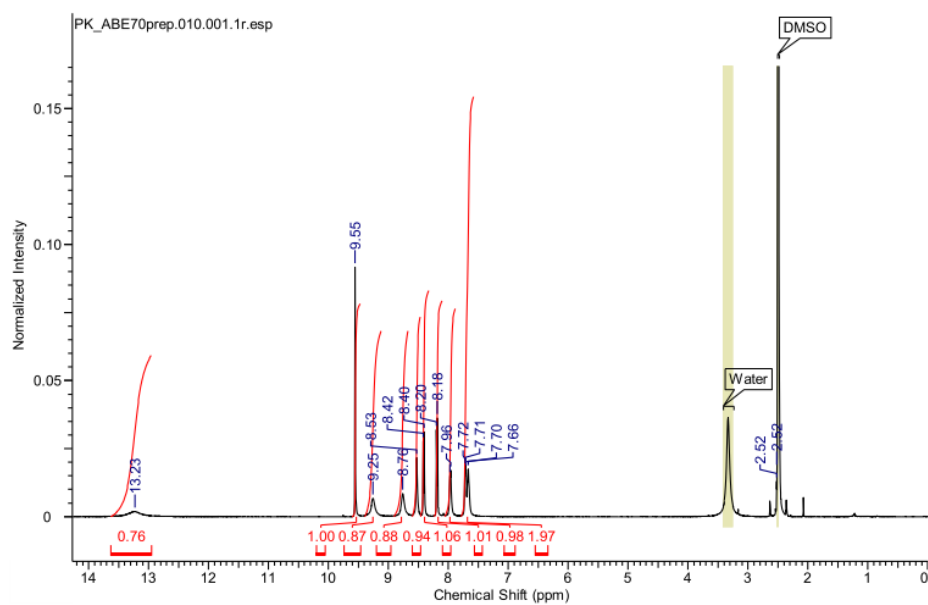


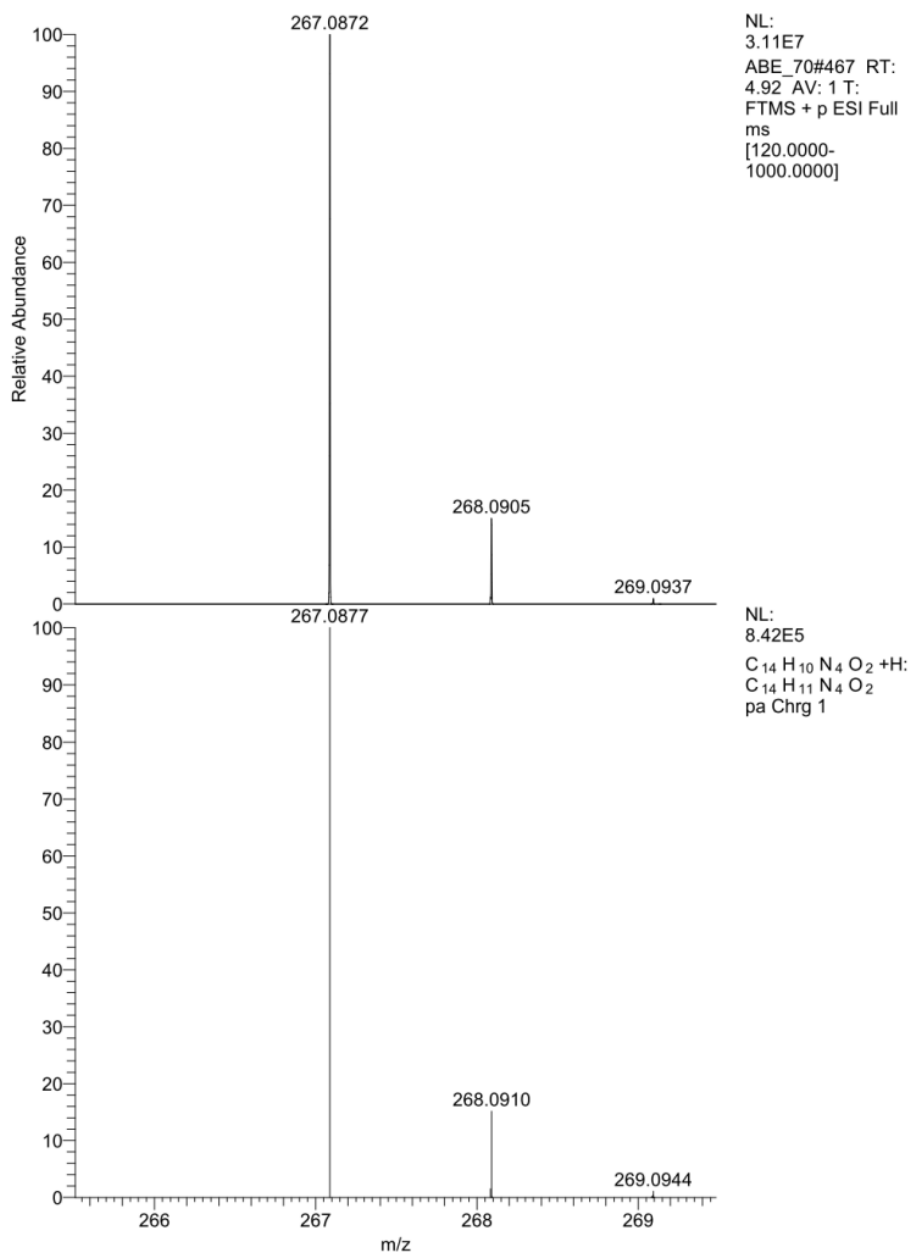
Figure S4: Dose-dependent EMSA experiments with compounds **26a**, **19n** and **50a-b**. Curve shows normalized data points (inhibition from 0 - 100%) representing averaged intensities of LANA-DNA-complex bands (upper bands) of duplicates \pm standard deviation. IC_{50} value was calculated using a four-parameter dose-response model.

1.4 ^1H and ^{13}C NMR Spectra and High Resolution Mass Spectrometry (HRMS)

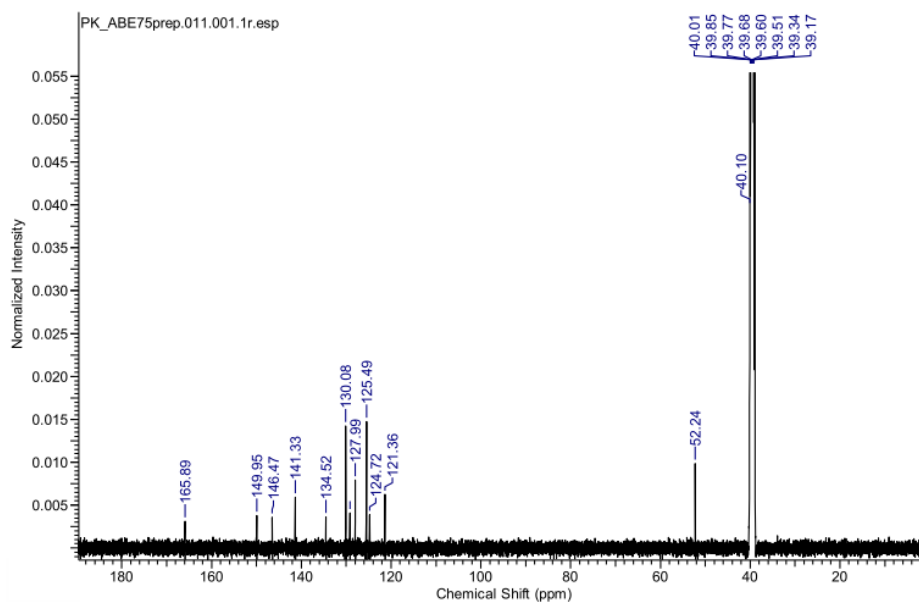
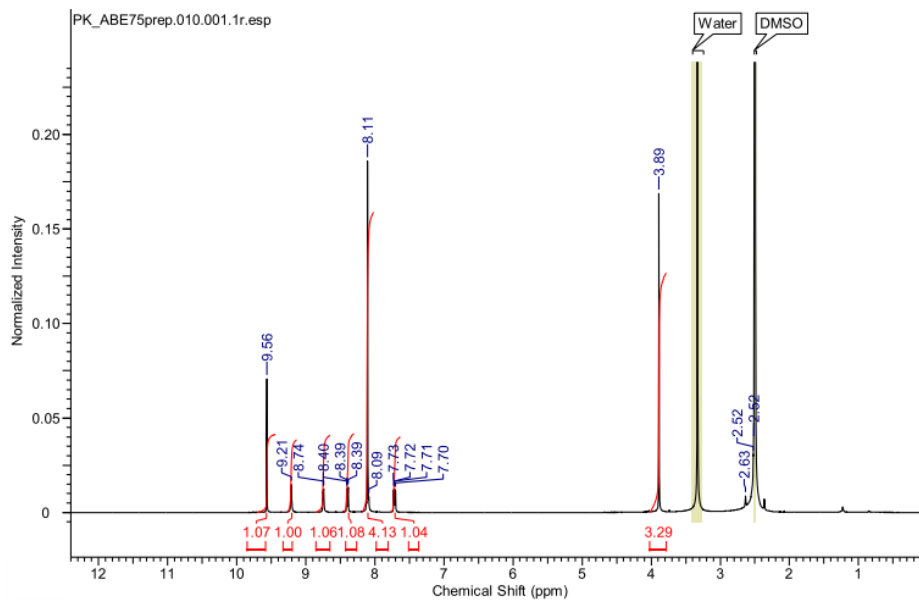
Representative ^1H and ^{13}C of each final compound were depicted in below. The high resolution masses of all final compounds were measured on a Thermo Scientific Q Exactive Focus (Germany) equipped with DIONEX ultimate 3000 UHPLC+ focused. For gradient elution, an EC 150/2 NUCLEODUR C18 Pyramid (3 μm) column (Machery-Nagel, Germany) was used with a mobile phase consisting of acetonitrile containing 0.1% formic acid (FA; [v/v]; eluent A) and water containing 0.1% FA ([v/v]; eluent B). Elution method was used with a total run time of 7.5 min and gradient conditions 10% A to 90% A. Mass spectrometry was used in positive or negative mode using electrospray ionization (ESI). Measured (upper spectrum) and calculated (lower spectrum) HRMS spectra of each final synthesized compound were depicted below.

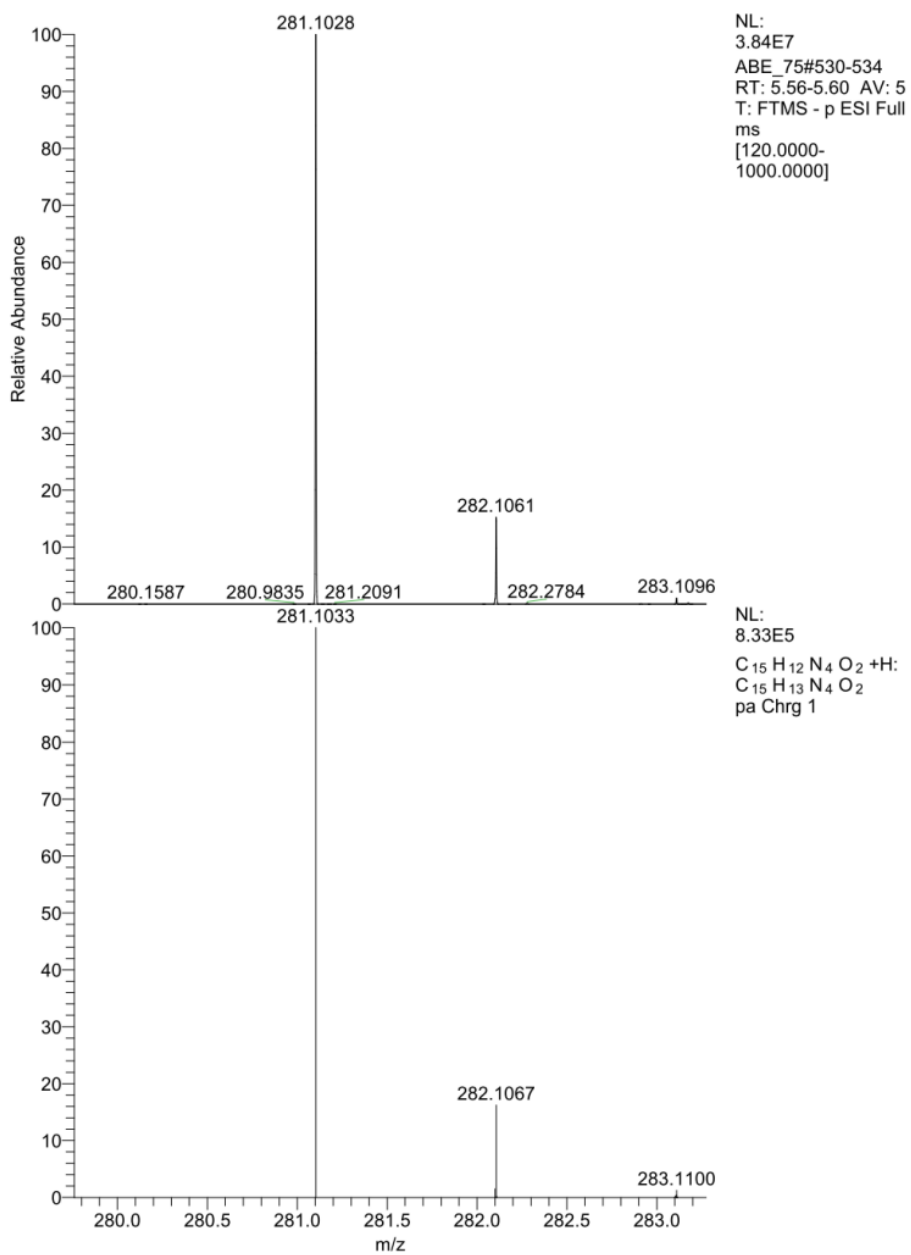
3-(1-(pyridin-3-yl)-1H-1,2,3-triazol-4-yl)benzoic acid (4):



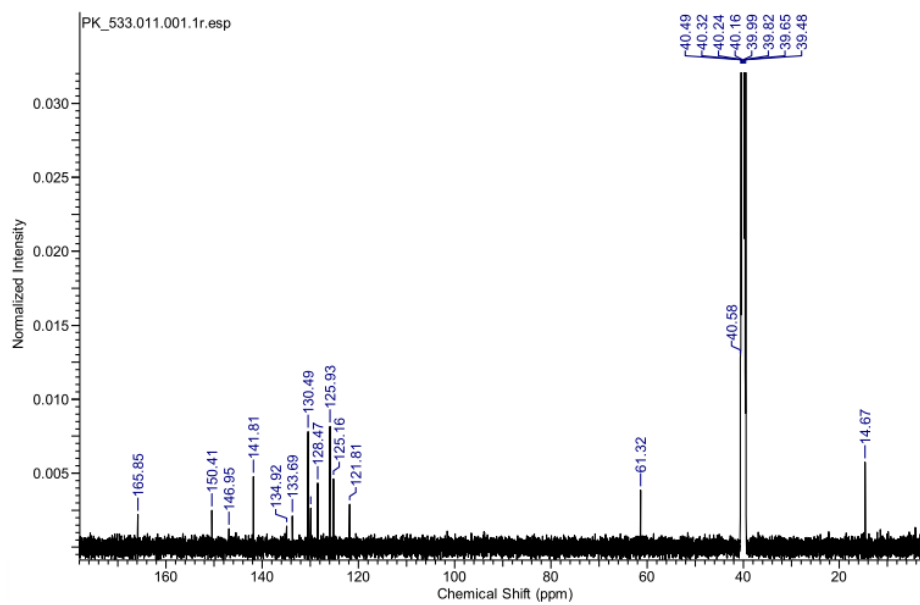
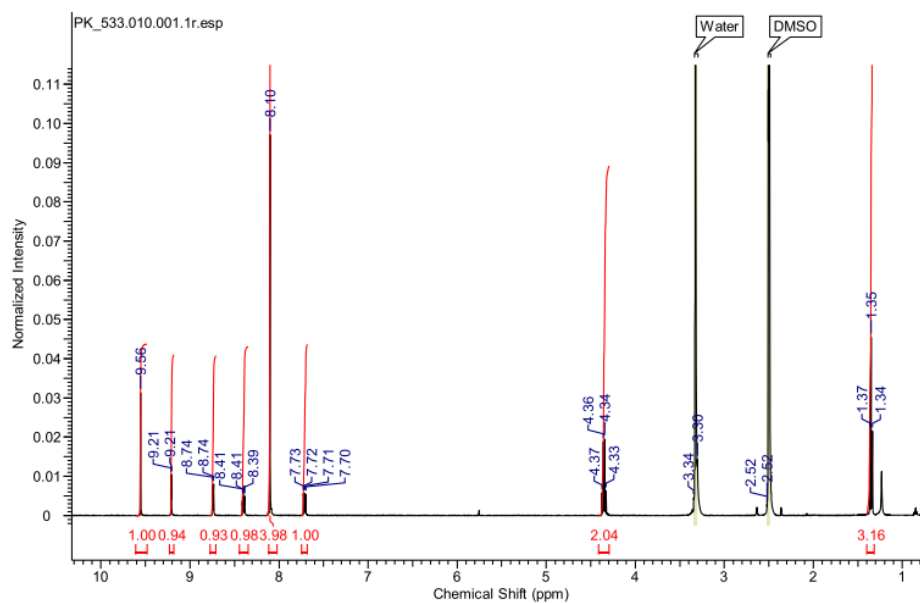


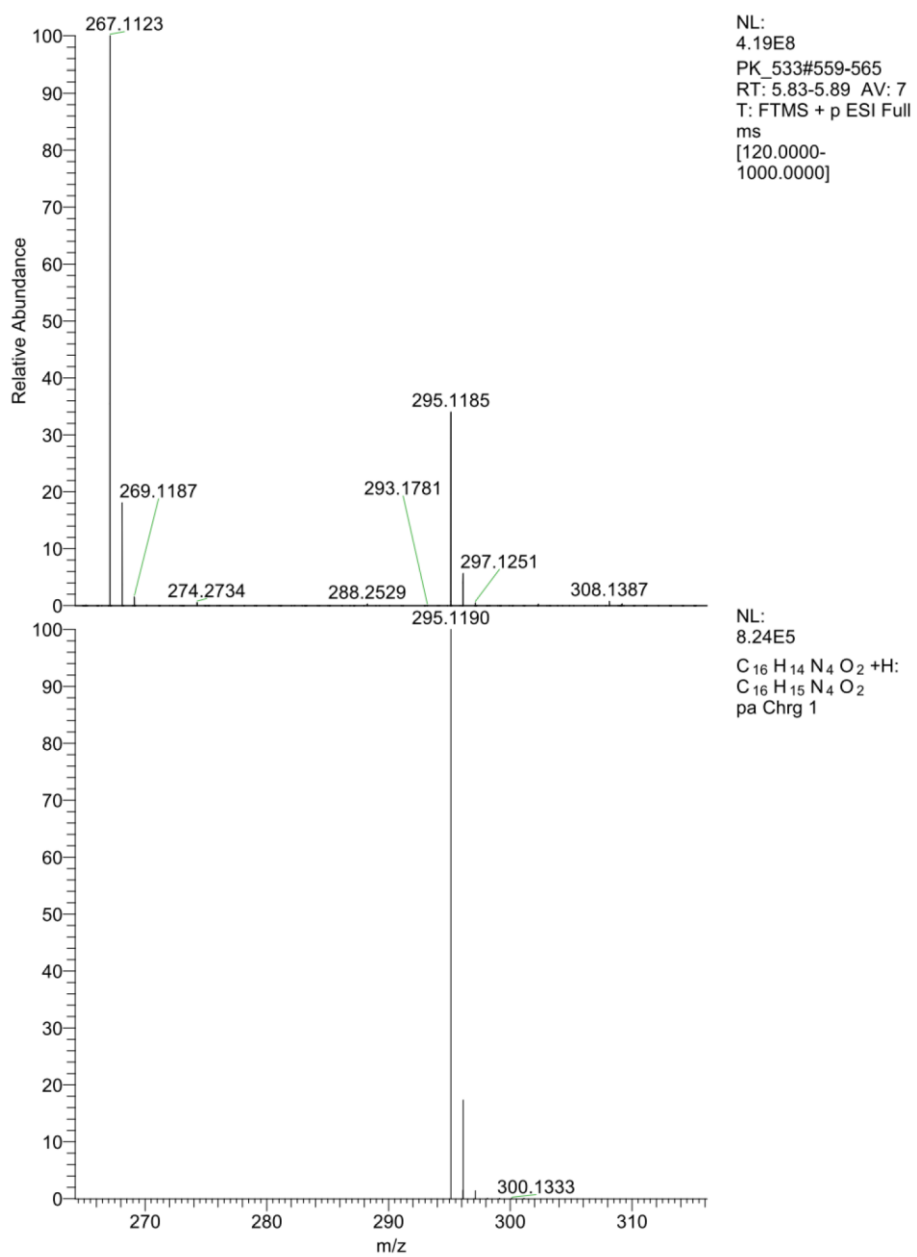
methyl 4-(1-(pyridin-3-yl)-1H-1,2,3-triazol-4-yl)benzoate (5):



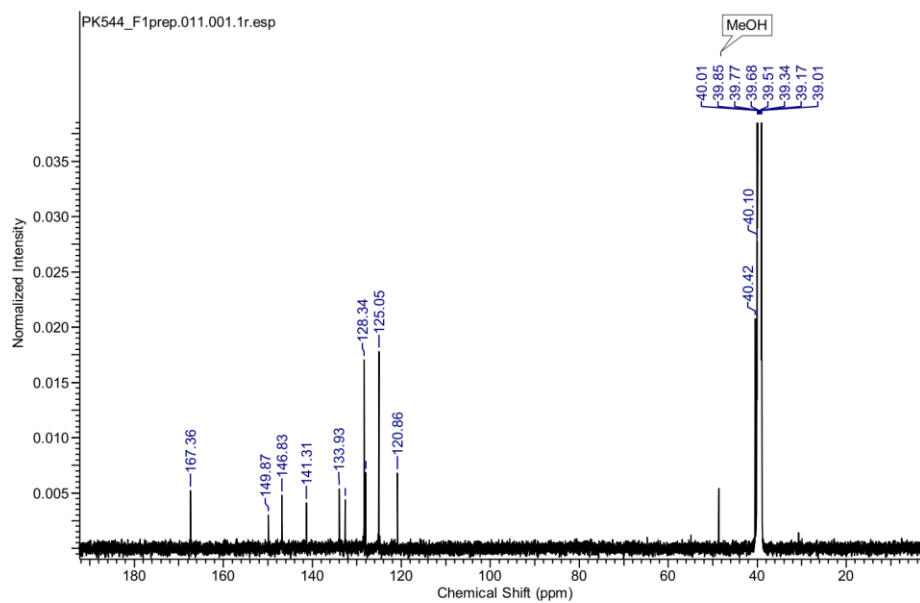
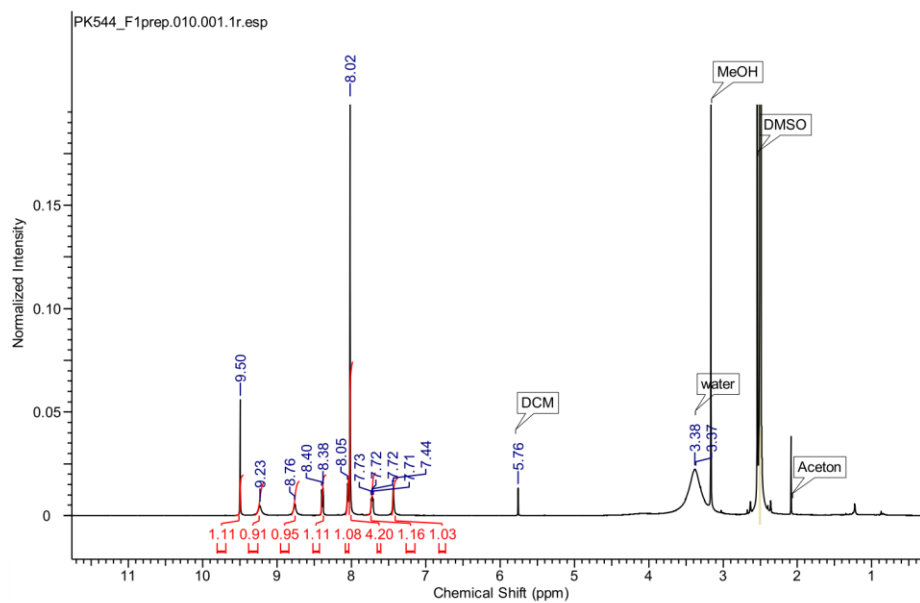


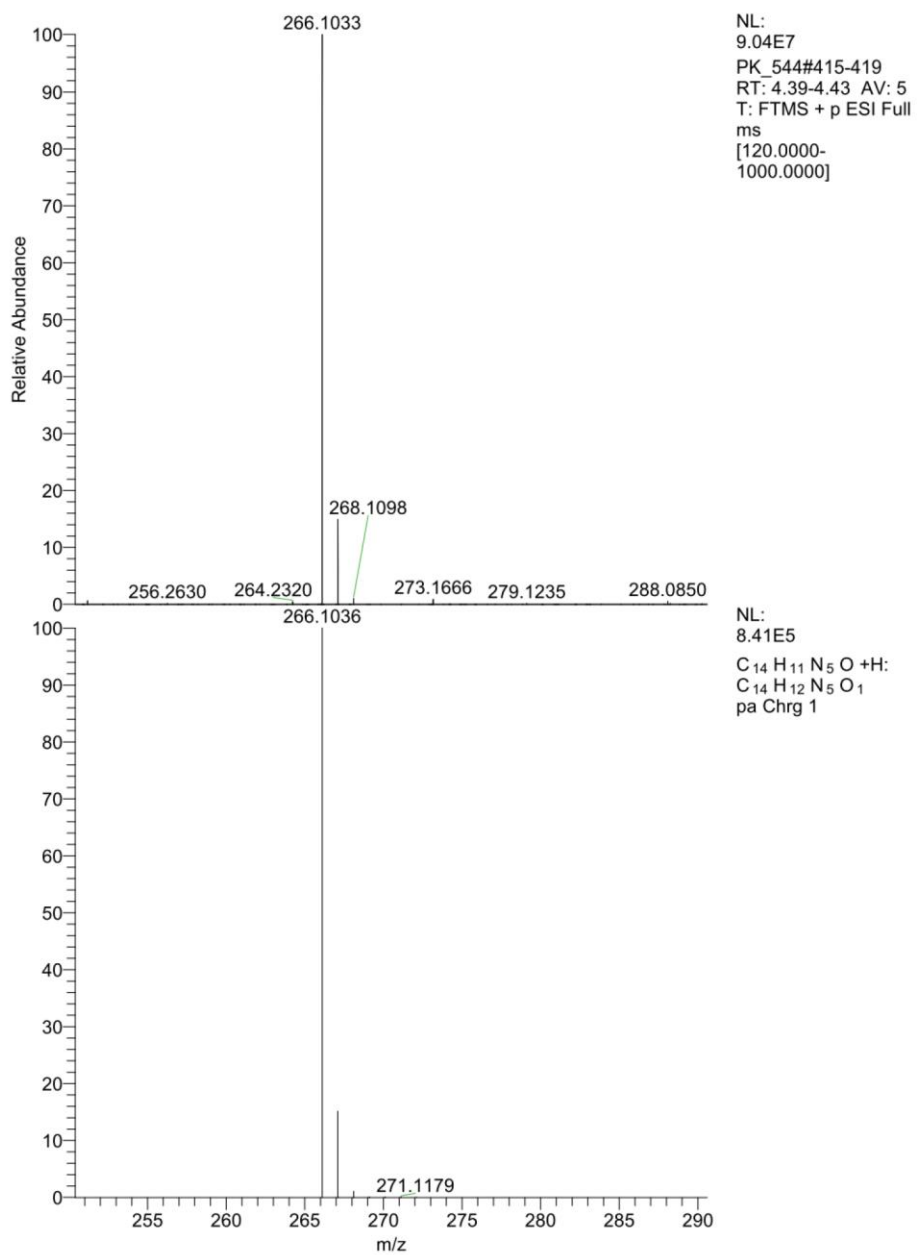
ethyl 4-(1-(pyridin-3-yl)-1H-1,2,3-triazol-4-yl)benzoate (6):

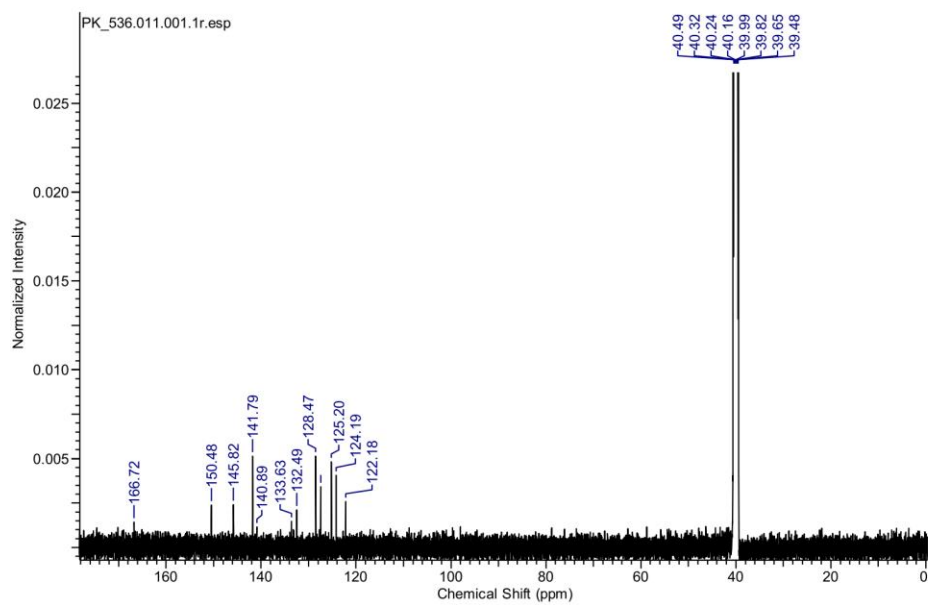
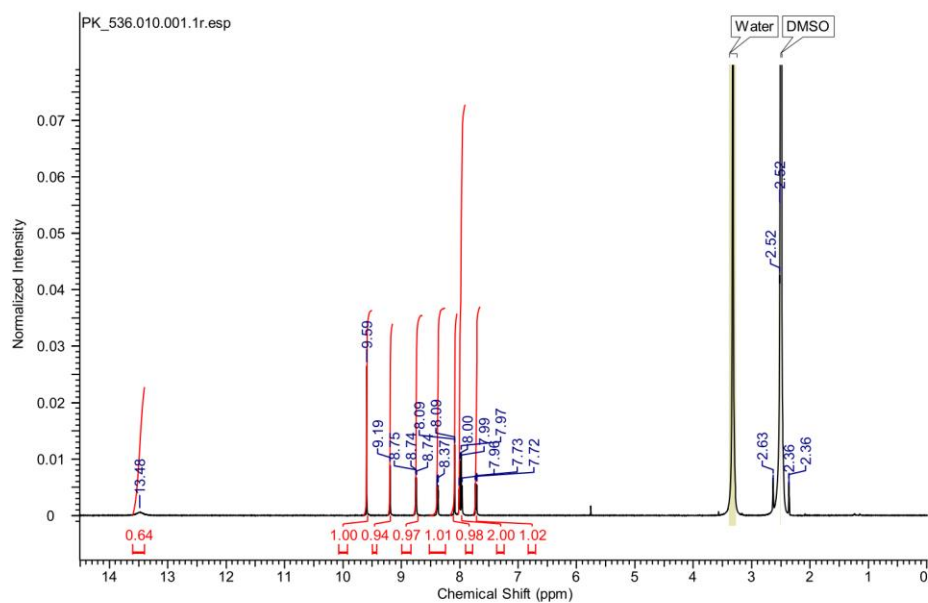


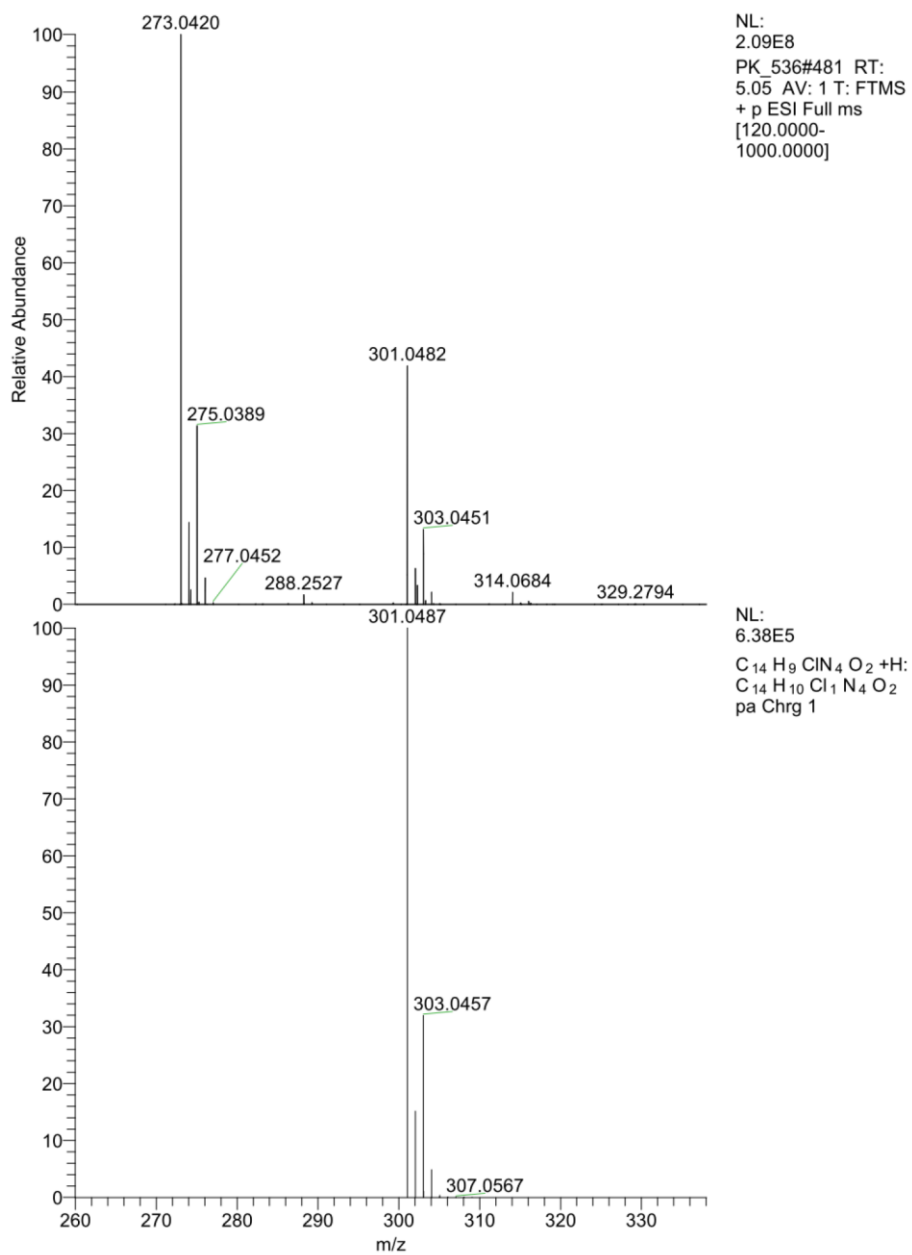


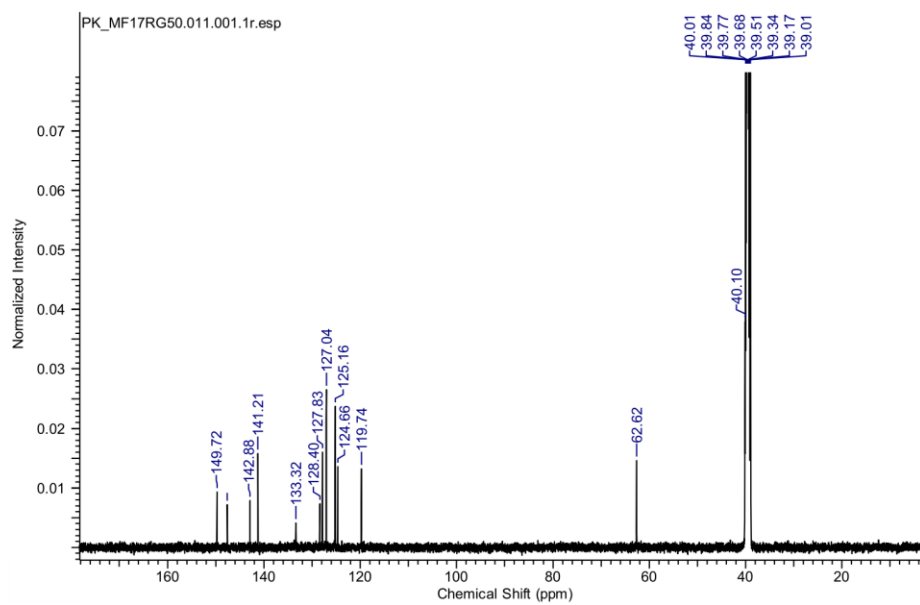
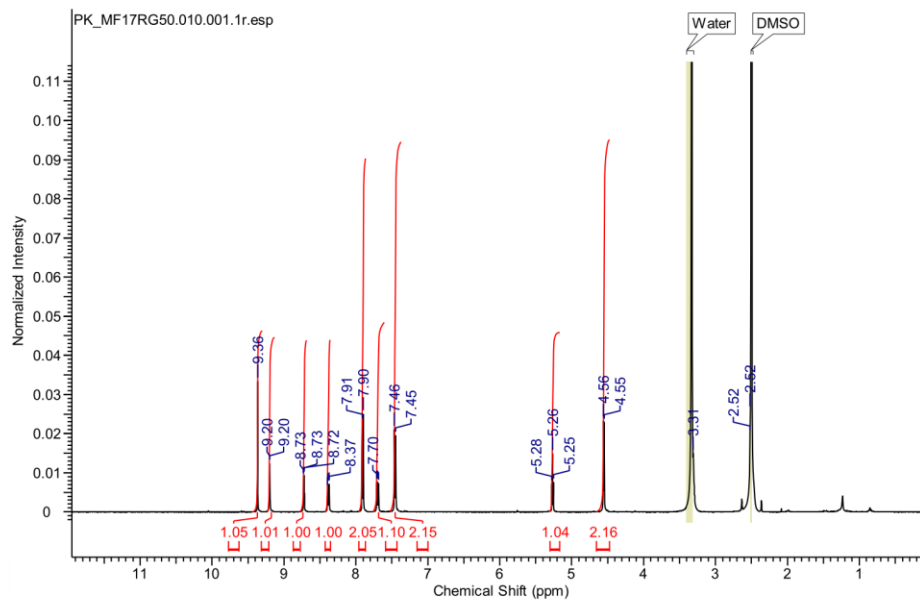
4-(1-(pyridin-3-yl)-1H-1,2,3-triazol-4-yl)benzamide (7):

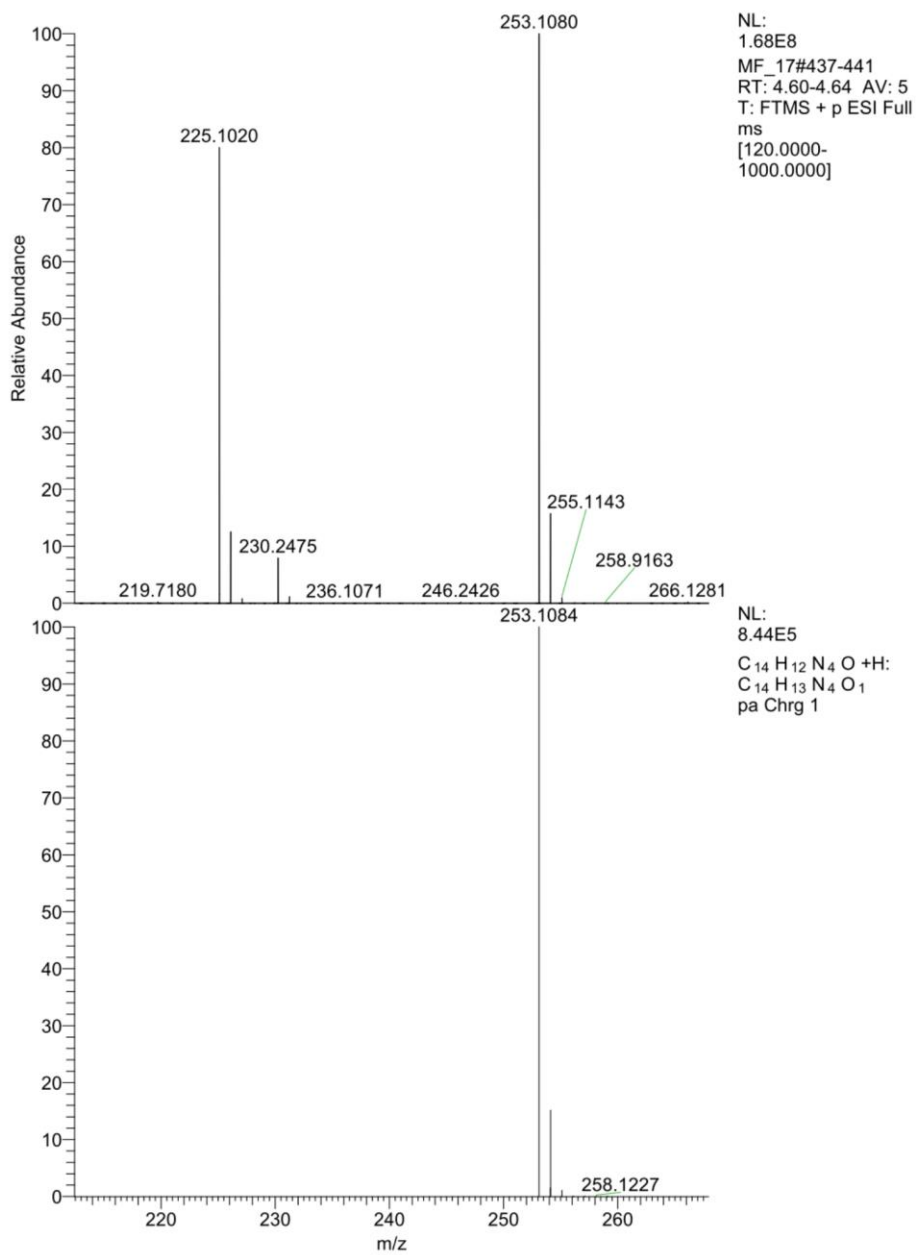


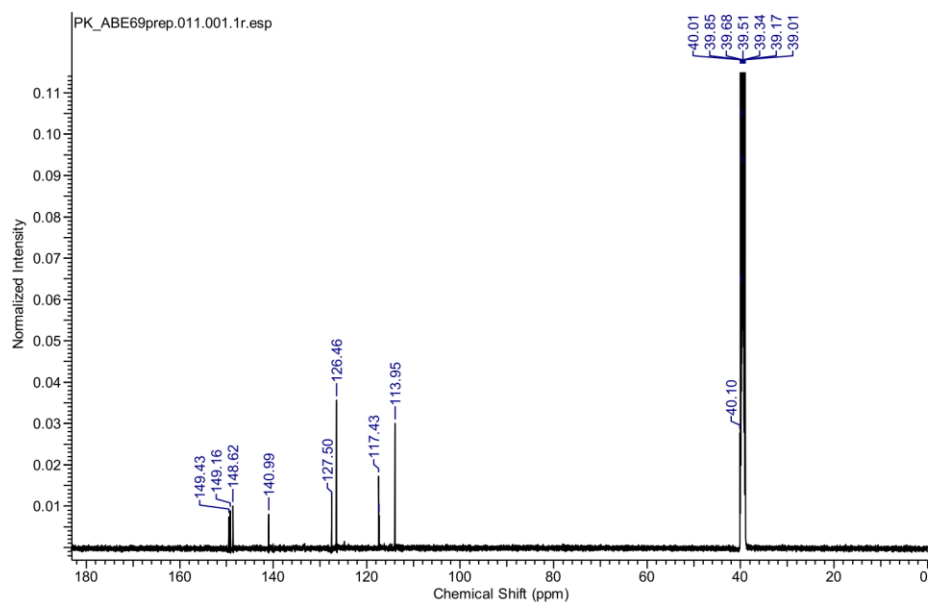
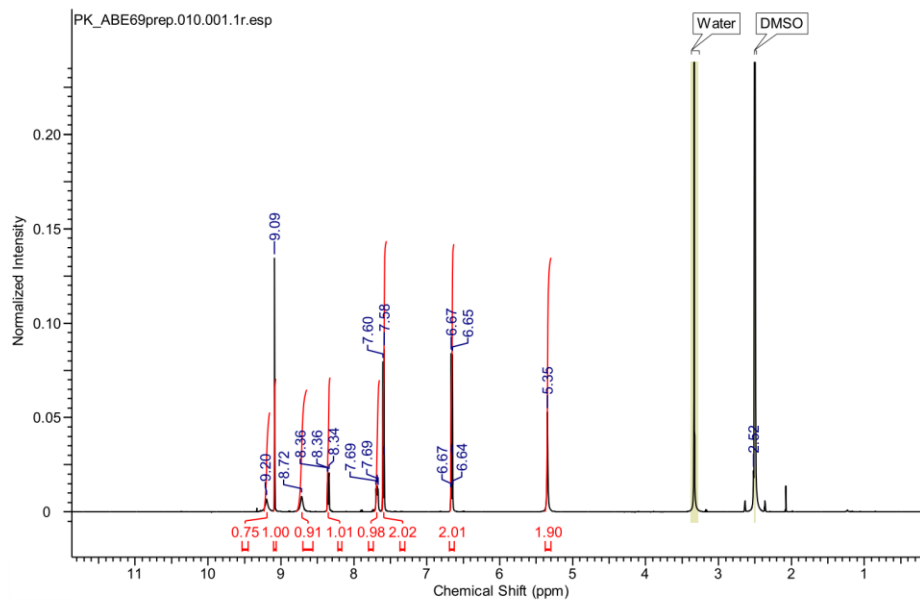


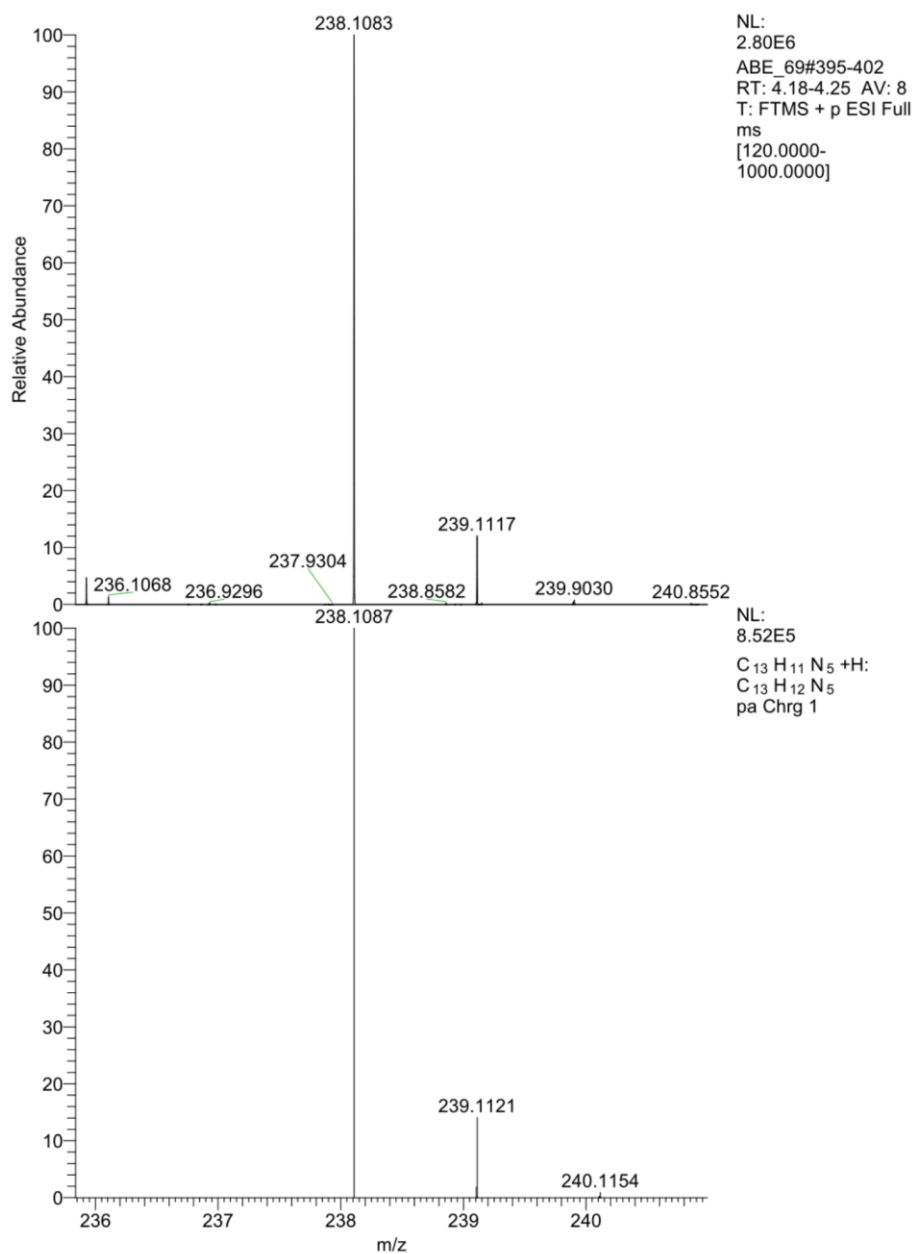
2-chloro-4-(1-(pyridin-3-yl)-1H-1,2,3-triazol-4-yl)benzoic acid (9):

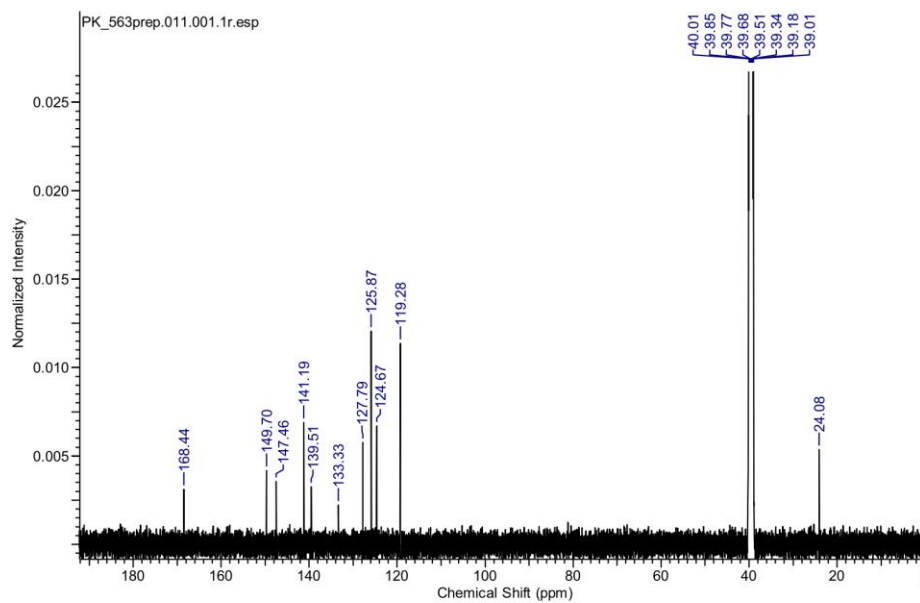
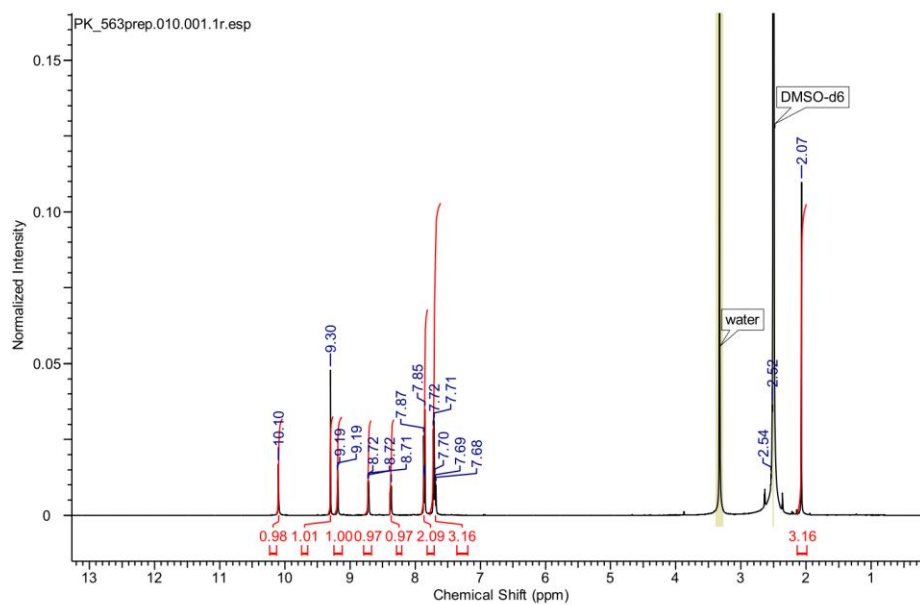


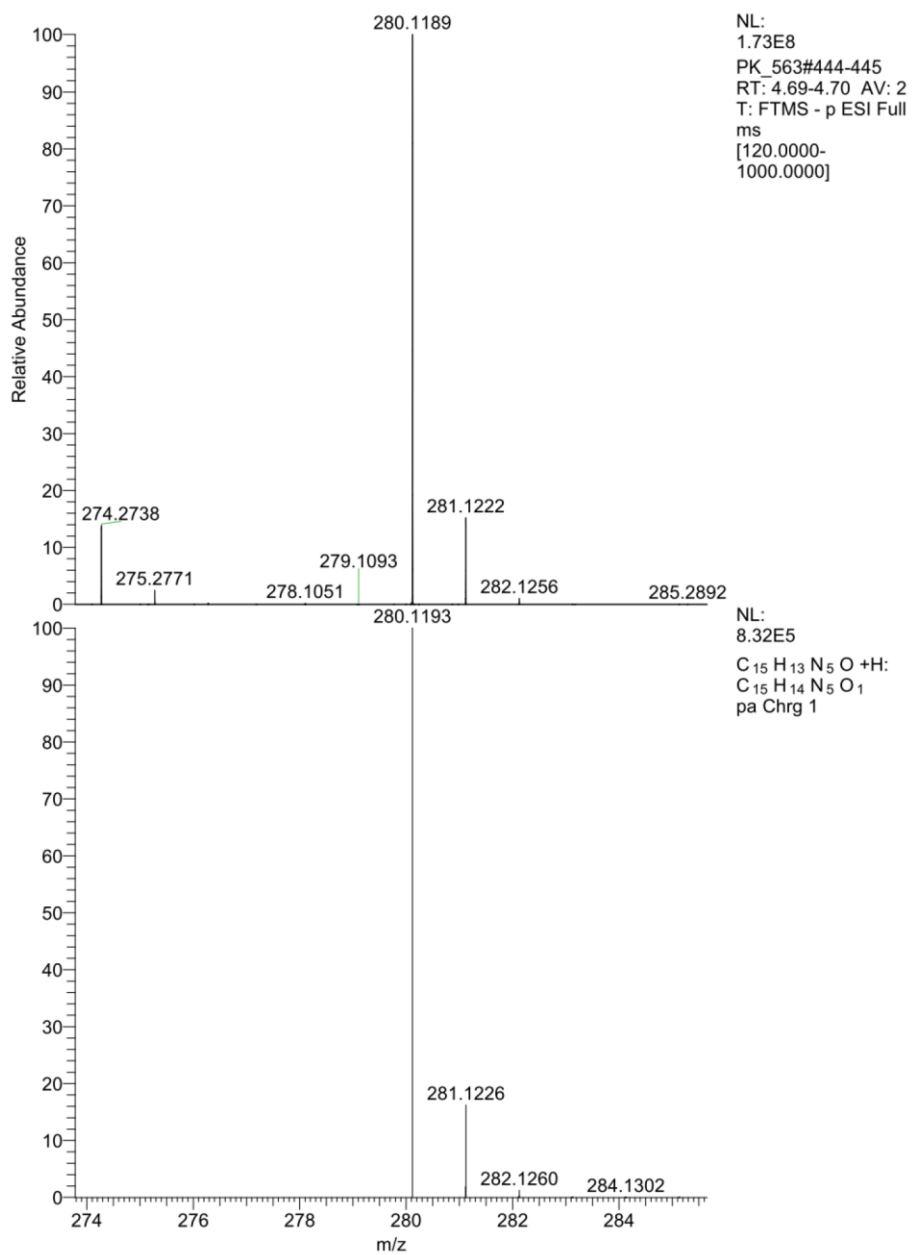
(4-(1-(pyridin-3-yl)-1H-1,2,3-triazol-4-yl)phenyl)methanol (10):



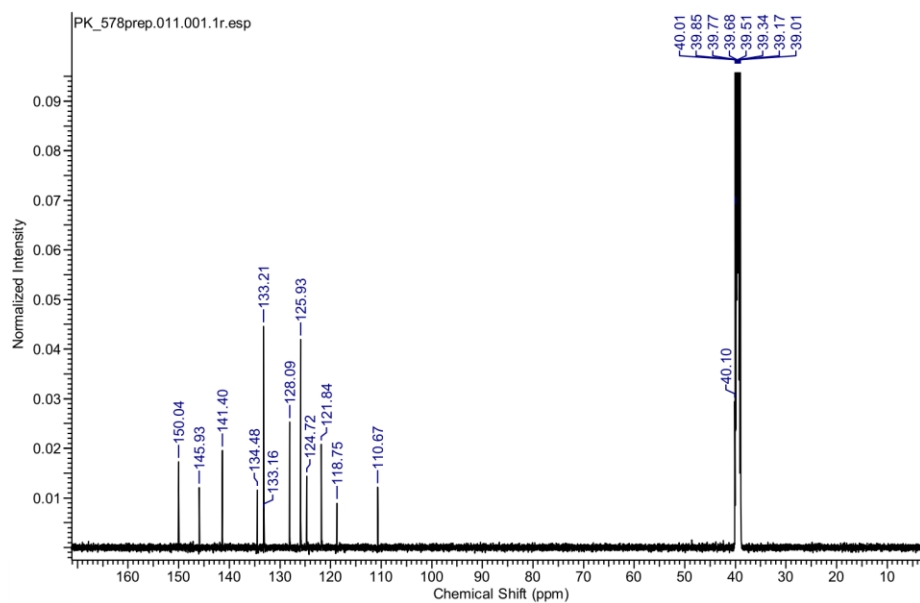
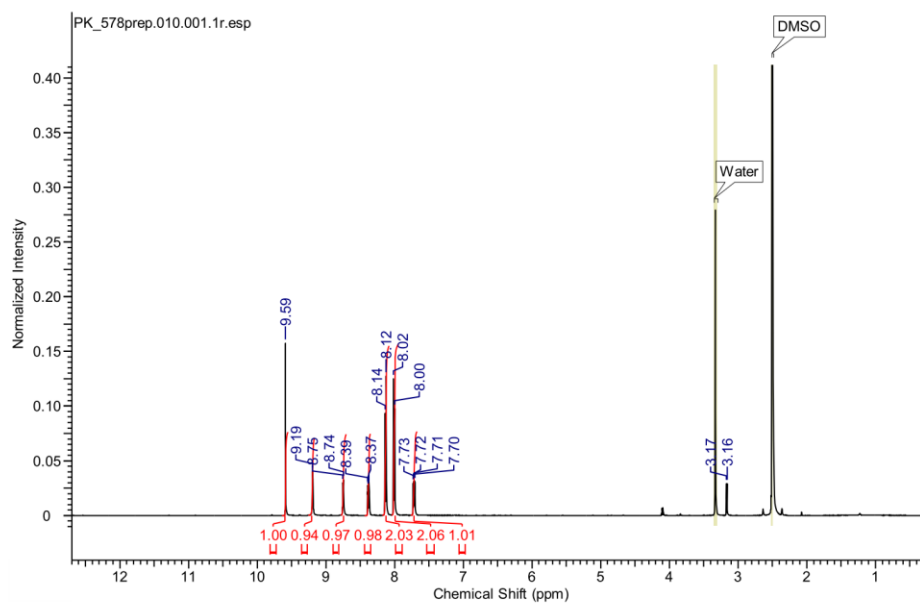
4-(1-(pyridin-3-yl)-1H-1,2,3-triazol-4-yl)aniline (11):

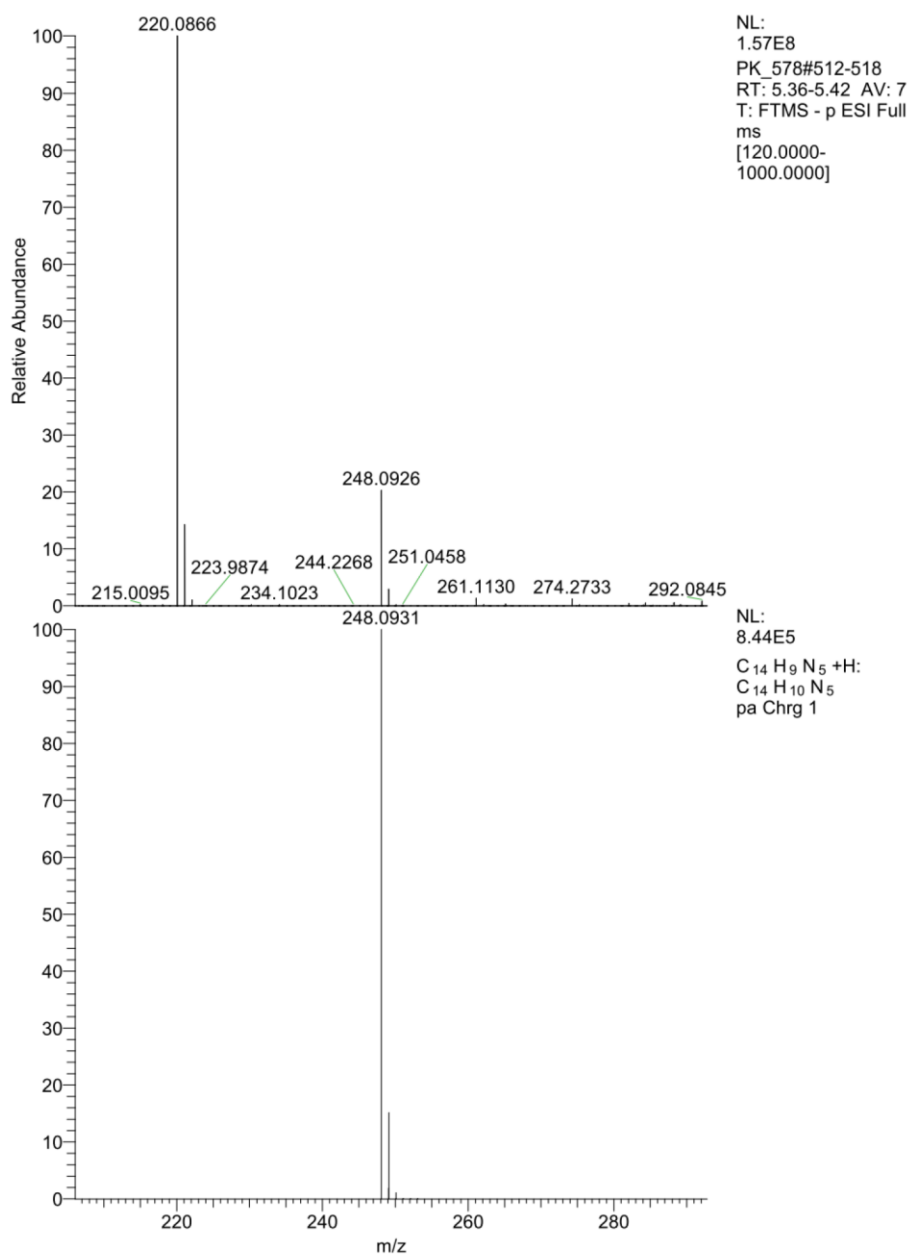


***N*-(4-(1-(pyridin-3-yl)-1*H*-1,2,3-triazol-4-yl)phenyl)acetamide (12):**

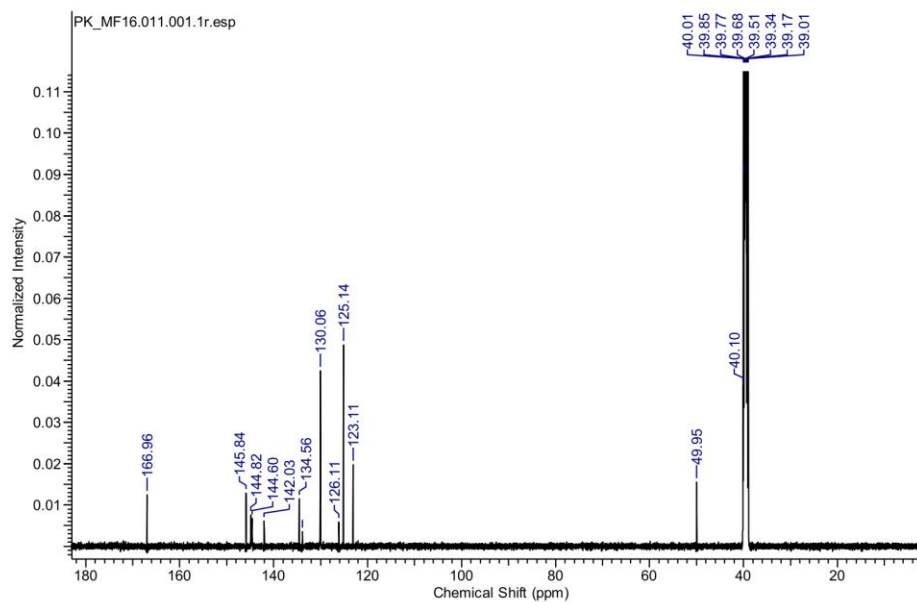
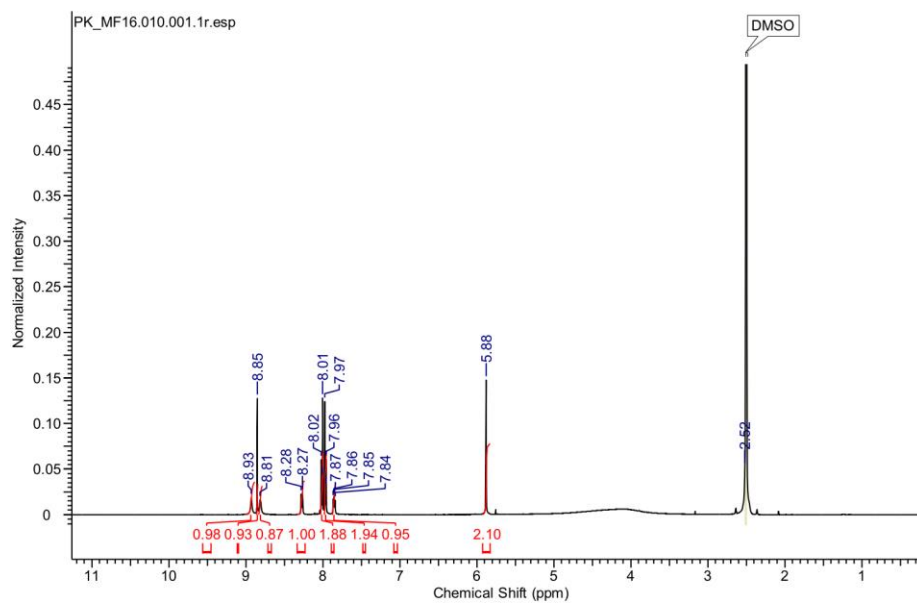


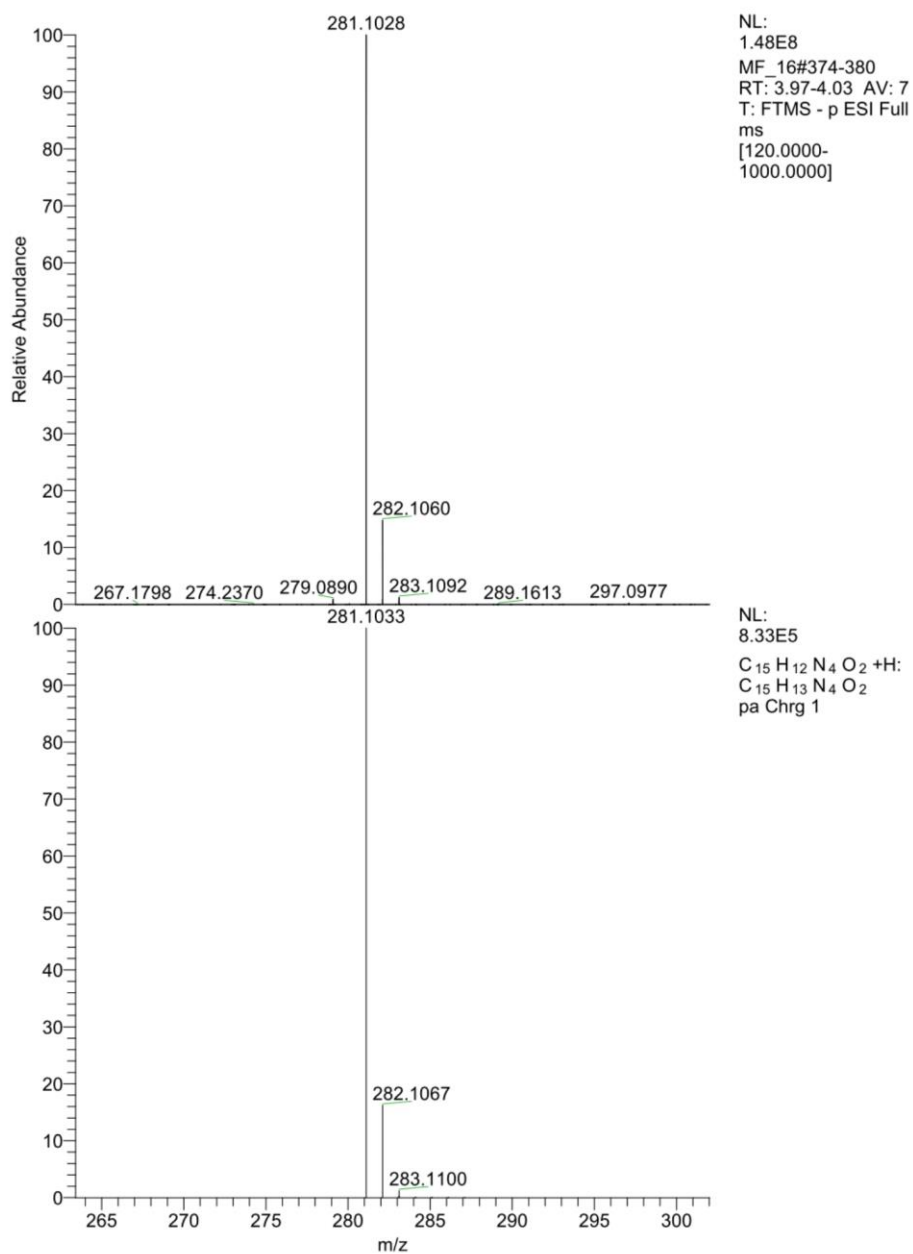
4-(1-(pyridin-3-yl)-1H-1,2,3-triazol-4-yl)benzotrile (13):

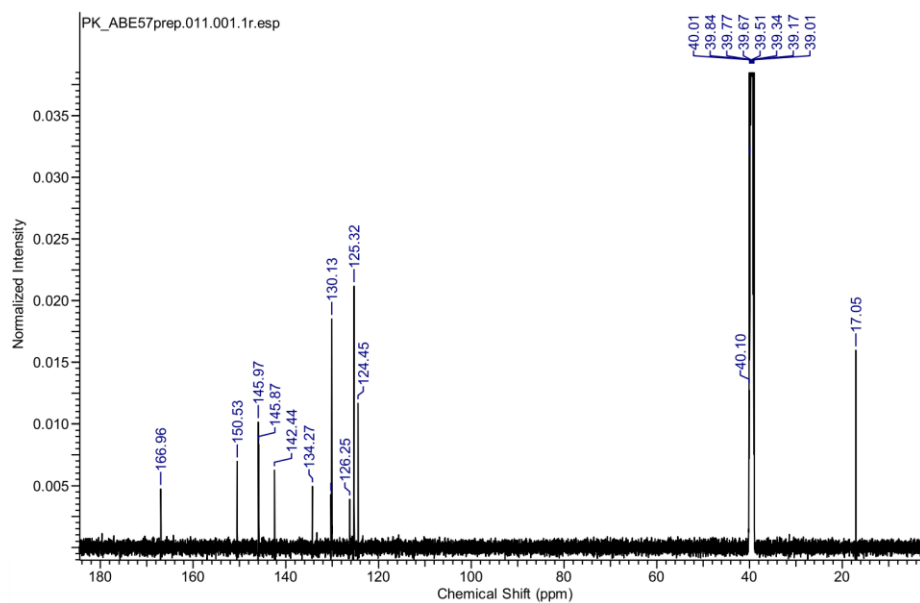
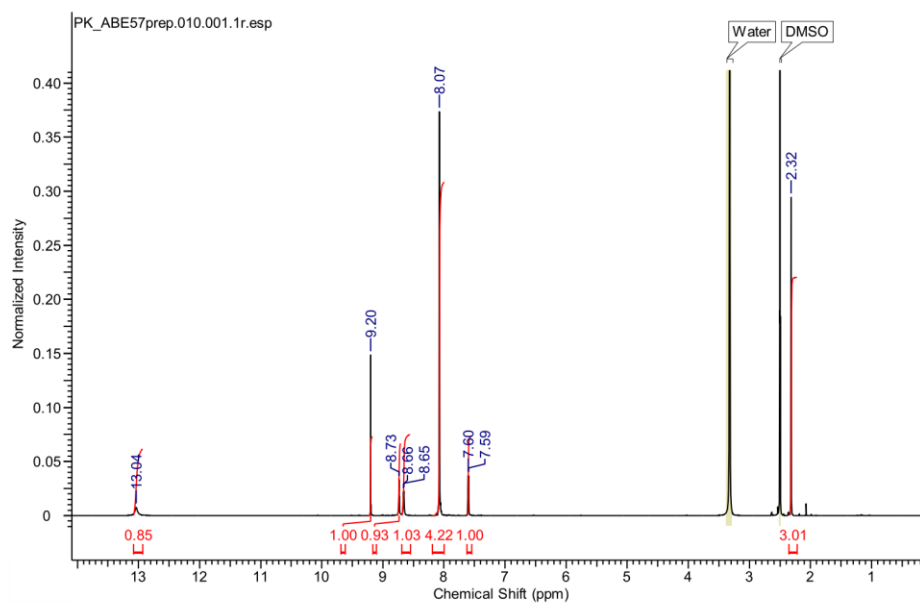


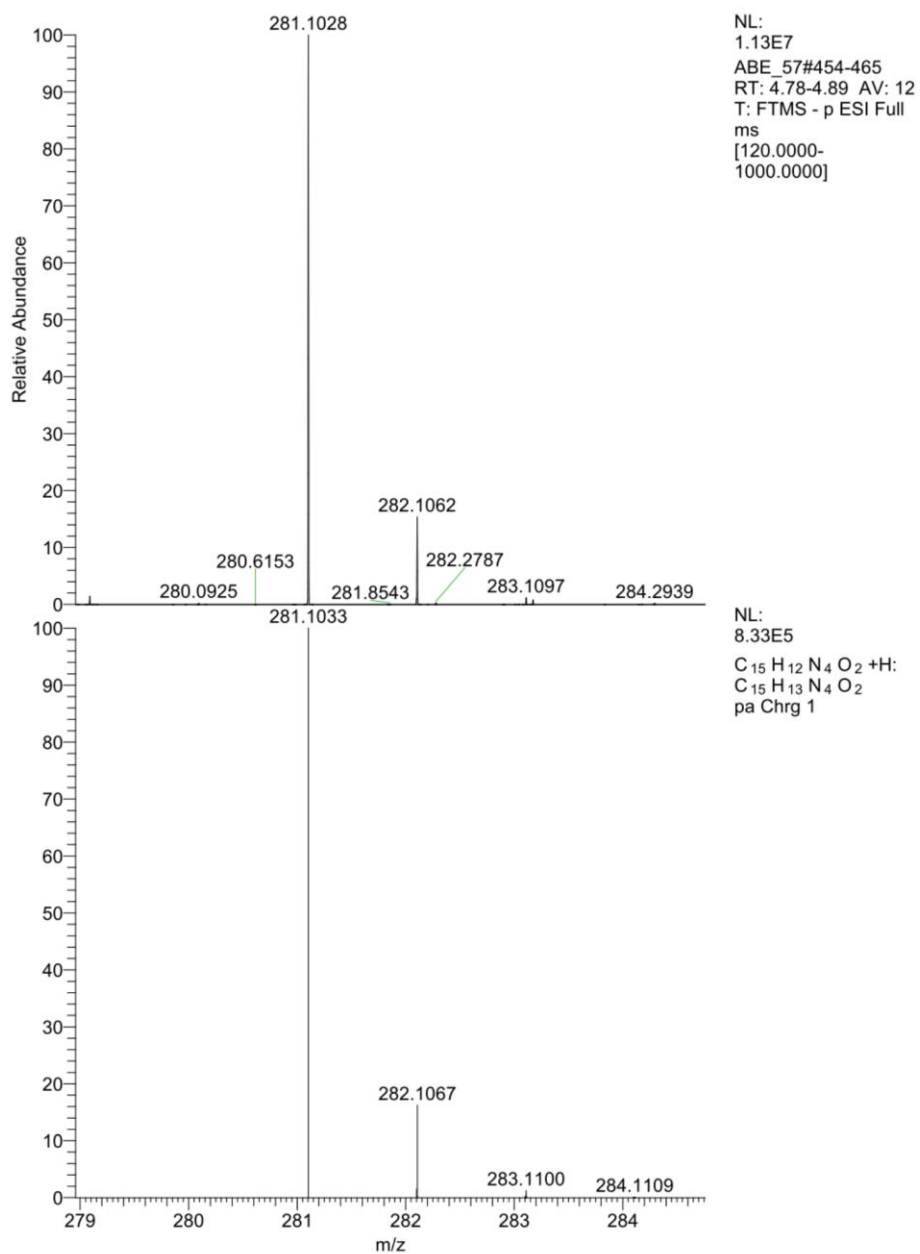


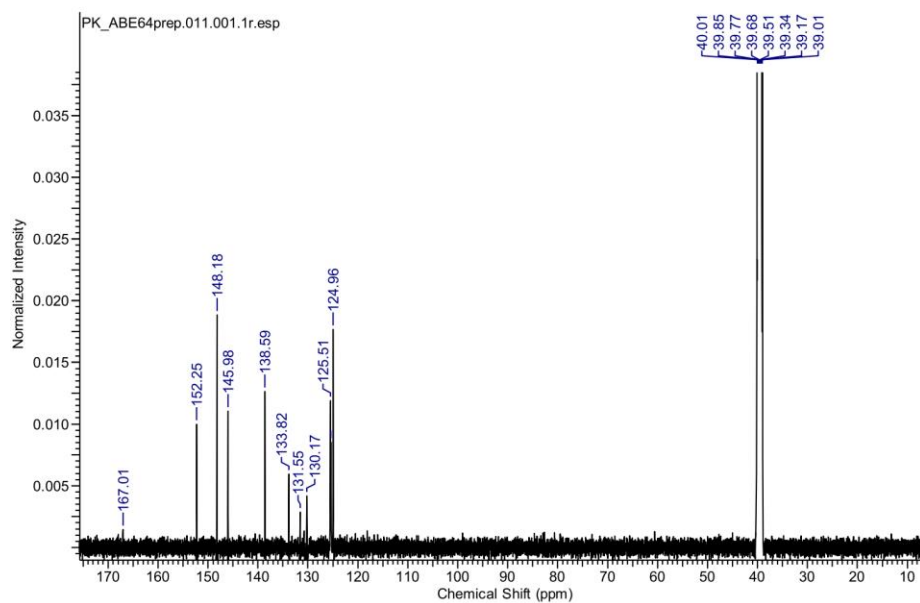
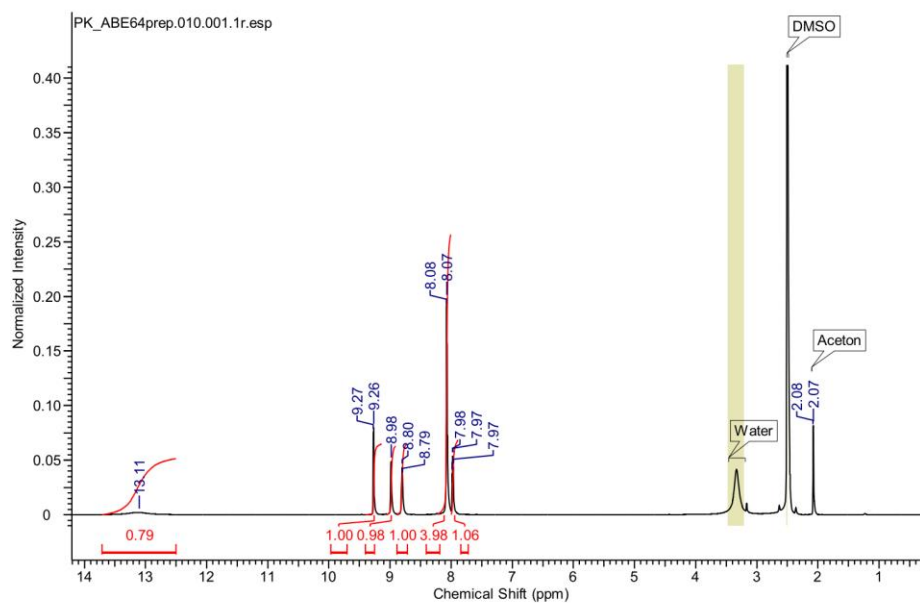
4-(1-(pyridin-3-ylmethyl)-1H-1,2,3-triazol-4-yl)benzoic acid (16):

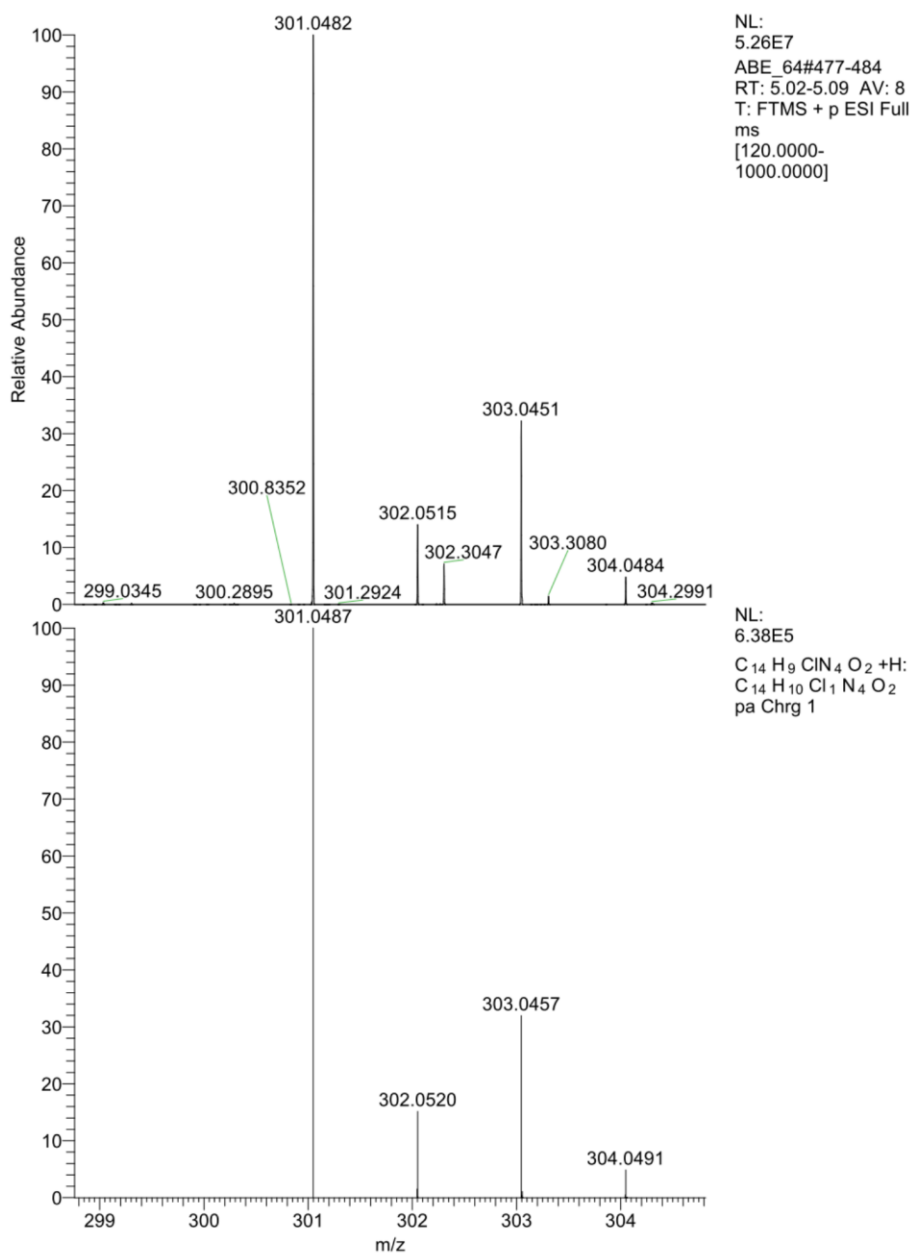




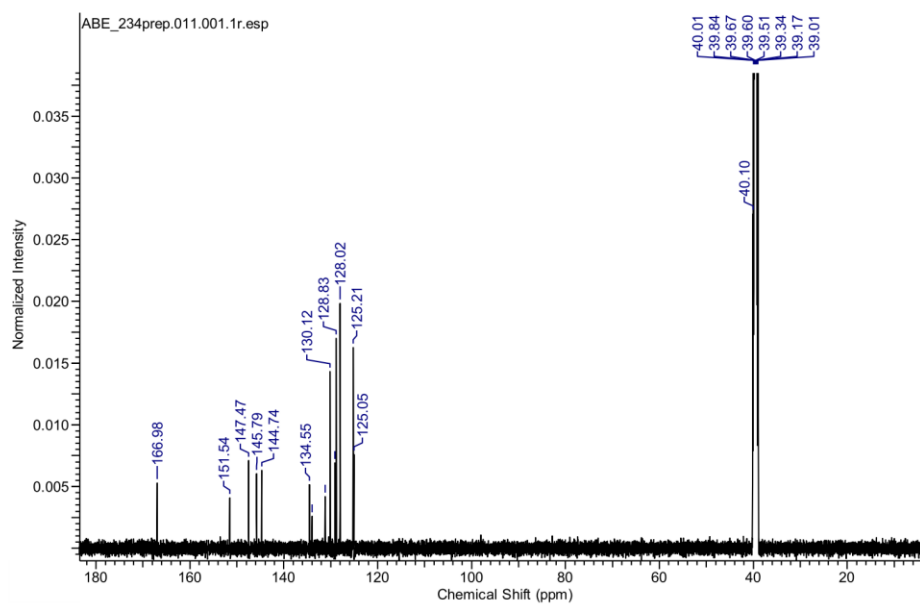
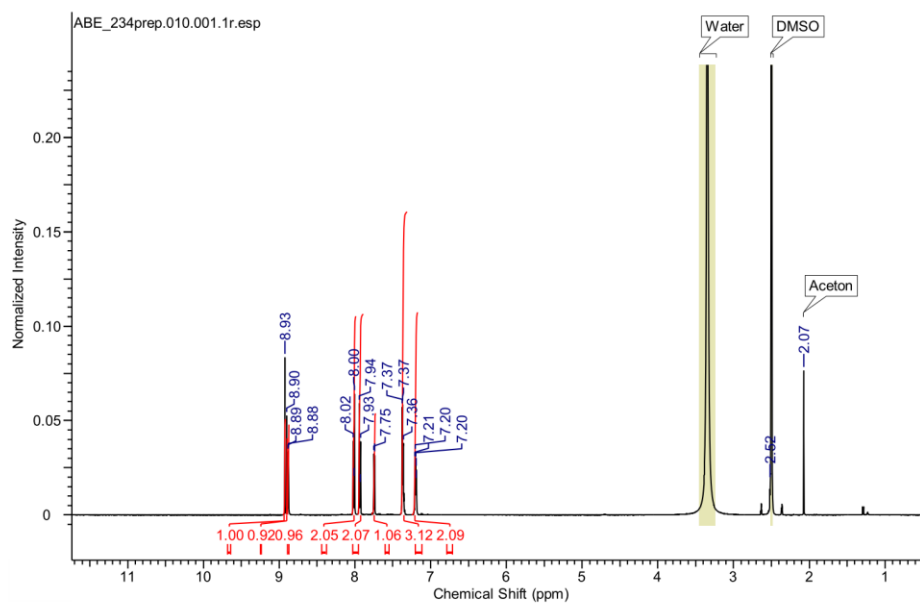
4-(1-(4-methylpyridin-3-yl)-1H-1,2,3-triazol-4-yl)benzoic acid (19a):

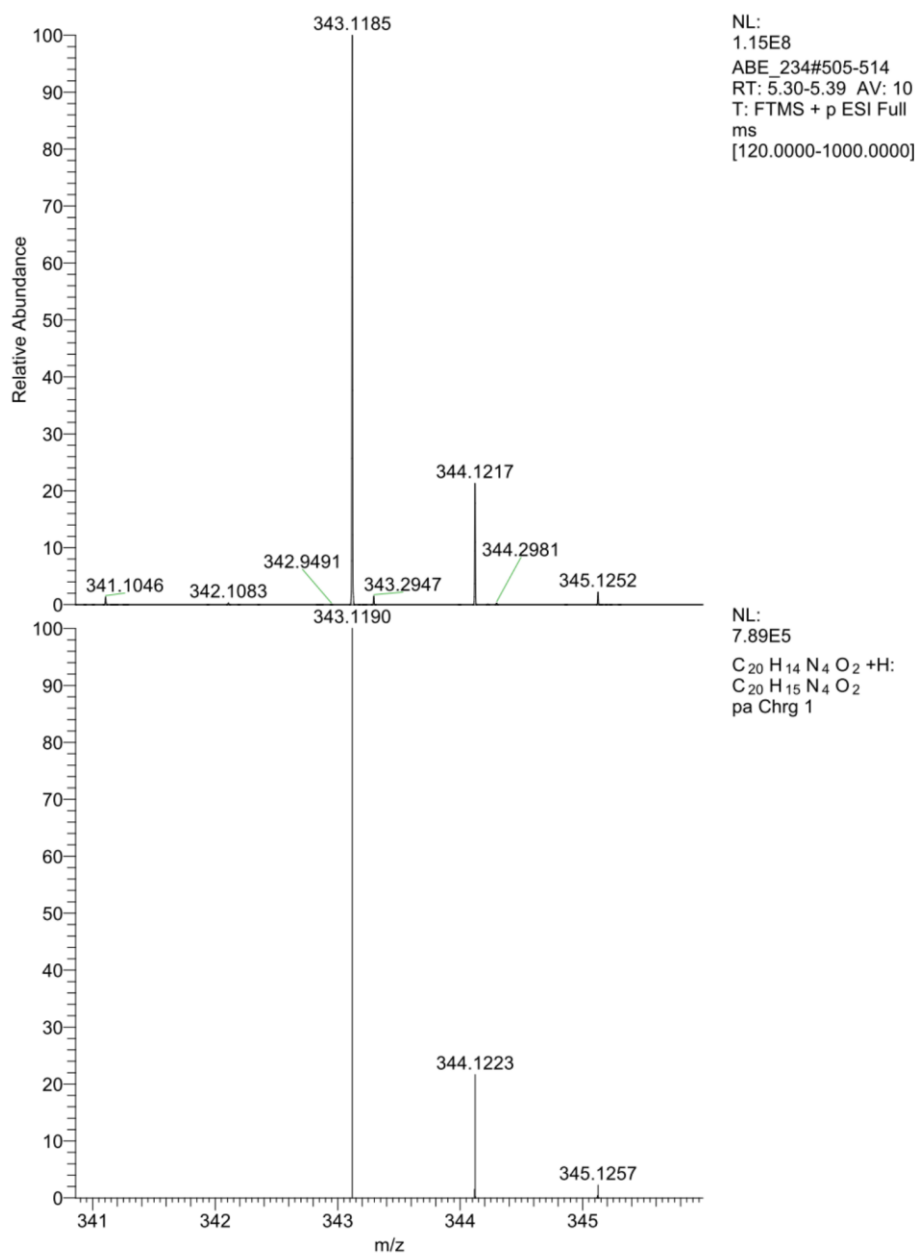


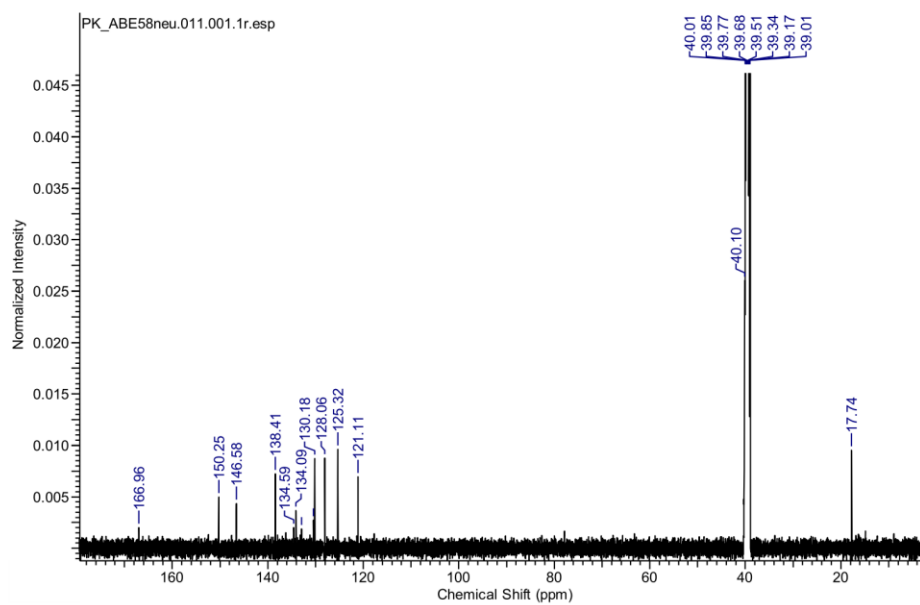
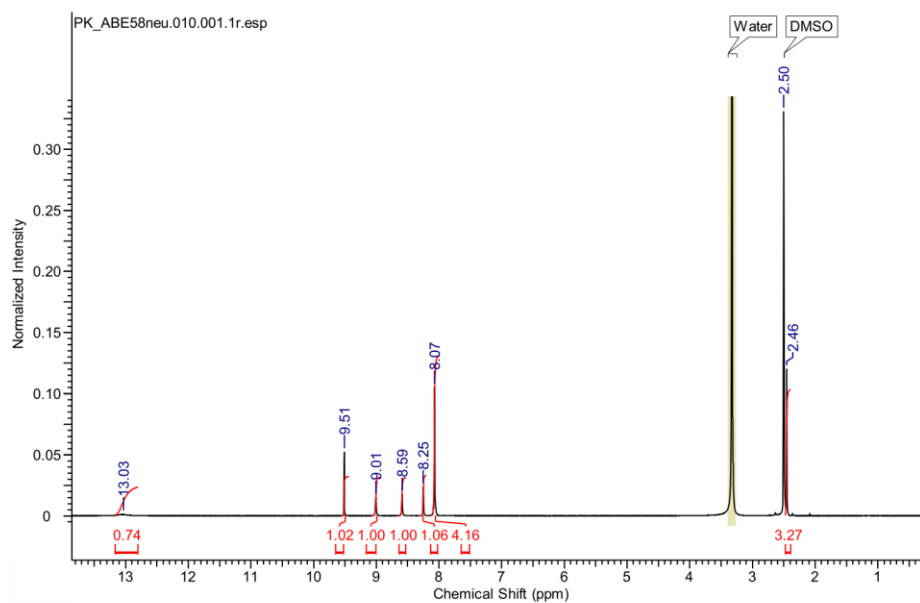
4-(1-(4-chloropyridin-3-yl)-1H-1,2,3-triazol-4-yl)benzoic acid (19b):

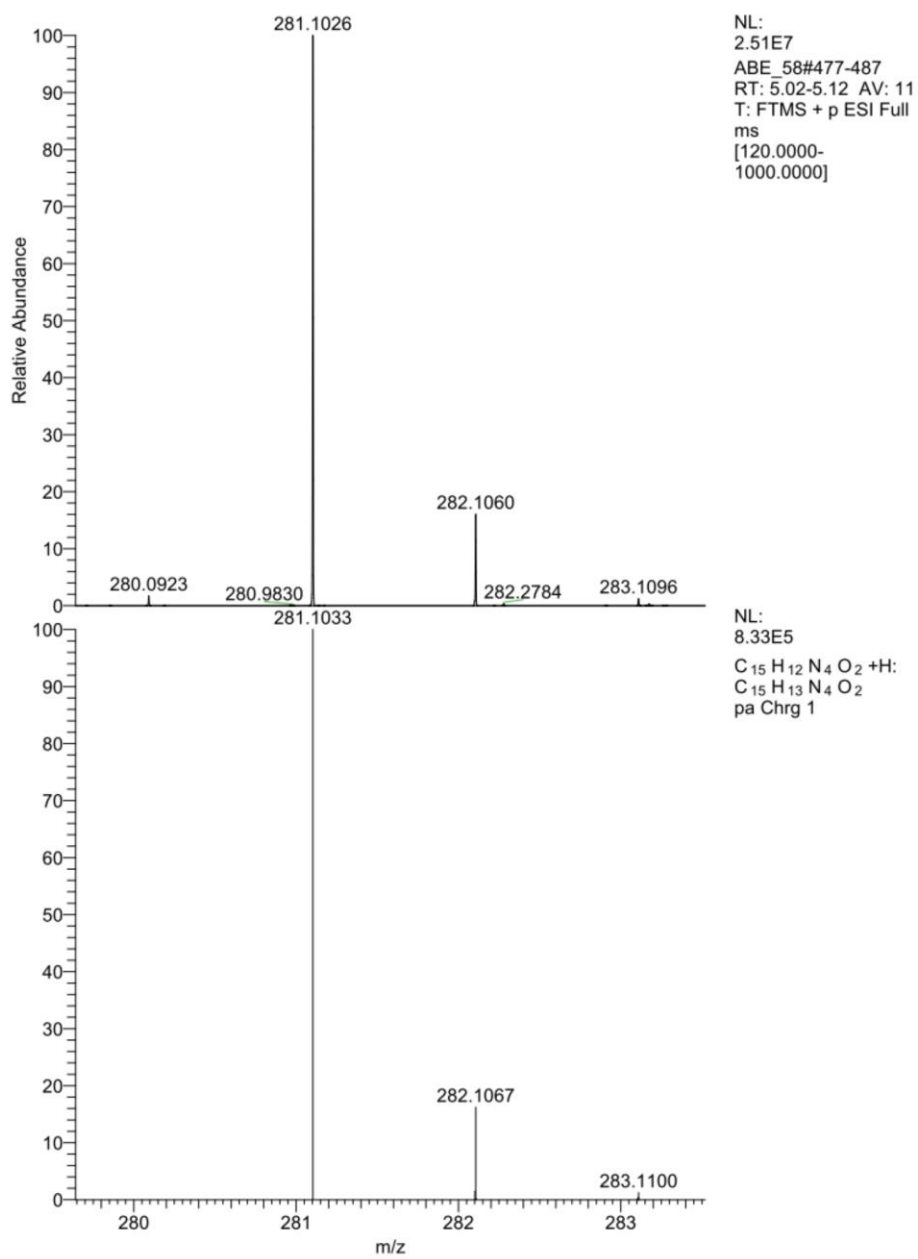


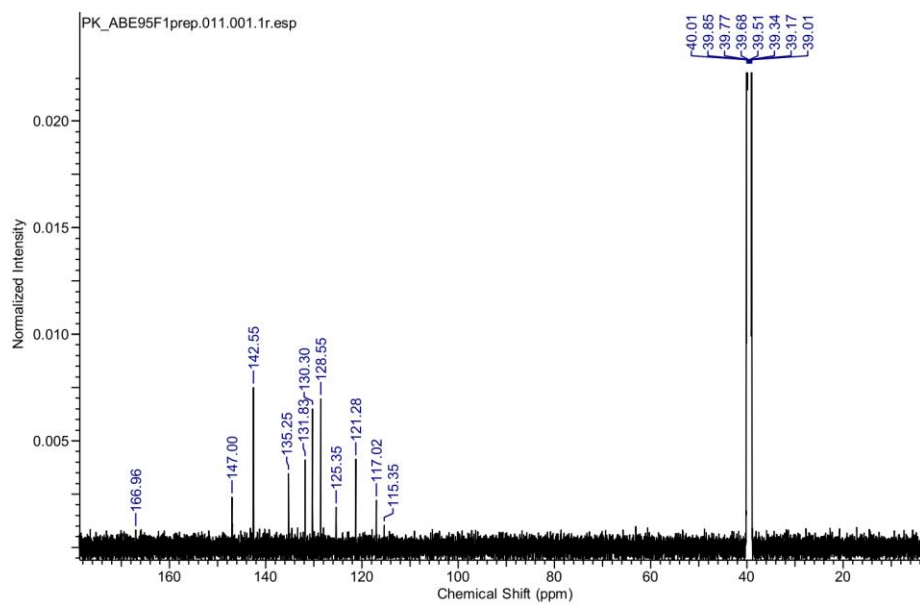
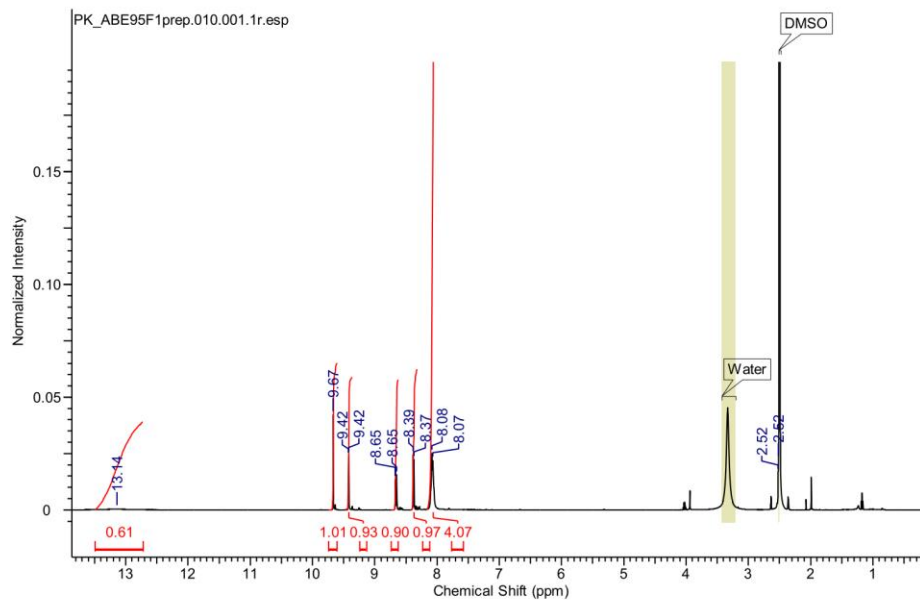
4-(1-(4-phenylpyridin-3-yl)-1H-1,2,3-triazol-4-yl)benzoic acid (19c):

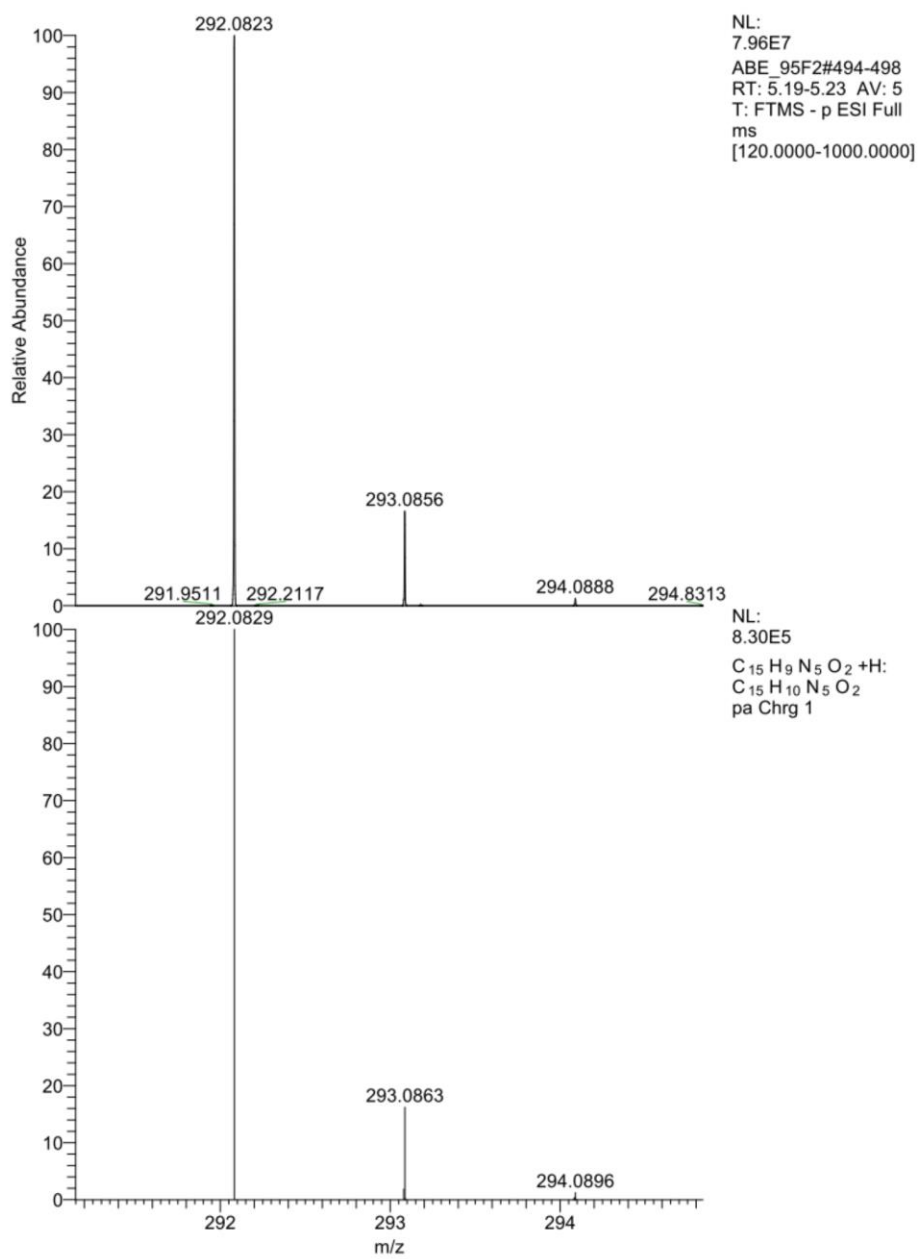


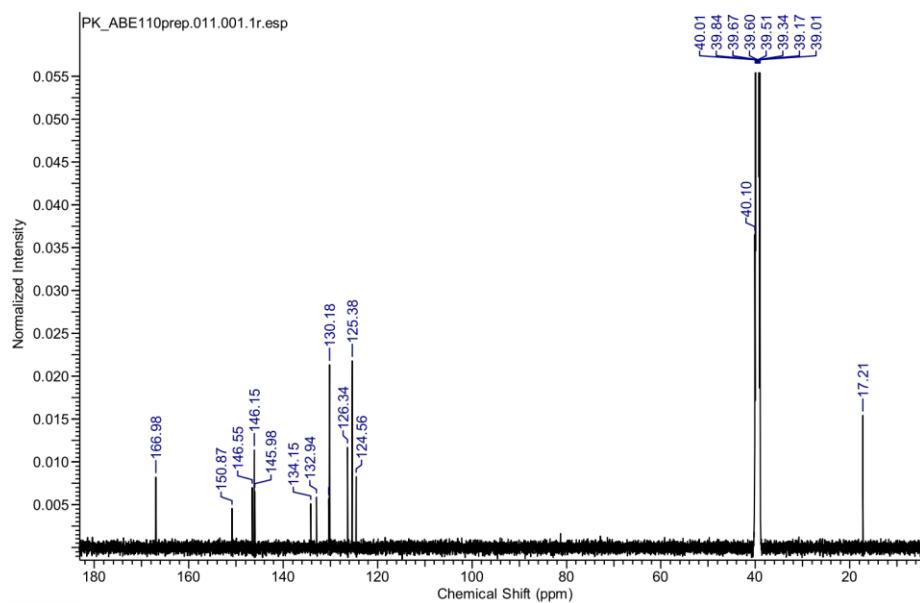
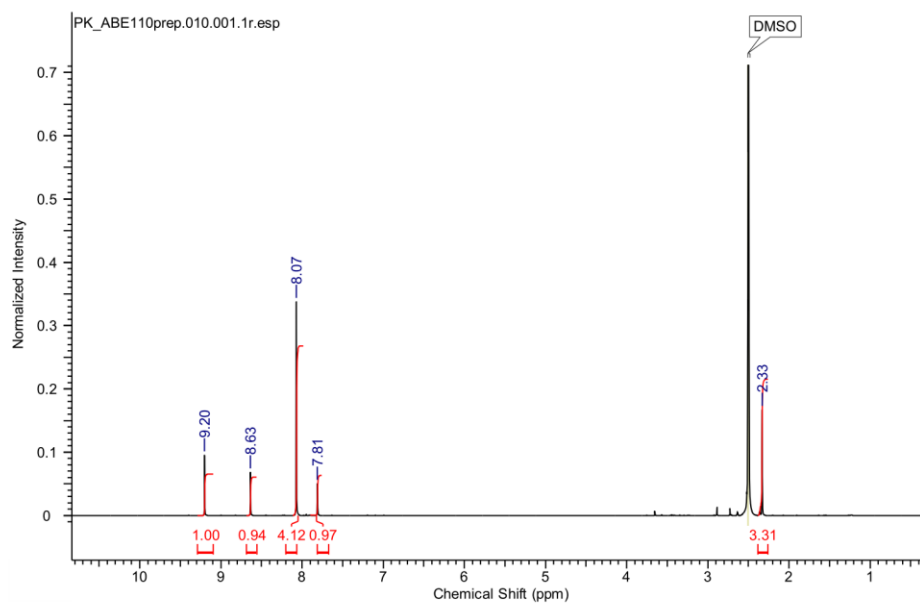


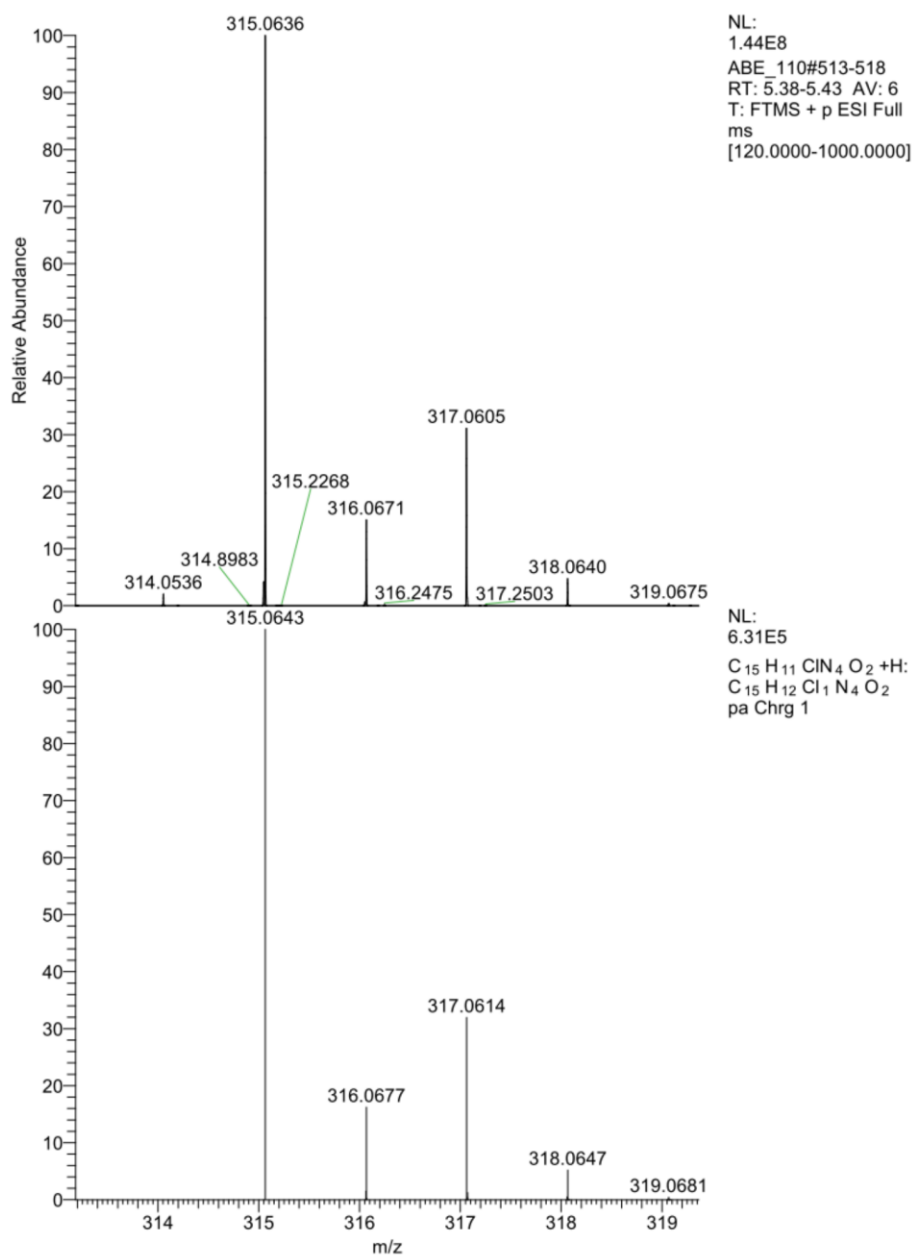
4-(1-(5-methylpyridin-3-yl)-1H-1,2,3-triazol-4-yl)benzoic acid (19d):



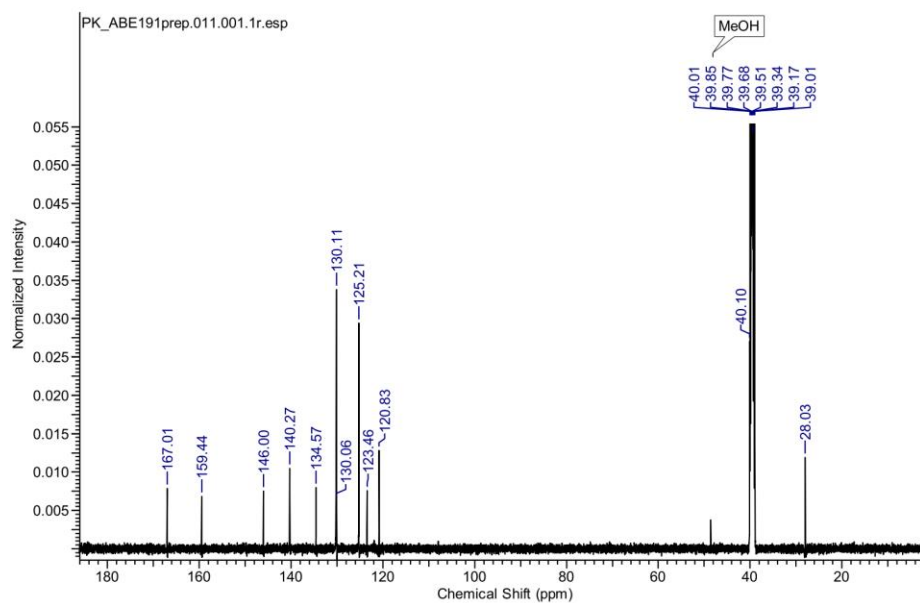
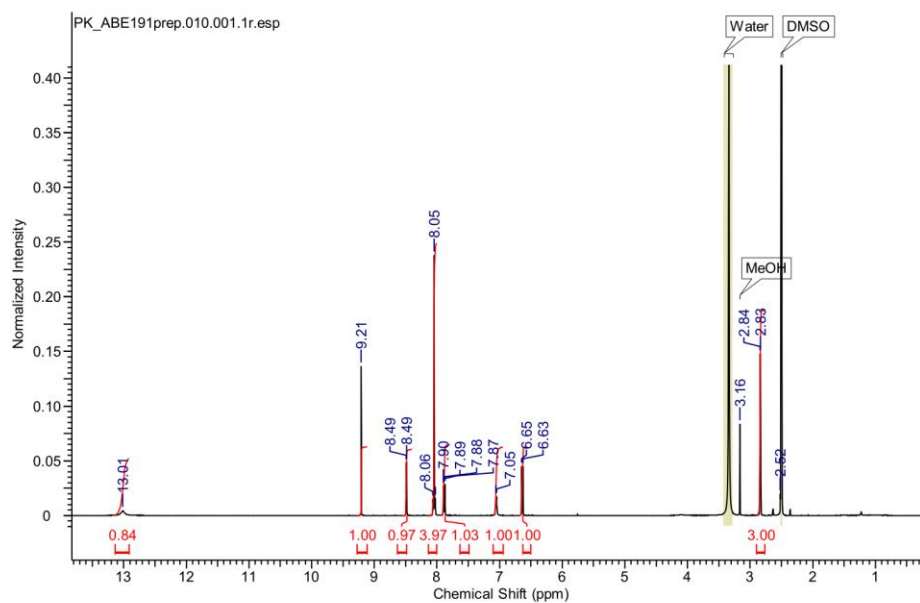
4-(1-(6-cyanopyridin-3-yl)-1H-1,2,3-triazol-4-yl)benzoic acid (19e):

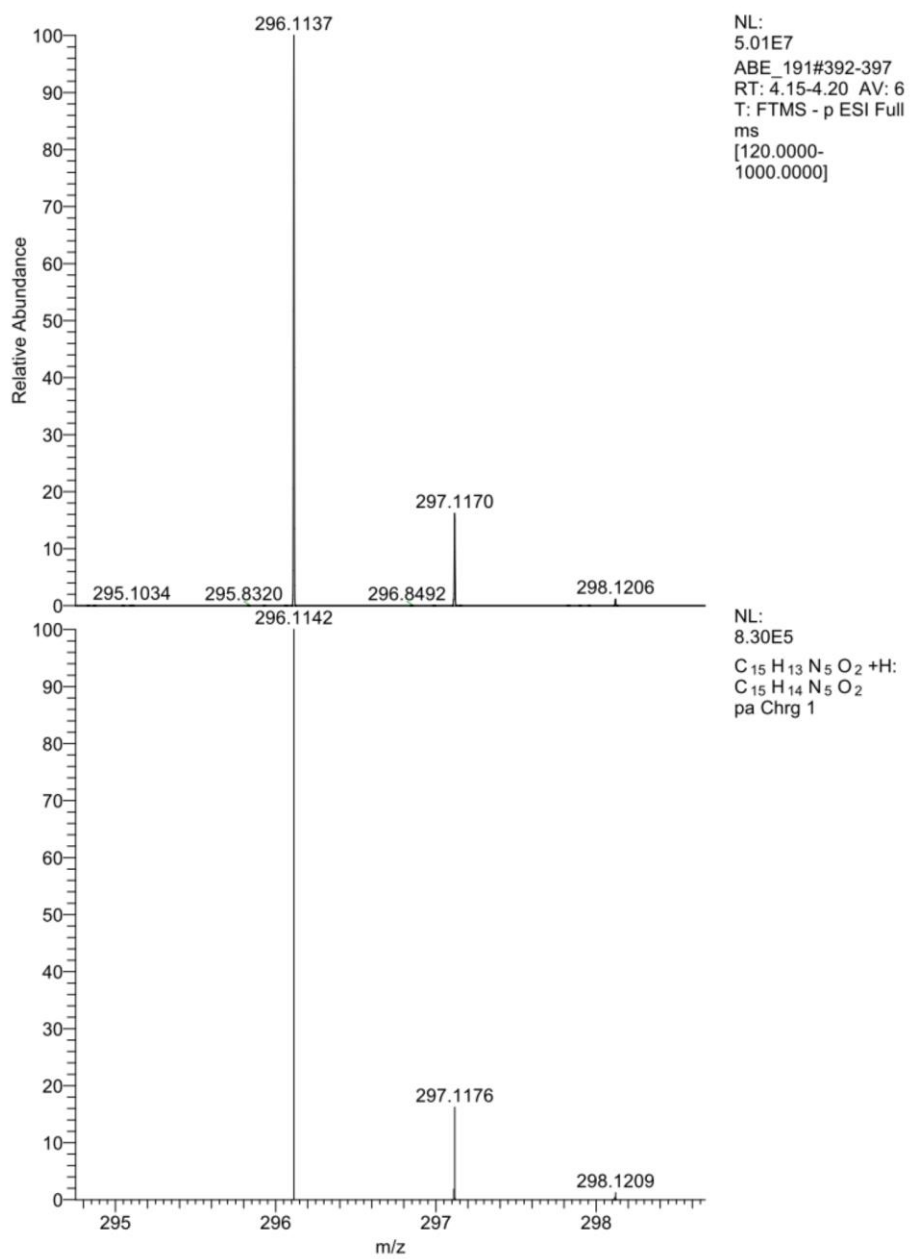


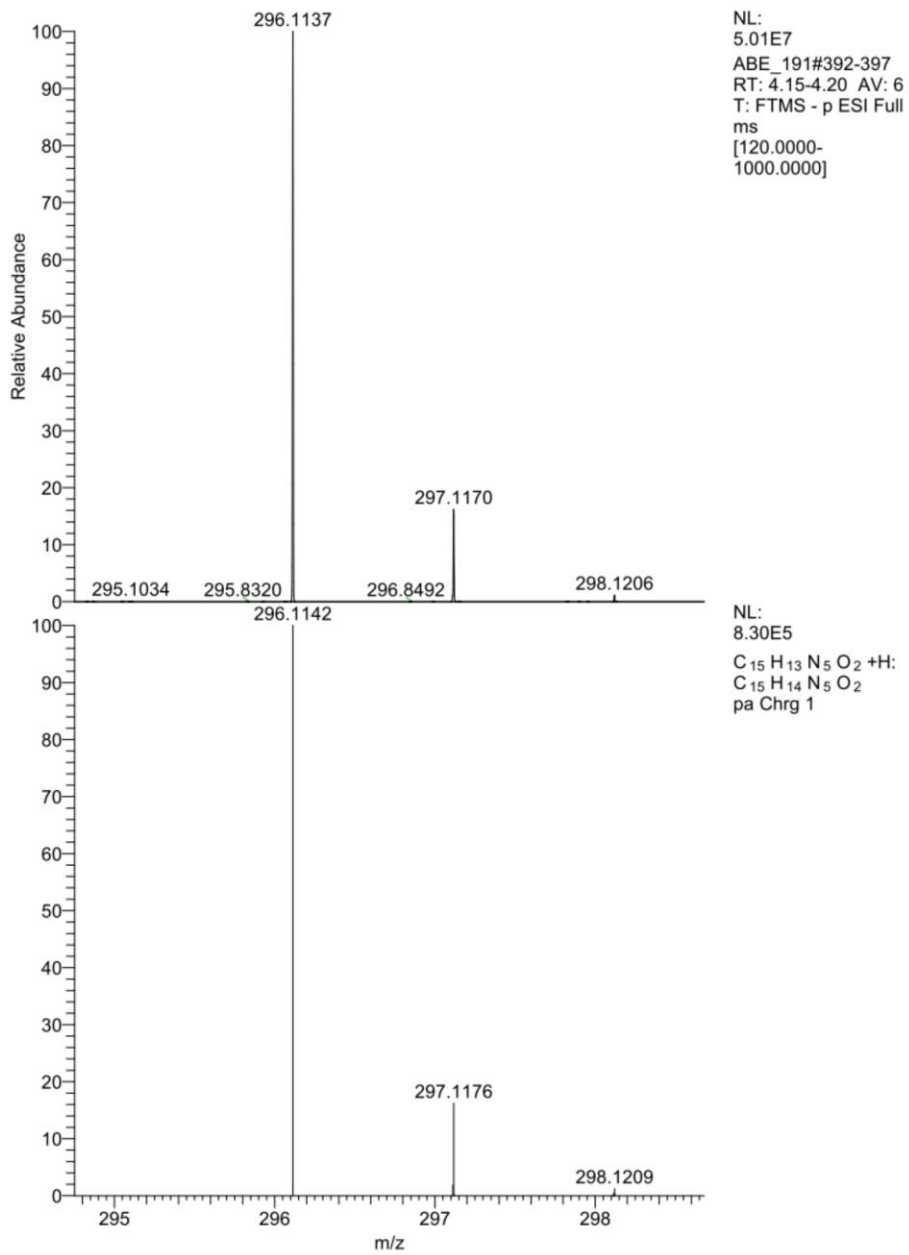
4-(1-(6-chloro-4-methylpyridin-3-yl)-1H-1,2,3-triazol-4-yl)benzoic acid (19f):

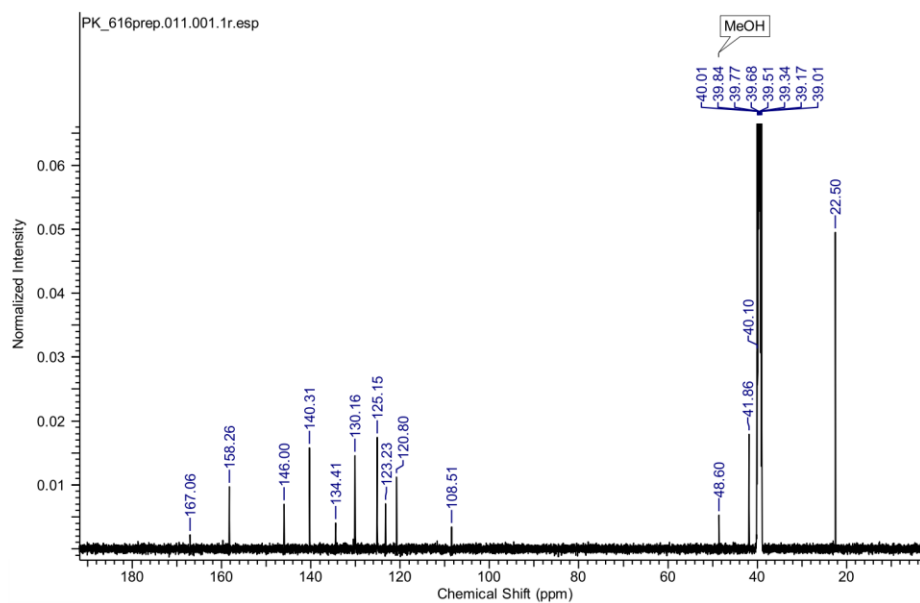
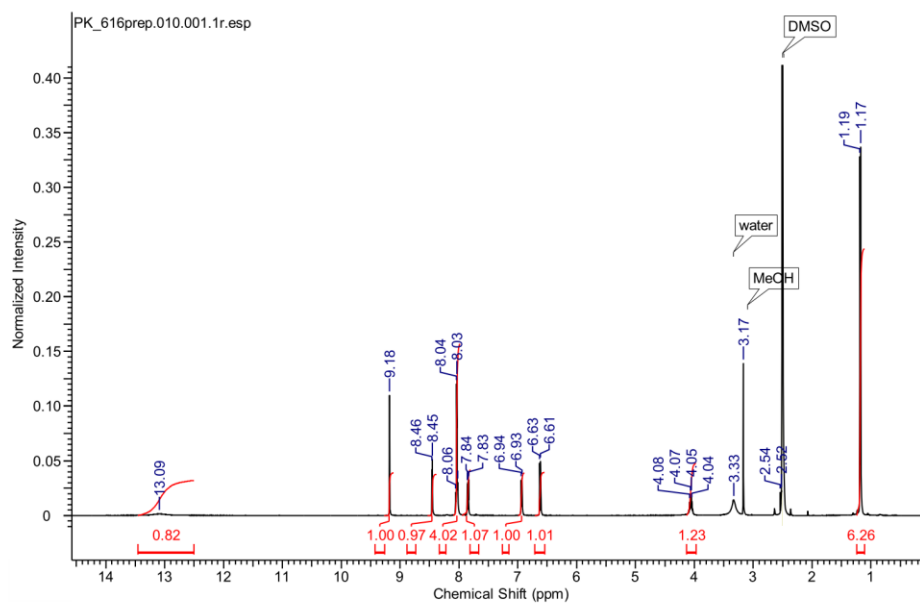


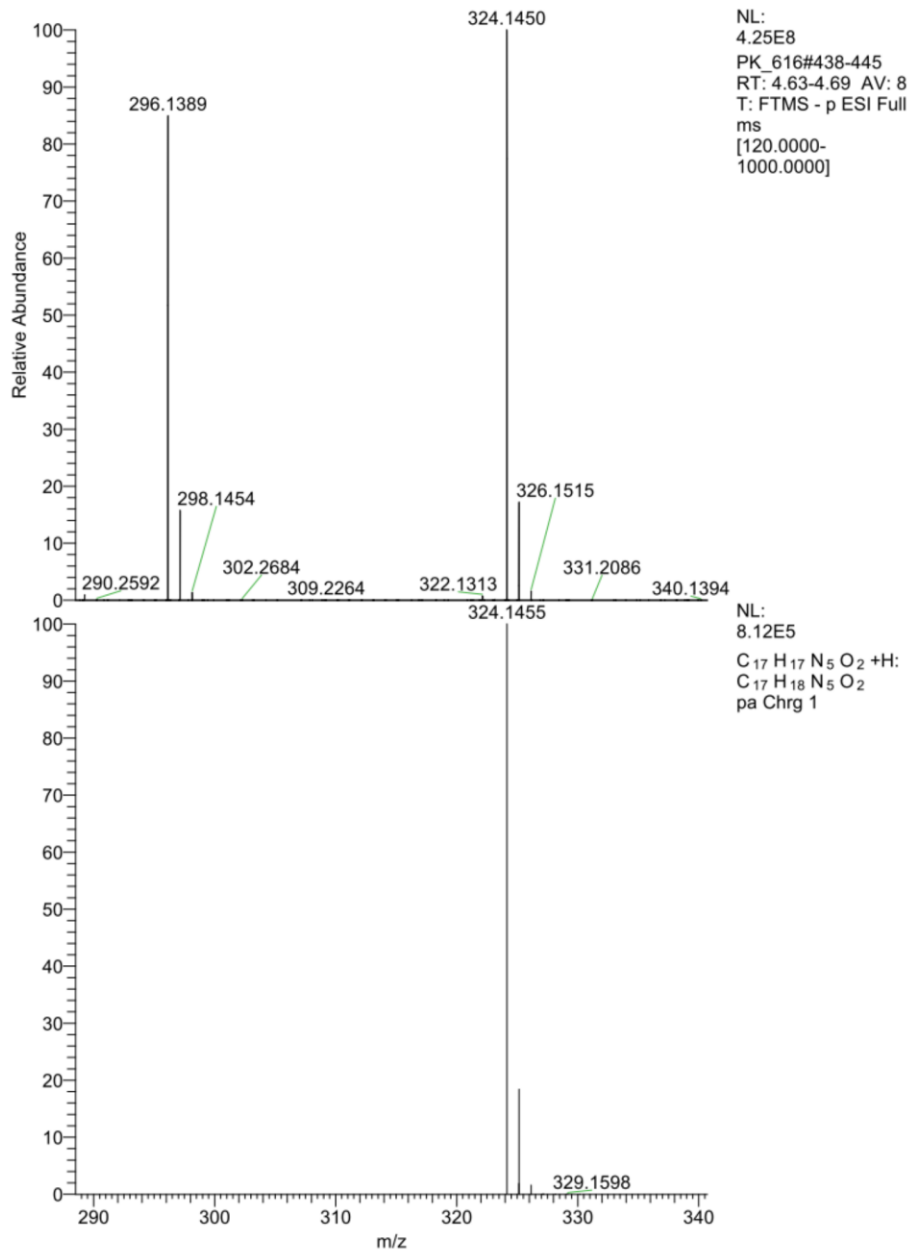
4-(1-(6-(methylamino)pyridin-3-yl)-1H-1,2,3-triazol-4-yl)benzoic acid (19g):

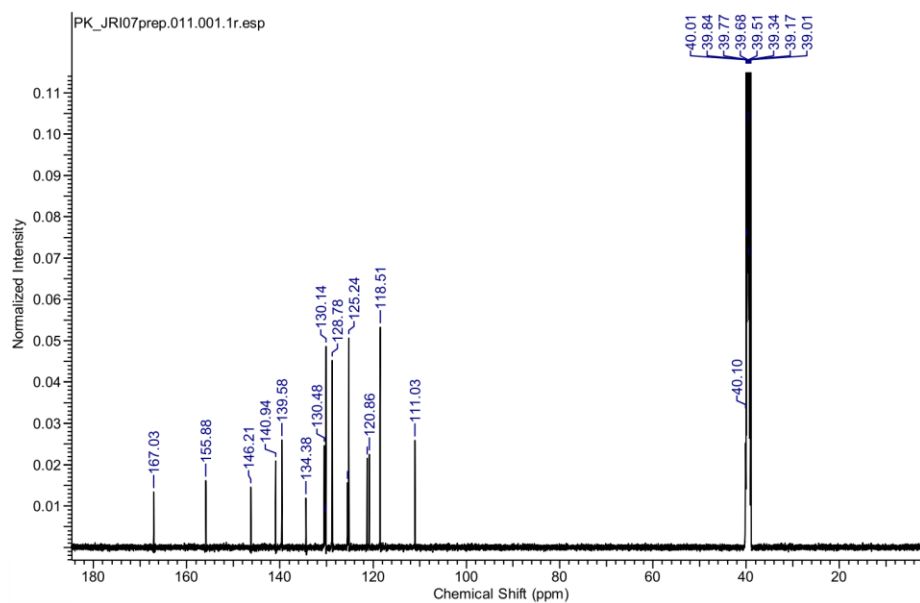
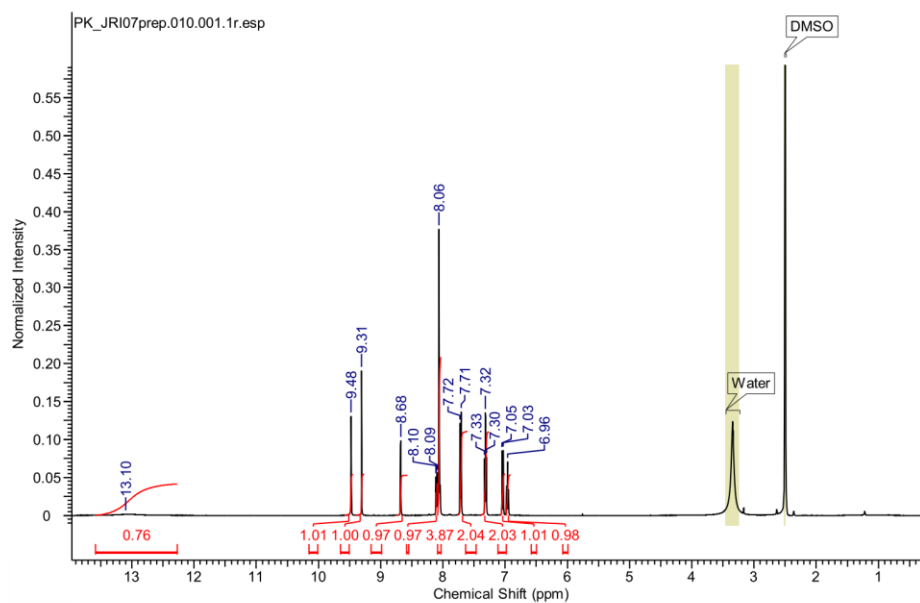


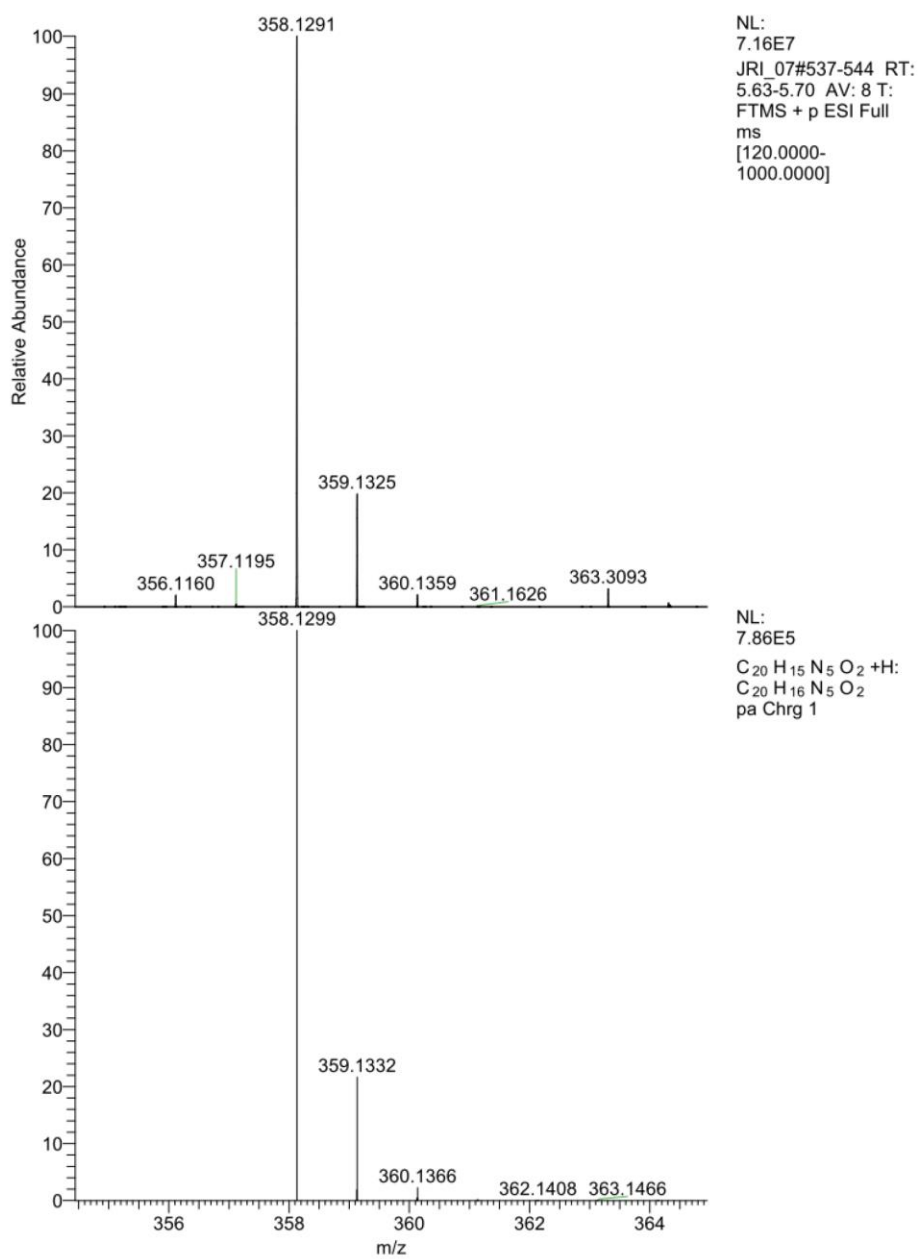


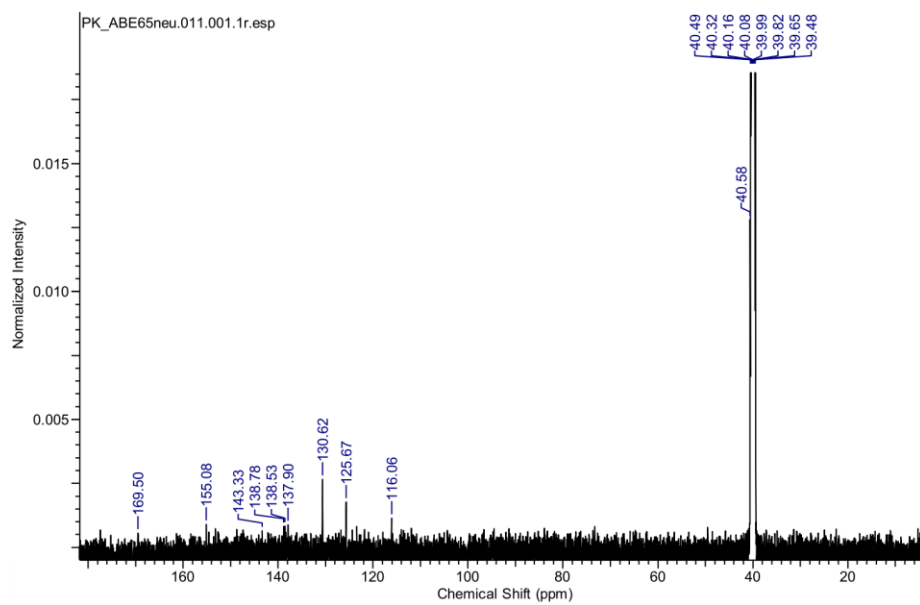
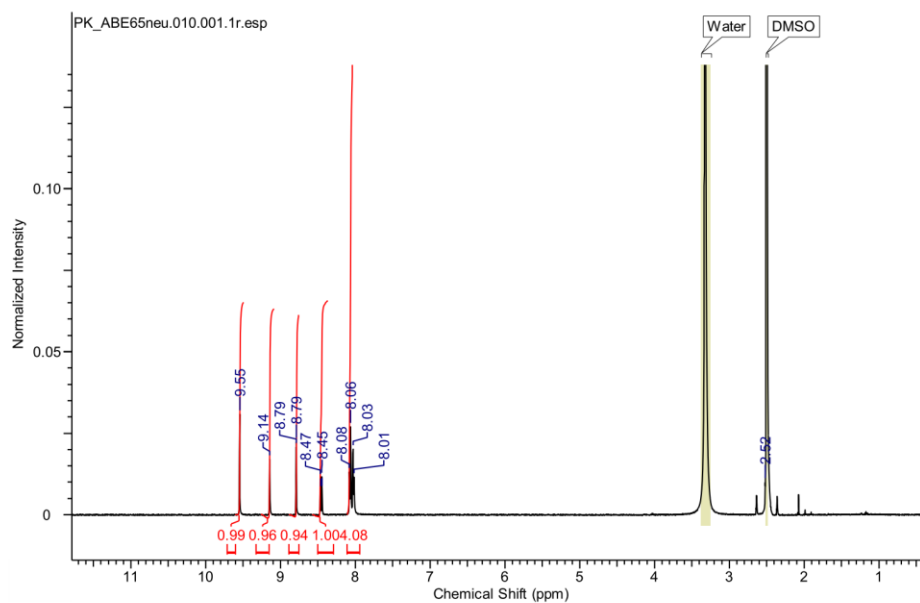


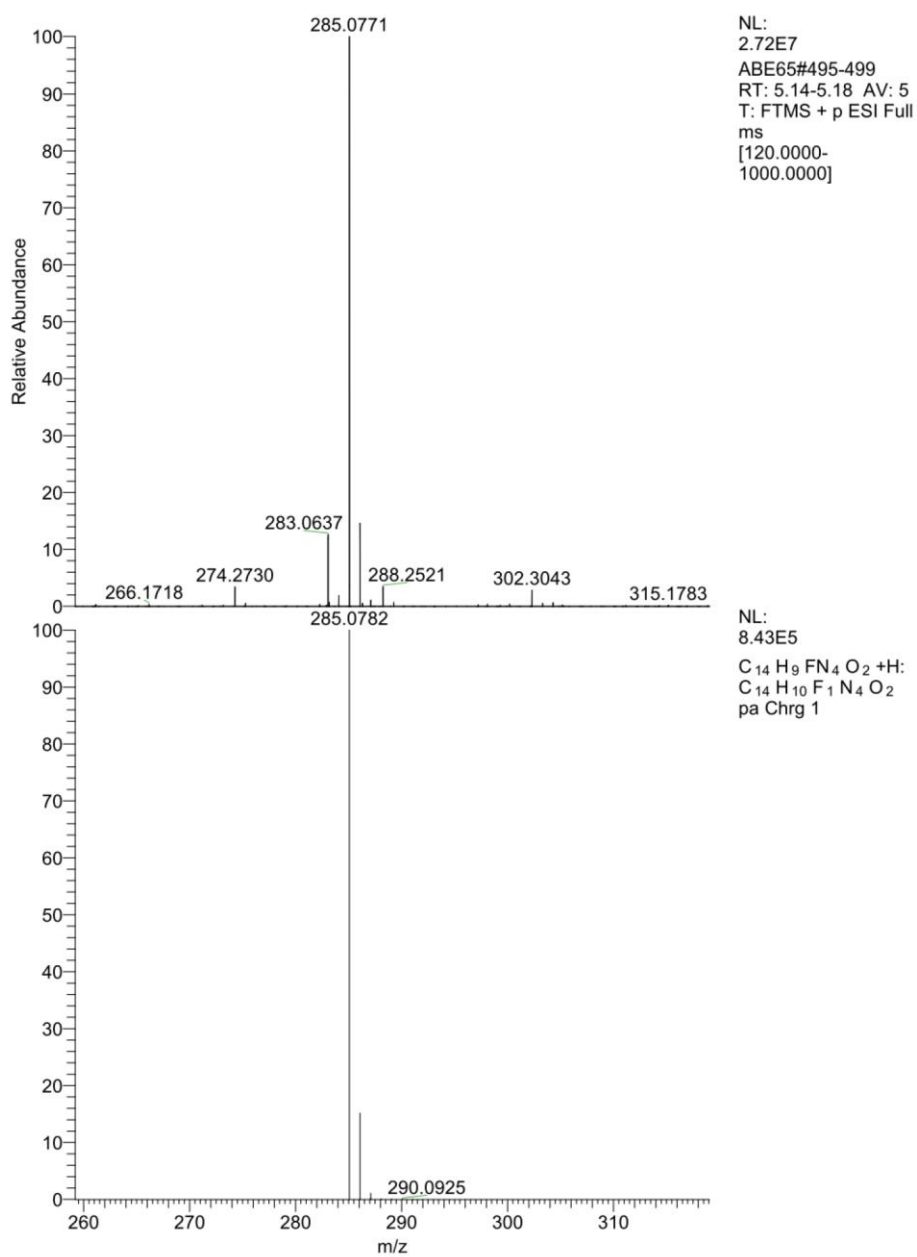
4-(1-(6-(isopropylamino)pyridin-3-yl)-1H-1,2,3-triazol-4-yl)benzoic acid (19h):



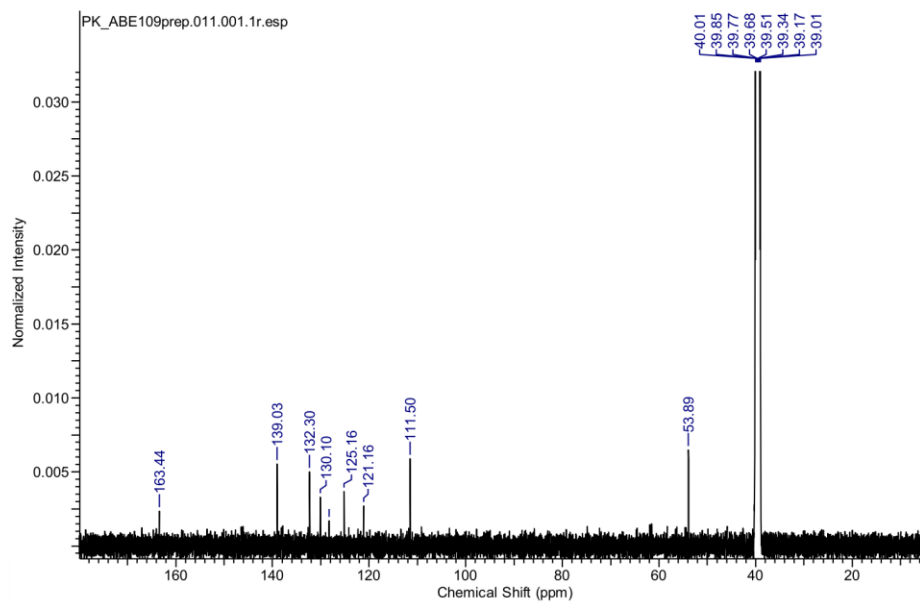
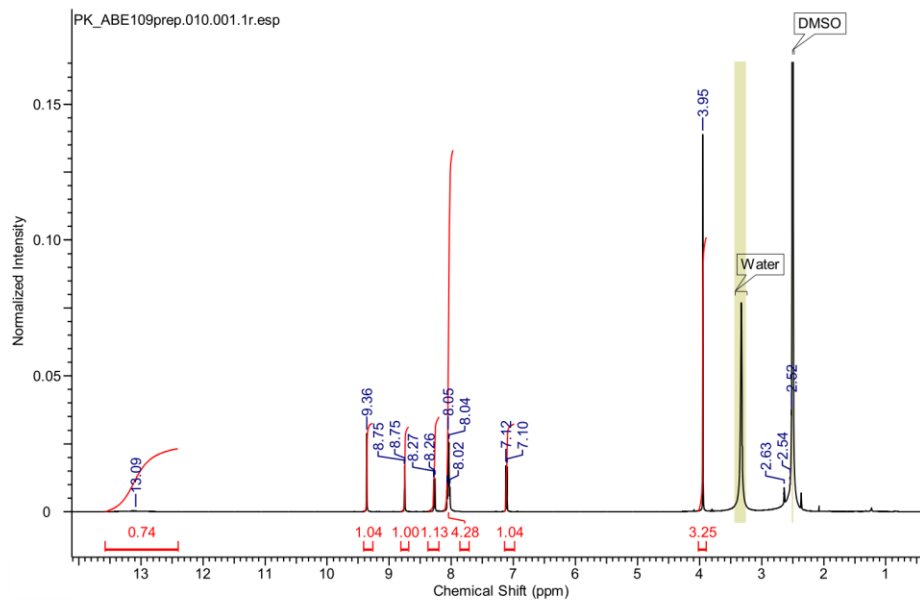
4-(1-(6-(phenylamino)pyridin-3-yl)-1H-1,2,3-triazol-4-yl)benzoic acid (19i):

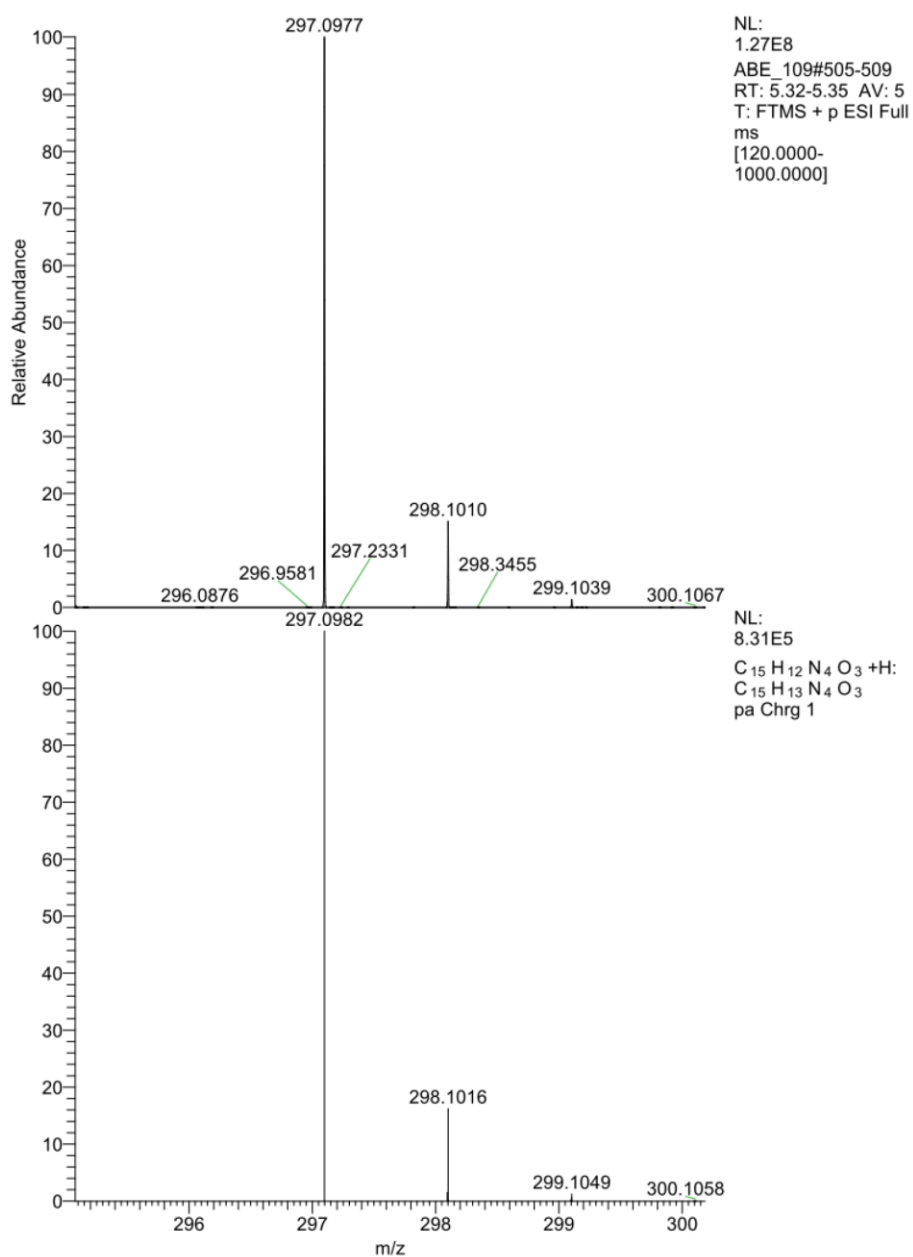


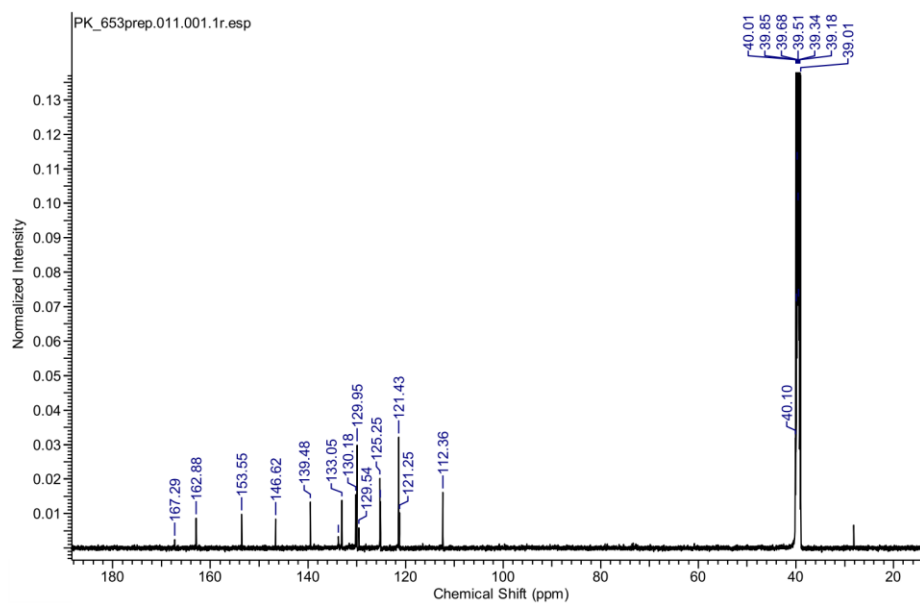
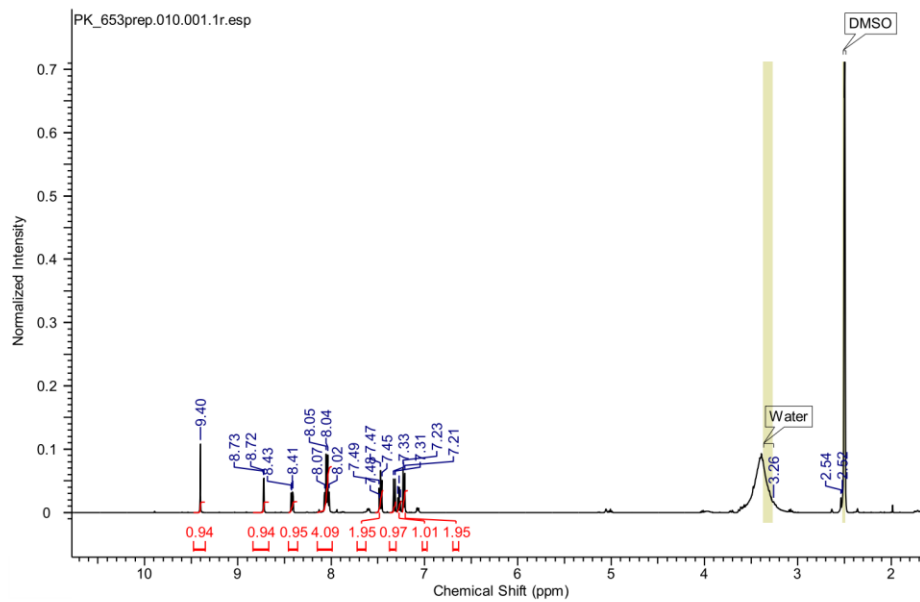
4-(1-(5-fluoropyridin-3-yl)-1H-1,2,3-triazol-4-yl)benzoic acid (19j):

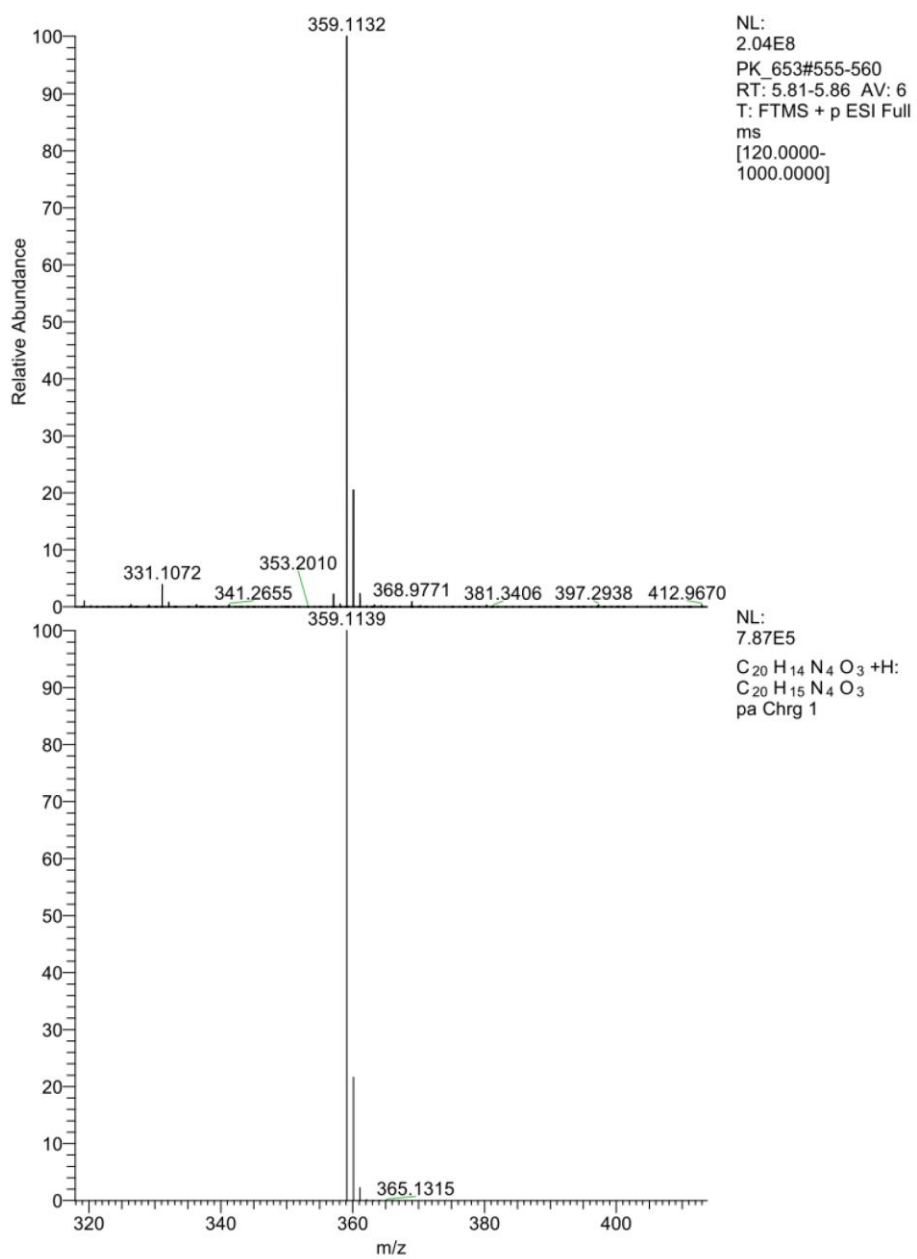


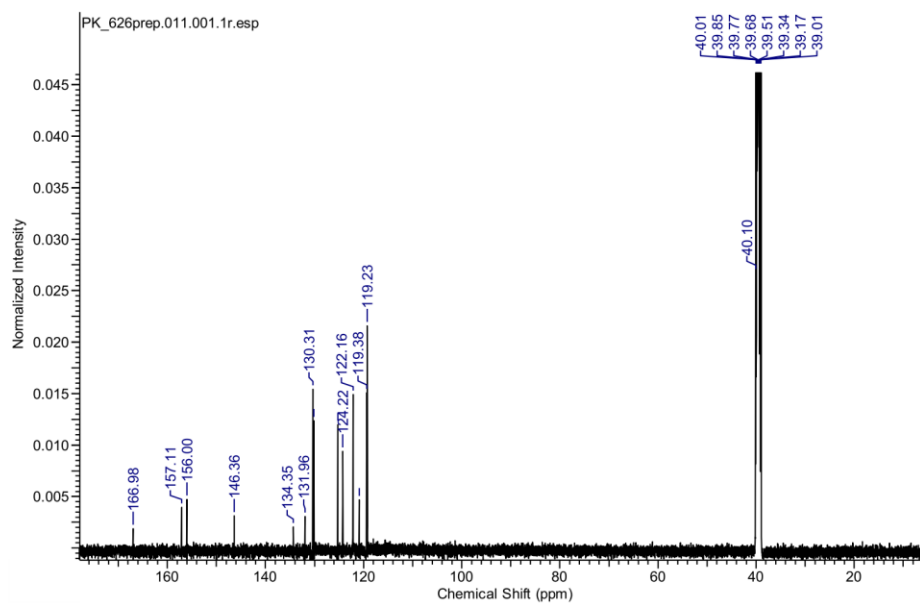
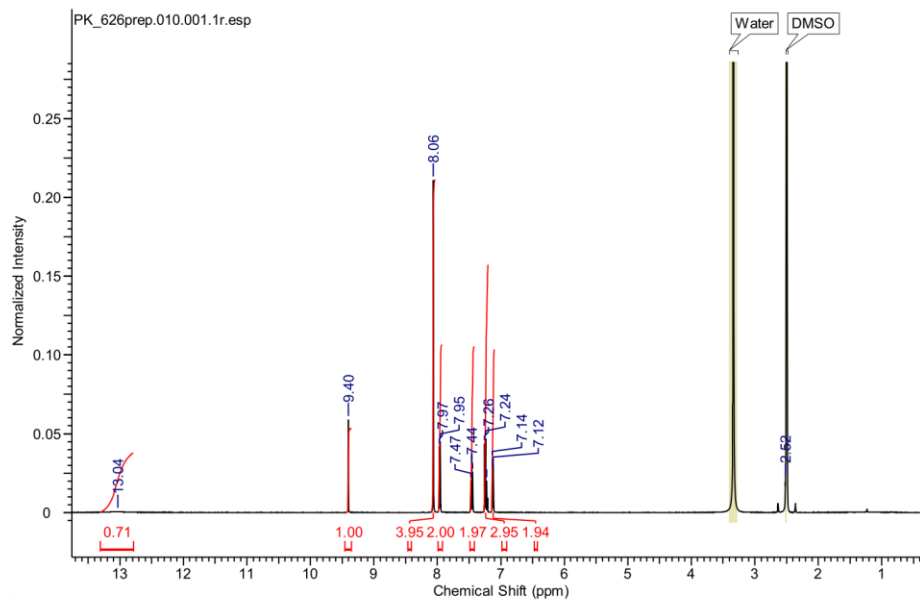
4-(1-(6-methoxypyridin-3-yl)-1H-1,2,3-triazol-4-yl)benzoic acid (19k):

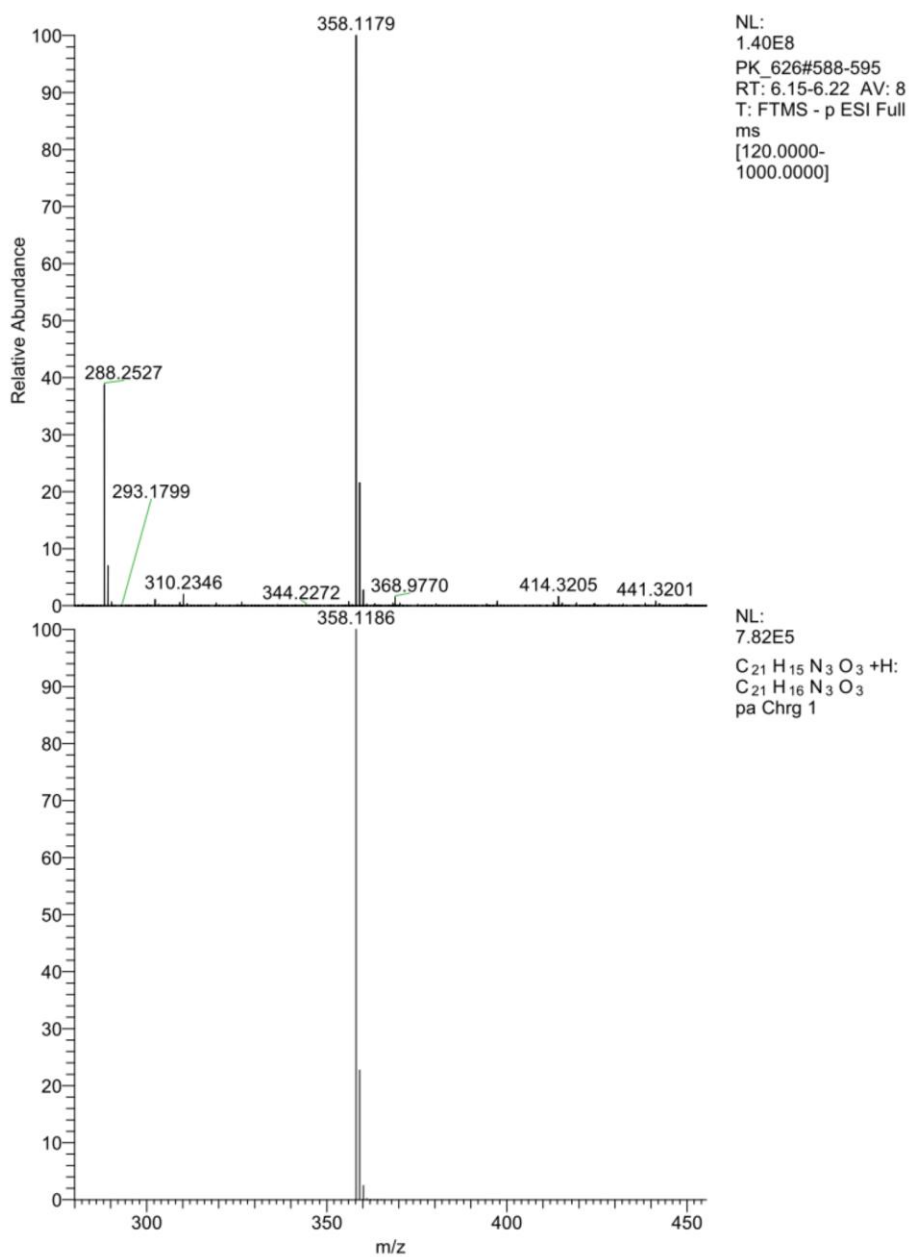


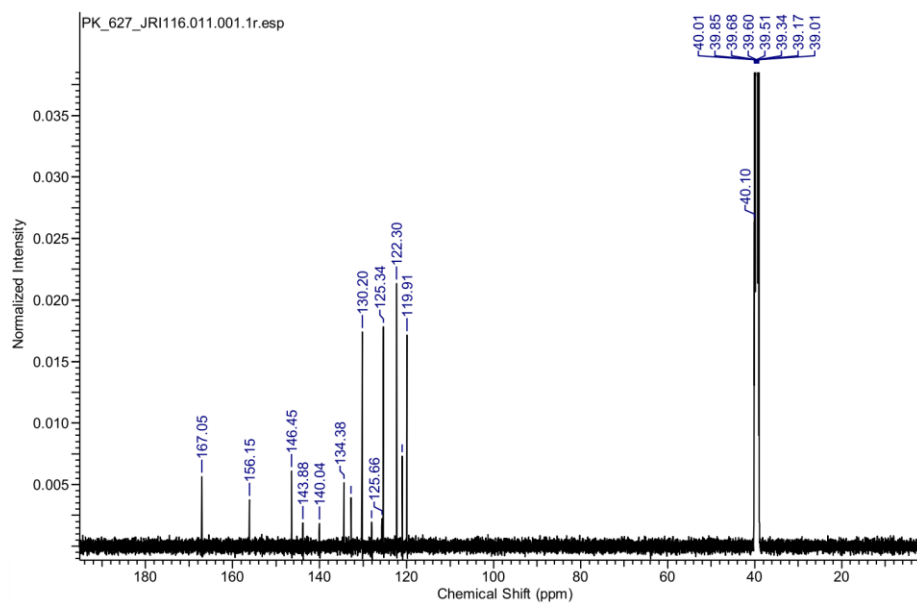
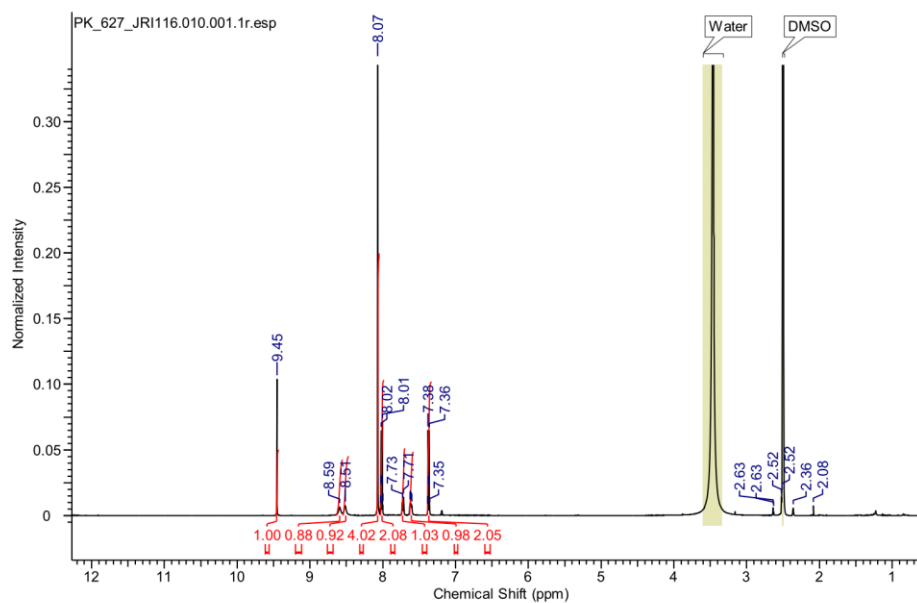


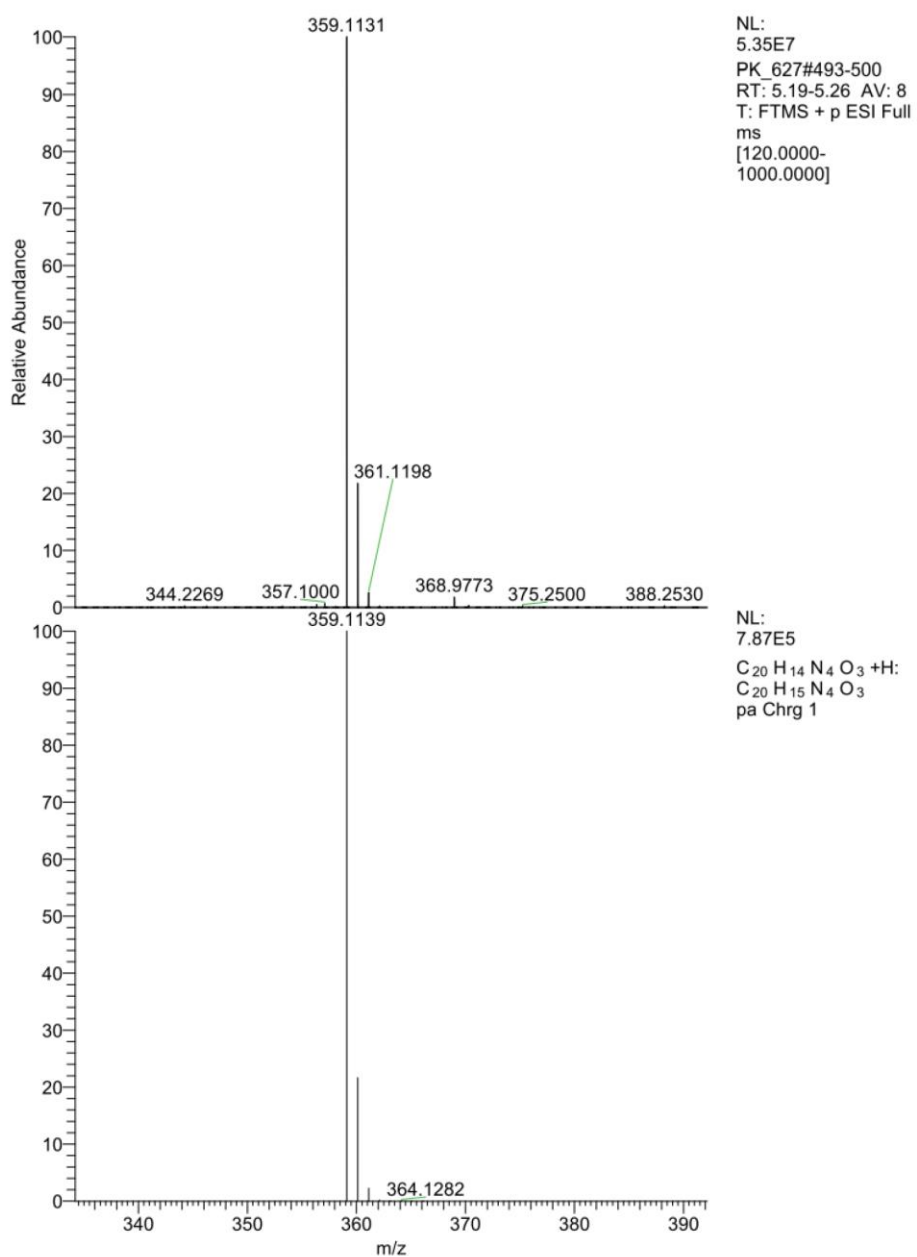
4-(1-(6-phenoxy pyridin-3-yl)-1H-1,2,3-triazol-4-yl)benzoic acid (19I):

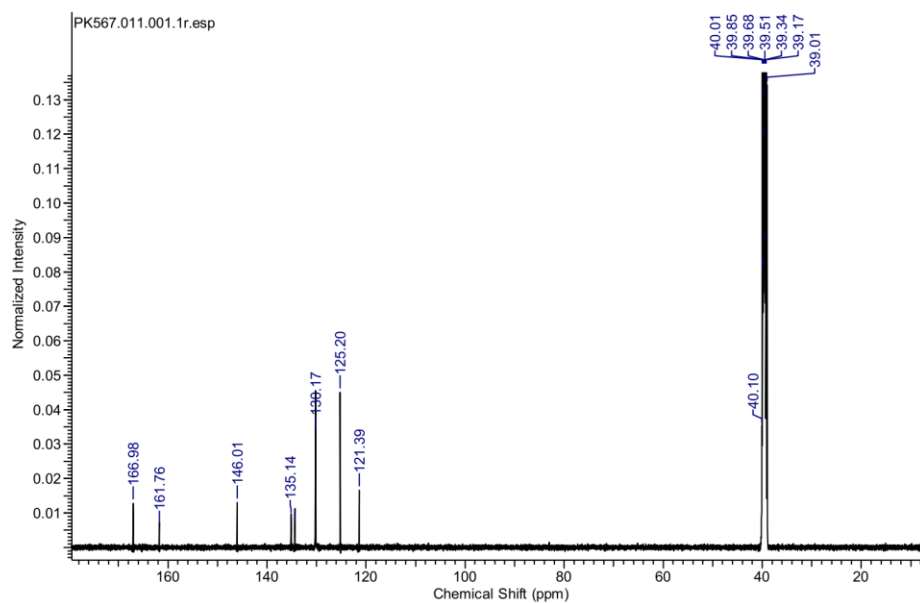
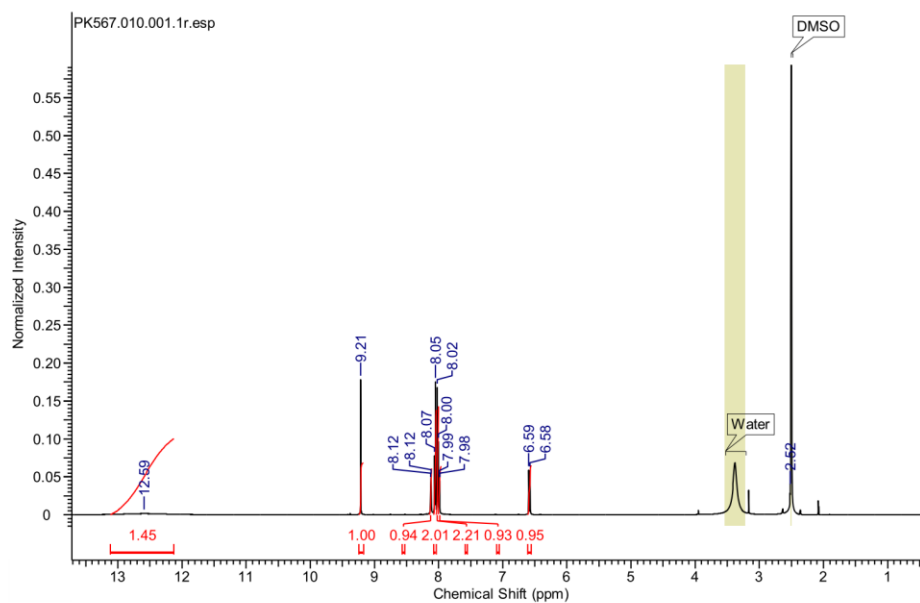


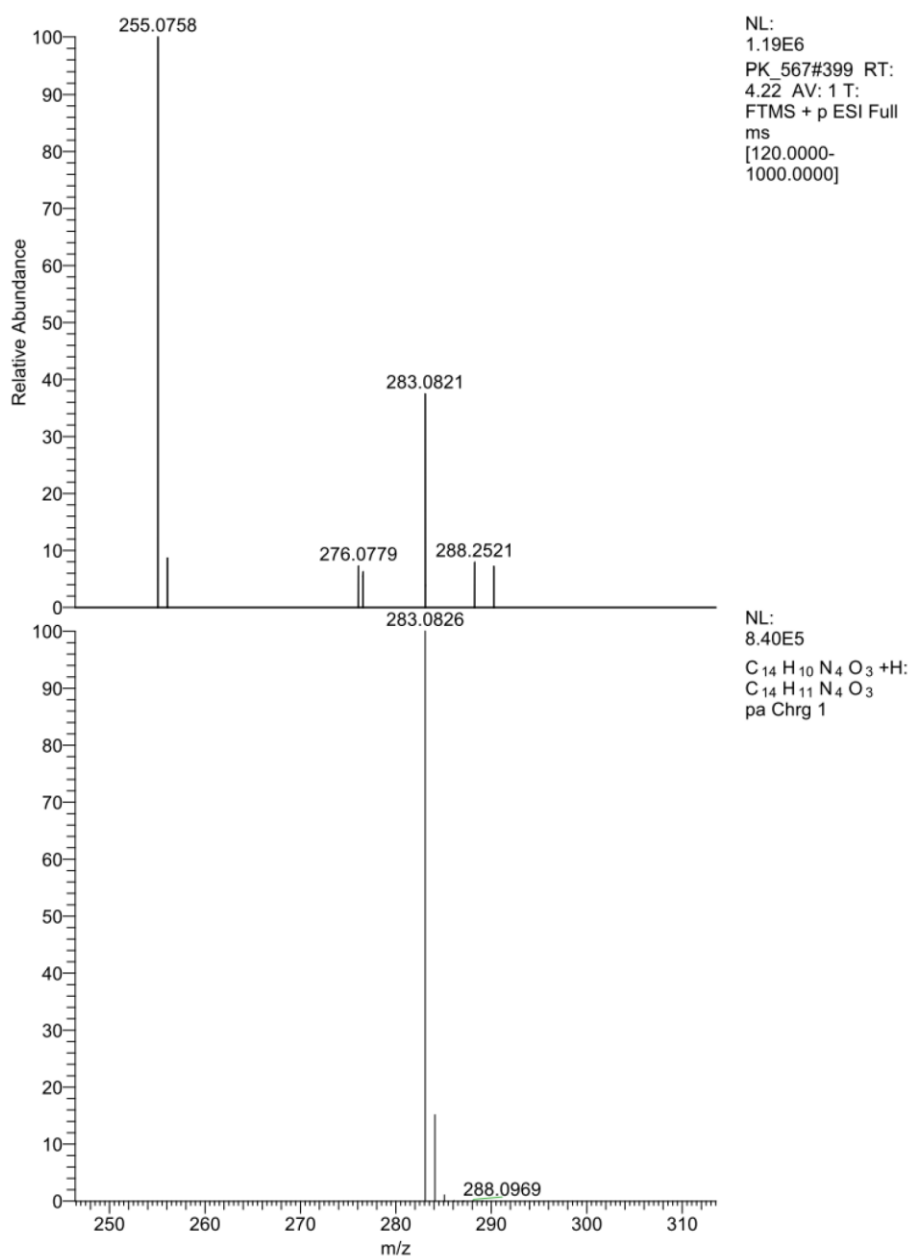
4-(1-(4-phenoxyphenyl)-1H-1,2,3-triazol-4-yl)benzoic acid (19m):

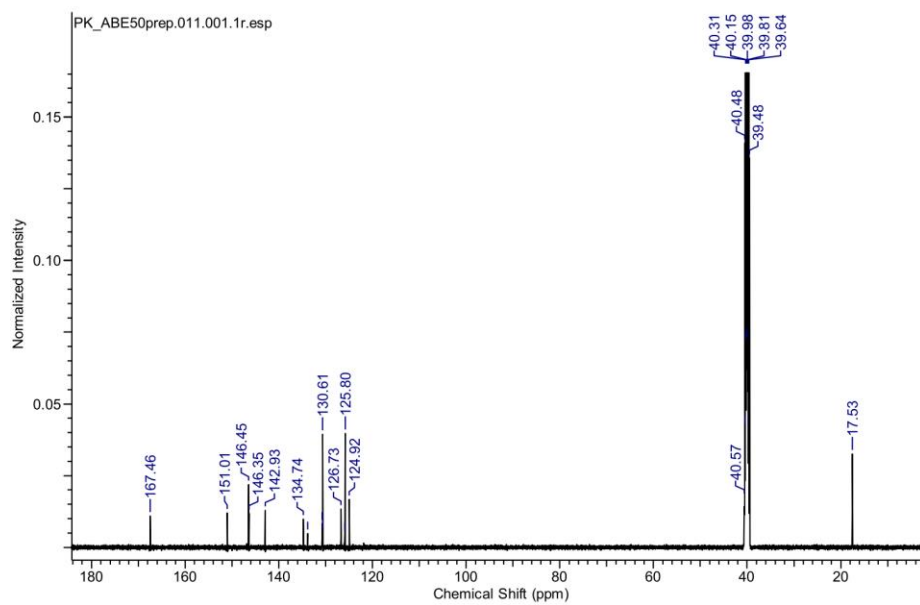
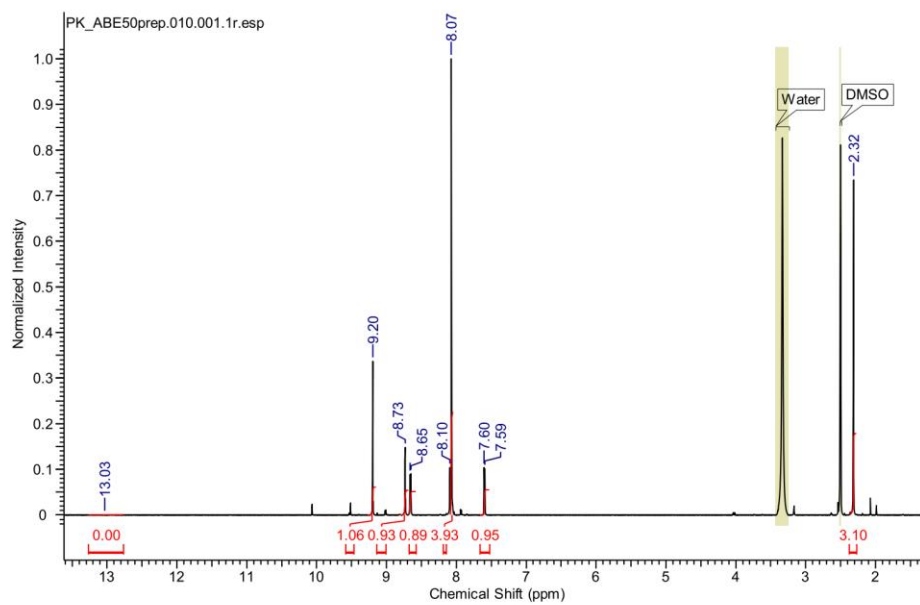


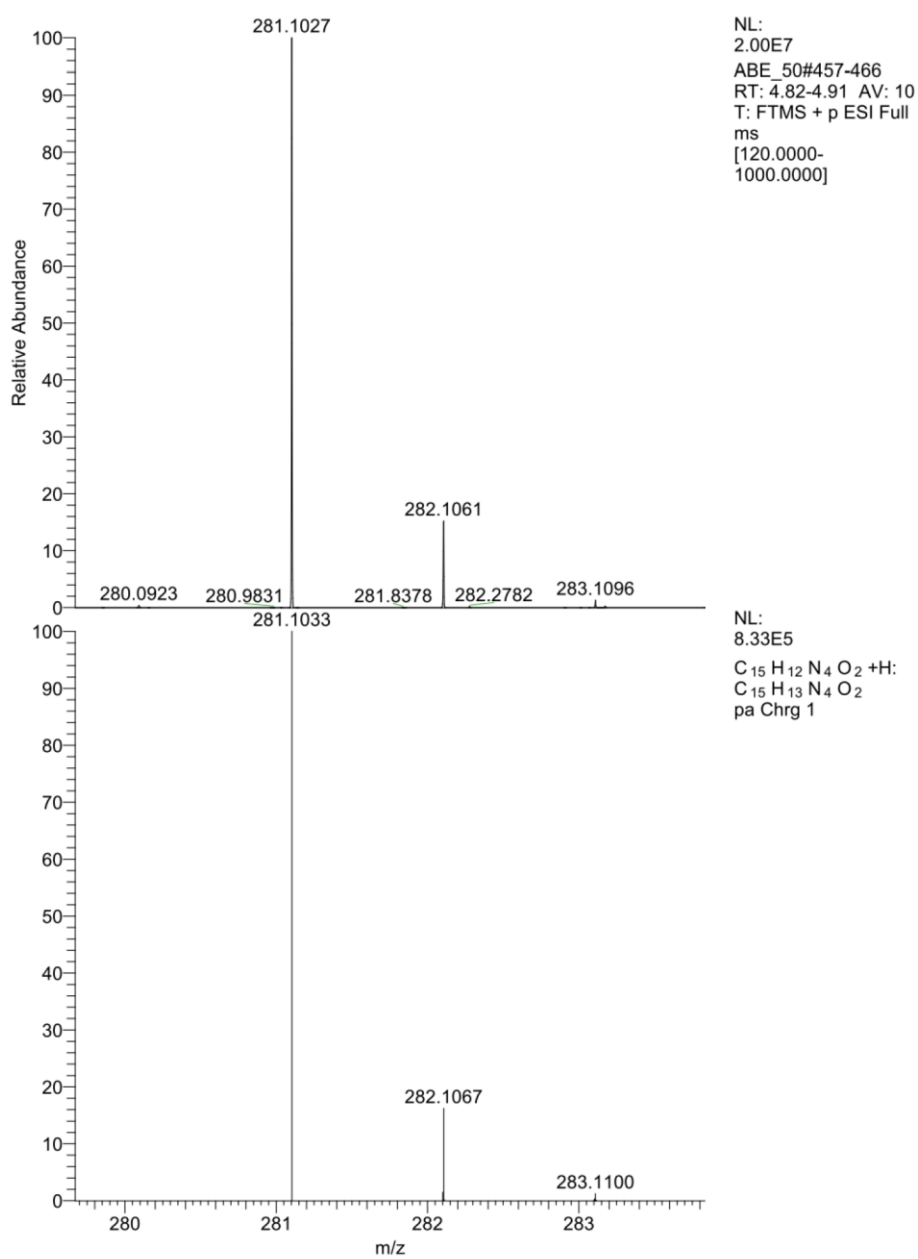
4-(1-(4-(pyridin-3-yloxy)phenyl)-1H-1,2,3-triazol-4-yl)benzoic acid (19n):

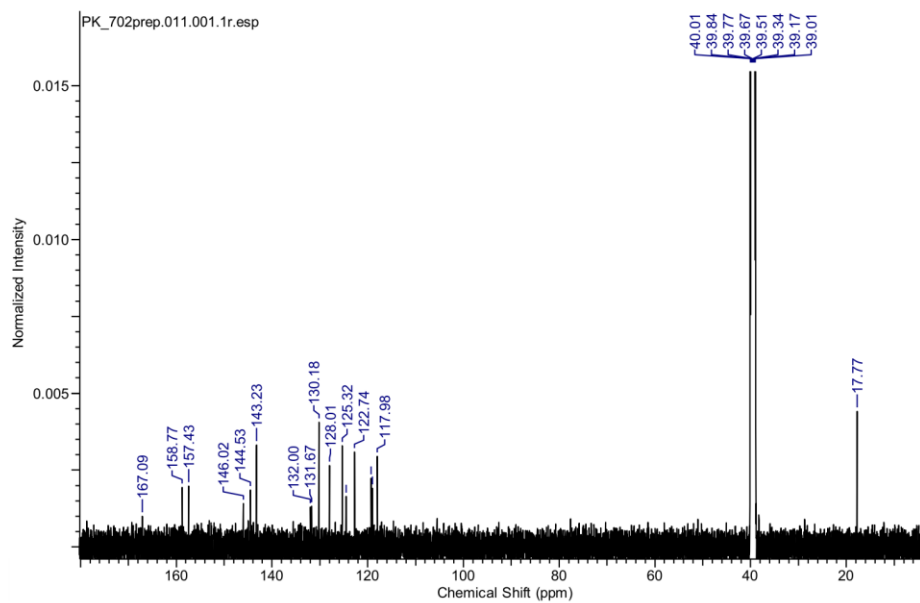
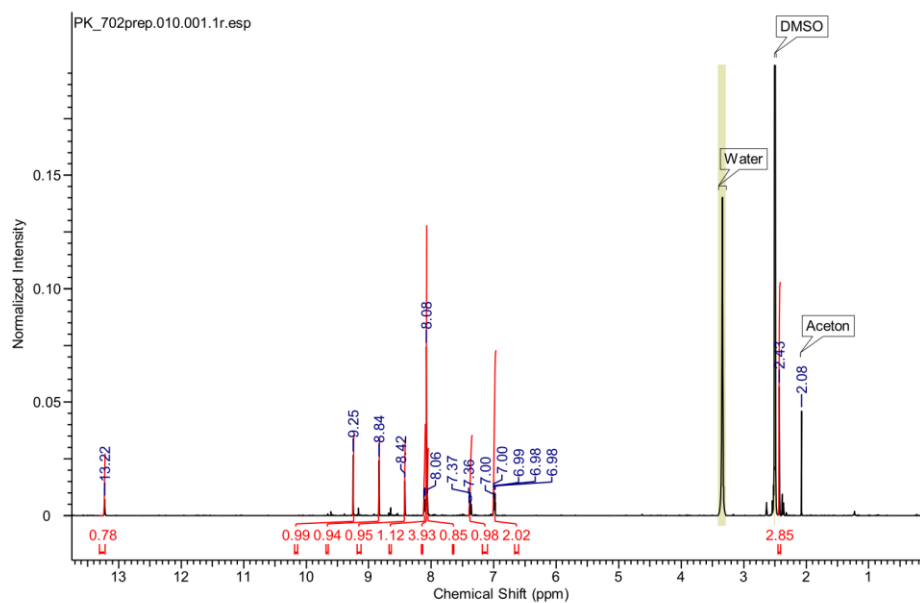


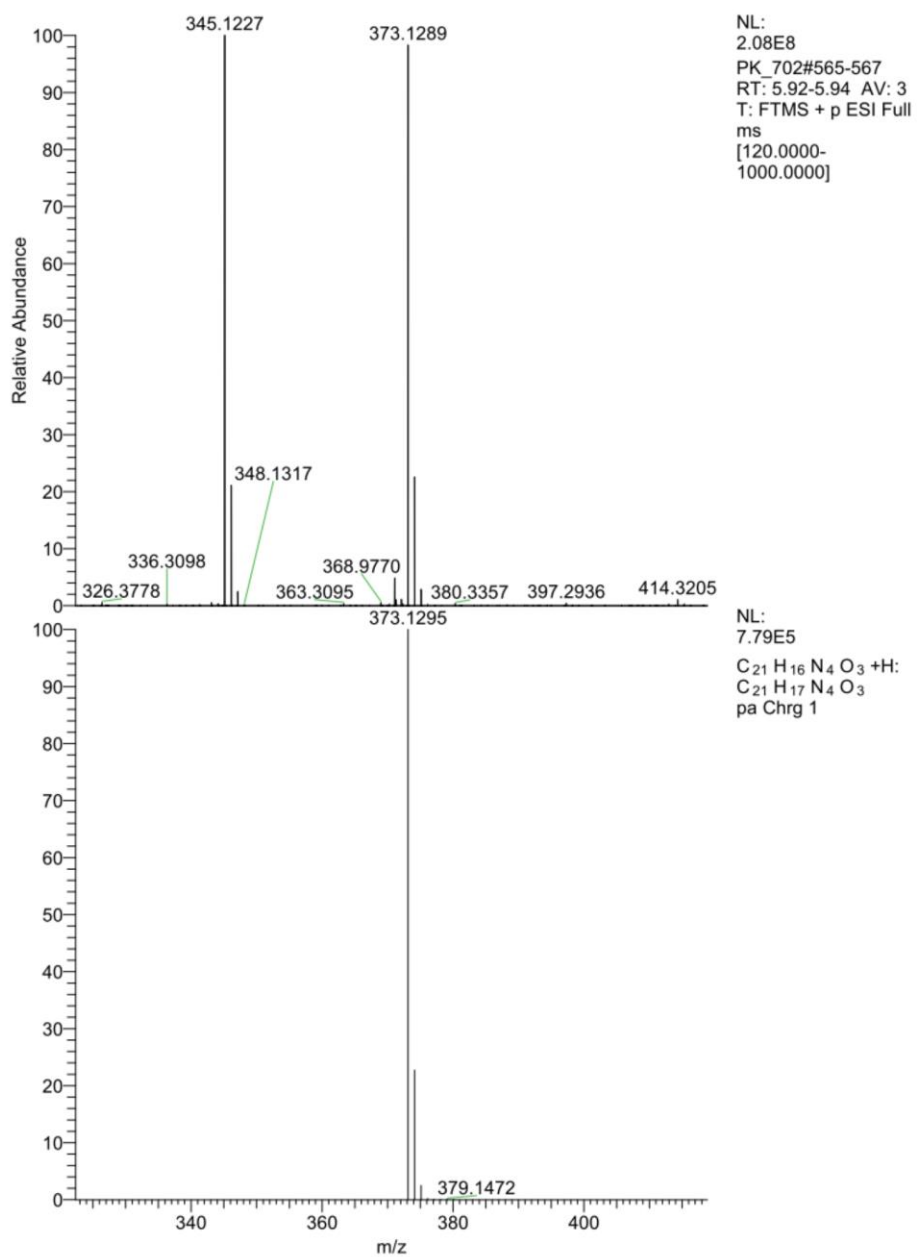
4-(1-(6-hydroxypyridin-3-yl)-1H-1,2,3-triazol-4-yl)benzoic acid (19o):

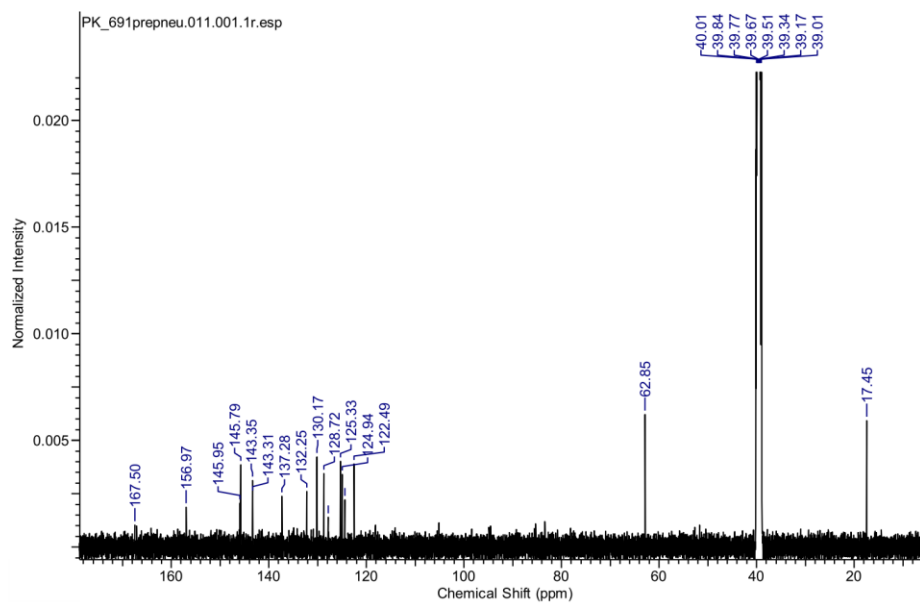
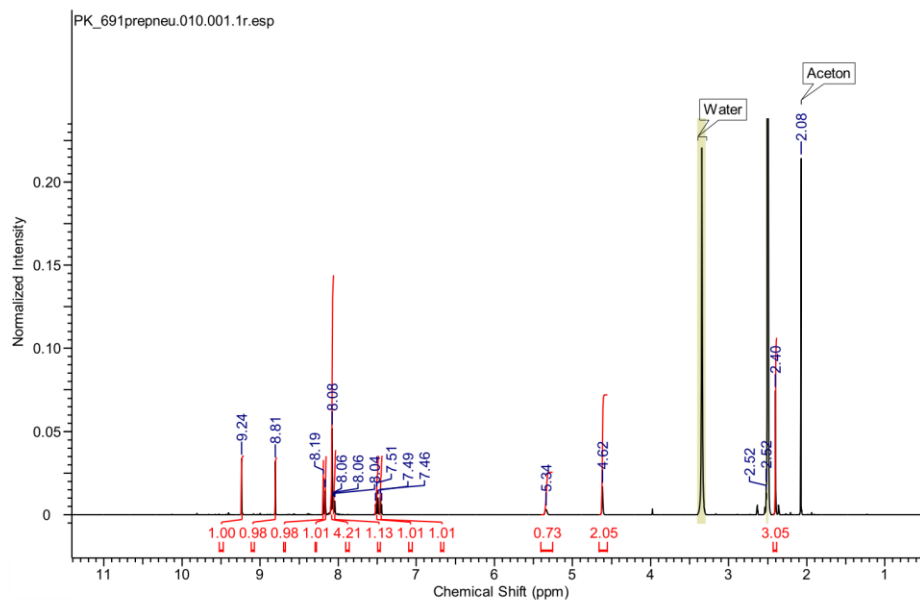


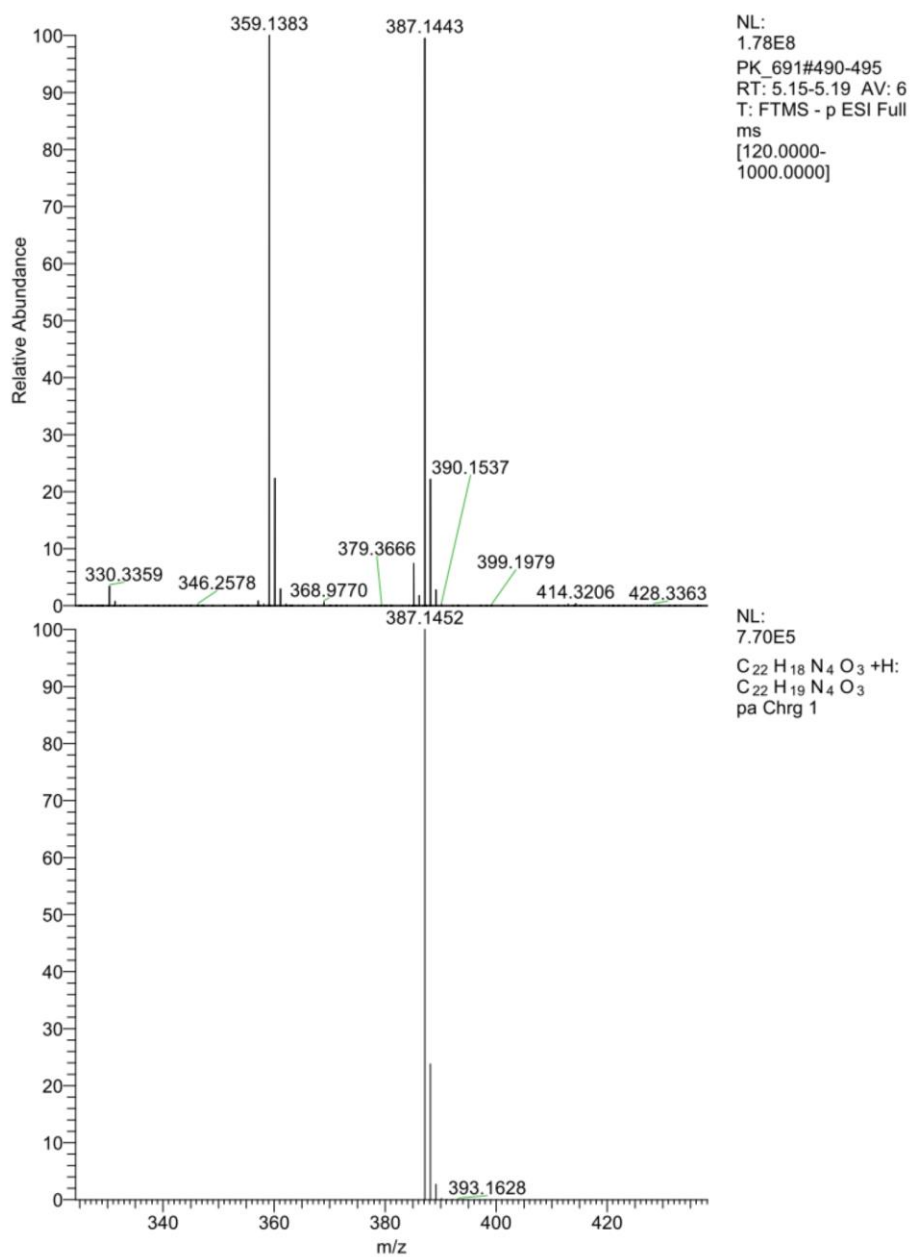
4-(1-(3-methylpyridin-4-yl)-1H-1,2,3-triazol-4-yl)benzoic acid (22):



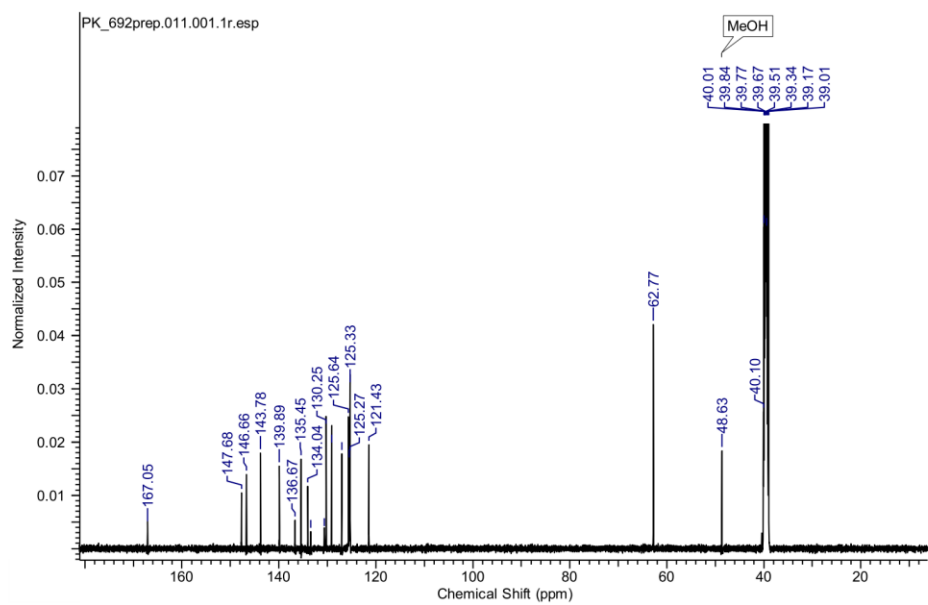
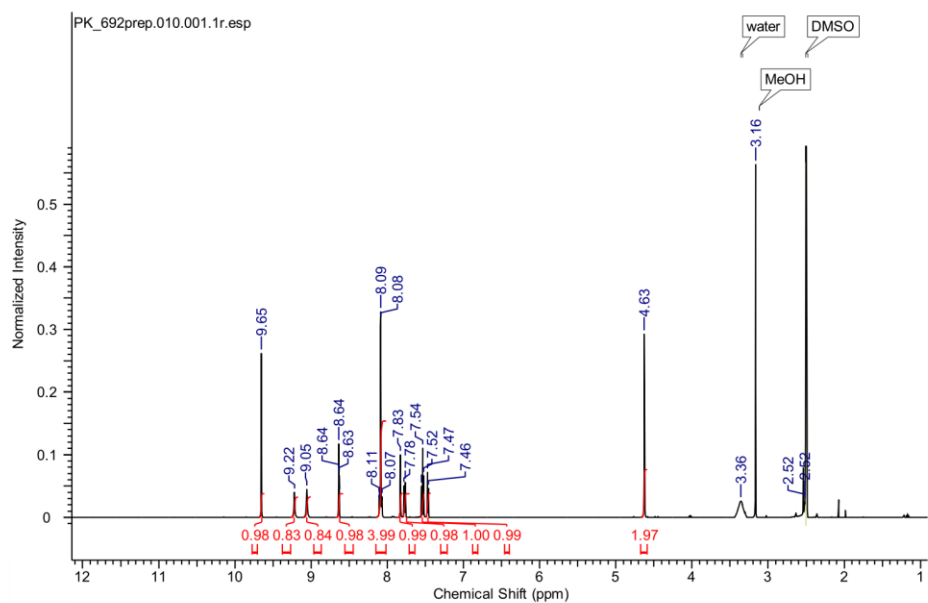
4-(1-(6-(2-hydroxyphenyl)-4-methylpyridin-3-yl)-1H-1,2,3-triazol-4-yl)benzoic acid (26a):

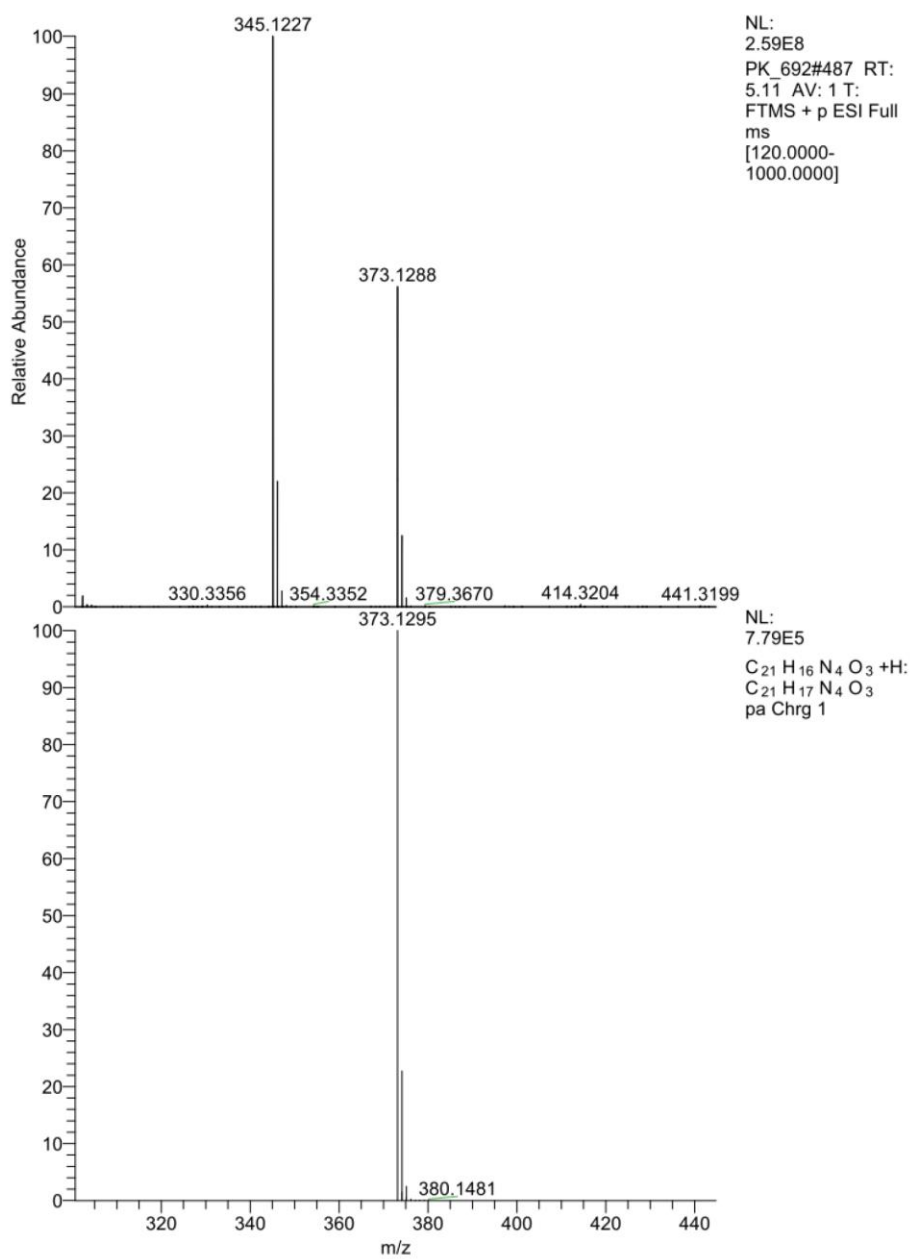


4-(1-(6-(3-(hydroxymethyl)phenyl)-4-methylpyridin-3-yl)-1H-1,2,3-triazol-4-yl)benzoic acid (26b):

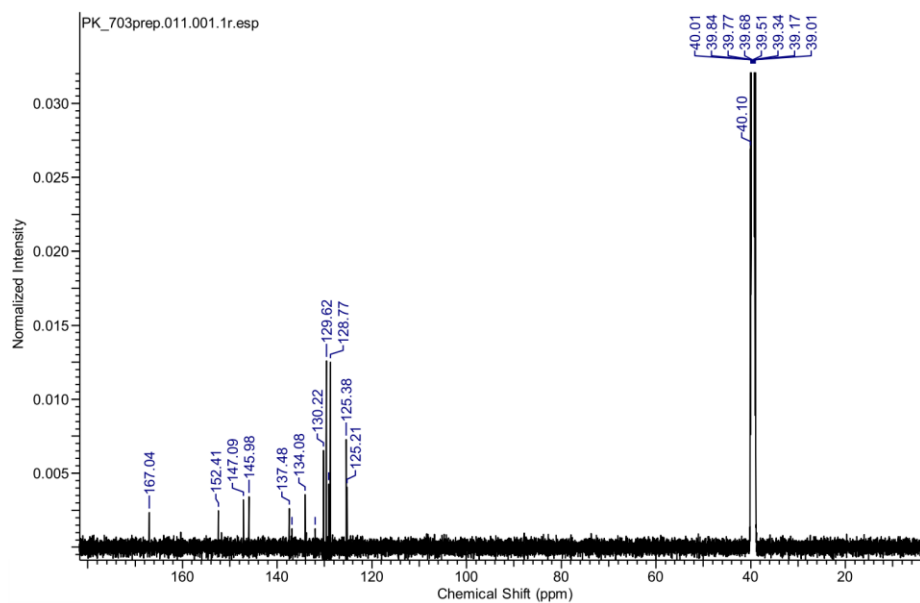
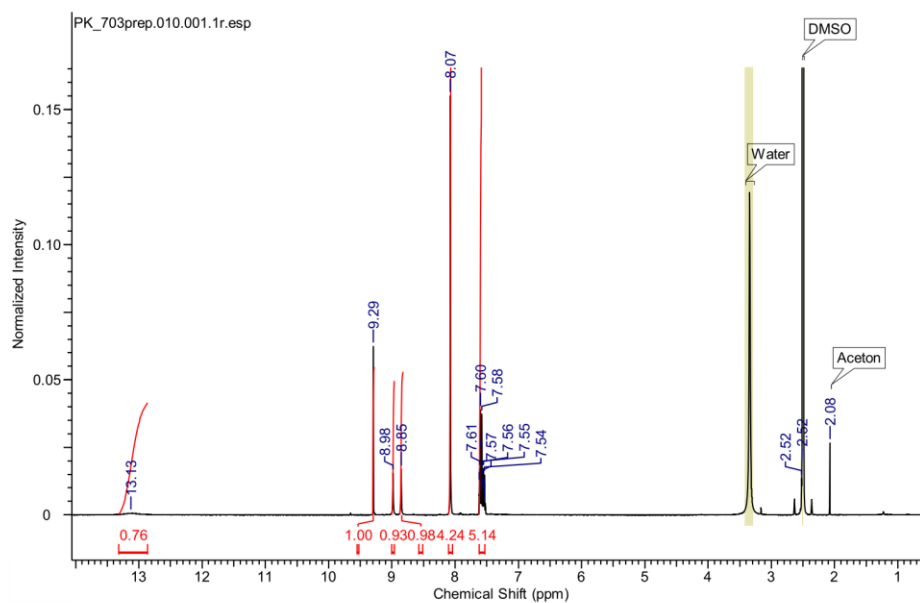


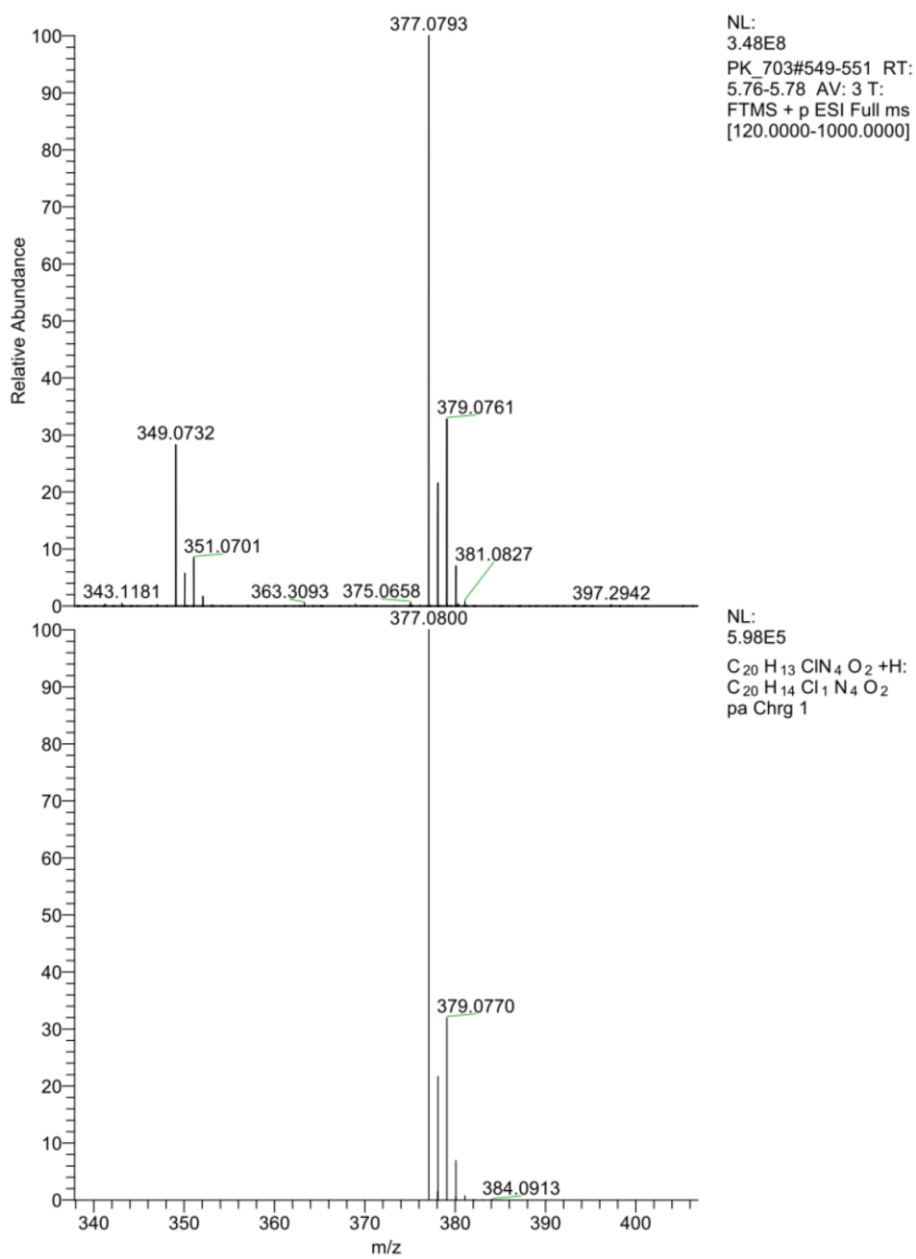
4-(1-(5-(3-(hydroxymethyl)phenyl)pyridin-3-yl)-1H-1,2,3-triazol-4-yl)benzoic acid (31a):

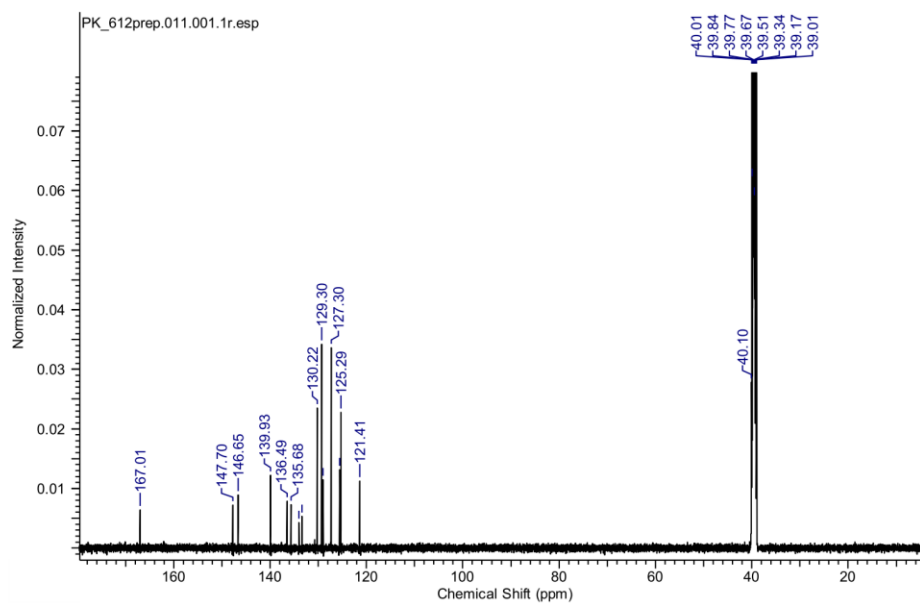
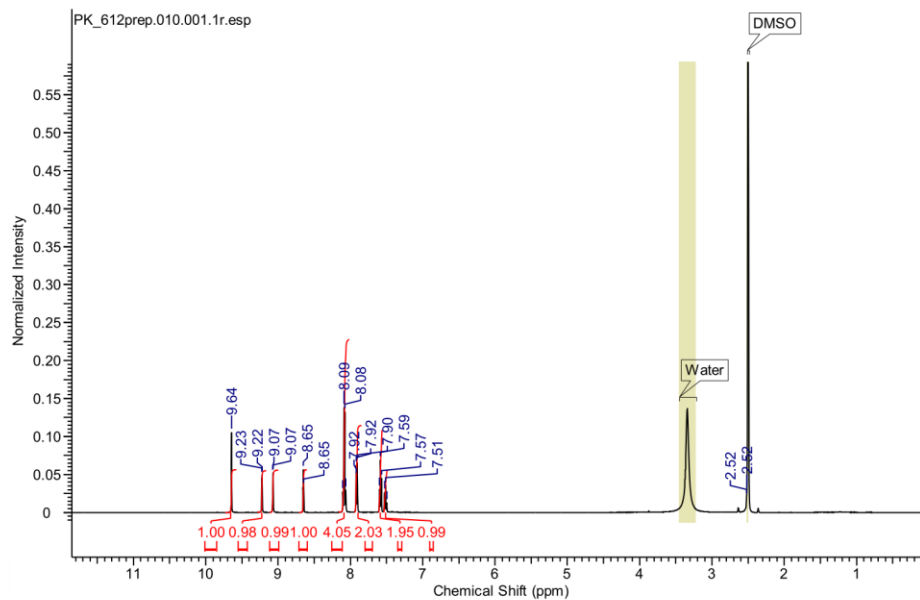


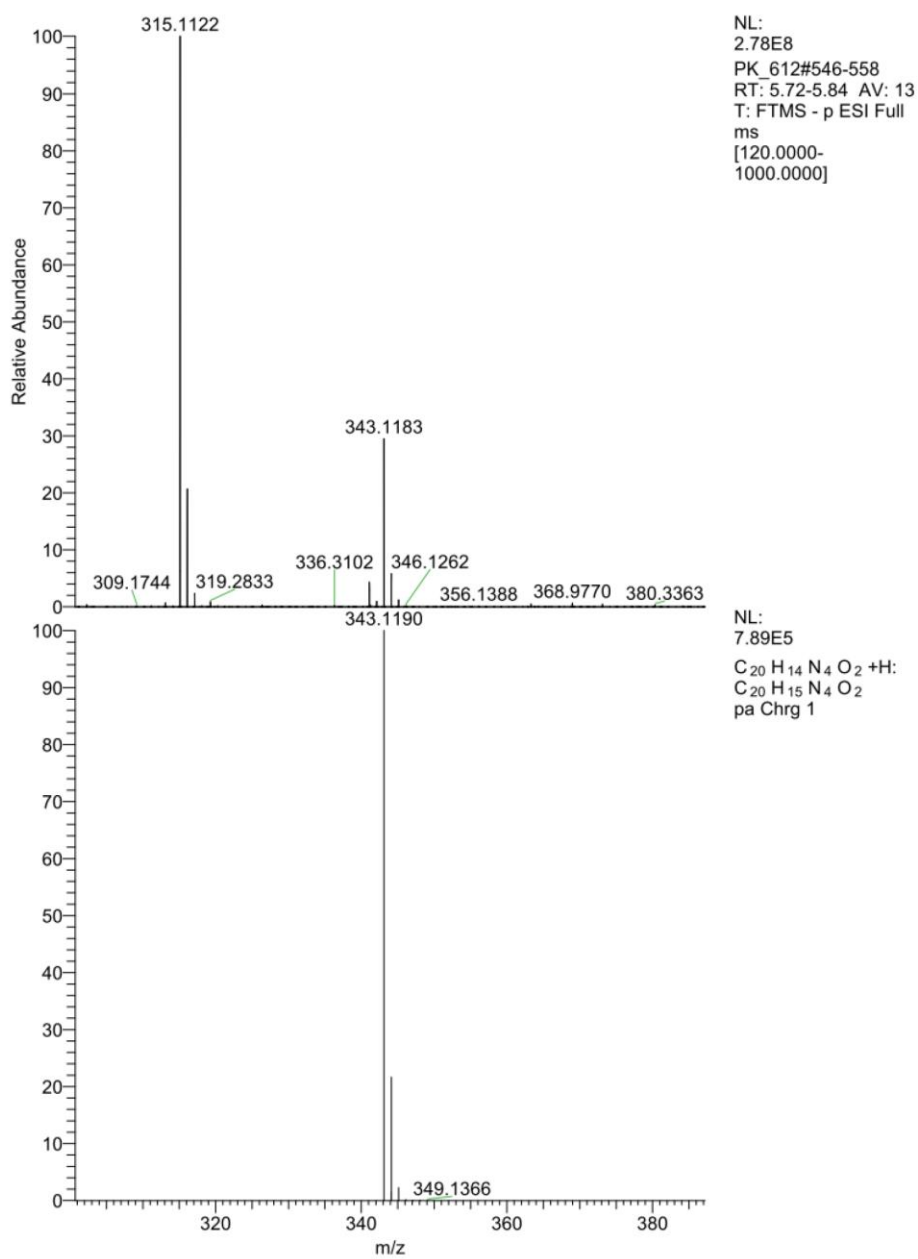


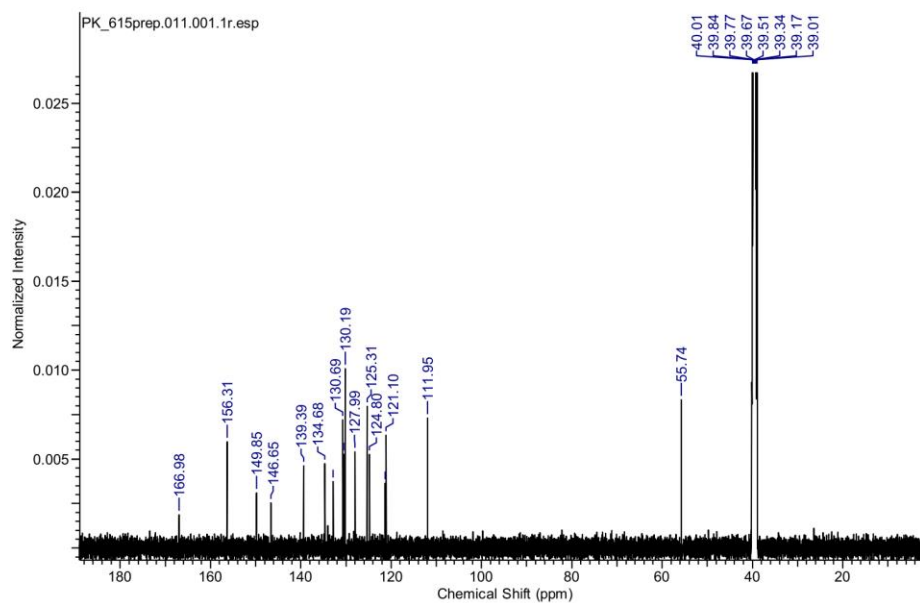
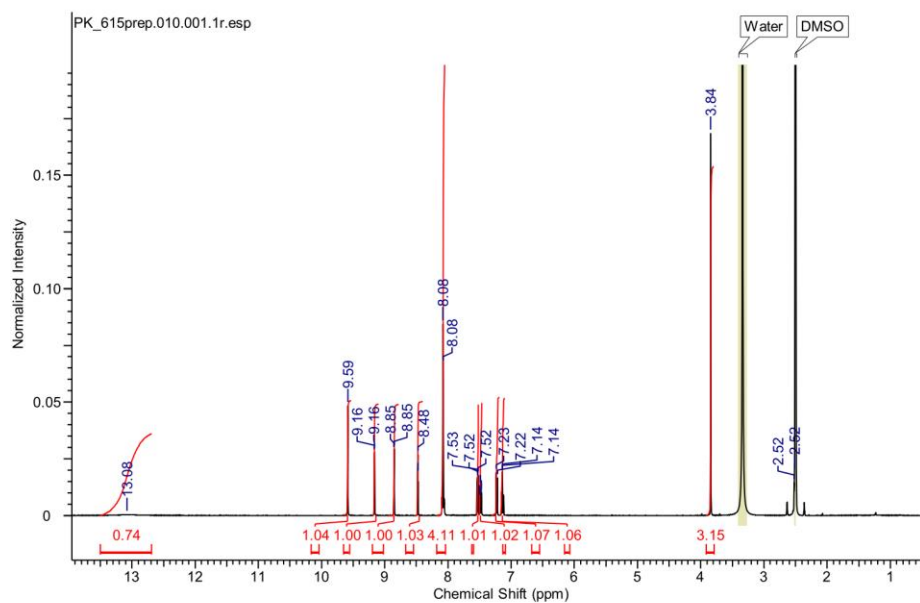
4-(1-(4-chloro-5-phenylpyridin-3-yl)-1H-1,2,3-triazol-4-yl)benzoic acid (31b):

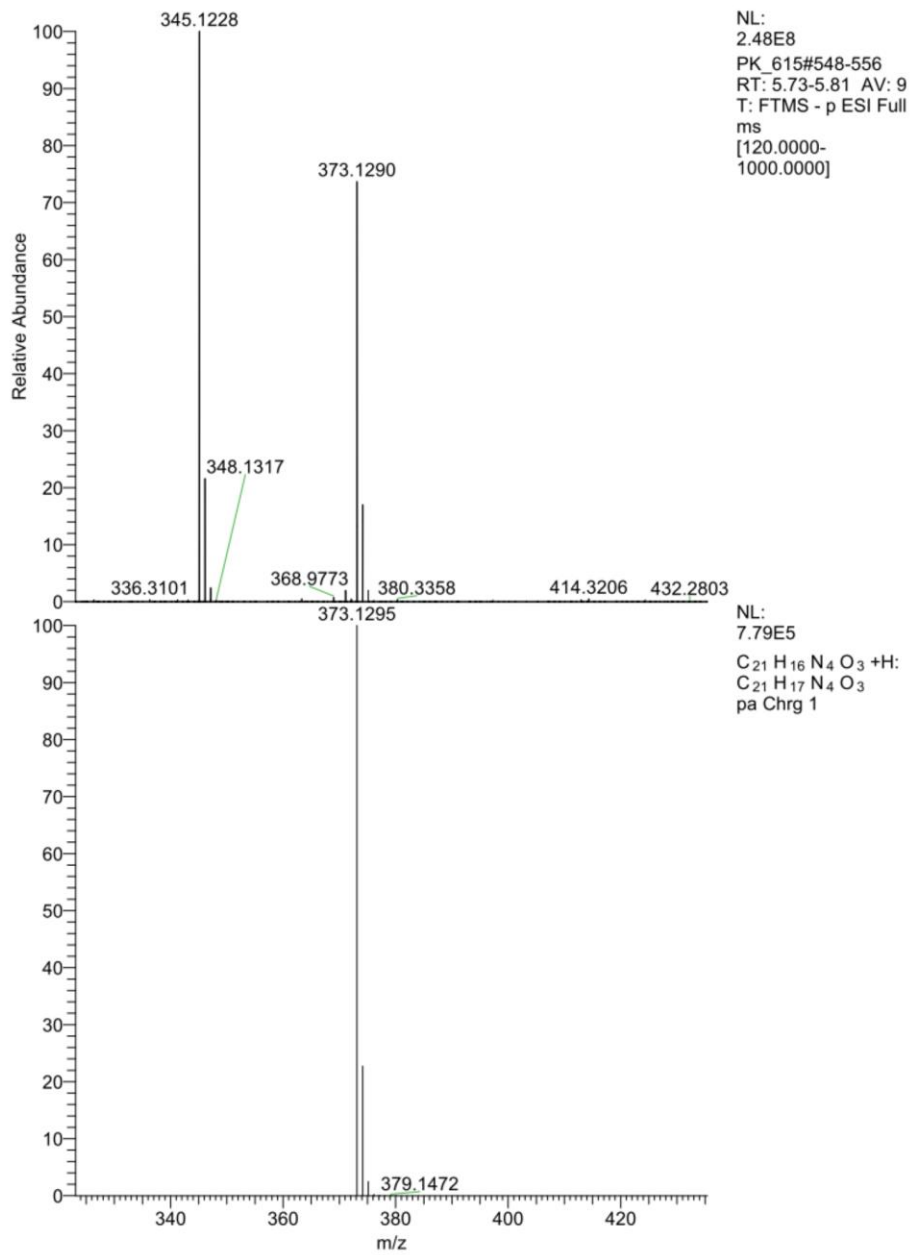


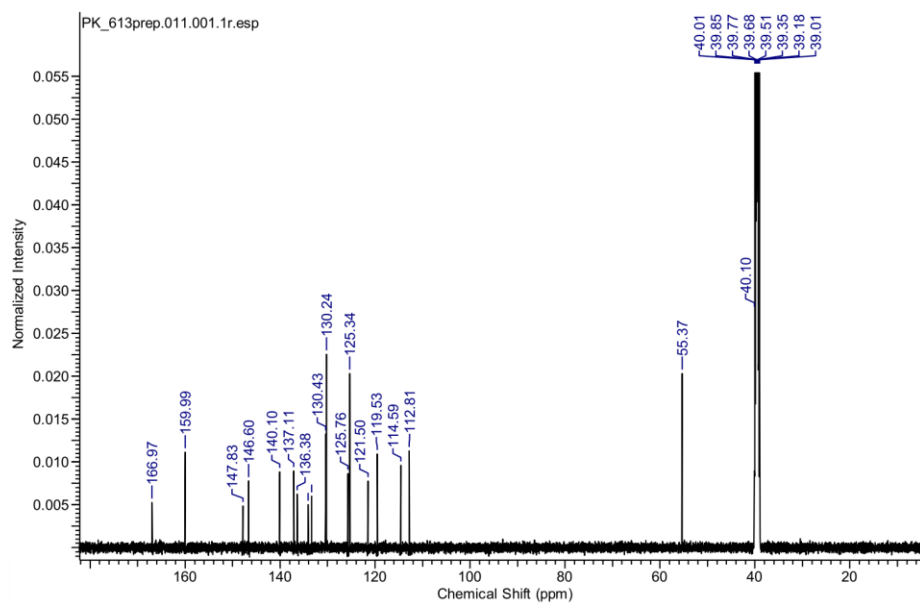
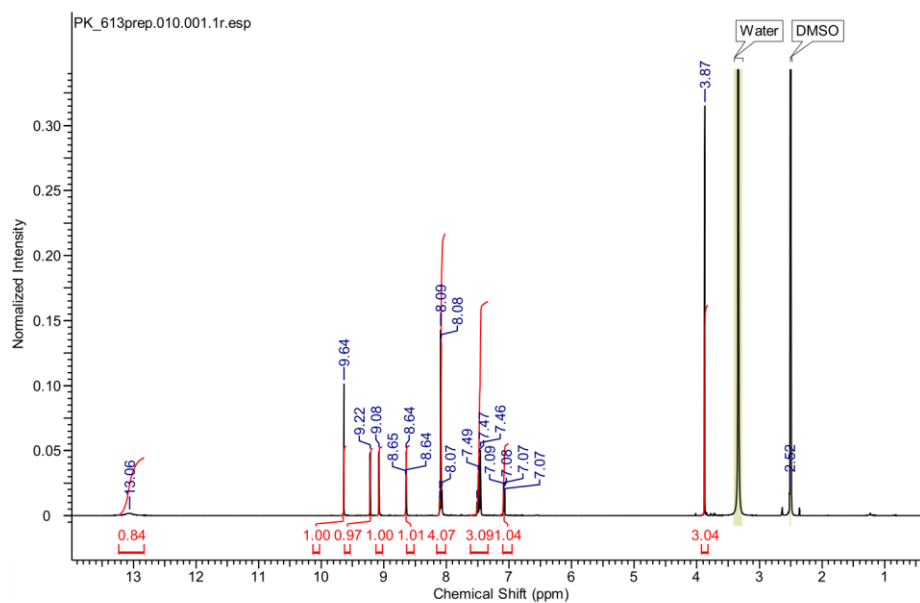


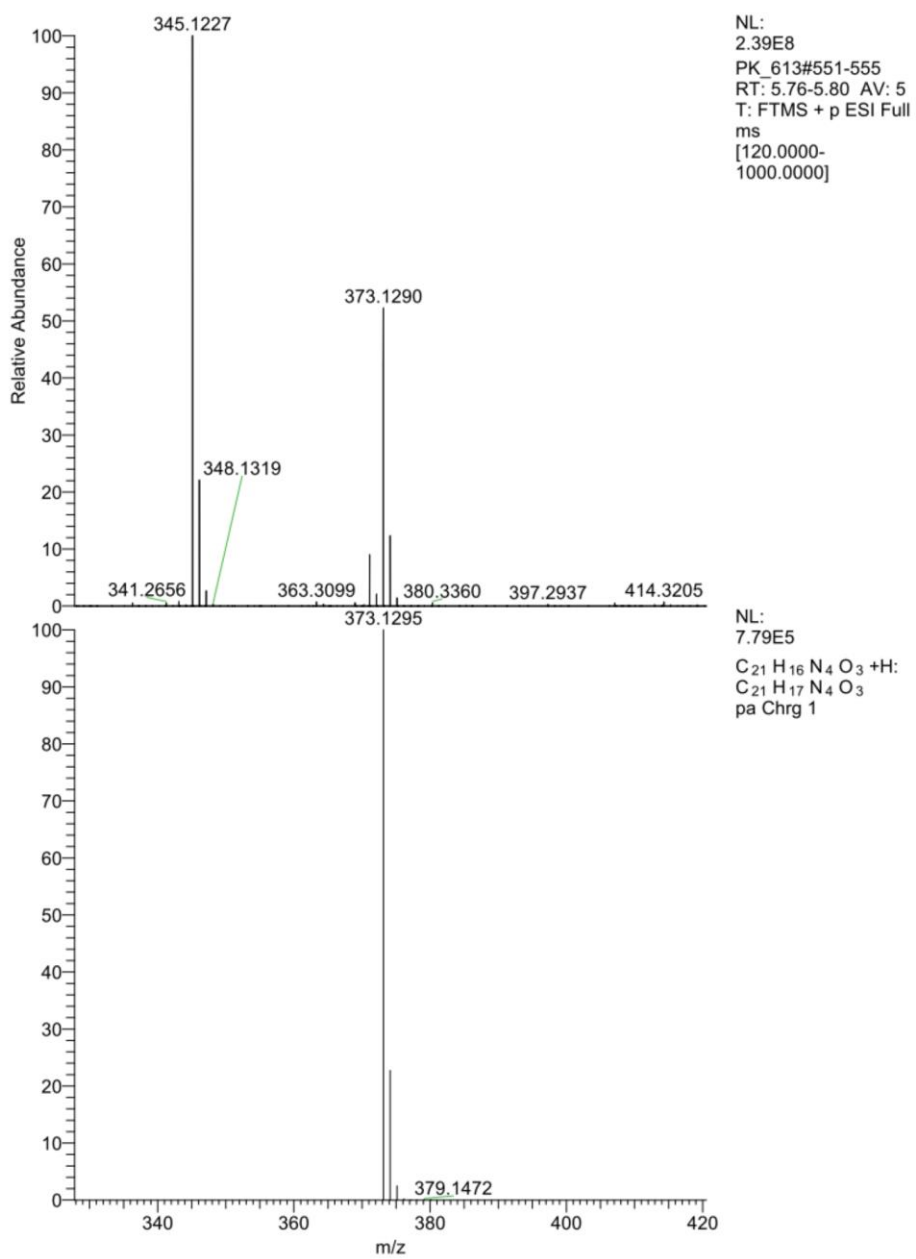
4-(1-(5-phenylpyridin-3-yl)-1H-1,2,3-triazol-4-yl)benzoic acid (36a):



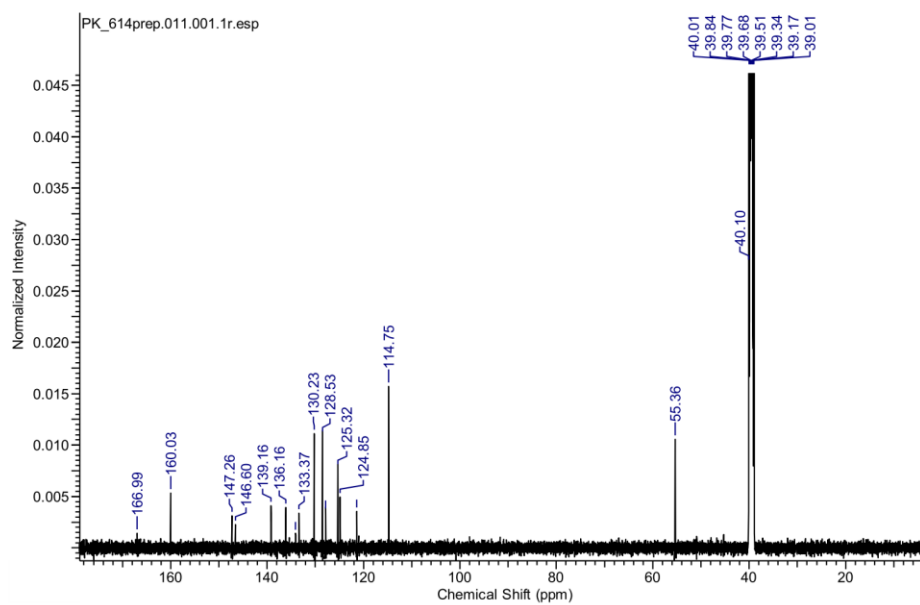
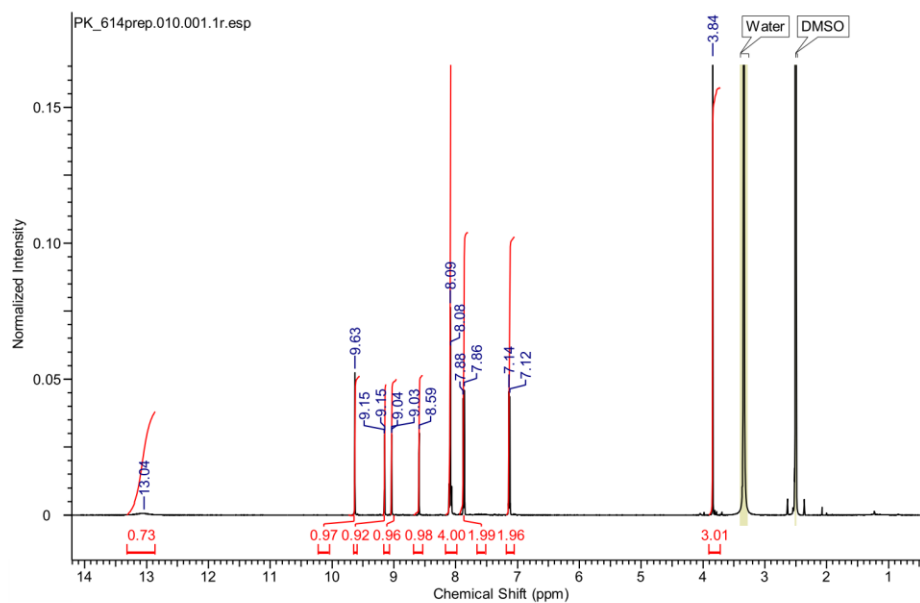
4-(1-(5-(2-methoxyphenyl)pyridin-3-yl)-1H-1,2,3-triazol-4-yl)benzoic acid (36b):

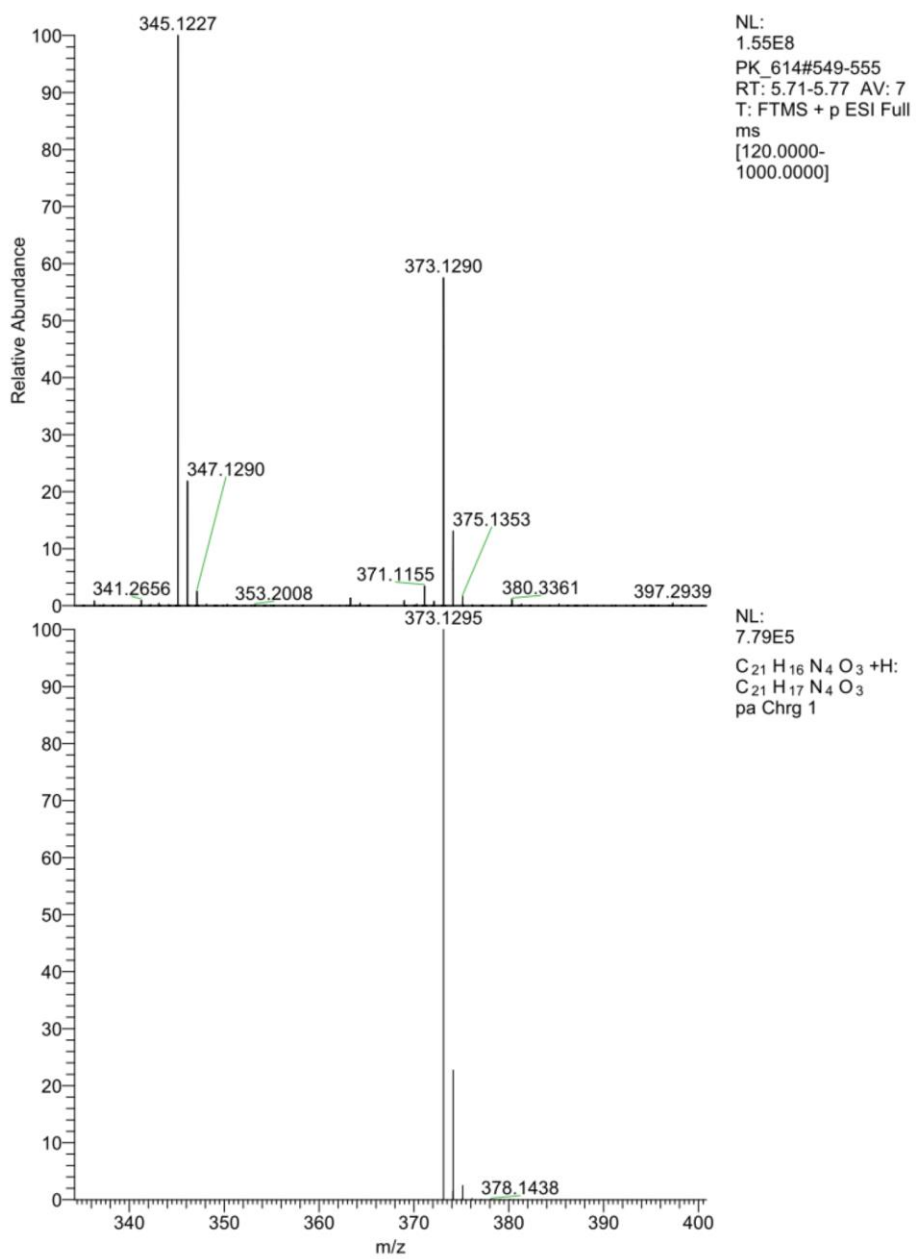


4-(1-(5-(3-methoxyphenyl)pyridin-3-yl)-1H-1,2,3-triazol-4-yl)benzoic acid (36c):

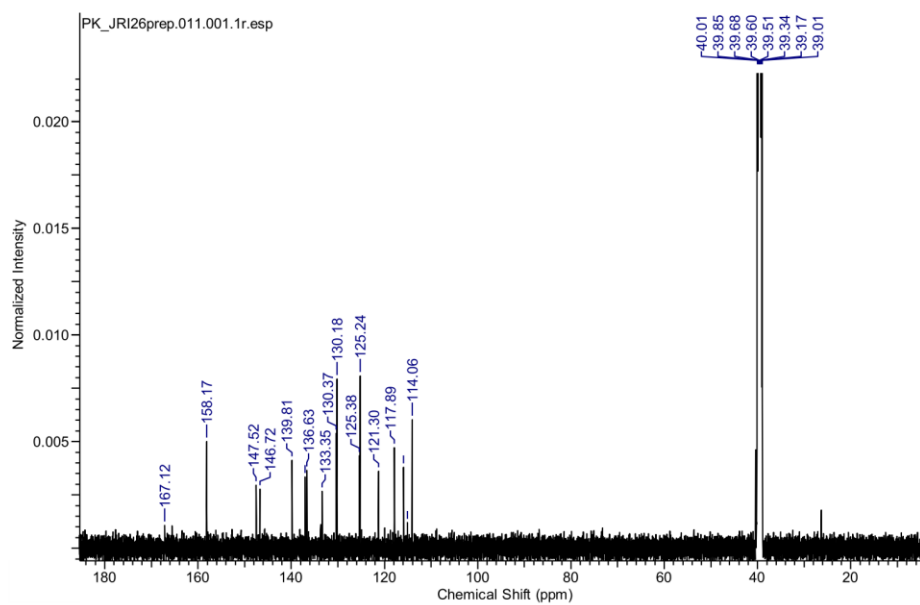
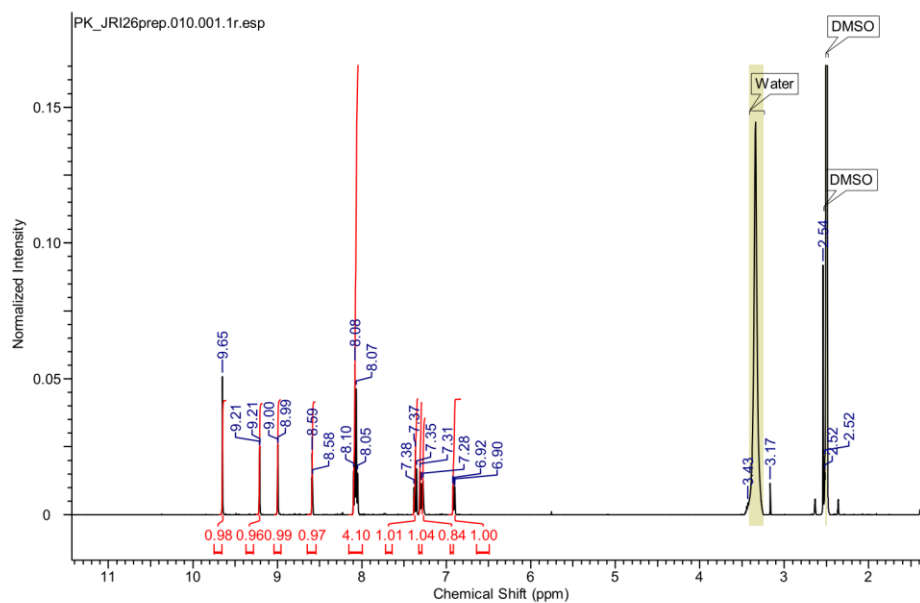


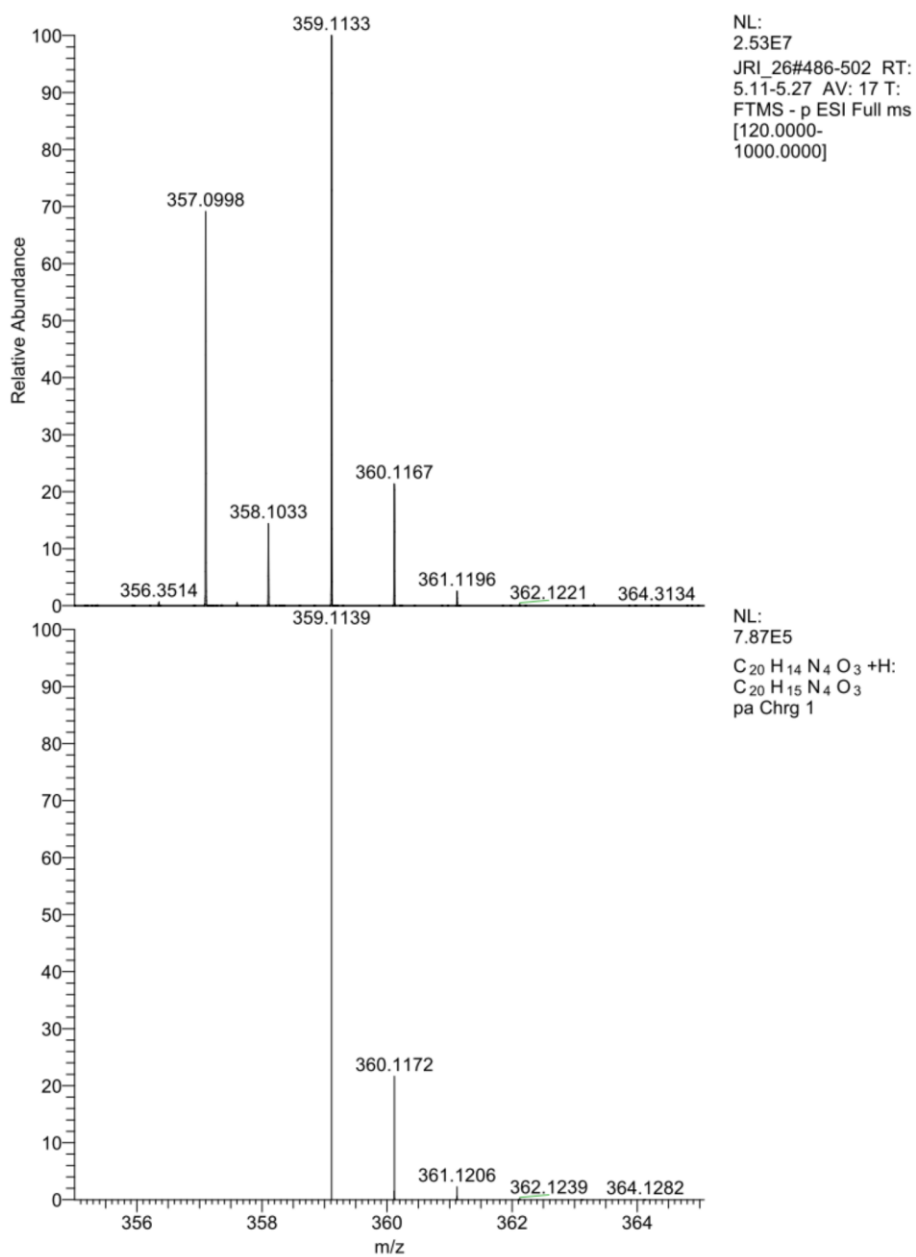
4-(1-(5-(4-methoxyphenyl)pyridin-3-yl)-1H-1,2,3-triazol-4-yl)benzoic acid (36d):

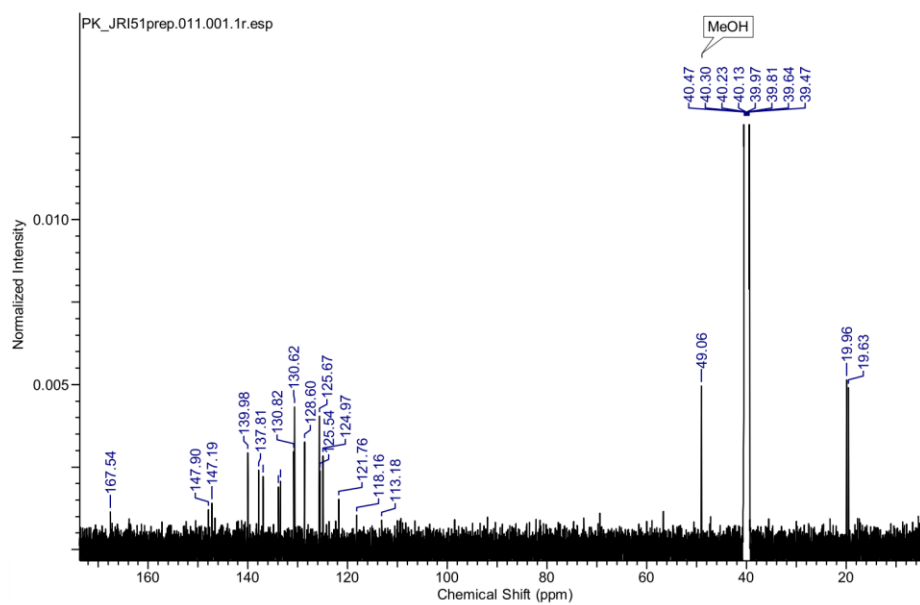
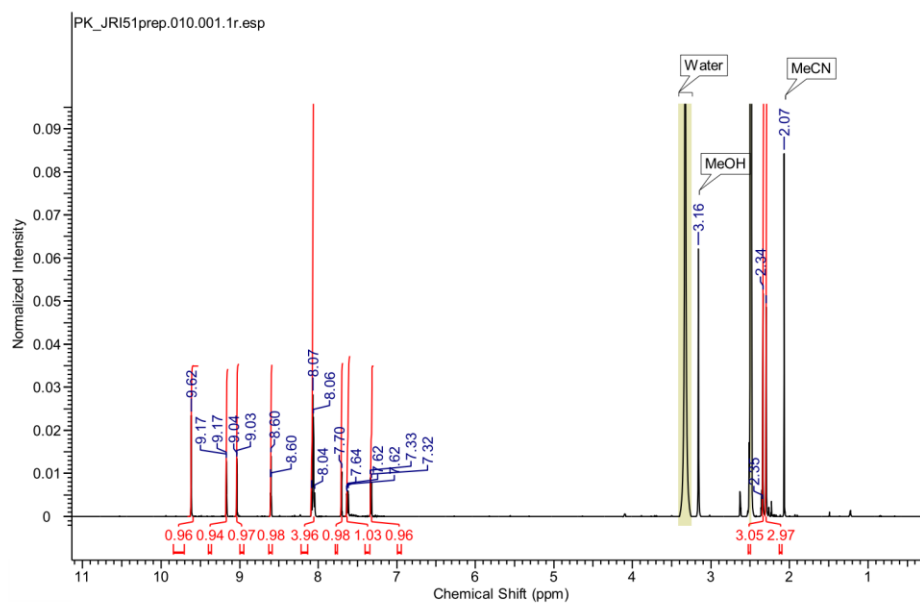


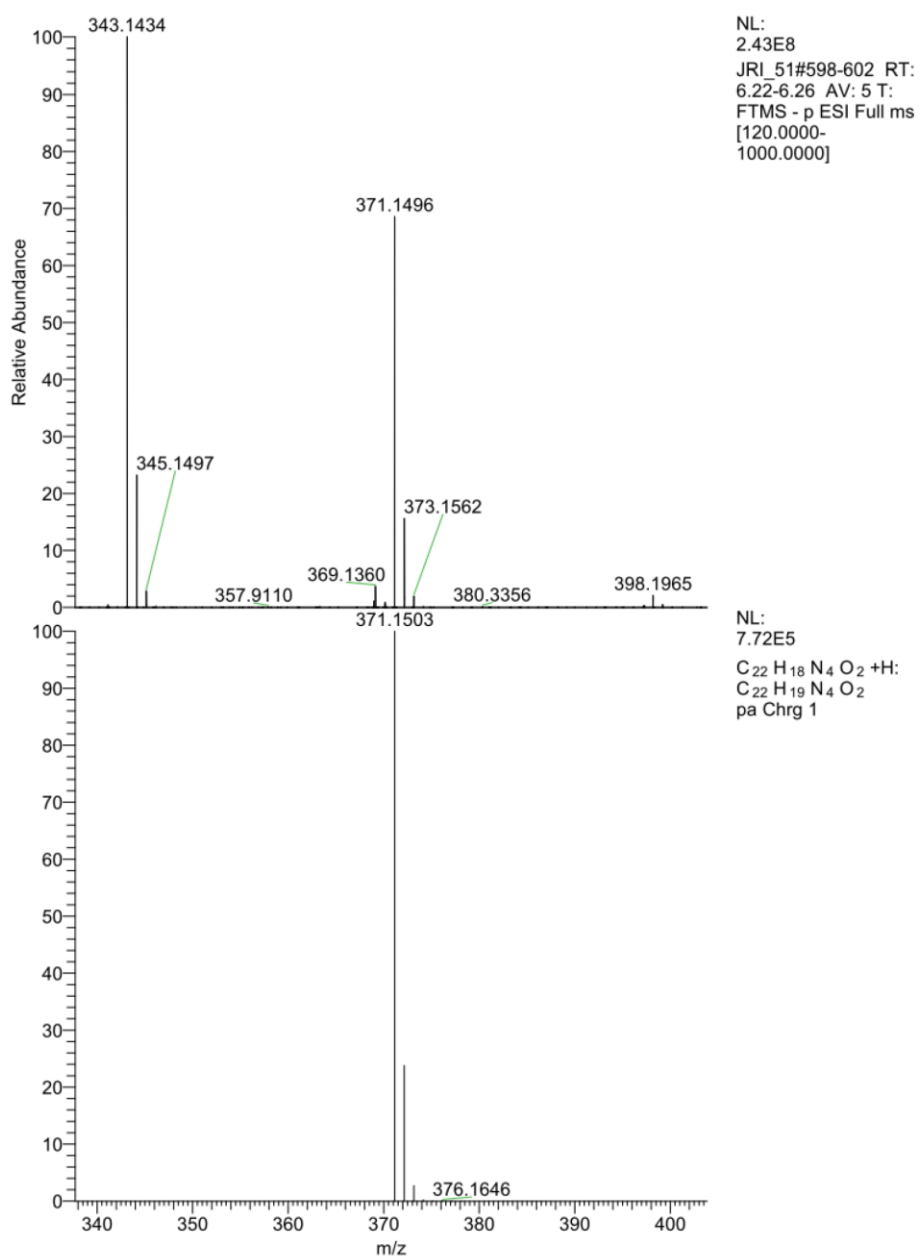


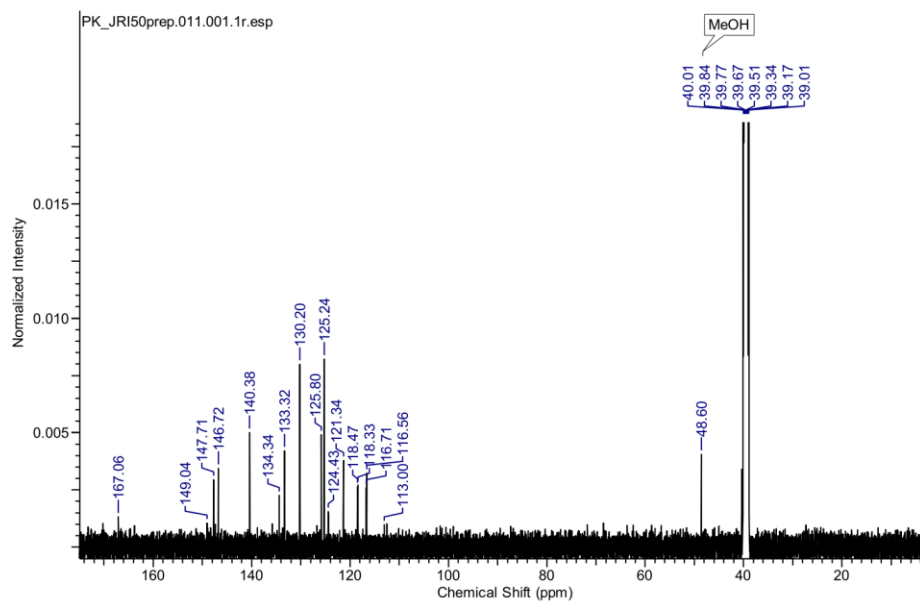
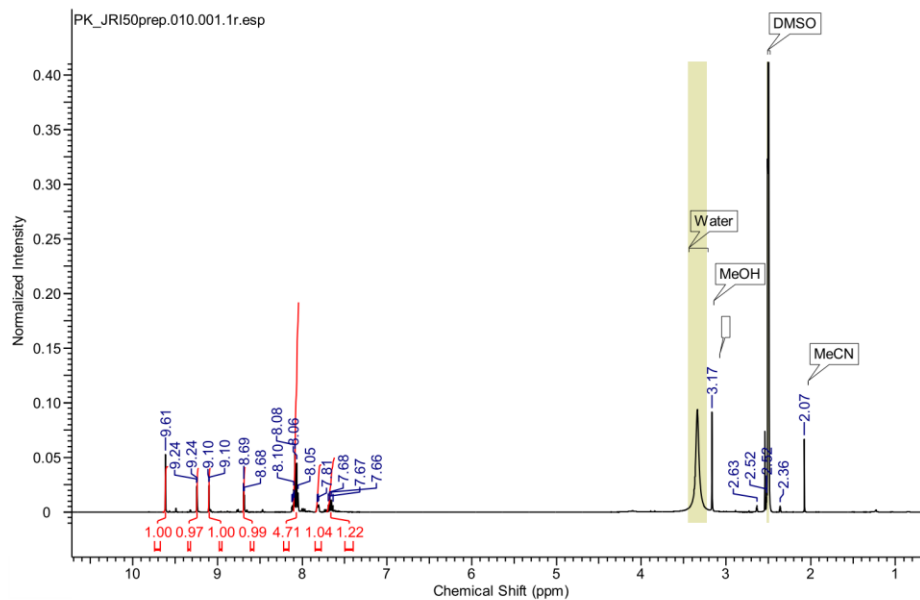
4-(1-(5-(3-hydroxyphenyl)pyridin-3-yl)-1H-1,2,3-triazol-4-yl)benzoic acid (36e):

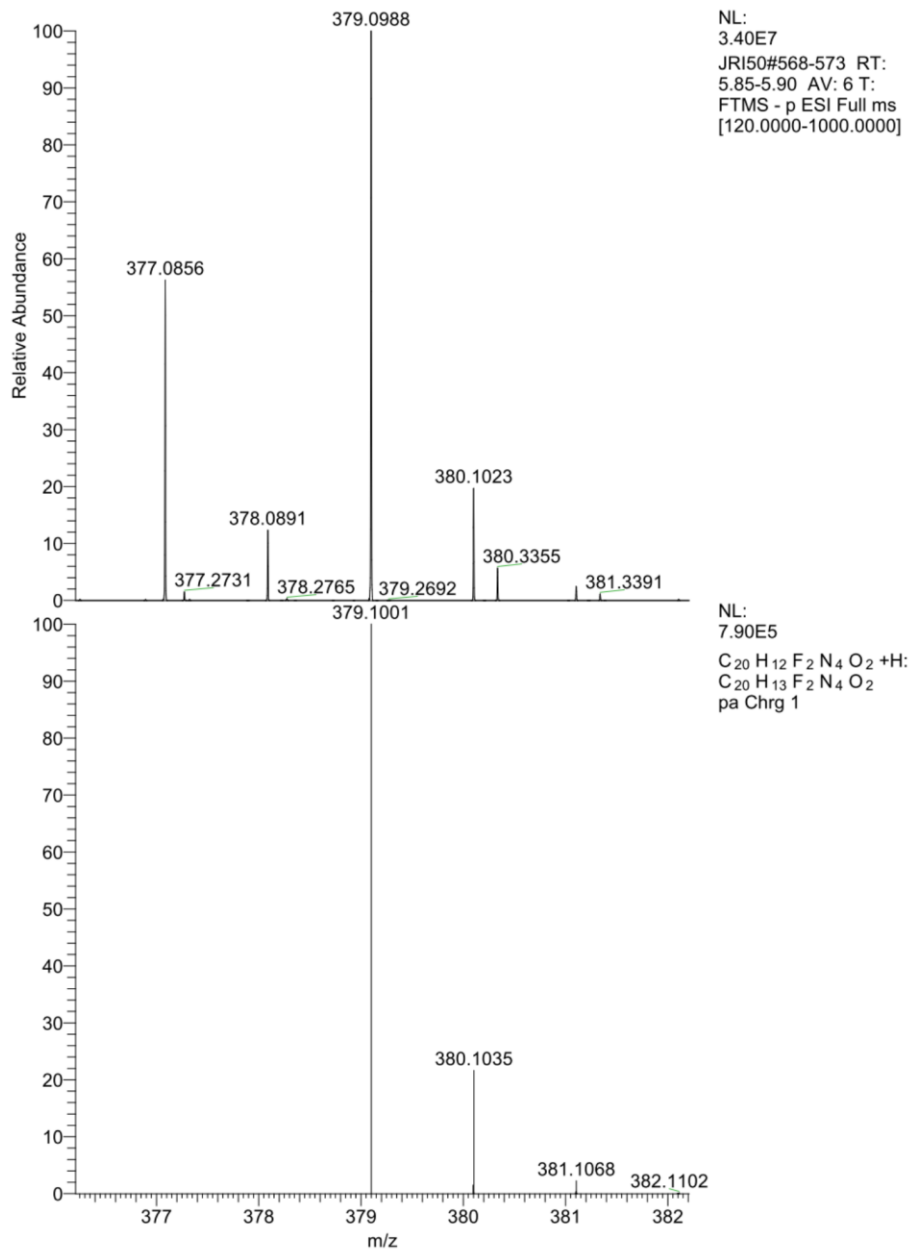


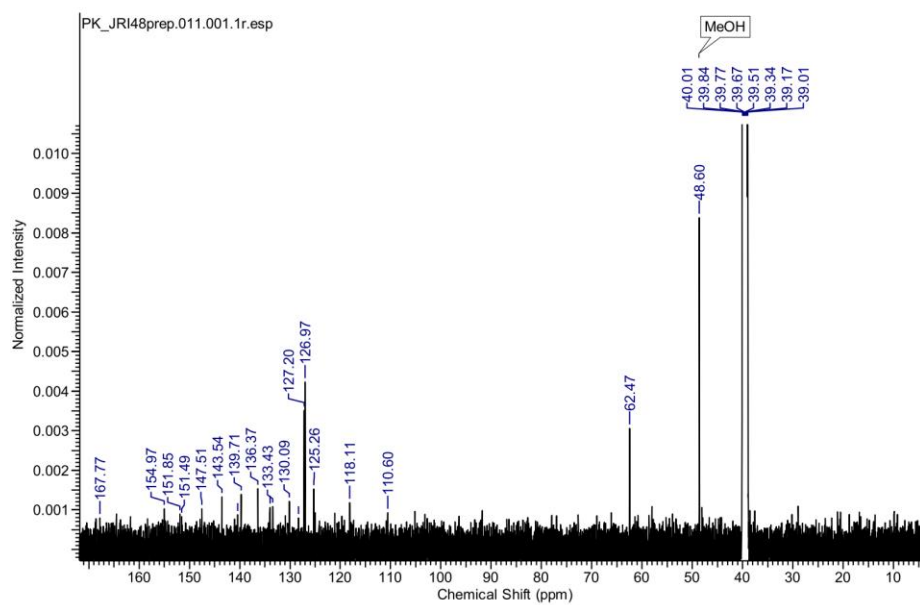
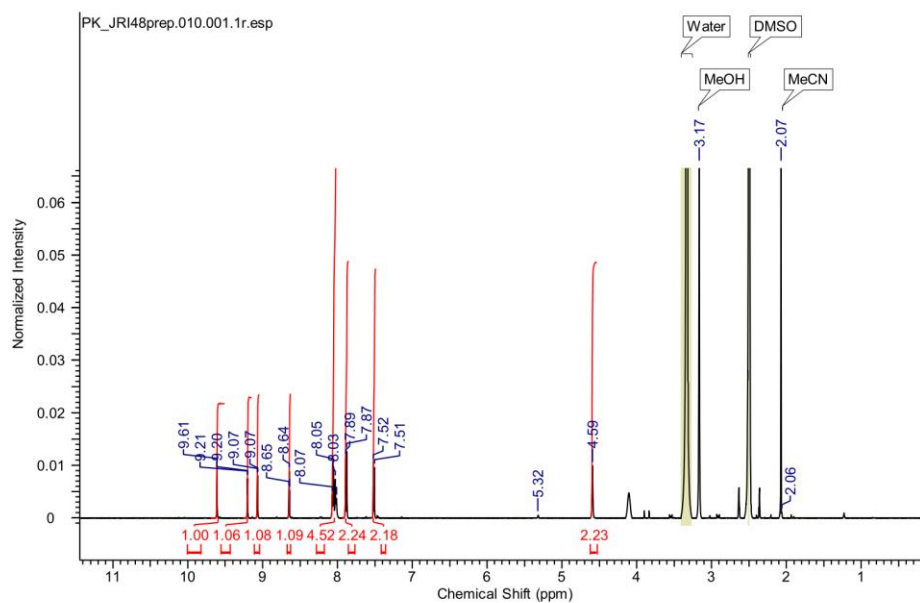


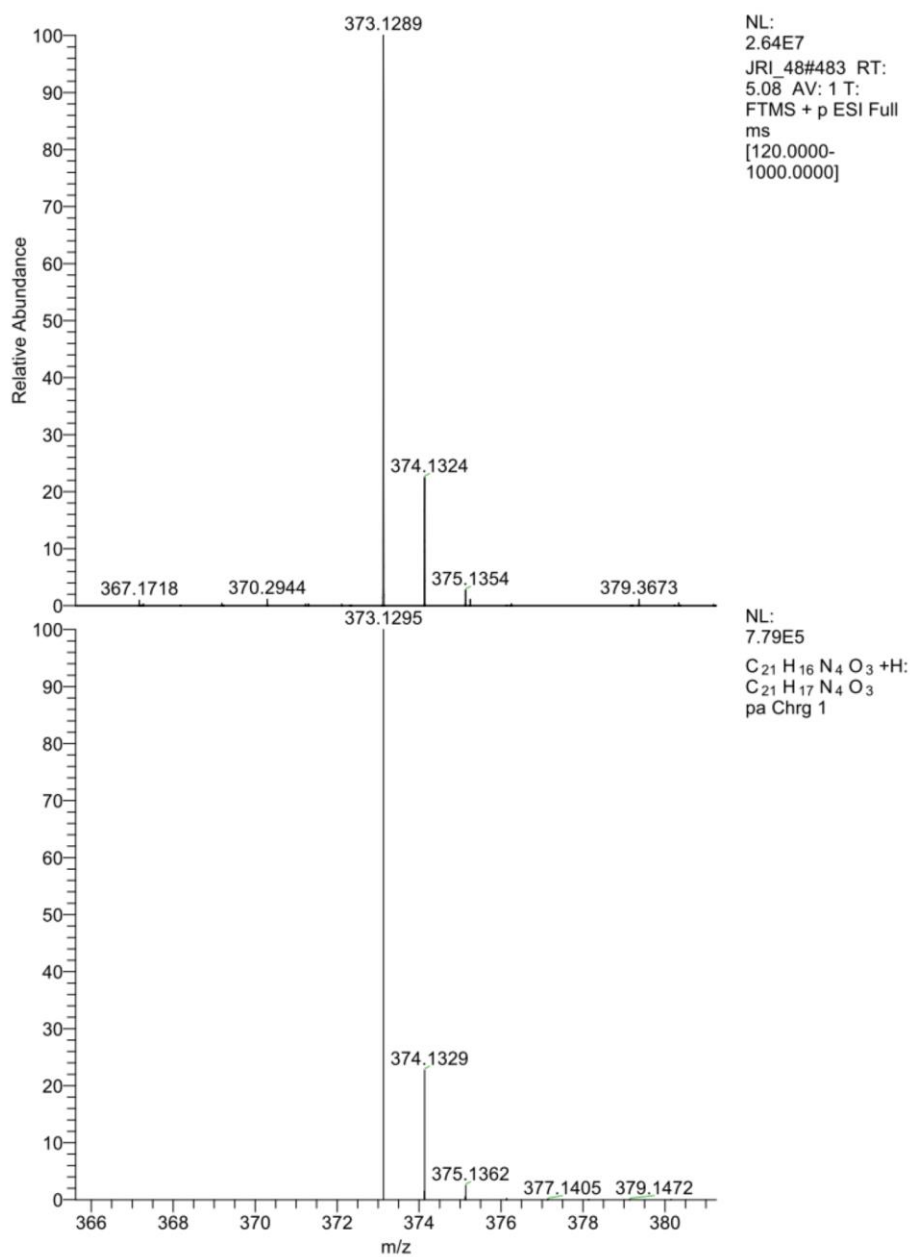
4-(1-(5-(3,4-dimethylphenyl)pyridin-3-yl)-1H-1,2,3-triazol-4-yl)benzoic acid (36f):



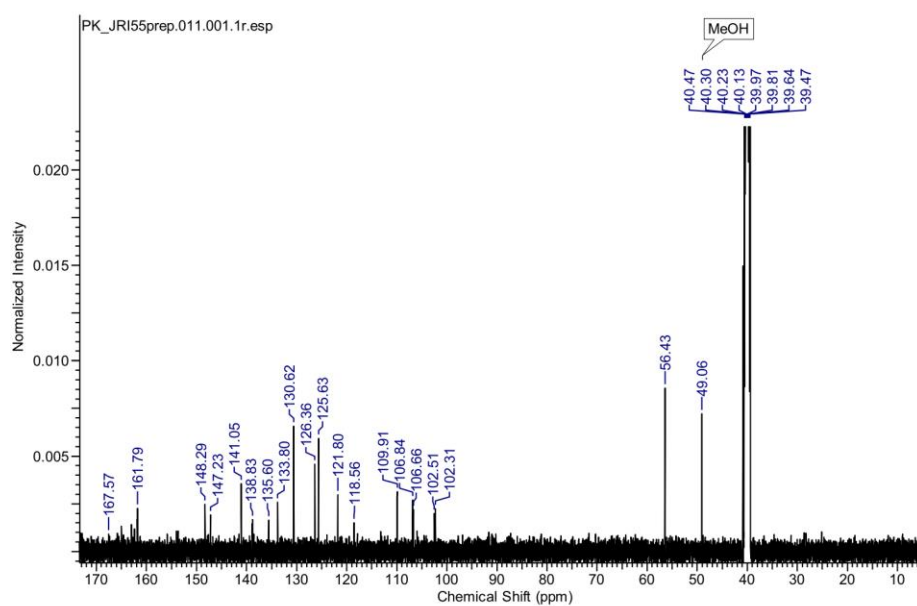
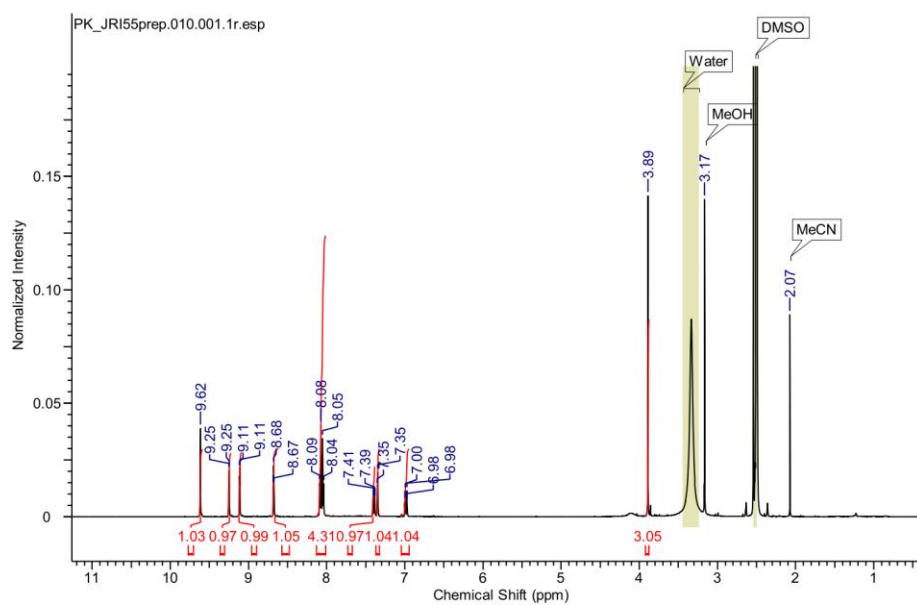
4-(1-(5-(3,4-difluorophenyl)pyridin-3-yl)-1H-1,2,3-triazol-4-yl)benzoic acid (36g):

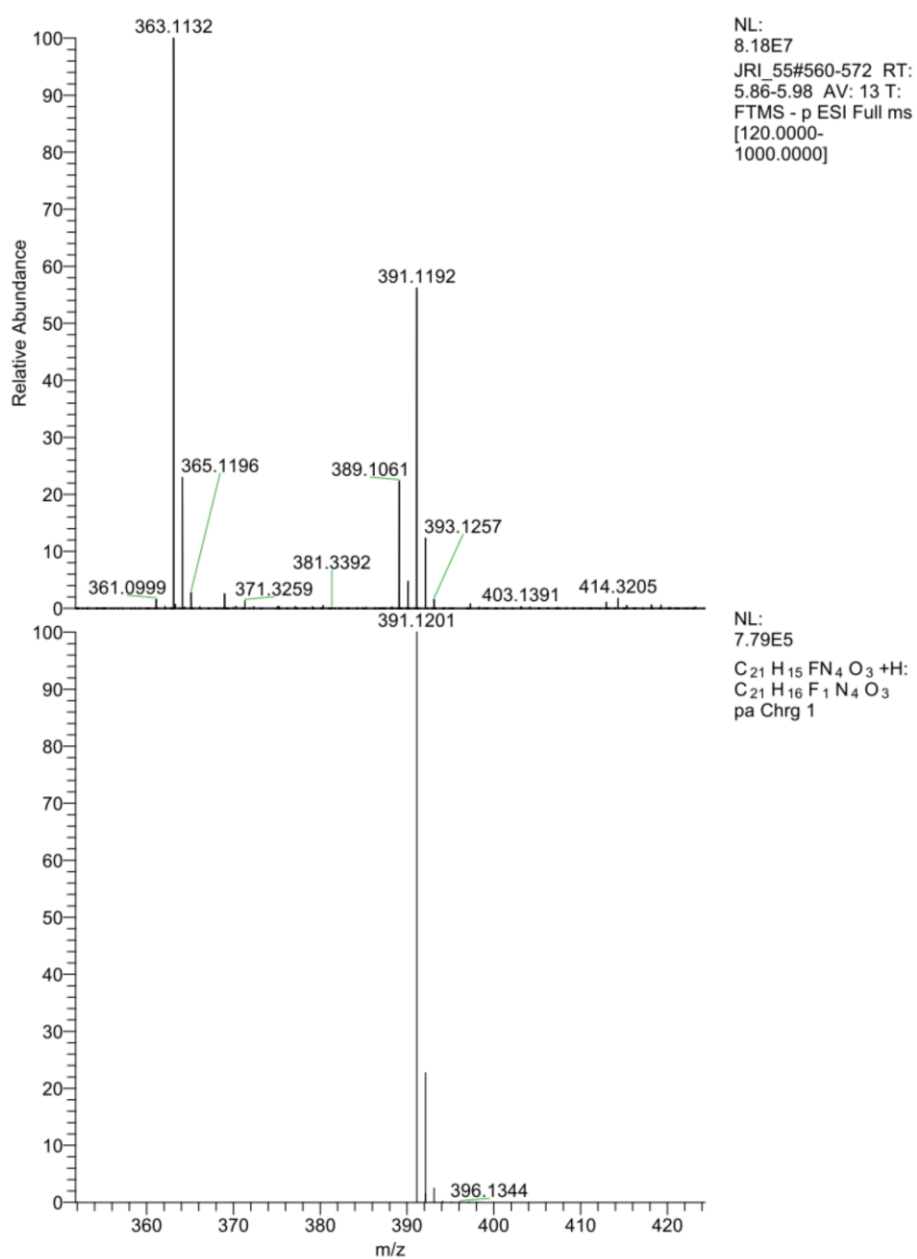


4-(1-(5-(4-(hydroxymethyl)phenyl)pyridin-3-yl)-1H-1,2,3-triazol-4-yl)benzoic acid (36h):

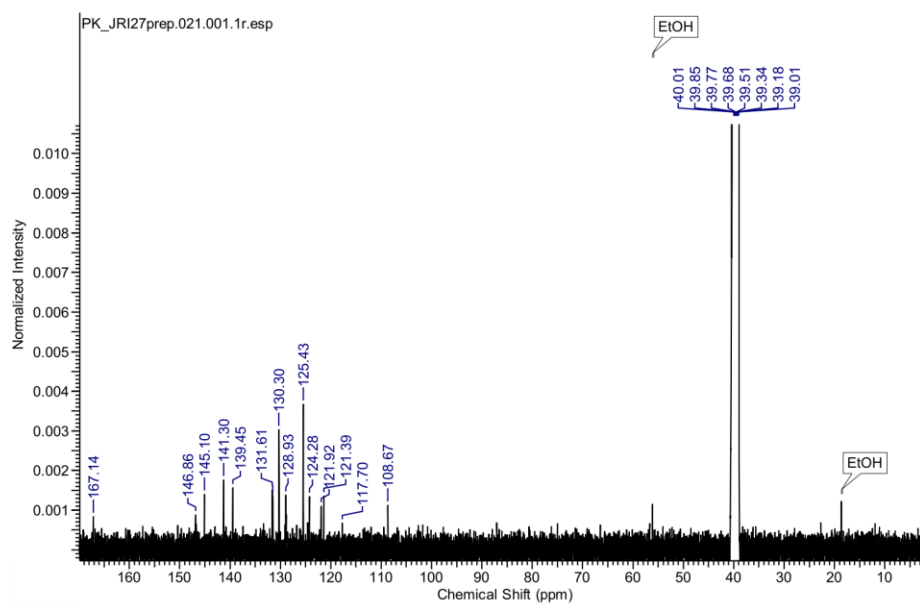
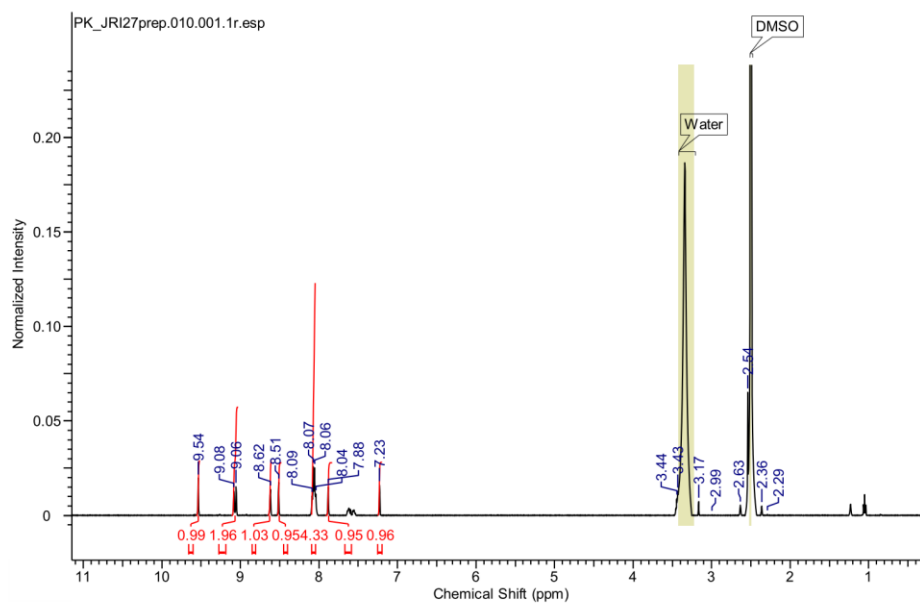


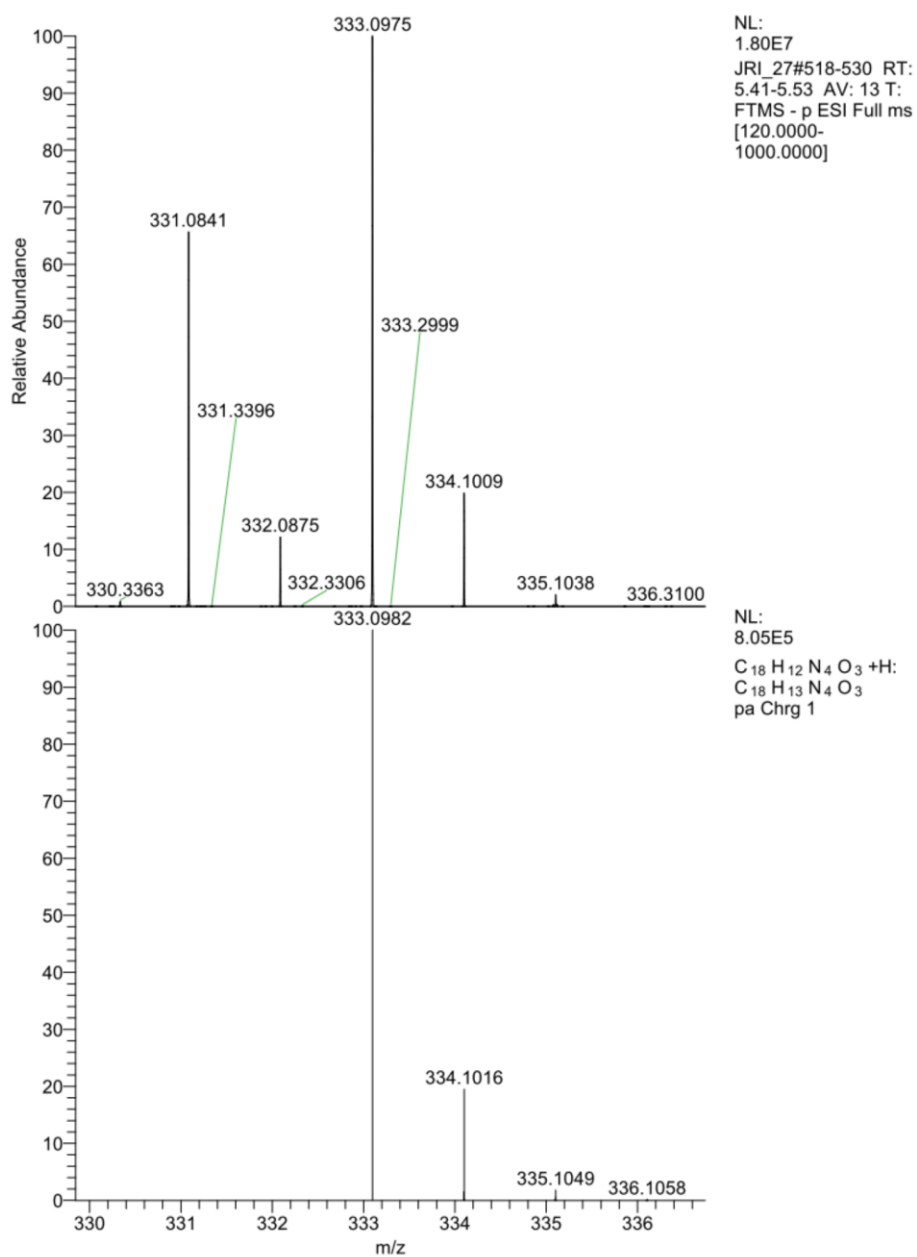
4-(1-(5-(3-fluoro-5-methoxyphenyl)pyridin-3-yl)-1H-1,2,3-triazol-4-yl)benzoic acid (36i):



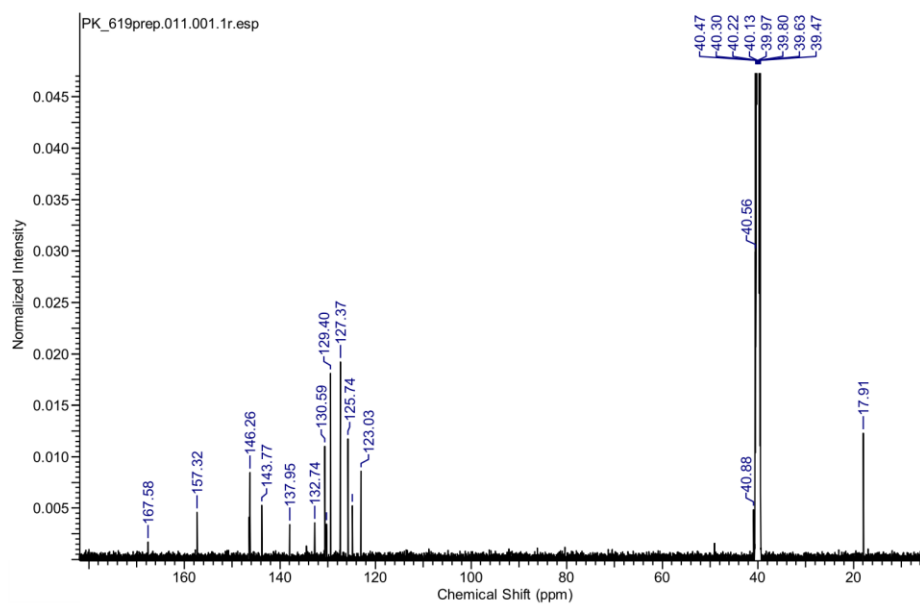
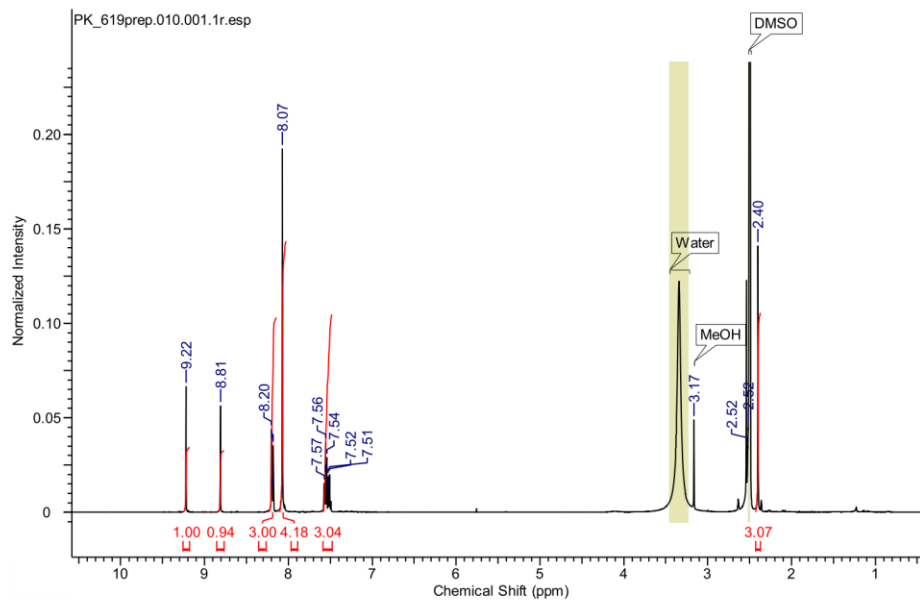


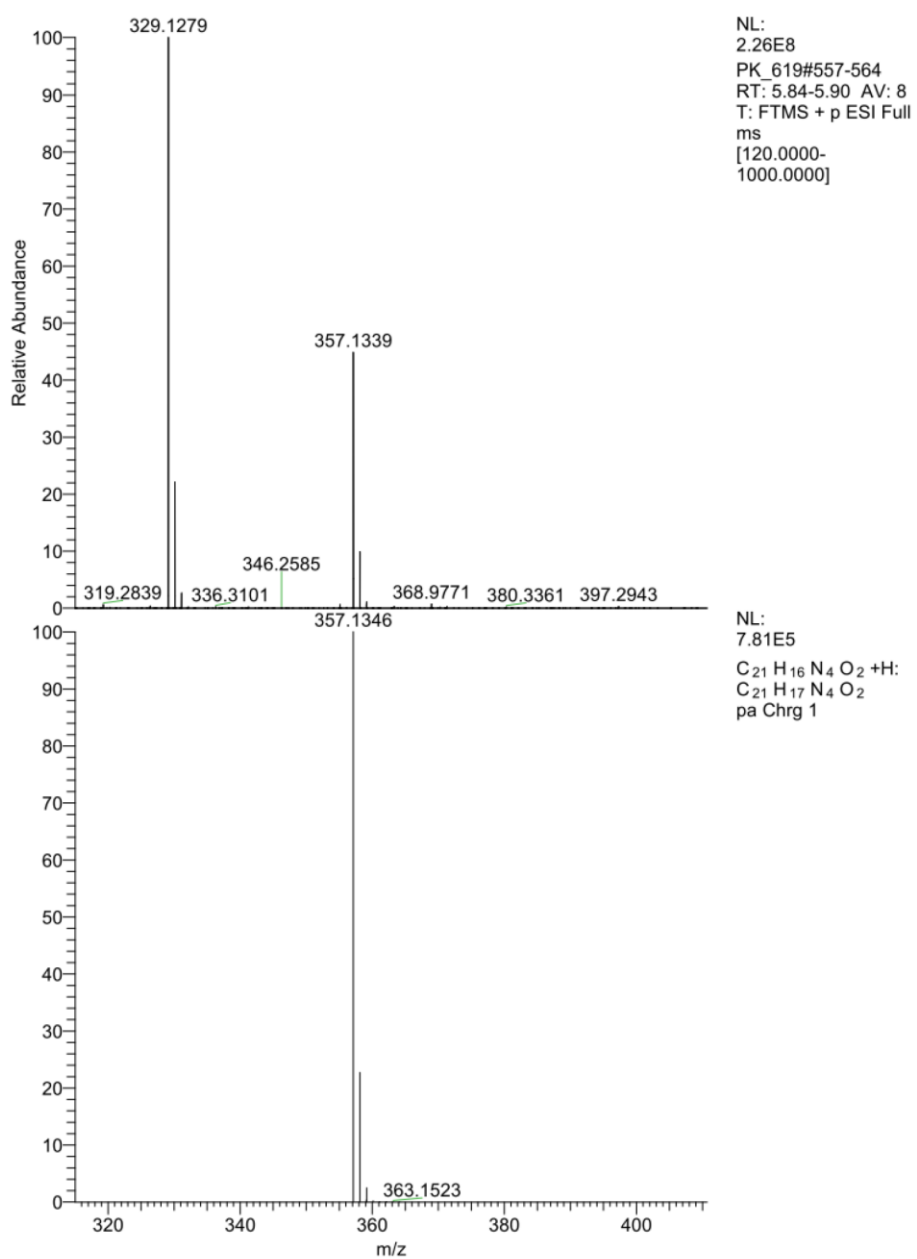
4-(1-(5-(furan-3-yl)pyridin-3-yl)-1H-1,2,3-triazol-4-yl)benzoic acid (36j):

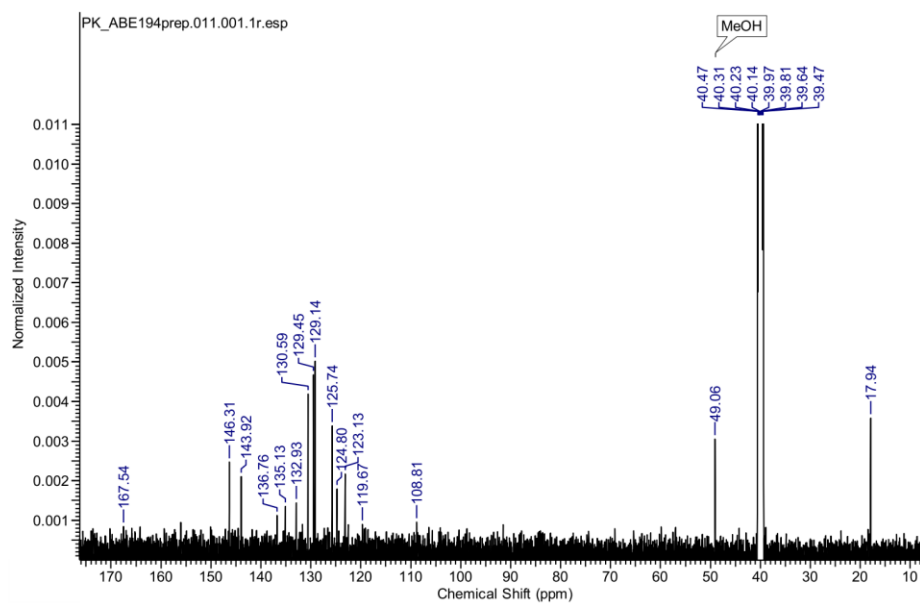
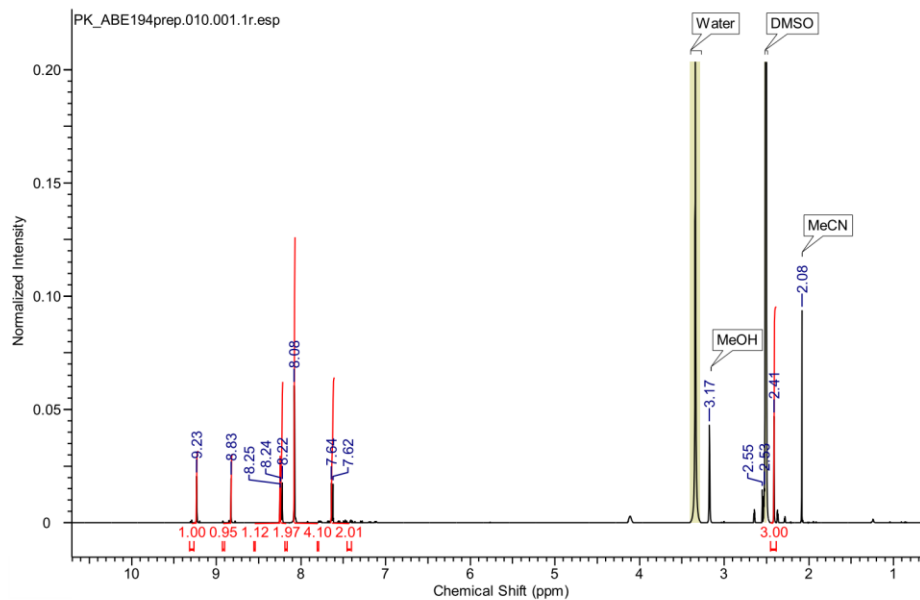


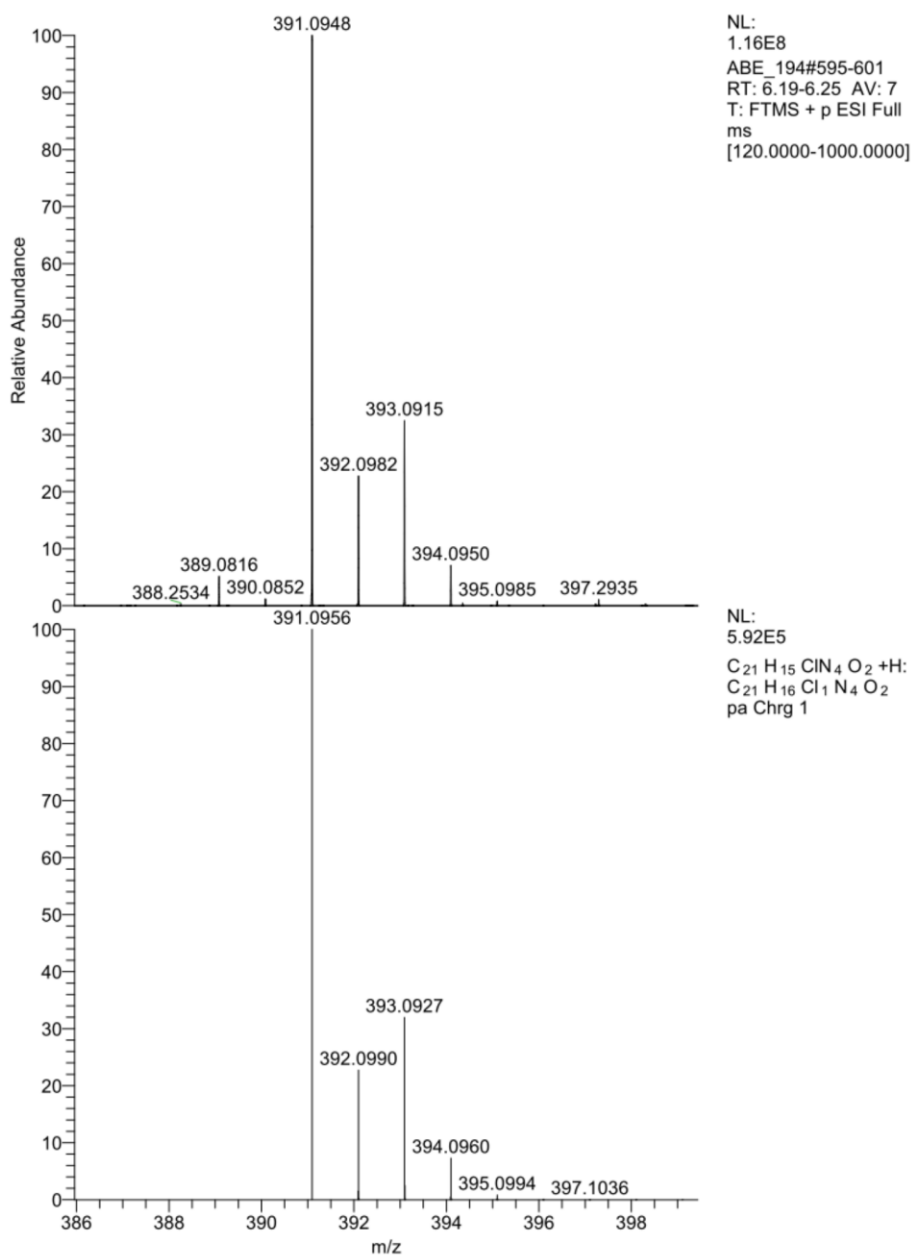


4-(1-(4-methyl-6-phenylpyridin-3-yl)-1H-1,2,3-triazol-4-yl)benzoic acid (36k):

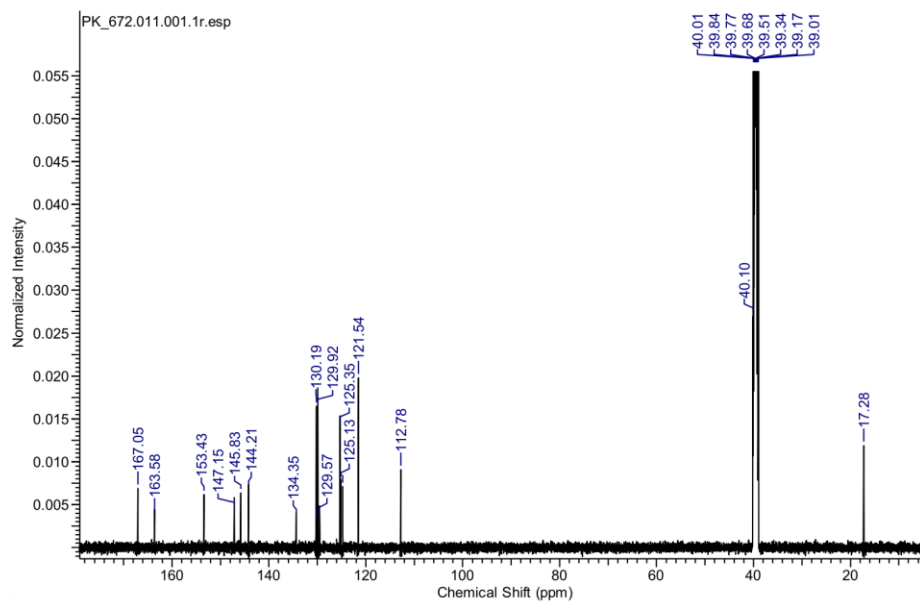
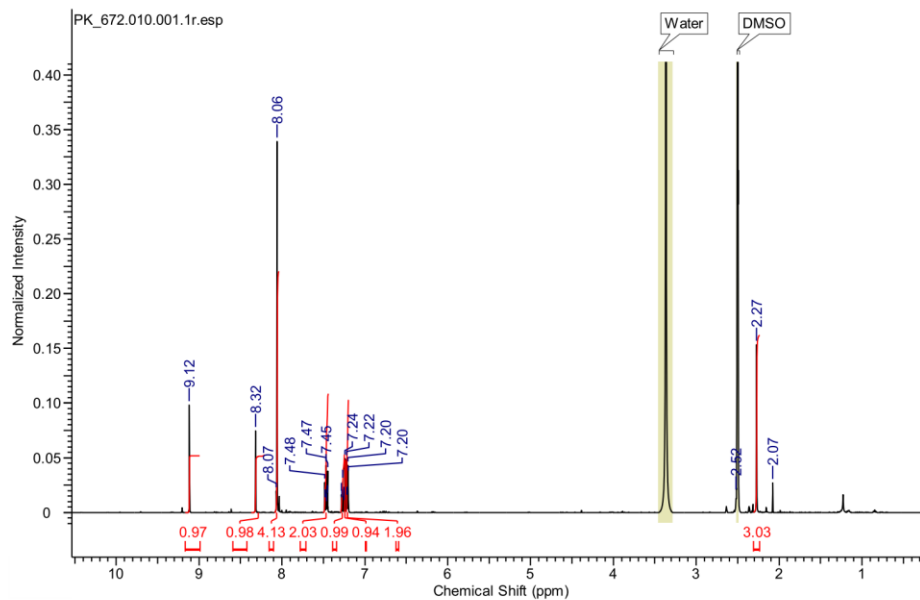


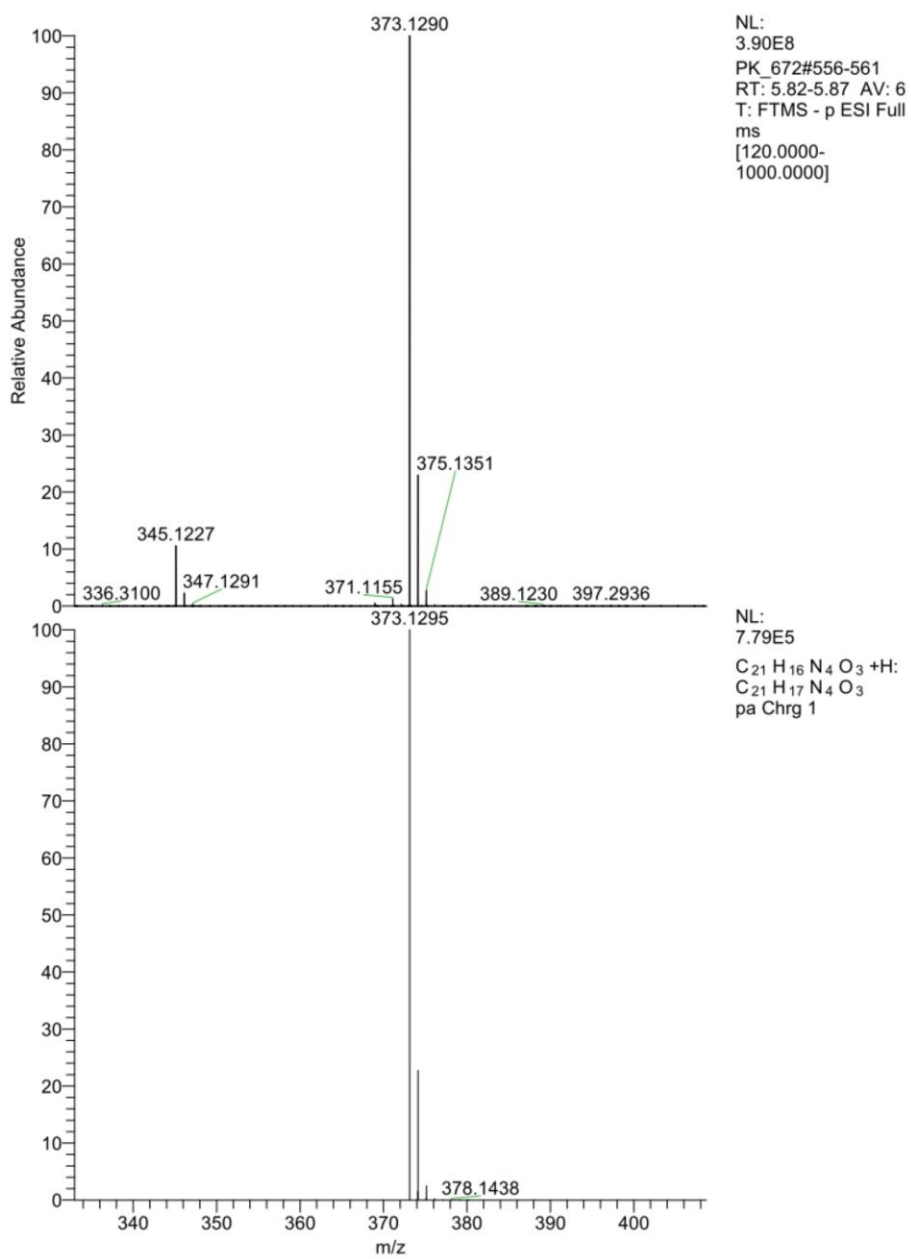


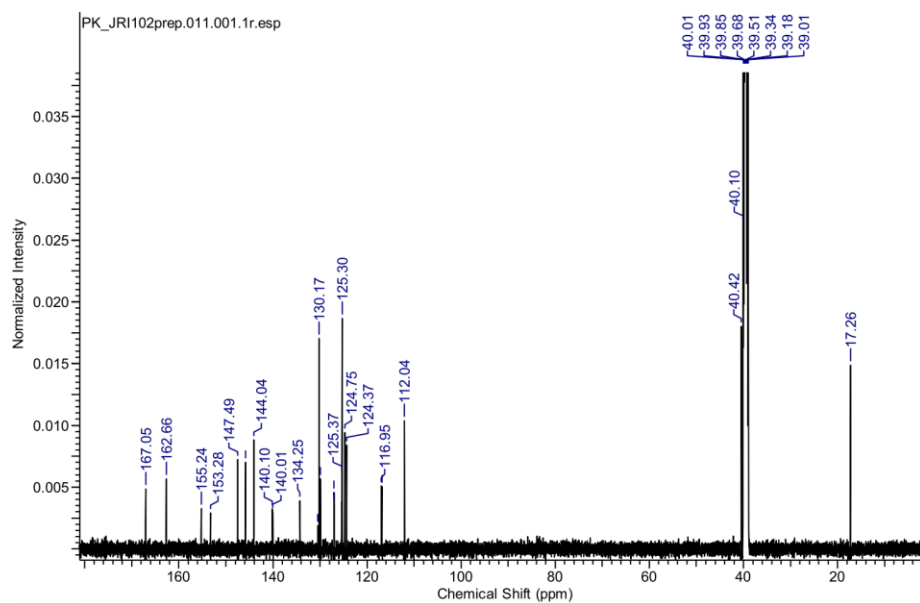
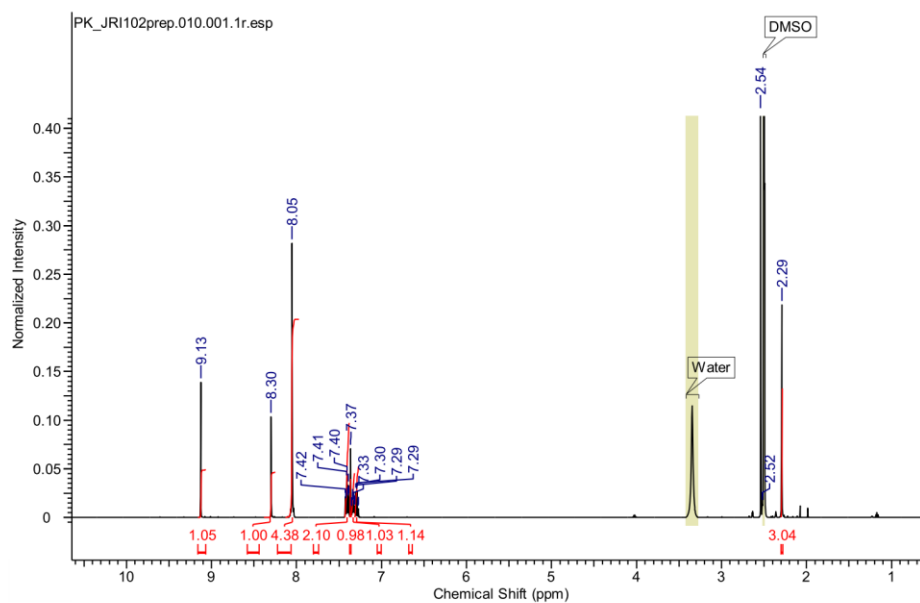
4-(1-(6-(4-chlorophenyl)-4-methylpyridin-3-yl)-1H-1,2,3-triazol-4-yl)benzoic acid (36L):

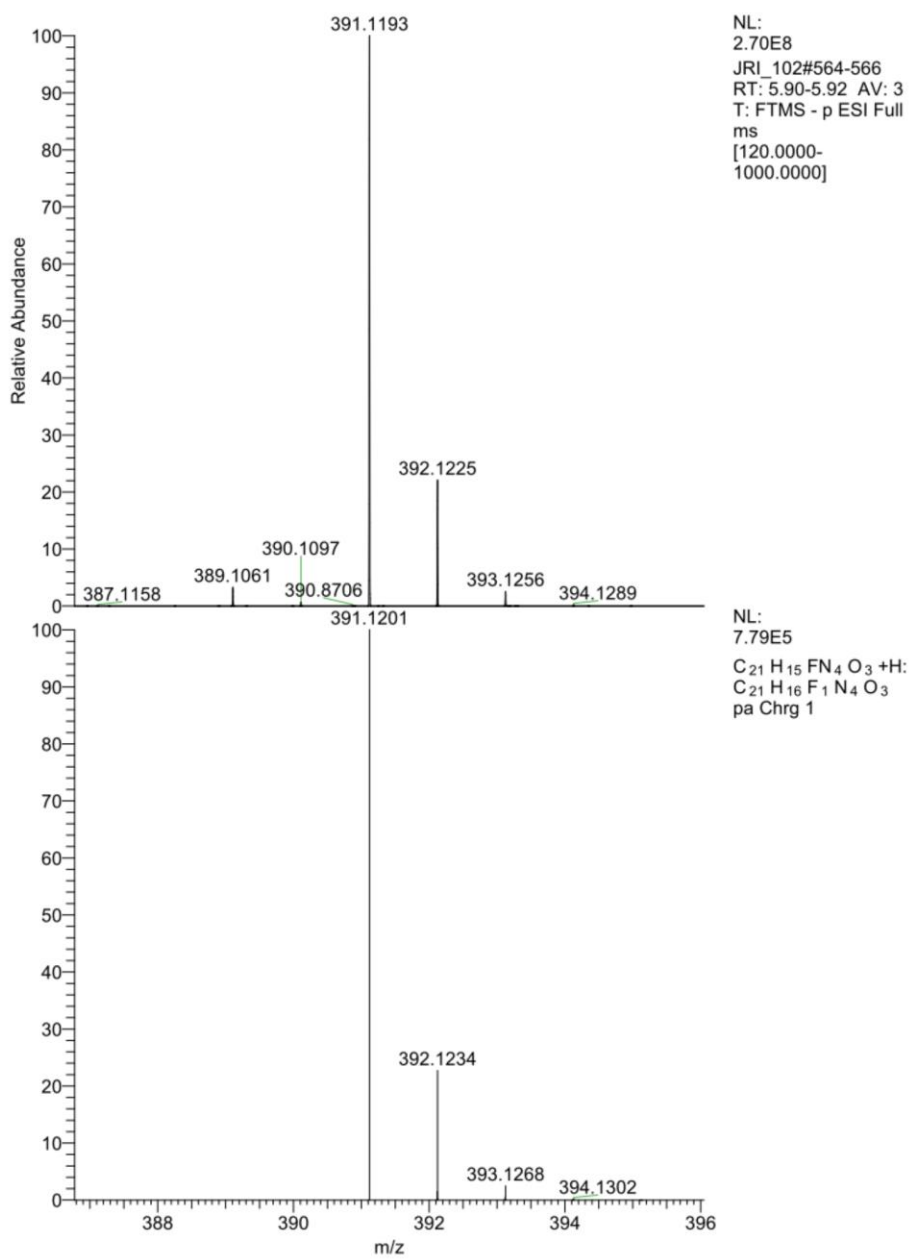


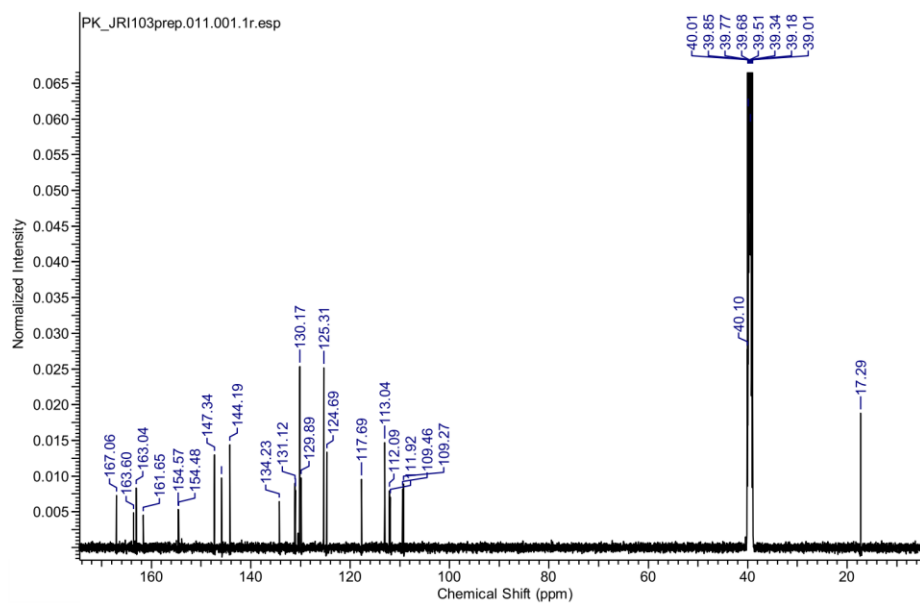
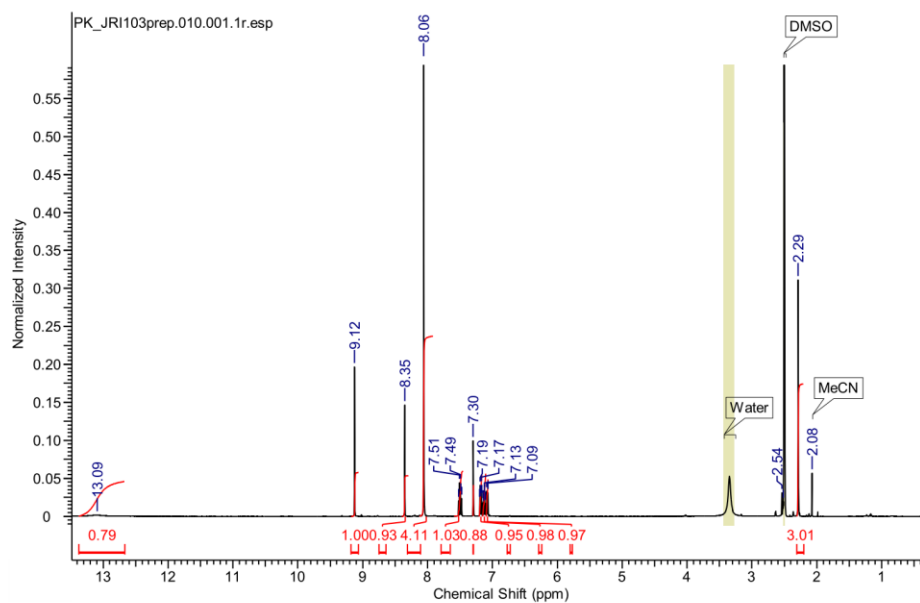
4-(1-(4-methyl-6-phenoxy-pyridin-3-yl)-1H-1,2,3-triazol-4-yl)benzoic acid (40a):

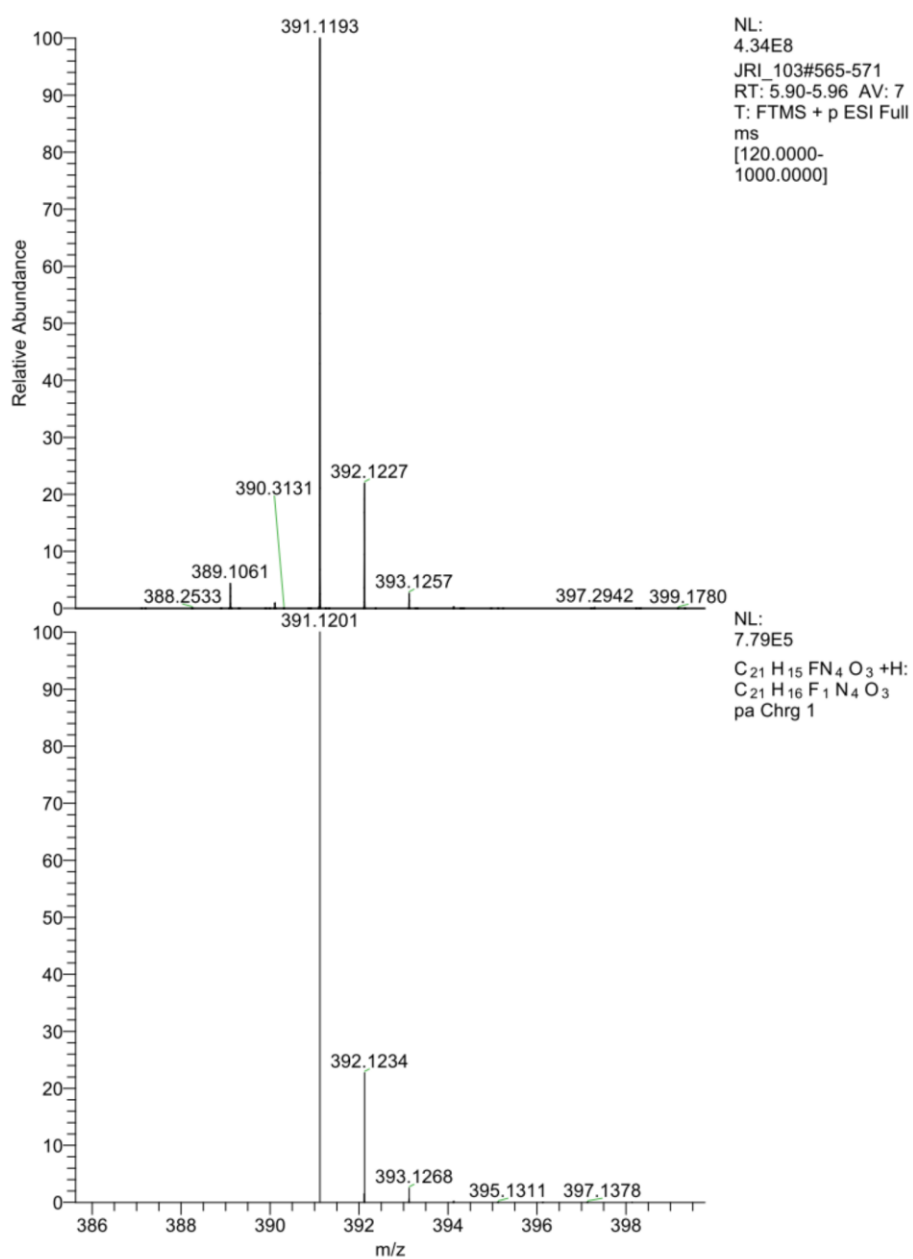


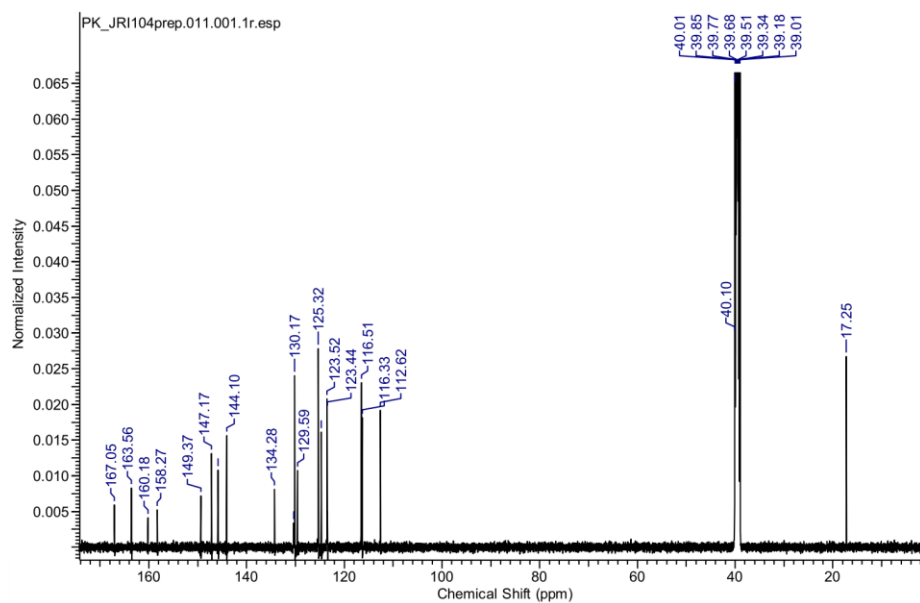
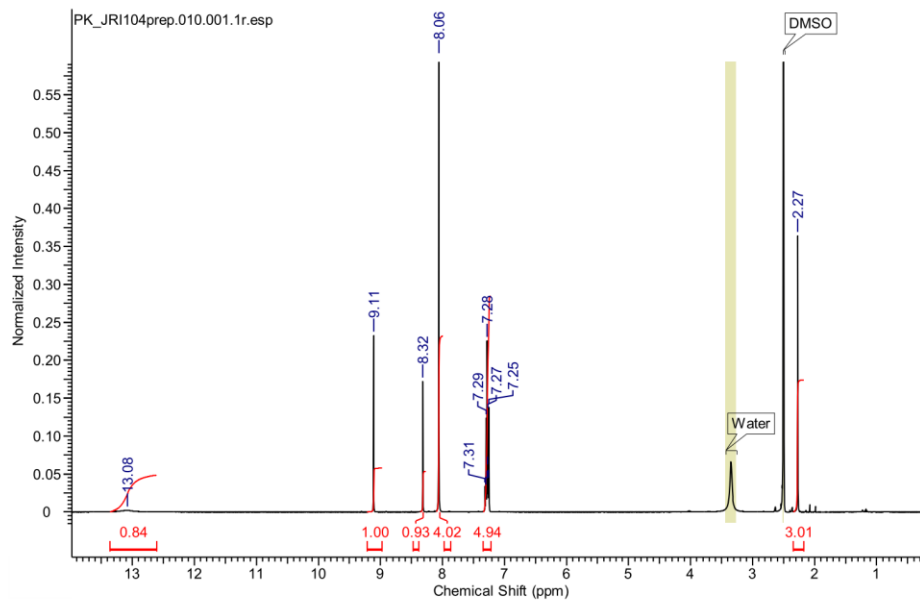


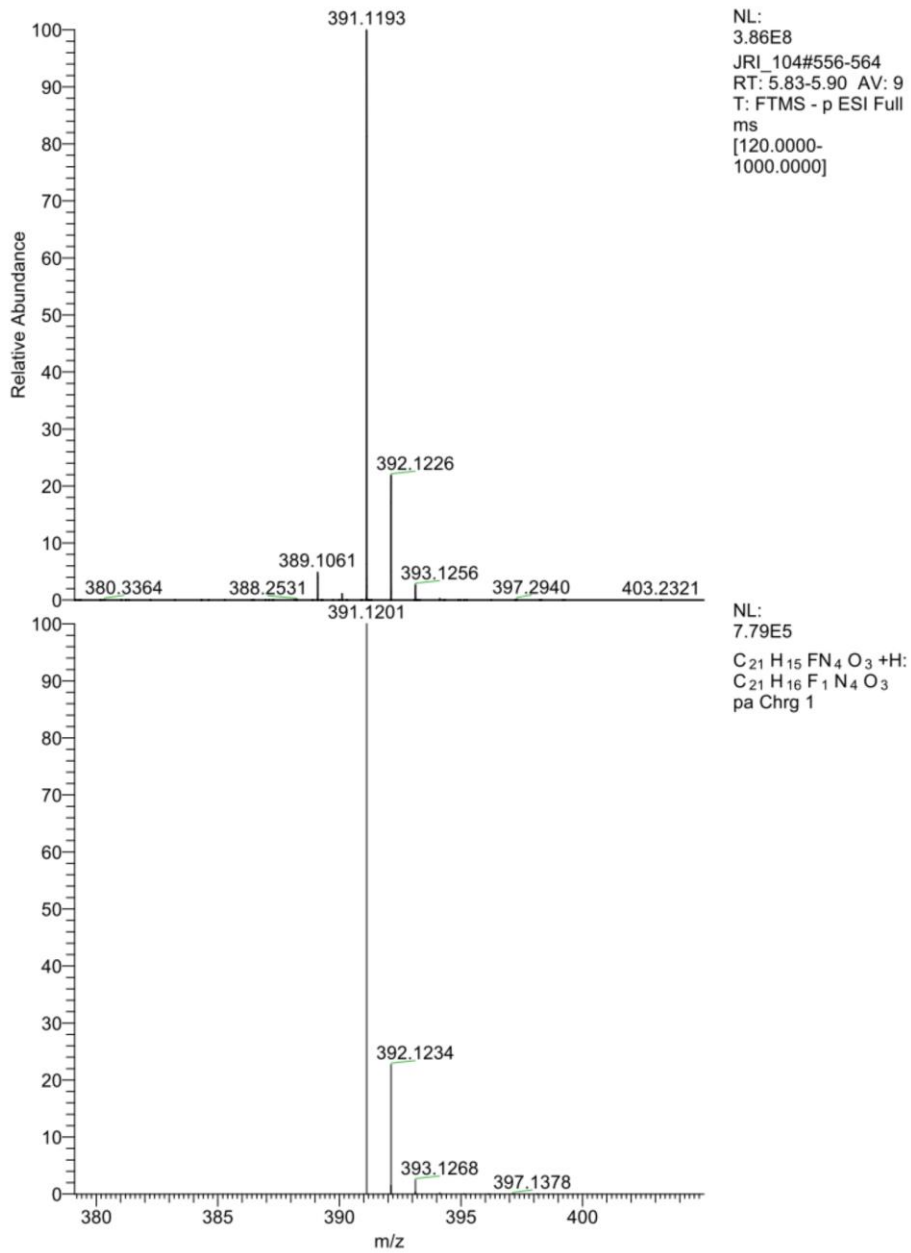
4-(1-(6-(2-fluorophenoxy)-4-methylpyridin-3-yl)-1H-1,2,3-triazol-4-yl)benzoic acid (40b):



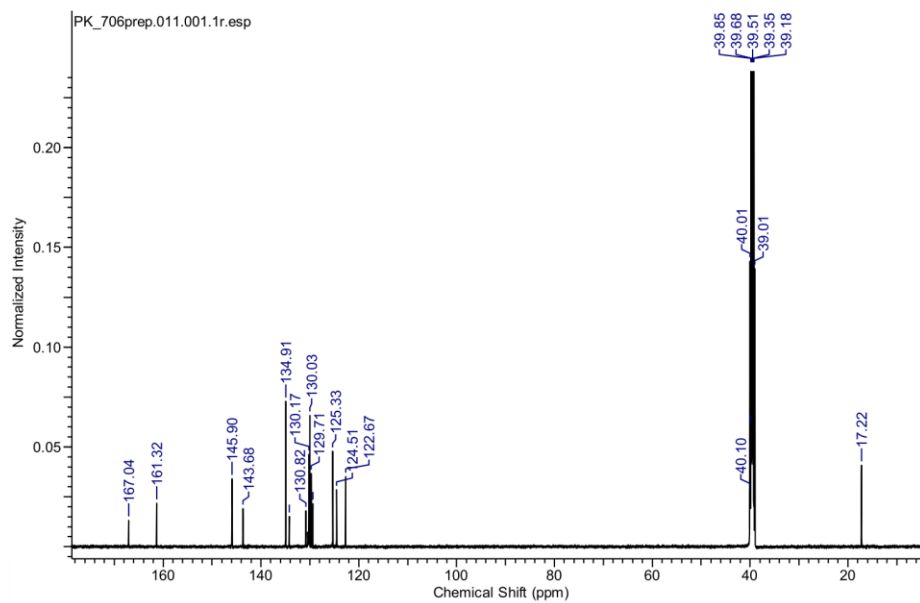
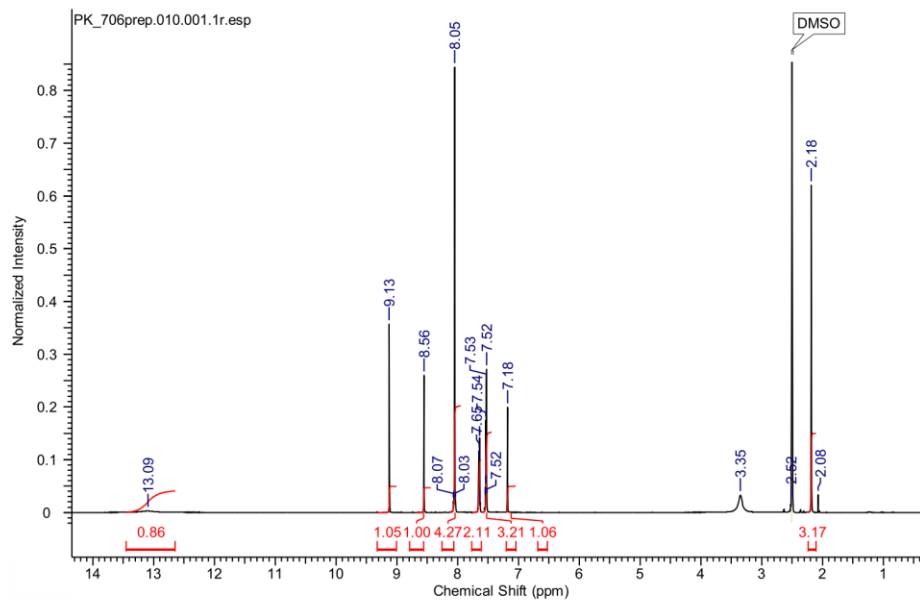
4-(1-(6-(3-fluorophenoxy)-4-methylpyridin-3-yl)-1H-1,2,3-triazol-4-yl)benzoic acid (40c):

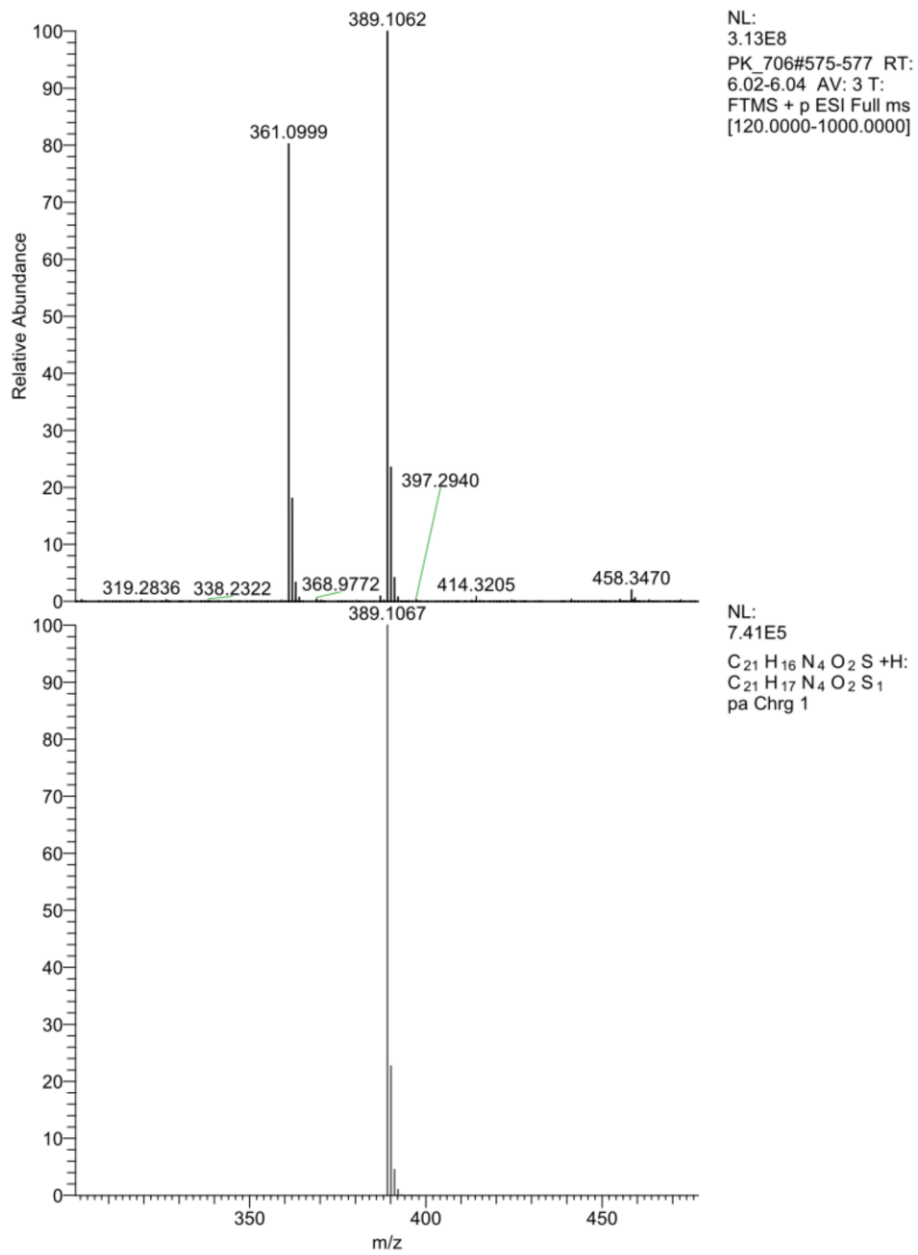


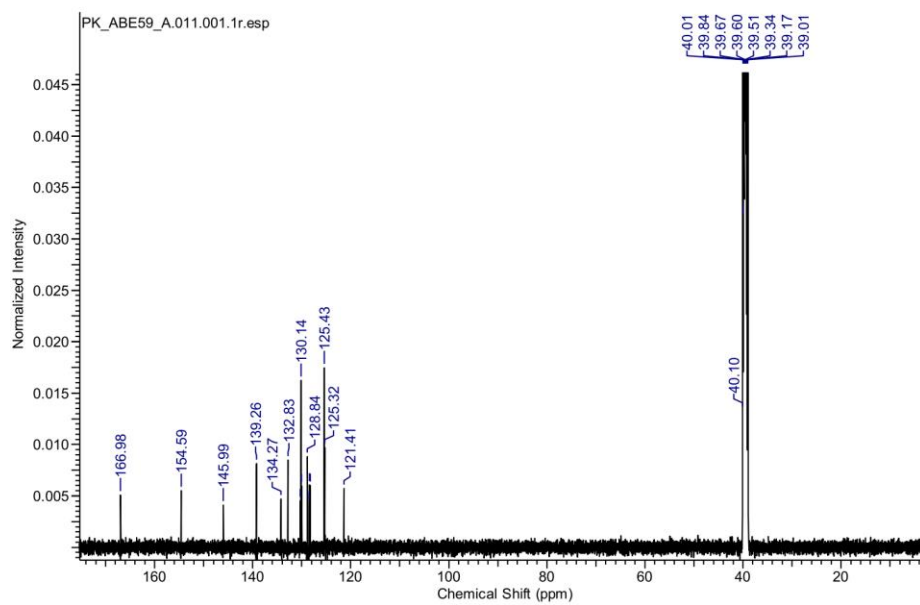
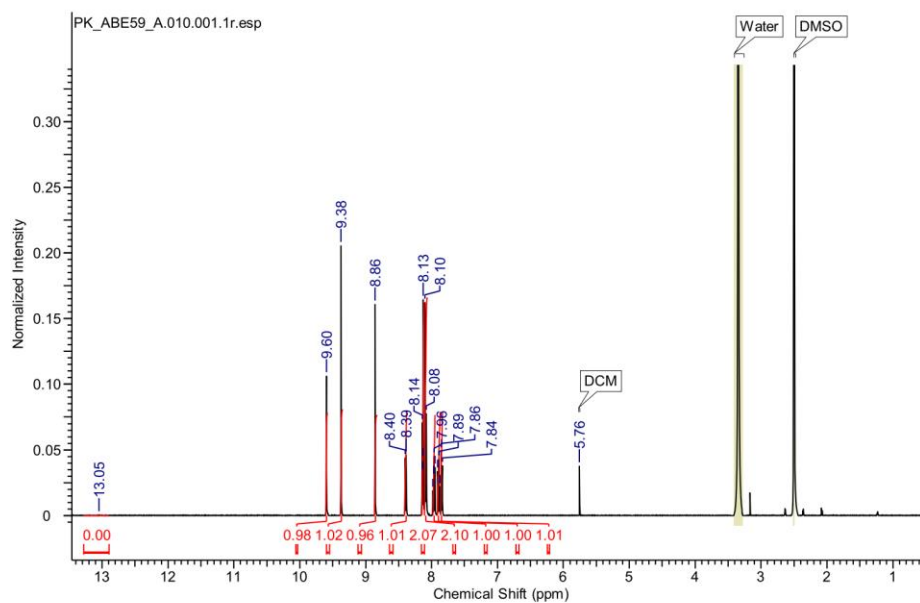
4-(1-(6-(4-fluorophenoxy)-4-methylpyridin-3-yl)-1H-1,2,3-triazol-4-yl)benzoic acid (40d):

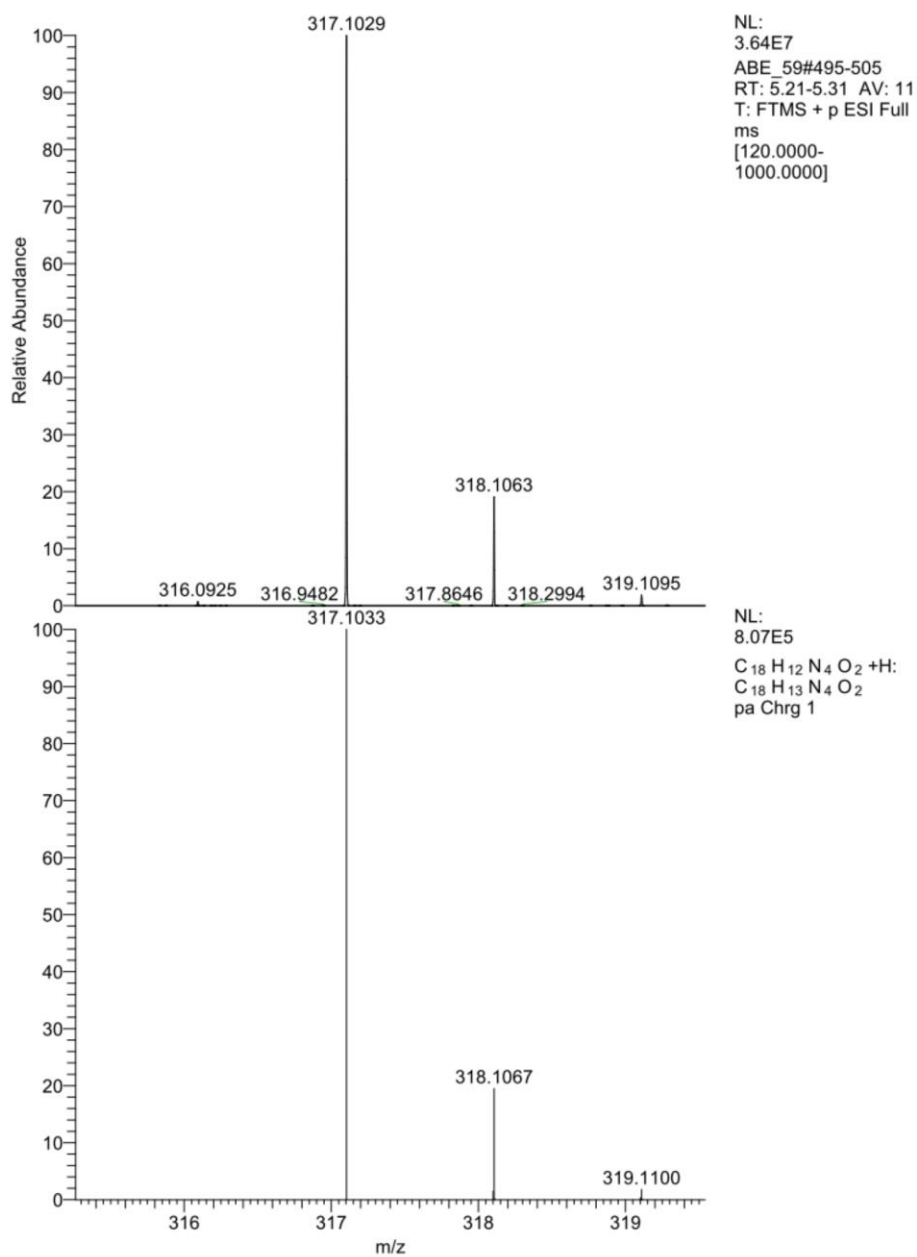


4-(1-(4-methyl-6-(phenylthio)pyridin-3-yl)-1H-1,2,3-triazol-4-yl)benzoic acid (40e):

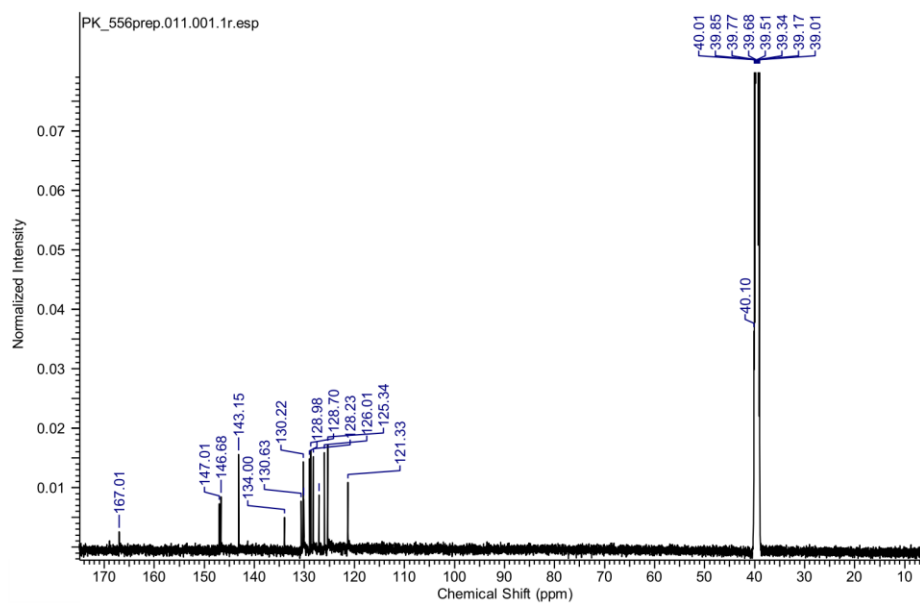
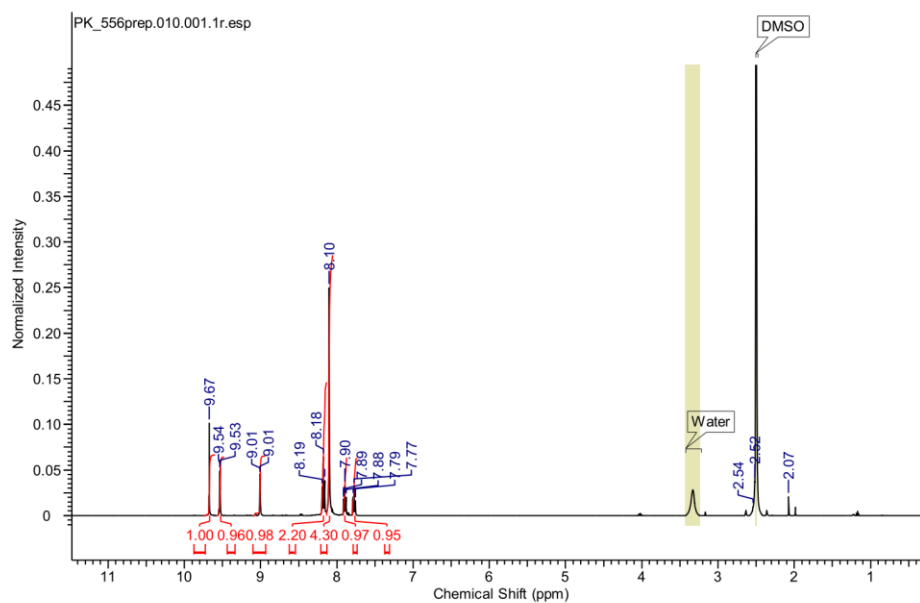


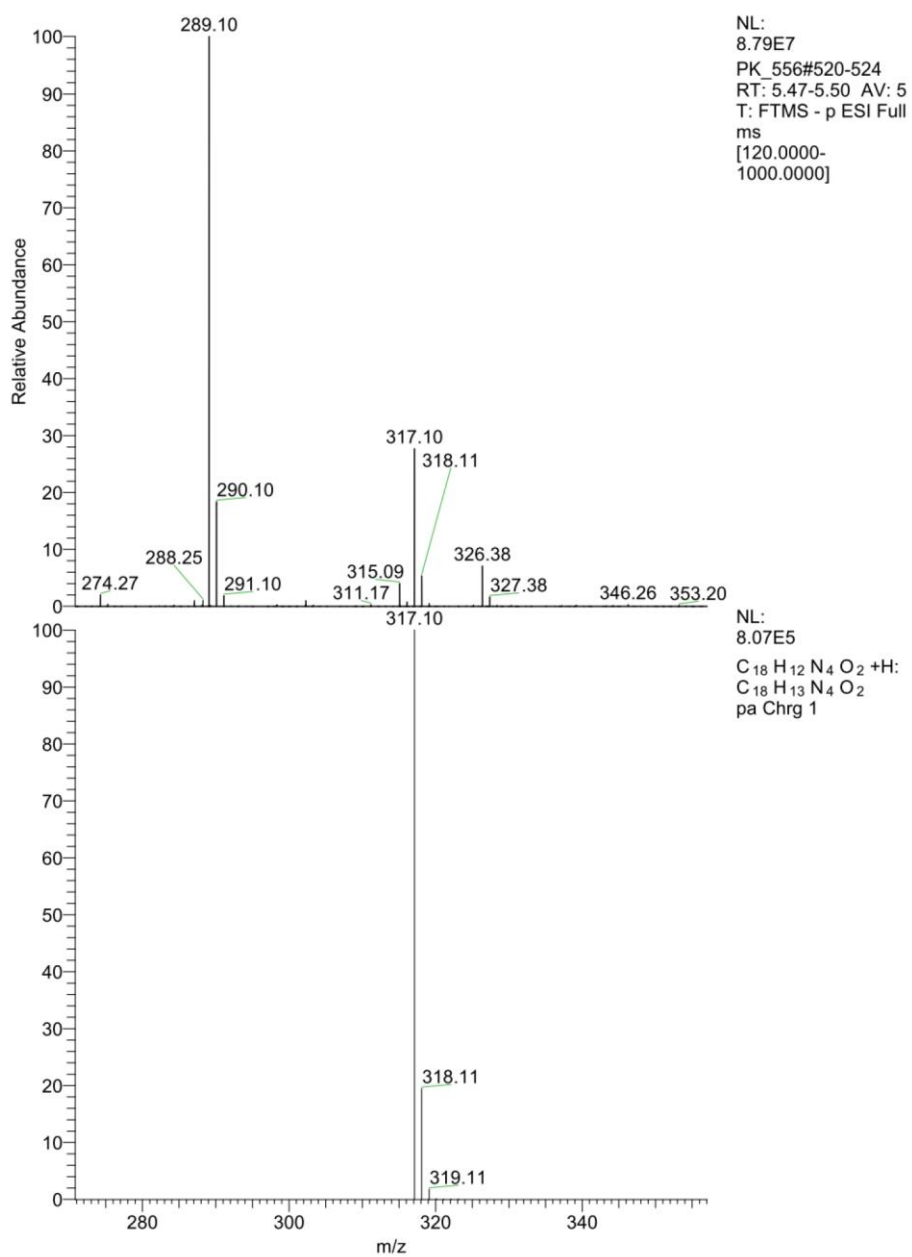


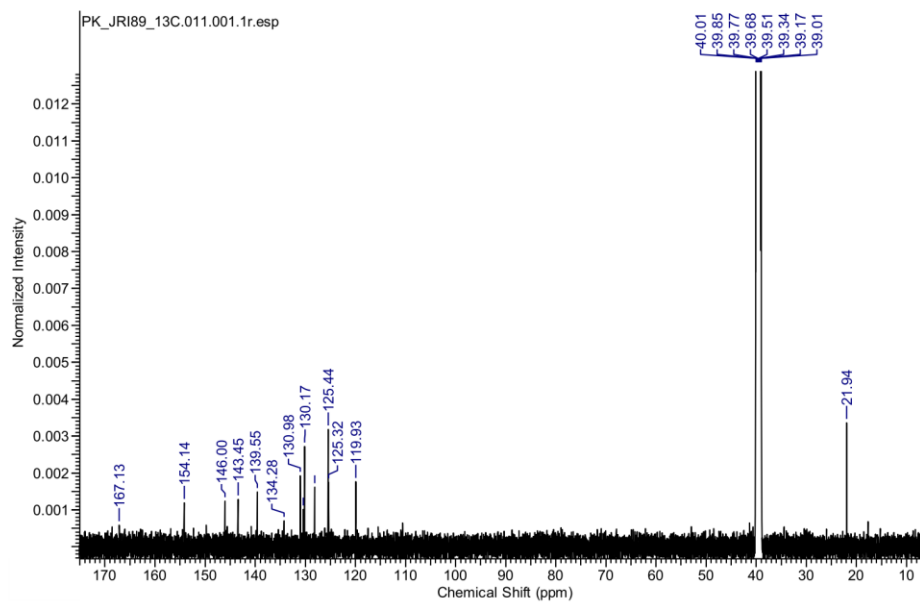
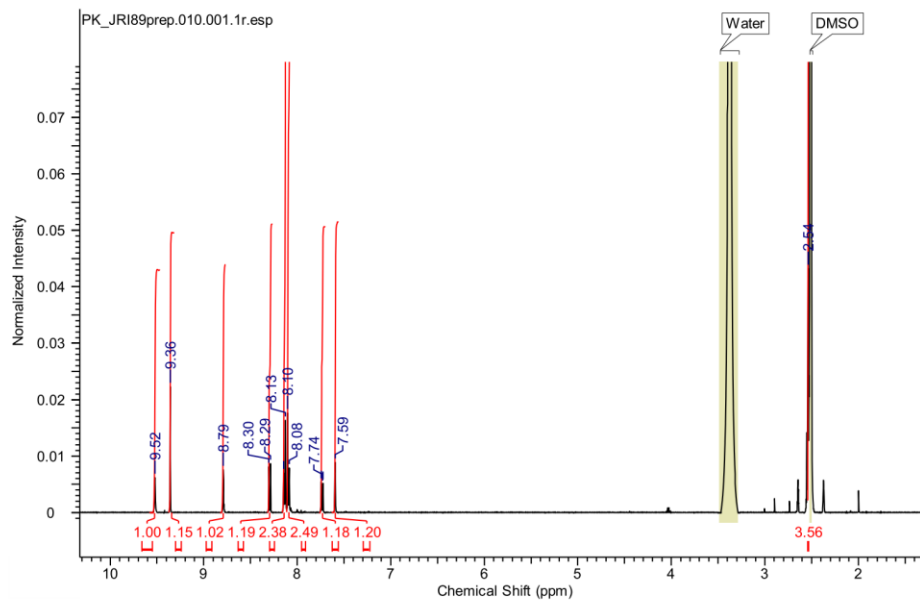
4-(1-(isoquinolin-4-yl)-1H-1,2,3-triazol-4-yl)benzoic acid (43):

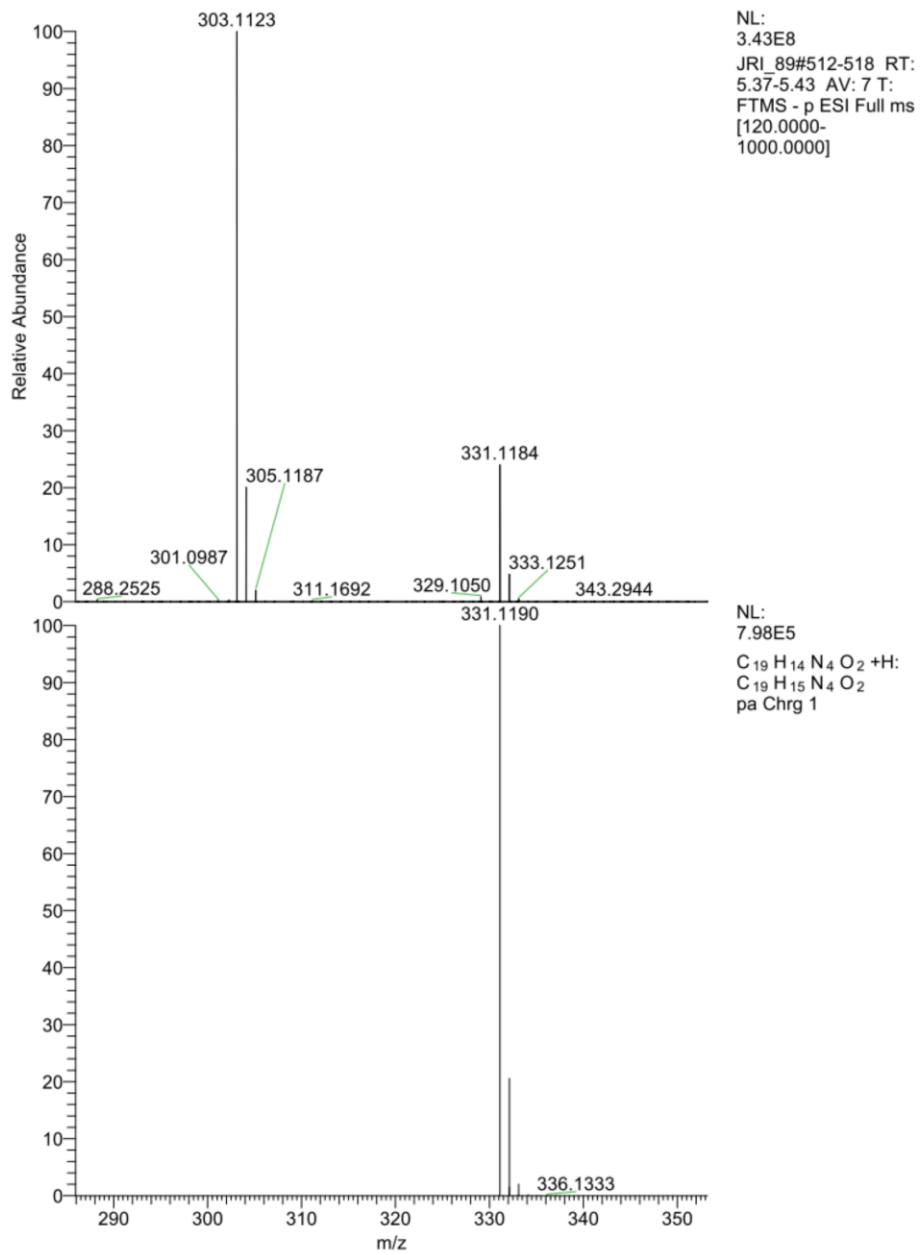


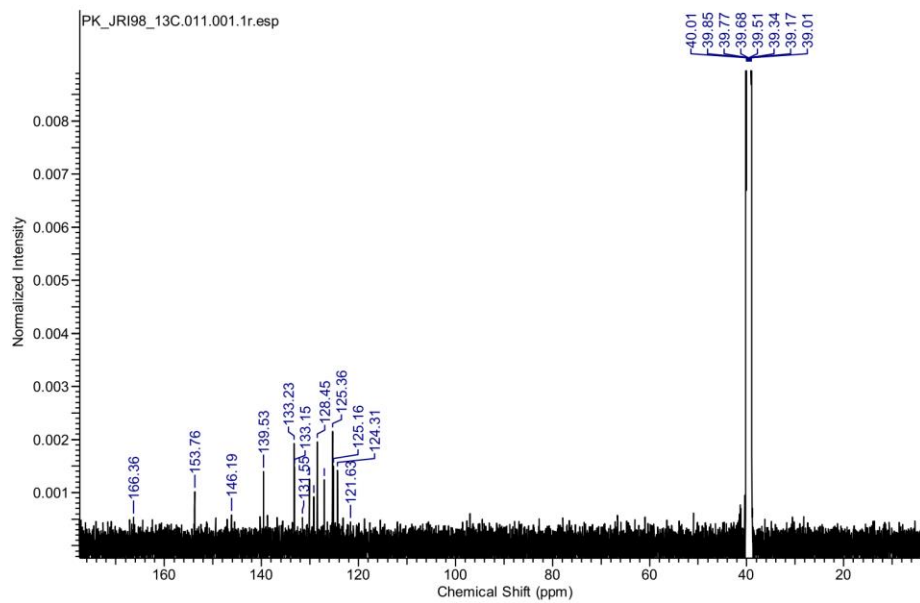
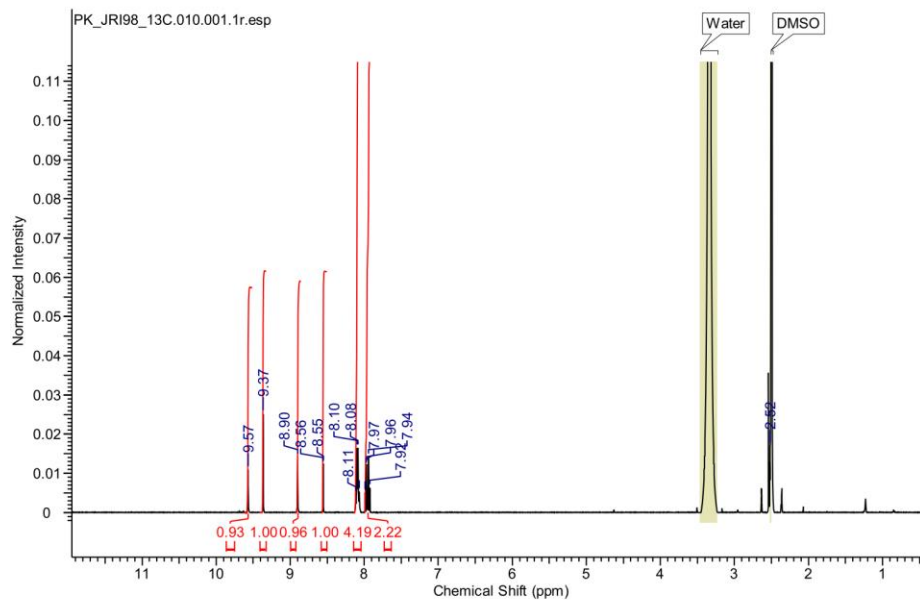
4-(1-(quinolin-3-yl)-1H-1,2,3-triazol-4-yl)benzoic acid (46):

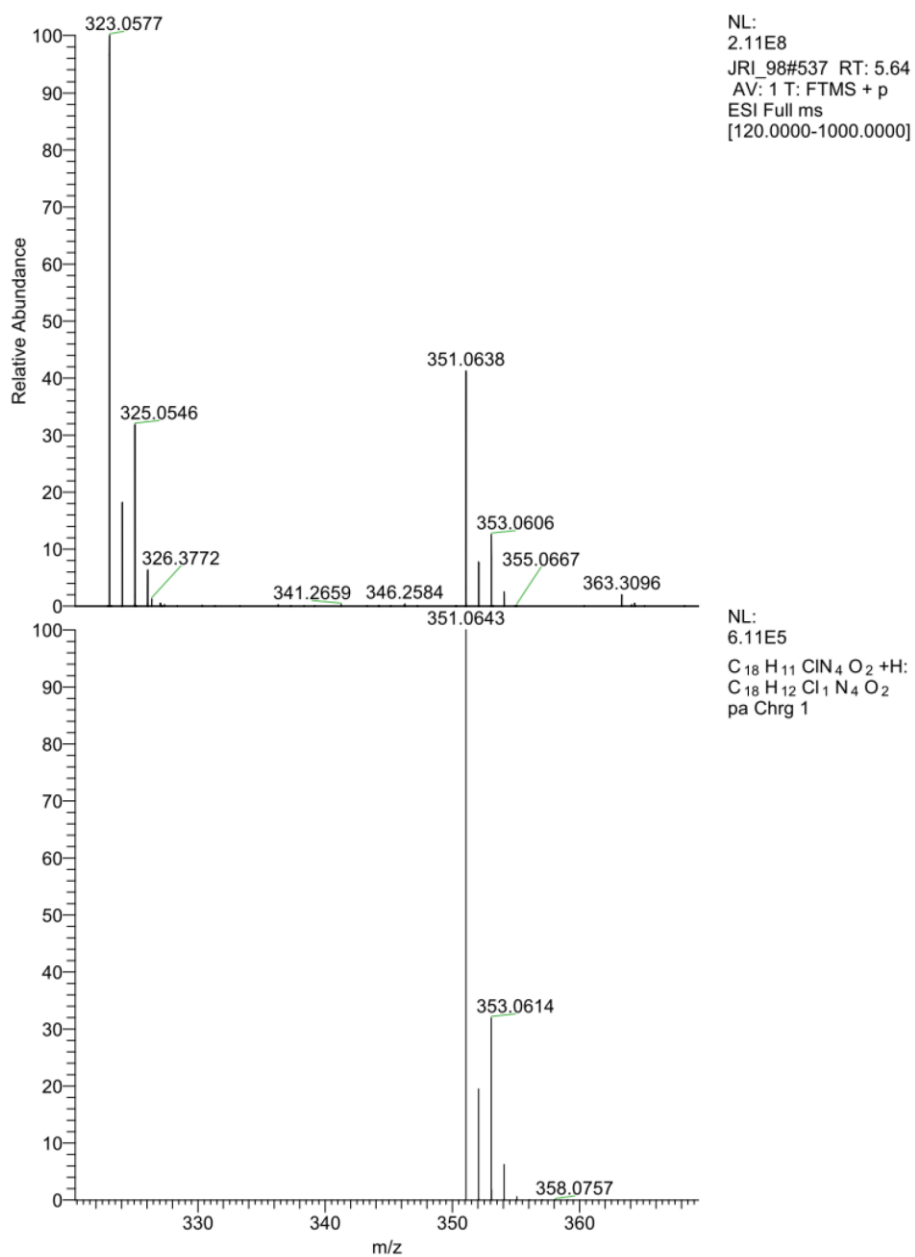


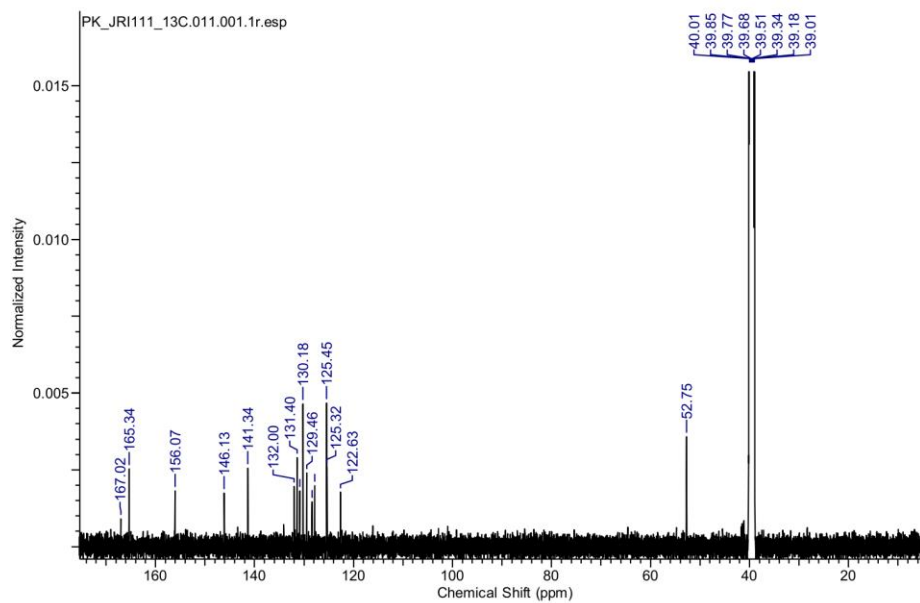
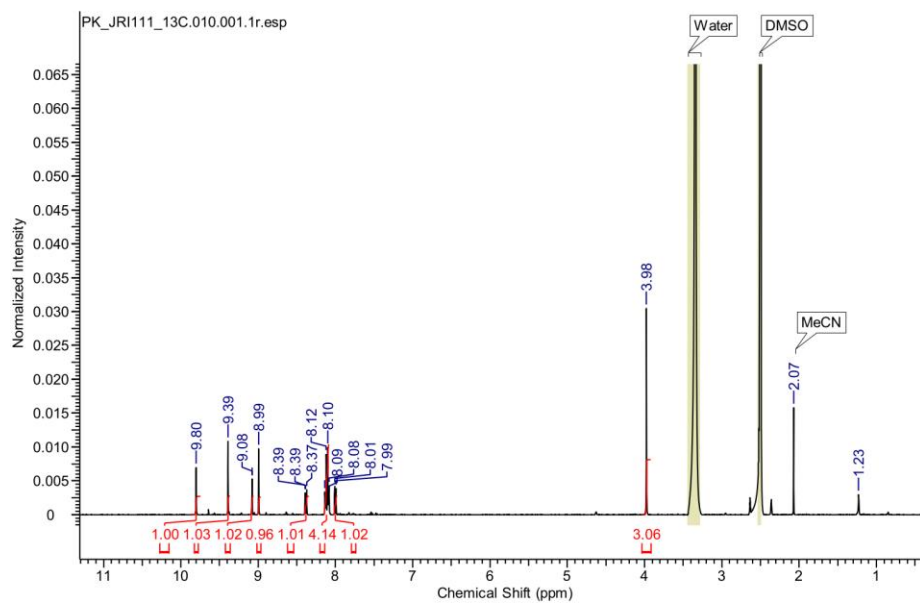


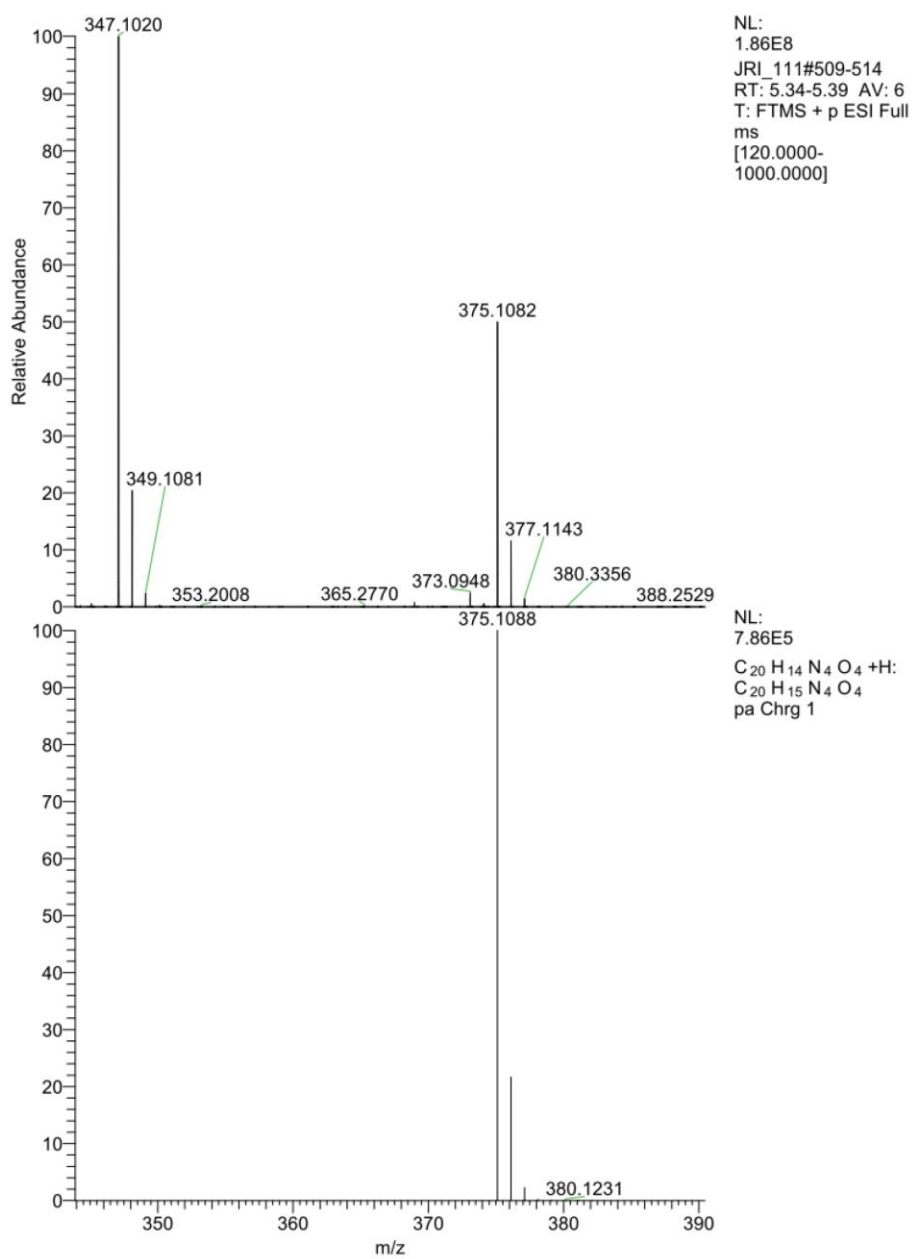
4-(1-(6-methylisoquinolin-4-yl)-1H-1,2,3-triazol-4-yl)benzoic acid (50a):



4-(1-(7-chloroquinolin-4-yl)-1H-1,2,3-triazol-4-yl)benzoic acid (50b):



4-(1-(7-(methoxycarbonyl)isoquinolin-4-yl)-1H-1,2,3-triazol-4-yl)benzoic acid (50c):



2 References

1. Kirsch, P.; Jakob, V.; Oberhausen, K.; Stein, S.C.; Cucarro, I.; Schulz, T.F.; Empting, M. Fragment-Based Discovery of a Qualified Hit Targeting the Latency-Associated Nuclear Antigen of the Oncogenic Kaposi's Sarcoma-Associated Herpesvirus/Human Herpesvirus 8. *J. Med. Chem.* **2019**, *62*, 3924–3939, doi:10.1021/acs.jmedchem.8b01827.